



UNIVERSITY OF  
**LIVERPOOL**

**Synthesis of Novel Polyester-Based  
Nanomedicines for Colorectal Cancer Drug  
Encapsulation.**

Thesis submitted in accordance with the requirements of the University of  
Liverpool for the degree of Doctor in Philosophy by:

**Sarah Louise Blackmore**

August 2020

## Acknowledgements

Firstly, I would like to thank my supervisor, Prof. Steve Rannard, for the opportunity to pursue my PhD project along with undergraduate projects over the last six years. His guidance and support have enabled me to gain more confidence in my abilities and the work I carry out.

I would also like to thank the whole of the Rannard Group, every individual has brought a positivity to my time within the team over the course of my studies, each in a unique way. In particular, I would like to thank Dr Pierre Chambon for his help and insight throughout all my projects, he has been instrumental to the development of my knowledge and skills within this field. I would also like to extend my gratitude to Dr Andrew Dwyer and Dr Sean Flynn for their advice throughout my PhD and Dr Faye Hern and Anika Shakil who I have always been able to turn to. To Claire Armstrong, I am grateful we got to share our PhD journeys together. I would also like to thank Usman Arshad for carrying out the pharmacological assessments of the material produced. My thanks also to Dr Marianne Ashford and Dr Kevin Treacher, both of whom aided in the discussion of this work and provided me with the opportunity to present my research and analyse materials *via* TASC analysis at AstraZeneca, Alderley Park.

I am immensely grateful to my family and friends for all of their support, there are not enough words to describe how much I value each one of you.

I am grateful to my partner, Connor, for his love and encouragement over the last 2 years; your confidence in me has helped me enormously. Even on the toughest days, I have always been able to count on you to find a way to spur me on, make me laugh and put a smile on my face. My sister, Charlotte, thank you for always being there no matter what, not only over the past four years but throughout my life sharing in the most exciting and hardest times. Your knowledge and insight have been invaluable in finalising my work. Thank you to my Dad for all the life lessons he has taught me and for the love and guidance that he has given me throughout my life to help shape me into the person I am today. Your enthusiasm and interest in my work has pushed me to always strive to be my best. I am also grateful to Janine for helping me on the path to pursue Chemistry at the University of Liverpool; the courage you gave me has helped develop my outlook on the things that I can achieve.

Finally, I dedicate my thesis to my Mum, whose drive and determination was ever inspiring; although you may not have been here to see me progress through university I know you have been with me every step of the way.

## Abstract

Drug encapsulation within nanocarriers provides a solution to the poor bioavailability and off-site toxicities seen for poorly water soluble active agents. Nanocarriers formulated from biodegradable, biocompatible polyesters such as PLA and PCL are capable of being cleared from the body whilst functionalisation of the monomer species offers pathways for the tuning of polymer physicochemical properties to aid drug encapsulation. Here the application of substituted caprolactone monomers in MSA catalysed ROP produced a range of  $\epsilon$ -CL-based polyesters of varying architecture with the ultimate goal of creating a range polymeric nanoparticles capable of encapsulating active metabolite 7-ethyl-10-hydroxycamptothecin, SN-38.

Baeyer Villiger oxidation allowed the synthesis of 4 new  $\epsilon$ -CL based monomers with increasing alkyl side chain lengths plus the additional bis-lactone monomer, 4,4'-bioxepanyl-7,7'-dione, *BOD*. Henceforth capabilities of MSA-catalysed ROP in the construction of a variety of polymer architectures was explored avoiding traditional SnOct<sub>2</sub> and mitigating the risk of residual metal in polymers bound for pharmacological use. PEG<sub>2/5K</sub>-OH macroinitiators were synthesised to complete the library of polymers taken forward for (co)nanoprecipitation studies. PCL polymers were initially used for more in depth studies producing stable aqueous nanoparticle dispersions with hydrodynamic diameters > 110 nm. Co-nanoprecipitation with amphiphilic PEG-*b*-PCL<sub>40</sub> polymers showed a reduction in zeta potential with increasing PEG-*b*-PCL<sub>40</sub> content with both M<sub>n</sub> for the hydrophilic PEG blocks. In view of these preliminary results, the full library of polymers were investigated and comparable nanoparticle characteristics such as size, PDI and zeta potential were achieved. Encapsulation ability of these systems was assessed with the introduction of guest molecules, such as oil red, docetaxel and SN-38 pentanoate, successfully producing stable nanoparticle dispersions at 2.43 wt% drug loading.

Conversely failure to yield SN-38 encapsulating nanoparticles *via* co-nanoprecipitation led to the employment of thin film hydration. This allowed drug loadings from 2.43 wt% to 95 wt% to be achieved with increasing particle size of 45 to 240 nm. Supplementary studies allowed the characterisation of both the thin films and resulting dispersions as well as the determination of stability both in dry and hydrated states. Finally, preliminary pharmacological analysis, *in vitro* gave an important comparison to free SN-38 highlighting retardation of release and reduced macrophage uptake that had been gained by encapsulating the active compound.

# Contents

## CHAPTER 1 – Introduction

<b>1.1 Colorectal cancer</b> .....	2
<b>1.2 Conventional chemotherapy</b> .....	4
<b>1.3 Nano-medical interventions</b> .....	7
1.3.1 Passive targeting.....	10
1.3.2 Active targeting .....	12
1.3.3 Nanostructures.....	15
<b>1.4 Homo- and co-polyesters</b> .....	24
<b>1.5 Functionalised monomers and polymers</b> .....	30
<b>1.6 Aims of the project</b> .....	36
<b>References</b> .....	39

## CHAPTER 2 – Synthesis and characterisation of caprolactone derived polyesters *via* acid catalysed ring opening polymerisation

<b>2.1 Introduction</b> .....	50
2.1.1 Ring opening polymerisation, <i>ROP</i> .....	50
2.1.2 Variation in polymer composition and architecture .....	55
2.1.2.1 Variation of polymer composition – co-polymerisation of polyesters .....	55
2.1.2.2 Variation of polymer architecture – branching of polyesters <i>via</i> ROP .....	58
2.1.3 Chapter aims.....	66
<b>2.2 Synthesis of substituted caprolactone monomers <i>via</i> Baeyer-Villiger oxidation</b> .....	67
<b>2.3 MSA catalysed ROP of <math>\epsilon</math>-caprolactone</b> .....	77
2.3.1 Linear polymerisation of $\epsilon$ -caprolactone <i>via</i> MSA catalysed ROP .....	77
2.3.1.1 Benzyl alcohol initiated, MSA catalysed ROP of $\epsilon$ -caprolactone .....	77
2.3.1.2 Poly(ethylene glycol) <sub>2K/5K</sub> initiated MSA catalysed ROP of $\epsilon$ -caprolactone .....	81
2.3.2 Mechanistic studies of linear polymerisation of $\epsilon$ -caprolactone <i>via</i> MSA catalysed ROP .....	84
2.3.2.1 Kinetic studies of linear MSA catalysed ROP of $\epsilon$ -caprolactone initiated by benzyl alcohol.....	84
2.3.2.2 Assessment of opportunistic side reactions present in linear MSA catalysed ROP of $\epsilon$ -caprolactone.....	93
2.3.2.3 Analysis of the potential transesterification during linear MSA catalysed ROP of $\epsilon$ -caprolactone initiated by benzyl alcohol .....	100
2.3.2.4 Overall outlook from mechanistic studies .....	104



2.3.3 Statistical co-polymerisation of $\epsilon$ -caprolactone and BOD <i>via</i> MSA catalysed ROP to achieve branched architecture .....	105
2.3.3.1 Benzyl alcohol initiated statistical co-polymerisation of $\epsilon$ -caprolactone and BOD <i>via</i> MSA catalysed ROP .....	106
2.3.3.1.1 Kinetic studies of the statistical co-polymerisation of $\epsilon$ -CL and BOD <i>via</i> MSA catalysed ROP .....	113
2.3.3.2 Poly(ethylene glycol) <sub>5K</sub> initiated, MSA catalysed ROP of $\epsilon$ -caprolactone and BOD .....	115
<b>2.4 MSA catalysed ROP of substituted caprolactone monomers .....</b>	<b>118</b>
2.4.1 MSA catalysed ROP of substituted caprolactone monomers to achieve linear architecture .....	119
2.4.1.1 Benzyl alcohol initiated, MSA catalysed ROP of substituted caprolactone monomers .....	119
2.4.1.2 Poly(ethylene glycol) <sub>5K</sub> initiated, MSA catalysed ROP of substituted caprolactone monomers .....	120
2.4.2 Statistical co-polymerisation of substituted caprolactone monomers and BOD <i>via</i> MSA catalysed ROP to achieve branched architecture.....	123
2.4.2.1 Benzyl alcohol initiated, MSA catalysed ROP of substituted caprolactone monomers .....	123
2.4.2.2 Poly(ethylene glycol) <sub>5K</sub> initiated, MSA catalysed ROP of substituted caprolactone monomers and BOD .....	125
<b>2.5 Differential scanning calorimetry, DSC .....</b>	<b>127</b>
<b>2.6 Conclusions .....</b>	<b>131</b>
<b>References .....</b>	<b>133</b>

## **CHAPTER 3 – Nanoparticle formation *via* nanoprecipitation and co-nanoprecipitation**

<b>3.1 Introduction.....</b>	<b>139</b>
3.1.1 Nanoparticle preparation <i>via</i> nanoprecipitation .....	139
3.1.1.1 Principles of small molecule nanoparticles prepared <i>via</i> nanoprecipitation .....	140
3.1.1.2 Principles of polymeric nanoparticles prepared <i>via</i> nanoprecipitation.....	142
3.1.2 Nanoparticle preparation <i>via</i> co-nanoprecipitation .....	145
3.1.3 Chapter aims.....	146
<b>3.2 (Co)-Nanoprecipitation studies with poly(<math>\epsilon</math>-caprolactone) based polymers.....</b>	<b>147</b>
3.2.1 (Co)-Nanoprecipitation studies using an acetone good solvent phase .....	147
3.2.1.1 Salt stability studies .....	155
3.2.2 (Co)-Nanoprecipitation studies of PCL polymers using a THF good solvent phase .....	158

3.2.2.1 Salt stability studies .....	165
<b>3.3 (Co)-nanoprecipitation utilising PSCM<sub>40</sub>-co-BOD<sub>0.7</sub>.....</b>	<b>169</b>
3.3.1 PEG- <i>b</i> -PCL <sub>40</sub> stabilised PSCM <sub>40</sub> -co-BOD <sub>0.7</sub> nanoparticles <i>via</i> co-nanoprecipitation .....	170
3.3.2 PEG- <i>b</i> -PSCM <sub>40</sub> stabilised PSCM <sub>40</sub> -co-BOD <sub>0.7</sub> nanoparticles <i>via</i> (co)-nanoprecipitation .....	174
<b>3.4 Model encapsulation <i>via</i> co-nanoprecipitation.....</b>	<b>178</b>
3.4.1 Encapsulation of Oil red O <i>via</i> co-nanoprecipitation .....	179
3.4.2 Encapsulation of docetaxel <i>via</i> co-nanoprecipitation.....	182
<b>3.5 Conclusions .....</b>	<b>184</b>
<b>References .....</b>	<b>186</b>

## **CHAPTER 4 – SN-38 encapsulation and pharmacological assessment**

<b>4.1 Introduction.....</b>	<b>190</b>
4.1.1 Chapter aims.....	191
<b>4.2 Encapsulation of SN-38-based drug molecules <i>via</i> co-nanoprecipitation.....</b>	<b>191</b>
4.2.1 Encapsulation of SN-38 penanoate, SN-38 P, <i>via</i> co-nanoprecipitation.....	192
4.2.2 Encapsulation of SN-38 <i>via</i> co-nanoprecipitation.....	197
4.2.2.1 Dilution studies of co-nanoprecipitation with guest molecules.....	198
<b>4.3 Evaluation of nanoparticle formation <i>via</i> a thin film hydration method using novel polyesters .....</b>	<b>206</b>
4.3.1 Thin film co-hydration using multiple polymeric species .....	207
4.3.2 Thin film hydration using single polymeric species .....	217
4.3.2.1 Thin film hydration of branched amphiphilic PEG <sub>5K</sub> /polyester block co-polymers .....	217
4.3.2.2 Stability of nanoparticles created <i>via</i> thin film hydration of an amphiphilic branched polyester co-polymer and SN-38 .....	226
4.3.2.2.1 Stability of dry thin films formed during the thin film hydration process ...	226
4.3.2.2.2 Stability of aqueous dispersions formed from thin film hydration .....	230
4.3.2.3 Thin film hydration comparison using linear amphiphilic PEG <sub>5K</sub> /polyester block co-polymers .....	234
4.3.3 Mechanistic studies of the thin film hydration method using an amphiphilic branched co-polymers and SN-38.....	236
4.3.3.1 SEM studies of the thin film hydration method using amphiphilic branched polyester co-polymers.....	237
4.3.3.1.1 SEM study of dry thin films formed before thin film hydration of PEG <sub>5K</sub> -PMOP <sub>40</sub> -BOD <sub>0.7</sub> and SN-38.....	237

4.3.3.1.2 SEM study of filtered thin film dispersions formed <i>via</i> thin film hydration of PEG <sub>5K</sub> -PCL <sub>40</sub> -BOD <sub>0.7</sub> and SN-38 .....	241
4.3.3.2 DSC of thin films formed before thin film hydration using PEG <sub>5K</sub> -b-PCL <sub>40</sub> -co-BOD <sub>0.7</sub> and SN-38 .....	254
4.3.3.3 TASC of thin films formed before thin film hydration using PEG <sub>5K</sub> -b-PCL <sub>40</sub> -co-BOD <sub>0.7</sub> and SN-38 .....	259
<b>4.4 Pharmacological studies of SN-38 containing dispersions produced <i>via</i> thin film hydration of branched PEG<sub>5K</sub>/polyester co-polymers .....</b>	<b>266</b>
4.4.1 Release rate studies .....	266
4.4.2 Cytotoxicity .....	271
4.4.3 Macrophage uptake .....	273
4.4.4 <i>In vivo</i> studies .....	274
<b>4.5 Conclusions .....</b>	<b>275</b>
<b>References .....</b>	<b>276</b>
<b>CHAPTER 5 – Conclusions and future work</b>	
<b>5.1 Conclusions.....</b>	<b>279</b>
<b>5.2 Future work.....</b>	<b>282</b>
5.2.1 Polymer synthesis.....	282
5.2.2 Nanoparticle formation and encapsulation <i>via</i> co-nanoprecipitation.....	283
5.2.3 Nanoparticle formation and encapsulation <i>via</i> thin film hydration.....	284
5.2.4 Pharmacological assessment .....	284
<b>References .....</b>	<b>286</b>
<b>CHAPTER 6 – Experimental procedures</b>	
<b>6.1 Materials .....</b>	<b>288</b>
<b>6.2 Instrumentation and characterisation .....</b>	<b>288</b>
6.2.1 Instrumentation.....	288
6.2.2 Summary of characterisation.....	289
<b>6.3 Methods for Chapter 2 – Polymer synthesis.....</b>	<b>290</b>
<b>6.4 Methods for Chapter 3 – Particle formation.....</b>	<b>296</b>
<b>6.5 Methods for Chapter 4 – Encapsulation of active drug molecules .....</b>	<b>298</b>
<b>References .....</b>	<b>306</b>
<b>APPENDIX.....</b>	<b>307</b>

## List of Abbreviations

<b><math>\delta</math>-VL</b>	$\delta$ -valerolactone
<b>5-FU</b>	Fluorouracil
<b>ATRP</b>	Atom transfer radical polymerisation
<b>bis-MPA</b>	2-bis(methylol)propionic acid
<b>BOD</b>	4,4'-bioxepanyl-7,7'-dione
<b>BOP</b>	5-( <i>tert</i> -butyl)oxepan-2-one
<b>BzA</b>	Benzyl alcohol
<b>CDCl<sub>3</sub></b>	Deuterated chloroform
<b>CES</b>	Carboxylesterase
<b>CHCl<sub>3</sub></b>	Chloroform
<b>CMC</b>	Critical micelle concentration
<b>CRC</b>	Colorectal cancer
<b>CT 26</b>	Murine colorectal cancer cell line
<b>D</b>	Dispersity
<b>DBU</b>	1,8-diazabicyclo[5.4.0]undec-7-ene
<b>DCM</b>	Dichloromethane
<b>DCR</b>	Derived count rate
<b>DIPEA</b>	<i>N,N</i> -diisopropylethylamine
<b>DLCA</b>	Diffusion limited cluster-cluster aggregation
<b>DLD-1</b>	Dukes' type C colorectal adenocarcinoma cell line
<b>DLS</b>	Dynamic light scattering
<b>DMAP</b>	4-(dimethylamino)pyridine
<b>DMF</b>	Dimethylformamide
<b>DNA</b>	Deoxyribonucleic acid
<b>DP<sub>i</sub></b>	Degree of polymerisation associated with the initiator
<b>DP<sub>n</sub></b>	Number average degree of polymerisation
<b>DP<sub>OH</sub></b>	Degree of polymerisation associated with the hydroxyl chain end
<b>DPP</b>	Diphenyl phosphate
<b>DP<sub>SEC</sub></b>	Degree of polymerisation from size exclusion chromatography
<b>DSC</b>	Differential scanning calorimetry
<b>DVLO</b>	Derjaguin-Landau-Verwey-Overbeek

<b>D<sub>z</sub></b>	Z-average diameter
<b>EGFR</b>	Epidermal Growth Factor Receptor
<b>EPR</b>	Enhanced permeation and retention
<b>FDA</b>	US Food and drug administration
<b>FOLFIRI</b>	US chemotherapy regimen of fluorouracil, leucovorin and irinotecan
<b>FOLFOX</b>	UK chemotherapy regimen of fluorouracil, leucovorin and oxaliplatin
<b>FR</b>	Folate receptor
<b>G4</b>	Generation four
<b>GUV</b>	Giant unilamellar vesicles
<b>HCT 116</b>	Human colorectal cancer cell line
<b>HER 2</b>	Human growth factor receptor 2
<b>IC<sub>50</sub></b>	Half maximal inhibitory concentration
<b>LiBr</b>	Lithium bromide
<b>LoVo</b>	Human colorectal adenocarcinoma cell line
<b>LUV</b>	Large unilamellar vesicles
<b>LV</b>	Leucovorin
<b>MLV</b>	Multilamellar vesicles
<b>M<sub>n</sub></b>	Number average molecular weight
<b>MOP</b>	5-methyloxepan-2-one
<b>MPS</b>	Mononuclear phagocyte system
<b>MRI</b>	Magnetic resonance imaging
<b>MS</b>	Mass spectrometry
<b>MSA</b>	Methanesulfonic acid
<b>M<sub>w</sub></b>	Weight average molecular weight
<b>NaCl<sub>(aq.)</sub></b>	Sodium chloride solution
<b>NHC</b>	<i>N</i> -heterocyclic carbene
<b>NMR</b>	Nuclear magnetic resonance
<b>PAMAM</b>	Poly(amidoamine)
<b>PBS</b>	Phosphate-saline buffer
<b>PCL</b>	Poly( $\epsilon$ -caprolactone)
<b>PdI</b>	Polydispersity index
<b>PEG</b>	Poly(ethylene glycol)
<b>PGA</b>	Poly(glycolide)

<b>PHLOP</b>	5-phenyloxepan-2-one
<b>pHPMA</b>	Poly(2-hydroxypropyl methacrylate)
<b>PLA</b>	Poly(lactide)
<b>PLGA</b>	Poly(lactide- <i>co</i> -glycolide)
<b>PMMA</b>	Poly(methyl methacrylate)
<b>POP</b>	5-propyloxepan-2-one
<b>PTFE</b>	Poly(tetrafluoroethylene)
<b>PVA</b>	Poly(vinyl alcohol)
<b>PVP</b>	Poly( <i>N</i> -vinyl pyrrolidone)
<b>RAFT</b>	Reverse addition-fragmentation chain-transfer polymerisation
<b>RED</b>	Rapid equilibrium dialysis
<b>RES</b>	Reticuloendothelial system
<b>RI</b>	Refractive index
<b>RLCA</b>	Reaction limited cluster-cluster aggregation
<b>ROMBP</b>	Ring opening multi-branching polymerisation
<b>ROP</b>	Ring opening polymerisation
<b>SAA</b>	Salicylic acid
<b>SCM</b>	Substituted caprolactone monomer
<b>SCROP</b>	Self-condensing ring opening polymerisation
<b>SCVP</b>	Self-condensing vinyl polymerisation
<b>SDN</b>	Solid drug nanoparticle
<b>SEC</b>	Triple detection size exclusion chromatography
<b>SEM</b>	Scanning electron microscopy
<b>Sn(Oct)<sub>2</sub></b>	Tin (II) octanoate
<b>SN-38</b>	7-ethyl-10-hydroxycamptothecin
<b>SN-38 P</b>	7-ethyl-10-hydroxycamptothecin pentanoate
<b>SN-38G</b>	7-ethyl-10-hydroxycamptothecin glucuronide
<b>SPIONS</b>	Superparamagnetic iron oxide nanoparticles
<b>SPR</b>	Surface plasmon resonance
<b>SUV</b>	Small unilamellar vesicles
<b>TASC</b>	Thermal analysis by structural characterisation
<b>TBD</b>	Triazabicyclodecene
<b>TEA</b>	Triethylamine

<b>TfOH</b>	Trifluoromethanesulfonic acid or 'triflic acid'
<b>TfR</b>	Transferrin receptor
<b>T<sub>g</sub></b>	Glass transition temperature
<b>THF</b>	Tetrahydrofuran
<b>TLC</b>	Thin layer chromatography
<b>T<sub>m</sub></b>	Melting point
<b>TOP 1</b>	Topoisomerase I
<b>UHP</b>	Urea hydrogen peroxide
<b>ε-CL</b>	ε-caprolactone

# **CHAPTER 1**

## **INTRODUCTION**



## 1.1 Colorectal cancer

Cancer, derived from the Greek word *karkinos*, describes the growth of many abnormal cells within the body resulting from disruption of their normal growth mechanism.<sup>1,2</sup> This disruption occurs as a consequence of gene mutations, as cells divide during mitosis, or by deoxyribonucleic acid, *DNA*, damage from environmental factors. This leads to unregulated cell proliferation as the cells fail to respond to signals for both proliferation and apoptosis, resulting in a number of regulatory cell mechanisms being affected, and giving cancer cells different characteristics to those of normal cells.<sup>3</sup> However uncontrolled cell growth can lead to both benign and malignant tumours of which only malignant tumours are commonly referred to as cancer. Benign tumours are non-invasive, remaining isolated to the location they formed in and are often susceptible to treatment by surgical intervention.<sup>3</sup> On the other hand, malignancy describes the capability of a tumour to spread and invade a number of tissues throughout the body *via* the circulatory and lymphatic systems; a process known as metastasis.<sup>4</sup> This characteristic of cancers develops through a series of multiple mutations, which can accumulate over a number of years, making many cancers more prolific in the aging population.<sup>3</sup>

The term colorectal cancer, *CRC*, refers to malignant tumours found in the early and/or late part of the bowel, colon (*'colo'*) and/or the rectum (*'rectal'*) respectively, and is often referred to as bowel cancer. Worldwide it is the third most common cancer after lung and breast cancer, estimated to account for 10.2 % of the 18.1 million new cases of cancer worldwide in 2018 for both sexes.<sup>5</sup> It is also estimated to be the second leading form of cancer mortality with 9.2 % of all 9.6 million cancer-related death cases (both sexes) in 2018 being attributed to *CRC*.<sup>5</sup> These statistics are only set to increase with the *CRC* global burden predicted to increase by 60 % by 2030, estimating 2.2 million new cases and 1.1 million deaths.<sup>6</sup> The incidence and mortality rates of *CRC* are vastly affected by the socioeconomic status of various countries, with first world countries exhibiting higher incidence rates due to dietary and obesity factors; even so the mortality rates within these countries are also lower due to more advanced screening and treatment processes.<sup>6</sup>

Although many developed countries have long standing screening processes to diagnose *CRC*, up to 25 % of patients have metastases at the time of diagnosis which in turn diminishes the prognosis for the patient in question.<sup>7-9</sup> 2.1 % of these patients have lung metastases, however the most common site for *CRC* metastasis is the liver due to the hepatic portal venous system being responsible for the majority of intestinal drainage.<sup>10</sup> Primary tumours are most commonly

treated with surgery and resection of the tumour, incurring a loss of part of the colon to prevent reoccurrence, additional chemotherapy and/or radiotherapy has been used to improve success rates.<sup>9,11,12</sup> In contrast secondary tumours in metastasis sites are commonly more difficult to treat, with a 5 year survival rate being predicted for ~50 % of patients.<sup>13</sup> Survival rates for hepatic metastasis are predicted by the operability of the tumour but only ~10-30 % of patients can undergo tumour resection.<sup>13</sup> The prognosis for the other 70- 90 % of patients is bleak; if the tumour has developed in an inoperable location patients must first undergo systemic chemo- and/or radiotherapy. This is to hopefully decrease the tumour to a size where resection is safe to perform and achieve complete/partial remission,\* however 70 % of these patients will typically develop reoccurrence.<sup>14</sup> If this is unsuccessful, the last resort for these patients is palliative chemotherapy and care which aims to maintain an acceptable quality of life for the patient for the remainder of their lifetime (Figure 1.1).

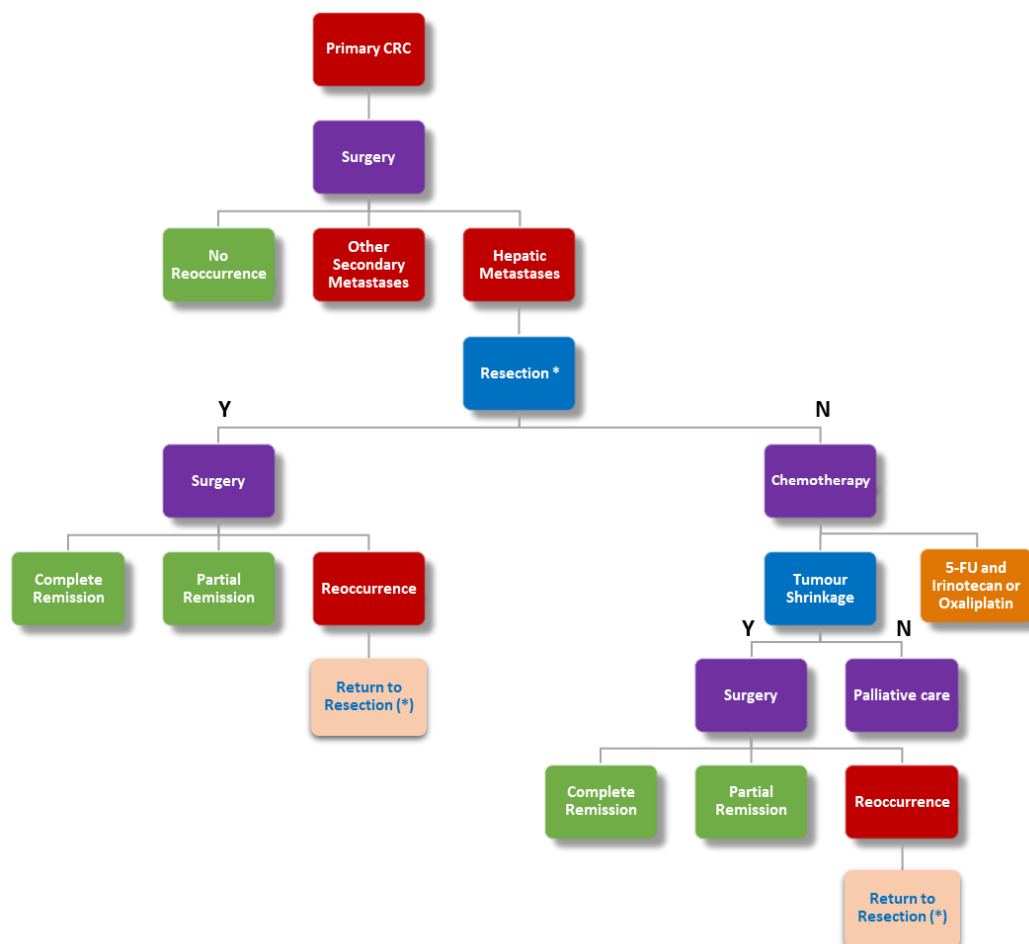


**Figure 1.1 – Flow chart showing the treatment process for CRC and liver metastases.**

\* A term used to describe the decrease in growth of an active tumour. Complete remission refers to the disappearance of all signs and symptoms of the cancer although reoccurrence is still possible.<sup>199</sup> Partial remission refers to the decrease in signs or symptoms of the cancer.<sup>200</sup>

Consequently research to advance and improve chemotherapy treatments has been a major topic at the forefront of cancer research. The increased effectiveness of these types of treatments could increase the number of patients that either achieve complete remission or are able to undergo resection and extend the life expectancy for CRC sufferers. In addition, with the consideration of currently available treatments, the improvement of chemotherapy regimens has potential to improve patient wellbeing and quality of life whilst undergoing such treatments.

## 1.2 Conventional chemotherapy

Systemic chemotherapy is broadly used across all stages of CRC tumour development, often being used in combination with surgical interventions, and most commonly involves the anti-metabolites fluorouracil, *5-FU* and leucovorin, *LV*.<sup>14,15</sup> These agents are often used in combination with other anti-cancer drugs, either irinotecan (US regimen FOLFIRI) or oxaliplatin (UK regimen FOLFOX).<sup>16–18</sup> Nonetheless both irinotecan and oxaliplatin are linked to inimical side effects specific to the liver, for example diarrhoea and leukopenia, which severely impair the level of safe dose of these compounds.<sup>19,20</sup> Although both of these anti-cancer drugs have disadvantages that require additional research and improvement, our research will focus on irinotecan and its active metabolite, 7-ethyl-10-hydroxycamptothecin, *SN-38*, in particular.

The camptothecin derivative irinotecan is a water soluble pro-drug that, when converted into its active metabolite, poorly water soluble *SN-38*, acts as a Topoisomerase I, *TOP 1*, inhibitor<sup>†</sup>. *SN-38* is of the most potent *TOP 1* inhibitors (100-1000 x more potent than irinotecan), and is classed as a *TOP 1* poison due to its mechanism of action.<sup>21</sup> Its main mechanism of inhibition of *TOP 1* occurs by stabilising the *TOP 1* cleavage complex after DNA strand scission by hydrophobic interactions with the DNA strands and hydrogen bonding to *TOP 1* (Figure 1.2).<sup>22–24</sup> This modifies the enzymes ability to recognise cleavage sites preventing the re-ligation of *TOP 1* and results in the definition of the cleavage complex as ‘suicide’ or ‘aborted’.<sup>21,25</sup> This inhibition of DNA relaxation during the replication process leads to breaks in the DNA double strand and ultimately cell death.<sup>21,26,27</sup>

---

<sup>†</sup> Topoisomerases are universal enzymes that regulate the cleavage of the DNA backbone to release supercoils that are created during replication and transcription. This is done by cleavage of one strand of the DNA double helix followed by rotation, before re-ligation. This allows replication and transcription to continue without strands breaking from strain.<sup>21</sup>

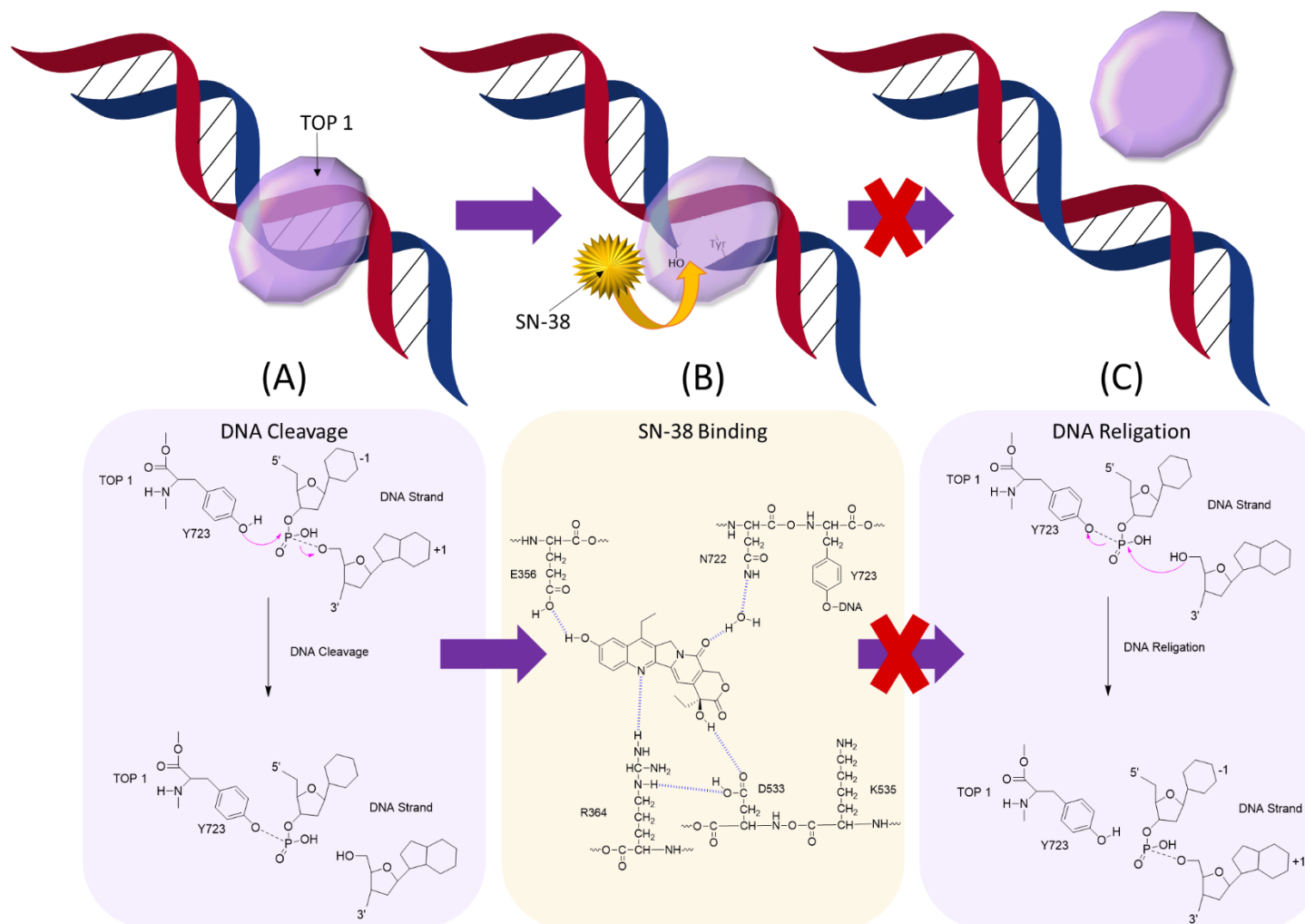


**Figure 1.2 – Scheme representing the mechanism of action of SN-38 and TOP 1.** (A) Binding of TOP 1 to a single DNA strand resulting in strand scission. (B) SN-38 binding *via* hydrogen bonding between SN-38 functional groups and TOP 1 amino acids. (C) Re-ligation of the DNA strand and release of TOP 1 which is prevented by the binding of SN-38.

Although these treatments have been common practice for treating liver CRC metastases, their effectiveness in achieving remission or preventing recurrence – as with the majority of chemotherapy regimens, regardless of cancer type - is limited by the adverse cumulative side effects from systemic chemotherapy and cancer cell mutations.<sup>10</sup> The conversion of irinotecan into the active metabolite occurs in the liver *via* carboxylesterases, *CES*, which is followed by the deactivation of SN-38 to SN-38 glucuronide, *SN-38G*,<sup>‡</sup> The SN-38G is excreted in urine and bile along with unconverted irinotecan and SN-38 (Figure 1.3) and the secretion of these compounds in bile has been shown to be a main contributor to the severe diarrhoea seen in most patients.<sup>19,28,29</sup>

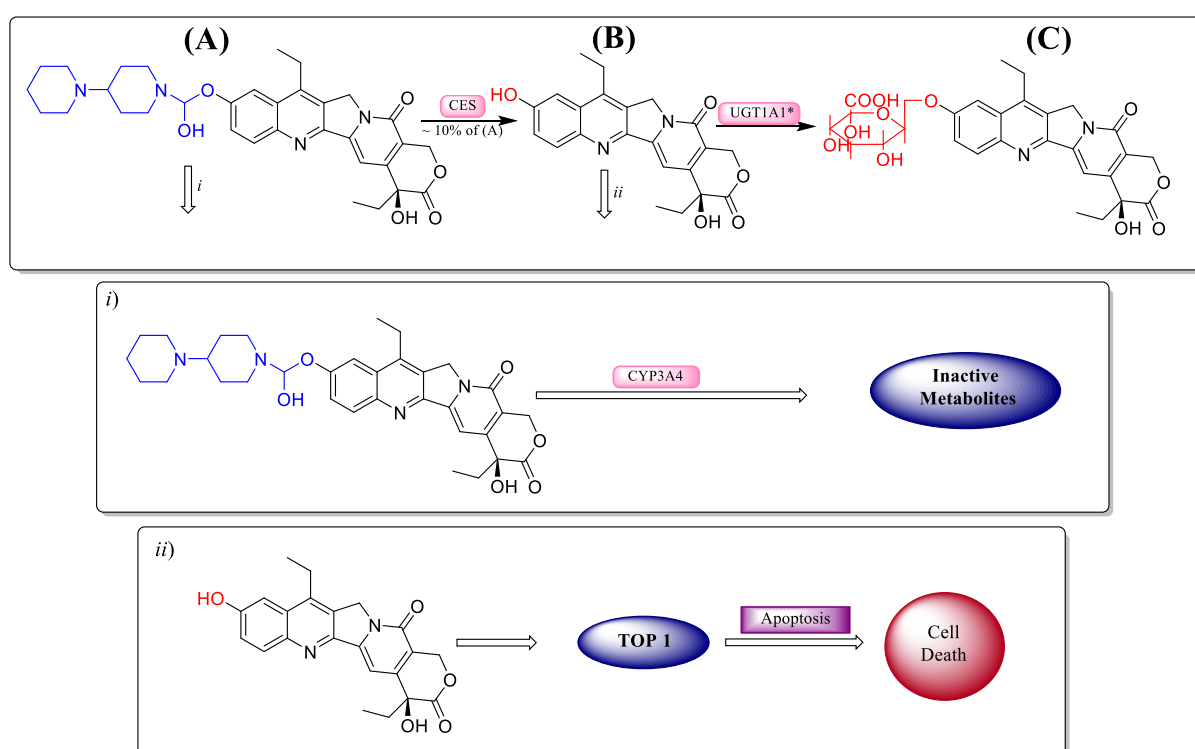


**Figure 1.3 – Scheme representing the metabolism of A (irinotecan, *pro-drug*) to B (SN-38, *active drug*) to C (SN-38-glucuronide, *inactive metabolite*).** *i*) Shows the side reaction of A to inactive metabolites *via* CYP3A4 enzyme. *ii*) Shows the side reaction of B to TOP 1 resulting in apoptosis. \*UGT1A1 is polymorphic affecting the metabolism of B.

Studies indicate that irinotecan and SN-38G can be converted back to the active SN-38 by bacterial  $\beta$ -glucuronidase as they pass through the intestines leading to increased cell apoptosis and consequentially severe colonic damage.<sup>19,29–31</sup> In turn this damage, in combination with

<sup>‡</sup> The conversion of SN-38 to SN-38G is mitigated by the polymorphic gene UGT1A1 producing UDP-glucuronosyltransferases. However mutations in this gene, specifically UGT1A1\*28 and UGT1A1\*6, can affect the secondary pathway to SN-38G contributing to the side effects of diarrhoea and neutropenia.<sup>201</sup>

increased mucus secretion and goblet cell mutation, leads to decreased absorption in the gut and therefore results in increased diarrhoea.<sup>19,28</sup> Another limitation linked to irinotecan is poor drug metabolism, with only ca. 10 % of the administered dose being converted into the active metabolite SN-38 with a significant patient-patient variability in SN-38 exposure.<sup>32</sup>

Consequently this has directed research to focus on delivery systems and interventions that tackle the problems on two fronts by mitigating side effects and increasing the drug efficacy by targeting tumour sites directly. The direct delivery of SN-38 to tumour sites, *via* systems such as nanocarriers, would avoid any patient-patient variability in dose. Additionally diminishing the presence of the active metabolite in the replication mechanisms of healthy cells would avoid triggered apoptosis of healthy cells, in turn alleviating some adverse side effects present from the current dosing regimens. Eventually the application of these delivery systems across the spectrum of all chemotherapy could prevent the unnecessary attack of healthy cells in most cases, which would contribute to a decrease in serious side effects seen with most chemotherapy treatments whilst increasing efficacy.

### **1.3 Nano-medical interventions**

Nano-medical drug delivery systems have been prevalent in research in recent decades due to the advantages they offer to many treatment and diagnostic interventions of diseases including chemotherapy, HIV and malaria treatments.<sup>33-35</sup> These systems arose from the necessity to find solutions for the direct delivery of highly toxic and/or poorly water soluble drugs to specific sites in the body, avoiding attack on healthy cells or tissues and increasing therapeutic effect. Direct delivery of the active agent using nanotechnology also facilitates increased efficacy, pharmacokinetics, lower doses and in some cases long acting formulations that are beneficial to both patients and industry.<sup>33,36-38</sup> As the field of nanotechnology expands, drug molecules can now be incorporated within a range of materials and structural forms, for example, polymer hydrogels,<sup>39</sup> solid lipid nanoparticles,<sup>40</sup> solid drug nanoparticles,<sup>35,41</sup> and inorganic nanoparticles,<sup>42,43</sup> along with the encapsulation of drug molecules within the hydrophobic domain of stable aqueously dispersed polymeric nanoparticles.<sup>44,45</sup>

These nanostructures are all of a size that is between 1-1000 nm although the exact definition of the nanoscale is disputed.<sup>46,47</sup> Their components are chosen to be biocompatible and must be able to be cleared from the body to minimise any toxicity that could arise from the carrier itself. These constituents can often be adapted to include functionality that can increase bioavailability, circulation time and stability in biological conditions.<sup>37</sup> For example, polymeric

nanoparticles often have a polyethylene glycol, *PEG*, ‘stealth’ corona that results in longer circulation times by avoiding the liver first pass metabolism and also increasing stability under biological conditions.<sup>38</sup> Biodegradability is also being introduced into some polymeric nanoparticle systems with the use of polyesters such as poly(lactide-*co*-glycolide), *PLGA*, or poly( $\epsilon$ -caprolactone), *PCL*, which can be cleared from the body *via* the Krebs cycle.<sup>48</sup> In addition, nanocarriers can be tailored to activate changes within a particular environment such as pH or chemical stimuli.<sup>49</sup> This variety in nanoparticle features, component characteristics and domains capable of carrying drug molecules has led to a vast number of nanomedicines that are either already approved and used in the clinical setting or being tested within clinical trials, showing how successful this field is developing to be (Table 1.1).

In addition to desirable properties of nanoparticle components, other advantages that are achieved by the use of nanoscale interventions can be derived from the ability to target a group of specific cells within the body. At this point nanomedical interventions can be split into two distinct groups based on their mechanism of targeting; either passive or active.<sup>50</sup> Both groups involve the exploitation of a number of biological pathways to achieve their respective targeting and often involve specific characteristics or components of the nanocarriers that are important for this purpose.

**Table 1.1-Drug delivery systems within preclinical and clinical trials as well as clinical use for cancer therapy.**

Material	Commercial Name	Description Of Carrier (Drug(s))	Passive or Active Targeting	Targets include	Outcome	Ref
<i>Liposome</i>	Doxil®	PEGylated liposome (doxorubicin)	Passive	Ovarian cancer; multiple myeloma; Kaposi's sarcoma; recurrent breast cancer	Decreased free drug toxicity; improved site specific delivery	51
	Onivyde®	Liposome (irinotecan)	Passive	Metastatic pancreatic ductal adenocarcinoma	Improved survival when administered with 5-FU and folinic acid.	52
	Thermodox®	Thermal sensitive lipid functionalised liposome (doxorubicin)	Passive	Primary liver cancer	Increased drug concentration in target tissue; decrease in adverse side effects	53
<i>Polymeric Nanoparticles</i>	Eligard®	PLGA nanoparticle (leuprolide)	Depot (N/A hormone suppressant)	Prostate cancer	More sustained release of drug overtime; decreased adverse effects	44
	CRLX101	Cyclodextrin-PEG (camptothecin)	Passive	Rectal, ovarian, tubal and peritoneal cancer	Decrease in side effects; improved site specific delivery	54
	-	Anti-EGFR functionalised PEG-PLGA (paclitaxel)	Active	Triple negative breast cancer	Increased therapeutic effect; improved site specific delivery	55
<i>Dendrimer</i>	-	Hyaluronic acid functionalised PAMAM G4 (cisplatin and doxorubicin)	Active	Breast cancer	Increased drug accumulation; increase in anticancer efficiency	56
	-	Biotin functionalised PEGylated PAMAM G4 (paclitaxil)	Active	Lung cancer	Increased cytotoxicity; inhibition of growth	57
<i>Micelle</i>	CALAA-01	Transferrin cyclodextrin micelle (siRNA)	Active	Solid organ tumours; RRM2 gene	Provides targeted delivery of functional siRNA (still to be fully assessed)	58,59
	AZD2811	Accurins; PEG-PLA	Passive	Aurora kinase B inhibitor; acute myeloid leukaemia; colorectal carcinoma	Improved site specific delivery; increased efficacy; decreased toxicity	60,61
	CriPec®	PEG-ylated poly(lactate) micelle (docetaxel)	Passive	Ovarian cancer; solid tumours	Preferential release in acidic conditions; reduction in dose limiting toxicities	62
<i>Inorganic Nanoparticles</i>	Nanotherm™	Aminosilane-coated SPION	Directly injected into the tumour	Glioblastoma	Local tissue hyperthermia – (non-) programmed cell death; increased survival by up to 12 months	43,63
	CYT-6091	Human tumour necrosis factor, rtTNF functionalised colloidal gold.	Passive	A variety of histologies	Increased maximum dose; possible preferential targeting of tumour tissue	42



### 1.3.1 Passive targeting

Passively targeting nanocarriers were the first of the two types of targeting to appear in clinical trials in the 1980s and have resulted in a number of approved products appearing on the market for clinical use. The most well-known example of this type of targeting drug vehicle is Doxil®, a liposomal doxorubicin used to target refractory Kaposi's sarcoma, ovarian cancer and recurrent breast cancers.<sup>37,51,64</sup> Doxil® is made up of doxorubicin loaded PEGylated liposomes, where the hydrophilic polymer acts as a 'stealth' surface coating which reduces the rapid clearance seen for many conventional liposomes in parallel with more effectively passive targeting of cancer cells.<sup>51</sup> Due to the clinical precedent set by Doxil® there have been a large number of liposomal formulations that have been US Food and Drug Administration, *FDA*, approved. One of the most recent of these is Onivyde® which is a liposomal irinotecan formulation for the treatment of metastatic pancreatic cancer.<sup>52</sup> Studies showed that when the nanoliposomal irinotecan was administered in combination with 5-FU and folinic acid there were significant improvements in a number of characteristics of the treatment.<sup>33,52</sup> The survival of patients was extended compared to that of traditional gemcitabine-based regimens. Moreover the efficacy and pharmacokinetics were also improved along with providing a controllable safety profiles.<sup>33,52</sup>

In addition passively targeting nanoparticles are not limited to liposomes. There are a number of other examples of nanocarriers, with a range of different structures and components that also illustrate the ability to passively target tumour cells. These nanostructures include polymeric nanoparticles and micelles such as PEGylated cyclodextrin nanoparticles and poly(ethylene glycol-*co*-lactide), *PEG-PLA*, micelles respectively.<sup>54,60</sup> Unlike liposomes, these structures are restricted to the encapsulating of hydrophobic compounds drugs within hydrophobic cores providing the prospect of the delivery of poorly water soluble drugs to target sites. For example, *PEG-PLA* micelles have allowed for the encapsulation of a number of drug molecules such as AstraZeneca drug AZD2811 and docetaxel for the treatment of leukaemia, CRC and ovarian cancers.<sup>60,62</sup> These vehicles have shown a reduction in drug related toxicities along with a number of other characteristics which reiterate the list of advantages that can be accessed by the utilisation of nanocarriers of various forms.<sup>60,62</sup>

The main mechanism that aids these drug delivery vehicles to selectively target tumour sites without any intentional targeting moiety is the enhanced permeability and retention, *EPR*, effect caused by tumour cell's biological composition (Figure 1.4).<sup>65-67</sup> As tumour cells rapidly divide and grow there is a need for oxygenated blood to be supplied to these masses which is

achieved by the angiogenesis of a new, rapidly growing, neovasculature and the engulfing of pre-existing blood vessels.<sup>67</sup> This in turn results in a number of abnormalities that set tumour vessels apart from normal blood vasculature, for example dilated saccular channels, irregular diameter and an abnormal branched pattern.<sup>67,68</sup> Included in this list of characteristics is the incomplete endothelial lining of the blood vessels causing the presence of pores between 0.1 and 3  $\mu\text{m}$  in diameter.<sup>69,70</sup> This, combined with a diminished pericyte coverage, allows nanocarriers to leak out of tumour vasculature into the tumour bed.<sup>66</sup> The accumulated nanoparticles are then retained in the tumour site due to the lack of an effective lymphatic drainage system<sup>§</sup>.<sup>65</sup>

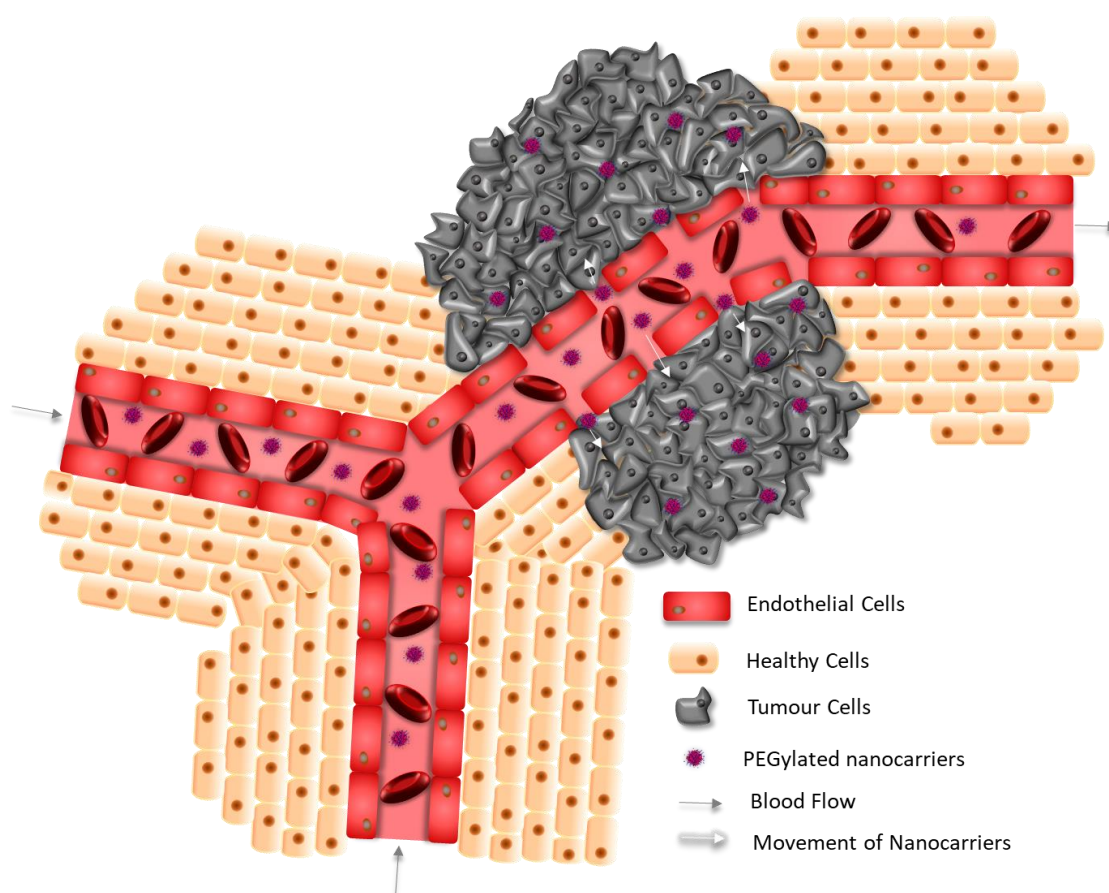


**Figure 1.4 – Schematic representation of passive tissue targeting *via* the enhanced permeation and retention, EPR, effect in a site with a limited lymphatic drainage system.<sup>71</sup>**

<sup>§</sup> The complex network of lymph nodes that facilitates the removal of unwanted material from cells grow at a slower rate than blood vessels. This results in tumours often having an extensive blood vessel network whilst lacking in normal lymphatic drainage from the cells and tissues.<sup>65</sup>

The EPR effect only provides approximately a 2-fold increase of accumulation of nanoparticles in the tumour compared to normal tissues and organs, which clear nanoparticles from circulation *via* glomerular filtration (kidneys) or the mononuclear phagocyte system, *MPS*.<sup>67</sup> Moreover there is a significant reduction in side effects as a consequence of low accumulation in healthy tissues equipped with non-leaky vasculature and a complete effective lymphatic drainage system. Therefore, exploiting the EPR effect phenomenon is key to increased efficacy, which is in turn facilitated by increasing circulation times for nanoparticles and preventing clearance through the kidneys or liver. This highlights the significance of nanocarrier physicochemical characteristics such as the size of the nanoparticles, the corona of these entities and their shape.<sup>38,65</sup> For instance, as seen with the examples Doxil® and Cripec®, passively targeting nanocarriers often have a PEGylated corona.<sup>51,62</sup> This not only offers a steric stability to particles but also prevents the binding of plasma proteins, shields the surface charge, adds hydrophilicity to the surface and induces repulsion in particle-blood component interactions.<sup>49</sup> This in turn protects the particle against opsonin interactions and reducing clearance by the reticuloendothelial system, *RES*.<sup>72</sup>

As highlighted, the exploitation of passive targeting, particle physicochemical properties and the EPR effect have successfully led to a number of nanomedicines that have decreased cytotoxicity whilst increasing bioefficacy. Nevertheless this method of targeting has limitations with regards to the achievable drug concentrations in tumours and consequently the therapeutic efficacy and the lack of ability to categorically distinguish between healthy and tumour cells.<sup>67</sup> These factors can be enhanced by the implementation of active targeting to deliver drugs and their metabolites to a chosen site within the body.

### **1.3.2 Active targeting**

Active targeting was developed to further increase the selectivity of nanoparticles to tumour sites by proactively exploiting a number of different characteristics associated with solid tumour masses. This is often achieved by the addition of covalently bonded targeting moieties, associated to a specific group of cells, to the corona of nanoparticles.<sup>50,73</sup> Optionally sites that are actively targeting nanoparticles can give a controlled and definite response when a specified stimuli is applied. This can be either an internal stimuli, such as pH or a chemical change, or can be an external environmental change inducing a response from the nanoparticles, such as heat or an oscillating magnetic field.<sup>49,74,75</sup>

There are a number of examples of targeting moieties including antibodies, dendrons and protein ligands (Figure 1.5) which allow for binding of the nanocarrier to the selected site with consequential internalisation of the receptor-ligand complex by the endocytosis/phagocytosis mechanism.<sup>76</sup> This internalisation is followed by liposomal degradation of the receptor-carrier complex which results in drug release.<sup>76</sup>

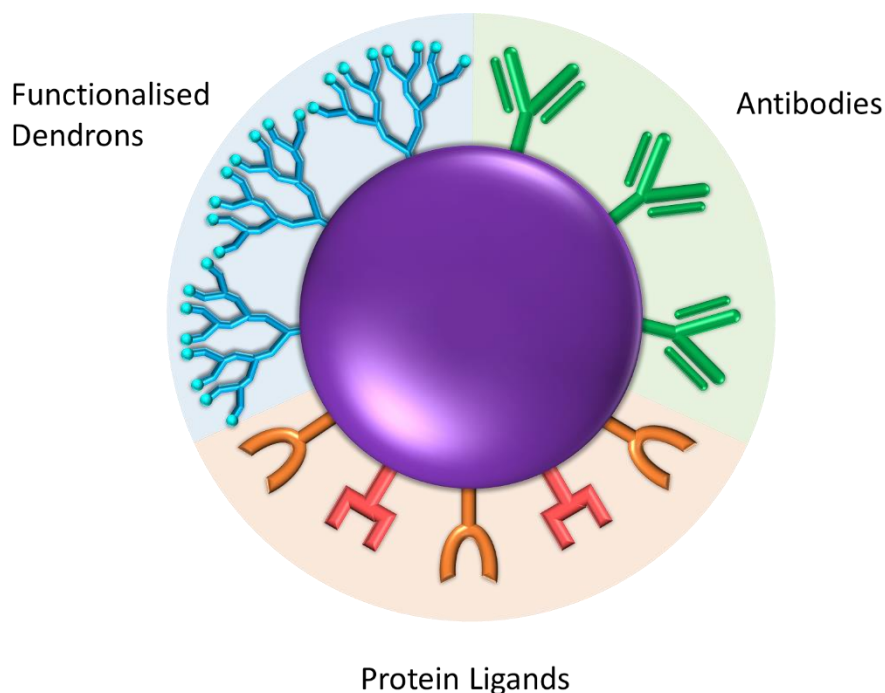


**Figure 1.5 – Examples of targeting moieties that can be used in nanocarriers designed for active targeting.**

Protein targeting ligands, for instance folic acid<sup>\*\*</sup> and iron rich transferrin<sup>††</sup>, can be used to decorate the corona of nanocarriers and highly selectively exploit the corresponding receptors that are over expressed on the surface of rapidly growing cancer cells.<sup>76</sup> Both these ligands are involved in a receptor-ligand pair on the surface of the cell and result in endocytosis into the cell cytoplasm.<sup>76,77</sup> They are desirable as targeting ligands due to their receptors being over-expressed in malignant cells, along with the internalisation of each ligand through folate receptor, *FR*, or transferrin receptor, *TfR*, respectively.<sup>73,77</sup> Folate, one the most extensively used targeting moiety, has been conjugated onto a number of particles,<sup>73</sup> for example, biodegradable PEG-PLGA polymeric micelles carrying doxorubicin.<sup>77,78</sup> These showed the

<sup>\*\*</sup> Folic acid or folate is a vitamin required for the biosynthesis of purines and pyrimidines within cells.<sup>202</sup> The most significant receptor for nanocarriers decorated with folate is the high-affinity phosphatidyl-inositol-linked folate receptor, *FR*, which is capable of internalising these nanocarriers and is over-expressed in tumour cells.<sup>203</sup> This receptor is minimally expressed in healthy cells of adults and therefore a good receptor for active targeting.<sup>73</sup>

<sup>††</sup> Transferrin is responsible for the transport of iron through the blood stream to cells resulting in internalisation at transferrin receptors.<sup>204</sup> These receptors expression is up to a 100 x higher in malignant cells compared to healthy cells making iron rich transferrin or transferrin mimics suitable as an active protein targeting ligands.<sup>73</sup>

active internalisation of the particles into the cell cytoplasm with increased cytotoxicity and cellular uptake compared to untargeted doxorubicin, whilst also demonstrating reduced cardiotoxicity indicating a differentiation between healthy and tumour cells.<sup>77,78</sup>

Monoclonal antibodies are also well-established targeting moieties due to their high selectivity and binding affinity to a certain target, owing to the presence of site specific binding sites on each molecule.<sup>73</sup> There are a number of antigens which are overexpressed in malignant cells and can be targeted by the complementary corresponding antibody. These include, but are not limited to, the epidermal growth factor receptor, *EGFR*; the human epidermal growth factor receptor 2, *HER2*; and the A33 antigen.<sup>77,79</sup> These allow for more specific differentiation between cancer and healthy cells which generally generates substantial improvement in therapeutic efficacy compared to the passive counterparts, as seen with studies conducted by Domínguez-Ríos and co-workers.<sup>80</sup> Here PLGA particles functionalised with trastuzumab an anti-HER2 antibody were used to actively target ovarian cancer cells for site specific delivery of cisplatin.<sup>80</sup> HER2 receptors are most commonly over expressed in a number of breast and ovarian cancers allowing for this targeting pathway to be exploited in this group of cancers.<sup>81</sup> The anti-HER2 decorated nanoparticles showed an increase in cytotoxicity and cellular uptake *in vitro*, demonstrating promising pathways for increasing efficacy whilst simultaneously lowering side effects.<sup>80</sup>

Not only can particles decorated with the corresponding antibodies to these receptors allow for the targeted delivery of anti-cancer drugs, but can also permit additional positive effects to be accessed. For example, antibodies that interact with the EGFR can diminish or stop cancer cell proliferation; combined with anti-cancer drug compounds such as cisplatin and doxorubicin, this can halt tumour growth or eradicate the tumour altogether.<sup>77</sup> These features have made these targeting moieties a popular choice despite their complexity.<sup>79</sup>

Whilst antibodies and protein ligands both present specific targets to interact with, dendrons offer the prospect to target sites by creating the opportunity to add random or zoned multi-functionality to the surface of nanoparticles.<sup>82</sup> This can be achieved by two synthesis pathways, resulting in either dendrimers or dendron functionalised polymers including hyperbranched polydendrons, *hyp-polydendrons*.<sup>83-86</sup> The most investigated of the two for drug delivery has been dendrimers, in particular those synthesised from polymers containing poly(amidoamine), *PAMAM*. PAMAM dendrimers have a large number of potential binding sites for the formation of dendrimer-ligand complexes at the target site and allowing for

additional functionalisation for increased targeting effects. For example, a single PAMAM-NH<sub>2</sub> dendrimer of the fourth generation, *G4*, used to encapsulate 5-FU has ca. 250 potential bonding sites (64 1° amine surface groups, 62 3° amine internal groups and 124 amide groups).<sup>85</sup> In a similar formulation, these numerous bonding sites have been exploited to aid PEGylation, the linking of biotin<sup>††</sup> and the conjugation of paclitaxel.<sup>57</sup> The conjugated Biotin components allowed for increased cytotoxicity and cell internalisation in multicellular cancer spheroids compared to conjugated materials and free paclitaxel.<sup>57</sup> Simultaneously PEG functionalities provided shielding of the cationic charged dendrimers to decrease toxicity.<sup>57</sup>

The development of both passively and actively targeting nanoparticles means that there is an extensive library of materials and formulations that can be used to deliver poorly targeting, hydrophobic drug molecules to their specified site. In spite of this, further refining of this library along with novel additions will solve problems with existing systems as well as create new systems that deliver drugs that have previously failed to be encapsulated in nanocarrier systems.

### 1.3.3 Nanostructures

As detailed in 1.3.1 and 1.3.2 there is an extensive library of nanomaterials that can achieve passive or active targeting by modifying the corona. However, focus must also be given to the general structure of the nanomaterials used. There is a wide range of structures that can be formed on the nanoscale that allow for the encapsulation and/or transportation of active pharmaceutical ingredients such as poorly water soluble or biologically unstable drug molecules. These include liposomes,<sup>87</sup> nanoemulsions,<sup>88</sup> micelles,<sup>89</sup> polymeric nanoparticles,<sup>90</sup> solid drug nanoparticles and dendrimers (summarised in Table 1.2).<sup>91,92</sup>

---

<sup>††</sup> Biotin is an essential micronutrient, more commonly known as vitamin B7 or vitamin H.<sup>205</sup> It is required as a co-factor in the function of 5 biotin dependant carboxylases. This results in cancer cells over-expressing biotin to increase uptake to achieve rapid proliferation and growth therefore making it a prime candidate as an active targeting molecule.<sup>57,205</sup>

**Table 1.2-Summary of various nanostructures used for drug delivery and tumour imaging.**

Structure	Typical size	Methods of Synthesis	Advantages	Disadvantages	Ref
<i>Liposome</i>	Average: 50-500 nm SUV (< 100 nm) LUV (100-1000 nm) GUV (> 1 µm) MLV (> 1 µm)	General overall method consists of 4 steps: <ul style="list-style-type: none"> <li>- Formation of a monolith/thin film from organic solvent</li> <li>- Dispersion in aqueous media (methods can include mechanical and solvent dispersion techniques; e.g. sonication and ether injection respectively)</li> <li>- Purification</li> <li>- Analysis</li> </ul> Drug loading can be achieved by passive and active methods.	<ul style="list-style-type: none"> <li>• Very low toxicity</li> <li>• Able to entrap both hydrophilic and hydrophobic molecules</li> <li>• Often biodegradable</li> <li>• Easy modulation of size by synthesis</li> <li>• Modification to achieve ‘stealth’ properties (by PEGylation) or active targeting</li> </ul>	<ul style="list-style-type: none"> <li>• Can be cleared by the RES by interactions with opsonins</li> <li>• High and low density lipoproteins, <i>HDLs</i> and <i>LDLs</i>, can decrease stability</li> <li>• High cost of synthesis</li> <li>• Difficult to scale synthesis</li> <li>• High variability between batches</li> </ul>	50,87,93,94
<i>Polymeric Micelle</i>	< 100 nm	Self-assembly and drug loading by: <ul style="list-style-type: none"> <li>- Dialysis</li> <li>- Film casting</li> </ul>	<ul style="list-style-type: none"> <li>• Small size and narrow distribution that allows for the accumulation in tumour tissues (EPR effect)</li> <li>• Possible to decorate the surface with PEG or targeting functionalities to improve targeting</li> <li>• Easy variation of the components to tune properties</li> </ul>	<ul style="list-style-type: none"> <li>• Poor <i>in vivo</i> stability due to the dilution of the micelles in the blood leading to a shift below the CMC causing partial micelle dissolution</li> <li>• Interaction with blood components (e.g. albumin and apolipoproteins) diminishes retention of the drug</li> </ul>	62,89,93
<i>Polymeric Nanoparticles</i>	10 nm-1 µm	These include but are not limited to : <ul style="list-style-type: none"> <li>- Nanoprecipitation</li> <li>- Solvent evaporation</li> <li>- High-pressure Homogenisation</li> <li>- Dialysis</li> <li>- Spray drying</li> </ul>	<ul style="list-style-type: none"> <li>• Reproducible synthesis technique</li> <li>• Easy modification of the components to tune the particle physicochemical properties;</li> <li>• Variety of polymers can be used</li> <li>• Drug retention due to diffusion in complex polymer matrix</li> </ul>	<ul style="list-style-type: none"> <li>• Method of synthesis makes it hard to tune the size</li> <li>• Scale up can be difficult</li> <li>• Small accumulation in target tissue can occur</li> <li>• Only a small number of formulations in clinical trials</li> </ul>	90,95,96
<i>Dendrimer</i>	< 15 nm	Convergent synthesis: <ul style="list-style-type: none"> <li>- Synthesis from the periphery of the dendrimer</li> <li>- Number of generations is pre-determined</li> <li>- Wedges coupled to a multivalent core to ultimately yield a dendrimer</li> </ul> Divergent synthesis: <ul style="list-style-type: none"> <li>- Starts from the multivalent core molecule</li> <li>- Step-wise synthesis to ‘grow’ the dendrimer, adding generations in each synthetic cycle.</li> </ul>	<ul style="list-style-type: none"> <li>• Reproducible synthesis</li> <li>• Monodisperse samples made</li> <li>• Easy addition of surface or targeting functionalities</li> <li>• Multiple ways of transporting a hydrophobic molecule.</li> <li>• Rapidly cleared from the blood due to small size – do not need to be biodegradable</li> </ul>	<ul style="list-style-type: none"> <li>• Modification required to decrease the toxicity induced by cationic amine groups</li> <li>• Lengthy manufacturing with many repetitive steps</li> <li>• Costly</li> <li>• A challenge for scale up to large volumes</li> </ul>	71,91,93,97

**Table 1.2 cont. -Summary of various nanostructures used for drug delivery and tumour imaging.**

Structure	Typical size	Typical Synthesis	Advantages	Disadvantages	Ref
<i>Solid Drug Nanoparticles</i>	< 1 $\mu\text{m}$	<p>Top-down (suitable for thermostable compounds):</p> <ul style="list-style-type: none"> <li>- Nano milling/ media milling</li> <li>- High pressure homogenisation</li> <li>- Micro-fluidization</li> </ul> <p>Bottom-up:</p> <ul style="list-style-type: none"> <li>- Nanoprecipitation under sonication</li> <li>- Emulsion template freeze drying</li> <li>- Spray drying</li> </ul> <p>High energy methods:</p> <ul style="list-style-type: none"> <li>- Emulsion Template Freeze Drying</li> <li>- Ultrasonic emulsification</li> <li>- High-pressure homogenisation</li> <li>- Micro-fluidics</li> <li>- Membrane emulsification</li> </ul> <p>Low energy methods:</p> <ul style="list-style-type: none"> <li>- Phase inversion temperature method</li> <li>- Spontaneous emulsification</li> <li>- Emulsion inversion point method</li> </ul>	<ul style="list-style-type: none"> <li>• Option for oral administration</li> <li>• Scalable synthesis techniques</li> <li>• Stability over time</li> <li>• Composed of 100 % drug</li> <li>• Sustained release profiles</li> <li>• Can allow for the decrease in dosing regimens</li> </ul>	<ul style="list-style-type: none"> <li>• Limited to solid drug compounds</li> <li>• Limited knowledge on the effects different stabilisers play on the properties of the SDNs</li> <li>• Pharmacokinetic variability with drug release and movement around the body</li> </ul>	41,92,98–100
<i>Nanoemulsions</i>	10-100 nm	<p>Magnetic nanoparticles such as iron oxide NPs:</p> <ul style="list-style-type: none"> <li>- Precipitation of salt in aqueous media</li> <li>- Polyol process, dissolution of magnetic salts</li> <li>- Degradation of metallic compounds in organic solvents</li> </ul> <p>Production of NPs with good crystallinity:</p> <ul style="list-style-type: none"> <li>- Hydrothermal synthesis (use of temperature and pressure)</li> </ul> <p>Metallic nanoparticles:</p> <ul style="list-style-type: none"> <li>- Spray/laser pyrolysis (spraying of salts into reactors or lasers heat precursor mixtures)</li> </ul> <p>Other methods:</p> <ul style="list-style-type: none"> <li>- Micro emulsions</li> </ul>	<ul style="list-style-type: none"> <li>• Option for oral administration</li> <li>• Ability to deliver multiple drugs simultaneously</li> <li>• Option for active targeting functionalities</li> <li>• Can be used for both solid and liquid drug compounds</li> <li>• Easily tuneable properties.</li> </ul>	<ul style="list-style-type: none"> <li>• Thermodynamically unstable, will separate into two macro-phases over time</li> <li>• Manufacturing processes can limit the types of compounds used</li> <li>• Scale up could be difficult due to the number of variable that have to be considered.</li> </ul>	88,101–103
<i>Inorganic Nanoparticles</i>	Variable depending on structure (~10 – 500nm)	<p>Magnetic nanoparticles such as iron oxide NPs:</p> <ul style="list-style-type: none"> <li>- Precipitation of salt in aqueous media</li> <li>- Polyol process, dissolution of magnetic salts</li> <li>- Degradation of metallic compounds in organic solvents</li> </ul> <p>Production of NPs with good crystallinity:</p> <ul style="list-style-type: none"> <li>- Hydrothermal synthesis (use of temperature and pressure)</li> </ul> <p>Metallic nanoparticles:</p> <ul style="list-style-type: none"> <li>- Spray/laser pyrolysis (spraying of salts into reactors or lasers heat precursor mixtures)</li> </ul> <p>Other methods:</p> <ul style="list-style-type: none"> <li>- Micro emulsions</li> </ul>	<ul style="list-style-type: none"> <li>• Gold nanoparticles are FDA approved</li> <li>• Drug delivery can be used in conjunction with another imaging or treatment pathway</li> <li>• Unique properties of metallic nanoparticles (SPR) can allow for simultaneous imaging of different tissues</li> <li>• SPIONs in an oscillating magnetic field can induce controlled cell death</li> </ul>	<ul style="list-style-type: none"> <li>• Carbon nanotubes and quantum dots are both hydrophobic and require polymer stabilisation</li> <li>• Drug molecules are generally required to be covalently attached with a cleavable linker</li> <li>• Some cytotoxicity can be induced by burst release of metallic nanoparticles, namely iron</li> <li>• Carbon nanotubes are cytotoxic and require polymer functionality to improve this.</li> </ul>	33,37,93,104



Liposomes are by far the most researched and widely used form of nanostructure. Composed of a lipid bi-layer formed from amphiphilic lipid and cholesterol molecules assembled in a spherical fashion to produce particles of sizes between 50 and 500 nm.<sup>50,93,94</sup> This results in clear segregated hydrophobic and hydrophilic domains, the hydrophobic domain is sandwiched between two hydrophilic layers, the outer layer stabilising the structure, with the inner layer creating a hydrophilic internal cavity.<sup>93</sup> In this way the liposome is set apart from other nanocarriers as it has the ability to simultaneously carry both hydrophobic and hydrophilic compounds within the two domains (Figure 1.6). Equally their chemical composition induces low toxicity and immunogenicity of these carriers as their components are analogous to the phospholipid bi-layer of biological cells.<sup>93</sup> Modifications can also be used to enhance the properties of these nanostructures, for example the conjugation of PEG to the corona of the liposomes prevents the binding of opsonins and therefore diminishes recognition and clearance by the RES.<sup>50,105</sup> Furthermore the easy modulation of the size, targeting mechanism and hydrophilic/hydrophobic character allow the liposome to maintain its status as the most studied and extensively used “injected” nanoscale drug-delivery system.

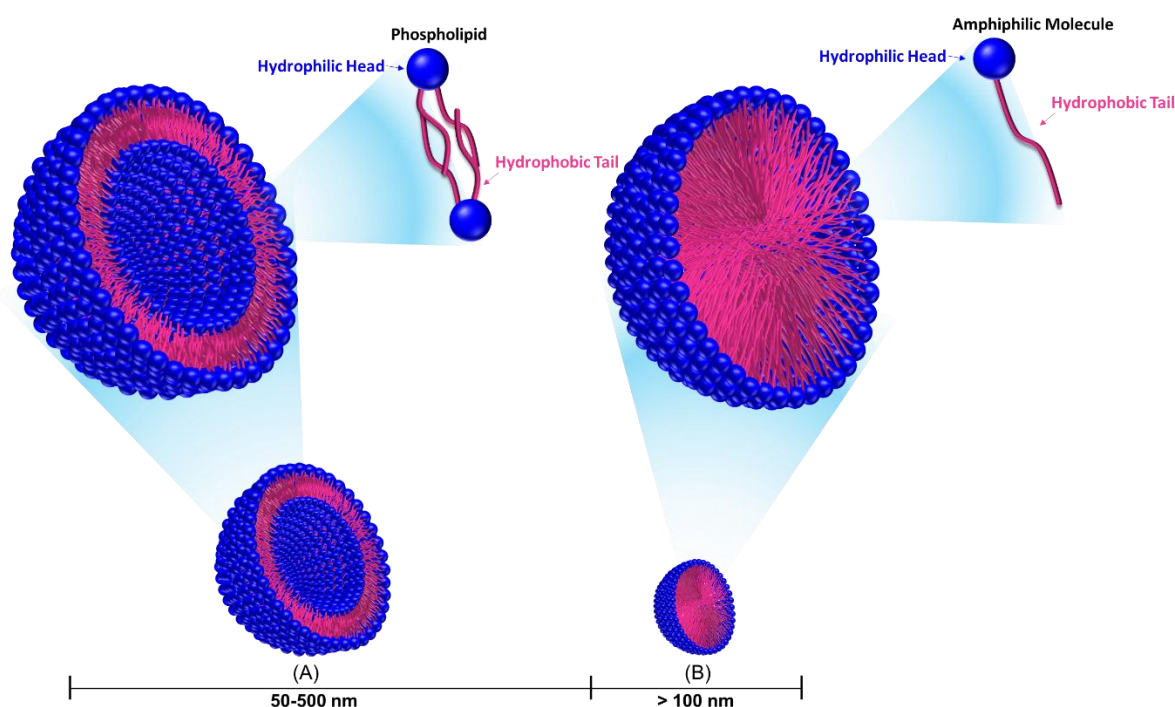


**Figure 1.6 – Example structure of a liposome (A) and micelle (B).**<sup>106</sup>

A similar nanostructure formed from the self-assembly of small molecule surfactants are micelles (Figure 1.6) which consists of a hydrophilic surface domain surrounding a hydrophobic environment but is void a hydrophilic inner cavity due to the lack of interdigitating hydrophobic chains of surfactant molecules.<sup>93</sup> Consequently this hydrophobic

environment is capable of encapsulating poorly water-soluble drug molecules. Micelles are typically under 100 nm in size and their amphiphilic components are generally surfactants, however block co-polymers have been used, which can be easily varied to allow for the tuning of the characteristics of the micelles.<sup>62,93</sup> For example, size, drug loading capabilities, drug retention and also drug release can be tuned by the adaptation of the micelle element's chemical composition and molecular weight.<sup>62</sup> Like liposomes, the corona can be decorated with PEG or targeting moieties, such as antibodies, to take advantage of both passive and active targeting pathways. On the other hand, these vehicles have a number of obstacles to overcome *in vivo* mainly related to the decrease in stability when the formulation is greatly diluted, below the critical micelle concentration,  $CMC^{65}$ , in the blood stream.<sup>62</sup> Further disadvantages related to drug retention are being tackled by the synthesis of amphiphilic polymer drug conjugates that are capable of self-assembly upon reaching the  $CMC$ .<sup>62</sup>

Another system that employs the use of polymeric species are polymeric nanoparticles (Figure 1.7), similarly to polymeric micelles these nanostructures consist of a hydrophobic core domain surrounded by a hydrophilic corona. Despite this, these structures differ from polymeric micelles in a number of ways including size, synthesis routes and composition. Commonly synthesised by nanoprecipitation, the polymer species collapse, upon desolvation, to form nanoparticles with a dense polymer core ranging in sizes from 10 nm to 1  $\mu\text{m}$ .<sup>95</sup> Drug encapsulation is achieved by dissolution in the organic solvent, containing the selected polymer, resulting in entrapment within the polymer core following nanoprecipitation. A number of biocompatible, and often biodegradable, synthetic polymers can be used to form these structures including PLGA and poly(2-hydroxypropyl methacrylate), *pHPMA*, co-polymers which induce slower release rates of the encapsulated drug as the molecules are required to diffuse through the polymer.<sup>37</sup> Additionally, these particles are commonly PEGylated which prevents phagocytosis and opsonisation and also induces stability under biological conditions.<sup>107</sup> Furthermore there is the ability to easily vary and modify the components used to tailor the physicochemical properties of the particles and in turn their polymer-drug interactions as well as corona functionality to vary the stability and method of cell targeting (Figure 1.7). Despite the multitude of promising characteristics these nanocarriers have, there are only a small number of formulations that have made it to clinical trials with only one of these capable of active targeting.<sup>108</sup> Nonetheless they still maintain their reputation

---

<sup>65</sup> The critical micelle concentration,  $CMC$ , is the concentration of surfactants at which micelles spontaneously form; shown by an abrupt change in solution property of the molecules, usually measured by surface tension.<sup>206</sup>

as one of the more popular forms of nanostructure for drug delivery research and development.<sup>108</sup>

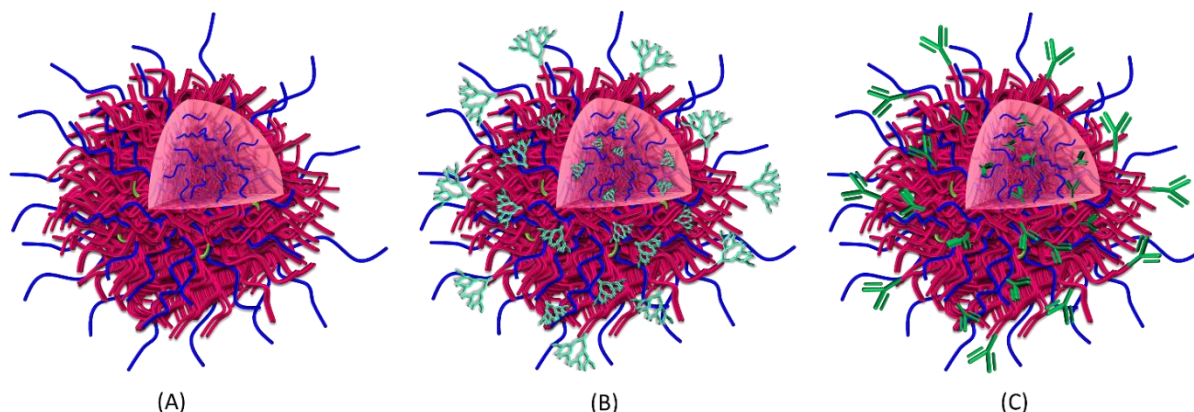


**Figure 1.7 – Examples of polymeric nanoparticles with varying corona functionality. (A) PEGylated, (B) dendrons and (C) anti-bodies.**<sup>109</sup>

Although research seems swayed towards polymer nanoparticles and liposomes there are a number of other structures that are also being investigated for the treatment and diagnosis of disease and cancer. Dendrimers offer an alternative way to transport hydrophobic drug molecules within their tree-like, three dimensional structures.<sup>50,93,94</sup> The active drug molecules can be transported either by being covalently bonded to the surface of the dendrimer or by encapsulation within internal cavities.<sup>50</sup> The synthesis of these species results in monodisperse, globular high molecular weight particles. The ease of surface functionality coupled with controlled and reproducible synthesis makes these nanostructures a promising group of drug vehicle.<sup>71,94</sup> On the contrary, many successful dendrimer syntheses result in the presence of tertiary amine groups, which act as sites of cationic charge; modification maybe required to overcome the inherent toxicity of polycationic materials. This is normally achieved by the addition of a hydrophilic polymer to the periphery of the dendrimer.<sup>93,97</sup>

In comparison to the nanostructures previously discussed in this section, which are all directed towards intravenous injection to avoid the gastrointestinal tract and the clearance issues linked with it, there are some nanostructures tailored to oral administration. In particular solid drug nanoparticles, *SDNs*, and nanoemulsions (Figure 1.8) which have properties tailored for oral administration allowing for alternatives where parenteral administration is undesirable.<sup>88,92</sup>

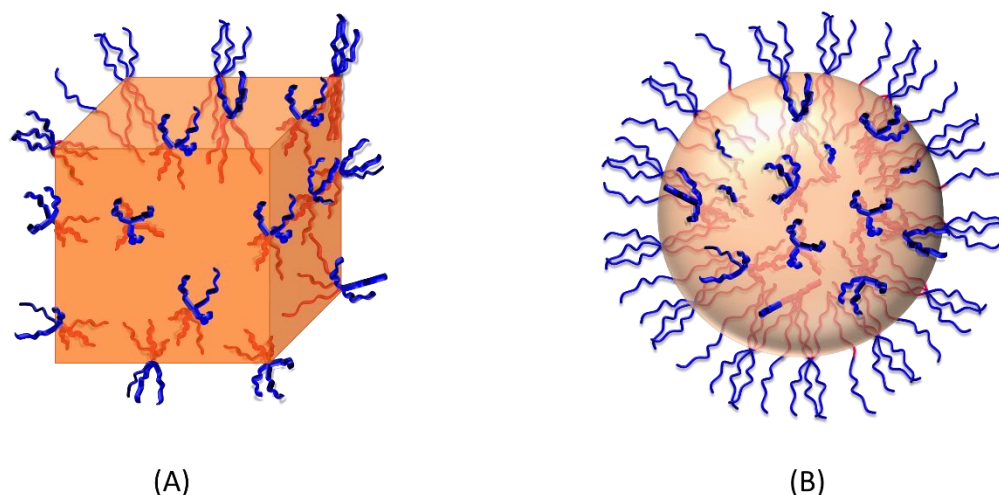


**Figure 1.8 – Example structures of (A) solid drug nanoparticles and (B) nanoemulsions.**

SDNs are nanoparticles made directly from poorly water-soluble drug compounds and stabilised by polymeric and/or surfactant species.<sup>98</sup> Although the poorly water soluble drug is not contained in or attached in this case, SDNs have shown to improve the bioavailability of drugs, induce slow sustained release and overcome effects linked to food with oral administration.<sup>110–112</sup> These in turn are linked to lower dosing regimens and lower pill burdens for patients due to enhanced drug absorption after oral administration.<sup>35,92</sup> Studies on SDNs for the treatment of HIV have shown little effect on the immune system, suggesting that these nanostructures may have an advantage in terms of immunogenicity compared to some nanostructures addressed earlier in this section, for example dendrimers.<sup>113</sup> Not only do these nanostructures offer pharmacological benefits, their manufacturing processes are scalable with both top-down and bottom-up routes available for their synthesis.<sup>100,114,115</sup> SDNs have been shown to be able to be stored over long periods of time proving they are one of the most commercially viable forms of nanostructure reflected by having the most FDA approved nanomedicines than any other technology.<sup>116</sup>

Nanoemulsions also allow for oral administration along with the options for topical and parenteral routes.<sup>88,101,102</sup> The composition of these nanostructures are mixtures of two immiscible liquids, an aqueous continuous phase and a non-aqueous dispersed phase of nano-sized droplets.<sup>50,101</sup> The size of these nano-droplets can be tuned by using different oils to create the non-aqueous phase, for example soybean oil, a long chain triglyceride, has been used to produce large particles of around 120 nm.<sup>101</sup> This can be combined with varying the structure and concentration of the stabilising polymers or surfactants as demonstrated by Hobson *et al.*<sup>88</sup> Similar to other nanostructures, the ability to contain drug molecules within the entity, by

encapsulation of poorly water soluble drugs within dispersed non-aqueous droplets, can decrease toxicity and increase bioavailability due to sustained circulation and protect the drug from degradation and clearance.<sup>101</sup> Additionally the supplementary functionalisation of the stabilising polymers used when forming nanoemulsions with targeting moieties can allow access to active targeting pathways.<sup>101</sup>

Lastly there are also a number of different inorganic particles (Figure 1.9) that have been studied as drug delivery agents, treatment and diagnostic applications of treating disease due to their unique properties. They also often have lower toxic side effects than organic based nanostructures and allow access to more imaging techniques.<sup>37</sup> Gold nanoparticles, for example, have unique optical and thermal properties which, combined with the ability to tune a number of physical characteristics such as size and surface functionality, make them one of the most researched inorganic nanoparticles for disease treatment.<sup>33</sup> There are a number of other particles associated with this diverse group of nanostructures which include, silver iron oxide and silica nanoparticles along with quantum dots and carbon nanotubes however, like gold, iron oxide nanoparticles are the most intensely studied.<sup>117</sup> These particles are being investigated for use in targeted drug delivery and contrast enhancement agents for magnetic resonance imaging, *MRI*, due to the magnetic properties they possess.<sup>33,118</sup> Magnetism is also used to treat tumours from controlled cell death with superparamagnetic iron oxide nanoparticles, *SPIONs*, in the presence of an oscillating magnetic field inducing a thermal effect local to the nanoparticles position.<sup>33,43,63</sup> Metallic inorganic nanoparticles allow access to surface plasmon resonance, *SPR*; the oscillation of metal-free electrons on the surface of the particles.<sup>117,119</sup> These oscillations are stimulated by interaction with light in the visible region and allow for ultra-sensitive imaging that can achieve clarity capable of differentiating between healthy cells and tumour cells.<sup>119</sup> There is also the opportunity to functionalise these nanoparticles with targeting moieties and drugs to permit dual action treatments.<sup>93,117,118</sup>

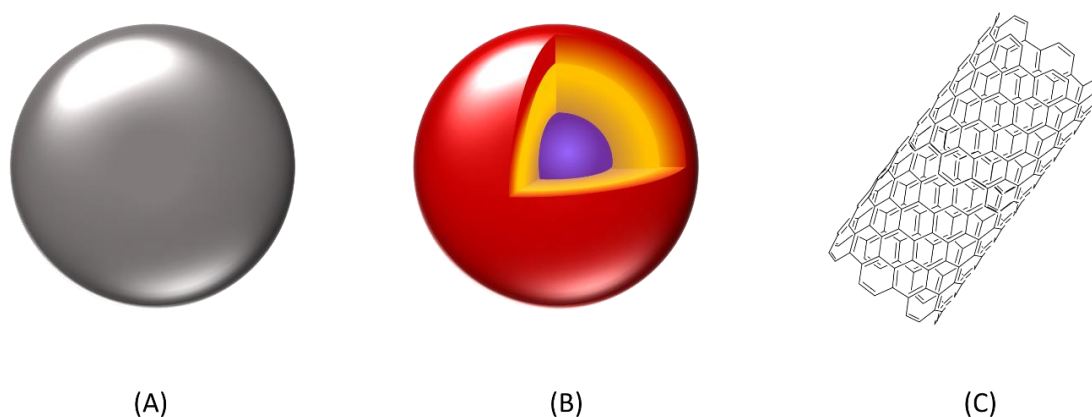


**Figure 1.9 – Examples of inorganic nanoparticles:** (A) metallic nanoparticles, (B) quantum dots and (C) carbon nanotubes. Not to respective scales.

Quantum dots are biocompatible, semiconducting nanocrystals that have a multitude of physicochemical properties that make them an attractive alternative to other nanostructures for cancer treatment and detection.<sup>93,120</sup> These include, but are not limited to, highly tuneable photoluminescence and multi-colour fluorescence.<sup>37</sup> The optical properties that make quantum dots ideal for targeted and traceable drug delivery are dependent on their size. Each size on quantum dot emits a different colour when excited by the same wavelength of light.<sup>93,121,122</sup> This means that different tissues could be imaged simultaneously by targeted delivery of different sized quantum dots to these selected tissues. Despite a large number of advantages, these structures do have shortcomings, they are inherently hydrophobic and are highly likely to aggregate and have high toxicity.<sup>123,124</sup> This can be avoided by coating the quantum dots with a polar species or mono/multi-layer ligand shells (usually formed from amphiphilic polymers).<sup>125</sup> This also provides an opportunity for the embedding of hydrophobic drug molecules or contrast agents beneath the hydrophilic shells and the attachment of hydrophilic guest molecules and targeting agents to the periphery of the particles.<sup>37,126</sup> In combination with the number of advantageous properties these structures have they prove to be a promising avenue for the imaging of tumour sites and aiding the drug delivery to them.

As a final example carbon nanotubes are rolled sheets of graphene rings made from  $sp^2$  hybridised carbon and are most well-known for near-infrared photothermal ablation therapy.<sup>37</sup> In this case the carbon nanotubes increase the temperature in the tumour sites and cause cell death. This effect can be tuned as it is dependent on the concentration of nanotubes and the light intensity.<sup>127,128</sup> These structures not only possess useful optical properties but also can penetrate cells, have a flexible structure and are intrinsically stable.<sup>127,128</sup> Like most of the structures we have addressed there is the opportunity for the functionalisation of the surface to

induce active targeting or carry drug molecules.<sup>129</sup> The internal cavity of carbon nanotubes can also serve as a carrier for hydrophobic guest molecules or plasmid DNA.<sup>129</sup> Nonetheless these structure also have their problems with poor water solubility, non-biodegradability and cytotoxicity which all require functionalisation with polymers to avoid and improve.<sup>94</sup> Even so, the advantageous characteristics and alternative therapy pathways they offer make them a good candidate for future drug delivery candidates in conjunction with new treatment options.

Although there is a wide variety of nanostructures that could be selected for the application of drug delivery, this body of work will focus on the use of polymeric nanoparticles.

### **1.4 Homo- and co-polyesters**

When designing new polymeric nanocarriers, a number of factors must be considered, one of which being the properties of the nanoparticle components. A review of the nanomedicine literature shows that polyesters account for a large proportion of the materials contributing to nanocarriers structures under development. These polymers are desirable as they possess a number of characteristics that are favourable for medicinal and biological use. Some of these properties are the ability to be bio-reabsorbed, tuneable biodegradability and crystallinity.<sup>130,131</sup> Polyesters of varying structures have also be shown to be biocompatible, meaning they do not illicit any toxicity or carcinogenic effects in local tissues when placed in the body.<sup>130,132</sup> Due to their biodegradation, by hydrolysis of the ester backbone, the degradation products of these particular polyesters can also be viewed as biocompatible as they do not interfere with tissue healing.<sup>130</sup> These properties have led to a number of applications for this class of polymers.

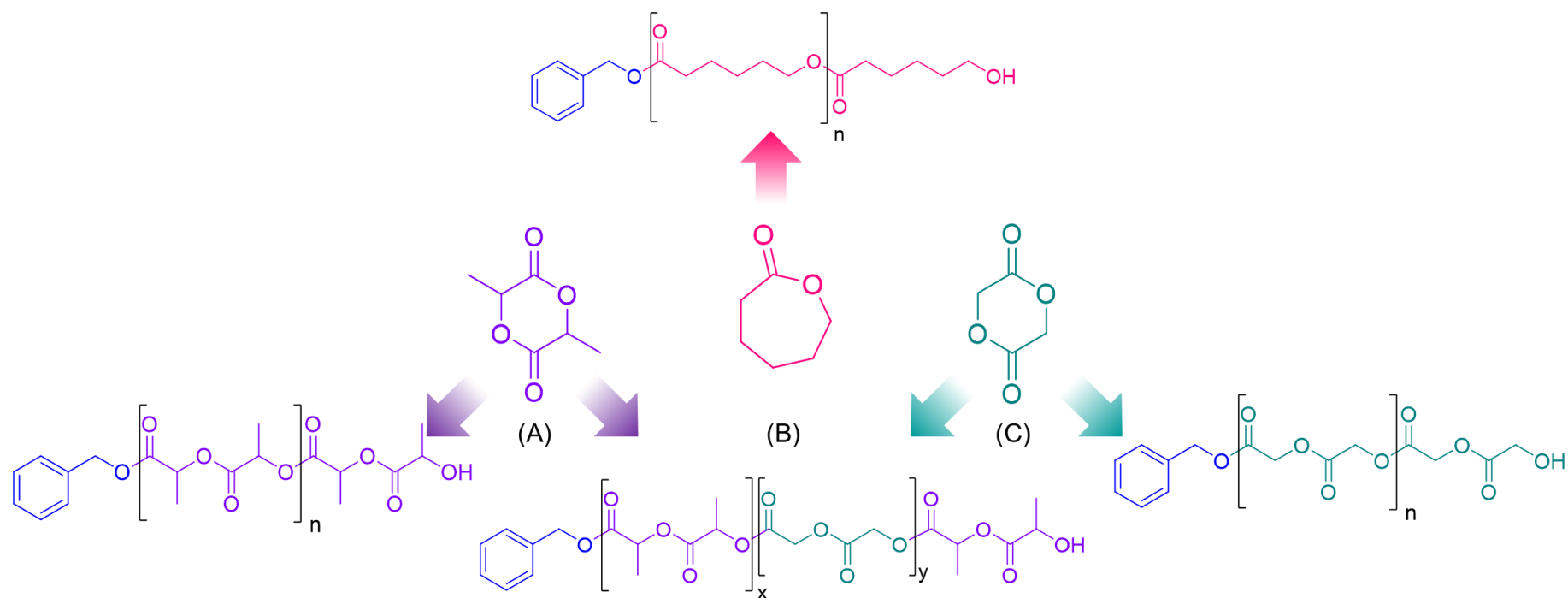


**Figure 1.10-** Scheme showing the various polyesters resulting from; (A) lactide, (B)  $\epsilon$ -caprolactone, and (C) glycolide.



Over the past 3 decades the most popular polymers in this category have been based on lactide and/or glycolide diesters\*\*\* cyclic monomers, namely PLA, and PLGA (Figure 1.10). After the FDA approval of formulations containing PLA, the research of these polymers was accelerated which increased their use in clinical settings with applications such as bone scaffolding, biodegradable implants and tissue sutures becoming prevalent.<sup>133–135</sup>

These polymers possess a number of characteristics, mentioned earlier, that have led to their implementation in the development of a number of nanomedical interventions such as polymeric nanoparticles. These characteristics can generally be tuned by adjusting the chemistry, for example adjusting the ratio of lactide to glycolide in PLGA polymers or by producing PLA with specific chiral conformations.<sup>36,130,136</sup> The degradation of PLA is quite slow, taking around 3-5 years to completely break down under biological conditions.<sup>130</sup> This can be tuned as the time taken to hydrolyse the ester backbone is dependent on numerous polymer properties including the molecular weight, crystallinity, morphology and stereoisomer content.<sup>130,137</sup> Furthermore the degradation products of PLA and PLGA, lactic and glycolic acid, are both present within the body and metabolised *via* the Cori and Krebs cycles (Figure 1.11) meaning they have a minimal toxicity when the polymers are broken down.<sup>36,136,138</sup> Further advantages over vinyl polymers are highlighted by the synthesis of the monomers themselves. Lactic acid, the precursor to its cyclic dimer, and the monomer lactide, can be produced by the fermentation of sugars.<sup>130,137,139</sup> This offers a method of synthesis that is sustainable and has low environmental impact adding to the benefits of the resulting polymers.

---

\*\*\* Diesters within this text refer to the saturated cyclic ring molecules that contain 2 ester functional groups within the dominant ring.

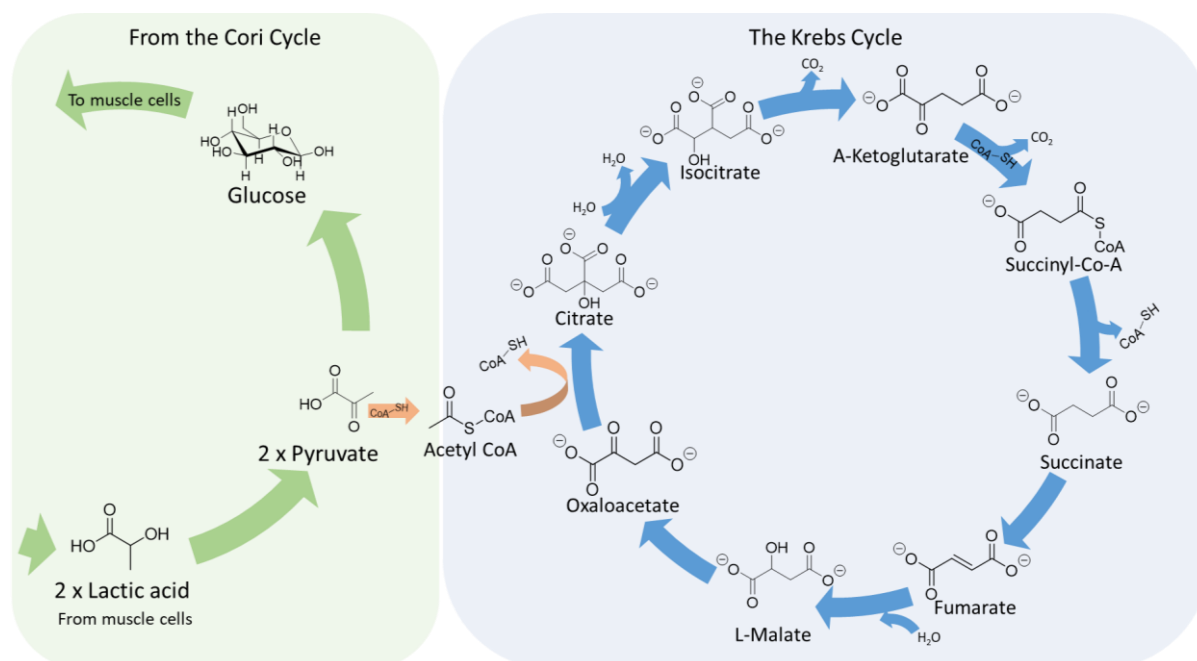


**Figure 1.11 –Scheme representing the degradation pathways of lactic acid *via* hydrolysis intermediates.**

The combination of these numerous desired properties has encouraged the creation of various nanomedical drug delivery vehicle examples based on PLA and PLGA polyesters. These systems are capable of encapsulating a range of molecules with a variety of molecular weights. Recent studies have resulted in a PLGA formulation that is capable of actively targeting epithelial ovarian cancer cells by the addition of an antibody to the corona of the PLGA nanoparticles.<sup>80</sup> After loading the particles with the highly hydrophobic drug cisplatin, a layer by layer method was used to coat chitosan onto the particles.<sup>80</sup> This consequently allowed the decoration of the corona with trastuzumab antibodies which resulted in greater cytotoxicity towards cancer cells and increased cellular uptake *in vitro*.<sup>80</sup> Drug release studies showed that cisplatin was released quicker from the nanoparticle when the pH of the release media was decreased.<sup>80</sup> This was characteristic of PLGA nanoparticles as the lower pH aids the hydrolysis of the polymer backbone releasing the drug molecules from the polymer network.<sup>140</sup>

Although there are numerous examples of nanomedicines that utilise the PLGA co-polymers, a large number of studies can be found using PEG-PLA in the nanoparticle composition. Chen *et al.* have recently formulated a new PEG-PLA system capable of co-encapsulating two anti-cancer drug molecules, erlotinib (an EGFR tyrosine kinase inhibitor) and fedratinib (a highly selective JAK2 inhibitor) for the treatment of erlotinib-resistant non-small cell lung cancer.<sup>141,142</sup> The encapsulation of these drug molecules within the PEG-PLA nanoparticles allowed control of a number of factors such as tumour accumulation, lower clearance,

improved drug solubility, reduction in toxicities.<sup>141,142</sup> Moreover the ability to incorporate two drug molecules within the same nanoparticle can allow for complementary effects to be obtained in the target tumour sites.<sup>142</sup> Interestingly *in vitro* release studies showed that, like PLGA particles, a decrease in pH led to an increased concentration of released drug after 48 hours.<sup>141</sup> This again is characteristic of PLA being subject to faster hydrolysis of the polyester backbone at acidic pH although the protonation of the amine groups in the drug molecules, causing them to be more hydrophilic, has also been eluded too.<sup>141</sup>

Alternatively the almost forgotten monomer, caprolactone, has started to increasingly be seen in research in recent years after a boom in examination the 1970s which declined with the increased exploration of lactide and glycolide based polymers. Similar to the 6-membered ring diesters,  $\epsilon$ -caprolactone is also biocompatible,<sup>†††</sup> bioresorbable, biodegradable and the monomer has potential to be made from renewable resources.<sup>131,143</sup> Moreover its slower degradation rates, due to greater hydrophobicity, made it initially more popular for long acting depot injections, releasing drugs over longer periods such as a year.<sup>131,144</sup> This became a very active research area for PCL applications, including studies of a suture material (Maxon<sup>TM</sup>) capable of degrading slowly, before numerous reports of faster releasing and faster degrading biomedical devices and drug carriers based on PLA, PGA and PLGA polymers.<sup>131,145</sup>

Nonetheless the pliability, low melting point and the ability to tune the degradation and crystallinity of poly( $\epsilon$ -caprolactone), *PCL*, based polymers (Figure 1.10, B) has seen a resurgence of interest both in the field of drug delivery and tissue engineering for this polymer.<sup>131</sup> Additionally the absence of isomerism in the polymer chains, unlike PLA, allows for more predictability in the resulting polymers allowing characteristics like solubility and thermal properties to be more consistent between polymer batches.<sup>130</sup> A further advantage is the ease in functionalisation of the monomer ring which therefore can provide opportunities for tuneable properties and targeting moieties.<sup>131,133</sup> Finally, similar to PLA, a number of PCL based nanoparticle systems have been FDA approved for drug delivery.<sup>131,146</sup>

New innovations are now being created which highlight the advantages of PCL based nanoparticles, although these are not in clinical trials as of yet. Paclitaxel and doxorubicin loaded PEG-PCL nanoparticles have shown the importance of the hydrophobic nature of the

---

<sup>†††</sup> The degradation products produced by the hydrolysis of the ester bonds in the poly( $\epsilon$ -caprolactone), *PCL*, backbone, namely 6-hydroxyl caproic acid is also incorporated into the Krebs cycle before excretion from the body.<sup>131</sup>

PCL chains to achieving higher drug loadings than nanoparticles based on PLA and PLGA.<sup>146-148</sup> Paclitaxel is a more hydrophobic drug than doxorubicin and therefore interacts more strongly with the PCL polymer segments.<sup>146</sup> This results in an increase in drug loading, from 0.2 to 5.1 %, with increasing PCL block lengths, from 1,100 to 23,500  $\text{gmol}^{-1}$ , in contrast this was not seen with doxorubicin as the interactions with the polymer chains are weaker.<sup>146-148</sup> This highly hydrophobic nature of PCL, which can be tuned when combined with hydrophilic PEG, allows for the encapsulation of a large number of drug molecules, such as ovalbumin and curcumin, with a range of computational  $\text{LogP}$  values<sup>\*\*\*</sup>, (-9.9 to 7.5) and a range of molecular weights.<sup>146</sup> Among the drugs encapsulated are SN-38 and cyclosporin A, two active compounds that have been difficult to encapsulate in a number of nanocarriers.<sup>146,149,150</sup> Cyclosporin A, a highly insoluble immunosuppressant used to reduce risk of transplant organ rejection, had previously been successfully encapsulated in lipid-based nanocarriers however these were shown to be unstable.<sup>149</sup> In contrast, when encapsulated within PEG-PCL polymeric micelles concentrations of cyclosporin A comparable to those in the clinical treatment Sandimmune® (an ethanol and cremophor EL formulation) were achieved.<sup>149</sup> Further studies on these particles showed that the release of the drug was slower for the PEG-PCL micelles compared to the clinical formulation, and resulted in decreased accumulation in the kidneys and reduced nephrotoxic effect.<sup>149,151</sup> This was attributed to reduced drug leakage due to greater interactivity between the drug molecules and the PCL core, increased stability of the polymer micelles and the 'stealth' properties<sup>§§§</sup> gained by the incorporation of a PEG corona.<sup>151</sup>

A selection of studies have explored the encapsulation of SN-38 in PEG-PCL nanoparticles, which is unable to be directly administered into the body due to its pH sensitivity and poor water solubility (Chapter 1.2).<sup>152</sup> To achieve encapsulation, different methods have been implemented which use characteristics of PCL polymers. Rychahou *et al.* achieved encapsulation of SN-38 along with a selection of other drugs by utilising a thin film hydration method, owing to PCL mechanical and physical properties.<sup>153</sup> The encapsulation of these drug molecules improved cytotoxicity and solubility both *in vitro* and *in vivo* showing an increased accumulation in target tissues and a decrease in lung cancer tumours after 72 hours.<sup>153</sup> Another study aiming to encapsulate SN-38 demonstrated the blending capabilities PCL polymers

---

\*\*\*  $\text{LogP}$  is a logarithm of the partition coefficient of a molecule between n-octanol and water and is used to measure its hydrophobicity. The more positive the value the more hydrophobic the compound is, the molecule will partition favourably into the octanol phase.<sup>207</sup>

§§§ Stealth refers to the common property associated with a PEG corona giving the nanoparticles the ability to avoid recognition and clearance by the RES by the prevention of opsonin and plasma proteins binding to the nanoparticles.

possess as pluronic F108 was used in conjunction with PEG-PCL to aid loading of SN-38 into the resulting nanoparticles.<sup>144,150</sup> The combination of these polymers in various ratios was critical to successfully achieve high drug loading and stabilise the micelles in aqueous medium.<sup>150</sup> These particles were not only able to retain the drug payload over several days but were also capable of combining several functions such as drug delivery and imaging shown by the introduction of fluorescent tags to aid drug tracking.<sup>150</sup>

## 1.5 Functionalised monomers and polymers

There are a range of unmodified monomers that can be used to create a library of homo- and co-polyesters, but a host of properties can be accessed by the modification of simple cyclic esters and diesters. The addition of functional groups to these monomers allows new properties to be unlocked once they have undergone polymerisation which would otherwise be unable to be accessed due to the lack of diversity in commercially available lactone monomers.<sup>154</sup> There have been a number of publications demonstrating ring opening polymerisation, *ROP*, involving multiple functionalised lactones derived from 4, 6 and 7 membered rings (Table 1.3).<sup>155</sup> *ROP* of monomers that have been functionalised with aromatic groups, amine groups and hydroxyl groups have produced a range of polymers.<sup>156</sup> Chemical properties such as the glass transition temperature and crystallinity of these resulting polymers varies with the substituents on the cyclic (di)ester monomers.<sup>155</sup> Polar functionalities such as amine and hydroxyl groups could increase the hydrophilicity of the polymers and allow for increased polymer-drug interactions when loaded into nanocarriers. In reality these require complicated pre- and post-polymerisation protection and de-protection procedures for successful *ROP*.<sup>156</sup> Conversely a recent study by Hao *et al.* has achieved the polymerisation of lactones carrying unprotected tertiary amine functionalities attaining polyesters with characteristics essential for gene delivery.<sup>157</sup>

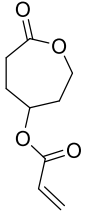
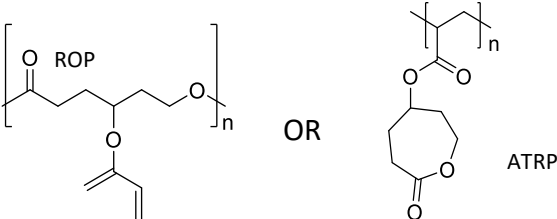
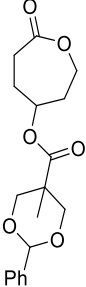
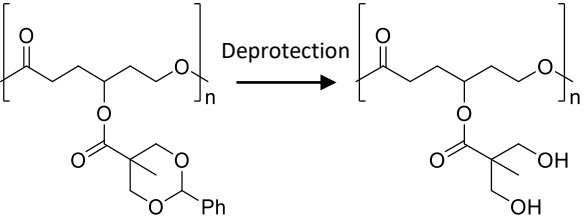
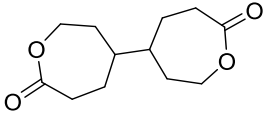
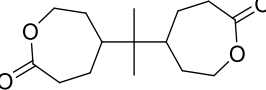
**Table 1.3 - Summary of select examples of functionalised lactone monomers, polymers and their resulting properties.**

Monomer	Polymer	Notable Properties of resulting polymer	Ref
<i>4-membered lactones</i>			
		<ul style="list-style-type: none"> <li>• Thiol-ene reactions can yield macro-initiators</li> <li>• Epoxidation and sulfonation resulted in polymers capable of inducing new bone growth and muscle regeneration</li> </ul>	158,159
		<ul style="list-style-type: none"> <li>• Polymers showed increasing crystallinity with increasing isotacticity.</li> </ul>	160
	 Quarterisation $\rightarrow$	<ul style="list-style-type: none"> <li>• Polymers have high crystallinity resulting in low solubility in organic solvents.</li> <li>• Resulting polymer hydrophobicity could be altered by quarterisation with pyridine to increase hydrophilicity.</li> </ul>	161,162
<i>6-membered lactones</i>			
	 Dihydroxylation $\rightarrow$	<ul style="list-style-type: none"> <li>• 20 wt% included in co-polymers with PCL gives more rigid polymers capable of undergoing dihydroxylation to produce polymers with greater stability than other hydroxyl polyesters.</li> <li>• Ability to graft PEG to the polymers post-polymerisation</li> </ul>	163
		<ul style="list-style-type: none"> <li>• Gives the potential for post-polymerisation click chemistry with selected groups.</li> <li>• For example, functionalisation with benzophenone groups produce photopatternable aliphatic polymers.</li> </ul>	164,165
		<ul style="list-style-type: none"> <li>• Polymers allow for modification for fluorescent dye attachment</li> <li>• Can also be functionalised with a peptides <i>via</i> click reactions to improve cell internalisation.</li> </ul>	166,167

**Table 1.3 cont. - Summary of select examples of functionalised lactone monomers, polymers and their resulting properties.**

Monomer	Polymer	Notable Properties of resulting polymer	Ref
	<p style="text-align: center;">Deprotection</p>	<ul style="list-style-type: none"> <li>• Deprotection of this polymer can yield poly(<math>\beta</math>-malic acid).</li> <li>• The pendant carboxylic acid groups on poly(<math>\beta</math>-malic acid) then provide a pathway for drug or targeting moiety conjugation.</li> </ul>	155,168
<i>7-membered lactones</i>			
		<ul style="list-style-type: none"> <li>• MRI-visible, hydrophobic co-polymers can be produced by the functionalisation with diethylene-triaminepentaacetic acid/<math>Gd^{3+}</math> complexes.</li> <li>• Possible to form organogels after click reaction functionalisation with cyclodextrin</li> </ul>	169,170
		<ul style="list-style-type: none"> <li>• Potential for radical thiol-ene reactions to functionalise the polymer with amines and subsequently fluorescein isothiocyanate <ul style="list-style-type: none"> <li>◦ The resulting polymers from this reaction are cationic and water soluble and have the potential for gene delivery.</li> </ul> </li> <li>• Thiol-ene reactions also possible with sugars and zwitterions</li> </ul>	171,172
		<ul style="list-style-type: none"> <li>• Radio-opaque and could allow for visualisation of drug delivery <i>via</i> X-ray radiology</li> </ul>	173
	<p style="text-align: center;">Deprotection</p>	<ul style="list-style-type: none"> <li>• Ability to modify the groups post polymerisation so introduce hydroxyl groups capable of reacting further to achieve fluorescent dye attachment or graft co-polymers.</li> <li>• For example; reactions with primary amines for use as macroinitiators</li> </ul>	158,174,175

**Table 1.3 cont. - Summary of select examples of functionalised lactone monomers, polymers and their resulting properties.**

Monomer	Polymer	Notable Properties of resulting polymer	Ref
		<ul style="list-style-type: none"> <li>• Both polyacrylates and polyesters can result from this monomer <i>via</i> atom transfer radical polymerisation or ROP respectively.</li> <li>• The resulting polyester is capable of intermolecular crosslinking, a flexible approach to small nanoparticles.</li> <li>• The polyester can also be grafted onto metallic surfaces to allow for coating and adhesion of poly(vinyl chloride) as a top coat.</li> </ul>	176
		<ul style="list-style-type: none"> <li>• The resulting polymer can be deprotected to yield a bis(hydroxymethyl) functionalised PCL .</li> <li>• This resulting polymer is capable of self-polymerisation to produce hyperbranched polyesters.</li> <li>• This pendant group can also be used in the divergent growth of dendrons along the polymer backbone. Generated up to G4 dendrons</li> </ul>	177,178
<i>Bifunctional monomers</i>			
	-	<ul style="list-style-type: none"> <li>• Allows the cross linking of polymer chains during polymerisation resulting in branched polymer architecture and high molecular weight</li> </ul>	179,180
	-	<ul style="list-style-type: none"> <li>• Allows the cross linking of polymer chains during polymerisation resulting in branched polymer architecture and high molecular weight</li> </ul>	155,180



A wide variety of monomers have been investigated in the production of polymers with the most variations being seen for 7-membered rings (i.e.  $\epsilon$ -CL type monomers).<sup>133</sup> The polymer properties accessed can in turn affect the physicochemical properties of the core of the nanoparticles formed from these species. These monomers can also allow for the adaptation of the biocompatible and biodegradable nature of the resulting polyesters which could aid their use as nanocarriers. For example, the incorporation of a carboxylic acid group in the polymer backbone, introduced by the ROP of malide dibenzyl ester followed by acid deprotection, achieves faster hydrolysis compared to non-functionalised PLA.<sup>181,182</sup> Modifications to the  $\epsilon$ -CL monomer ring can be introduced at 3 different positions on the lactone ring,  $\alpha$ -,  $\beta$ - or  $\gamma$ -positions.<sup>158</sup> Functionalisation at the  $\gamma$ -position include the addition of *tert*-butyldimethylsilane groups (1), ketal functionality (2), ketones (3) or carboxylate groups (4) some of which can serve as protecting groups that can be removed after polymerisation to ultimately achieve hydroxyl groups (Figure 1.12, Table 1.3).<sup>155,183–185</sup> Reports of  $\beta$ -substituted  $\epsilon$ -caprolactones are significantly more rare in the literature with only a small number of publications dedicated to them.<sup>158</sup> Nonetheless  $\alpha$ -substituted  $\epsilon$ -caprolactones have yielded numerous monomers with functionalities that include (5) halogenated, (6) alkyne and (7) alkene functionalities which allow for click and thiol-ene reactions to be undertaken post-polymerisation (Figure 1.12, Table 1.3).<sup>158,169,171,186</sup> Further complex adaptations can include the incorporation of an initiating group that can be used in sub-sequential polymerisations, for example atom transfer radical polymerisation (8), allowing the formation of co-polymers with various architecture which could further tune the physicochemical properties of the resulting materials.<sup>187</sup> Additional modifications can be made to yield difunctional monomers, such as 2,2-bis( $\epsilon$ -caprolactone-4-yl) and 4,4'-bioxepanyl-7,7'-dione, *BOD*, which are capable of cross-linking polyester chains when employed in ROP polymerisations (Table 1.3).<sup>155,180</sup>

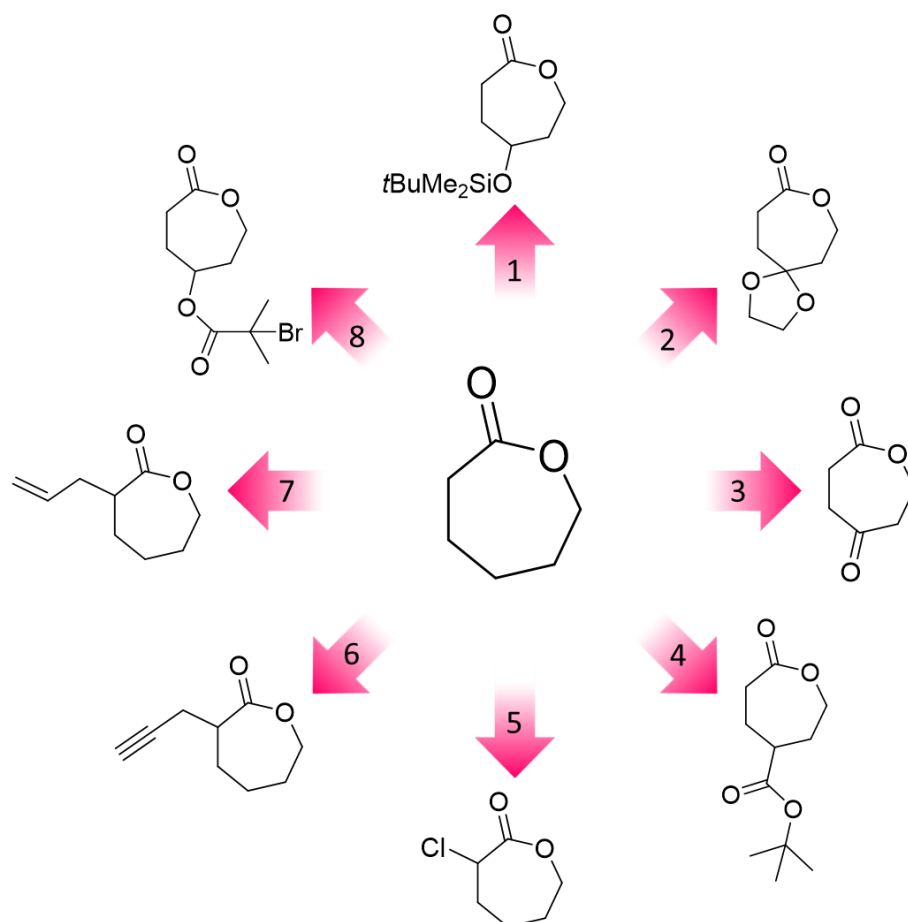


**Figure 1.12 – Examples of functionalised 7-membered lactones used as monomers.**

(1) 5-((tert-butyl dimethylsilyl)oxy)oxepan-2-one, (2) 5-ethylene ketal  $\epsilon$ -caprolactone, (3) oxepane-2,5-dione, (4)  $\gamma$ -tert-butyl carboxylate- $\epsilon$ -caprolactone, (5)  $\alpha$ -chloro-caprolactone, (6)  $\alpha$ -propargyl- $\epsilon$ -caprolactone, (7)  $\alpha$ -allyl- $\epsilon$ -caprolactone and (8)  $\gamma$ -(2-bromo-2-methyl propionyl)- $\epsilon$ -caprolactone.

These modifications are achieved in numerous different ways and vary depending on the ring size and the desired functionality. These synthetic routes often arise from the adaptation of the methods used to synthesise the basic monomer forms. For example functionalised 4-membered  $\beta$ -lactones are yielded from either a [2+2] cycloaddition of a ketene and an aldehyde or the metal-based Lewis acid catalysed carbonylation of epoxides, the latter of which has been shown to yield both *cis*- and *trans*-  $\beta$ -lactones.<sup>154,188–190</sup> 6-membered lactide monomers have a number of routes to formation and therefore have a number of routes to introduce functionality, two examples being dimerization of  $\alpha$ -hydroxyl acids (which can only yield homo-bifunctional lactide monomers) and the condensation of  $\alpha$ -haloacyl halides/-halocarboxylic acids and  $\alpha$ -hydroxyl acids followed by lactonisation (can yield hetero-bifunctional lactide monomers).<sup>154,191–193</sup> 7-membered functional lactones can also be created *via* lactonisation, but this is difficult due to competing reactions and results in low yields.<sup>154,194</sup> The preferred method of synthesis is Baeyer-Villiger oxidation of cyclic ketones following Chapman-Stevens

oxidation of cyclic alcohols.<sup>185,195,196</sup> This is an attractive route to monomers due to the diversity in both available cyclic ketones and catalysts.<sup>154</sup> Its success has effectively yielded numerous monomers with varying ring functionality from ketones and halides to ethers.<sup>154,184,197,198</sup>

Although many complex modifications have been made to 6 and 7 membered lactone rings to widely vary the properties of the polymers produced, literature seems to be lacking for the investigations and effects that simpler modifications might have on the resulting polyesters. These, unlike the monomers detailed above in Table 1.3, require less complex synthesis and remove the need to protect any functional groups that may take part in the reaction (e.g. hydroxyl, carboxylic acid and amine groups).<sup>155</sup> Investigating smaller modifications by adding and varying an alkyl side chain could allow for fine tuning of properties, creating subtle changes to the polymers physical properties (e.g.  $T_g$  and crystallinity) that could significantly impact the interactions of the polymer with drug molecules.

Comparatively for most of these functionalised monomers their controlled ROP is usually achieved by the use of metal based catalysts such as aluminium alkoxide or tin (II) octanoate (see Scheme 1) and also high reaction temperatures.<sup>155</sup> This results in polymers that are usually hard to purify due to metal residue. Few reports have shown the use of organo-catalysts in the case of functionalised polyesters, most polymerisations of this nature utilise tin (II) octanoate.<sup>156</sup> This allows for the opportunity to explore new boundaries by implementing organo-catalysed ROP along with the novel monomers to produce a series of polymers with tailored physical properties.

### **1.6 Aims of the project**

The following PhD research aims to ultimately create a number of nanoparticle formulations centred on caprolactone-based polymers. These nanoparticle dispersions' capability of encapsulating and delivering the active drug metabolite of irinotecan, SN-38 will be explored. Leading to this ultimate outcome this research will investigate the potential to vary the polymer backbone to achieve varying physicochemical properties of the resulting polymers.

The synthesis of a number of substituted caprolactone monomers that have varying alkyl groups of increasing chain length (Figure 1.13) will be attempted by Baeyer-Villiger oxidation. The addition of these side chains is hypothesised to effect the thermal properties of the resulting polymers allowing the potential for the tuning of the semi-crystallinity seen with PCL. Implementation of these monomers in an acid catalysed ring opening polymerisation method

will allow for the creation of linear polymers with the potential to create polymers of varying architecture. The inclusion of a branching bis-lactone monomer BOD should allow access to a modified ‘Strathclyde’ approach (discussed in Chapter 2, Section 2.1.2.2) within the polymerisations to achieve branched architectures. Furthermore the variation of the initiator used in these polymerisations to include PEG is expected to result in the production of linear and branched block co-polymers (Figure 1.13)

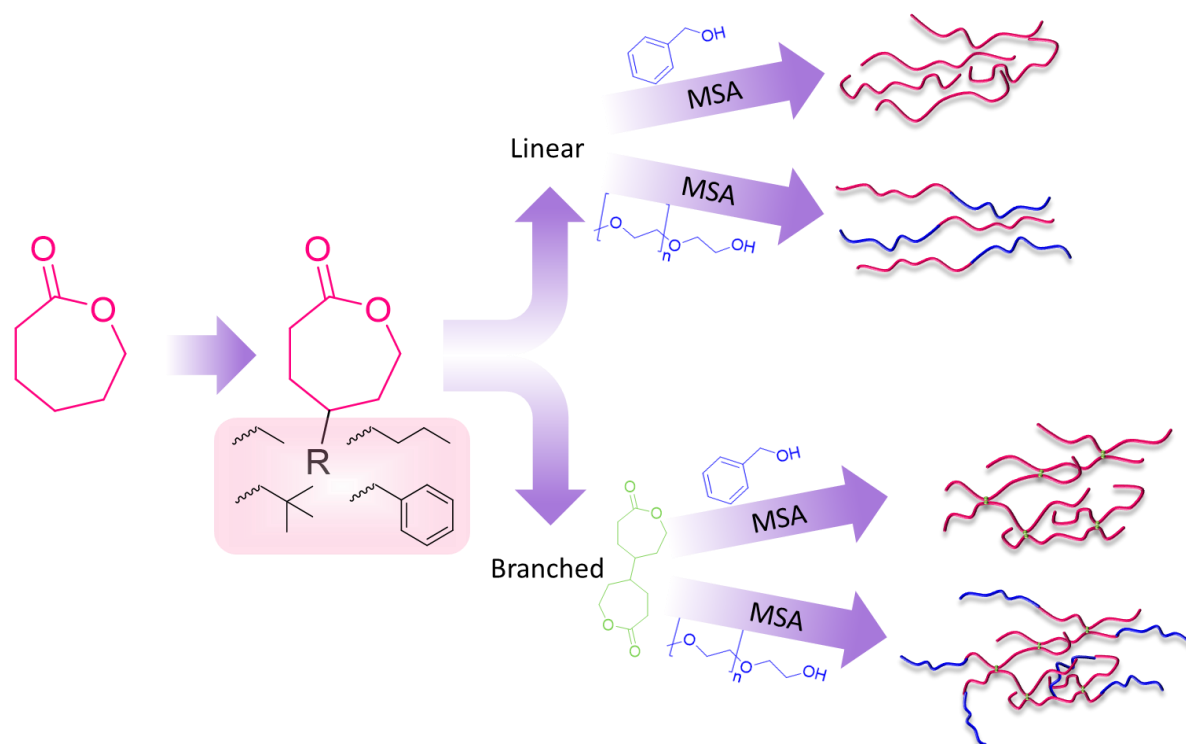


**Figure 1.13- Schematic representation of aims of the project involving polymerisation to produce linear and branched species.**

As there are a variety of methods to form polymeric nanoparticles the library of polymers, resulting from the synthetic programme, will initially be studied using a rapid (co)nanoprecipitation method. This should allow for the testing of the hypothesis that composition and architecture of the polymeric species affect the characteristics and stability of the resulting polyester nanoparticles (Figure 1.14). Salt studies could also provide complementary data to further analyse the roles of architecture and PEGylation. Considering previous research within the Rannard group, it is hypothesised that the implementation of a branched architecture would result in the production of smaller nanoparticles when compared to polymers of linear architecture. Additionally the presence of hydrophilic PEG coronas should result in increased salt stability due to the induction of steric stability in contrast to charge stabilisation.

Finally the ability of the nanoparticles to encapsulate guest molecules and ultimately SN-38 must be explored to permit comparisons to similar systems within the literature (Figure 1.14). Development of the encapsulation method would allow for the evaluation of optimum drug loading potential and the stability of the resulting dispersions. The aim to create nanoparticle systems capable of encapsulating SN-38, possessing stability over time and decorated with a PEGylated corona will open up the opportunity for pharmacological studies to evaluate the rate of drug release, the cytotoxicity of nanoparticles with and without drug. *In vitro* studies evaluating release, toxicity and cellular uptake of nanoparticle systems should help to establish the viability of these systems. It is expected that the collection of results during *in vitro* investigations will enable selections for *in vivo* studies to be undertaken. It is hypothesised that the nanoparticle dispersions will induce slower release rates when compared to free SN-38 and the encapsulation of the drug within the polymer matrix will mitigate the offsite toxicities linked to SN-38 *in vivo*.

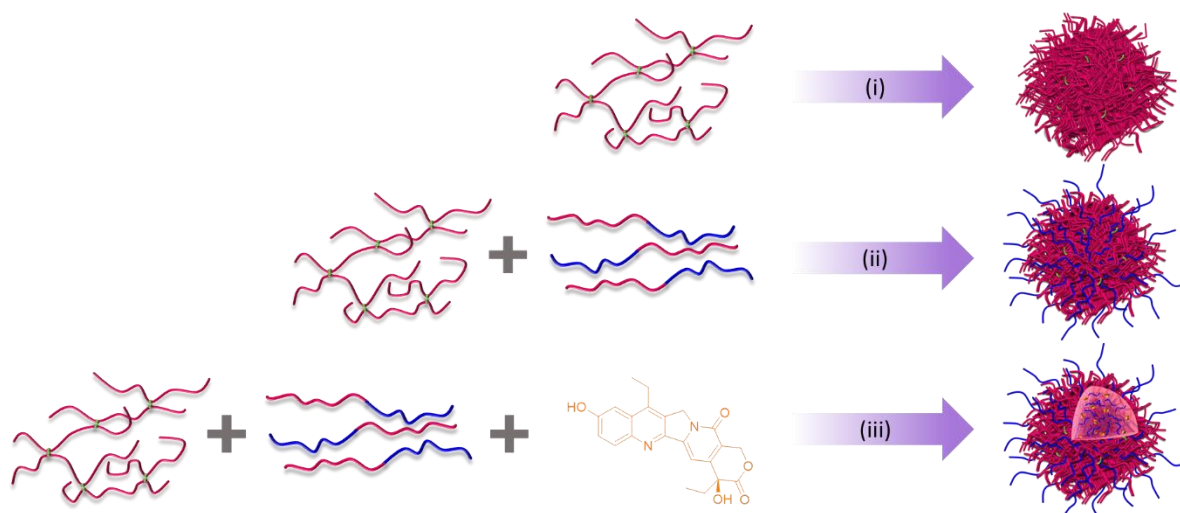


**Figure 1.14 – Schematic representation of the nanoprecipitation aims of this work.**

Involving the (i) nanoprecipitation of singular species, (ii) co-nanoprecipitation of two species simultaneously and (iii) encapsulation of hydrophobic guest molecules, in particular SN-38.

## References

- 1 Oxford Dictionary, Main definitions of Cancer in English, <https://en.oxforddictionaries.com/definition/cancer>, (accessed 4 February 2019).
- 2 National Cancer Institute, What Is Cancer?, <https://www.cancer.gov/about-cancer/understanding/what-is-cancer>, (accessed 4 February 2019).
- 3 G. M. Cooper, *A Cell: A Molecular Approach*, Sinauer Associates, Sunderland (MA), 2nd Ed., 2000.
- 4 National Cancer Institute, NCI Dictionary of Cancer Terms - Malignancy, <https://www.cancer.gov/publications/dictionaries/cancer-terms/def/malignancy>, (accessed 29 July 2019).
- 5 F. Bray, J. Ferlay, I. Soerjomataram, R. L. Siegel, L. A. Torre and A. Jemal, *CA A Cancer J. Clin.*, 2018, **68**, 394–424.
- 6 M. Arnold, M. S. Sierra, M. Laversanne, I. Soerjomataram, A. Jemal and F. Bray, *Gut*, 2017, **66**, 683–691.
- 7 M. Kekelidze, L. D’Errico, M. Pansini, A. Tyndall and J. Hohmann, *World J. Gastroenterol.*, 2013, **19**, 8502–8514.
- 8 A. M. Leufkens, M. A. A. J. van den Bosch, M. S. van Leeuwen and P. D. Siersema, *Scand. J. Gastroenterol.*, 2011, **46**, 887–894.
- 9 M. De Rosa, U. Pace, D. Rega, V. Costabile, F. Duraturo, P. Izzo and P. Delrio, *Oncol. Rep.*, 2015, **34**, 1087–1096.
- 10 L. R. Zarour, S. Anand, K. G. Billingsley, W. H. Bisson, A. Cercek, M. F. Clarke, L. M. Coussens, C. E. Gast, C. B. Geltzeiler, L. Hansen, K. A. Kelley, C. D. Lopez, S. R. Rana, R. Ruhl, V. L. Tsikitis, G. M. Vaccaro, M. H. Wong and S. C. Mayo, *Cell. Mol. Gastroenterol. Hepatol.*, 2017, **3**, 163–173.
- 11 W. Hohenberger, K. Weber, K. Matzel, T. Papadopoulos and S. Merkel, *Color. Dis.*, 2009, **11**, 354–364.
- 12 K. Sondenaa, P. Quirke, W. Hohenberger, K. Sugihara, H. Kobayashi, H. Kessler, G. Brown, V. Tudyka, A. D’Hoore, R. H. Kennedy, N. P. West, S. H. Kim, R. Heald, K. E. Storli, A. Nesbakken and B. Moran, *Int. J. Colorectal Dis.*, 2014, **29**, 419–428.
- 13 G. P. Kanas, A. Taylor, J. N. Primrose, W. J. Langeberg, M. A. Kelsh, F. S. Mowat, D. D. Alexander, M. A. Choti and G. Poston, *Clin Epidemiol.*, 2012, **4**, 283–301.
- 14 E. P. Misiakos, N. P. Karidis and G. Kouraklis, *World J. Gastroenterol.*, 2011, **17**, 4067–4075.
- 15 S. R. Alberts and L. D. Wagman, *Oncologist*, 2008, **13**, 1063–1073.
- 16 G. F. Gustavsson B, Carlsson G, D Machover, Petrelli N, Roth A, Schmoll HJ, Tveit KM, *Clin. Colorectal Cancer*, 2014, **14**, 1–10.
- 17 D. B. Longley, D. P. Harkin and P. G. Johnston, *Nat Rev Cancer*, 2003, **3**, 330–8.
- 18 K. Chen, Y. Gong, Q. Zhang, Y. Shen and T. Zhou, *Medicine (Baltimore)*, 2016, **95**, e5221–e5221.

- 19 R. J. Gibson and D. M. K. Keefe, *Support. Care Cancer*, 2006, **14**, 890–900.
- 20 N. Zdenkowski, S. Chen, A. van der Westhuizen and S. Ackland, *Oncologist*, 2012, **17**, 201–211.
- 21 Y. Pommier, P. Pourquier, Y. Fan and D. Strumberg, *Biochim. Biophys. Acta - Gene Struct. Expr.*, 1998, **1400**, 83–106.
- 22 M. Huang, H. Gao, Y. Chen, H. Zhu, Y. Cai, X. Zhang, Z. Miao, H. Jiang, J. Zhang, H. Shen, L. Lin, W. Lu and J. Ding, *Clin. Cancer Res.*, 2007, **13**, 1298–1307.
- 23 C. Marchand, S. Antony, K. W. Kohn, M. Cushman, A. Ioanoviciu, B. L. Staker, A. B. Burgin, L. Stewart and Y. Pommier, *Mol. Cancer Ther.*, 2006, **5**, 287–296.
- 24 G. S. Laco, *PLoS One*, 2011, **6**, 1–7.
- 25 A. Y. Chen and L. F. Liu, *Annu. Rev. Pharmacol. Toxicol.*, 1994, **34**, 191–218.
- 26 Y. Hsiang, M. G. Lihou and L. F. Liu, *Cancer Res.*, 1989, **49**, 5077–5082.
- 27 C. Holm, J. M. Covey, D. Kerrigan and Y. Pommier, *Cancer Res.*, 1989, **49**, 6365–6368.
- 28 R. J. Gibson, J. M. Bowen, M. R. B. Inglis, A. G. Cummins and D. M. K. Keefe, *J. Gastroenterol. Hepatol.*, 2003, **18**, 1095–1100.
- 29 A. Alimonti, A. Gelibter, I. Pavese, F. Satta, F. Cognetti, G. Ferretti, D. Rasio, A. Vecchione and M. Di Palma, *Cancer Treat. Rev.*, 2004, **30**, 555–562.
- 30 M. Fittkau, W. Voigt, H. J. Holzhausen and H. J. Schmoll, *J. Cancer Res. Clin. Oncol.*, 2004, **130**, 388–394.
- 31 M. Ma and H. McLeod, *Curr. Med. Chem.*, 2003, **10**, 41–49.
- 32 R. P. Jones, P. Sutton, R. M. D. Greensmith, A. Santoyo-Castelazo, D. F. Carr, R. Jenkins, C. Rowe, J. Hamlett, B. K. Park, M. Terlizzo, E. O’Grady, P. Ghaneh, S. W. Fenwick, H. Z. Malik, G. J. Poston and N. R. Kitteringham, *Cancer Chemother. Pharmacol.*, 2013, **72**, 359–368.
- 33 D. Bobo, K. J. Robinson, J. Islam, K. J. Thurecht and S. R. Corrie, *Pharm. Res.*, 2016, **33**, 2373–2387.
- 34 M. Kurd, S. Sadegh Malvajerd, S. Rezaee, M. Hamidi and K. Derakhshandeh, *Artif. cells, nanomedicine, Biotechnol.*, 2019, **47**, 2123–2133.
- 35 R. P. Bakshi, L. M. Tatham, A. C. Savage, A. K. Tripathi, G. Mlambo, M. M. Ippolito, E. Nenortas, S. P. Rannard, A. Owen and T. A. Shapiro, *Nat. Commun.*, 2018, **9**, 1–8.
- 36 A. Kumari, S. K. Yadav and S. C. Yadav, *Colloids Surfaces B Biointerfaces*, 2010, **75**, 1–18.
- 37 S. Senapati, A. Kumar Mahanta, S. Kumar and P. Maiti, *Signal Transduct. Target. Ther.*, 2018, **3**, 1–19.
- 38 A. Jurj, C. Braicu, L. A. Pop, C. Tomuleasa, C. D. Gherman and I. Berindan-Neagoe, *Drug Des. Devel. Ther.*, 2017, **11**, 2871–2890.
- 39 A. R. Town, J. Taylor, K. Dawson, E. Niezabitowska, N. M. Elbaz, A. Corker, E. Garcia-tun and T. O. McDonald, *J. Mater. Chem. B*, 2019, **7**, 373–383.

- 40 A. Gordillo-Galeano and C. E. Mora-Huertas, *Eur. J. Pharm. Biopharm.*, 2018, **133**, 285–308.
- 41 J. J. Hobson, A. Al-khouja, P. Curley, D. Meyers, C. Flexner, M. Siccardi, A. Owen, C. F. Meyers and S. P. Rannard, *Nat. Commun.*, 2019, **10**, 1–10.
- 42 S. K. Libutti, G. F. Paciotti, A. A. Byrnes, H. R. Alexander, W. E. Gannon, M. Walker, G. D. Seidel, N. Yuldasheva and L. Tamarkin, *Clin. Cancer Res.*, 2010, **16**, 6139–6149.
- 43 B. Thiesen and A. Jordan, *Int. J. Hyperth.*, 2008, **24**, 467–474.
- 44 R. Berges, *Eur. Urol. Suppl.*, 2005, **4**, 20–25.
- 45 J. Ford, P. Chambon, J. North, F. L. Hatton, M. Giardiello, A. Owen and S. P. Rannard, *Macromolecules*, 2015, **48**, 1883–1893.
- 46 K. Riehemann, S. W. Schneider, T. A. Luger, B. Godin, M. Ferrari and H. Fuchs, *Angew. Chemie Int. Ed.*, 2009, **48**, 872–897.
- 47 G. Lövestam, H. Rauscher, G. Roebben, B. S. Klüttgen, N. Gibson, J. Putaud and H. Stamm, *Considerations on a Definition of Nanomaterial for Regulatory Purposes*, 2010.
- 48 O. Dechy-Cabaret, B. Martin-Vaca and D. Bourissou, *Chem. Rev.*, 2004, **104**, 6147–6176.
- 49 V. P. Torchilin, *AAPS J.*, 2007, **9**, 128–147.
- 50 H. Boulaiz, P. J. Alvarez, A. Ramirez, J. A. Marchal, J. Prados, F. Rodríguez-Serrano, M. Perán, C. Melguizo and A. Aranega, *Int. J. Mol. Sci.*, 2011, **12**, 3303–3321.
- 51 N. D. James, R. J. Coker, D. Tomlinson, J. R. W. Harris, M. Gompels, A. J. Pinching and J. S. W. Stewart, *Clin. Oncol.*, 1994, **6**, 294–296.
- 52 A. Wang-Gillam, C. P. Li, G. Bodoky, A. Dean, Y. S. Shan, G. Jameson, T. MacArulla, K. H. Lee, D. Cunningham, J. F. Blanc, R. A. Hubner, C. F. Chiu, G. Schwartzmann, J. T. Siveke, F. Braiteh, V. Moyo, B. Belanger, N. Dhindsa, E. Bayever, D. D. Von Hoff and L. T. Chen, *Lancet*, 2016, **387**, 545–557.
- 53 R. Lencioni and D. Cioni, *Hepatic Oncol.*, 2016, **3**, 193–200.
- 54 X. Tian, M. Nguyen, H. P. Foote, J. M. Caster, K. C. Roche, C. G. Peters, P. Wu, L. Jayaraman, E. G. Garmey, J. E. Tepper, S. Eliasof and A. Z. Wang, *Cancer Res.*, 2017, **77**, 112–122.
- 55 V. Venugopal, S. Krishnan, V. R. Palanimuthu, S. Sankarankutty, J. K. Kalaimani, S. Karupiah, N. S. Kit and T. T. Hock, *PLoS One*, 2018, **13**, 1–17.
- 56 X. Guo, X. Kang, Y. Wang, X. Zhang, C. Li and Y. Liu, *Acta Biomater.*, 2019, **84**, 367–377.
- 57 S. V. K. Rompicharla, P. Kumari, H. Bhatt, B. Ghosh and S. Biswas, *Int. J. Pharm.*, 2019, **557**, 329–341.
- 58 M. E. Davis, *Mol. Pharm.*, 2009, **6**, 659–668.
- 59 A. C. Eifler and C. S. Thaxton, *Biomedical Nanotechnology: Methods and Protocols*, 2011, vol. 726.



- 60 S. Ashton, Y. H. Song, J. Nolan, E. Cadogan, J. Murray, R. Odedra, J. Foster, P. A. Hall, S. Low, P. Taylor, R. Ellston, U. M. Polanska, J. Wilson, C. Howes, A. Smith, R. J. A. Goodwin, J. G. Swales, N. Strittmatter, Z. Takáts, A. Nilsson, P. Andren, D. Trueman, M. Walker, C. L. Reimer, G. Troiano, D. Parsons, D. De Witt, M. Ashford, J. Hrkach, S. Zale, P. J. Jewsbury and S. T. Barry, *Sci. Transl. Med.*, 2016, **8**, 1–11.
- 61 N. Floc'h, S. Ashton, D. Ferguson, P. Taylor, L. S. Carnevalli, A. M. Hughes, E. Harris, M. Hattersley, S. Wen, N. J. Curtis, J. E. Pilling, L. A. Young, K. Maratea, E. J. Pease and S. T. Barry, *Mol. Cancer Ther.*, 2019, **18**, 1–33.
- 62 A. Varela-Moreira, Y. Shi, M. H. A. M. Fens, T. Lammers, W. E. Hennink and R. M. Schiffelers, *Mater. Chem. Front.*, 2017, **1**, 1485–1501.
- 63 K. Maier-Hauff, F. Ulrich, D. Nestler, H. Niehoff, P. Wust, B. Thiesen, H. Orawa, V. Budach and A. Jordan, *J. Neurooncol.*, 2011, **103**, 317–324.
- 64 D. Peer, J. M. Karp, S. Hong, O. C. Farokhzad, R. Margalit and R. Langer, *Nat. Nanotechnol.*, 2007, **2**, 751–760.
- 65 K. Greish, J. Fang, T. Inutsuka, A. Nagamitsu and H. Maeda, *Clin. Pharmacokinet.*, 2003, **42**, 1089–1105.
- 66 J. Fang, H. Nakamura and H. Maeda, *Adv. Drug Deliv. Rev.*, 2011, **63**, 136–151.
- 67 Y. Nakamura, A. Mochida, P. L. Choyke and H. Kobayashi, *Bioconjug. Chem.*, 2016, **27**, 2225–2238.
- 68 H. Hashizume, P. Baluk, S. Morikawa, J. W. McLean, G. Thurston, S. Roberge, R. K. Jain and D. M. McDonald, *Am. J. Pathol.*, 2000, **156**, 1363–1380.
- 69 M. K. Danquah, X. A. Zhang and R. I. Mahato, *Adv. Drug Deliv. Rev.*, 2011, **63**, 623–639.
- 70 D. M. McDonald, G. Thurston and P. Baluk, *Microcirculation*, 1999, **6**, 7–22.
- 71 D. Peer, J. M. Karp, S. Hong, O. C. Farokhzad, R. Margalit and R. Langer, *Nat. Nanotechnol.*, 2007, **2**, 751–760.
- 72 J. H. Senior, *Crit. Rev. Ther. Drug Carrier Syst.*, 1987, **3**, 123–193.
- 73 R. Bazak, M. Houry, S. El Achy, S. Kamel and T. Refaat, *J. Cancer Res. Clin. Oncol.*, 2014, **141**, 769–784.
- 74 D. Le Garrec, J. Taillefer, J. E. Van Lier, V. Lenaerts and J. C. Leroux, *J. Drug Target.*, 2002, **10**, 429–437.
- 75 S. Gammas, K. Suzuki, C. Sone, Y. Sakurai, K. Kataoka and T. Okano, *J. Control. Release*, 1997, **48**, 157–164.
- 76 G. Pillai, *Nanotechnology Toward Treating Cancer*, Elsevier Inc., 2018.
- 77 S. D. Steichen, M. Caldorera-Moore and N. A. Peppas, *Eur. J. Pharm. Sci.*, 2013, **48**, 416–427.
- 78 H. S. Yoo and T. G. Park, *J. Control. Release*, 2004, **96**, 273–283.
- 79 R. K. Jani and G. Krupa, *J. Drug Deliv. Ther.*, 2019, **9**, 408–415.

- 80 R. Domínguez-Ríos, D. R. Sánchez-Ramírez, K. Ruiz-Saray, P. E. Ocegüera-Basurto, M. Almada, J. Juárez, A. Zepeda-Moreno, A. del Toro-Arreola, A. Topete and A. Daneri-Navarro, *Colloids Surfaces B Biointerfaces*, 2019, **178**, 199–207.
- 81 D. P. English, D. M. Roque and A. D. Santin, *Mol. Diagnosis Ther.*, 2013, **17**, 85–99.
- 82 F. Y. Hern, A. Hill, A. Owen and S. P. Rannard, *Polym. Chem.*, 2018, **9**, 1767–1771.
- 83 F. L. Hatton, L. M. Tatham, L. R. Tidbury, P. Chambon, T. He, A. Owen and S. P. Rannard, *Chem. Sci.*, 2015, **6**, 326–334.
- 84 F. L. Hatton, P. Chambon, T. O. McDonald, A. Owen and S. P. Rannard, *Chem. Sci.*, 2014, **5**, 1844–1853.
- 85 A. Buczkowski, S. Sekowski, A. Grala, D. Palecz, K. Milowska, P. Urbaniak, T. Gabryelak, H. Piekarski and B. Palecz, *Int. J. Pharm.*, 2011, **408**, 266–270.
- 86 K. Ulbrich, K. Holá, V. Šubr, A. Bakandritsos, J. Tuček and R. Zbořil, *Chem. Rev.*, 2016, **116**, 5338–5431.
- 87 A. Akbarzadeh, R. Rezaei-Sadabady, S. Davaran, S. W. Joo, N. Zarghami, Y. Hanifehpour, M. Samiei, M. Kouhi and K. Nejati-Koshki, *Nanoscale Res. Lett.*, 2013, **8**, 1–8.
- 88 J. J. Hobson, S. Edwards, R. A. Slater, P. Martin, A. Owen and S. P. Rannard, *RSC Adv.*, 2018, **8**, 12984–12991.
- 89 K. Letchford and H. Burt, *Eur. J. Pharm. Biopharm.*, 2007, **65**, 259–269.
- 90 M. Rangasamy, *J. Appl. Pharm. Sci.*, 2011, **1**, 08–16.
- 91 E. Abbasi, S. F. Aval, A. Akbarzadeh, M. Milani, H. T. Nasrabadi, S. W. Joo, Y. Hanifehpour, K. Nejati-Koshki and R. Pashaei-Asl, *Nanoscale Res. Lett.*, 2014, **9**, 1–10.
- 92 A. C. Savage, L. M. Tatham, M. Siccardi, T. Scott, M. Vourvahis, A. Clark, S. P. Rannard and A. Owen, *Eur. J. Pharm. Biopharm.*, 2019, **138**, 30–36.
- 93 J. K. Patra, G. Das, L. F. Fraceto, E. V. R. Campos, M. D. P. Rodriguez-Torres, L. S. Acosta-Torres, L. A. Diaz-Torres, R. Grillo, M. K. Swamy, S. Sharma, S. Habtemariam and H. S. Shin, *J. Nanobiotechnology*, 2018, **16**, 1–33.
- 94 D. Lombardo, M. A. Kiselev and M. T. Caccamo, *J. Nanomater.*, 2019, **2019**, 1–26.
- 95 C. J. Martínez Rivas, M. Tarhini, W. Badri, K. Miladi, H. Greige-Gerges, Q. A. Nazari, S. A. Galindo Rodríguez, R. Á. Román, H. Fessi and A. Elaissari, *Int. J. Pharm.*, 2017, **532**, 66–81.
- 96 B. V. N. Nagavarma, H. K. S. Yadav, A. Ayaz, L. S. Vasudha and H. G. Shivakumar, *Asian J. Pharm. Clin. Res.*, 2012, **5**, 16–23.
- 97 R. Duncan and L. Izzo, *Adv. Drug Deliv. Rev.*, 2005, **57**, 2215–2237.
- 98 H. Zhang, D. Wang, R. Butler, N. L. Campbell, J. Long, B. Tan, D. J. Duncalf, A. J. Foster, A. Hopkinson, D. Taylor, D. Angus, A. I. Cooper and S. P. Rannard, *Nat. Nanotechnol.*, 2008, **3**, 506–511.
- 99 A. Owen and S. Rannard, *Adv. Drug Deliv. Rev.*, 2016, **103**, 144–156.

- 100 S. Verma, R. Gokhale and D. J. Burgess, *Int. J. Pharm.*, 2009, **380**, 216–222.
- 101 E. Sánchez-López, M. Guerra, J. Dias-Ferreira, A. Lopez-Machado, M. Ettcheto, A. Cano, M. Espina, A. Camins, M. L. Garcia and E. B. Souto, *Nanomaterials*, 2019, **9**, 821.
- 102 A. Gupta, H. B. Eral, T. A. Hatton and P. S. Doyle, *Soft Matter*, 2016, **12**, 2826–2841.
- 103 N. Sharma, S. Mishra, S. Sharma, R. D. Deshpande and R. Kumar Sharma, *Int. J. Drug Dev. Res.*, 2013, **5**, 37–48.
- 104 G. Romero and S. E. Moya, *Synthesis of organic nanoparticles*, 2012, vol. 4.
- 105 H. Koide, T. Asai, K. Hatanaka, S. Akai, T. Ishii, E. Kenjo, T. Ishida, H. Kiwada, H. Tsukada and N. Oku, *Int. J. Pharm.*, 2010, **392**, 218–223.
- 106 Health Products Distributors, Liposomes, <http://www.integratedhealth.com/supplements/liposomes.html?mode=list>, (accessed 13 March 2020).
- 107 F. Masood, *Mater. Sci. Eng. C*, 2016, **60**, 569–578.
- 108 S. P. Egusquiaguirre, J. L. Pedraz, R. M. Hernández and M. Igartua, *Nanotherapeutic Platforms for Cancer Treatment: From Preclinical Development to Clinical Application*, Elsevier Inc., 2016.
- 109 F. L. Hatton, P. Chambon, A. C. Savage and S. P. Rannard, *Chem. Commun.*, 2016, **52**, 3915–3918.
- 110 M. Siccardi, P. Martin, D. Smith, P. Curley, T. McDonald, M. Giardiello, N. Liptrott, S. Rannard and A. Owen, *J. Interdiscip. Nanomedicine*, 2016, **1**, 110–123.
- 111 M. Farha, E. Masson, H. Tomkinson and G. Mugundu, *J. Clin. Pharmacol.*, 2019, **59**, 463–471.
- 112 C. Tistaert, T. Heimbach, B. Xia, N. Parrott, T. S. Samant and F. Kesisoglou, *J. Pharm. Sci.*, 2019, **108**, 592–602.
- 113 N. J. Liptrott, M. Giardiello, T. O. McDonald, S. P. Rannard and A. Owen, *J. Nanobiotechnology*, 2018, **16**, 1–15.
- 114 R. J. Malcolmson and J. K. Embleton, *Pharm. Sci. Technol. Today*, 1998, **1**, 394–398.
- 115 R. H. Muller and K. Peters, *Int. J. Pharm.*, 1998, **160**, 229–237.
- 116 M. Giardiello, N. J. Liptrott, T. O. McDonald, D. Moss, M. Siccardi, P. Martin, D. Smith, R. Gurjar, S. P. Rannard and A. Owen, *Nat. Commun.*, 2016, **7**, 1–10.
- 117 A. Z. Mirza and F. A. Siddiqui, *Int. Nano Lett.*, 2014, **4**, 1–7.
- 118 V. Mody, R. Siwale, A. Singh and H. Mody, *J. Pharm. Bioallied Sci.*, 2010, **2**, 282.
- 119 P. K. Jain, X. Huang, I. H. El-Sayed and M. A. El-Sayed, *Plasmonics*, 2007, **2**, 107–118.
- 120 P. N. Prasad, *Nanophotonics*, John Wiley & Sons Inc., 2004.
- 121 G. Xu, S. Zeng, B. Zhang, M. T. Swihart, K. T. Yong and P. N. Prasad, *Chem. Rev.*, 2016, **116**, 12234–12327.

- 122 J. Liu, T. Liu, S. Nie, S. K. Lau, V. A. Varma, J. A. Petros, A. O. Osunkoya, R. A. Moffitt, M. Caldwell, M. D. Wang, A. N. Young, T. Krogstad and B. Leyland-Jones, *ACS Nano*, 2010, **4**, 2755–2765.
- 123 C. B. Murray, D. J. Norris and M. G. Bawendi, *J. Am. Chem. Soc.*, 1993, **115**, 8706–8715.
- 124 R. Bilan, I. Nabiev and A. Sukhanova, *ChemBioChem*, 2016, **17**, 2103–2114.
- 125 V. Noireaux, B. Dubertret, P. Skourides, D. J. Norris, V. Noireaux, A. H. Brivanlou and A. Libchaber, *Science (80-. )*, 2002, **298**, 1759–1762.
- 126 G. J. Halder, C. J. Kepert, B. Moubaraki, K. S. Murray and J. D. Cashion, *Science (80-. )*, 2002, **298**, 1762–1765.
- 127 N. Huang, H. Wang, J. Zhao, H. Lui, M. Korbelik and H. Zeng, *Lasers Surg. Med.*, 2010, **42**, 638–648.
- 128 N. Ahmed, H. Fessi and A. Elaissari, *Drug Discov. Today*, 2012, **17**, 928–934.
- 129 K. H. Son, J. H. Hong and J. W. Lee, *Int. J. Nanomedicine*, 2016, **11**, 5163–5185.
- 130 S. Farah, D. G. Anderson and R. Langer, *Adv. Drug Deliv. Rev.*, 2016, **107**, 367–392.
- 131 M. A. Woodruff and D. W. Hutmacher, *Prog. Polym. Sci.*, 2010, **35**, 1217–1256.
- 132 Houghton Mifflin Company, *The American Heritage Medical Dictionary*, Houghton Mifflin Company, 2007.
- 133 C. K. Williams, *Chem. Soc. Rev.*, 2007, **36**, 1573–1580.
- 134 J. Lunt, *Polym. Degrad. Stab.*, 2002, **59**, 145–152.
- 135 U. F. and D. Administration, Inventory of Effective Food Contact Substance (FCS) Notifications, [https://www.accessdata.fda.gov/scripts/fdcc/?set=FCN&id=475&sort=FCN\\_No&order=DESC&startrow=1&type=basic&search=lactide](https://www.accessdata.fda.gov/scripts/fdcc/?set=FCN&id=475&sort=FCN_No&order=DESC&startrow=1&type=basic&search=lactide), (accessed 24 July 2019).
- 136 K.-T. Kim, J.-Y. Lee, D.-D. Kim, I.-S. Yoon and H.-J. Cho, *Pharmaceutics*, 2019, **11**, 280.
- 137 K. Hamad, M. Kaseem, H. W. Yang, F. Deri and Y. G. Ko, *Express Polym. Lett.*, 2015, **9**, 435–455.
- 138 S. Sun, H. Li, J. Chen and Q. Qian, *Physiology*, 2017, **32**, 453–463.
- 139 L. W. McKeen, *Plastics Used in Medical Devices*, Elsevier Inc., 2013.
- 140 B. S. Zolnik and D. J. Burgess, *J. Control. Release*, 2007, **122**, 338–344.
- 141 D. Chen, F. Zhang, J. Wang, H. He, S. Duan, R. Zhu, C. Chen, L. Yin and Y. Chen, *Front. Pharmacol.*, 2018, **9**, 1–9.
- 142 A. Pardanani, C. Harrison, J. E. Cortes, F. Cervantes, R. A. Mesa, D. Milligan, T. Masszi, E. Mishchenko, E. Jourdan, A. M. Vannucchi, M. W. Drummond, M. Jurgutis, K. Kuliczowski, E. Gheorghita, F. Passamonti, F. Neumann, A. Patki, G. Gao and A. Tefferi, *JAMA Oncol.*, 2015, **1**, 643–651.
- 143 M. Labet and W. Thielemans, *Chem. Soc. Rev.*, 2009, **38**, 3484–3504.

- 144 R. P. Brannigan and A. P. Dove, *Biomater. Sci.*, 2017, **5**, 9–21.
- 145 S. A. Metz, N. Chegini and B. J. Masterson, *Biomaterials*, 1990, **11**, 41–45.
- 146 P. Grossen, D. Witzigmann, S. Sieber and J. Huwyler, *J. Control. Release*, 2017, **260**, 46–60.
- 147 X. Shuai, T. Merdan, A. K. Schaper, F. Xi and T. Kissel, *Bioconjug. Chem.*, 2004, **15**, 441–448.
- 148 X. Shuai, H. Ai, N. Nasongkla, S. Kim and J. Gao, *J. Control. Release*, 2004, **98**, 415–426.
- 149 H. M. Aliabadi, A. Mahmud, A. D. Sharifabadi and A. Lavasanifar, *J. Control. Release*, 2005, **104**, 301–311.
- 150 Q. Gu, J. Z. Xing, M. Huang, C. He and J. Chen, *Nanotechnology*, 2012, **23**, 1–10.
- 151 H. M. Aliabadi, S. Elhasi, D. R. Brocks and A. Lavasanifar, *J. Pharm. Sci.*, 2008, **97**, 1916–1925.
- 152 K. K. Vangara, J. L. Liu and S. Palakurthi, *Int. J. Cancer Res. Treat.*, 2013, **33**, 2425–2434.
- 153 P. Rychahou, Y. Bae, D. Reichel, Y. Y. Zaytseva, E. Y. Lee, D. Napier, H. L. Weiss, N. Roller, H. Frohman, A. T. Le and B. Mark Evers, *J. Control. Release*, 2018, **275**, 85–91.
- 154 R. Tong, *Ind. Eng. Chem. Res.*, 2017, **56**, 4207–4219.
- 155 X. Lou, C. Detrembleur and R. Jérôme, *Macromol. Rapid Commun.*, 2003, **24**, 161–172.
- 156 H. Seyednejad, A. H. Ghassemi, C. F. Van Nostrum, T. Vermonden and W. E. Hennink, *J. Control. Release*, 2011, **152**, 168–176.
- 157 J. Hao, S. Elkassih and D. J. Siegwart, *Synlett*, 2016, **27**, 2285–2292.
- 158 G. Becker and F. R. Wurm, *Chem. Soc. Rev.*, 2018, **47**, 7739–7782.
- 159 C. G. Jaffredo and S. M. Guillaume, *Polym. Chem.*, 2014, **5**, 4168–4194.
- 160 J. W. Kramer and G. W. Coates, *Tetrahedron*, 2008, **64**, 6973–6978.
- 161 X.-Q. Liu, Z.-C. Li, F.-S. Du and F.-M. Li, *Macromol. Rapid Commun.*, 1999, **20**, 470–474.
- 162 X.-Q. Liu, M.-X. Wang, Z.-C. Li and F.-M. Li, *Macromol. Chem. Phys.*, 1999, **200**, 468–473.
- 163 B. Parrish and T. Emrick, *Macromolecules*, 2004, **37**, 5863–5865.
- 164 B. Parrish, R. B. Breitenkamp and T. Emrick, *J. Am. Chem. Soc.*, 2005, **127**, 7404–7410.
- 165 D. Chen, C. C. Chang, B. Cooper, A. Silvers, T. Emrick and R. C. Hayward, *Biomacromolecules*, 2015, **16**, 3329–3335.
- 166 D. E. Borchmann, R. Tarallo, S. Avendano, A. Falanga, T. P. Carberry, S. Galdiero and M. Weck, *Macromolecules*, 2015, **48**, 942–949.
- 167 D. E. Borchmann, N. Ten Brummelhuis and M. Weck, *Macromolecules*, 2013, **46**,

- 4426–4431.
- 168 J. Y. Ljubimova, M. Fujita, A. V. Ljubimov, V. P. Torchilin, K. L. Black and E. Holler, *Nanomedicine*, 2008, **3**, 247–265.
- 169 S. El Habnoui, B. Nottelet, V. Darcos, B. Porsio, L. Lemaire, F. Franconi, X. Garric and J. Coudane, *Biomacromolecules*, 2013, **14**, 3626–3634.
- 170 O. Jazkewitsch, A. Mondrzyk, R. Staffel and H. Ritter, *Macromolecules*, 2011, **44**, 1365–1371.
- 171 E. M. Pelegri-O’Day, S. J. Paluck and H. D. Maynard, *J. Am. Chem. Soc.*, 2017, **139**, 1145–1154.
- 172 V. Darcos, S. Antoniacomi, C. Paniagua and J. Coudane, *Polym. Chem.*, 2012, **3**, 362–368.
- 173 S. El Habnoui, V. Darcos and J. Coudane, *Macromol. Rapid Commun.*, 2009, **30**, 165–169.
- 174 W. Dai, J. Zhu, A. Shangguan and M. Lang, *Eur. Polym. J.*, 2009, **45**, 1659–1667.
- 175 E. L. Prime, Z. A. Abdul Hamid, J. J. Cooper-White and G. G. Qiao, *Biomacromolecules*, 2007, **8**, 2416–2421.
- 176 H. Li, R. Jérôme and P. Lecomte, *Polymer (Guildf.)*, 2006, **47**, 8406–8413.
- 177 M. Trollsas, P. Lowenhielm, V. Y. Lee, M. Moller, R. D. Miller and J. L. Hedrick, *Macromolecules*, 1999, **32**, 9062–9066.
- 178 C. C. Lee, S. M. Grayson and J. M. J. Fréchet, *J. Polym. Sci. Part A Polym. Chem.*, 2004, **42**, 3563–3578.
- 179 N. T. Nguyen, K. J. Thurecht, S. M. Howdle and D. J. Irvine, *Polym. Chem.*, 2014, **5**, 2997–3008.
- 180 R. Palmgren, S. Karlsson and A. C. Albertsson, *J. Polym. Sci. Part A Polym. Chem.*, 1997, **35**, 1635–1649.
- 181 H. Tian, Z. Tang, X. Zhuang, X. Chen and X. Jing, *Prog. Polym. Sci.*, 2012, **37**, 237–280.
- 182 Y. Kimura, K. Shirotani, H. Yamane and T. Kitao, *Macromolecules*, 1988, **21**, 3338–3340.
- 183 D. Tian, O. Halleux, P. Dubois, R. Jérôme, R. Sobry and G. Van den Bossche, *Macromolecules*, 1998, **31**, 924–927.
- 184 J. P. Latere, P. Lecomte, P. Dubois and R. Jérôme, *Macromolecules*, 2002, **35**, 7857–7859.
- 185 M. Trollsås, V. Y. Lee, D. Mecerreyes, P. Löwenhielm, M. Möller, R. D. Miller, J. L. Hedrick, M. Trollsas, V. Y. Lee, D. Mecerreyes, P. Lowenhielm, M. Moller, R. D. Miller and J. L. Hedrick, *Macromolecules*, 2000, **33**, 4619–4627.
- 186 R. Riva, S. Schmeits, C. Jérôme, R. Jérôme and P. Lecomte, *Macromolecules*, 2007, **40**, 796–803.

- 187 D. Mecerreyes, B. Atthoff, K. A. Boduch, M. Trollsa and J. L. Hedrick, *Macromolecules*, 1999, **32**, 5175–5182.
- 188 J. E. Wilson and G. C. Fu, *Angew. Chemie - Int. Ed.*, 2004, **43**, 6358–6360.
- 189 S. G. Nelson, C. Zhu and X. Shen, *J. Am. Chem. Soc.*, 2004, **126**, 14–15.
- 190 M. Mulzer and G. W. Coates, *J. Org. Chem.*, 2014, **79**, 11851–11862.
- 191 W. W. Gerhardt, D. E. Noga, K. I. Hardcastle, A. J. García, D. M. Collard and M. Weck, *Biomacromolecules*, 2006, **7**, 1735–1742.
- 192 D. E. Noga, T. A. Petrie, A. Kumar, M. Weck, A. J. García and D. M. Collard, *Biomacromolecules*, 2008, **9**, 2056–2062.
- 193 R. J. Pounder and A. P. Dove, *Biomacromolecules*, 2010, **11**, 1930–1939.
- 194 C. Galli and L. Mandolini, *J. Chem. Soc. Chem. Commun.*, 1982, 251–253.
- 195 M. Renz and B. Meunier, *Eur. Journal Org. Chem.*, 1999, **1999**, 737–750.
- 196 G. J. ten Brink, I. W. C. E. Arends and R. A. Sheldon, *Chem. Rev.*, 2004, **104**, 4105–4123.
- 197 C. Detrembleur, M. Mazza, O. Halleux, P. Lecomte, D. Mecerreyes, J. L. Hedrick and R. Jérôme, *Macromolecules*, 2000, **33**, 14–18.
- 198 T. Mathisen, K. Masus and A. C. Albertsson, *Macromolecules*, 1989, **22**, 3842–3846.
- 199 National Cancer Institute, NCI Dictionary of Cancer Terms - Complete Remission, <https://www.cancer.gov/publications/dictionaries/cancer-terms/def/complete-remission>, (accessed 28 May 2019).
- 200 National Cancer Institute, NCI Dictionary of Cancer Terms - Remission, <https://www.cancer.gov/publications/dictionaries/cancer-terms/def/remission>, (accessed 28 May 2019).
- 201 L. Iyer, S. Das, L. Janisch, M. Wen, J. Ramírez, T. Karrison, G. F. Fleming, E. E. Vokes, R. L. Schilsky and M. J. Ratain, *Pharmacogenomics J.*, 2002, **2**, 43–47.
- 202 M. Talekar, J. Kendall, W. Denny and S. Garg, *Anticancer. Drugs*, 2011, **22**, 949–962.
- 203 B. Yu, H. C. Tai, W. Xue, L. J. Lee and R. J. Lee, *Mol. Membr. Biol.*, 2010, **27**, 286–298.
- 204 Z. M. Qian and P. L. Tang, *BBA - Mol. Cell Res.*, 1995, **1269**, 205–214.
- 205 D. M. Mock, *Biotin: Pharmacology, Pathophysiology, and Assessment of Biotin Status*, 2004.
- 206 T. Tadros, *Encyclopedia of Colloid and Interface Science*, 2013.
- 207 ScienceDirect, Lipophilicity, <https://www.sciencedirect.com/topics/pharmacology-toxicology-and-pharmaceutical-science/lipophilicity>, (accessed 30 July 2019).

# **CHAPTER 2**

## **SYNTHESIS AND CHARACTERISATION OF CAPROLACTONE DERIVED POLYESTERS VIA ACID CATALYSED RING OPENING POLYMERISATION**



## 2.1 Introduction

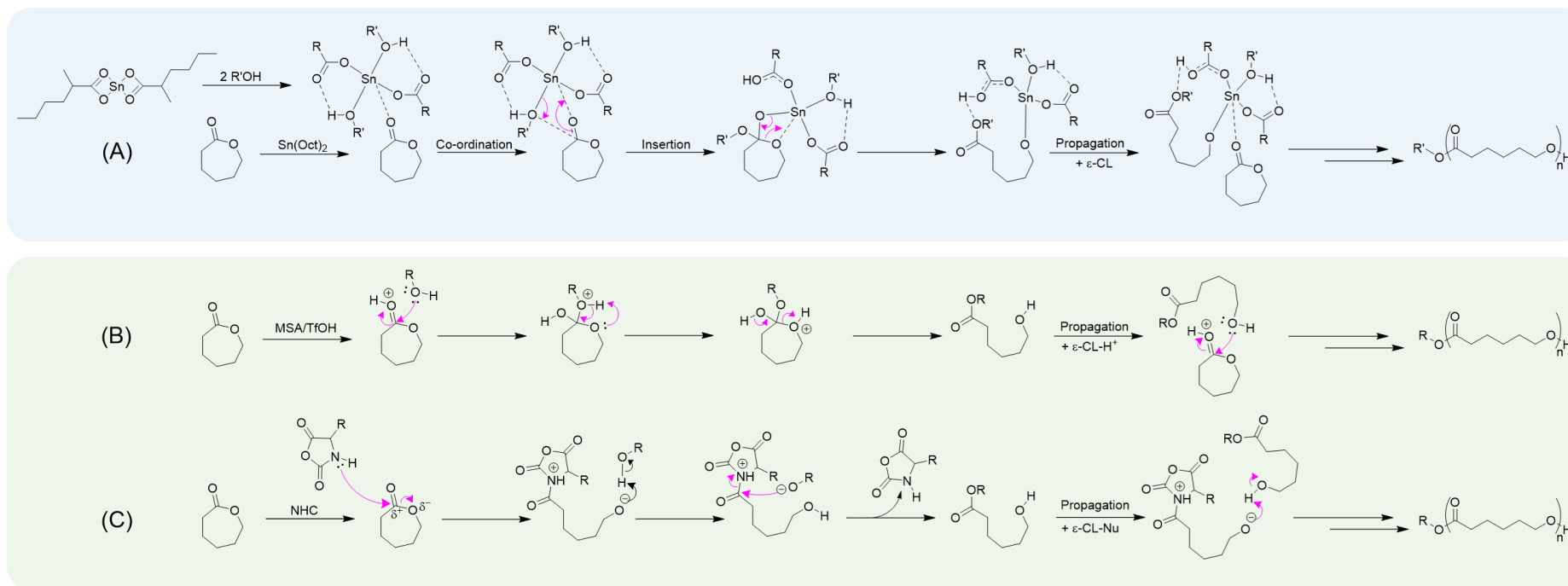
### 2.1.1 Ring opening polymerisation, *ROP*

Polyesters can be synthesised from two distinct routes, involving either linear or cyclic monomer units; for non-cyclic monomers, such as hydroxyl-acids, step growth polycondensation is the route to polymers.<sup>1</sup> The polymerisation of cyclic lactones however has been mainly achieved by the “controlled/living” technique of ring opening polymerisation, *ROP*, allowing for the de-cyclisation of each monomer unit as the polymerisation progresses.<sup>2–</sup>

<sup>4</sup> Unlike other controlled polymerisations, such as atomic transfer radical polymerisation, *ATRP*, where the driving force is the enthalpy change when C=C bonds move to C-C, *ROP* is driven by the loss of ring strain also equating to a loss of enthalpy.<sup>5</sup>

This technique is of high industrial importance contributing to the synthesis of numerous polymers for wide ranging applications such as polyethylene oxide, polysiloxane, Nylon-6 (polycaprolactam) and increasingly polylactide and polyglycolide.<sup>5</sup> Due to the industrial relevance of *ROP*, the polymers it produces, and their advantageous properties with regards to biological applications research into this area has increased. For example, variation of polymerisation conditions has allowed well-defined polyesters to be achieved under mild conditions. As the reaction is catalysed, through activation of either the growing polymer chain end or the monomer (to facilitate hydroxide attack), modified catalysis conditions have been highly explored. These catalysts can be categorised dependant on the properties and method of action of the species in question. Considering the *ROP* of lactones in particular there are 4 main routes for the reaction to proceed namely anionic, cationic, monomer activated and coordination-insertion mechanisms.<sup>4,6</sup>

The most common method of *ROP* of  $\epsilon$ -CL is driven by metal based catalysts, with reports of tin (II) octanoate regularly found in literature.<sup>4</sup> These catalysts proceed by a coordination/insertion mechanism (Scheme 2.1, A), a pseudo anionic route, which allows for the attack of a new monomer molecule by the metal catalyst forming a hydrogen bond between the metal ion and the carbonyl oxygen thus initiating the reaction.<sup>7</sup> The propagation of the polymerisation continues by the insertion of the monomer into the metal-oxygen bond followed by ring opening of the monomer to extend the polymer chain. The metal bond to the polymer chain end is maintained throughout the reaction only being cleaved by proton transfer in the termination step to form a hydroxyl group chain end.<sup>4,7,8</sup>



**Scheme 2.1 – Schematic representation of three ROP mechanisms;** (A) coordination/insertion mechanism (metal catalysed), (B) electrophilic activated monomer mechanism (methanesulfonic acid, *MSA*/trifluoromethanesulfonic acid, *TfOH* catalysed) and (C) nucleophilic activated monomer mechanism (N-heterocyclic carbene catalysed).

Although this is the most commonly used technique for the ROP of  $\epsilon$ -CL it is not without some drawbacks which make it undesirable for the synthesis of polyesters bound for biological use. The most significant drawbacks stem from the difficult removal of the catalyst in its entirety leading to residual metal within the polymers coupled with the necessity for high temperatures that promote both inter- and intramolecular reactions, thereby broadening the polydispersity of resulting polymers.<sup>1,4,9</sup> In an attempt to achieve metal free polymerisation, gain easy catalyst removal and lower polymerisation temperatures several research groups have investigated a whole host of alternatives. These include enzymes, which can prove difficult to work with (polymerisation, degradation and enzyme deactivation occur simultaneously) and organocatalysts.<sup>4</sup> This latter group that consists of a number of molecules with advantageous properties over the traditional metal catalysis routes.<sup>1,5,10-12</sup>

Organocatalysts were first reported by Nederberg *et al.* in 2001 using 4-(dimethylamino)pyridine, *DMAP*, as catalyst for ROP of lactide.<sup>13</sup> Since then the range of molecules, and combinations of such, has expanded greatly to include a wide range of compounds capable of ROP catalysis.<sup>11,13</sup> Among these are thiourea amines, *N*-heterocyclic carbenes, *NHCs*, organic bases and acids (Figure 2.1) many of which are commercially available and easily stored.<sup>1,4,5,10,11,14,15</sup> The approach for each of these groups falls into an activated monomer (Scheme 2.1, B & C) or activated chain end mechanism dependant on the catalyst nature and monomer susceptibility to polymerisation.<sup>6,10</sup>

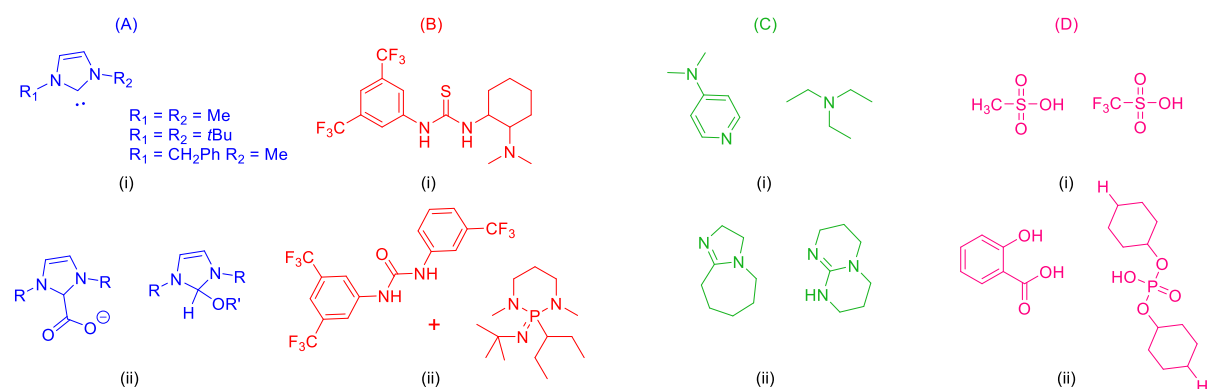


**Figure 2.1 – Examples of organocatalysts that have been applied to ROP;** (A) *N*-heterocyclic carbenes, *NHC*, (i) free *NHC* examples, (ii) examples of protected *NHC*s; (B) (thio)urea amines, (i) thiourea containing both H-donor and acceptor groups within same molecule, (ii) bicomponent urea and base (2-*tert*-Butylimino-2-diethylamino-1,3-dimethylperhydro-1,3,2-diazaphosphorine, *BEMP*) catalytic system; (C) organic bases, (i) 4-(dimethylamino)pyridine, *DMAP*, and triethylamine, *TEA*, (ii) 1,8-diazabicyclo[5.4.0]undec-7-ene, *DBU*, and triazabicyclodecene, *TBD*; and (D) organic acids, (i) sulfonic acids, methanesulfonic acid, *MSA*, and trifluoromethanesulfonic acid, *TFOH*, (ii) carboxylic acid, salicylic acid, *SAA*, and phosphoric acid, diphenyl phosphate, *DPP*, catalysts.<sup>10,15</sup>

*NHC*s are highly popular due to their successful application to the polymerisation of a range of monomers including epoxides, siloxanes and cyclic carbonates but in particular lactide (Figure 2.1, A).<sup>11,16–18</sup> First applied by Connor *et al.* in 2002,<sup>14</sup> *NHC*s offer highly reactive catalysis for ROP when coupled with an alcohol initiator and have since been extensively studied in the catalysis of ROP.<sup>10</sup> Despite their clear success, *NHC*s are seen as inaccessible to a large number of researchers due to being highly unstable in air and requiring inert atmospheres. More recently, “protected” *NHC*s have more frequently been applied.<sup>11</sup> These compounds allow for more air stable adducts that generate a free carbene that can catalyse the polymerisation when triggered by a stimulus such as temperature or solvent.<sup>10,19</sup> This group of molecules includes examples such as *NHC*-carboxylates and *NHC*-alcohol adducts which, although provide a solution to air instability, generally have lower activity than unprotected *NHC*s due to the reliance on complete generation of the active catalyst within the reaction mixture.<sup>10</sup>

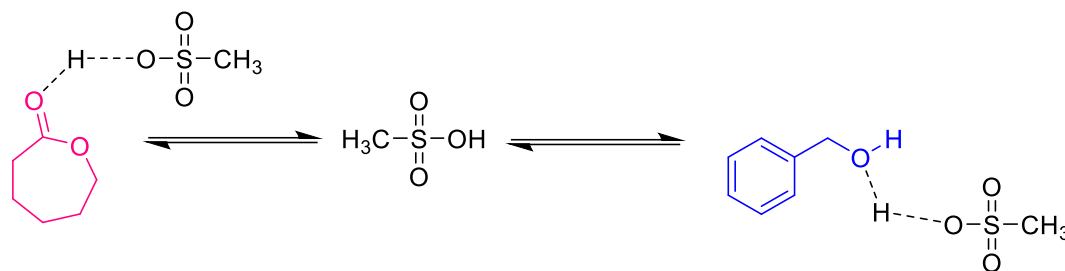
Supramolecular chemistry has also been applied to the catalysis of ROP by the use of thiourea amines and similar molecules (Figure 2.1, B). The combination of both H-acceptors (amine base) and H-donors (thiourea, N-H) in the same catalyst (either joined in the same molecule or dual component) allows for activation of both the chain end and the monomer giving a polymerisation that is highly selective to chain propagation with respect to transesterification

and broad functional group tolerance.<sup>11,15</sup> Recent studies have shown the rate of polymerisation when using bicomponent catalysts can be optimised by the selective pairing of (thio)urea and amine. Lin and Waymouth showed that the rate of polymerisation increased with increased basicity of the amine pair to a given (thio)urea and that optimum rate was reached when the acidity of the (thio)urea was closely matched to that of the protonated base.<sup>15</sup> When comparing ureas to thioureas it was found that ureas were more active when paired with a base compared to the corresponding thiourea pairings. These findings gave insight into the mechanism of action of these catalysts showing there are 2 potential mechanisms dependant on base strength, however, both mechanisms result in the activation of the chain end and the monomer.<sup>15</sup>

In a similar manner to supramolecular catalysts, base and acid catalysis allow for a more accessible metal free ROP than seen with NHCs with a broad spectrum of molecules that can be implemented. For example the first organocatalyst DMAP, a Brønsted base, is one of several pyridine derivatives that behave as nucleophiles that have been shown to catalyse the ROP of a variety of monomers such as glucose, cyclodextrin, and lactones (Figure 2.1, C).<sup>10,14,20</sup> Further examples of bases capable of catalysing ROP are numerous including guanidines and amidines such as 1,8-diazabicyclo[5.4.0]undec-7-ene, *DBU*, which shows high activity to lactide and can be used in combination with a H-bond donor to broaden the library of monomers that can be successfully polymerised.<sup>11,21,22</sup> Furthermore, phosphazene bases have been shown to be capable of low temperature ROP as well as promote co-polymerisation with methacrylate monomers.<sup>4,10,11</sup> However, these catalysts seem to have limited monomer tolerability with each showing limitations in activity with respect to the monomer chosen.<sup>11</sup>

Among the various acids, including carboxylic acids and phosphoric acids, that have been studied to catalyse ROP of lactones there is a group of strong sulfonic acids that have been widely investigated (Figure 2.1, D).<sup>10</sup> This group includes methanesulfonic acid, *MSA*, and trifluoromethanesulfonic acid, *TfOH*, which have been shown to successfully catalyse the ROP of lactones in various solvents, such as dichloromethane, *DCM*, toluene and water.<sup>10,23</sup> *TfOH* has been shown to successfully catalyse the polymerisation of five and six membered rings (butyrolactone and lactide), which have the lowest ring strain, showing the activity of this catalyst is related to the higher acidity. Nonetheless, weaker *MSA* is capable of catalysing the ROP of  $\epsilon$ -caprolactone,  $\epsilon$ -*CL*, more efficiently and with more control than *TfOH*, showing that the reactivity of the catalyst does not solely correlate with the strength of the acid.<sup>23</sup> This phenomenon was attributed to the increased acidity of *TfOH* resulting in an increased

deactivation of the initiating alcohol that is in direct competition with the activation of the monomer (Scheme 2.2).<sup>4,23</sup>



**Scheme 2.2 – Deactivation and activation of the monomer and initiating species by an acid catalyst (e.g. methanesulfonic acid, *MSA*, and trifluoromethanesulfonic acid, *TfOH*).**<sup>23</sup>

These acids have been shown to promote an activated monomer mechanism (Scheme 2.1, B) which can be referred to as pseudo cationic due to the generation of a positively charged species after protonation of the monomer.<sup>10</sup> This is the result of the catalyst activating the monomer and facilitating attack of the carbonyl group by the alcohol initiator. Following the exchange of protons, the ring opens allowing the propagation of the polymer chain. The polymerisation propagates through attack of the chain end hydroxyl functionality at the carbonyl of another activated monomer molecule. As with all ring opening polymerisations, this can be seen as a “controlled/living” polymerisation where chain-extension will occur after the addition of more monomer after full conversion of the initial monomer feed.

## 2.1.2 Variation in polymer composition and architecture

The modification of polyesters to tune their polymer properties is not limited to the use of functionalised monomers and/or post-polymerisation reactions. Other strategies, applied during polymer synthesis, allow the resulting polymers to exhibit physicochemical properties that would have otherwise been unexploited. These methods can be divided into two groups; (1) composition - to alter the polymer backbone by the addition of co-monomers, co-polymerisation, and (2) architecture - to vary the way the polymer chains are linked together, branching.

### 2.1.2.1 Variation of polymer composition – co-polymerisation of polyesters

The introduction of two or more monomers into a linear polymer chain *via* co-polymerisation may lead to a number of different structures that vary in the relative ordering of the monomers along each chain (Figure 2.2). The most common co-polymers seen in the application of nanoparticle formation are amphiphilic block co-polymers, formed from a hydrophilic block

(frequently PEG or poly(vinylpyrrolidone), *PVP*) and a hydrophobic block (any hydrophobic polymer including polyesters and polymethacrylates) (Figure 2.2, A).<sup>24–27</sup> These are normally synthesised by sequential polymerisations, polymerisation of one monomer before the addition of a second monomer, yielding two separate blocks with distinct hydrophobicity. These structures are advantageous in the formation of nanoparticles due to various properties of the polymer segments that allow clear domains to be created during nanoparticle formation thus allowing for greater particle stability. For example, and as discussed in Chapter 1, PEG-*b*-PLA co-polymers can be used to form drug containing polymeric micelles with a hydrophobic core surrounded by a hydrophilic corona inducing stability within the aqueous phase.<sup>28</sup> Among numerous examples, PCL has also been reported to provide the hydrophobic block within PEG co-polymers which have subsequently been used for the formation of polymeric nanoparticles or micelles.<sup>25,29,30</sup> The polyester blocks are most commonly synthesised using metal catalysis and PEG macroinitiators to achieve such architecture; along with the most widely used Sn(Oct)<sub>2</sub> catalyst other inorganic compounds have been utilised to catalysed the ROP of  $\epsilon$ -CL from monomethoxy-PEG such as tin oxide, zinc and antimony trioxide.<sup>25,29,30</sup> Block co-polymer structures that contain two hydrophobic segments have also been synthesised using novel catalytic approaches; using a catalyst “switch” technique that directs block segment synthesis from reactions containing monomer mixtures.<sup>26,31</sup> Wang *et al.* have shown that by utilising organocatalysts, such as MSA, that are active for  $\epsilon$ -CL or  $\delta$ -valerolactone but not lactide and the switching to a catalytic system that is only active for lactide, such as DBU, multi-block co-polymers can be synthesised without the need for purification between each block formation.<sup>31</sup>

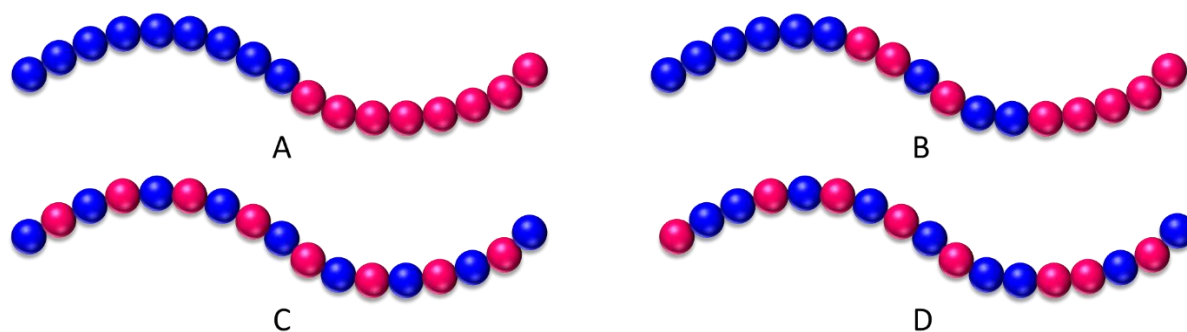


**Figure 2.2 – Representation of the different possibilities of monomer sequence when altering polymer composition using co-polymerisation.** (A) Block co-polymer, (B) gradient co-polymer, (C) alternating co-polymer and (D) statistical co-polymer.

Alongside block co-polymers, the most common co-polyester structure found within literature are statistical co-polyesters such as PLGA (Figure 2.2, D). Statistical (previously known as “random”) co-polymer composition relies on a one-pot synthetic approach where both monomers are present at the start of the polymerisation. This can result in a mixture of polymer compositions dependant on the ratios of the monomers used, their subsequent reactivity’s with respect to each other and the catalyst used. In the case of PLGA, glycolide possesses a greater reactivity with regards to ROP therefore it is likely that large segments of the polymer chain will comprise of glycolide blocks, however protocols have been explored to prevent this.<sup>32-34</sup> Hoyer and co-workers, studied methods to control the statistical addition of lactide and glycolide monomers to the polymer chain during propagation.<sup>34</sup> It was found that the implementation of a semi-batch polymerisation involving the continuous addition of glycolide to the polymerisation mixture at a rate that mitigated the increased reactivity of the monomer resulted in the ability to control the monomer sequence within the polymer.<sup>34</sup> The most significant advantage to this method is the ease in the ability to vary polymer composition within the reaction allowing tailoring of the resulting polymer properties. The properties of PLGA can be tuned by varying the lactide to glycolide ratio in the final polymer composition. PLGA polymers which are rich in lactide often have more hydrophobic character than glycolide rich counterparts leading to slow degradation times.<sup>32,33</sup> Nonetheless, these effects cannot be readily predicted from the feedstock monomer ratio within the reaction mixture; this is most clearly demonstrated by the disappearance of crystallinity in PLGA co-polymers despite poly(glycolide) being highly crystalline.<sup>32</sup>

Alternatively, the simultaneous polymerisation of dicyano-substituted  $\epsilon$ -CL by Pahovnik and co-workers yielded statistical co-polymers with  $\epsilon$ -CL confirmed by  $^1\text{H}$  and  $^{13}\text{C}$  nuclear magnetic resonance, *NMR*.<sup>35</sup> A difference in reactivity of the monomers was controlled by the use of a solvent system in which the more reactive monomer was only partially soluble, thereby minimising monomer concentration in the reaction mixture.  $^{13}\text{C}$  NMR also revealed that like to like monomer interactions were slightly more favourable which would indicate more zonal or gradient type co-polymerisation.<sup>35</sup>

Although significantly less common in the literature, examples of gradient co-polymers have been achieved relying on the differing reactivity of the monomers inducing a composition shift as the polymerisation proceeds.<sup>36</sup> The co-polymerisation of caprolactone and lactide highlighted that the monomer’s reactivity within the co-polymerisation differ from each other in both co-ordination/insertion and activated monomer mechanisms with lactide being seen to



preferably polymerised.<sup>37</sup> This difference in reactivity would suggest that the synthesis of gradient co-polymers predominate; however, due to the presence of transesterification reactions, statistical co-polymers are achieved.<sup>37,38</sup> The successful synthesis of gradient co-polymers has been achieved with  $\delta$ -valerolactone, *VL*, and  $\epsilon$ -caprolactone utilising organocatalysed ROP in the presence of 1,3-diethyl-4,5-dimethylimidazol-2-ylidene.<sup>38,39</sup> Here, Shin *et al.* confirmed the gradient structure of the co-polymers by <sup>13</sup>C NMR, indicating larger fractions of CL-CL and VL-VL bonds within the polymer structures and the difference inferred in the thermal properties of the resultant polymers.<sup>39</sup> The study of the thermal properties highlighted the advantages of accessing a number of different co-polymer structures as the melting point of gradient co-polymers was lower than that of the block co-polymer analogue but higher than the statistical co-polymer.<sup>38,39</sup> These structures are also considered a cheaper alternative to block co-polymers, removing the need for purification of the separate polymer chains before complete synthesis of the co-polymer structure.<sup>36</sup> Combined with recent advances in the use of vinyl gradient co-polymers in polymeric micelles, the area of co-polymerisation is expected to continue to grow over the coming years.<sup>36</sup>

### **2.1.2.2 Variation of polymer architecture – branching of polyesters *via* ROP**

Variation in polymer architecture, often along with the formation of high molecular weight polymers, may be achieved by the linking of primary polymer chains and the creation of branching. The synthesis of branched polymers, and the components used within them, allows for the tuning of numerous physicochemical properties such as rate of degradability, lower viscosities and improved nanoparticle formation coupled with additional functionality that can be gained from the large number of chain ends.<sup>40-43</sup> There are several routes to achieve branched architectures in polyesters, with both ROP and polycondensation techniques yielding such polymers. In all cases, the polymerisations achieve a higher number of chain ends within each macromolecule, and such branching generally requires more simplistic, less time consuming syntheses than those used for perfect dendritic branching.<sup>40,44-46</sup> Although there is a significant body of literature concerning the polycondensation of monomers such as 2-bis(methylol)propionic acid, *bis-MPA*, to form branched polyesters, the use of ROP allows for the controlled production of branched polymers using lactone monomers, such as PCL and PLA, with potentially high molecular weight.<sup>43,47</sup> Several ROP methods have been reported that yield particular branched architectures such as graft, star, dendritic and hyperbranched polymers (Figure 2.3); all of these have been largely explored using traditional catalysts such as Sn(Oct)<sub>2</sub>.<sup>43,47</sup>

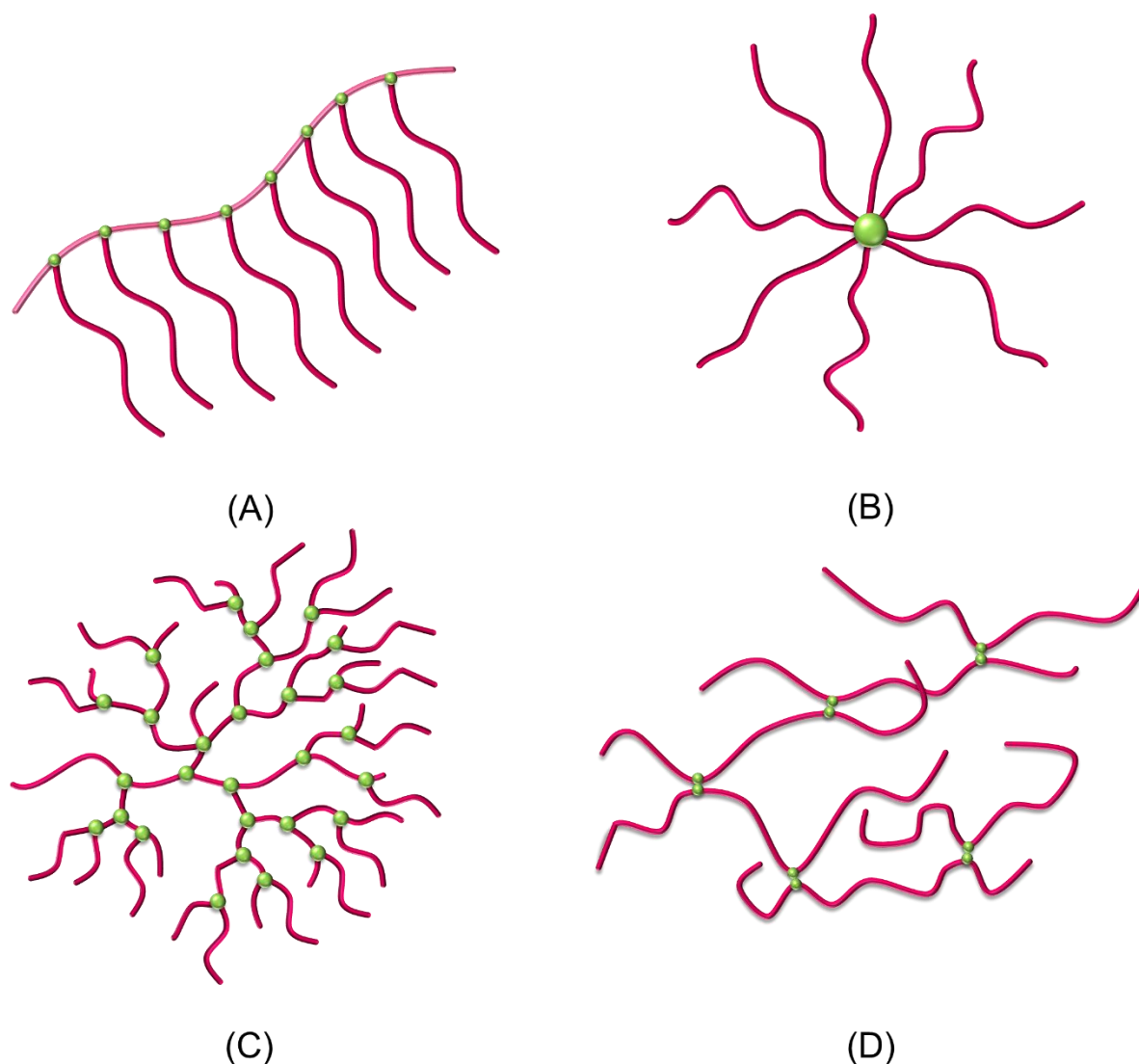


**Figure 2.3- Representation of the types of branched architectures resulting from ROP methods;** (A) graft co-polymers, (B) star polymers, (C) dendritic polymers and (D) hyperbranched co-polymers.

Graft and star branched architectures commonly require the use of polymeric macroinitiators or post-functionalisation of polymer chains *via* click chemistry to achieve their unique structures (Figure 2.3, A & B).<sup>48</sup> Graft co-polymers commonly are a form of branched copolymer that employ multifunctional macroinitiators to allow the growth of polymers from numerous functional sites either randomly or equally spaced along the macroinitiator polymer chain.<sup>43</sup> There are three methods to achieve this architecture which have all been explored with ROP of cyclic lactones (Figure 2.4). For example, PLGA has been ‘grafted onto’ poly(vinyl alcohol), *PVA*, chains through the conversion of hydroxyl terminal groups to carboxylic acid groups which could subsequently be used to graft onto *PVA* polymer chains before further polymerisation to form hydrogels (Figure 2.4, A).<sup>47,49</sup> Additionally, a more complex

architecture has recently been explored by the grafting of PEG chains onto a co-polymer of caprolactone and 3,3-bis(chloromethyl)oxacyclobutane *via* a Janus polymerisation\*\*\*\* in the presence of propylene oxide.<sup>50</sup> ‘Grafting from’, another common method, involves the polymerisation of monomers from initiating points along a polymer backbone (Figure 2.4, B). This has been demonstrated by Shang *et al.*, where  $\alpha$ -chloro- $\epsilon$ -CL was co-polymerised with  $\epsilon$ -CL from PEG macroinitiators then reacted together to form a tri-block polymer backbone with pendant chlorine groups. Subsequently the ATRP of 2-(2-methoxy ethoxy)ethyl methacrylate and oligoethylene glycol methyl methacrylate from these pendant groups yielded a graft co-polymer which, following azide end-functionalisation and click-reactions with a cross linker, possessed the ability to form hydrogels.<sup>51</sup> Alternatively, Kissel and co-workers successfully polymerised lactide and glycolide *via* Sn(Oct)<sub>2</sub> catalysed ROP from OH groups along a PVA chain producing polymers with number averaged molecular weight,  $M_n$ , values between 5000 and 30,000 g mol<sup>-1</sup>; these materials were capable of being tuned for slow degradation using additional sulfonate modification.<sup>52</sup> Finally, ‘grafting through’ presents an alternative route to branched co-polymer architectures; this strategy involves the (co)polymerisation of macromonomers (Figure 2.4, C), commonly short polyester chains functionalised by a vinyl monomer containing an hydroxyl functional group in order to synthesise a polymer backbone, such as *N*-(2-hydroxypropyl)methacrylamide.<sup>43,53</sup> This results in branched architecture often referred to as ‘comb’ polymers which can self-assemble to form micelles and other nanostructures.<sup>43,48,53</sup>

---

\*\*\*\* Janus polymerisation is a variation of ROP in which anionic and cationic polymerisations are combined at the chain ends of a single propagating chain.<sup>98</sup>

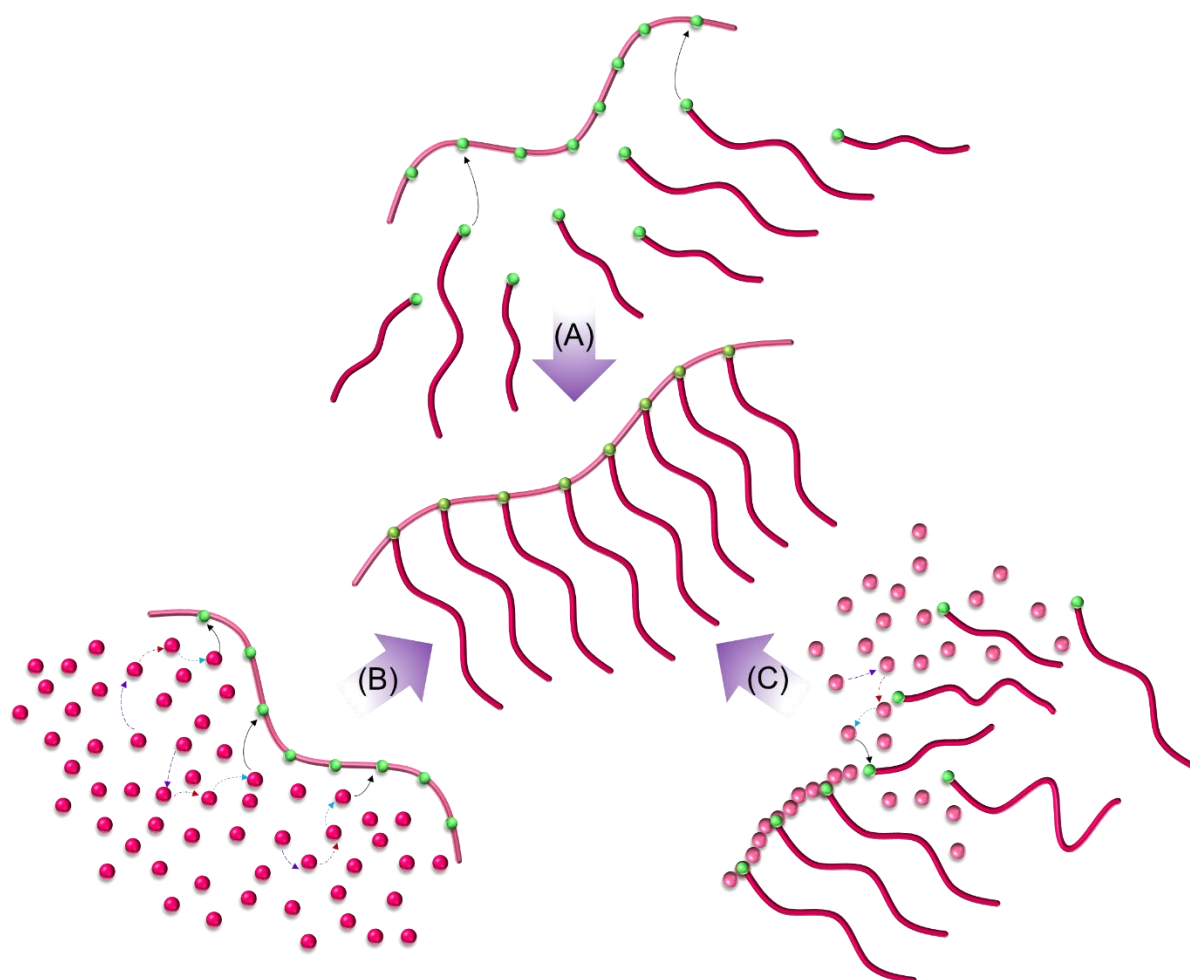


**Figure 2.4 – Representation of the routes to achieve graft co-polymers;** (A) ‘grafting onto’, (B) ‘grafting from’ and (C) ‘grafting through’; arrows showing propagation of polymer chain with addition of the, (black) first, (blue) second, (red) third and (purple) fourth, monomer in polymerisation sequence.

Star polymers have a single point of branching at the centre of the structure that is surrounded by linear polymer chains. High molecular weight star polymers can be achieved *via* two routes, either ‘core-first’ or ‘arm-first’ (Figure 2.5).<sup>43,47,48</sup> Core-first begins with the ROP of a lactone monomer initiated by a chosen polyol to give hydrophobic linear arms extending from the core which can then be functionalised by a hydrophilic polymer such as PEG.<sup>48</sup> The degree of branching within these structures is determined by the number of alcohol groups present in the core polyol.<sup>48</sup> Variation has been created with this method by both post-functionalising PCL chain ends and utilising macromolecules such as cyclodextrin as a core molecule.<sup>43</sup> Conversion of PCL hydroxyl end groups to thiols successfully allowed the growth of *N*-(2-hydroxypropyl)methacrylamide to act as the hydrophilic block within amphiphilic star polymers.<sup>43,54</sup> Alternatively, regioselective functionalisation of cyclodextrin has been shown to

allow for the creation of mikroarm<sup>†††</sup> Janus star polymers with both PCL and PEG polymers originated from the cyclodextrin core which was shown to prolong drug release.<sup>43,55</sup>

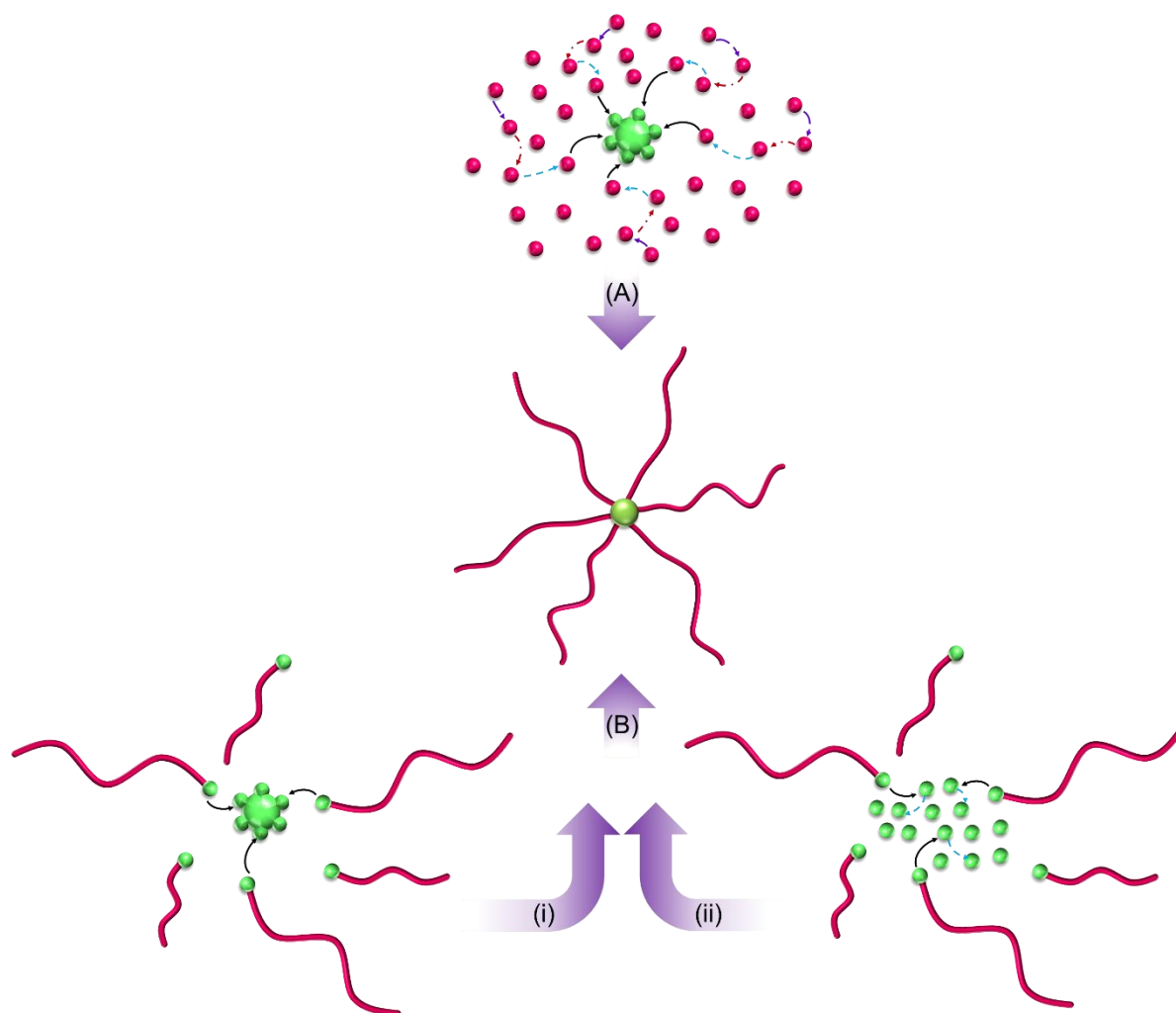


**Figure 2.5 – Two synthesis routes to star polymers;** (A) core-first and (B) arm-first: (i) coupling to a singular multi-functional molecule and (ii) polymerisation of highly branched core initiated by arm segments; arrows showing propagation of polymer chain with addition of the, (black) first, (blue) second, (red) third and (purple) fourth, monomer in polymerisation sequence.

Arm-first synthesis of star polymers often has poor coupling between the arm and core sections due to steric hindrance therefore it has become more common to see highly branched cross-linked cores within star polymers made *via* an arm-first strategy.<sup>43,48</sup> This route removes the requirement for precise reactions to a single multi-armed molecule to gain the desired star architecture (Figure 2.5, B i).<sup>43</sup> MSA has been used as a catalyst in the synthesis of such branched structures by exploiting 4,4'-bioxepanyl-7,7'-dione, *BOD*, as a bis-lactone to achieve

<sup>†††</sup> Mikroarm star polymers refer to star polymers that have arms of varying chemical nature, for example arms that are either hydrophobic and hydrophilic in the same structure.<sup>48</sup>

star co-polymers with a cross-linked core and linear PCL arms (Figure 2.6).<sup>10,56</sup> Despite previous reports of such structures being synthesised using  $\text{Sn}(\text{Oct})_2$ , MSA was shown to be a viable catalyst for the polymerisation of both the PCL arm macroinitiators and subsequent cross-linked BOD core.<sup>10,56</sup> Ren *et al.* explored the use of MSA in the synthesis of star co-polymers, derived from PCL and BOD, in both one and two-pot reactions and showed that both methods produced polymers at faster rates and lower dispersities when compared to similar reactions using  $\text{Sn}(\text{Oct})_2$ .<sup>10,56</sup> Here, BOD is used as the sole monomer within the second polymerisation allowing for the synthesis of a highly cross-linked core in the star polymer to produce molecular weight values between 9,900 and 36,200  $\text{g mol}^{-1}$ .<sup>56</sup> This method was also shown to produce higher star purity than polymers synthesised using traditional tin-based catalysts.<sup>56</sup>

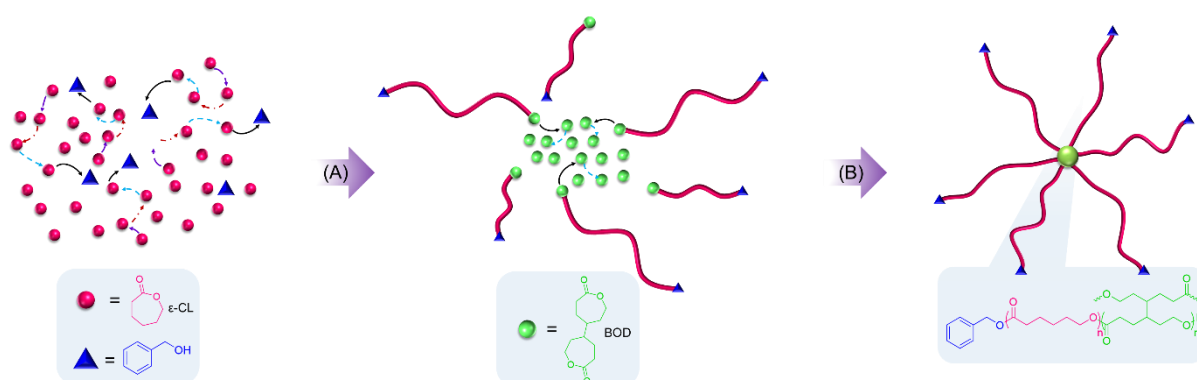


**Figure 2.6 - Representation of ‘arm first’ star polymer synthesis detailed by Ren *et al.*;** (A) ROP of  $\epsilon$ -CL resulting in linear ‘arm’ macroinitiators followed by (B) ROP of BOD resulting in a highly branched cross linked core;<sup>56</sup> arrows showing propagation of polymer chain with addition of the, (black) first, (blue) second, (red) third and (purple) fourth, monomer in polymerisation sequence.

Dendritic-like branched architectures are common within the literature, being created *via* ring opening multi-branching polymerisation, *ROMBP*, also referred to as self-condensing ring opening polymerisation, *SCROP*. Based on the concept of self-condensing vinyl polymerisation, *SCVP*, latent  $\text{AB}_2$  monomers, referred to as inimers, are polymerised to give polymers with branched architecture and increased terminal functionality towards the periphery of the polymers.<sup>43–45,47,57,58</sup> Inimers, frequently hydroxyl functionalised cyclic monomers, are capable of acting as both a monomer and initiating species allowing branching points to be created as the polymerisation progresses, and generating highly branched architecture from a single origin point.<sup>43,47,59</sup> The study of this method of polymerisation originated with both cyclic ester monomers, namely 4-(2-hydroxyethyl)- $\epsilon$ -caprolactone, being explored by Fréchet and co-workers; and cyclic ethers, such as glycidol, reported by Frey and

co-workers.<sup>45,60</sup> Considering 4-(2-hydroxyethyl)- $\epsilon$ -caprolactone as an example,  $\text{Sn}(\text{Oct})_2$  catalysed SCROP yielded polymers with  $M_n$  values between 65,000–85,000  $\text{g mol}^{-1}$  and analysis indicated that the structure produced consisted of three structural units (linear, dendritic and terminal groups) that are consistent with conventional  $\text{AB}_n$  branching (Figure 2.7).<sup>45</sup> Since these first reports, this method has been further explored with a range of monomers, for example the latent  $\text{AB}_3$ -like bis(hydroxymethyl)-substituted- $\epsilon$ -caprolactone and a number of different catalysts such as Lewis acids.<sup>43,47,58,61–64</sup> Additionally, the methodology has been refined to enable the polymerisation of more well defined dendritic polymers with lower dispersity values by utilising a slow monomer addition technique.<sup>59,62,65</sup>

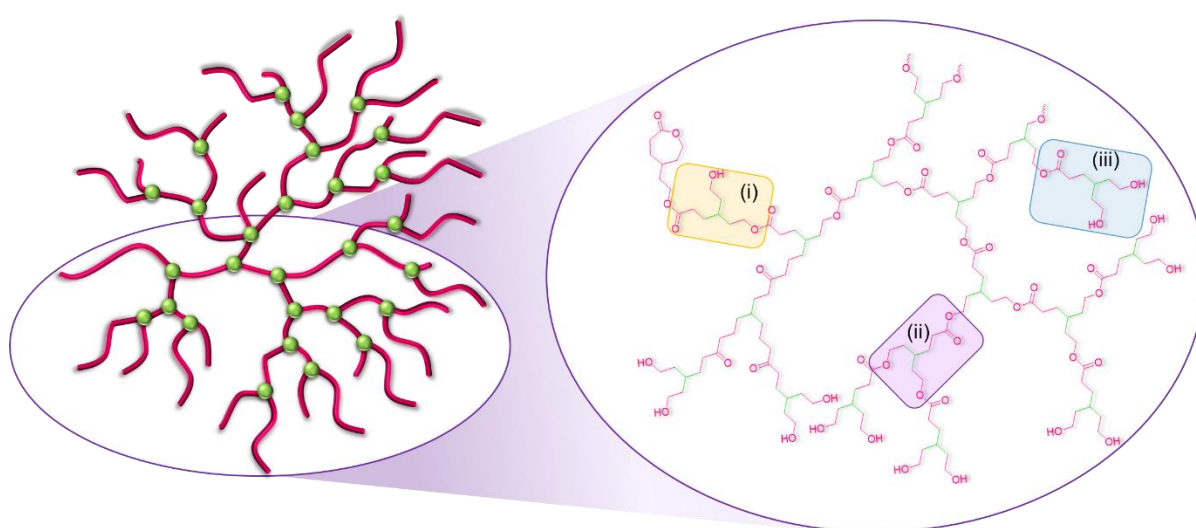


**Figure 2.7 – Dendritic branched polymer based on 4-(2-hydroxyethyl)- $\epsilon$ -caprolactone;** indicating (i) linear, (ii) dendritic and (iii) terminal units.

Finally, soluble hyperbranched architectures can be achieved by the implementation of a modified ‘Strathclyde route’. This is a one pot synthesis which is an adaptation of the Strathclyde method developed by Sherrington and co-workers in 2000 using free radical polymerisation of mono- and di-vinyl monomers in the presence of a chain transfer agent.<sup>40,46,66</sup> The method was subsequently referred to as the ‘modified Strathclyde method’ when it was applied to controlled radical polymerisation techniques such as ATRP and reversible addition-fragmentation chain-transfer polymerisation, *RAFT*, where control in radical concentration regulated the primary chain length and number of branching points per chain to prevent gelation.<sup>40</sup> The basis of this method is the statistical co-polymerisation of a bifunctional monomer and monofunctional monomer under standard polymerisation conditions.<sup>40,46</sup> When employing the ‘modified Strathclyde method’, the polymerisation can be split into 3 separate stages, initiation, propagation and branching (Figure 2.8).<sup>67</sup> Firstly, for controlled radical co-



polymerisations, all polymer chains grow and propagate under identical conditions and near-identical rates. Additionally, Flory-Stockmayer theory suggests that as long as the incorporation of a bi-functional monomer is controlled to less than one per polymer chain, the product will not gel.<sup>68</sup> Finally, at the latter stage of the polymerisation and high monomer conversion polymer chains start to form branched architectures through intermolecular reactions, leading to a high molecular weight soluble polymer. (Figure 2.8).<sup>67</sup>

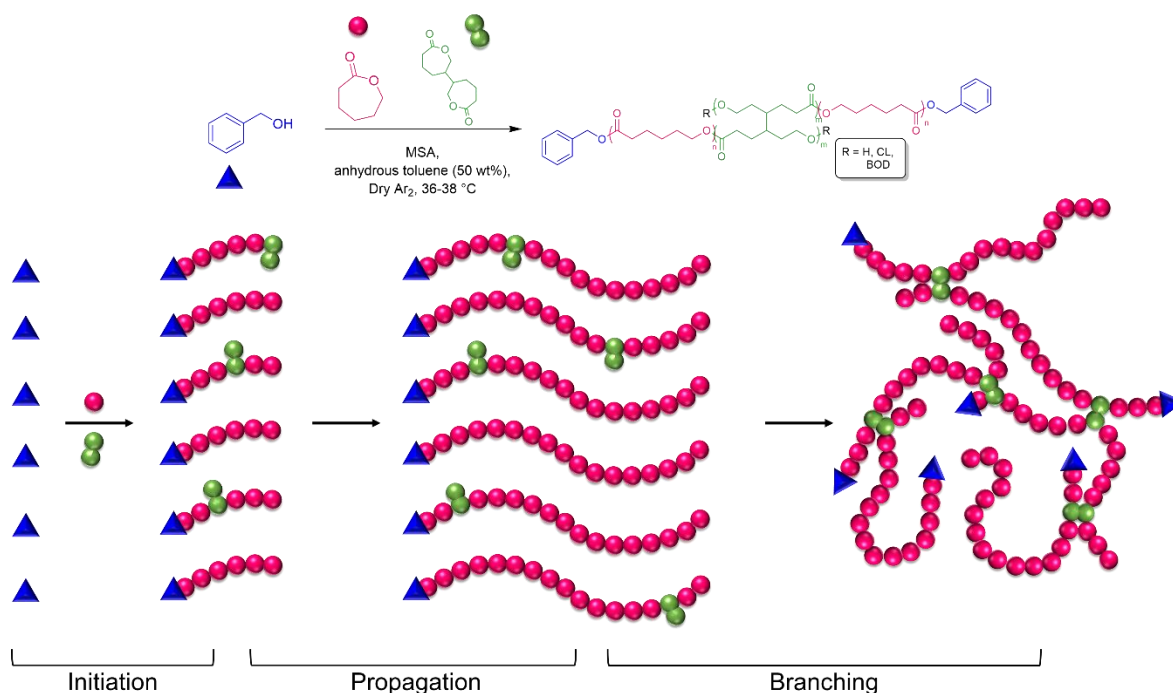


**Figure 2.8 – Representation of the evolution of branching from the application of a modified ‘Strathclyde route’ to hyperbranched polymers to ROP.**

Amongst other researchers, the Rannard group has shown the versatility of the ‘modified Strathclyde method’, implementing it in numerous radical polymerisations to yield branched architectures that include polymethacrylates, such as poly(butyl methacrylate) and poly(2-hydroxypropyl methacrylate) and poly(oligo(ethyleneglycol) methacrylate).<sup>69–73</sup> Furthermore this method has allowed the introduction of a new polymer architecture, hyperbranched polydendrons, a unique structure that combines the segmental nature of block co-polymers, surface functionality opportunities of dendrons and branched architecture into a single macromolecule.<sup>70,72,74</sup> Consequently these polymers have then been studied in a number of applications that have demonstrated the advantages that can be drawn from such architecture.<sup>71,72</sup> Hatton *et al.* showed, by the isolation of highly branched, high molecular weight species within a hyperbranched polydendrons distribution, that nanoprecipitation could



be influenced significantly and the resulting nanoparticles could be tuned in size and stability.<sup>41,75</sup>

Literature regarding the application of a ‘modified Strathclyde method’ to ROP, however, is lacking with only a few papers reporting the combination of a cyclic ester with bis-lactone. Bulk ROP of caprolactone with bis-lactone BOD was initially reported by Nguyen *et al.* utilising a Sn(Oct)<sub>2</sub> catalyst which yielded polymers of molecular weights above 30,000 g mol<sup>-1</sup>.<sup>42</sup> Researchers showed that, unlike controlled radical polymerisations where molecular weight rapidly increases at ~ 70 % monomer conversion due to the linking of linear chains, tin catalysed ROP showed a similar behaviour at ~90 % monomer conversion.<sup>42</sup> This was hypothesised to be due to the steric hindrance induced by the incorporation of BOD into the polymeric species. Once incorporated, the significant steric bulk of the pendant CL group would be likely to impede catalyst coordination, and favour activation of free mono-functional  $\epsilon$ -CL; at high monomer conversions, coordination to the pendant CL rings of the BOD groups would encourage intermolecular reactions and subsequent branching.<sup>42</sup>

Nonetheless, literature within this area of branched polyesters is lacking with significantly less publications than star, graft and dendritic architectures, inviting the exploration of avenues into this area of study. When coupled to the lack of investigation into the synthesis of all branched architecture types, in particular highly branched soluble polymers *via* a ‘modified Strathclyde routes’, organocatalysed ROP, investigation into this area could bring additional advantages.

### 2.1.3 Chapter aims

This chapter aims to lay foundations for the work to be addressed in following chapters, providing information in key ideas and concepts that have either been previously explored in a limited fashion or yet to be investigated. Given the variety of branched architectures that has been achieved with polyesters, yet the lack of exploration implementing a ‘modified Strathclyde method’, this work aims to further develop the area. Furthermore, although co-polymers again have been widely explored, particularly with PEG, amphiphilic branched co-polyesters within literature have only been obtained via star and graft co-polymer structures. It is hypothesised that, given the advantages and variety of physicochemical properties that are made available by a high level of branching and presence of separate hydrophobic and hydrophilic segments, structures achieved via a ‘modified Strathclyde method’ will be instrumental in future chapters. The implementation of MSA catalysed ROP, and the inclusion of BOD, should allow access to these structures whilst providing a valuable alternative to metal

catyalsed routes (Figure 2.9). Although polymerisation studies are expected to begin with  $\epsilon$ -caprolactone, development of a number of substituted caprolactone monomers, *SCM*, are theorised to allow for the tuning of the resulting polyester properties, such as  $T_g$ , crystallinity and hydrophobicity (Figure 2.9, B). Therefore this chapter ultimately aims to study the synthesis of a range of new branched polyesters and their resulting properties.

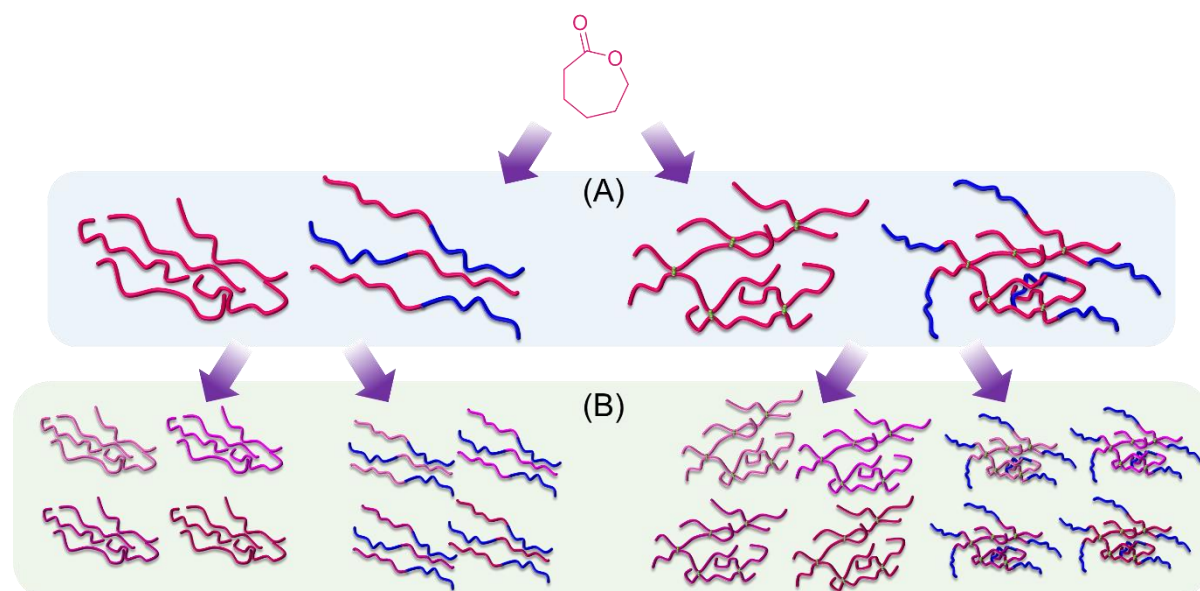
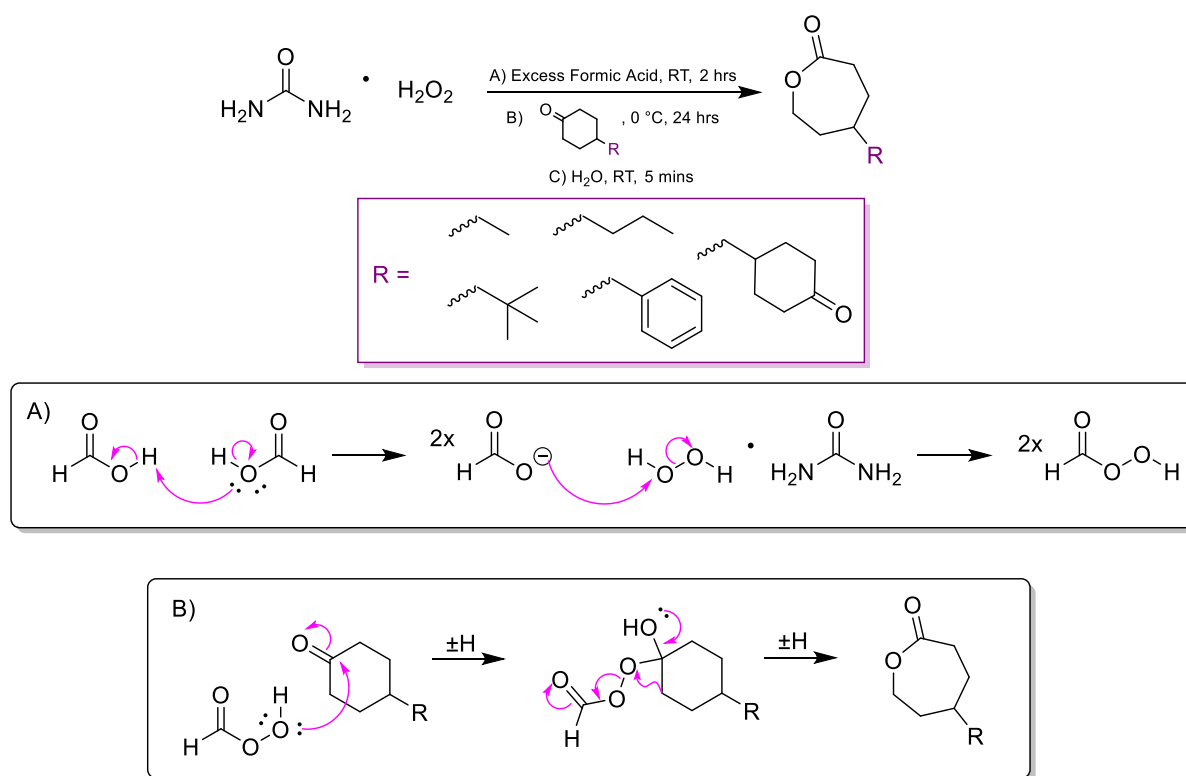


**Figure 2.9 – Representation of the aims of this chapter;** (A) synthesis of a library of polymers of varying architecture based on  $\epsilon$ -caprolactone and (B) implementation of a variety of substituted caprolactone monomers in these syntheses.

## 2.2 Synthesis of substituted caprolactone monomers *via* Baeyer-Villiger oxidation

As detailed in Section 1.5, there has been an absence of studies in the literature of polymers made by simple modifications to the caprolactone monomer ring, and the effects these have on the properties of polymers that would result from their polymerisation. As mentioned previously, one aim of this research was to study the effects of backbone substitution, using various pendant groups, on the physiochemical properties of the resulting polymers. As part of this study, the viability of substituted monomers in the production of polymers of varying architecture *via* MSA catalysed ROP was also important to understand. The use of substituted monomers within branched architecture is ultimately hypothesised to yield control of nanoparticle formation and guest molecule encapsulation and release (Section 1.6).

The selection of substituted caprolactone monomer structures targeted for this study was aided by a review of commercially available cyclic ketone precursors that may be utilised in the well-reported Baeyer Villiger oxidation reaction (Scheme 2.3).<sup>76–78</sup>



**Scheme 2.3 – Scheme representing the synthesis of substituted caprolactone monomers via Baeyer-Villiger oxidation.**

Four commercially available cyclic ketones were selected due to their chemical diversity and the potential for the substituted groups to impact the resulting polymer glass transition temperature and crystallinity. Two target monomers aimed to introduce straight chain methyl and propyl substituents, analogous to varying side-chain lengths within vinyl polymers that would be expected to lead to a decrease in glass transition temperature.<sup>79,80</sup> The introduction of a *tert*-butyl substituent was also selected to increase glass transition temperature, drawing upon the analogy of the impact of moving from *n*-butyl side chains to *t*-butyl side chains, within (meth)acrylate structures; whilst the addition of an aromatic pendant group was expected to introduce the potential for  $\pi$ - $\pi$  stacking between chains or between chains and guest molecules.<sup>79–81</sup> In summary, the target substituted caprolactone monomers were 5-methyloxepan-2-one, *MOP*, 5-propyloxepan-2-one, *POP*, 5-(*tert*-butyl)oxepan-2-one, *BOP* and 5-phenyloxepan-2-one, *PHLOP* (Figure 2.10, F to I respectively).

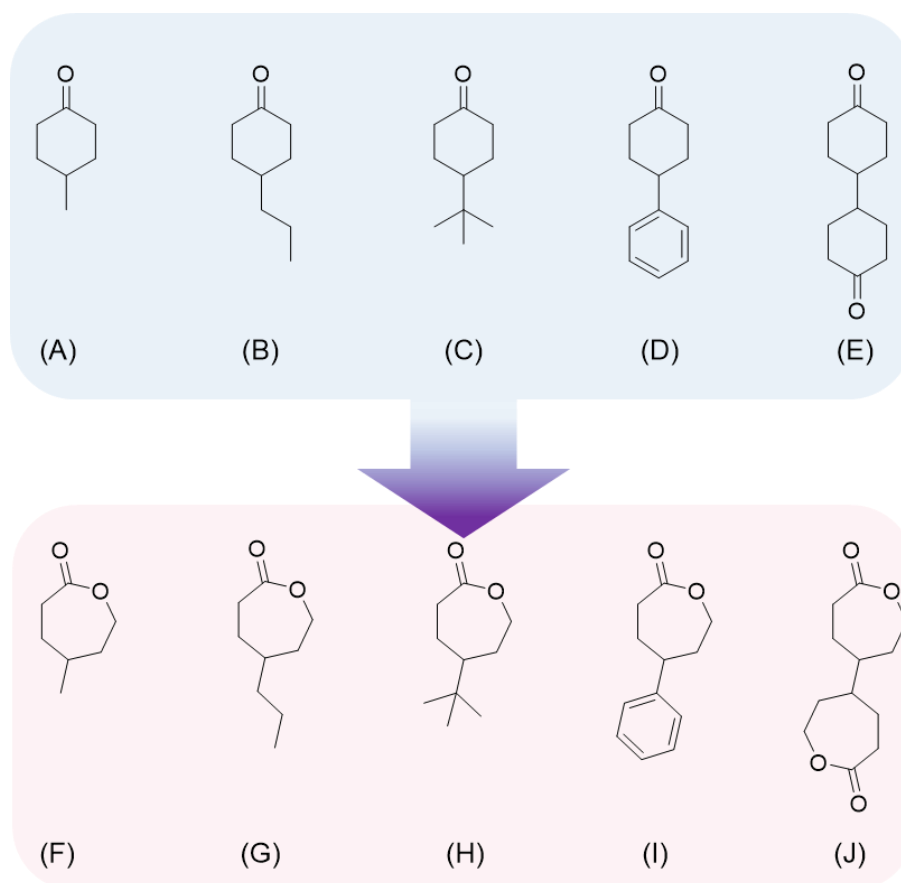


**Figure 2.10 – Molecular structures of substituted caprolactone monomers produced from cyclic ketones;** (A) 4-methylcyclohexanone, (B) 4-propylcyclohexanone, (C) 4-(*tert*-butyl)cyclohexanone, (D) 4-phenylcyclohexanone and (E) bicyclohexanone Producing (F) 5-methyloxepan-2-one, *MOP*, (G) 5-propyloxepan-2-one, *POP*, (H) 5-(*tert*-butyl)oxepan-2-one, *BOP*, (I) 5-phenyloxepan-2-one, *PHLOP* and (J) 4,4'-bioxepanyl-7,7'-dione, *BOD*.

The target monomers all possess substitution at position 5 on the ring for consistency and to minimise any potential for steric hindrance in the activated monomer mechanism during ROP. In addition to the four new substituted caprolactone monomers, a bi-functional ketone, bicyclohexanone, allowed the production of bis-lactone, *BOD*, for the synthesis of polyesters with branched architecture (Figure 2.10, J).

Baeyer-Villiger oxidation allows the addition of an oxygen atom into a C-C bond adjacent to a C=O ketone bond, and relies upon the cleavage of a O-O bond commonly within peroxide or peroxy-acid reagents.<sup>76-78</sup> When using a cyclic ketone, for example a 6-membered ring, the migration of the oxygen atom from the O-O bond produces a 7-membered ring ester (a lactone). The four substituted caprolactone monomers were readily achieved using the same method of Baeyer-Villiger oxidation, detailed by Nguyen *et al.* to achieve *BOD*, where a reactive peroxy-acid was created *in-situ* by a reaction of formic acid and urea hydrogen peroxide, *UHP*,<sup>42</sup> the

resulting formate subsequently reacts with hydrogen peroxide to form the peroxy-acid (Scheme 2.3, A). Upon the addition of the selected ketone, nucleophilic attack proceeds by the migration of oxygen from the O-O bond within the peroxy-acid into the cyclic ring yielded the desired lactone (Scheme 2.3, B).<sup>76-78</sup>

Optimisation of the reported reaction conditions was achieved by extending the reaction time of the cyclic ketone with the peroxy-acid from 2 to 24 hours. This allowed the reaction to proceed to completion and considerably reduced the amount of unreacted ketone to be removed from the products. The equivalents of reactants used gave a 3:1 molar ratio of peroxy-acid to ketone for the oxygen migration step (assuming the complete reaction of all UHP), also promoting the production of the cyclic ester. Water was added to quench the reaction after 24 hours, to decompose the remaining peroxy-acid to the starting formic acid and UHP, hence enabling safe purification in the absence of large concentrations of residual peroxy-acid. A simple water-chloroform extraction allowed the removal of any remaining peroxy-acid and the excess formic acid and UHP into the aqueous phase and the concentration of the product lactone with the chloroform layer. After the final washes with saturated sodium bicarbonate solution, thin layer chromatography, *TLC*, analysis showed the presence of residual formic acid and each starting cyclic ketone (*R<sub>f</sub>* values 0 (formic acid) and between 0.46 and 0.84 (cyclic ketones) Section 6.3.1.1) along with the desired final products (*R<sub>f</sub>* values MOP = 0.20, POP = 0.25, BOP = 0.33, PHLOP = 0.15). These impurities were removed by column chromatography with a solvent mixture of ethyl acetate:hexane (25:75). Achieving high purity was necessary to allow for accurate targeted degrees of polymerisation (*via* monomer mass) and, in the case of BOD, which had previously been used without purification by column chromatography, the addition of accurate equivalents to avoid gelation during ROP; removal of formic acid was also essential to eliminate any interference with MSA used as the polymerisation catalyst. This procedure was followed for all the monomers; reactions for MOP, POP, BOP and PHLOP were conducted on a 15 g scale (3 x 5 g scales to work safely with the peroxy-acid) which resulted in recovered yields of: MOP = 56.3 %, POP = 39.8 %, BOP = 63.3 % and PHLOP = 64.8 %. BOD synthesis was carried out on a 5 g scale and resulted in a recovered yield of 62 %.

Analysis of all monomers was achieved by <sup>1</sup>H NMR, <sup>13</sup>C NMR and chemical ionisation mass spectrometry, *MS*. For all substituted caprolactone monomers, the presence of the ester group was confirmed by a number of hydrogen and carbon environments within the NMR spectra; these environments and chemical shifts correlated with caprolactone NMR spectra (Appendix, Figure A1 & A2). Each monomer had a proton environment between 4 and 4.5 ppm with

multiplet splitting and could be assigned to the CH<sub>2</sub> group next to the C-O ester bond within the cyclic newly formed lactone ring; MOP = 4.42 - 4.12 ppm (Figure 2.11, A, proton environment *e*), POP = 4.39 - 4.10 ppm (Figure 2.12, A, proton environment *e*), BOP = 4.46 - 4.05 ppm (Figure 2.13, A, proton environment *e*), PHLOP = 4.43 - 4.23 ppm (Figure 2.14, A, proton environment *e*) and BOD = 4.22 ppm (Figure 2.15, A, proton environment *e*).

The <sup>13</sup>C NMR further confirmed the formation of the lactone ester group with peaks at 175-176 and 68 ppm corresponding to the C=O ester carbonyl and the CH<sub>2</sub> next to the ester oxygen in correlation with caprolactone (Appendix, Figure A1 & A2); MOP = 176.06 ppm and 68.09 ppm (Figure 2.11, B, carbon environments *a* and *f*), POP = 176.14 ppm and 68.19 ppm (Figure 2.12, B, carbon environments *a* and *f*), BOP = 176.28 ppm and 68.63 ppm (Figure 2.13, B, carbon environments *a* and *f*), PHLOP = 175.72 ppm and 68.26 ppm (Figure 2.14, B, carbon environments *a* and *f*) and BOD = 175.38 ppm and 68.07 ppm (Figure 2.15, B, carbon environments *a* and *f*). Chemical ionisation MS in all cases had peaks corresponding to both the protonated ions, [MH<sup>+</sup>], and ammonium adducts, [MNH<sub>4</sub><sup>+</sup>]; [MH<sup>+</sup>] peaks generated for each monomer were, MOP = 129.1 Da (Figure 2.11, C), POP = 157.1 Da (Figure 2.12, C), BOP = 171.1 Da (Figure 2.13, C), PHLOP = 191.1 Da (Figure 2.14, C) and BOD = 227.1 Da (Figure 2.15, C). Further confirmation of successful syntheses was provided by elemental analysis, *CHN*, which showed highly comparable measurements to the calculated percentages of carbon, oxygen and hydrogen in each case (Section 6.3.1.1).

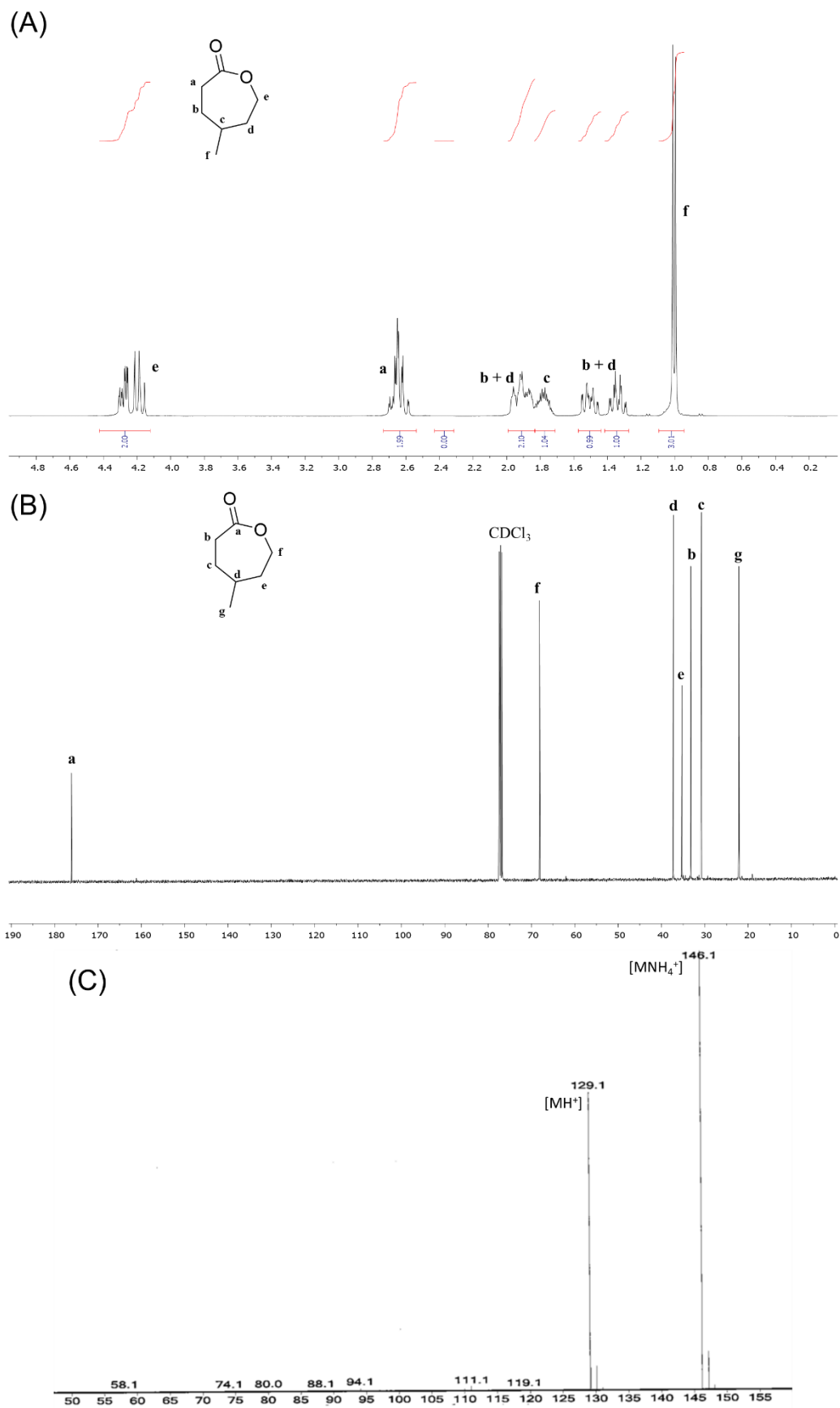


**Figure 2.11** – Analysis undertaken to confirm structure of 5-methyloxepan-2-one, *MOP*;  
 (A)  $^1\text{H}$  NMR in  $\text{CDCl}_3$ , (B)  $^{13}\text{C}$  NMR in  $\text{CDCl}_3$  and (C) Chemical ionisation MS (ammonium gas).

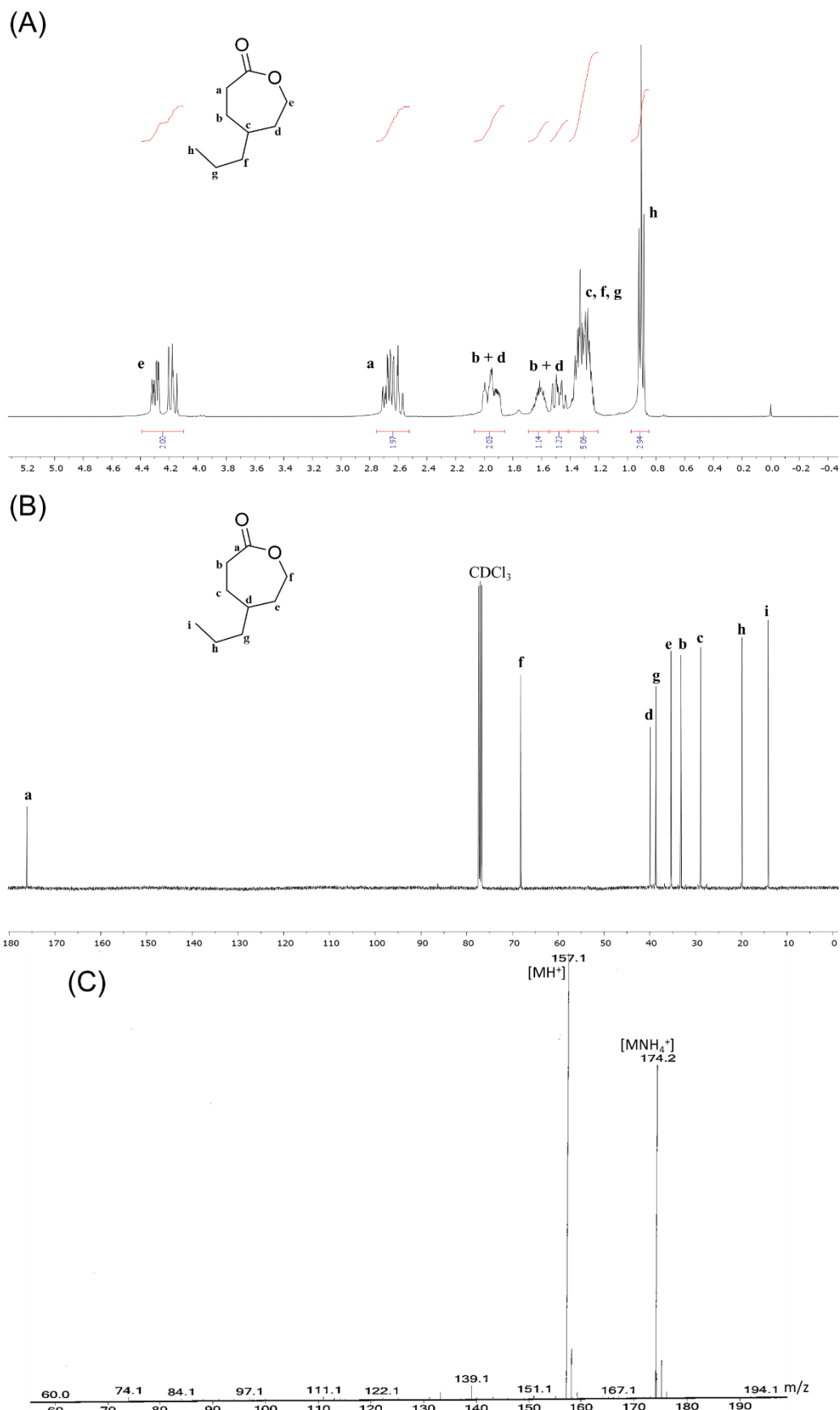


**Figure 2.12 – Analysis undertaken to confirm structure of 5-propyloxepan-2-one, POP;**  
 (A)  $^1\text{H}$  NMR in  $\text{CDCl}_3$ , (B)  $^{13}\text{C}$  NMR in  $\text{CDCl}_3$  and (C) Chemical ionisation MS (ammonium gas).



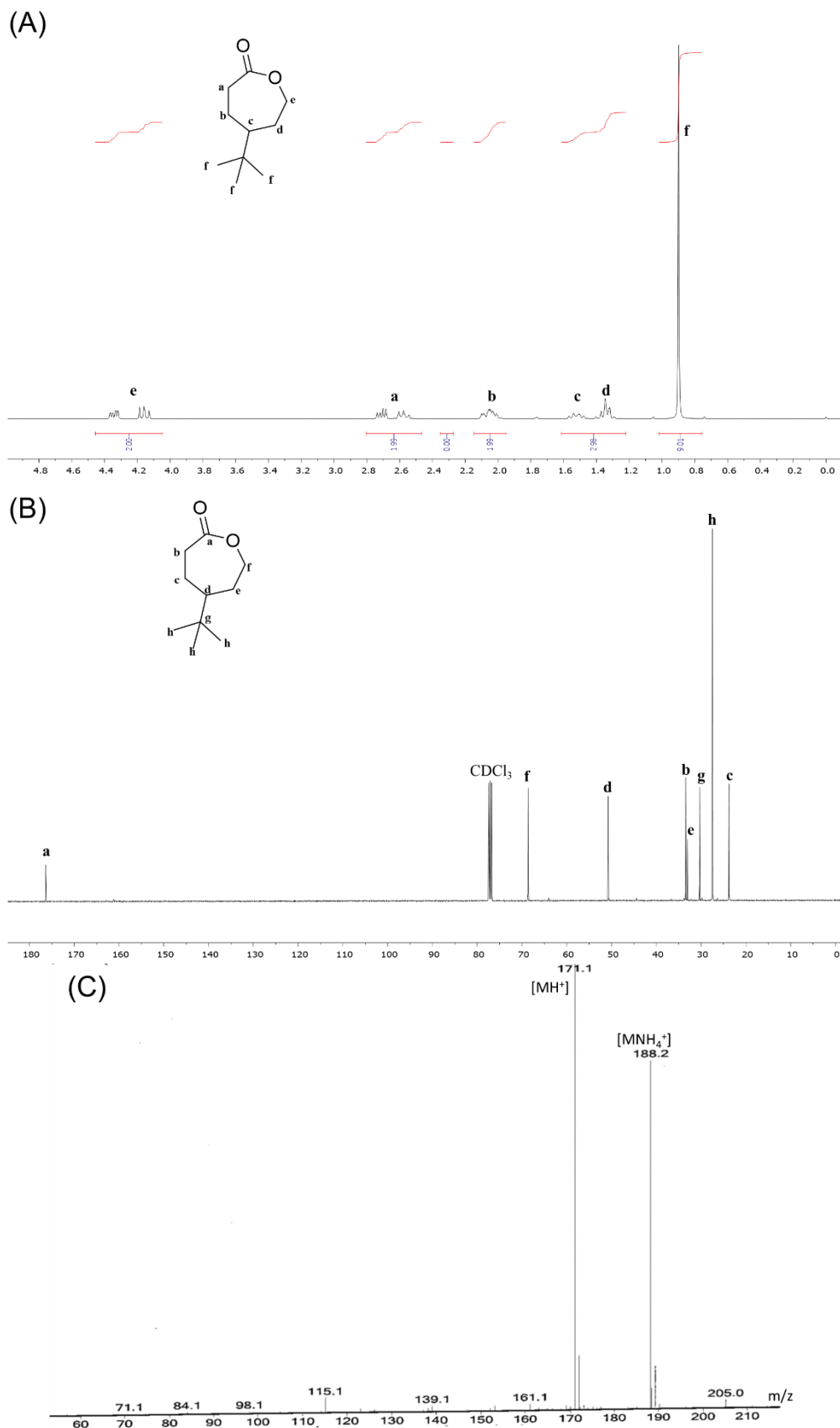


**Figure 2.13** – Analysis undertaken to confirm structure of 5-(*tert*-butyl)oxepan-2-one, *BOP*; (A)  $^1\text{H}$  NMR in  $\text{CDCl}_3$ , (B)  $^{13}\text{C}$  NMR in  $\text{CDCl}_3$  and (C) Chemical ionisation MS (ammonium gas).

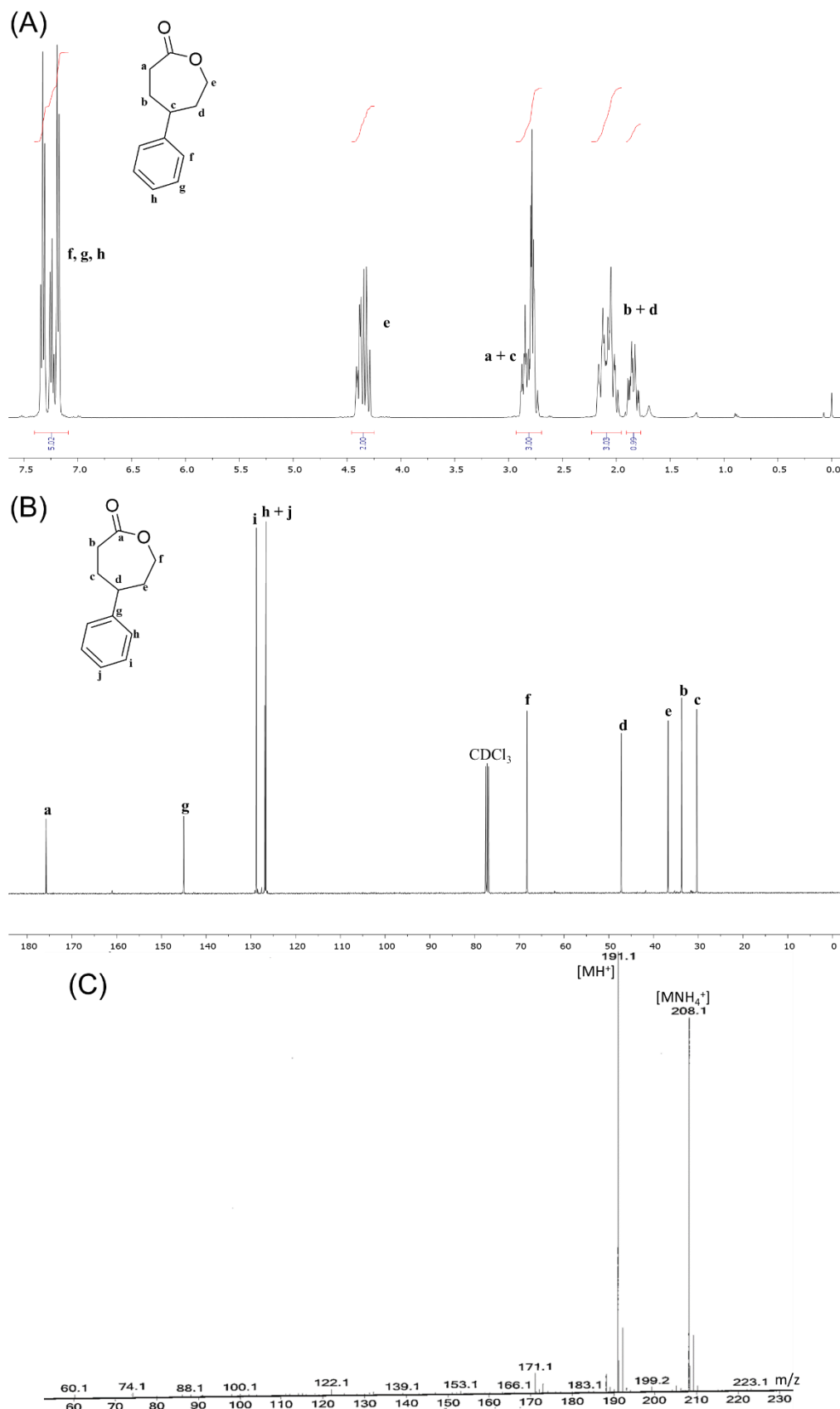


**Figure 2.14** – Analysis undertaken to confirm structure of **5-phenyloxepan-2-one**, *PHLOP*; (A)  $^1\text{H}$  NMR in  $\text{CDCl}_3$ , (B)  $^{13}\text{C}$  NMR in  $\text{CDCl}_3$  and (C) Chemical ionisation MS (ammonium gas).

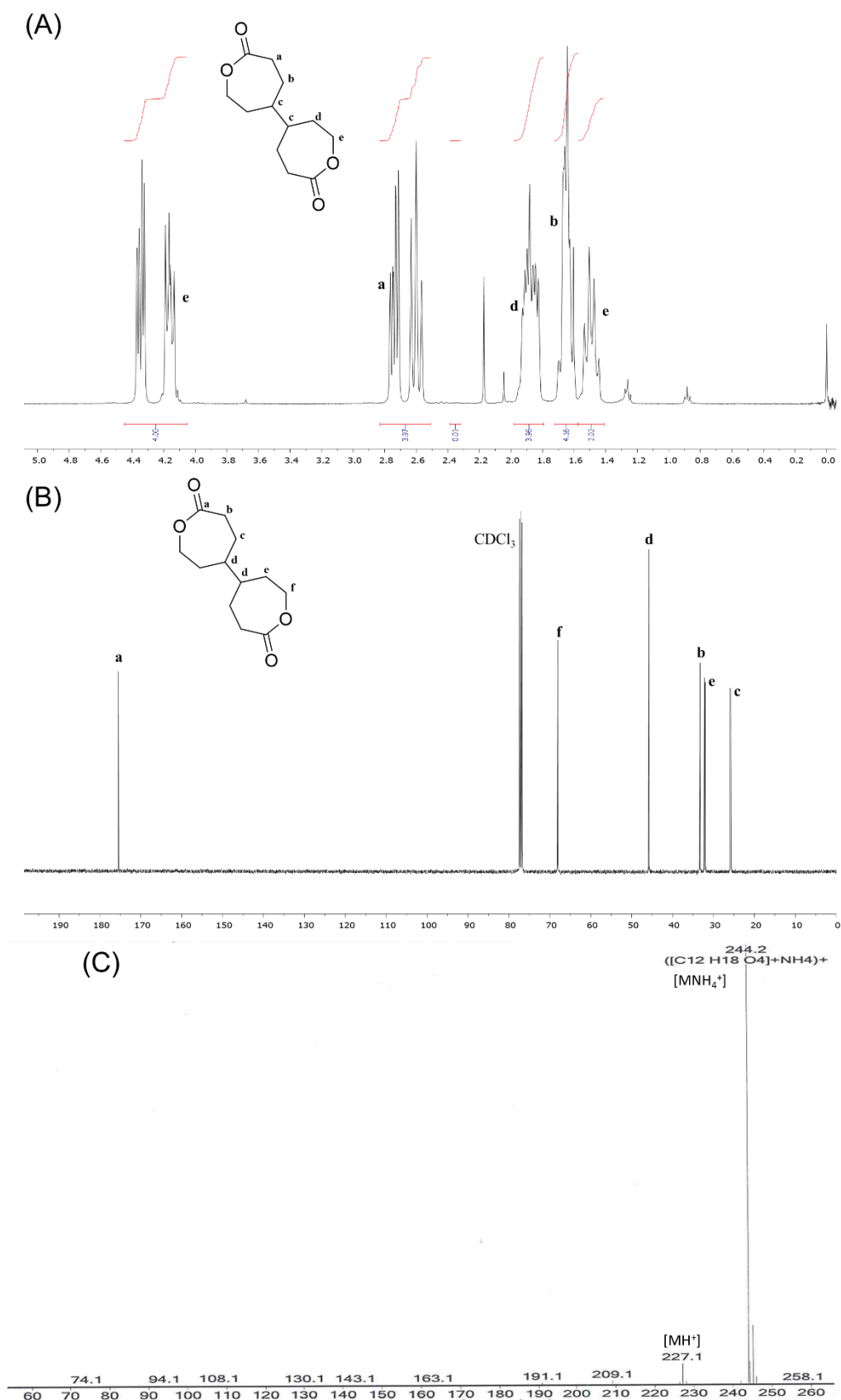


**Figure 2.15** – Analysis undertaken to confirm structure of 4,4'-bioxepanyl-7,7'-dione, *BOD*; (A)  $^1\text{H}$  NMR in  $\text{CDCl}_3$ , (B)  $^{13}\text{C}$  NMR in  $\text{CDCl}_3$  and (C) Chemical ionisation MS (ammonium gas).

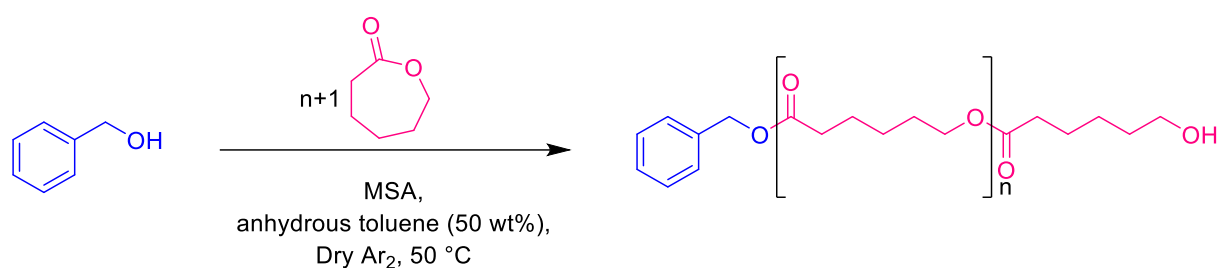
## 2.3 MSA catalysed ROP of $\epsilon$ -caprolactone

The investigation of lactone polymerisations commenced with a comprehensive study of MSA-catalysed ROP of commercially available  $\epsilon$ -CL, to investigate previously reported findings by Gazeau-Bureau *et al.* which detailed the higher activity of MSA for  $\epsilon$ -CL than the stronger acid TfOH.<sup>23</sup> Furthermore, following success reported by Nguyen *et al.*, it was hoped that by exploring the possibility of utilising MSA in co-polymerisation using a ‘modified Strathclyde method’ variation in architecture may be achieved.<sup>42</sup> Finally the incorporation of macroinitiators in MSA-catalysed co-polymerisations, again somewhat lacking in literature, was hypothesised to offer further insight into the capabilities of this type of ROP and help define reaction conditions.

### 2.3.1 Linear polymerisation of $\epsilon$ -caprolactone *via* MSA catalysed ROP

#### 2.3.1.1 Benzyl alcohol initiated, MSA catalysed ROP of $\epsilon$ -caprolactone

Homopolymerisation of  $\epsilon$ -CL was investigated in a series of experiments where the number average degree of polymerisation,  $DP_n$ , was increased from 10 to 200 monomer units. The reactions were carried out at 50 wt% in toluene at 30 °C and were initiated with benzyl alcohol, *BzA* (Scheme 2.4). An argon atmosphere within the reaction vessel was utilised to reduce the possibility of water being introduced into the reaction and acting as an initiator. Upon addition of the MSA catalyst, at a molar ratio of 1:1 initiator: catalyst, homogeneous clear reaction mixtures were observed.



**Scheme 2.4 – Benzyl alcohol initiated MSA catalysed ROP of  $\epsilon$ -caprolactone in toluene at 30 °C.**

Reaction times were increased by intervals of ca. 30 minutes per additional 10 monomer units to allow for the reactions to proceed to completion and ranged from 15 minutes to 9 hours for  $DP_n$  10 to 200. Termination of the reactions was achieved by the dilution of the reaction mixture with chloroform,  $\text{CHCl}_3$ , and the addition of basic alumina to neutralise the catalyst. After a

short basic alumina filtration to remove the catalytic system an aliquot of the resulting liquid was taken for NMR analysis of the crude product.

$^1\text{H}$  NMR determined that the reactions achieved high conversion with values  $>99\%$  in all cases except PCL<sub>200</sub> which only reached 44 % after 9 hours (Table 2.1). Triple detection size exclusion chromatography, SEC, in DMF/LiBr (0.01 M), showed an increase in the number average,  $M_n$ , and weight average,  $M_w$ , molecular weights ranging from 4,060 and 5,540  $\text{g mol}^{-1}$  to 8,760 and 10,630  $\text{g mol}^{-1}$  (Table 2.1) respectively for PCL<sub>30</sub> to PCL<sub>100</sub>. Although reaction times spanned from only 15 minutes for PCL<sub>10</sub> to 9 hours for PCL<sub>200</sub> the dispersity,  $D$ , of each polymer fell within the range of 1.09 to 1.36 when analysed by SEC reiterating the high amount of control that can be achieved with this catalyst.<sup>23</sup> Unfortunately, as the SEC instrument available had columns that were unable to accurately separate very low molecular weights from the solvent front, PCL<sub>10</sub> and PCL<sub>20</sub> were unable to be analysed by SEC. These low  $D$  values indicate that there are limited transesterification reactions occurring in this set of reactions, which is advantageous for the targeting of branched polymers using a high concentration of bis-lactone monomer as described in Section 2.3.1. Furthermore, as demonstrated by Gazeau-Bureau *et al.*, the control of these reaction, demonstrated by low  $D$  values, correlates to the low pKa of MSA which reduces the deactivation of the initiating BzA which is direct competition with the activated monomer (Section 2.1.1, Scheme 2.2).<sup>4,10,23</sup>

**Table 2.1 - Series of MSA catalysed ROP of  $\epsilon$ -CL, initiated by benzyl alcohol, with varied degree of polymerisation 10 to 200 monomer units, normalised with dn/dc value 0.06044 (calculation given in Appendix (Table A1));**

Target polymer	Reaction time (hours)	<sup>1</sup> H NMR				SEC <sup>c</sup>			
		Monomer conversion <sup>a</sup>	DP <sub>1</sub> by NMR (Initiator) <sup>d</sup>	M <sub>n</sub> by NMR (Initiator) (g mol <sup>-1</sup> ) <sup>e</sup>	M <sub>n</sub> Theory <sup>b</sup> (g mol <sup>-1</sup> )	M <sub>n</sub> (g mol <sup>-1</sup> )	M <sub>w</sub> (g mol <sup>-1</sup> )	Đ	$\alpha$
PCL <sub>10</sub>	0.25	>99%	12	1,480	1,250		<i>f</i>		
PCL <sub>20</sub>	0.66	>99%	21	2,510	2,390		<i>f</i>		
PCL <sub>30</sub>	1	>99%	33	3,870	3,530	4,060	5,540	1.36	0.76
PCL <sub>40</sub>	1.5	>99%	41	4,790	4,670	4,680	5,650	1.21	0.82
PCL <sub>50</sub>	2	>99%	66	7,640	5,820	6,510	7,660	1.18	0.84
PCL <sub>60</sub>	2.5	>99%	66	7,640	6,960	6,920	7,960	1.15	0.98
PCL <sub>80</sub>	4	>99%	99	11,410	9,240	7,560	9,720	1.29	0.69
PCL <sub>100</sub>	5	>99%	137	15,750	11,520	8,760	10,630	1.21	0.71
PCL <sub>200</sub>	9	44 %	110	12,670	10,150	7,150	7,770	1.09	0.92

*a* Determined by <sup>1</sup>H NMR (CDCl<sub>3</sub>, 400 MHz) of the crude samples and calculated using equation 1 in Appendix, *b* Calculated using the equation:  $M_{n\text{theory}} = (DP_{\text{targeted}} \times \text{conv.} \times M_{r\text{CL}}) + M_{r\text{BzA}}$ , *c* Determined by triple detection SEC with a mobile phase of DMF/LiBr 0.01 M (60 °C) at 1 mL min<sup>-1</sup>, *d* Calculated using the equation;  $DP_1 = (J4.05/2 \div J5.1/2)$ , *e* Calculated using the equation:  $M_{n\text{NMR}} = (DP_{1(\text{Eq. 2.14})} \times M_{r\text{CL}}) + M_{r\text{BzA}}$ , *f* insufficient light scattering for calculation but RI chromatograms indicated monomodal distribution.

SEC analysis also showed monomodal chromatograms for all polymers (Figure 2.16), with high molecular weight shoulders beginning to appear at the highest targeted  $DP_n$  values. The ability to accurately control the polymerisation at low targeted  $DP_n$  values, using MSA catalysed ROP, is important to understand to allow accurate design of branched polymers and avoid gelation. Therefore ideal branching is more likely to occur for polymers with a targeted  $DP_n \leq 50$  for each linear chain linked together to allow for control of water impurity concentrations.

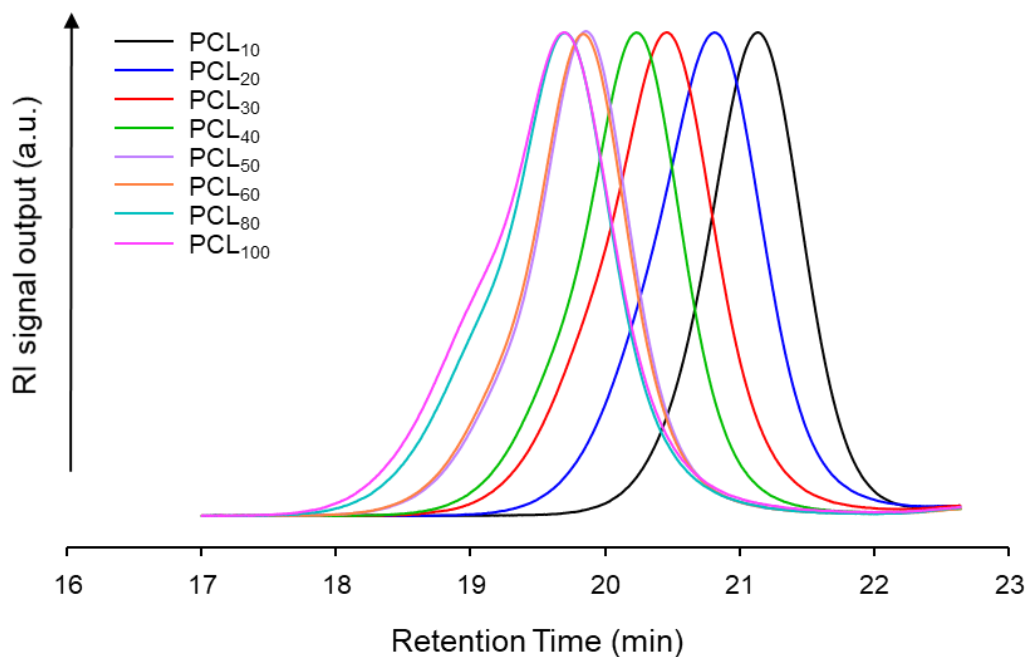
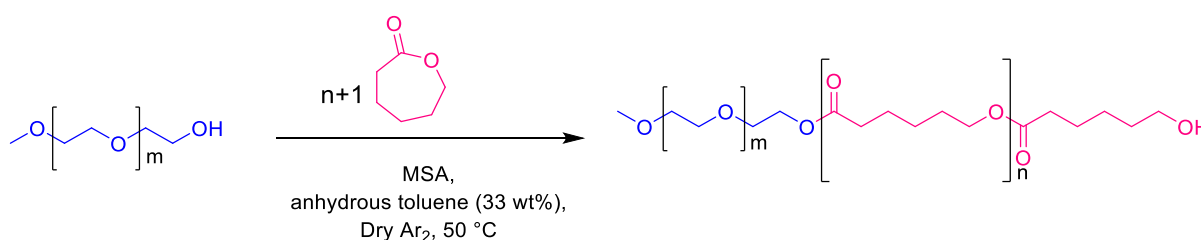


**Figure 2.16 - Refractive index,  $RI$ , detector output chromatograms of linear  $PCL_x$  polymers ( $x = 10-100$ ) generated by MSA catalysed ROP.** Obtained by triple detection SEC; Mobile phase: DMF/ 0.01 M LiBr at 60 °C.

### 2.3.1.2 Poly(ethylene glycol)<sub>2K/5K</sub> initiated MSA catalysed ROP of $\epsilon$ -caprolactone

MSA catalysed ROP using a hydrophilic macroinitiator, in this case poly(ethylene glycol), *PEG-OH*, was studied to form amphiphilic A-B block co-polymers (Scheme 2.5). Two *PEG-OH* polymers of differing molecular weight were selected to allow for the exploration of the effect hydrophilic block length on nanoparticle formation.  $M_n$  values of 2000 g mol<sup>-1</sup>, *PEG<sub>2K</sub>-OH*, and 5000 g mol<sup>-1</sup>, *PEG<sub>5K</sub>-OH*, were selected to allow variation in amphiphilicity when the target  $DP_n$  of the hydrophobic PCL block was maintained at 40 monomer units. Similar initiating conditions to those used for linear homo-polymerisations were utilised (initiator: catalyst ratio - 1:1 molar equivalents), however, the reaction dilution was increased to 33 wt%, with respect to monomer, using toluene heated to 50 °C to enable *PEG-OH* to completely dissolve.



**Scheme 2.5 – PEG-OH initiated MSA catalysed ROP of  $\epsilon$ -CL in toluene at 50 °C.**

As seen with the BzA initiated linear homo-polymers, <sup>1</sup>H NMR analysis showed both *PEG-b-PCL* polymerisations reached >99% conversion (Table 2.2). This indicated that the use of a large macroinitiator does not retard the rate of polymerisation and supports the monomer activated mechanism, induced by the catalyst. The propagating polymer chain is surrounded by activated monomer species which decreases the impact of steric hindrance that is reported in classic chain end activated polymerisations where, as the polymerisation progresses and monomer concentrations decrease, the probability of reaction reduce.



**Table 2.2 - MSA catalysed ROP of  $\epsilon$ -CL initiated by PEG-OH with Degree of Polymerisation 40 monomer units.**

Target polymer	<sup>1</sup> H NMR			SEC <sup>c</sup>			
	DP <sub>I</sub> by NMR (Initiator) <sup>d</sup>	M <sub>n</sub> by NMR (Initiator) (g mol <sup>-1</sup> ) <sup>e</sup>	M <sub>n</sub> Theory <sup>b</sup> (g mol <sup>-1</sup> )	M <sub>n</sub> (g mol <sup>-1</sup> )	M <sub>w</sub> (g mol <sup>-1</sup> )	Đ	$\alpha$
PEG <sub>2K</sub> - <i>b</i> -PCL <sub>40</sub> <sup>e</sup>	41	6,680	6,570	5,470	6,260	1.15	0.59
PEG <sub>5K</sub> - <i>b</i> -PCL <sub>40</sub> <sup>f</sup>	42	9,790	9,570	7,540	8,400	1.12	0.70
PEG <sub>2K</sub> -OH		-			- <sup>g</sup>		
PEG <sub>5K</sub> -OH		-		4,970	5,250	1.06	0.76

Both polymers reached > 99% monomer conversion following a reaction time of 2 hours; *a* Determined by <sup>1</sup>H NMR (CDCl<sub>3</sub>, 400 MHz) of the crude samples, *b* Calculated using the equation:  $M_{n\text{theory}} = (DP_{\text{targeted}} \times \text{conv.} \times M_{r\text{CL}}) + M_{r\text{BZA}}$ , *c* Determined by triple detection SEC with a mobile phase of DMF/LiBr 0.01 M (60 °C) at 1 mL min<sup>-1</sup>, *d* Calculated using the equation;  $DP_I = (4.05/2 \div 3.36/2)$ , *e* Calculated using the equation:  $M_{n\text{NMR}} = (DP_{I(\text{Eq. 2.14})} \times M_{r\text{CL}}) + M_{r\text{BZA/PEG-OH}}$ , *e* dn/dc value 0.0588 used, *f* dn/dc value 0.0605 used, *g* insufficient light scattering for calculation but RI chromatograms indicated monomodal distribution

Triple detection SEC analysis (DMF/ 0.01 M LiBr, 60 °C) was undertaken after purification, following the same catalyst removal as detailed in Section 2.3.1.1, and precipitation into cold hexane. Good control of the polymerisation was evident from this analysis, with monomodal and narrow molecular weight distributions for both PEG<sub>2K</sub>-*b*-PCL<sub>40</sub> and PEG<sub>5K</sub>-*b*-PCL<sub>40</sub>; Đ 1.12 and 1.15 respectively (Table 2.2), indicating good initiator efficiency. Refractive index, RI, chromatogram comparisons between the initial macroinitiators and the A-B block co-polymers also showed an increase in molecular weight (Figure 2.17, A & B) and extension of the polymer chains with the new PCL<sub>40</sub> blocks. Additionally, comparative overlays of chromatograms of PEG<sub>2K</sub>-*b*-PCL<sub>40</sub> and PEG<sub>5K</sub>-*b*-PCL<sub>40</sub> highlights the different molecular weights of the final block co-polymers, derived from either the PEG<sub>2K</sub>-OH or larger PEG<sub>5K</sub>-OH blocks (Figure 2.17, C). However there was seen to be small discrepancies between the between theoretical (by <sup>1</sup>H NMR) and calculated (by SEC) M<sub>n</sub> values with the SEC given M<sub>n</sub> values being lower than expected when M<sub>n</sub> was calculated based the initiator proton environment in the <sup>1</sup>H-NMR. (Table 2.2).

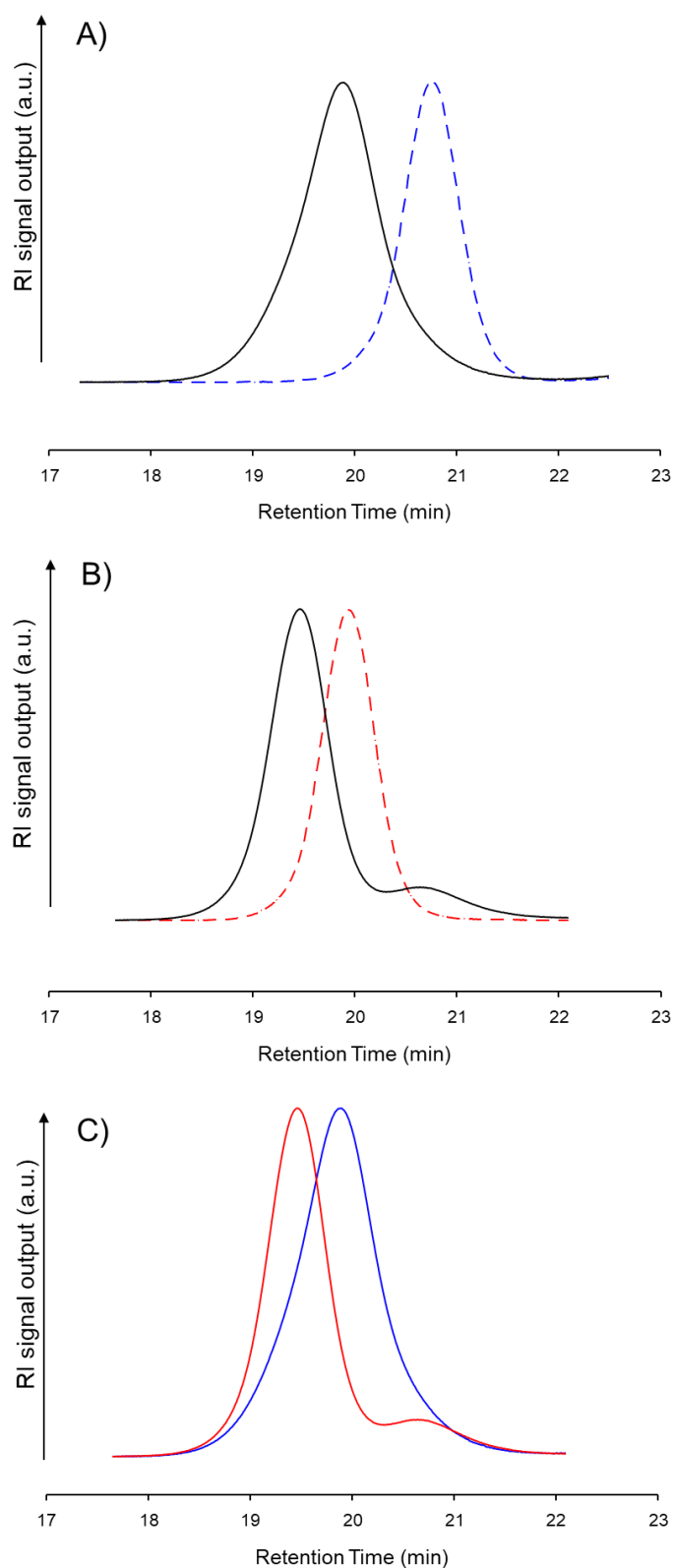


**Figure 2.17 - Refractive index,  $RI$ , detector output chromatograms of  $PEG_x-b-PCL_{40}$ , obtained by MSA catalysed ROP, overlaid with the corresponding  $PEG_x-OH$  macroinitiator; A)  $PEG_{2K}-b-PCL_{40}$  (black, solid) overlaid with  $PEG_{2K}-OH$  (blue, dashed); B)  $PEG_{5K}-b-PCL_{40}$  overlaid with  $PEG_{5K}-OH$  (red, dashed) and C)  $PEG_{2K}-b-PCL_{40}$  (blue) overlaid with  $PEG_{5K}-b-PCL_{40}$  (red). Triple detection SEC; Mobile phase: DMF/ 0.01 M LiBr at 60 °C.**

### **2.3.2 Mechanistic studies of linear polymerisation of $\epsilon$ -caprolactone *via* MSA catalysed ROP**

As MSA catalysed ROP provides a fast synthetic route to controlled polymers and given the favourable reaction conditions when compared to traditional metal catalysed ROP routes polymerisations of  $\epsilon$ -CL were undertaken with commercial scale up in mind. Therefore stringent anhydrous conditions were not followed throughout the investigations detailed in this chapter. However the implementation of less stringent conditions can lead to a number of complications which could affect the success of this ROP route in a commercial setting. Firstly the speed of the polymerisation could be affected by the lack of strict anhydrous conditions which also generates potential for opportunistic initiation of polymer chains (possibly by water). Finally the possibility of side reactions, such as transesterification, could affect the controlled nature of the resultant polymers therefore mechanistic studies were undertaken to explore these concerns.

#### **2.3.2.1 Kinetic studies of linear MSA catalysed ROP of $\epsilon$ -caprolactone initiated by benzyl alcohol**

In order to fully understand the role MSA plays in the polymerisation of  $\epsilon$ -CL detailed kinetic studies were conducted. These were also useful as a comparison for kinetics later performed on the branched PCL polymers giving insight into how the introduction of a bis-lactone monomer affects the kinetics of the polymerisation. This study was performed with a molar ratio of BzA:  $\epsilon$ -CL set to 1:40 monomer units, therefore targeting PCL<sub>40</sub>, and was conducted in the same fashion as the standard linear polymerisations and left to react over 1.5 hours before termination. Samples were initially taken every 5 minutes after the addition of MSA for the first 30 minutes, and then every 10 minutes until 1.5 hours was reached; the catalyst was removed using basic alumina as previously. The resulting crude samples were consequently analysed by <sup>1</sup>H NMR spectroscopy and SEC to determine the progression of monomer conversion and molecular weight as the reaction advanced.

Upon the execution of initial kinetic studies, and subsequent <sup>1</sup>H NMR analysis, it appeared that the basic alumina was removing excess unreacted monomer upon filtration, therefore, accurate monomer conversion values could not be deduced. In order to develop the best experimental protocol, two acid neutralisation methods applied in parallel to a limited number of time points on a model polymerisation.

Firstly, rather than passing the samples through a small basic alumina column, a small amount of basic alumina was instead added to each sample after first dissolving the aliquot from the reaction in chloroform; a simple filtration was then used to remove the solid alumina. Secondly, triethylamine, *TEA*, was dissolved in toluene and added to each sample aliquot at an equimolar concentration to the MSA; a simple filtration was utilised to remove the solid salt precipitate. The samples were analysed by  $^1\text{H}$  NMR to determine monomer conversions for each sample removed during the polymerisation. Importantly, monomer conversion appeared to not follow any consistent trend between time points when the samples were treated with basic alumina, but the conversion data generated from samples treated with TEA followed a clear trend during the polymerisation (Figure 2.18).

### Comparison of MSA neutralisation for kinetic analysis

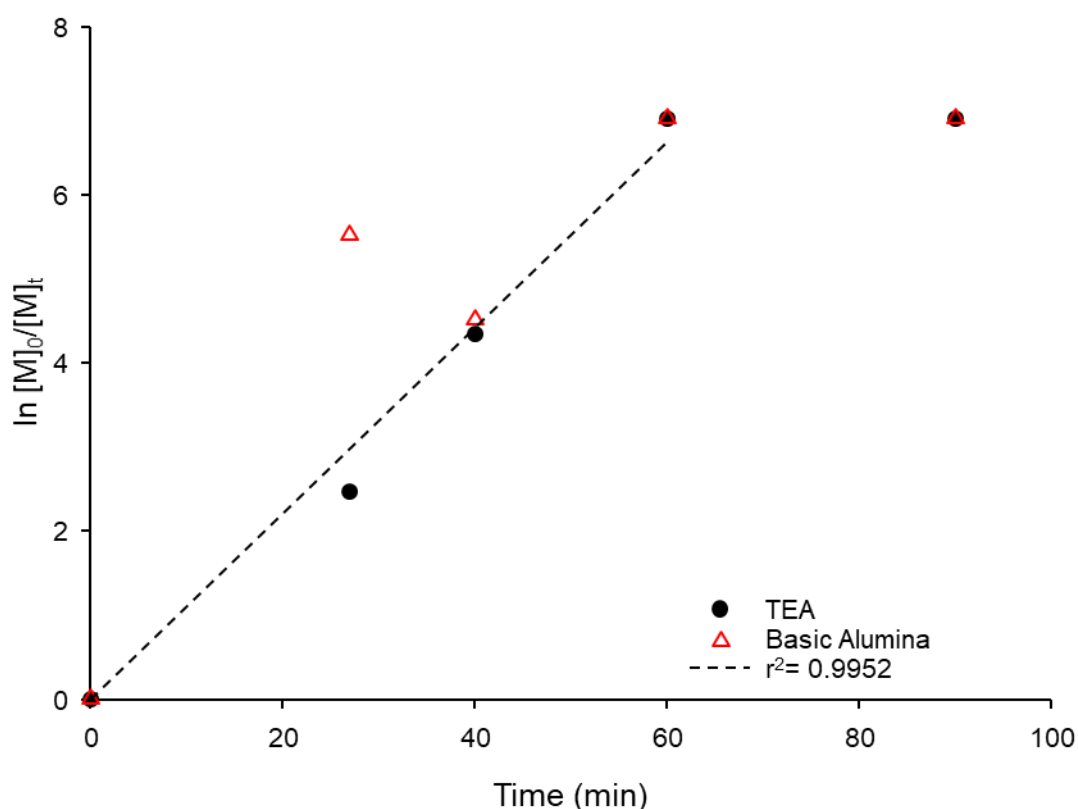


**Figure 2.18-** Semi-log plot vs time of  $\text{PCL}_{40}$  synthesis drawing comparisons between acid neutralisation techniques for kinetic analysis studies calculated by  $^1\text{H}$  NMR in  $\text{CDCl}_3$ . (A) TEA neutralisation ( $\bullet$ ) against basic alumina ( $\Delta$ ) with best fit line fitted to TEA time points excluding  $t_{90}$  as  $t_{60} = t_{90}$ ,  $r^2 = 0.9952$ .

This preliminary model reaction indicated that 91.5 % monomer conversion had been reached after 27 minutes, therefore, the reaction was repeated with samples taken every 3 minutes after

MSA addition up to a reaction time of 30 minutes, and additional samples taken every 5 until 1.5 hours. Analysis of samples taken in the first 30 minutes by  $^1\text{H}$  NMR showed that the polymerisation had achieved 17.8 % conversion after just 3 minutes with 99 % conversion being surpassed at 27 minutes. Analysis of all the time points after  $t_{27}$  showed a consistent plateau at  $> 99$  % conversion. Consequently, kinetics plots were constructed using  $^1\text{H}$  NMR analysis from time points  $t_0$  to  $t_{30}$  at which point 99.9 % conversion was indicated (Figure 2.19). The first order integration law was applied to the data to plot  $\ln([M]_0/[M]_t)$  versus time (Figure 2.19, A) where  $[M]_0$  is the monomer concentration at  $t_0$  and  $[M]_t$  is the monomer concentration at a specific time. In contrast to the linear relationship expected between  $\ln([M]_0/[M]_t)$  and time, an upward curve trending to an increased rate with increased time was observed with a regression of only  $r^2 = 0.8485$  (Figure 2.19, A). Literature illustrates that the use of acid catalysts in ROP does in fact follow first order kinetics, particularly in the case of lactide polymerisation; however, the polymerisation proceeding by an activated monomer mechanism adds an extra layer of complexity to the kinetics of cationic ROP.<sup>6,37,82,83</sup>

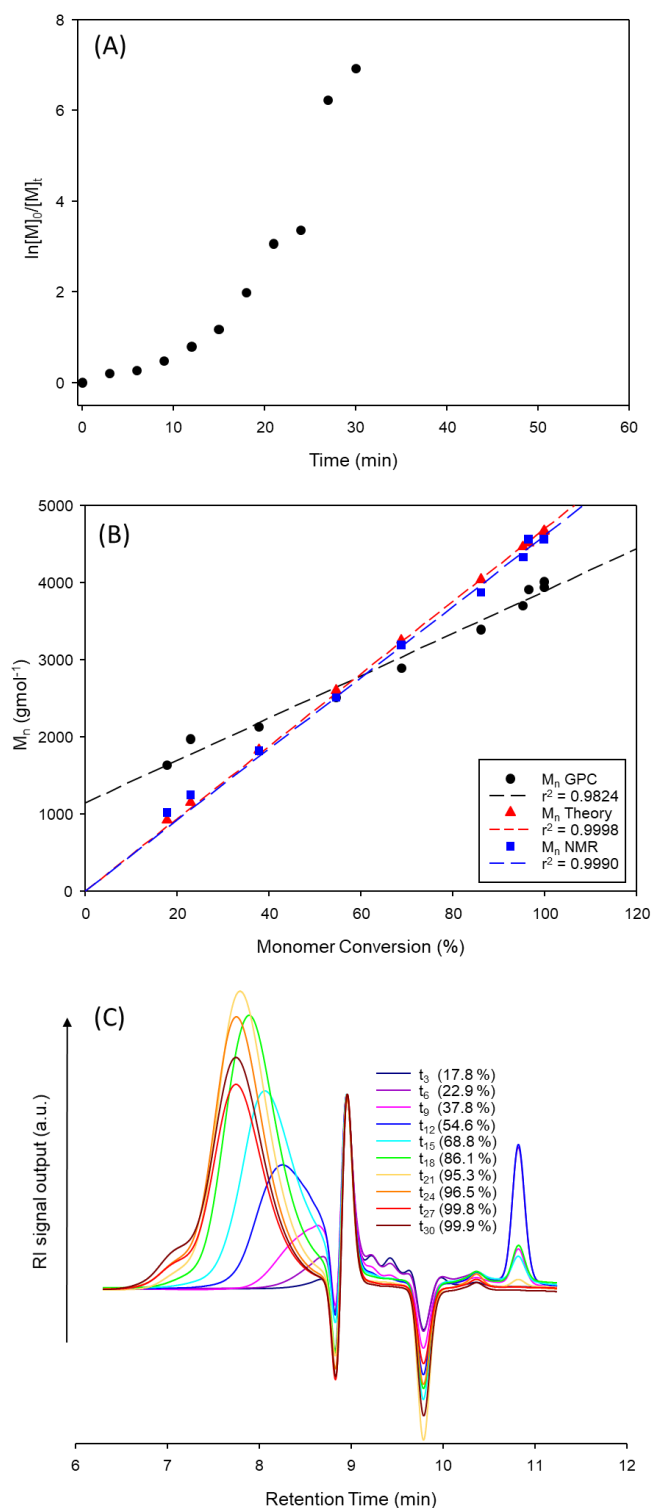


**Figure 2.19-** Analysis for kinetic study of PCL<sub>40</sub> synthesis completed with TEA acid neutralisation, between 0 to 30 minutes (when full monomer conversion reached-calculated by <sup>1</sup>H NMR in CDCl<sub>3</sub>). (A) semi-log plot from 0 – 99.9 % conversion ( $t_0$  to  $t_{30}$ ) calculated by <sup>1</sup>H NMR in CDCl<sub>3</sub>, (B) evolution of molecular weight with conversion calculated by <sup>1</sup>H NMR in CDCl<sub>3</sub> and RI detection SEC (DMF/LiBr 0.01 M at 1 mL min<sup>-1</sup> w.r.t to poly(methyl methacrylate, PMMA, calibrants), (C) overlay of RI traces from 17.8 – 99.9 % conversion ( $t_3$  to  $t_{30}$ ) using RI detection, single detection SEC (DMF/LiBr 0.01 M at 1 mL min<sup>-1</sup> w.r.t to PMMA calibrants).

Considering first order rate equations seen for other “controlled/living” polymerisations a common feature is the rate dependence on the concentration of monomer and radicals where radical concentration remains constant (Eq. 2.1).<sup>84</sup>

$$-\frac{d[M]}{dt} = k_p [M][R^*] \quad \text{Equation 2.1}$$

Where  $[M]$  is monomer concentration,  $k_p$  is the propagation constant and  $[R^*]$  is the concentration of radicals.<sup>84</sup> Therefore as the polymerisation proceeds and monomer concentrations decrease plotting  $\ln([M]_0/[M]_t)$  versus time yields a linear relationship. On the other hand, the propagation in an activated monomer mechanism involves reactions between a hydroxyl group on the initiator or growing chain end and a protonated monomer generating Eq. 2.2;

$$-\frac{d[M]}{dt} = k[H-M^+][OH] \quad \text{Equation 2.2}$$

where  $[H-M^+]$  is the concentration of protonated monomer,  $[OH]$  is the concentration of OH groups and  $k$  is a rate constant. Moreover the concentration of protonated monomer and its proportionality to the overall monomer concentration is determined by the basicity of the unreacted monomer and the monomer units in the polymer chain.<sup>37,83,85</sup>

The inclusion of monomer concentration,  $[M]$ , in the kinetic equation of propagation required the derivation of the term for the concentration of protonated monomer,  $[H-M^+]$ . This must begin with the definition of the equilibrium constants of protonation for the OH groups,  $K_{OH}$ , monomer,  $K_M$ , and polymer,  $K_{P\oplus}$ :

$$K_{OH} = \frac{[OH_2]}{[OH][H^+]} \quad \text{Equation 2.3}$$

where  $[OH_2]$  is the concentration of water and  $[H^+]$  is the concentration of protons.

$$K_M = \frac{[H-M^+]}{[M][H^+]} \quad \text{Equation 2.4}$$

$$K_{P\oplus} = \frac{[H-P^+]}{[P][H^+]} \quad \text{Equation 2.5}$$

Where  $[H-P^+]$  is the concentration protonated monomer units within the polymer chain and  $[P]$  is the concentration of monomer units within the polymer chain.

## CHAPTER 2

The total concentration of protons,  $[H^+]$ , is defined as:

$$[H^+] = [H - M^+] + [H - P^+] + [OH_2] \quad \text{Equation 2.6}$$

This can be re-written utilising equations 2.3 to 2.5:

$$[H^+] = K_M[M][H^+] + K_{P\oplus}[P][H^+] + K_{OH}[OH][H^+] \quad \text{Equation 2.7}$$

Therefore:

$$\frac{[H - M^+]}{K_M[M][H^+]} = \frac{[H^+]}{K_M[M][H^+] + K_{P\oplus}[P][H^+] + K_{OH}[OH][H^+]} \quad \text{Equation 2.8}$$

Equation 2.8 can now be simplified (Eq. 2.9) and subsequently rearranged (Eq. 2.10):

$$[H - M^+] = \frac{K_M[M][H^+]}{K_M[M] + K_{P\oplus}[P] + K_{OH}[OH]} \quad \text{Equation 2.9}$$

$$[H - M^+] = \frac{[M][H^+]}{[M] + \frac{K_{P\oplus}}{K_M}[P] + \frac{K_{OH}}{K_M}[OH]} \quad \text{Equation 2.10}$$

Therefore the term  $[H - M^+]$  can be represented by the equation:

$$[H - M^+] = B[M] \quad \text{Equation 2.11}$$

$$\text{where } B = \frac{[H^+]}{\{[M] + [P]\left(\frac{K_{P\oplus}}{K_M}\right) + [OH]\left(\frac{K_{OH}}{K_M}\right)\}}$$

Monomer concentration,  $[M]$ , can now appear in the kinetic equation of propagation adapted from equation 2.2:

$$-\frac{d[M]}{dt} = kB[M][OH] \quad \text{Equation 2.12}$$

$$\ln \frac{[M]_0}{[M]} = kB[OH]t \quad \text{Equation 2.13}$$

where  $[M]_0$  is the concentration of monomer at  $t_0$  and  $t$  is time.

After considering equations 2.2 to 2.13 it is clear that the linear relationship between  $\ln([M]_0/[M]_t)$  and time is dependent on the equilibrium constants of protonation for the monomer, monomer units in the polymer chain and the OH groups.  $[OH]$  remains constant throughout the reaction and  $K_{OH}/K_M$  can be assumed to also be constant and thus disregarded in term B (Eq. 2.11). Therefore, knowing that  $[M]$  and  $[P]$  (which are non-constant) vary



according to the equation  $[M] + [P]$  if  $C^{\text{ste}} = [M]_0$ , the term B can only then be considered a constant when the ratio  $K_{P\oplus}/K_M$  is close to 1.

The term  $K_{P\oplus}/K_M$  is dependent on the relative basicity of the unreacted monomer and the monomer units in the polymer chain.<sup>37</sup> Lactide, for example, has similar basicity in both ring closed and open (polymerised) forms therefore protonation can be regarded as equally distributed between polymer chains and unreacted monomer at any given time.<sup>37,85</sup> In this case  $K_{P\oplus}/K_M$  can be assumed to be close to 1 thus generating a linear relationship between  $\ln([M]_0/[M]_t)$  and time. In contrast,  $\epsilon$ -caprolactone has a significantly higher basicity as a closed ring, unreacted monomer, when compared to the open polymerised counterpart.<sup>37</sup> At the beginning of the polymerisation the concentration of activated monomer,  $[M-H^+]$ , is in equilibrium with the concentration of free acid,  $[H^+]$ , and inactivated monomer,  $[M]$ , (Equation 2.4) defining a certain concentration of activated monomer. During propagation the number of polyester groups (open ring polymerised monomers),  $[P]$ , increases. As the acid does not bind well to the ester groups within the polymer chain (i.e.  $K_{P\oplus}$  is  $< 1$ ), the effective concentration of acid in the equilibrium that is activating unreacted monomer,  $[H^+]$ , increases and therefore the effective concentration of activated monomer,  $[M-H^+]$ , increases. This means that, as the polymerisation progresses, and the growing polymer chain is less likely to become protonated, the amount of activated monomer per hydroxyl chain end increases.<sup>\*\*\*</sup> This increases the probability of reaction and therefore the rate of polymerisation (Figure 2.19, B).  $K_{P\oplus}/K_M$  can now be considered as  $< 1$  producing an upward curving plot in the semi-log graph as rate increases with time ( $[M] + (K_{P\oplus}/K_M)[P] \neq [M]_0$ ) (Figure 2.19, A). Figure 2.20 B shows a cartoon representation of the reaction assuming  $[H^+] = [H-M^+]$  (i.e.  $K_M = 1$ ). However due to the equilibrium between the free acid and protonated monomer,  $K_M$ , (Equation 2.4) and the fact  $K_M$  would be greater than 1, this process is likely to be more complex than the one depicted this figure.

A plot of  $M_n$  vs monomer conversion, using SEC analysis, generated a linear relationship (Figure 2.19, B), indicating control of the polymerisation. However, when plotted with both  $M_n$  by NMR and  $M_n$  theory vs time plots it is clear that the gradient produced with  $M_n$  by SEC was significantly different from these plots. Additionally, the regression line for  $M_n$  by SEC failed to pass through the origin of the graph. This deviation in gradient and intercept is not

---

<sup>\*\*\*</sup> This also suggests that transesterification reactions are kept at a minimum when monomer is present in the reaction mixture due to the decreased probability of the polymer chain becoming protonated by MSA.

unexpected as SEC analyses are known to be inaccurate at relatively short chain lengths and the single detection SEC instrument used here was only fitted with oligomer column; additionally single detection analysis (RI in this case) relies on poly(methyl methacrylate), *PMMA*, calibrants to calculate molecular weight values. In this case, the RI chromatograms (Figure 2.19, C) for the early and late time points lay on the upward and downward curve of the cubic plot produced by the *PMMA* calibrants which again leads to inaccuracies within the calculations of molecular weight values. Nonetheless both  $M_n$  by SEC and  $M_n$  by NMR have a linear relationship with conversion confirming all chains are apparently growing at a similar rate and suggesting control of the polymerisation.<sup>84</sup> The data here, and the strong indication of polymerisation control, indicates that the formation of branched polymer architectures using MSA-catalysed ROP should be possible using similar considerations to those previously reported for the monovinyl/divinyl monomer mixtures.<sup>69,86</sup>

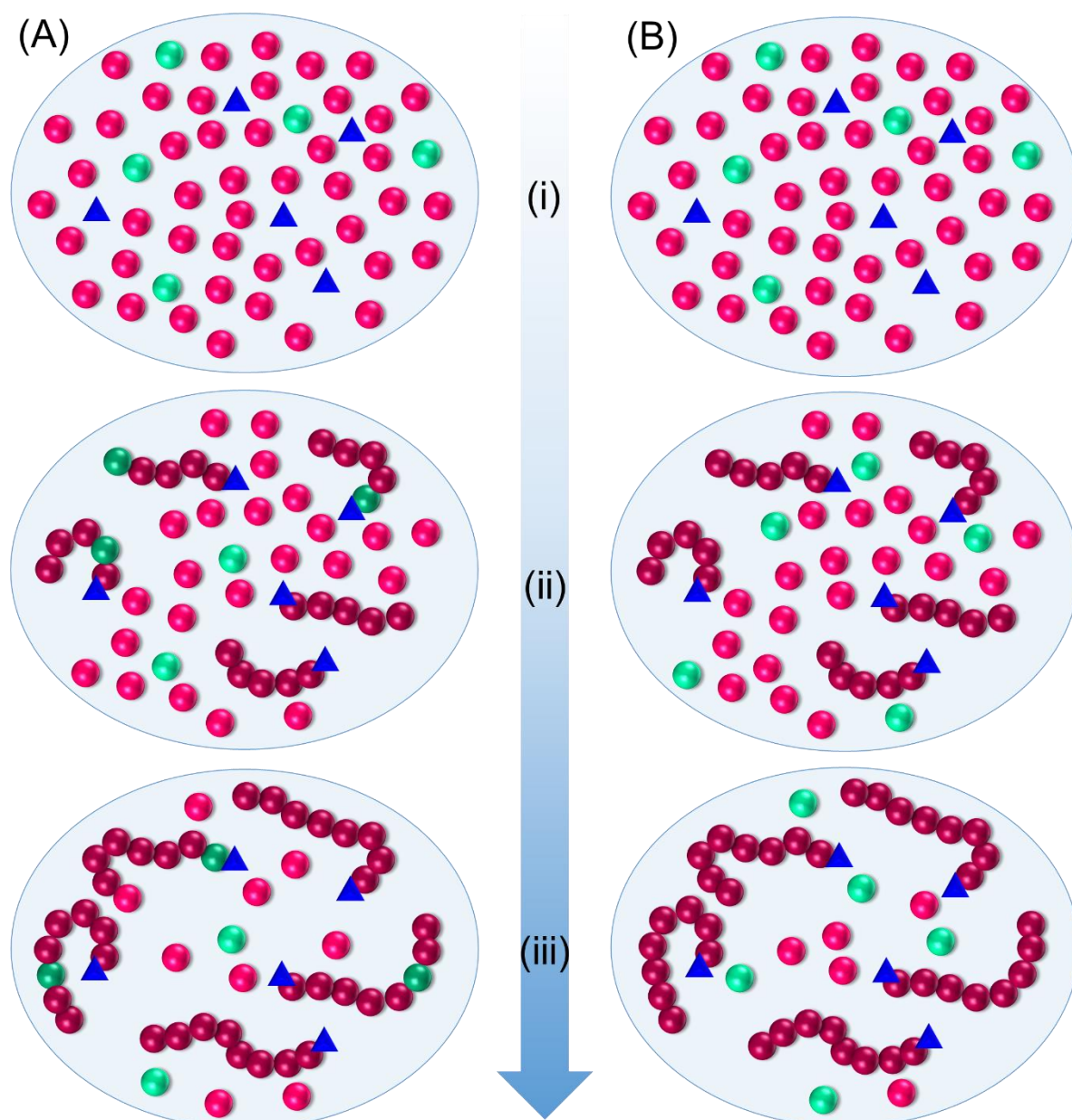


**Figure 2.20-** Schematic representation of the effects differing basicity of unreacted monomer and polymerised monomer has on the rate of polymerisation (assuming all free acid (1 eq. per BzA) results in a protonated monomer,  $K_M = 1$ ). (A) Basicity of both species are similar therefore  $K_{P^{\oplus}}/K_M \sim 1$ , (B) basicity of the unreacted monomer is much greater than the polymerised monomer therefore  $K_{P^{\oplus}}/K_M \ll 1$ . Insight into the reaction given at (i) 0 % monomer conversion, (ii) 50 % monomer conversion and (iii) 80 % monomer conversion. (Green circles) protonated monomer units, (dark pink circles) polymerised monomer units, (pink circles) unreacted monomer units and (blue triangles) initiating species.

### 2.3.2.2 Assessment of opportunistic side reactions present in linear MSA catalysed ROP of $\epsilon$ -caprolactone

As mentioned in Section 2.3.2 stringent anhydrous conditions were avoided for MSA catalysed ROP to target a polymerisation more suitable for industrial scale up.  $\epsilon$ -CL required the most labour intensive drying process, frequently distilled over calcium hydride,  $\text{CaH}_2$ , at 92 °C, which also generated problematic waste disposal. Therefore a short study was undertaken to assess molecular sieves as an alternative drying method mitigating both waste disposal and distillation difficulties. Targeting a  $\text{DP}_n = 40$  monomer units and implementing the polymerisation method detailed in Section 2.3.1.1 PCL polymers were generated from  $\epsilon$ -CL stocks either as received, dried over  $\text{CaH}_2$  or dried over molecular sieves (Table 2.3). Reaction times were extended to 2.5 hours in an attempt to emphasise any differences that may occur between the three reactions.

**Table 2.3 - Series of MSA catalysed ROP of  $\epsilon$ -CL ( $\text{DP}_n = 40$  monomer units), initiated by benzyl alcohol, exploring the effects of monomer drying methods on polymer control;**

Drying method	$^1\text{H NMR}$				SEC <sup>c</sup>				
	Monomer conversion <sup>a</sup>	$\text{DP}_1$ by NMR (Initiator)	$M_n$ by NMR (Initiator) ( $\text{g mol}^{-1}$ ) <sup>d</sup>	$M_n$ Theory <sup>b</sup> ( $\text{g mol}^{-1}$ )	$M_n$ ( $\text{g mol}^{-1}$ )	$M_w$ ( $\text{g mol}^{-1}$ )	$\mathcal{D}$	$\alpha$	$\text{dn/dc}$
As purchased	>99 %	41	4,790	4,670	5,020	5,350	1.07	0.78	0.0776
$\text{CaH}_2$ distillation	>99 %	42	4,900	4,670	5,320	5,930	1.12	0.87	0.0703
Molecular sieves	>99 %	44	5,130	4,670	5,320	5,580	1.05	0.77	0.0723

Polymerisations undertaken at 30 °C for 2.5 hours; *a* Determined by  $^1\text{H NMR}$  ( $\text{CDCl}_3$ , 400 MHz) of the crude samples, *b* Calculated using the equation:  $M_{n\text{theory}} = (\text{DP}_{\text{targeted}} \times \text{conv.} \times M_{r\text{CL}}) + M_{r\text{BZA}}$ , *c* Determined by triple detection SEC with a mobile phase of THF/ 2 v/v % TEA at 1 mL  $\text{min}^{-1}$ , *d* Calculated using the equation:  $M_{n\text{NMR}} = (\text{DP}_{\text{I(Eq. 2.14)}} \times M_{r\text{CL}}) + M_{r\text{BZA/PEG-OH}}$ .

$^1\text{H-NMR}$  analysis revealed that all three polymerisations reached >99 % monomer conversion suggesting that the polymerisation rate was unaffected by the lack of anhydrous monomer. Furthermore triple detection SEC (THF/ 2 v/v % TEA) revealed that all three polymers possess  $M_n$  values close to targeted and  $\mathcal{D} \leq 1.12$  in all cases. Therefore, as molecular sieves was thought to diminish the concentration of water compared to the commercially available monomer this method of drying was implemented for all future reactions.

## CHAPTER 2

As this alteration of drying method was hypothesised to affect the water content in the reaction mixture, in turn decreasing the possibilities of opportunistic initiation by this species, the monomer mass was normalised and set, and the targeted  $DP_n$  was increased by systematically decreasing the BzA mass. Therefore it could be stipulated that the concentration of water in a given mass of  $\epsilon$ -CL would increase relative to BzA concentration with increasing  $DP_n$ . The assessment of opportunistic initiation was assessed by studying  $^1H$ -NMR and triple detection SEC analysis of PCL polymers, determining the  $DP_n$  values generated by different treatment of the analysis. Studies began with BzA initiated polymerisation and later expanded to include PEG initiated PCL reactions (Table 2.4).

**Table 2.4 - Series of MSA catalysed ROP of  $\epsilon$ -CL, initiated by benzyl alcohol and PEG-OH, with varied degree of polymerisation 10 to 200 monomer units, with extended  $^1\text{H}$ -NMR analysis;**

Target polymer	Reaction time (hours)	Monomer conversion <sup>a</sup>	$^1\text{H}$ NMR				SEC <sup>c</sup>				
			DP <sub>I</sub> by NMR (Initiator)	DP <sub>OH</sub> by NMR (OH Chain End)	% of chains initiated by initiator	M <sub>n</sub> by NMR (Initiator) (g mol <sup>-1</sup> ) <sup>d</sup>	M <sub>n</sub> Theory <sup>b</sup> (g mol <sup>-1</sup> )	M <sub>n</sub> (g mol <sup>-1</sup> )	M <sub>w</sub> (g mol <sup>-1</sup> )	Đ	$\alpha$
PCL <sub>10</sub>	0.25	>99%	12	12	99	1,480	1,250		– <sup>g</sup>		
PCL <sub>20</sub>	0.66	>99%	21	20	94	2,510	2,390		– <sup>g</sup>		
PCL <sub>30</sub>	1	>99%	33	29	89	3,870	3,530	4,060	5,540	1.36	0.76
PCL <sub>40</sub>	1.5	>99%	41	39	95	4,790	4,670	4,680	5,650	1.21	0.82
PCL <sub>50</sub>	2	>99%	66	57	86	7,640	5,820	6,510	7,660	1.18	0.84
PCL <sub>60</sub>	2.5	>99%	66	58	88	7,640	6,960	6,920	7,960	1.15	0.98
PCL <sub>80</sub>	4	>99%	99	71	71	11,410	9,240	7,560	9,720	1.29	0.69
PCL <sub>100</sub>	5	>99%	137	79	58	15,750	11,520	8,760	10,630	1.21	0.71
PCL <sub>200</sub>	9	44 %	110	55	50	12,670	10,150	7,150	7,770	1.09	0.92
PEG <sub>2K</sub> - <i>b</i> -PCL <sub>40</sub> <sup>e</sup>	2	>99%	41	38	93	6,680	6,570	5,470	6,260	1.15	0.59
PEG <sub>5K</sub> - <i>b</i> -PCL <sub>40</sub> <sup>f</sup>	2	>99%	42	28	68	9,790	9,570	7,540	8,400	1.12	0.70

BzA initiated PCL polymer normalised with dn/dc value 0.06044, *a* Determined by  $^1\text{H}$  NMR ( $\text{CDCl}_3$ , 400 MHz) of the crude samples, *b* Calculated using the equation:  $M_{n\text{theory}} = (\text{DP}_{\text{targeted}} \times \text{conv.} \times M_{r\text{CL}}) + M_{r\text{BZA}}$ , *c* Determined by triple detection SEC with a mobile phase of DMF/LiBr 0.01 M (60 °C) at 1 mL min<sup>-1</sup>, *d* Calculated using the equation:  $M_{n\text{NMR}} = (\text{DP}_{\text{I(Eq. 2.14)}} \times M_{r\text{CL}}) + M_{r\text{BZA/PEG-OH}}$ , *e* dn/dc value 0.0588 used, *f* dn/dc value 0.0605 used, *g* insufficient light scattering for calculation but RI chromatograms indicated monomodal distribution.

Firstly,  $^1\text{H}$  NMR analysis was used to determine the  $\text{DP}_n$  of linear PCL polymers (Table 2.4) and draw comparisons between the  $\text{DP}_n$  values obtained from either the proton environment located on the  $\text{CH}_2$  immediately prior the first ester functionality of polymer chain, directly associated with the initiating group,  $\text{DP}_I$ , (Equation 2.14, Figure 2.21, environment b) or the  $\text{DP}_n$  derived from utilising the proton environment directly adjacent to the hydroxyl chain end that terminates all polymers,  $\text{DP}_{OH}$  (Equation 2.15, Figure 2.21, environment g). A strong correlation between these values would represent a lack of opportunistic initiation by impurities within the reaction mixture.

$$\frac{\left(\frac{\int \text{Polymer}}{nH_{RU}}\right)}{\left(\frac{\int \text{Initiator}}{nH_I}\right)} = \text{DP}_I \quad \text{Equation 2.14}$$

Where  $\int \text{Polymer}$  is the integration of the last  $\text{CH}_2$  proton environment of the monomer repeat unit at 4.05 ppm (Figure 2.21, environment f);  $nH_{RU}$  is the number of protons that correspond to this  $\text{CH}_2$  environment of each repeat unit, defined as environment f in Figure 2.21, known to be 2;  $\int \text{Initiator}$  is the integration of the  $\text{CH}_2$  environment directly before the first ester bond within the polymer chain at 5.1 ppm (Figure 2.21, environment b) and  $nH_I$  is the number of protons associated this  $\text{CH}_2$  environment of the initiating species defined as environment b in Figure 2.21, known to be 2.

$$\frac{\left(\frac{\int \text{Polymer}}{nH_{RU}}\right)}{\left(\frac{\int \text{Chain End (OH)}}{nH_{CE}}\right)} = \text{DP}_{OH} \quad \text{Equation 2.15}$$

Where  $\int \text{Chain End}$  is the integration of the  $\text{CH}_2$  proton environment, of the last repeat unit, next to the terminal OH of the polymer (Figure 2.21, environment g) and  $nH_{CE}$  is the number of protons associated with this  $\text{CH}_2$  environment of the last repeat unit defined as environment g in Figure 2.21, known to be 2.

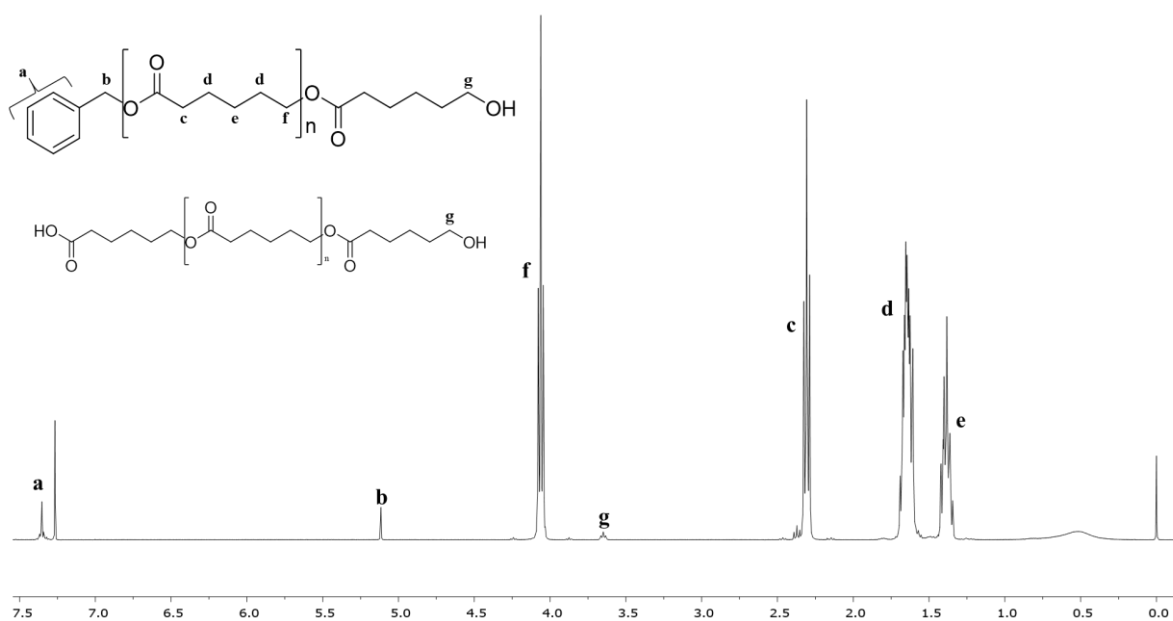


**Figure 2.21** –  $^1\text{H}$  NMR ( $\text{CDCl}_3$ , 400 MHz) of purified PCL<sub>40</sub>; illustrating the polymer proton environments (4.05 ppm) and highlighting the peaks corresponding to the environments of the benzyl alcohol, BzA, initiator (5.1 ppm) and the chain end (3.6 ppm).

Firstly concentrating on BzA initiated PCL polymer (Table 2.4), comparison of the  $\text{DP}_I$  and  $\text{DP}_{\text{OH}}$  values calculated from the different  $^1\text{H}$  NMR end group analyses show a good correlation for chain lengths below a targeted  $\text{DP}_n$  of 50 monomer units. This was also reflected by a good correlation between the  $M_n$  by NMR (based on  $\text{DP}_I$ ) and the  $M_n$  by SEC and indicates that BzA initiation efficiency of these reactions was high at chain lengths  $\leq 50$  monomer units. At higher  $\text{DP}_n$  values (PCL<sub>50</sub> to PCL<sub>100</sub>) significant discrepancies were seen between the  $M_n$  determined by NMR (based on  $\text{DP}_I$ ) and  $M_n$  values determined by SEC; this may suggest an increase in water impurity being introduced into the reaction vessel with increasing  $\text{DP}_n$ .<sup>87</sup> This would lead to a larger number of OH chain ends within the polymer sample than would be expected, i.e. a BzA: OH molar ratio of  $< 1$ .

Therefore, to further study the potential for co-initiation by water impurities, the values determined by using both Eq. 2.14 and Eq. 2.15 when analysing  $^1\text{H}$  NMR spectra from purified polymers (Figure 2.21) were more closely considered and a clear relationship could be seen between  $\text{DP}_{\text{OH}}$ ,  $\text{DP}_I$ , the percentage of chains initiated by BzA (Equation 2.16) and the  $\text{DP}_n$  of each polymer by SEC,  $\text{DP}_{\text{SEC}}$ .

$$\frac{\left(\frac{\int \text{Initiator}}{nH_I}\right)}{\left(\frac{\int \text{Chain End (OH)}}{nH_{CE}}\right)} \times 100 = \% \text{ chains by Initiator} \quad \text{Equation 2.16}$$



Two illustrative examples are PCL<sub>40</sub> and PCL<sub>100</sub> (Table 2.4); both polymers achieved high conversion (>99 %), which provides confidence that unreacted monomer has not been lost in purification. Each polymer, however, has a very different comparison of DP<sub>I</sub> and target DP<sub>n</sub> values with PCL<sub>40</sub> very closely matching the target.<sup>§§§§</sup> In comparison, DP<sub>OH</sub> calculations for PCL<sub>40</sub> and PCL<sub>100</sub> yielded values of 39 and 79 monomer units; excellent control was, therefore, achieved at low targeted DP<sub>n</sub> values but this much lower DP<sub>OH</sub> value for PCL<sub>100</sub> suggests a higher number of hydroxyl chain ends, than expected, which may be generated by initiation by water impurities. A greater understanding can be determined using Eq. 2.16.

When the NMR analysis for PCL<sub>40</sub> was applied to Eq. 2.16, where the integration of the CH<sub>2</sub> proton environment of BzA (Figure 2.21, environment b),  $\int Initiator$ , was normalised to 2 and the integration of the CH<sub>2</sub> proton environment next to the terminal OH of the polymer (Figure 2.21, environment g),  $\int Chain End$ , was calculated as 2.11, the percentage of chains initiated by BzA was calculated to be 94.8 % (Table 2.4). In contrast, an identical comparison for PCL<sub>100</sub> led to <sup>1</sup>H NMR calculated values for  $\int Initiator$  and  $\int Chain End$  of 2 and 3.48 respectively, generating a percentage of BzA initiated chains of 57.5 %.

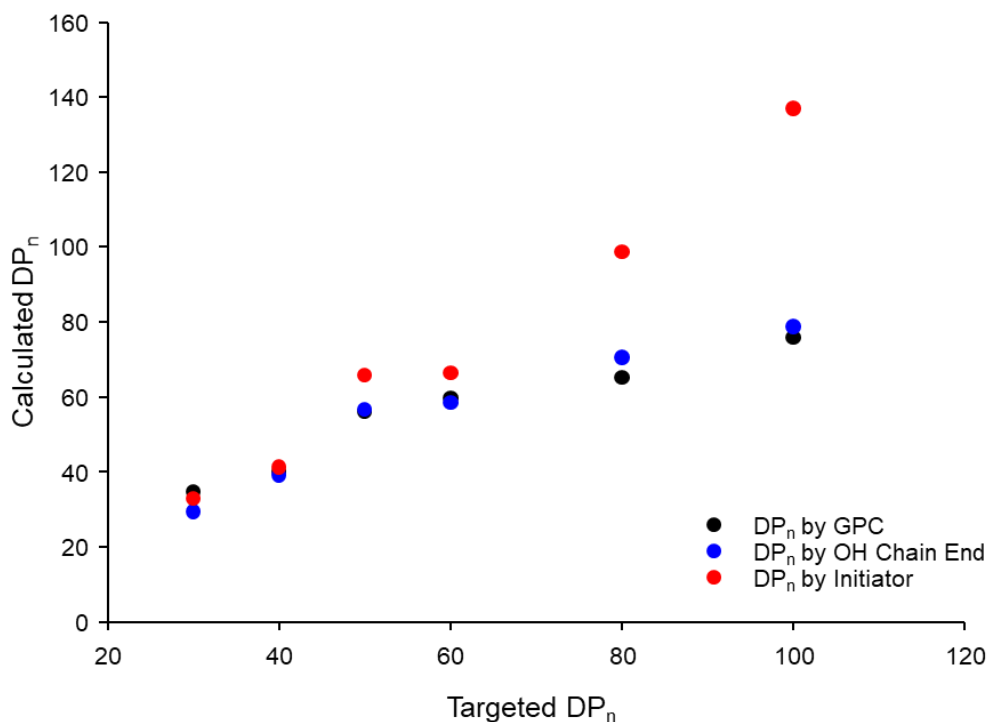
Utilising SEC for the determination of DP<sub>n</sub> is not a highly accurate technique, however, analysis of the SEC data allowed a DP<sub>SEC</sub> value to be derived *via* Eq.2.17; where  $Mn_{SEC}$  is the  $M_n$  generated by SEC analysis,  $Mr_I$  is the molecular weight of the initiator and  $Mr_{monomer}$  is the molecular weight of the monomer.

$$\frac{(Mn_{SEC})-(Mr_I)}{(Mr_{monomer})} = DP_{SEC} \quad \text{Equation 2.17}$$

A good correlation was obtained between DP<sub>SEC</sub> and calculated values of DP<sub>OH</sub> throughout the whole polymer series (Figure 2.22), illustrating that calculating DP<sub>OH</sub> allows relatively good representation of the polymer sample. Clearly, at DP<sub>n</sub> values < 50 monomer units, DP<sub>I</sub> calculated using Eq. 2.14 correlated well to DP<sub>SEC</sub> and also acts as a good representative value.

---

<sup>§§§§</sup> A high DP<sub>I</sub> value signifies that the ratio of initiator to monomer units at 99 % conversion has decreased from the targeted DP<sub>n</sub> ratio added at the start of the polymerisation. This can be attributed to some initiator being lost during purification due to a lower number of chains initiated by BzA. Therefore, although Eq. 2.14 allows the number of chains initiated by BzA to be determined it does not account for any chains initiated by moisture, calculated by Eq. 2.15.

Comparison of the various calculated  $DP_n$  values

**Figure 2.22 – Comparison of calculated  $DP_n$  values for linear PCL polymers (targeted  $DP_n$  – 30 to 100) by both  $^1H$  NMR and SEC; (●)  $DP_n$  calculated by SEC (Eq. 2.4), (●)  $DP_n$  calculated by  $^1H$  NMR and  $[Chain\ End\ (OH)]$  (Eq. 2.2), (●)  $DP_n$  calculated by  $^1H$  NMR and  $[Initiator]$  (Eq. 2.1).**

Studies were continued with the assessment of opportunistic initiation in the  $PEG_x-b-PCL_{40}$  copolymers synthesised in Section 2.3.1.2. As the targeted  $DP_n$  was 40 monomer units it was expected that a good correlation of PCL chain length would be seen when comparing  $DP_I$  (calculated by  $^1H$  NMR using the PEG initiating end group) and  $DP_{SEC}$ , as seen with the linear polymers, synthesised in Section 2.3.1.1. The  $DP_I$  and  $DP_{SEC}$  values for the hydrophobic PCL block of  $PEG_{2K}-b-PCL_{40}$  and  $PEG_{5K}-b-PCL_{40}$  were calculated to be 41 and 30 or 42 and 22 monomer units respectively indicating a potential initiation by water impurities within both samples (Table 2.3). Additionally further analysis of the purified polymers by  $^1H$  NMR gave  $DP_{OH}$  (calculated using the  $CH_2$  proton environment directly preceding the OH functionality of the PCL block chain end) at the values of 38 monomer units for  $PEG_{2K}-b-PCL_{40}$  and 28 for  $PEG_{5K}-b-PCL_{40}$ , further suggesting the presence of water impurity in the reaction mixtures. This could be associated with the difficulty in removing all water impurities, when using a vacuum oven, from the macroinitiators prior to polymerisation resulting in a deviation from the expected results based on BzA initiated  $PCL_{40}$ . However it is important to note that the deviation in  $DP_n$  values calculated by  $^1H$  NMR could also be the result of inaccuracies in the

mass of macroinitiator added to the polymerisation due the nominal molecular weights of 2000 and 5000 g mol<sup>-1</sup> for these species. Therefore greater deviation of DP<sub>I</sub> from DP<sub>SEC</sub> for PEG<sub>5K</sub>-*b*-PCL<sub>40</sub> could be the result of two possibilities; there may more water impurity entrapped within the longer PEG chains or greater inaccurate measurements were made during the preparation of this polymerisation due to the lower concentration of hydroxyl end groups in PEG<sub>5K</sub>-OH and mixture of chain lengths within the sample. This, in turn, could either introduce further water impurity to the reaction or a number of lower molecular weight species due to the presence shorter initiating species in the PEG<sub>5K</sub>-OH sample, which could account for the small artefact in the RI chromatogram of the polymer. Even so the low Đ values for both polymers indicates the reaction is still highly controlled with good initiator efficiency and allows for accurate targeting of a chosen DP<sub>n</sub>.

The ability to synthesise well-defined linear A-B block co-polymers with good control suggests that progression to attempting to synthesise amphiphilic branched architectures that are key to the study is justified using MSA catalysis. This also points towards a ROP method capable of challenging traditional tin-catalysed routes to allow a library of both homo and co-polymers of varying architecture to be produced.

### **2.3.2.3 Analysis of the potential transesterification during linear MSA catalysed ROP of ε-caprolactone initiated by benzyl alcohol**

Further investigations of MSA catalysed ROP were undertaken to achieve a greater understanding of the polymerisation before proceeding to varying initiators, architectures or monomer structures. The potential for transesterification within linear polymerisations was studied to identify side reactions that may impact the control within the polymerisation.<sup>4</sup> This was achieved by repeating the linear polymerisation targeting a DP<sub>n</sub> of 40 monomer units in toluene at 30 °C and sampling the reaction mixture at four time points. The first of these before catalyst addition, *t*<sub>0</sub>, to determine the experimental starting ratios of each reagent; the second, taken at 1.5 hours, *t*<sub>1.5</sub>, was previously shown to allow >99 % conversion for PCL<sub>40</sub> (Table 2.5) and, finally, samples were taken at 24 hours, *t*<sub>24</sub>, and 48 hours, *t*<sub>48</sub>, after the polymer had reached full conversion (Table 2.5). The catalyst was removed from each sample using basic alumina before analysis was undertaken by <sup>1</sup>H NMR and single detection SEC, equipped with an oligomer column, using a conventional calibration with PMMA calibrants with a mobile phase of DMF/LiBr 0.01 M at 60 °C with a flow rate of 1 mL min<sup>-1</sup>. The final polymer sample was also purified via precipitation (as with polymers synthesised in Section 2.3.1.1) and the final

pure  $^1\text{H}$  NMR and SEC samples subsequently analysed using the oligomer SEC equipment (Table 2.5).

**Table 2.5 - Experiment to determine the presence of transesterification reactions during MSA catalysed ROP of  $\epsilon$ -caprolactone with a  $\text{DP}_n$  of 40 monomer units.**

Time point	$^1\text{H}$ NMR <sup>b</sup>		SEC <sup>c</sup>		
	Monomer conversion <sup>a</sup>	$M_n$ (g mol <sup>-1</sup> )	$M_w$ (g mol <sup>-1</sup> )	$\bar{D}$	$\alpha$
t <sub>1.5</sub>	>99%	5,070	6,220	1.23	0.7
t <sub>24</sub>	>99%	7,770	11,520	1.48	0.7
t <sub>48</sub>	>99%	7,100	11,030	1.55	0.7
Polymer after precipitation		7,130	10,960	1.54	0.7

<sup>a</sup> Determined by  $^1\text{H}$  NMR ( $\text{CDCl}_3$ , 400 MHz) of the crude samples, <sup>b</sup> Calculated using the equation:  $M_{n\text{theory}} = (\text{DP}_{\text{targeted}} \times \text{conv.} \times M_{\text{CL}}) + M_{\text{BZA}} = 4,670 \text{ g mol}^{-1}$  for all polymers, <sup>c</sup> Determined by single detection SEC with a mobile phase of DMF/LiBr 0.01 M at 1 mL min<sup>-1</sup> w.r.t to poly(methyl methacrylate), PMMA, calibrants.

As the polymerisation progressed passed 1.5 hours, having reached >99 % conversion as shown by  $^1\text{H}$  NMR, the viscosity of the polymerisation mixture appeared to increase with sampling becoming more difficult at latter time points. Although, this could not confirm the specific type of secondary reaction occurring (e.g. transesterification), it was an important observation to note. The NMR spectra generated from the pure material showed no change or no additional proton environments when compared to the material synthesised in Section 2.3.1.1 confirming that the observed viscosity change was not the result of any additional material. SEC analysis indicated a dramatic increase in molecular weight between samples t<sub>1.5</sub> and t<sub>24</sub> which was clearly seen by a decrease in retention time of the molecular weight distribution, generated by the RI detector (Figure 2.23).

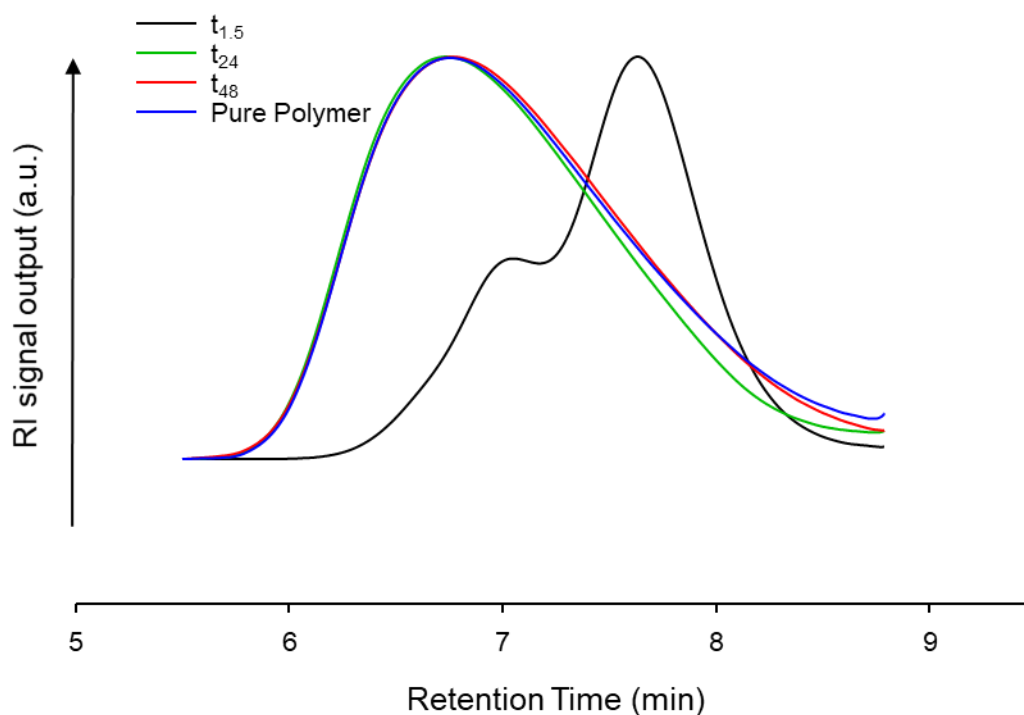


**Figure 2.23 – Analysis of samples (at time points  $t_{1.5}$ ,  $t_{24}$ ,  $t_{48}$  and after purification) obtained during the linear MSA catalysed ROP of  $\epsilon$ -caprolactone over 48 hours; refractive index,  $RI$ , detector output chromatograms of time points of  $PCL_{40}$  polymerisation, analysed utilising a single detection SEC, equipped with an oligomer column, w.r.t PMMA calibrants; Mobile phase: DMF/ 0.01 M LiBr at 60 °C.**

Here it is important to note that the bimodal distribution<sup>\*\*\*\*\*</sup> generated by the RI detector, for the sample  $t_{1.5}$  was due to the increased resolution of the oligomer column used with the single detection SEC. This is in keeping with the appearance of a shoulder of PCL polymers of increasing  $DP_n$  (from  $PCL_{40}$  to  $PCL_{100}$ ) analysed with a triple detection SEC in Section 2.3.1.1 (Figure 2.16). The higher molecular weight fraction highlighted by the second environment at a lower retention time also suggests that transesterification could have occurred before  $t_{1.5}$ . This coupled with the  $M_n$  and  $M_w$  values of 5,070 and 6,220  $g\ mol^{-1}$  for  $t_{1.5}$  and 7,770 and 11,520  $g\ mol^{-1}$  for  $t_{24}$  respectively indicated that inter- and intramolecular reactions were occurring once full conversion had been reached causing a dramatic reorganisation and broadening of the molecular weight distribution. There is little literature on the subject of acid catalysed transesterification within MSA catalysed ROP; however, it is theorised that the presence of MSA in the reaction mixture is critical in this phenomenon. Once the polymerisation has

<sup>\*\*\*\*\*</sup> The bimodal distribution observed in Figure 2.23, B was hypothesised to be a result of transesterification reactions occurring between 30 minutes and 1.5 hours, after full conversion was reached following the lower  $\bar{D}$  of the polymer at  $t_{30}$  compared to  $t_{90}$  in Section 2.3.2.1. This was supported by the appearance of a shoulder in the RI chromatograms for kinetic samples  $t_{24}$  to  $t_{30}$  (Figure 2.19, C).

reached >99 % monomer conversion, as there are no monomer molecules left that can be protonated/activated by MSA. Ester groups within the PCL chain are now protonated and are, subsequently, more susceptible to attack by the chain end hydroxyl groups.<sup>4</sup> Following chain end attack and proton transfer the chain is cleaved, liberating two new PCL chains of differing length (Figure 2.24, A). Not only is it possible for one chain to cleave another but at the same time a single chain can cleave itself subsequently forming a new polymer chain and a cyclic polymer chain which now does not contain an initiating molecule (BzA in this case); (Figure 2.24, B). Furthermore, as these multiple transesterification reactions increase as time progresses, the dispersity of the polymer sample will increase as some chains increase in length during coupling and other fragments of shorter chains are formed.

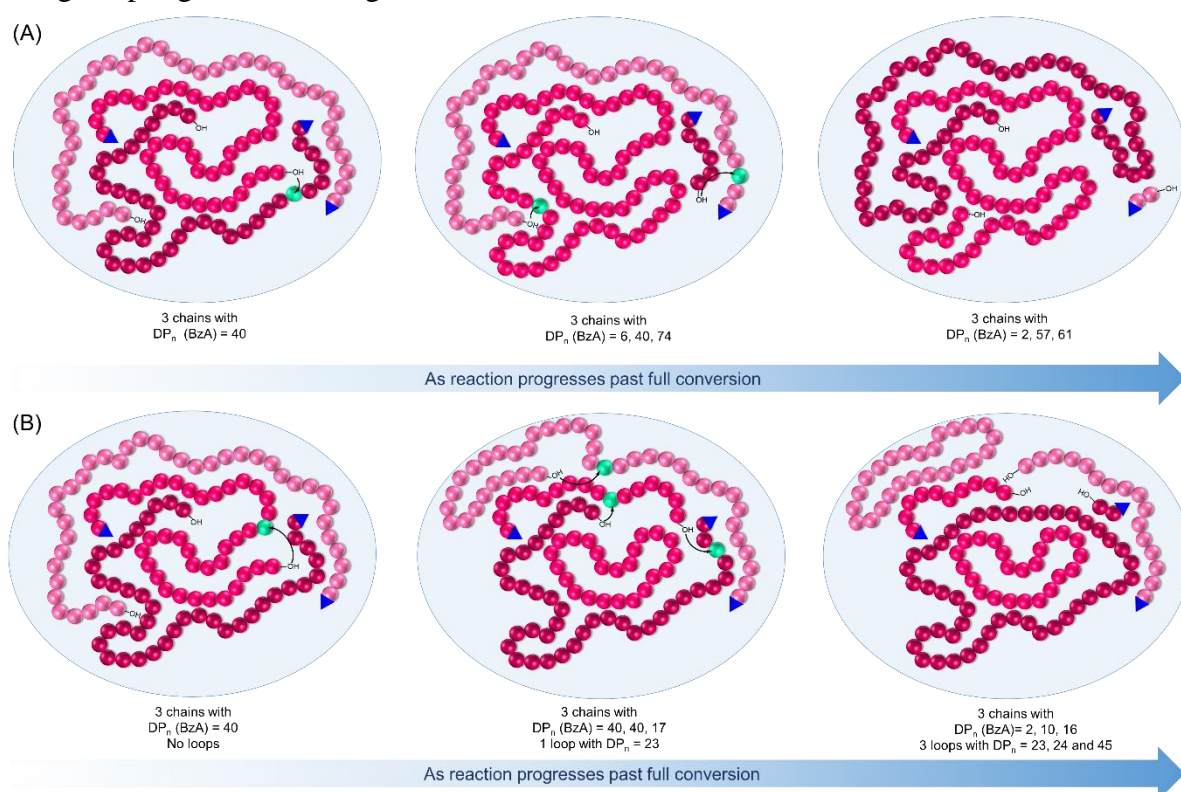
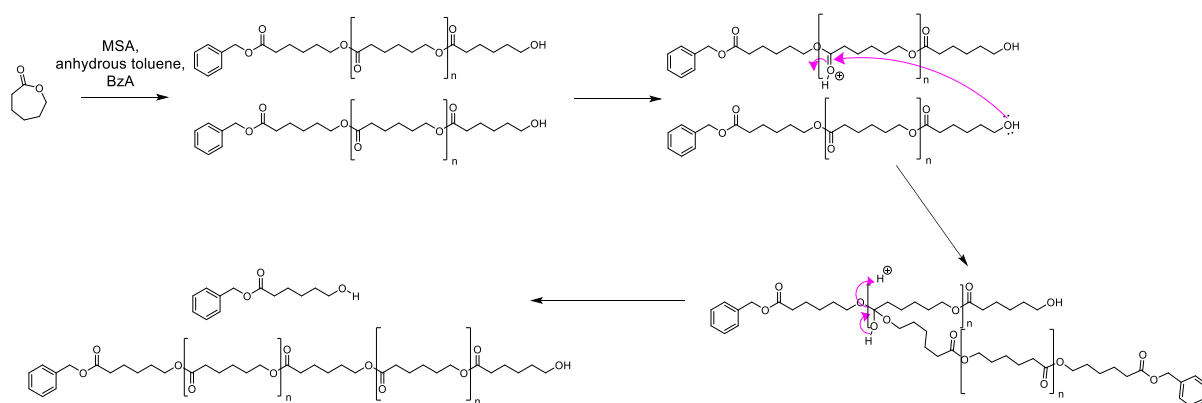


**Figure 2.24-** Schematic representation of transesterification reaction between linear polymer chains following the attack of a chain end OH resulting in; (A) two new chains of differing  $DP_n$  when chains initiated by BzA = 100 % and (B) cyclic polymers and chain of differing  $DP_n$  when chains initiated by BzA = 100 %.

Finally, only a small decrease in  $M_n$  and  $M_w$  values was observed between  $t_{24}$  and  $t_{48}$  (NB this could be due to the error inherent to SEC analysis). This indicates no significant change of the molecular weight distribution after 24 hours however this does not necessarily indicate that transesterification reactions had stopped. Most significantly the  $\bar{D}$  values for  $t_{1.5}$ ,  $t_{24}$  and  $t_{48}$  showed there was an increase in the dispersity of the polymer mixture as reaction time

progressed, from 1.23 to 1.55, which further confirms the presence of excessive transesterification reactions between chains (Figure 2.23).

In light of these observations, it is important to note that ROP does allow control of the polymerisation, allowing the targeting of a specific  $DP_n$  and producing polymers with low  $\bar{D}$ , (Section 2.3.1.1) as during propagation it is likely that the reaction with cyclic monomers is the dominant process. At high conversion, the decreasing unreacted monomer concentrations will lead to an increased likelihood of intramolecular transesterification reactions as MSA is more likely to protonate repeat units within the polymer chain (Scheme 2.6).<sup>4</sup> This is a well-known phenomenon in polyesterification and also occurs in industrial linear polymerisations containing di-acid and diol mixtures.<sup>4,56,87,88</sup> Preventative measures would allow transesterification reactions to be kept at a minimal level and this requires additional understanding of the kinetics of the ROP in question to terminate the polymerisation reaction closest to the time full monomer conversion is reached.



**Scheme 2.6 – Example of intermolecular transesterification of PCL chains resulting after high monomer conversion is reached.**

### 2.3.2.4 Overall outlook from mechanistic studies

The mechanistic studies of MSA catalysed ROP of  $\epsilon$ -CL revealed that although both opportunistic initiation and transesterification were present to some extent these phenomena should not be considered a significant problem for the targeting of highly branched PCL material via a modified ‘Strathclyde’ method. Opportunistic initiation was shown to be low when  $DP_n < 50$  monomer units therefore initially targeting a  $DP_n$  of 40 monomer units for branched architecture is hypothesised to mitigate this issue As  $DP_n$  increases, more chains are likely to not bear a benzyl initiating group, however, the relevance of this will decrease due to

the linking of most of the polymer chains during the polymerisation to achieve branched architecture.

Transesterification can also be considered as not significant for the formation of branched architecture via MSA catalysed ROP for several reasons. Firstly polymerisations are to be terminated after 1.5 hours following results gained in Section 2.3.2.1 indicating full conversion was reached after 30 minutes therefore transesterification is expected to be low. Furthermore literature regarding the implementation of a modified ‘Strathclyde’ route to branched architecture with various polymerisation techniques reveal that branched architecture often occurs at higher monomer conversion  $> 50\%$ . Therefore transesterification could possibly help achieve higher molecular weight structures once high monomer conversion is reached and ultimately not greatly affect the average primary chain length within the structure (Figure 2.25).

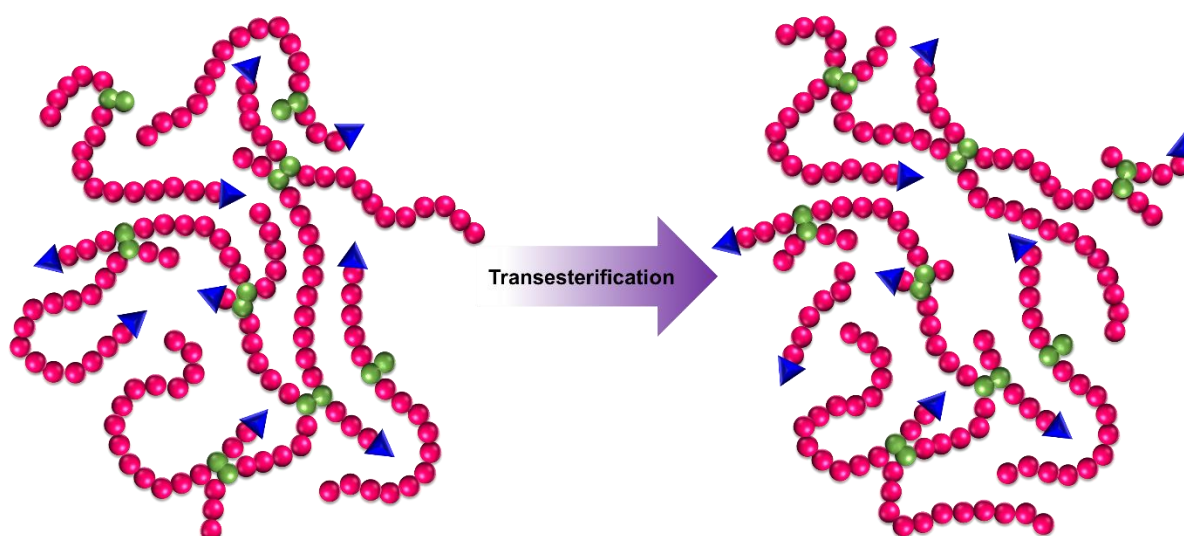


**Figure 2.25-** Representation of transesterification within a branched polymer species; altering the length of the primary chain however the average  $DP_n$  of all the primary chains within the polymer remains constant.

### 2.3.3 Statistical co-polymerisation of $\epsilon$ -caprolactone and BOD *via* MSA catalysed ROP to achieve branched architecture

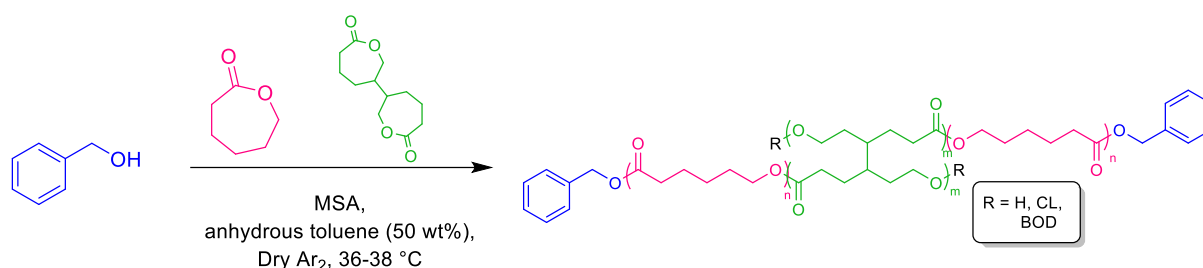
The synthesis of branched PCL structures have been achieved in literature *via* a number of methods as discussed in Section 2.1.2.2; however, achieving branched architectures *via* the combination of a modified ‘Strathclyde approach’ using the bis-lactone molecule BOD and MSA catalysed ROP, is previously unexplored. Previous work has utilised BOD and  $Sn(Oct)_2$  catalysed ROP; most literature mechanistic reports also utilise this catalyst although MSA catalysed reactions in DCM have been reported to produce cross-linked star polymers (however this was achieved by the homo-polymerisation of BOD).<sup>10,42,56</sup> In order to capitalise on the



advantages of MSA catalysed ROP, especially that lack of residual metal catalyst in polymers targeted for pharmacological use, the ability to achieve branched architecture *via* this route was explored using commercially available  $\epsilon$ -CL as the co-monomer.

### 2.3.3.1 Benzyl alcohol initiated statistical co-polymerisation of $\epsilon$ -caprolactone and BOD via MSA catalysed ROP

Polymerisations to explore the branching polymerisations using MSA catalysed ROP of BOD and  $\epsilon$ -CL (Scheme 2.7) were initially set to a  $DP_n$  of 40 monomer units for the primary chain length<sup>++++</sup> and sought to establish conditions leading to gelation. The gelation point was determined by decreasing the molar ratio of BOD: BzA until a soluble branched polymer was produced. Unpublished research by Blackmore *et al.* showed that soluble branched PCL polymers could be produced with a BOD: initiator molar ratio of 1:1; the polymers showed  $M_n$  and  $M_w$  values of 13,400 and 332,600  $g\ mol^{-1}$  respectively when analysed by triple detection SEC using a tetrahydrofuran, THF/TEA (2 v/v%) eluent and appeared to be in accordance with Flory-Stockmayer theory.<sup>68,89</sup> The polymers were also of higher molecular weight than similar material reported by Nguyen *et al.* when using a  $Sn(Oct)_2$  catalysed ROP method which displayed gelation above a BOD: initiator molar ratio of 0.6:1.<sup>42</sup>



**Scheme 2.7 – Benzyl alcohol initiated MSA catalysed ROP of  $\epsilon$ -CL and BOD in toluene at 36-38 °C.**

Within the current work, a refined purification of BOD has been employed, detailed in Section 2.2 and subsequently, a new gelation point was observed at BOD: BzA molar ratios of  $> 0.7:1$  within the MSA catalysed ROP targeting a primary chain length of 40 monomer units (Table 2.6). This polymer yielded  $M_n$  and  $M_w$  values of 12,430 and 261,900  $g\ mol^{-1}$  respectively ( $\bar{D} = 21.1$ ) when analysed by triple detection SEC (DMF/LiBr 0.01 M at 60 °C), corresponding to

<sup>++++</sup> Primary chain length refers to the  $DP_n$  of the linear portion of branched polymer architecture that would be produced if all branched points were severed.

## CHAPTER 2

an average of 56 linear primary chains linked together, on a weight average basis<sup>\*\*\*\*</sup>. Further reduction of the BOD: BzA molar ratio to 0.6:1, yielded a polymer that had a notable decrease in  $M_w$  and  $\bar{D}$  to  $74,650 \text{ g mol}^{-1}$  and 6.63 respectively, and a relatively small change in  $M_n$  values as expected. This shows the significance of BOD concentration in joining together linear primary chains and creating of highly branched architecture.

---

<sup>\*\*\*\*</sup> Calculated by dividing the  $M_w$  of the branched polymer by the  $M_n$  of the corresponding linear polymer synthesised in the absence of BOD.

**Table 2.6 - Series of BzA initiated MSA catalysed ROP of  $\epsilon$ -CL with BOD with varied Degree of Polymerisation 40 to 200 monomer units normalised with dn/dc value 0.06044.**

Target polymer	Reaction time (hours)	<sup>1</sup> H NMR		SEC <sup>b</sup>				
		Monomer conversion <sup>a</sup>	DP <sub>I</sub> of primary chain by NMR <sup>c</sup> (Initiator)	M <sub>n</sub> (g mol <sup>-1</sup> )	M <sub>w</sub> (g mol <sup>-1</sup> )	Đ	$\alpha$	No. of primary chains (weight averaged)
PCL <sub>40-co</sub> -BOD <sub>0.8</sub>	1.5			<i>Gel</i>				
PCL <sub>40-co</sub> -BOD <sub>0.75</sub>	1.5	>99%	51	<i>Gel</i>				
PCL <sub>40-co</sub> -BOD <sub>0.7</sub>	1.5	>99%	51	12,430	261,900	21.1	0.35	56
PCL <sub>40-co</sub> -BOD <sub>0.6</sub>	1.5	>99%	47	11,250	74,650	6.63	0.35	16
PCL <sub>60-co</sub> -BOD <sub>0.7</sub>	2.5	>99%	74	12,380	76,740	6.20	0.35	11
PCL <sub>80-co</sub> -BOD <sub>0.7</sub>	4	>99%	98	12,050	88,570	7.35	0.35	12
PCL <sub>100-co</sub> -BOD <sub>0.7</sub>	5	>99%	116	13,500	63,900	4.73	0.36	7
PCL <sub>200-co</sub> -BOD <sub>0.7</sub>	9	51 %	122	7,910	8,700	1.10	0.57	-

<sup>a</sup> Determined by <sup>1</sup>H NMR (CDCl<sub>3</sub>, 400 MHz) of the crude samples, <sup>b</sup> Determined by triple detection SEC with a mobile phase of DMF/LiBr 0.01 M (60 °C) at 1 mL min<sup>-1</sup>, <sup>c</sup> Calculated using the equation:  $M_{n,NMR} = (DP_{I(Eq. 2.14)} \times Mr_{CL}) + Mr_{BzA}$

To explore the influence of an increased primary chain length on the molecular weight of the resulting polymers the targeted  $DP_n$  of the primary chain was increased to 60, 80, 100 and 200 monomer units with a fixed BOD: BzA molar ratio of 0.7:1. As seen with the linear polymerisations targeting long chain lengths, PCL<sub>200-co</sub>-BOD<sub>0.7</sub> failed to reach high conversion after 9 hours, which indicated that the polymerisation may have a limit to the  $DP_n$  that can be targeted or the kinetics of this particular reaction are more complicated than those targeting  $\leq$  100 monomer units. Branched polymers with a targeted primary chain  $DP_n$  of 60 and 80 monomer units showed high values for both  $M_w$  and  $\bar{D}$ ; however, these results were also attainable for PCL<sub>40-co</sub>-BOD<sub>0.6</sub>. This, combined with SEC analysis of PCL<sub>100-co</sub>-BOD<sub>0.7</sub> indicating a polymer with an  $M_w$  of 63,900 g mol<sup>-1</sup> suggests that increased primary chain length decreases the overall potential for branching to occur due to a lower BOD:  $\epsilon$ -CL molar ratio and increased probability of forming polymer ‘loops’.

Confirmation of the formation of branched architectures can be achieved for each of the polymers produced from SEC analysis; namely, higher than targeted molecular weights, broad molecular weight distributions and the calculated Mark-Houwink alpha values,  $\alpha$ . All of the branched polymers produced exhibited a multimodal molecular weight distribution when compared to the linear equivalent polymerisations conducted in the absence of BOD (Figure 2.26).

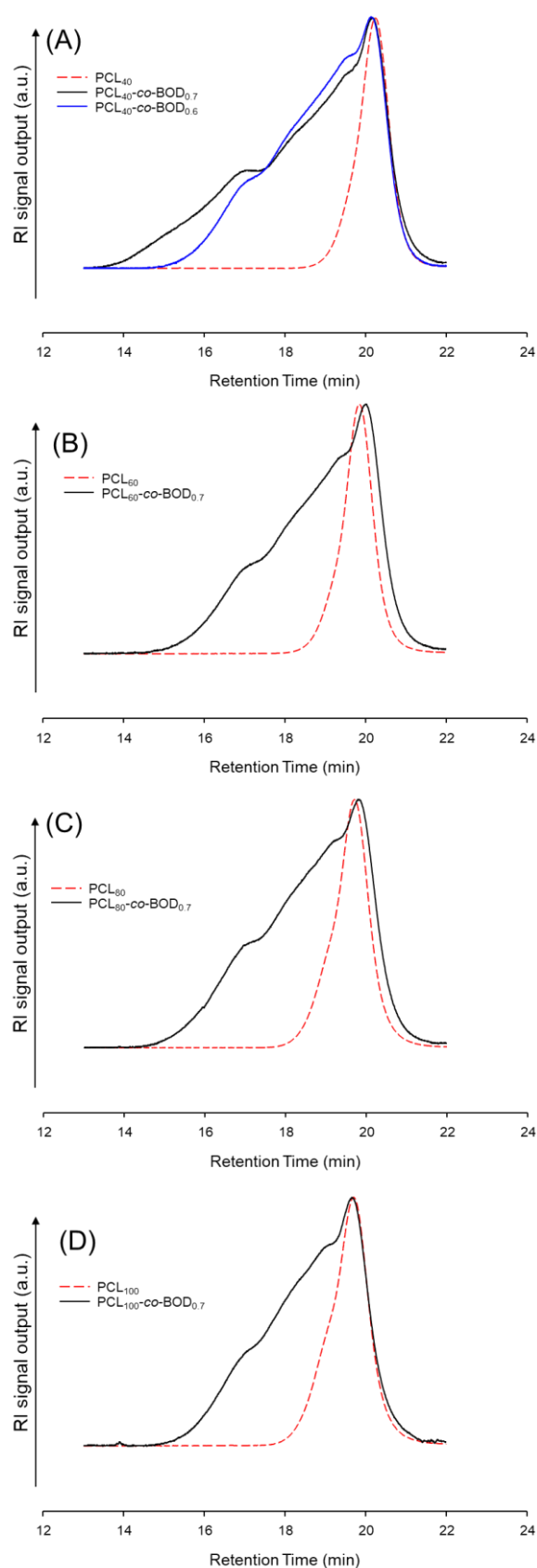


**Figure 2.26 - Refractive index,  $RI$ , detector output chromatograms of PCL<sub>x</sub>-co-BOD<sub>y</sub>, obtained by MSA catalysed ROP, overlaid with the corresponding linear PCL polymer; Triple detection SEC; Mobile phase: DMF/ 0.01 M LiBr at 60 °C.**

An overlay of the corresponding linear polymers within their branched analogues (Figure 2.26), shows a linear population within the broad distributions; this is characteristic of branched polymers obtained *via* a conventional and modified “Strathclyde” methods and can be attributed to the presence of BOD having little effect on the formation of primary chains (Figure 2.19).<sup>4,90,91</sup> This has been broadly studied with the creation of branched vinyl polymer architectures *via* a modified ‘Strathclyde’ route with several concepts being published within the literature. Bannister et al. demonstrated the statistical nature in which double bonds react during the polymerisation leading to the presence of unreacted pendant vinyl groups.<sup>86</sup> Monomer dilution has also been shown to be related to the linear population within the polymer species; an increased monomer dilution within the reaction mixture increases the number of wasteful intramolecular reactions due to the decreased interpenetration of propagating polymer chains.<sup>90,91</sup> However <sup>1</sup>H NMR analysis of the polymers produced in this section, by MSA catalysed ROP, would suggest that ‘loop’ formation is minimal. Furthermore it is important to note that although the vinyl polymerisation studies, detailed above, provide a small indication of what may be occurring during ROP, they cannot be fully applied to this technique due to its complex nature. As shown in Section 2.3.2.3 transesterification, both inter- and intra-molecular (Figure 2.27), is more likely to influence the branched architecture of polymers resulting from ROP and may aid the synthesis of highly branched architecture.

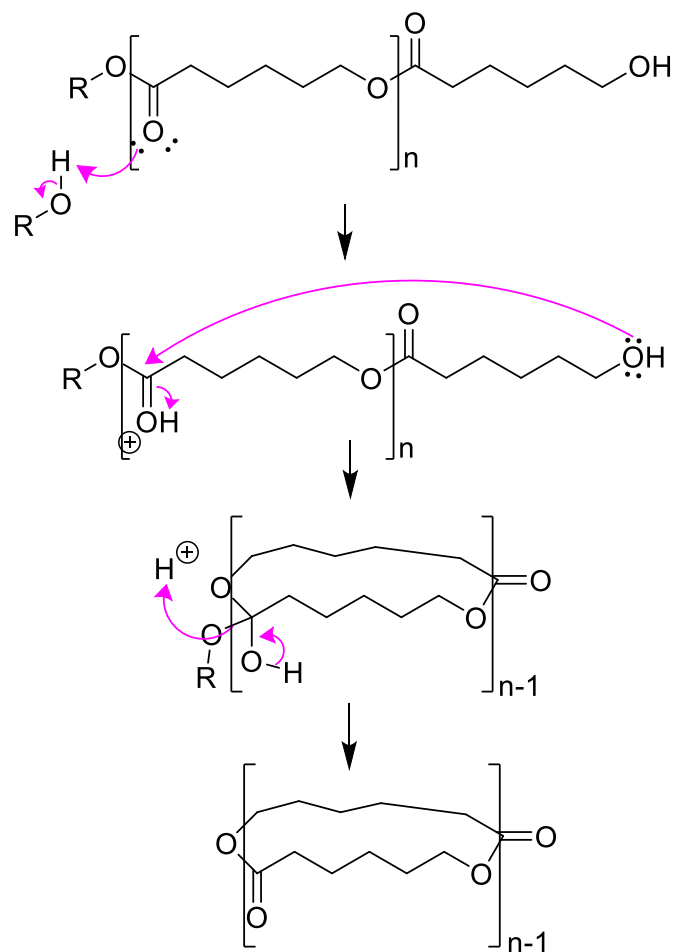


**Figure 2.27 – Example of intramolecular cyclisation reaction of a PCL chain during ROP of  $\epsilon$ -CL.**

Furthermore a clear trend can be seen when comparing the  $\alpha$  values of BzA initiated linear PCL to the corresponding branched species giving further confirmation of the achievement of branched architecture. As the Mark-Houwink equation (Equation 2.18);

$$[\eta] = KM^\alpha \quad \text{Equation 2.18}$$

used to calculate the  $\alpha$  values of a polymer, defines the relationship of intrinsic viscosity,  $[\eta]$ , and molecular weight,  $M$ , these values can be used to determine the rigidity of a polymer and in turn their architecture.<sup>92</sup>  $K$  and  $\alpha$  are constants where  $\alpha$  signifies the architecture of the polymer within a given solvent.<sup>92</sup>

In all cases for PCL-*co*-BOD that reached high conversion,  $\alpha$  values  $< 0.4$  were observed (Table 2.6) which corresponds to a compact branched architecture. The consistency of these values is remarkable and shows very similar solution behaviour of all branched PCL-*co*-BOD polymers in DMF. As seen in literature reports, it may be expected that the  $\alpha$  values would increase with

decreasing degree of branching (branching density); however, these values may indicate specific solution and coiling behaviour of branched PCL-derived polymers in DMF.<sup>92</sup>

In summary, the generation of a library of branched PCL-*co*-BOD polymers, with varying primary chain DP<sub>n</sub> and BOD:BzA molar ratios may be reliably synthesised using MSA catalysed ROP *via* a modified ‘Strathclyde method’. The promising success of this investigation not only provides a route to metal free branched PCL-*co*-BOD co-polymers, but also allows control of many of the structural parameters within the co-polymer which may be valuable in further studies.

### *2.3.3.1.1 Kinetic studies of the statistical co-polymerisation of ε-CL and BOD via MSA catalysed ROP*

A study of the kinetics of the branched ROP polymerisations was conducted in a similar manner to those already described above for analogous linear polymerisations (Section 2.3.2.1). As with previous studies, the primary chain length was targeted at DP<sub>n</sub> = 40 monomer units and the polymerisation was conducted at 36 °C for a total of 1.5 hours to achieve high monomer conversion. Following removal of the catalyst utilising equimolar TEA, the crude samples were analysed by <sup>1</sup>H NMR and triple detection SEC (DMF/LiBr 0.01 M at 60 °C).

<sup>1</sup>H NMR analysis showed that monomer conversion at each time point did not greatly differ from the corresponding linear time points with the branched polymerisation having slightly higher conversion over time. Furthermore, the application of the first order rate law Eq. 2.17, as derived in Section 2.3.2.1 yielded a kinetic plot that mirrored the trend seen with PCL<sub>40</sub> with an upward curve as the reaction progressed (Figure 2.28, A). This confirmed that the addition of BOD had very little effect on the rate of polymerisation.

Although the modified ‘Strathclyde method’ requires only a small molar concentration of the bi-functional monomer, following Flory-Stockmayer theory, the basicity of BOD has not been reported with respect to MSA catalyst ROP.<sup>40,68</sup> Therefore it was not obvious that the incorporation of BOD would have a negligible impact on the kinetics of the reaction. As no discernible effect on the kinetics was seen, it is safe to assume that due to the chemical similarity of the seven-membered lactones of BOD and ε-CL, the basicity of the two monomers will not be significantly different and their inclusion in the polymer backbone creates near-identical ester environments.<sup>37,85</sup>



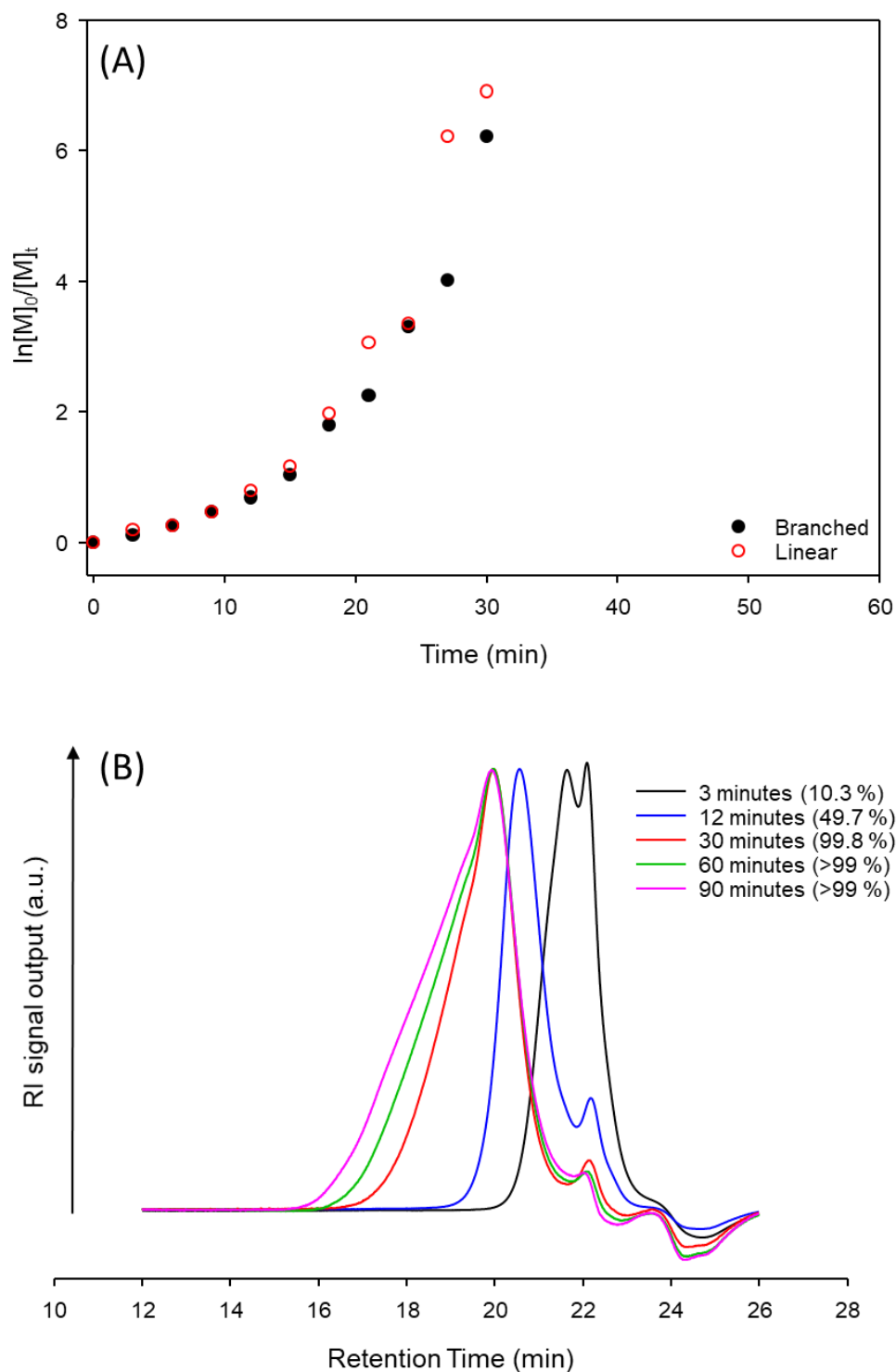


**Figure 2.28-** Analysis of kinetic study of  $\text{PCL}_{40}\text{-co-BOD}_{0.7}$  synthesis completed with TEA acid neutralisation, 0 to 30 minutes (full monomer conversion reached - calculated by  $^1\text{H}$  NMR in  $\text{CDCl}_3$ ). (A) semi-log plots from 0 – 99.8 % conversion ( $t_0$  to  $t_{30}$ ) calculated by  $^1\text{H}$  NMR in  $\text{CDCl}_3$  overlaid with linear PCL semi-log plot and (B) overlay of selected RI traces between 3 and 90 minutes using triple detection SEC ( $\text{DMF/LiBr}$  0.01 M at  $1 \text{ mL min}^{-1}$ ).

Triple detection SEC (DMF/LiBr 0.01 M at 60 °C) was unable to provide accurate analysis for the  $M_n$ ,  $M_w$  and  $\bar{D}$  of the polymer at each time point due to the presence of the monomer within each chromatogram. However a visual inspection of RI chromatograms at selected time points indicated a broadening of the molecular weight distribution from a monomodal peak 12 minutes (49.7 % monomer conversion) after the reaction began to the appearance of a shoulder at full monomer conversion (Figure 2.28, B). The broadening of the molecular weight distributions continued after monomer conversion reached >99 %, between 30 and 90 minutes (Figure 2.28, B). Therefore it is possible that although  $\epsilon$ -CL has surpassed 99 % conversion unreacted pendant BOD groups are still present leading to the increased branching of the polymer overtime. Furthermore this could also be an indication that transesterification, which was shown to be present at high monomer conversion (Section 2.3.2.3), maybe contributing a gain in molecular weight of the branched polymer.

### 2.3.3.2 Poly(ethylene glycol)<sub>5K</sub> initiated, MSA catalysed ROP of $\epsilon$ -caprolactone and BOD

The formation of amphiphilic branched polymers was studied by the inclusion of BOD in PEG-initiated A-B block co-polymerisations described in Section 2.3.1.2. A number of researchers have reported that significant circulation benefits for PEGylated nanoparticles can be derived from PEG chains with an  $M_n$  of 5000 g mol<sup>-1</sup>, therefore, PEG<sub>5K</sub>-OH was selected for these studies after successful linear co-polymerisations (Section 2.3.1.2). Considering the success of PCL<sub>40-co</sub>-BOD<sub>0.7</sub> in Section 2.3.3.1 the same primary chain length ( $DP_n = 40$  monomer units) and BOD: initiator molar ratios (0.7:1) were utilised.

As with the linear PEG<sub>5K-b</sub>-PCL<sub>40</sub> A-B block co-polymer synthesis, the polymerisation was conducted at 50 °C with 33 wt% solids in toluene (based on monomer mass) and terminated after 2 hours. <sup>1</sup>H NMR studies confirmed the reactions had achieved >99 % conversion and triple detection SEC analysis (DMF/LiBr 0.01 M at 60 °C) of PEG<sub>5K-b</sub>-PCL<sub>40-co</sub>-BOD<sub>0.7</sub> showed the purified sample to have  $M_n$ ,  $M_w$  and  $\bar{D}$  values of 10,370 g mol<sup>-1</sup>, 17,530 g mol<sup>-1</sup> and 1.69 respectively (Table 2.7). These values indicated that although a branched species had been formed the weight average number of primary chains linked together was only 2.3. This was most likely a result of the greater monomer dilution needed for the solubilisation of PEG<sub>5K</sub>-OH compared to BzA initiated branched ROP.

**Table 2.7 - Series of MSA catalysed ROP of  $\epsilon$ -CL with PEG<sub>5K</sub>-OH and BOD to achieved branched amphiphilic architecture;**

Target polymer	Reaction time (hours)	<sup>1</sup> H NMR		SEC <sup>b</sup>				
		Monomer conversion <sup>a</sup>	M <sub>n</sub> (g mol <sup>-1</sup> )	M <sub>w</sub> (g mol <sup>-1</sup> )	Đ	dn/dc	$\alpha$	No. of primary chains (weight averaged)
PEG <sub>5K</sub> - <i>b</i> -PCL <sub>40</sub>	2	>99%	7,540	8,400	1.12	0.0605	0.70	1
PEG <sub>5K</sub> - <i>b</i> -PCL <sub>40</sub> - <i>co</i> -BOD <sub>0.7</sub>	2.5	>99 %	10,370	17,530	1.69	0.0585	0.36	2.3
PEG <sub>5K</sub> - <i>b</i> -PCL <sub>40</sub> - <i>co</i> -BOD <sub>0.8</sub>	2.5	>99 %	11,860	20,410	1.73	0.0593	0.36	2.7
PEG <sub>5K</sub> - <i>b</i> -PCL <sub>40</sub> - <i>co</i> -BOD <sub>0.9</sub>	2.5	>99 %	11,490	23,600	2.05	0.0563	0.40	3.1
PEG <sub>5K</sub> - <i>b</i> -PCL <sub>40</sub> - <i>co</i> -BOD <sub>1</sub>	2.5	>99 %	12,410	26,590	2.14	0.0563	0.38	3.5
PEG <sub>5K</sub> - <i>b</i> -PCL <sub>40</sub> - <i>co</i> -BOD <sub>1.2</sub>	2.5	>99 %	12,280	35,960	2.93	0.0579	0.35	4.8
PEG <sub>5K</sub> - <i>b</i> -PCL <sub>40</sub> - <i>co</i> -BOD <sub>1.5</sub>	2.5	>99 %			<i>Gel</i>			
PEG <sub>5K</sub> - <i>b</i> -PCL <sub>80</sub> - <i>co</i> -BOD <sub>0.8</sub>	4	98.5 %	13,730	25,900	1.89	0.0597	0.37	-

<sup>a</sup> Determined by <sup>1</sup>H NMR (CDCl<sub>3</sub>, 400 MHz) of the crude samples, <sup>b</sup> Determined by triple detection SEC with a mobile phase of DMF/LiBr 0.01 M (60 °C) at 1 mL min<sup>-1</sup>.

The BOD: initiator molar ratio was increased in order to find the gel point and to evaluate whether the increase in BOD: initiator molar ratio greatly affects the  $M_n$  and  $M_w$  of the resulting branched polymers. As the polymers approached the gelation point, increasing  $M_w$  would be expected; however, the relatively dilute reaction conditions (33 wt% monomer) were suspected to require a significant increase in the BOD: initiator molar ratio to overcome loop formation and create effective cross-linking between primary chains, leading gelation. These studies confirmed a gel point at a BOD: initiator molar ratio of between 1.2:1 and 1.5:1; microscopic gelation was observed and, therefore, it was possible to dissolve the soluble fraction and conduct  $^1\text{H}$  NMR studies (Table 2.7). NMR showed that the primary chain length to have a  $DP_1$  of 38 monomer units and a  $DP_{OH}$  of 25 monomer units. SEC analysis was unable to be completed.

The polymerisations leading to soluble  $\text{PEG}_{5K}\text{-}b\text{-PCL}_{40}\text{-}co\text{-BOD}_x$  (where  $x = 0.8$  to  $1.2$ ) were studied by triple detection SEC analysis (DMF/0.01 M LiBr) and showed a clear trend of increasing  $M_w$  and  $\bar{D}$  with increasing BOD content (Figure 2.29). Although these species again are not highly branched, the trend of increasing weight average molecular weight supports the mechanism of a modified ‘Strathclyde’ strategy where increased intramolecular reactions may dominate at high dilutions, even within a ROP reaction.<sup>90,91</sup> The inability to produce highly branched, high molecular weight material is probably due to the large macroinitiator creating steric hindrance around the polymer chains and preventing primary chains from linking as efficiently as when low molecular weight initiators are used. Clearly, very high molecular weights are formed at the gel points but these appear to be hard to control reproducibly.

A further polymer was synthesised with the BOD: initiator molar ratio of 0.8:1 but targeting a  $DP_n$  of 80 monomer units for the primary chains. This was studied to understand whether an increase in  $DP_n$  of the primary chain would result in a more dramatic increase in  $M_n$  and  $M_w$ . However, upon SEC analysis this polymer was shown to provide materials with very similar molecular weight compared to the  $DP_n$  40 equivalent and increasing primary chain length does not seem to provide a simple solution to accessing higher molecular weight species.

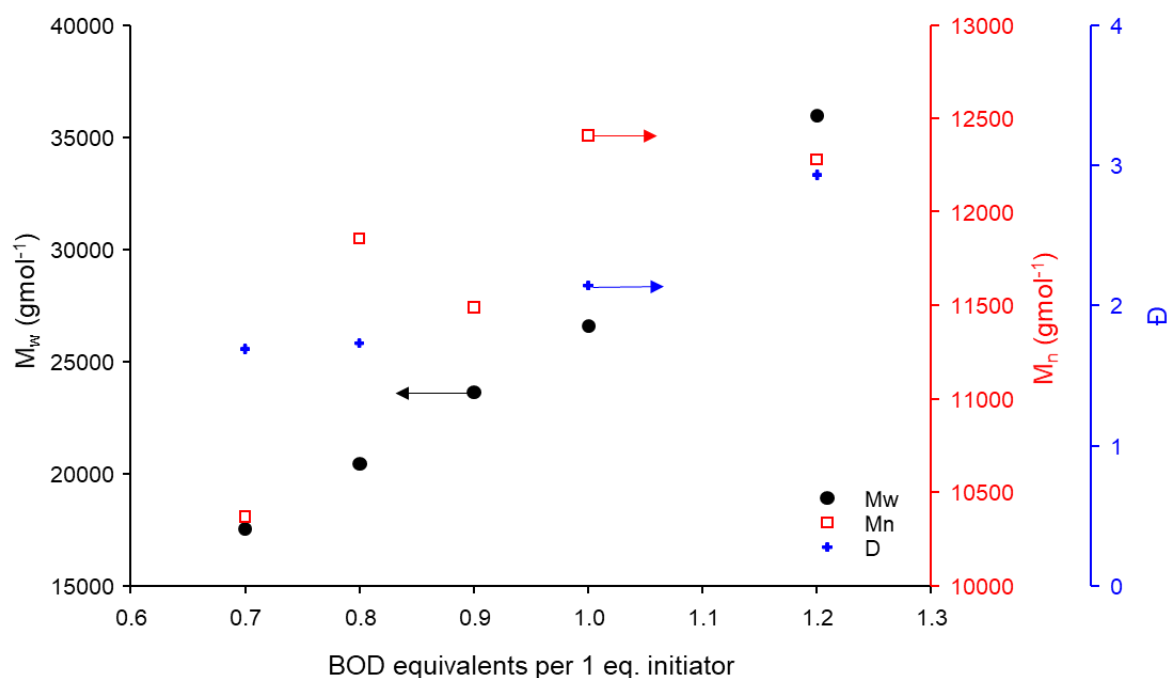


**Figure 2.29 - Change in  $M_n$ ,  $M_w$  and  $\bar{D}$  of  $PEG_{5K}\text{-}b\text{-}PCL_{40}\text{-}co\text{-}BOD_x$  with increasing BOD content.**

## 2.4 MSA catalysed ROP of substituted caprolactone monomers

The MSA catalysed ROP of the substituted caprolactone monomers was studied, following insights gained and procedures utilised during the investigation of  $\epsilon\text{-CL}$  polymerisation described above. The main aim for ROP including the substituted caprolactone monomers was to generate a library of polymers, varying in monomer chemistry, architecture and amphiphilicity for further studies of drug encapsulation and release. Given the strong similarity of the substituted caprolactone monomers with  $\epsilon\text{-CL}$  it was assumed that these monomers would have little effect on the overall kinetics of the ROP polymerisations when compared to  $\epsilon\text{-CL}$ , especially as the presence of BOD appeared to show no discernible effects (Section 2.3.3.1.1).<sup>23</sup> Reaction times were however slightly extended to 3.5 hours to ensure reactions were likely to have reached high conversion at the time of termination.

## 2.4.1 MSA catalysed ROP of substituted caprolactone monomers to achieve linear architecture

### 2.4.1.1 Benzyl alcohol initiated, MSA catalysed ROP of substituted caprolactone monomers

As in depth studies undertaken with the synthesis of PCL *via* MSA catalysed ROP highlighted accurate targeting of polymers with a  $DP_n$  of 40 monomer units, identical polymers were targeted. BzA initiated polymerisations of MOP, POP and BOP were undertaken at 30 °C (in toluene) at 50 wt% (monomer content); polymerisation of PHLOP was performed at 48 °C at 25 wt% in toluene (monomer content) to achieve full dissolution of the monomer. Following termination of the polymerisations by the addition of  $CHCl_3$  and basic alumina to quench the catalytic system which was removed using basic alumina filtration before crude samples were taken for  $^1H$  NMR analysis (Table 2.8). Polymers, which were then purified by trituration in hexane, were then analysed by  $^1H$  NMR and triple detection SEC (DMF/LiBr 0.01 M at 60 °C).

**Table 2.8 - MSA catalysed ROP of substituted caprolactone monomers with a targeted  $DP_n$  of 40 monomer units initiated by BzA;**

Target Polymer	$^1H$ NMR				SEC <sup>c</sup>				
	Monomer conversion <sup>a</sup>	$DP_n$ by NMR (Initiator)	$M_n$ by NMR (Initiator) (g mol <sup>-1</sup> ) <sup>d</sup>	$M_n$ Theory <sup>b</sup> (g mol <sup>-1</sup> )	$M_n$ (g mol <sup>-1</sup> )	$M_w$ (g mol <sup>-1</sup> )	$\bar{D}$	$\alpha$	dn/dc
PMOP <sub>40</sub>	>99 %	57	7,410	5,230	5,440	6,570	1.21	0.61	0.0603
PPOP <sub>40</sub>	>99 %	46	7,290	6,360	6,810	8,180	1.20	0.67	0.0594
PBOP <sub>40</sub>	>99 %	43	7,430	6,920	7,320	8,870	1.21	0.57	0.0678
PPHLOP <sub>40</sub>	99 %	66	12,660	7,720	8,140	9,570	1.18	0.67	0.1692

Polymerisations undertaken at 30 °C (MOP, POP, BOP) and 48 °C (PHLOP) for 3.5 hours; *a*

Determined by  $^1H$  NMR ( $CDCl_3$ , 400 MHz) of the crude samples, *b* Calculated using the equation:

$M_{n,theory} = (DP_{targeted} \times conv. \times Mr_{BM}) + Mr_{BzA}$ , *c* Determined by triple detection SEC with a mobile phase

of DMF/LiBr 0.01 M (60 °C) at 1 mL min<sup>-1</sup>, *d* Calculated using the equation:  $M_{n,NMR} = (DP_{I(Eq. 2.14)} \times$

$Mr_{BM}) + Mr_{BzA/PEG-OH}$ .

Subsequent NMR analysis of crude reaction mixture samples showed that high conversion  $\geq 99\%$  was achieved in all cases, suggesting that the addition of the substitution to the lactone rings do not significantly affect the polymerisation under these conditions.

Analysis by triple detection SEC revealed that each monomer appears to polymerise with similar control to  $\epsilon$ -CL with  $\bar{D}$  values ranging from 1.18 to 1.21, with monomodal molecular weight distributions, indicating that any transesterification reactions were relatively limited in these cases.

$^1\text{H-NMR}$  analysis of the purified polymer samples, and utilising equation 2.14 showed discrepancies between the calculated  $\text{DP}_1$  and the targeted  $\text{DP}_n$  values, with PPHLOP<sub>40</sub> and PMOP<sub>40</sub> showing significantly higher  $\text{DP}_1$  values than 40 monomer units. Unfortunately, due to the complexity of the  $^1\text{H-NMR}$  spectra of the purified polymers and overlap of proton environments  $\text{DP}_{\text{OH}}$  was unable to be calculated for these samples. The observed  $M_n$  values derived from triple detection SEC analysis (Table 2.8) show an excellent correlation with the theoretical values.

#### **2.4.1.2 Poly(ethylene glycol)<sub>5K</sub> initiated, MSA catalysed ROP of substituted caprolactone monomers**

Each of the four substituted caprolactone monomers was used to create amphiphilic A-B block co-polymers using MSA catalysed ROP and the PEG<sub>5K</sub>-OH macroinitiator described in studies with  $\epsilon$ -CL (Section 2.3.1.2); and the polyester block was again targeted to a  $\text{DP}_n$  of 40 monomer units, allowing for comparisons between PEG<sub>5K</sub>-*b*-PCL<sub>40</sub> and the resulting block co-polymers. As described in Section 2.3.1.2 and 2.4.1.1, the polymerisations were undertaken at 50 °C and for 3.5 hours at 33 wt% dilution (with regards to monomer), although this was reduced to 25 wt% for polymerisations using PHLOP due to its reduced solubility.

All four polymerisations achieved  $\geq 94\%$  conversion (Table 2.9) with the decrease potentially due to increased steric hindrance from the macroinitiator.  $\text{DP}_1$  values for the four polymers were all calculated to be lower than 40 monomer units but this was to be expected as all 4 reactions did not reach full monomer conversion. As mentioned in Section 2.4.1.1 due to overlap of proton environments within the  $^1\text{H NMR}$  of the pure polymer species  $\text{DP}_{\text{OH}}$  could not be determined.

**Table 2.9 – AB block co-polymers generated by PEG<sub>5K</sub>-OH initiated, MSA catalysed ROP of substituted caprolactone monomers with a targeted DP<sub>n</sub> of 40 monomer units;**

Target Polymer	<sup>1</sup> H NMR				SEC <sup>c</sup>			
	Monomer conv. <sup>a</sup>	DP <sub>I</sub> by NMR (Initiator)	M <sub>n</sub> by NMR (Initiator) (g mol <sup>-1</sup> ) <sup>d</sup>	M <sub>n</sub> Theory <sup>b</sup> (g mol <sup>-1</sup> )	M <sub>n</sub> (g mol <sup>-1</sup> )	M <sub>w</sub> (g mol <sup>-1</sup> )	Đ	α
PEG <sub>5K</sub> - <i>b</i> -PMOP <sub>40</sub>	96%	35	9,490	9,920	9,710	10,330	1.064	0.78
PEG <sub>5K</sub> - <i>b</i> -PPOP <sub>40</sub>	97%	36	10,620	11,060	10,870	11,490	1.058	0.78
PEG <sub>5K</sub> - <i>b</i> -PBOP <sub>40</sub>	94%	30	10,110	11,400	10,970	11,540	1.052	0.78
PEG <sub>5K</sub> - <i>b</i> -PPHLOP <sub>40</sub>	98%	38	12,230	12,460	12,090	12,840	1.062	0.78

Polymerisations undertaken at 50 °C for 3.5 hours; *a* Determined by <sup>1</sup>H NMR (CDCl<sub>3</sub>, 400 MHz) of the crude samples (see Appendix A for equations), *b* Calculated using the equation:  $M_{n\text{theory}} = (DP_{\text{targeted}} \times \text{conv.} \times Mr_{\text{BM}}) + Mr_{\text{BzA}}$ , *c* Determined by triple detection SEC with a mobile phase of DMF/LiBr 0.01 M (60 °C) at 1 mL min<sup>-1</sup>, *d* Calculated using the equation:  $M_{n\text{NMR}} = (DP_{\text{I(Eq. 2.14)}} \times Mr_{\text{BM}}) + Mr_{\text{BzA/PEG-OH}}$ .

Triple detection SEC (DMF/LiBr 0.01 M at 60 °C) analysis of the four A-B block co-polymers showed a small peak at higher retention times (Figure 2.30) despite a clearly monomodal molecular weight distribution being observed for the main separate signal. The small peak at a retention times of 20.5-22 minutes is very similar to peaks seen within chromatograms of PEG<sub>5K</sub>-*b*-PCL<sub>40</sub> samples (Figure 2.17, B), but does not overlay with that of the PEG<sub>5K</sub>-OH macroinitiator and appears to increase for PEG<sub>5K</sub>-*b*-PPHLOP<sub>40</sub> samples. Although this peak has not been directly identified, it may indicate opportunistic initiation by trace water as the resulting polymer would correspond to a linear homo-polyester and not bear the PEG<sub>5K</sub> block segment. Molecular weight determination excluded this additional peak to allow direct comparison to PEG<sub>5K</sub>-*b*-PCL<sub>40</sub> (Table 2.9) and the four polymers displayed a close comparison with the theoretical targeted values and Đ values < 1.10. Similarly, M<sub>n</sub> values determined by NMR correlated well with SEC values.



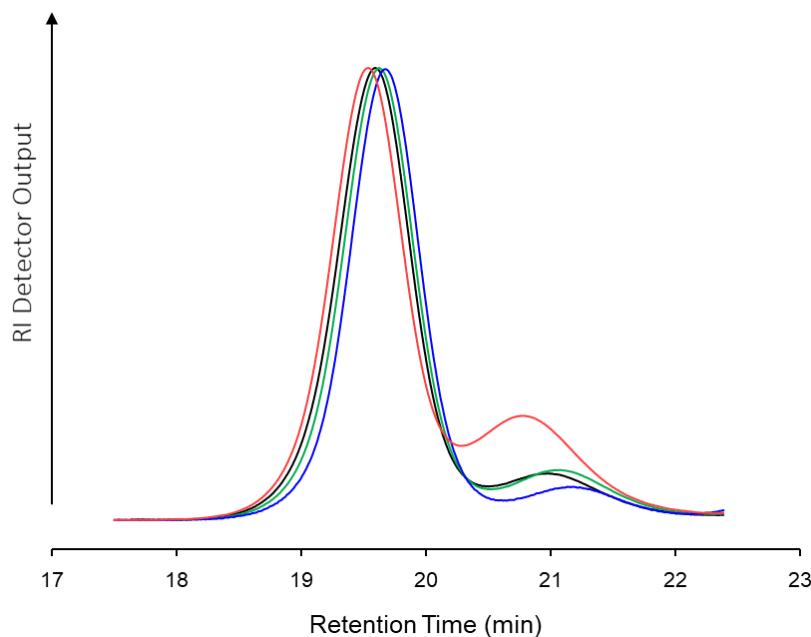


**Figure 2.30-** Refractive index, *RI*, detector output chromatograms of PEG<sub>5K</sub>-*b*-PBM<sub>40</sub>; PEG<sub>5K</sub>-*b*-PMOP<sub>40</sub> (black), PEG<sub>5K</sub>-*b*-PPOP<sub>40</sub> (green), PEG<sub>5K</sub>-*b*-PBOP<sub>40</sub> (blue) and PEG<sub>5K</sub>-*b*-PPHLOP<sub>40</sub> (red). Obtained by triple detection SEC; Mobile phase: DMF/ 0.01 M LiBr at 60 °C.

For completeness, SEC analysis was conducted with the inclusion of the lower molecular weight peak (Table 2.10) leading to a decrease in the calculated  $M_n$  values; however, these values were generally similar to the theoretical values and  $\bar{D}$  values remained  $< 1.10$ . This could be a result of water impurity within this reaction which is most likely a result of the initiator which, although was dried overnight in a vacuum oven before use, retaining water within its solid form.

**Table 2.10 – AB block co-polymers generated by PEG<sub>5K</sub>-OH initiated, MSA catalysed ROP of substituted caprolactone monomers with a targeted DP<sub>n</sub> of 40 monomer units including secondary population;**

Target Polymer	Monomer conv. <sup>a</sup>	<sup>1</sup> H NMR		SEC <sup>b</sup>			
		DP <sub>I</sub> by NMR (Initiator)	M <sub>n</sub> by NMR (Initiator) (g mol <sup>-1</sup> ) <sup>c</sup>	M <sub>n</sub> (g mol <sup>-1</sup> )	M <sub>w</sub> (g mol <sup>-1</sup> )	Đ	DP <sub>SEC</sub>
PEG <sub>5K</sub> - <i>b</i> -PMOP <sub>40</sub>	96%	35	9,490	8,280	8,910	1.076	26
PEG <sub>5K</sub> - <i>b</i> -PPOP <sub>40</sub>	97%	36	10,620	9,020	9,780	1.084	26
PEG <sub>5K</sub> - <i>b</i> -PBOP <sub>40</sub>	94%	30	10,110	10,020	10,570	1.055	33
PEG <sub>5K</sub> - <i>b</i> -PPHLOP <sub>40</sub>	98%	38	12,230	8,990	9,560	1.064	24

Polymerisations undertaken at 50 °C for 3.5 hours; *a* Determined by <sup>1</sup>H NMR (CDCl<sub>3</sub>, 400 MHz) of the crude samples, *b* Determined by triple detection SEC with a mobile phase of DMF/LiBr 0.01 M (60 °C) at 1 mL min<sup>-1</sup>, *c* Calculated using the equation:  $M_{nNMR} = (DP_{I(Eq. 2.14)} \times M_{rBM}) + M_{rBzA/PEG-OH}$ .

## 2.4.2 Statistical co-polymerisation of substituted caprolactone monomers and BOD via MSA catalysed ROP to achieve branched architecture

### 2.4.2.1 Benzyl alcohol initiated, MSA catalysed ROP of substituted caprolactone monomers

Branched polymer architectures were synthesised using the four substituted caprolactone monomers using approaches described in Sections 2.3.3.1 and 2.4.1.1 and, again, targeting a DP<sub>n</sub> = 40 monomer units for all polyester primary chains; all reactions were conducted for 3.5 hours at 38 °C to allow for BOD dissolution, with the exception of ROP reactions containing PHLOP which required a higher temperature of 60 °C to aid dissolution of both the solid monomer and BOD. Unlike PCL-*co*-BOD<sub>0.7</sub>, additional toluene was required to achieve homogenous reaction mixtures and polymerisations were conducted at 33 wt% for MOP, POP and BOP, and at 25 wt% (w.r.t monomer) for PHLOP. The BOD: BzA molar ratio was initially set to 0.8:1 and a series of soluble polymers were synthesised, however gelation of PMOP<sub>40</sub>-*co*-BOD<sub>0.8</sub> and PPOP<sub>40</sub>-*co*-BOD<sub>0.8</sub> was noticed during purification and analysis. This was also seen for PBOP<sub>40</sub>-*co*-BOD<sub>0.8</sub> and PPHLOP<sub>40</sub>-*co*-BOD<sub>0.8</sub> after short periods of storage at ambient temperature. All polymerisations were, therefore, conducted at a BOD: initiator ratio molar ratio of 0.7:1 to avoid further microscopic gelation behaviour; gelation was avoided with this ratio. <sup>1</sup>H NMR studies of crude reaction mixture samples showed all polymerisations reached

above 99 % conversion. (Table 2.11). Primary chain length was also shown to be relatively controlled for the polymerisation undertaken at 38 °C with  $DP_1$  values of  $\leq 50$  monomer units. However PHLOP<sub>40-co-BOD0.7</sub> was shown to have an average primary chain length of 76 monomer units which suggests that the higher temperature of the polymerisation may contribute to increased transesterification reactions preventing the accurate targeting of primary chain length in this case.

**Table 2.11 - Series of MSA catalysed ROP of substituted caprolactone monomers with BOD (0.7 molar equivalents w.r.t initiator) to achieved branched architecture;**

Target Polymer	<sup>1</sup> H NMR		SEC <sup>b</sup>					
	Monomer conversion <sup>a</sup>	DP <sub>1</sub> of primary chain by NMR <sup>c</sup> (Initiator)	M <sub>n</sub> (g mol <sup>-1</sup> )	M <sub>w</sub> (g mol <sup>-1</sup> )	Đ	α	dn/dc	No. of primary chains (weight averaged)
PMOP <sub>40-co-BOD0.7</sub>	99 %	44	9,920	89,470	9.02	0.34	0.0627	16.4
PPOP <sub>40-co-BOD0.7</sub>	>99 %	50	12,490	83,830	6.71	0.28	0.0564	12.3
PBOP <sub>40-co-BOD0.7</sub>	> 99 %	43	13,340	78,230	5.85	0.21	0.0649	10.7
PPHLOP <sub>40-co-BOD0.7</sub>	99 %	76	37,110	457,910	12.34	0.38	0.1326	56.3

Polymerisations undertaken at 38 °C (MOP, POP, BOP) and 60 °C (PHLOP) for 3.5 hours; *a* Determined by <sup>1</sup>H NMR (CDCl<sub>3</sub>, 400 MHz) of the crude samples, *b* Determined by triple detection SEC with a mobile phase of DMF/LiBr 0.01 M (60 °C) at 1 mL min<sup>-1</sup>, *c* Calculated using the equation:  $Mn_{NMR} = (DP_{I(Eq. 2.14)} \times Mr_{BM}) + Mr_{BzA/PEG-OH}$ .

As seen in Table 2.9, triple detection SEC analysis (DMF/LiBr 0.01 M at 60 °C) of the branched polymers indicated weight average molecular weights of  $> 78,000$  g mol<sup>-1</sup> with broad distributions (Figure 2.31), indicative of statistical branching, with  $\alpha$  values  $< 0.4$ . Furthermore the weight average number of primary chains linked together for each polymer species was  $> 10$ . The reason for the lower branched architecture of PBOP<sub>40-co-BOD0.7</sub> is unclear at this time. However characteristic multimodal chromatograms were produced for all four polymer species further confirming the presence of branched architecture.

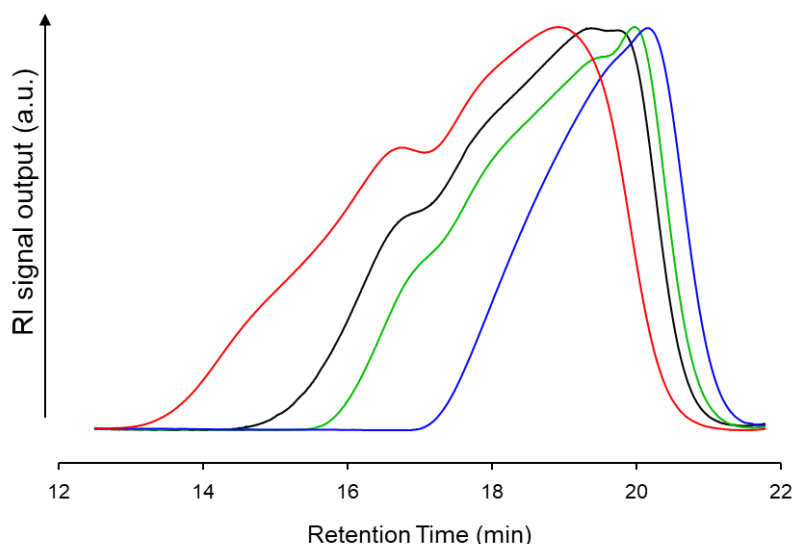


**Figure 2.31- Refractive index, *RI*, detector output chromatograms of PSCM<sub>40-co</sub>-BOD<sub>0.7</sub>; PMOP<sub>40-co</sub>-BOD<sub>0.7</sub> (black), PPOP<sub>40-co</sub>-BOD<sub>0.7</sub> (green), PBOP<sub>40-co</sub>-BOD<sub>0.7</sub> (blue) and PPHLOP<sub>40-co</sub>-BOD<sub>0.7</sub> (red). Obtained by triple detection SEC; Mobile phase: DMF/ 0.01 M LiBr at 60 °C.**

#### **2.4.2.2 Poly(ethylene glycol)<sub>5K</sub> initiated, MSA catalysed ROP of substituted caprolactone monomers and BOD**

The four substituted caprolactone monomers were used to synthesise a range of branched A-B block co-polymers using the PEG<sub>5K</sub>-OH macroinitiator, as described in Section 2.3.3.2 and Section 2.4.2.1. As described earlier, when using PHLOP, a lower solids content of 25 wt% (w.r.t monomer) was required and a molar ratio of BOD: PEG of 0.7:1 was employed to avoid gelation.

<sup>1</sup>H NMR analysis indicated that after 4 hours all four polymers had reached >97 % conversion (Table 2.12), and triple detection SEC analysis was undertaken on the purified polymers using an DMF/ 0.01 M LiBr eluent at 60 °C. As seen above (Section 2.3.3.2), the use of the PEG<sub>5K</sub>-OH macroinitiator in branching polymerisations led to low levels of branching and M<sub>w</sub> values <26,000 g mol<sup>-1</sup> in all cases (Table 2.12). Dispersity values were also low ( $\bar{D}$  <2.5), although  $\alpha$  values were < 0.4 indicating that branched architectures had indeed been achieved.

**Table 2.12 - Series of MSA catalysed ROP of substituted caprolactone monomers with PEG<sub>5K</sub>-OH and BOD to achieved branched amphiphilic architecture;**

Target polymer	<sup>1</sup> H NMR	SEC <sup>b</sup>					No. of primary chains (weight averaged)
	Monomer conversion <sup>a</sup>	M <sub>n</sub> (g mol <sup>-1</sup> )	M <sub>w</sub> (g mol <sup>-1</sup> )	Đ	dn/dc	α	
PEG <sub>5K</sub> - <i>b</i> -PMOP <sub>40-co</sub> -BOD <sub>0.7</sub>	98 %	11,960	22,350	1.87	0.0584	0.31	2.7
PEG <sub>5K</sub> - <i>b</i> -PPOP <sub>40-co</sub> -BOD <sub>0.7</sub>	99 %	12,110	19,950	1.65	0.0581	0.31	2.2
PEG <sub>5K</sub> - <i>b</i> -PBOP <sub>40-co</sub> -BOD <sub>0.7</sub>	99 %	11,450	18,360	1.6	0.0662	0.30	1.8
PEG <sub>5K</sub> - <i>b</i> -PPHLOP <sub>40-co</sub> -BOD <sub>0.7</sub>	98 %	15,400	25,130	1.6	0.0959	0.33	2.8
PEG <sub>5K</sub> - <i>b</i> -PMOP <sub>40-co</sub> -BOD <sub>0.7</sub> <sup>c</sup>	98 %	9,020	20,420	2.27	0.0612	0.31	2.5
PEG <sub>5K</sub> - <i>b</i> -PPOP <sub>40-co</sub> -BOD <sub>0.7</sub> <sup>c</sup>	99 %	7,870	17,490	2.22	0.0622	0.31	1.9
PEG <sub>5K</sub> - <i>b</i> -PBOP <sub>40-co</sub> -BOD <sub>0.7</sub> <sup>c</sup>	99 %	10,500	18,350	1.75	0.0671	0.30	1.8
PEG <sub>5K</sub> - <i>b</i> -PPHLOP <sub>40-co</sub> -BOD <sub>0.7</sub> <sup>c</sup>	98 %	12,920	21,030	1.63	0.1064	0.33	2.3

Polymerisations undertaken at 50 °C for 4 hours *a* Determined by <sup>1</sup>H NMR (CDCl<sub>3</sub>, 400 MHz) of the crude samples, *b* Determined by triple detection SEC with a mobile phase of DMF/LiBr 0.01 M (60 °C) at 1 mL min<sup>-1</sup>, *c* includes the low molecular weight peak in SEC analysis.

Interestingly the RI molecular weight distributions revealed the same smaller peak at a retention time of approximately 21 mins (Figure 2.32) and may indicate the opportunistic initiation speculated above (Section 2.4.1.2). The inclusion of this peak in SEC analysis, again, resulted in the decrease in  $M_n$  and  $M_w$  values; for example, PEG<sub>5K</sub>-*b*-PPHLOP<sub>40-co</sub>-BOD<sub>0.7</sub> shown a decrease in  $M_w$  from 25,130 to 21,030 g mol<sup>-1</sup>, when the smaller secondary population was included in the SEC analysis (Table 2.12). However this decrease in  $M_w$  did not greatly affect the number of chains linked together which remained < 3 in all 4 cases;  $\bar{D}$  did increase, as expected, due the inclusion of the smaller peak. (Table 2.12). The lack of high molecular weight, branched polymers reflected the results seen with PEG<sub>5K</sub>-*b*-PCL<sub>40-co</sub>-BOD<sub>0.7</sub> in Section 2.3.3.2 and may have been a result of increased dilution of these reactions or the steric hindrance created by bringing together large PEG chains during branching.

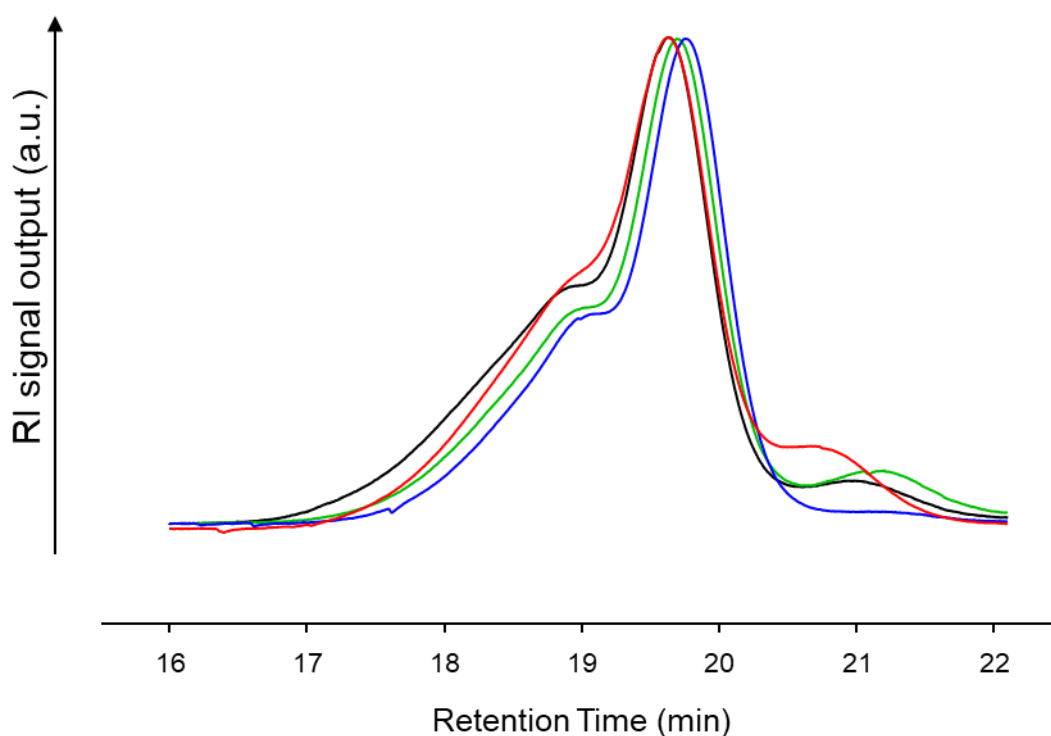


**Figure 2.32-** Refractive index, *RI*, detector output chromatograms of PEG<sub>5K</sub>-*b*-PSCM<sub>40-co</sub>-BOD<sub>0.7</sub>; PEG<sub>5K</sub>-*b*-PMOP<sub>40-co</sub>-BOD<sub>0.7</sub> (black), PEG<sub>5K</sub>-*b*-PPOP<sub>40-co</sub>-BOD<sub>0.7</sub> (green), PEG<sub>5K</sub>-*b*-PBOP<sub>40-co</sub>-BOD<sub>0.7</sub> (blue) and PEG<sub>5K</sub>-*b*-PPHLOP<sub>40-co</sub>-BOD<sub>0.7</sub> (red). Obtained by triple detection SEC; Mobile phase: DMF/ 0.01 M LiBr at 60 °C.

## 2.5 Differential scanning calorimetry, *DSC*

The library of polymers containing varying architecture and chemistry were studied using differential scanning calorimetry, *DSC*, in order to understand the variation in physical properties that may be available through these subtle changes in polymer structure and was

used as indicator as to thermal properties each polymer possessed. Analysis used a heat-cool-heat cycle from -90 to 250 °C to fully erase then capture the thermal properties of each sample including both glass transition temperature changes,  $T_g$ , and melting points,  $T_m$  (Table 2.13).

**Table 2.13- DSC analysis of the complete polyester library;**

Sample	$T_g$ (°C)	$T_m$ (°C)	Peak Enthalpy (J/g)
PCL <sub>40</sub>	-62	52	90
PMOP <sub>40</sub>	-----	Did not run	-----
PPOP <sub>40</sub>	-66	-	-
PBOP <sub>40</sub>	-23	-	-
PPHLOP <sub>40</sub>	-1	-	-
PCL <sub>40</sub> -BOD <sub>0.7</sub>	-60	48	71
PMOP <sub>40</sub> -BOD <sub>0.7</sub>	-63	-	-
PPOP <sub>40</sub> -BOD <sub>0.7</sub>	-----	Did not run	-----
PBOP <sub>40</sub> -BOD <sub>0.7</sub>	-20	-	-
PPHLOP <sub>40</sub> -BOD <sub>0.7</sub>	4	-	-
PEG <sub>5K</sub> -PCL <sub>40</sub>	-58	52	136
PEG <sub>5K</sub> -PMOP <sub>40</sub>	-63	53	94
PEG <sub>5K</sub> -PPOP <sub>40</sub>	-66	53	85
PEG <sub>5K</sub> -PBOP <sub>40</sub>	-28.8	51	79
PEG <sub>5K</sub> -PPHLOP <sub>40</sub>	4	49	75
PEG <sub>5K</sub> -PCL <sub>40</sub> -BOD <sub>0.7</sub>	-61	52	112
PEG <sub>5K</sub> -PMOP <sub>40</sub> -BOD <sub>0.7</sub>	-60	53	91
PEG <sub>5K</sub> -PPOP <sub>40</sub> -BOD <sub>0.7</sub>	-63	52	82
PEG <sub>5K</sub> -PBOP <sub>40</sub> -BOD <sub>0.7</sub>	-17	52	86
PEG <sub>5K</sub> -PPHLOP <sub>40</sub> -BOD <sub>0.7</sub>	13	50	70
PEG <sub>5K</sub> -OH	49	58	200

Heat-cool-heat cycle in the range of -90 to 250 °C at a rate of 5 °Cmin<sup>-1</sup>.

Initial analysis was carried out with caprolactone based polymers due to the access to literature values to corroborate the experimental values obtained from this study. PCL is known to be semi-crystalline meaning that the polymer has both amorphous and crystalline character. DSC analysis of the second heat cycle for both PCL<sub>40</sub> and PCL<sub>40</sub>-*co*-BOD<sub>0.7</sub> showed the presence of both  $T_g$  and  $T_m$  peaks at -62 °C and -60 °C and 52 °C and 48 °C respectively (Figure 2.33, Table 2.13). The values obtained for linear PCL<sub>40</sub> correlated closely with literature values of -60 °C and 63 °C for  $T_g$  and  $T_m$  values respectively.<sup>4,93</sup> The presence of  $T_m$  peaks for both linear and branched PCL-derived structures confirmed that these polymers were semi-

crystalline as expected and that the branched architecture does not greatly impact the crystallinity of the resultant polymer although it is clearly reduced. Across all the polymers studied, the introduction of branching led to an increase in  $T_g$ . The impact of branching on  $T_g$  has been studied in the literature, and similar results were seen for different polymers. Although not fully understood, it has been reported that an increase in  $T_g$  values may be due to the restriction of segmental mobility or the increasing compactness of the structure resulting in more chain ends, for amorphous polymers; however, this is unlikely in the case of materials created by a modified 'Strathclyde' approach as the number of chain ends present is identical to a linear polymer of the same  $DP_n$  as the primary chains within the branched structure.<sup>94-96</sup>



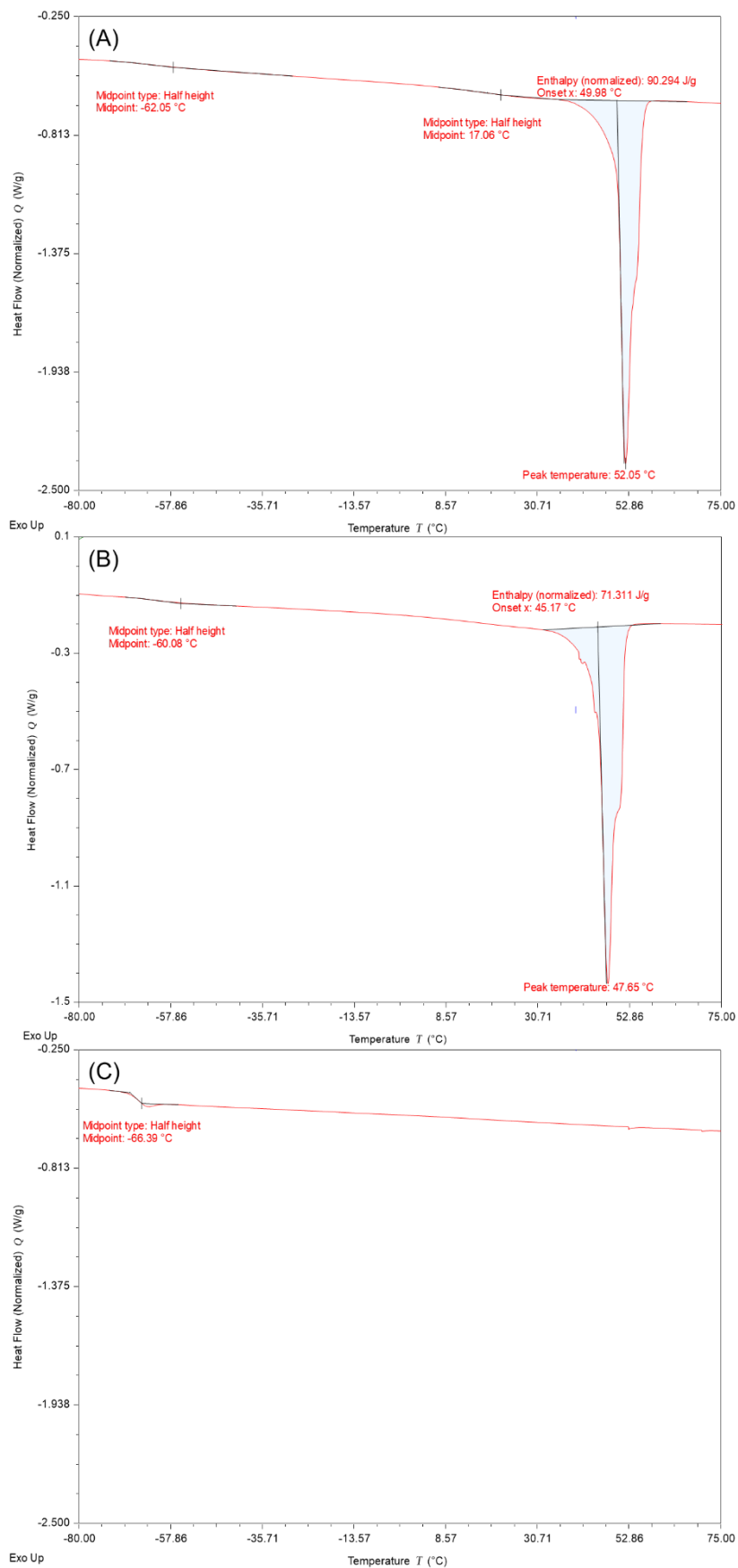


Figure 2.33- DSC traces generated from the second heat cycle from -80 to 75 °C, rate 5 °Cmin<sup>-1</sup>; (A) PCL<sub>40</sub>, (B) PCL<sub>40</sub>-co-BOD<sub>0.7</sub> and (C) PPOP<sub>40</sub>.

PMOP<sub>40</sub> was unavailable for this study and therefore omitted from the table. Importantly, substitution of the lactone ring led to a near complete disappearance of a  $T_m$  peak in all linear and branched polymer samples initiated by BzA, indicating a significant disruption of the crystallinity of the polymers and highly amorphous structure compared to PCL (Figure 2.33, C). Although an impact on crystallinity was hypothesised, a complete disruption of crystallinity was unexpected.

Finally, examination of all linear and branched A-B PEG-derived co-polymers revealed some clear trends with respect to the lactone monomer. Analysis of the PEG<sub>5K</sub>-OH macroinitiator confirmed that the  $T_m$  peak overlaid the  $T_m$  peak for PCL, therefore generating a  $T_m$  peak for all the block co-polymers regardless of monomer used or architecture (Table 2.13).

Within both the linear and branched A-B block co-polymers  $T_g$  became more negative as the side group substitution lengthened from a methyl side group to a flexible alkyl propyl group. This indicates that the extending side chain is acting like a plasticiser, preventing the tight packing of polymer chains and aiding movement by increasing the free volume in the polymer. Conversely the inclusion of a presence of a tertiary butyl side chain led to a dramatic increase in  $T_g$  and substitution with a phenyl ring led to a further increase. The t-butyl group is most likely acting as an ‘anchor’ trapping chains together and preventing free movement therefore increasing the energy needed to move the polymer above its  $T_g$ .<sup>79</sup> The pendant benzyl group is likely to act in a similar fashion with the additionally capability of aromatic interactions with other benzyl groups only the polymer backbone decreasing the flexibility and further increasing the energy needed to make the polymer pliable and flexible above its  $T_g$ .<sup>79</sup> This behaviour mirrors behaviour that would be seen with vinyl polymers of varying side chain chemistry.<sup>79,80</sup>

## 2.6 Conclusions

In conclusion, the aims of this chapter were to investigate MSA catalysed ROP and its application in the synthesis of polyester-derived polymers of varying architecture and monomer chemistry. This successfully generated a library of polymer species that can be taken forward for future nanoparticle formation studies and drug encapsulation evaluation. More in depth studies with caprolactone based polymers not only set a baseline for future studies with a new series of substituted caprolactone monomers but also provided a valuable insight into the broad applicability of MSA catalysed ROP.

Kinetic experiments for linear and branched PCL highlighted the complexity of this polymerisation technique given that the first order kinetics of the reaction were dependant on protonated monomer. This highlighted the relevance of the basicity of the monomer species and importance of its consideration when implementing new unexplored monomer species.

Highly stringent anhydrous conditions were avoided during these polymerisations as future scalability was an important consideration, given that scalable techniques would have more long term value and commercial relevance. Molecular weight chain end and  $^1\text{H}$  NMR analysis of linear PCL polymers indicated that opportunistic initiation was occurring, most likely from low levels of residual water within the monomer. However this does not appear to be a significant issue, particularly when  $\text{DP}_n$  is  $< 50$  monomer units, as the tying together of primary polymer chains during the statistical branching process will lead to structures that approximate closely to the targeted materials in the overall composition.<sup>97</sup> Further mechanistic studies revealed the presence of transesterification reactions once high monomer conversion had been surpassed although this should not pose a problem during branched polymer synthesis. Moreover these transesterification reaction could in fact aid the synthesis of highly branched, high molecular weight material.

Amphiphilic A-B block co-polymer synthesis with long PEG chains, that have been shown to be of clinical relevance, highlighted the significant effects steric hindrance proved to have on the successful formation of high molecular weight branched species. Nonetheless structural, chemical and physical property diversity within the available library of polymers, synthesised with the inclusion of substituted caprolactone monomers, motivates exploration of nanoparticle formation and guest encapsulation.

**References**

- 1 C. Jérôme and P. Lecomte, *Adv. Drug Deliv. Rev.*, 2008, **60**, 1056–1076.
- 2 A. Kowalski, A. Duda, Stanis and S. Penczek, *Macromol. Rapid Commun.*, 1998, **19**, 567–572.
- 3 A. Duda, S. Penczek, A. Kowalski and J. Libiszowski, *Macromol. Symp.*, 2000, **153**, 41–53.
- 4 M. Labet and W. Thielemans, *Chem. Soc. Rev.*, 2009, **38**, 3484–3504.
- 5 O. Nuyken and S. D. Pask, *Polymers (Basel)*, 2013, **5**, 361–403.
- 6 P. Kubisa and S. Penczek, *Prog. Polym. Sci.*, 1999, **24**, 1409–1437.
- 7 A. Khanna, Y. S. Sudha, S. Pillai and S. S. Rath, *J. Mol. Model.*, 2008, **14**, 367–374.
- 8 K. M. Stridsberg, M. Ryner and A. C. Albertsson, *Controlled Ring-Opening Polymerization: Polymers with designed Macromolecular Architecture*, Springer-Verlag Berlin Heidelberg, 1st edn., 2002.
- 9 M. Möller, R. Kånge and J. L. Hedrick, *J. Polym. Sci. Part A Polym. Chem.*, 2000, **38**, 2067–2074.
- 10 W. N. Ottou, H. Sardon, D. Mecerreyes, J. Vignolle and D. Taton, *Prog. Polym. Sci.*, 2016, **56**, 64–115.
- 11 A. P. Dove, *ACS Macro Lett.*, 2012, **1**, 1409–1412.
- 12 H. Seyednejad, A. H. Ghassemi, C. F. Van Nostrum, T. Vermonden and W. E. Hennink, *J. Control. Release*, 2011, **152**, 168–176.
- 13 F. Nederberg, E. F. Connor, M. Möller, T. Glauser and J. L. Hedrick, *Angew. Chemie - Int. Ed.*, 2001, **40**, 2712–2715.
- 14 E. F. Connor, G. W. Nyce, M. Myers, A. Möck and J. L. Hedrick, *J. Am. Chem. Soc.*, 2002, **124**, 914–915.
- 15 B. Lin and R. M. Waymouth, *Macromolecules*, 2018, **51**, 2932–2938.
- 16 J. Raynaud, W. N. Ottou, Y. Gnanou and D. Taton, *Chem. Commun.*, 2010, **46**, 3203–3205.
- 17 F. Nederberg, B. G. G. Lohmeijer, F. Leibfarth, R. C. Pratt, J. Choi, A. P. Dove, R. M. Waymouth and J. L. Hedrick, *Biomacromolecules*, 2007, **8**, 153–160.
- 18 L. He, H. Guo, Y. Wang, G. F. Du and B. Dai, *Tetrahedron Lett.*, 2015, **56**, 972–980.
- 19 S. Naumann and M. R. Buchmeiser, *Catal. Sci. Technol.*, 2014, **4**, 2466–2479.
- 20 Y. Miao, C. Rousseau, A. Mortreux, P. Martin and P. Zinck, *Polymer (Guildf)*, 2011, **52**, 5018–5026.
- 21 D. J. Coady, K. Fukushima, H. W. Horn, J. E. Rice and J. L. Hedrick, *Chem. Commun.*, 2011, **47**, 3105–3107.
- 22 B. G. G. Lohmeijer, R. C. Pratt, F. Leibfarth, J. W. Logan, D. A. Long, A. P. Dove, F. Nederberg, J. Choi, C. Wade, R. M. Waymouth and J. L. Hedrick, *Macromolecules*,

- 2006, **39**, 8574–8583.
- 23 S. Gazeau-Bureau, D. Delcroix, B. Martín-Vaca, D. Bourissou, C. Navarro and S. Magnet, *Macromolecules*, 2008, **41**, 3782–3784.
- 24 J. Ford, P. Chambon, J. North, F. L. Hatton, M. Giardiello, A. Owen and S. P. Rannard, *Macromolecules*, 2015, **48**, 1883–1893.
- 25 J. Rieger, C. Passirani, J. P. Benoit, K. Van Butsele, R. Jérôme and C. Jérôme, *Adv. Funct. Mater.*, 2006, **16**, 1506–1514.
- 26 H. U. Kang, Y. C. Yu, S. J. Shin, J. Kim and J. H. Youk, *Macromolecules*, 2013, **46**, 1291–1295.
- 27 Q. Gu, J. Z. Xing, M. Huang, C. He and J. Chen, *Nanotechnology*, 2012, **23**, 1–10.
- 28 S. Ashton, Y. H. Song, J. Nolan, E. Cadogan, J. Murray, R. Odedra, J. Foster, P. A. Hall, S. Low, P. Taylor, R. Ellston, U. M. Polanska, J. Wilson, C. Howes, A. Smith, R. J. A. Goodwin, J. G. Swales, N. Strittmatter, Z. Takáts, A. Nilsson, P. Andren, D. Trueman, M. Walker, C. L. Reimer, G. Troiano, D. Parsons, D. De Witt, M. Ashford, J. Hrkach, S. Zale, P. J. Jewsbury and S. T. Barry, *Sci. Transl. Med.*, 2016, **8**, 1–11.
- 29 J. S. Lee, S. J. Hwang and D. S. Lee, *Macromol. Res.*, 2009, **17**, 72–78.
- 30 X. W. Wei, C. Y. Gong, M. L. Gou, S. Z. Fu, Q. F. Guo, S. Shi, F. Luo, G. Guo, L. Y. Qiu and Z. Y. Qian, *Int. J. Pharm.*, 2009, **381**, 1–18.
- 31 X. Wang, J. J. Liu, S. Xu, J. Xu, X. Pan, J. J. Liu, S. Cui, Z. Li and K. Guo, *Polym. Chem.*, 2016, **7**, 6297–6308.
- 32 C. D’Avila Carvalho Erbeta, R. J. Alves, J. M. Resende, R. Fernando de Souza Freitas and R. Geraldo de Sousa, *J. Biomater. Nanobiotechnol.*, 2012, **3**, 208–225.
- 33 O. Dechy-Cabaret, B. Martin-Vaca and D. Bourissou, *Chem. Rev.*, 2004, **104**, 6147–6176.
- 34 H. Qian, A. R. Wohl, J. T. Crow, C. W. MacOsco and T. R. Hoye, *Macromolecules*, 2011, **44**, 7132–7140.
- 35 M. Toplishek, E. Žagar and D. Pahovnik, *Eur. Polym. J.*, 2019, **119**, 438–444.
- 36 C. Zheng, *Soft Matter*, 2019, **15**, 5357–5370.
- 37 M. Basko and P. Kubisa, *J. Polym. Sci. Part A Polym. Chem.*, 2006, **44**, 7071–7081.
- 38 Q. lei Song, S. yan Hu, J. peng Zhao and G. zhao Zhang, *Chinese J. Polym. Sci. (English Ed.)*, 2017, **35**, 581–601.
- 39 E. J. Shin, H. A. Brown, S. Gonzalez, W. Jeong, J. L. Hedrick and R. M. Waymouth, *Angew. Chemie - Int. Ed.*, 2011, **50**, 6388–6391.
- 40 R. M. England and S. Rimmer, *Polym. Chem.*, 2010, **1**, 1533–1544.
- 41 F. L. Hatton, P. Chambon, A. C. Savage and S. P. Rannard, *Chem. Commun.*, 2016, **52**, 3915–3918.
- 42 N. T. Nguyen, K. J. Thurecht, S. M. Howdle and D. J. Irvine, *Polym. Chem.*, 2014, **5**, 2997–3008.

- 43 R. d’Arcy, J. Burke and N. Tirelli, *Adv. Drug Deliv. Rev.*, 2016, **107**, 60–81.
- 44 J. M. J. Frechet, M. Henmi, I. Gitsov, S. Aoshima, M. R. Leduc and R. B. Grubbs, *Science*, 1995, **269**, 1080–1083.
- 45 M. Liu, N. Vladimirov and J. M. J. Fréchet, *Macromolecules*, 1999, **32**, 6881–6884.
- 46 N. O’Brien, A. McKee, D. C. Sherrington, A. T. Slark and A. Titterton, *Polymer (Guildf)*., 2000, **41**, 6027–6031.
- 47 M. Bednarek, *Prog. Polym. Sci.*, 2016, **58**, 27–58.
- 48 A. Michalski, M. Brzezinski, G. Lapienis and T. Biela, *Prog. Polym. Sci.*, 2019, **89**, 159–212.
- 49 E. Vidovic, D. Klee and H. Hocker, *Polymer (Guildf)*., 2007, **45**, 4536–4544.
- 50 H. Qiu, Z.-N. Yang and J. Ling, *Chinese J. Polym. Sci.*, 2019, **37**, 858–865.
- 51 P. Shang, J. Wu, X. Shi, Z. Wang, F. Song and S. Liu, *Polymers (Basel)*., 2019, **11**, 1–15.
- 52 X. Wang, X. Xie, C. Cai, E. Rytting, T. Steele and T. Kissel, *Macromolecules*, 2008, **41**, 2791–2799.
- 53 O. Soga, C. F. Van Nostrum, A. Ramzi, T. Visser, F. Soulimani, P. M. Frederik, P. H. H. Bomans and W. E. Hennink, *Langmuir*, 2004, **20**, 9388–9395.
- 54 B. S. Lele and J. Leroux, *Polymer (Guildf)*., 2002, **43**, 5595–5606.
- 55 P. F. Gou, W. P. Zhu and Z. Q. Shen, *Biomacromolecules*, 2010, **11**, 934–943.
- 56 J. M. Ren, Q. Fu, A. Blencowe and G. G. Qiao, *ACS Macro Lett.*, 2012, **1**, 681–686.
- 57 M. Alger, *Polymer Science Dictionary*, Springer Nature, 3rd Editio., 2017.
- 58 B. I. Voit and A. Lederer, *Chem. Rev.*, 2009, **109**, 5924–5973.
- 59 M. Smet, in *Encyclopedia of Polymeric Nanomaterials*, eds. S. Kobayashi and K. Mullen, Springer Reference, 2015 Editio., 2015, pp. 2446–2459.
- 60 A. Sunder, R. Hanselmann, H. Frey and R. Mülhaupt, *Macromolecules*, 1999, **32**, 4240–4246.
- 61 M. Jikei and M. Kakimoto, *Prog. Polym. Sci.*, 2001, **26**, 1233–1285.
- 62 A. Goodwin and D. Baskaran, *Macromolecules*, 2012, **45**, 9657–9665.
- 63 D. Yan, J. Hou, X. Zhu, J. J. Kosman and H.-S. Wu, *Macromol. Rapid Commun.*, 2000, **21**, 557–561.
- 64 M. Trollsas, P. Lowenhielm, V. Y. Lee, M. Moller, R. D. Miller and J. L. Hedrick, *Macromolecules*, 1999, **32**, 9062–9066.
- 65 T. Satoh, *Int. J. Polym. Sci.*, 2012, **2012**, 1–8.
- 66 P. A. Costello, I. K. Martin, A. T. Slark, D. C. Sherrington and A. Titterton, *Polymer (Guildf)*., 2002, **43**, 245–254.
- 67 I. Bannister, N. C. Billingham, S. P. Armes, S. P. Rannard and P. Findlay,

- Macromolecules*, 2006, **39**, 7483–7492.
- 68 P. J. Flory, *J. Am. Chem. Soc.*, 1941, **63**, 3083–3090.
- 69 A. B. Dwyer, P. Chambon, A. Town, F. L. Hatton, J. Ford and S. P. Rannard, *Polym. Chem.*, 2015, **6**, 7286–7296.
- 70 F. L. Hatton, P. Chambon, T. O. McDonald, A. Owen and S. P. Rannard, *Chem. Sci.*, 2014, **5**, 1844–1853.
- 71 J. J. Hobson, S. Edwards, R. A. Slater, P. Martin, A. Owen and S. P. Rannard, *RSC Adv.*, 2018, **8**, 12984–12991.
- 72 F. Y. Hern, A. Hill, A. Owen and S. P. Rannard, *Polym. Chem.*, 2018, **9**, 1767–1771.
- 73 H. E. Rogers, P. Chambon, S. E. R. Auty, F. Y. Hern, A. Owen and S. P. Rannard, *Soft Matter*, 2015, **11**, 7005–15.
- 74 F. L. Hatton, L. M. Tatham, L. R. Tidbury, P. Chambon, T. He, A. Owen and S. P. Rannard, *Chem. Sci.*, 2015, **6**, 326–334.
- 75 R. A. Slater, T. O. McDonald, D. J. Adams, E. R. Draper, J. V. M. Weaver and S. P. Rannard, *Soft Matter*, 2012, **8**, 9816–9827.
- 76 M. Renz and B. Meunier, *Eur. Journal Org. Chem.*, 1999, **1999**, 737–750.
- 77 L. Zhou, X. Liu, J. Ji, Y. Zhang, X. Hu, L. Lin and X. Feng, *J. Am. Chem. Soc.*, 2012, **134**, 17023–17026.
- 78 G. J. ten Brink, I. W. C. E. Arends and R. A. Sheldon, *Chem. Rev.*, 2004, **104**, 4105–4123.
- 79 Polymer Science Learning Center, The Glass Transition, <https://pslc.ws/macrog/tg.htm#one>, (accessed 23 January 2020).
- 80 N. R. Jadhav, V. L. Gaikwad, K. J. Nair and H. M. Kadam, *Asian J. Pharm.*, 2009, **3**, 82–89.
- 81 T. Nakano, *Polym. J.*, 2010, **42**, 103–123.
- 82 D. Bourissou, B. Martin-Vaca, A. Dumitrescu, M. Graullier and F. Lacombe, *Macromolecules*, 2005, **38**, 9993–9998.
- 83 S. Penczek, *J. Polym. Sci. Part A Polym. Chem.*, 2000, **38**, 1919–1933.
- 84 P. G. Matyjaszewski, Features of Controlled/"Living" Radical Polymerizations, <https://www.cmu.edu/maty/crp/features.html>, (accessed 29 January 2020).
- 85 G. Bouchoux, D. Drancourt and D. Leblanc, *New J. Chem.*, 1995, **19**, 1243–1257.
- 86 I. Bannister, N. C. Billingham, S. P. Armes, S. P. Rannard and P. Findlay, *Macromolecules*, 2006, **39**, 7483–7492.
- 87 L. Mezzasalma, A. P. Dove and O. Coulembier, *Eur. Polym. J.*, 2017, **95**, 628–634.
- 88 A. Duda and S. Penczek, *Symp. A Q. J. Mod. Foreign Lit.*, 2001, 160–198.
- 89 S. L. Blackmore, P. Chambon and S. P. Rannard, *Ring Opening Polymerisation of Biodegradable Polyesters of Various Architecture [Unpublished work]*, 2016.

## CHAPTER 2

- 90 J. Rosselgong and S. P. Armes, *Polym. Chem.*, 2015, **6**, 1143–1149.
- 91 J. Rosselgong, S. P. Armes, W. R. S. Barton and D. Price, *Macromolecules*, 2010, **43**, 2145–2156.
- 92 H. Chen and J. Kong, *Polym. Chem.*, 2016, **7**, 3643–3663.
- 93 S. Direct, Polycaprolactone - an overview, <https://www.sciencedirect.com/topics/engineering/polycaprolactone>, (accessed 10 March 2020).
- 94 A. Khalyavina, L. Häußler and A. Lederer, *Polymer (Guildf.)*, 2012, **53**, 1049–1053.
- 95 Q. Zhu, J. Wu, C. Tu, Y. Shi, L. He, R. Wang, X. Zhu and D. Yan, *J. Phys. Chem. B*, 2009, **113**, 5777–5780.
- 96 T. Alhilfi, P. Chambon and S. P. Rannard, *J. Polym. Sci.*, 2020, **1**, 1–13.
- 97 F. Y. Hern, A. Hill, A. Owen and S. P. Rannard, *Polym. Chem.*, 2018, **9**, 1767–1771.
- 98 L. You and J. Ling, *Macromolecules*, 2014, **47**, 2219–2225.



# **CHAPTER 3**

## **NANOPARTICLE FORMATION VIA NANOPRECIPITATION AND CO-NANOPRECIPITATION**

### 3.1 Introduction

As research exploring the application of nanostructures in biomedical and industrial environments increases, investigations into the formation of these particles also proliferates. These studies focus on a wide range of areas which include scalability, uniformity and transferability from a research to an industrial setting. This wide ranging research has resulted in the development of a variety of routes to forming nanoparticles on a number of scales. As detailed in Section 1.3.3, there are numerous synthetic routes to form nanoparticles of a specific structure. Example of these are thin film hydration for liposomes or more synthetically-focussed routes to materials such as dendrimers *via* convergent or divergent synthesis, however these are more consistently seen in a research laboratory setting.<sup>1,2</sup> Industrial scale formation of nanostructures is most commonly achieved by batch or flow reactors, for instance with the production of carotene nanoparticles for natural colouring and taste modulation for food and drink.<sup>3,4</sup>

Focusing on the research laboratory scale, with the formation of polymeric nanoparticles in particular, there are numerous methods of preparation that have been developed to achieve uniform nanoparticle dispersions.<sup>5</sup> Among these techniques, nanoprecipitation has become prevalent in literature, favoured due to its reproducibility, accessibility and easy variation in the production of polymeric nanoparticles.<sup>6-8</sup>

#### 3.1.1 Nanoparticle preparation *via* nanoprecipitation

First developed in the 1980s when the process was patented, nanoprecipitation of macromolecules, also referred to as solvent displacement, can be defined as the rapid addition of a sole hydrophobic or amphiphilic polymeric species into an aqueous dispersion (Figure 3.1).<sup>9</sup> This triggers the collapse of the polymer chains into nuclei which grow until colloidal stability is reached.<sup>7,8,10,11</sup> This simple facile technique relies on the low energy mixing of two solvents, here referred to as a '*good*' solvent, capable of solubilising polymer components plus any drug molecules, and a '*bad*' solvent, an anti-solvent for both the polymer and guest molecules, commonly water. The addition of a good solvent, containing polymer/drug components, to a bad solvent results in a three step process, detailed below, leading to the formation of nanoparticle dispersions.<sup>7</sup> The creation of nanoparticle dispersions with narrow size distribution and low polydispersity requires that the nucleation and growth steps within the process remain separate, occurring consecutively and not at any point simultaneously.<sup>12-14</sup>

The complexity of the mechanism of nanoprecipitation requires a review of small molecule nanoprecipitation to provide a more comprehensive view of the technique.

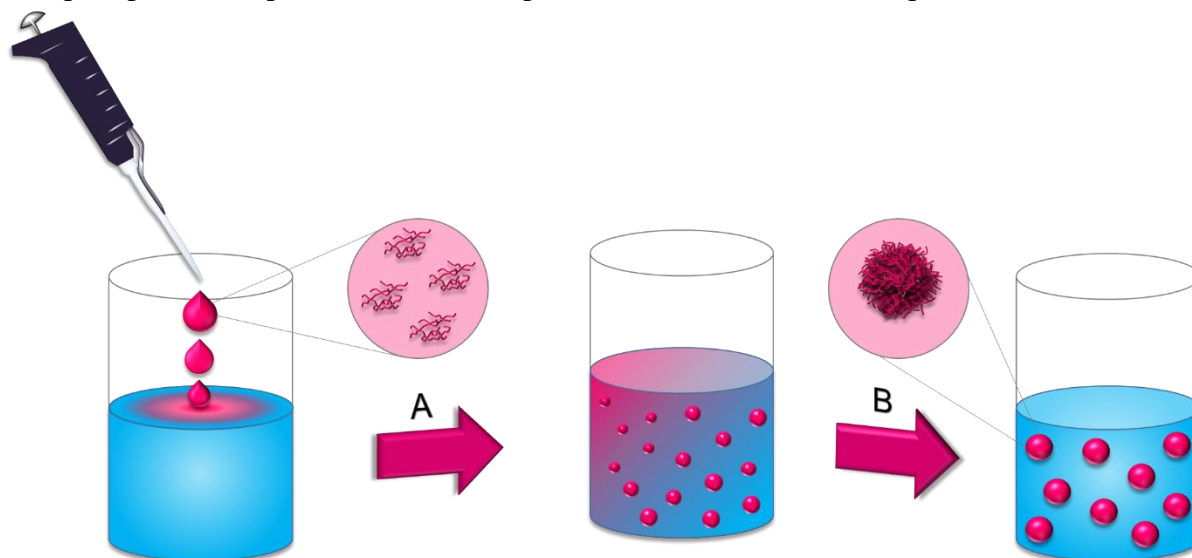


**Figure 3.1 – Representation of the nanoprecipitation of a branched hydrophobic polymer to form polymeric nanoparticles by (A) rapid addition of the miscible organic phase containing the polymeric species and (B) evaporation of the organic phase to yield an aqueous dispersion of nanoparticles.**

### 3.1.1.1 Principles of small molecule nanoparticles prepared *via* nanoprecipitation

Initial nanoprecipitation techniques involved the precipitation of small molecules, such as drug compounds. The first step in this nanoparticle formation, the generation of supersaturation, is achieved upon addition of good solvent to bad solvent decreasing the overall mixed solvent environment's ability to dissolve the solute (drug) (Figure 3.2).<sup>6,7,12</sup> This means that the supersaturation ratio,  $S_r$ , is dependent on the concentration of the solutes within the solvent mixture.  $S_r$  can be defined via Equation 3.1; when solvent exchange occurs by the addition of a good solvent to a large volume of bad solvent, where  $C$  is mass of solute divided by the final solution volume and  $C_\infty$  is the bulk solubility or the equilibrium concentration.<sup>6,7,12</sup>

$$S_r \equiv \frac{C}{C_\infty} \quad \text{Equation 3.1}$$

$$\text{where } C = \frac{\text{Total mass of solute added}}{\text{Final solution volume}}$$

Once the point at which supersaturation and a metastable<sup>§§§§§</sup> dispersion is reached, the need to minimise the energy of the system and gain thermodynamic stability drives nucleation to occur.<sup>8</sup> The concentration at which this arises within the good solvent/solute/bad solvent mixture is commonly defined as the “ouzo effect”, named after the Greek drink, defined as the instantaneous formation of nanoparticles without the need for surfactants.<sup>8,14</sup> The small region in which nucleation can occur, also referred to as the “ouzo domain”, is dependent on both solute concentration and the ratio of good to bad solvent. It is only within this region that uniform particles with narrow particle distributions will be achieved.<sup>14,15</sup>

Following supersaturation the formation of nanoparticles can now be divided into two mechanisms defined by the compounds nanoprecipitated and is dependent on the supersaturation of the solution:

- if supersaturation,  $S_r$ , is low, nucleation and diffusion limited growth is dominant (more likely for small molecules); Nucleation-growth is considered most likely for small molecules where nucleation is most commonly explained by the classic model which states that the onset of supersaturation causes phase separation to reduce the free energy within the system.<sup>6,14</sup> In the case of drug molecules the formation of nuclei is often achieved by crystallisation.<sup>6,7,14</sup> The formation and subsequent growth of these nuclei depletes the solution supersaturation thereby lowering the free energy of the system; the decrease in energy only stops once the supersaturation is below the concentration at which nuclei spontaneously form.<sup>7</sup> Diffusion limited growth, also known as growth *via* condensation, can then take place. This characterises the two step mechanism of the diffusion of solutes to the nuclei surface from the bulk, followed by the integrating the solute molecules to the nuclei matrix.<sup>6,7,14</sup>
- In contrast, supersaturation is high it induces diffusion limited cluster-cluster aggregation, *DLCA* (more likely for polymers) with the collection of smaller particles resulting larger entities, this will be fully addressed in Section 3.1.1.2 .<sup>14,16</sup>

---

<sup>§§§§§</sup> A state in which an energy barrier must be overcome to access a more stable thermodynamic state and is not a reversible process. In the case of nanoparticle formation the nucleation of the solute allows the system to overcome the energy barrier minimising thermodynamic instability.<sup>8,14</sup>

### 3.1.1.2 Principles of polymeric nanoparticles prepared *via* nanoprecipitation

Nanoparticle formation via the nanoprecipitation of polymer is considered to be more complex than small molecules however some principles addressed in Section 3.1.1.1 can be applied such as the formation of a supersaturated solution. First nucleation occurs by the collapse of polymer chains; a strong entropic effect, due to the desolvation of polymers chains by the diffusion of good solvent into the anti-solvent. This is followed by their congregation to form defined nuclei of a critical size (Figure 3.2).

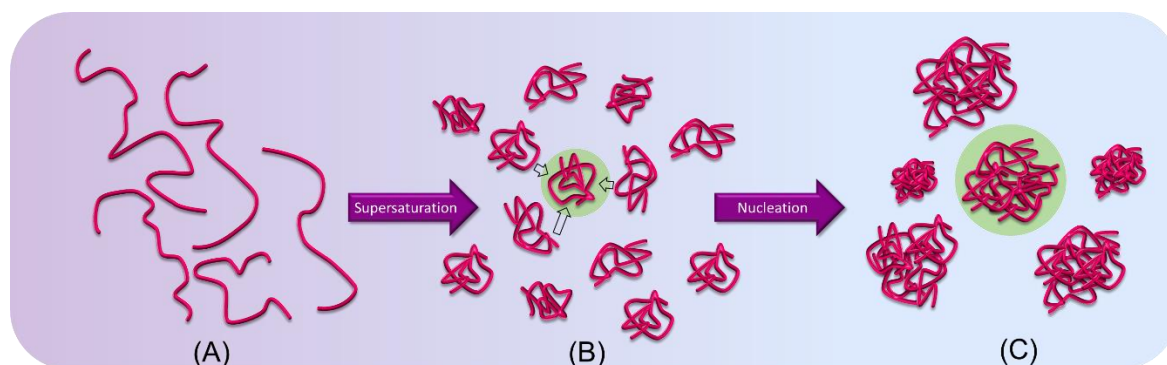


**Figure 3.2 – Representation of creation of supersaturation leading to polymeric nuclei formation during the nanoprecipitation process;** (A) polymer chains dissolved in good solvent, (B) addition to bad solvent creates supersaturation, polymer chains collapse to minimise energy, (C) congregation of polymer chains form nuclei of a critical size depleting supersaturation until nuclei formation stops.

The behaviour of these nuclei can then be defined by DLCA which refers to the aggregation of two particles within the solution which results in the growth of a single larger particle (Figure 3.3). This mechanism relies on a high number of nuclei which causes a high number of collisions between ‘clusters’ and assumes each collision results in the aggregation<sup>\*\*\*\*\*</sup> of the two species involved.<sup>14,16,17</sup> The moment at which the growth phase stops for polymeric nanoparticles is dependent on particles gaining colloidal stability and preventing aggregates forming from excessive growth.

\*\*\*\*\* There is an alternative mechanism and mathematical description for the growth of nanoparticles *via* cluster-cluster aggregation known as reaction limited cluster-cluster aggregation, *RLCA*. In this model clusters only undergo a reaction to permanently join together after a large number of collisions has occurred, taking into account the characteristics of the clusters themselves, for example repulsive forces of alike charged particles.<sup>17,37</sup>

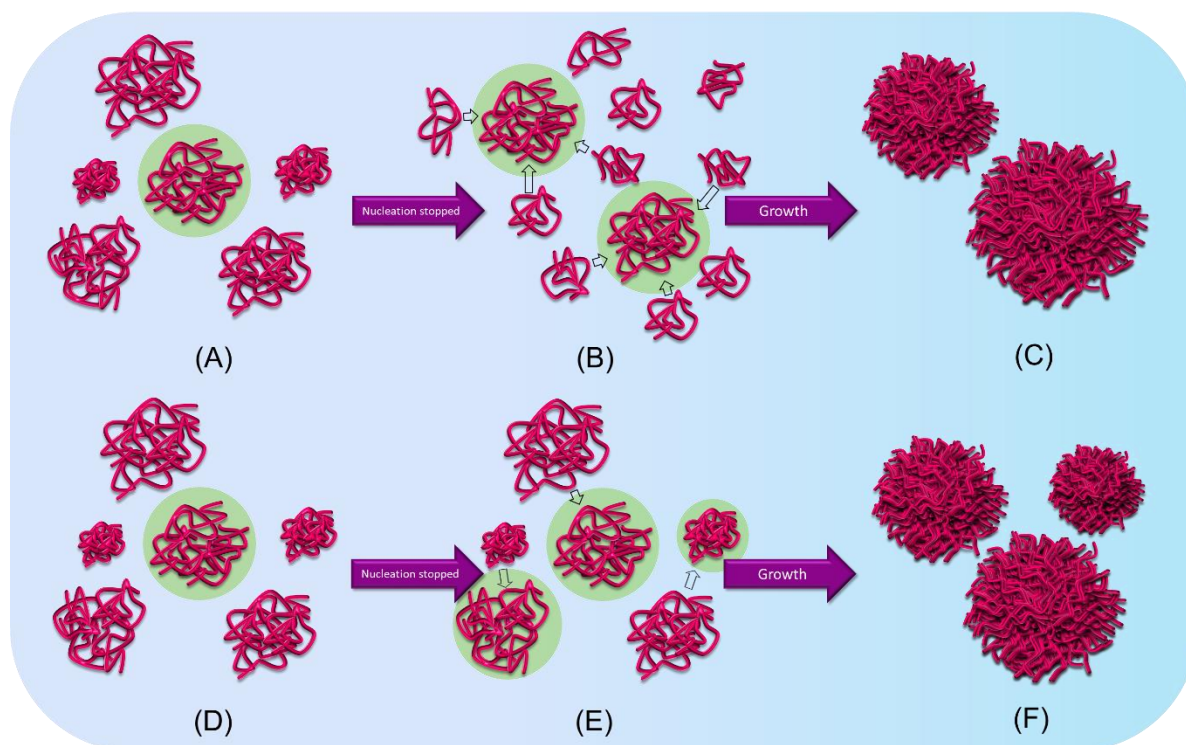


**Figure 3.3 – Representation of the growth mechanisms of nuclei to form nanoparticles, adapted from Lepeltier *et al.*<sup>14</sup>** (A & D) nucleation halted when nuclei reach critical size, (B) diffusion limited growth; solutes diffusing through solution and adsorbing onto the surface of the nuclei, (E) DLCA, aggregation of 2 particles resulting in growth of a single particle, (C & F) growth by both mechanisms resulting in the formation of nanoparticle dispersions.

The mechanism of polymeric nanoparticle formation from nanoprecipitation has been studied further by Rannard and co-workers to gain a more detailed understanding of the roles both polymer species play in the formation of the nanoparticles and the definition of their resulting properties.<sup>18,19</sup> Investigations by Hatton *et al.* showed the inclusion of just 1 wt% highly branched polymeric species with a hydrophobic linear dendritic hybrid during nanoprecipitation reduced the hydrodynamic radius and polydispersity of the particles compared to the nanoprecipitation of a linear dendritic hybrid alone.<sup>18</sup> Further exploration of this phenomenon, by varying the components within the good solvent, increasing amounts of branched polymer, produced a trend of decreasing hydrodynamic radius with increased branched polymer concentration.<sup>18</sup>

The colloidal stability of nanoparticles formed from nanoprecipitation can be split into two groups defined by the nanoparticle components. The nanoprecipitation of a solely hydrophobic polymer into an aqueous phase would rely on electrostatic stabilisation (Figure 3.4, A), explained by the Derjaguin-Landau-Verwey-Overbeek, *DLVO*, theory.<sup>20–23</sup> This theory

describes the colloidal stability of a system to be the result of two opposite forces acting on the nanoparticles; attractive van der Waals forces induced by dipole-dipole moments, and repulsive electrostatic forces induced by an electrostatic double layer that forms around a charged particle.<sup>22-24</sup> The balance of these two forces determines the stability of the colloidal system. When electrostatic repulsion is greater than the attractive van der Waals forces, an energy barrier between flocculation (the reversible joining of two particles) and aggregation (permanent joining of two particles) is generated, resulting in a stable system.<sup>20,24</sup> However this energy barrier is subject to change if the environment in which the particles exist changes, specifically with respect to salt concentration. The addition of charged salt ions into the system results in the masking of the charged double layer around the particles, reducing their surface potential, and in turn the energy barrier, resulting in aggregation and instability.<sup>20</sup>

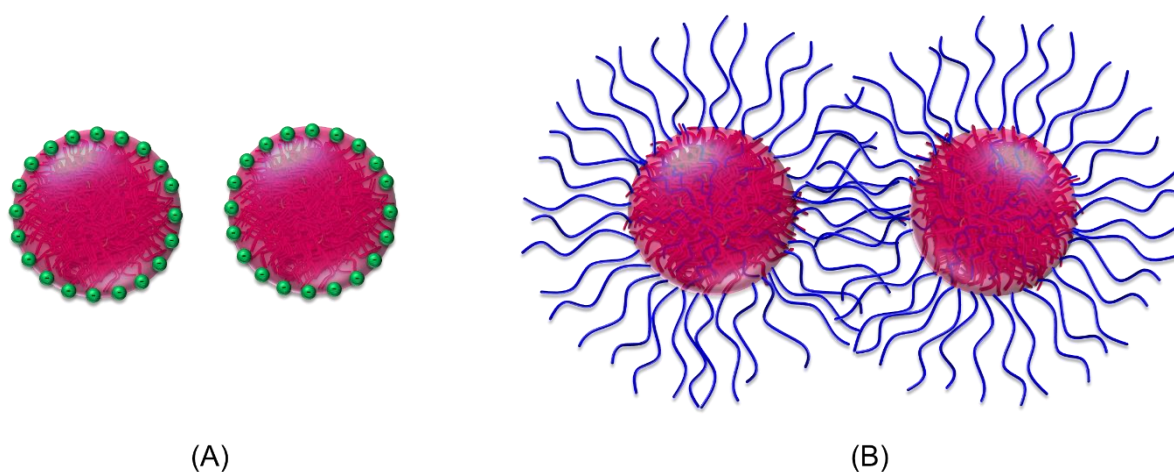


**Figure 3.4 – Representation of the different types of stabilisation induced in polymeric nanoparticle formation.** (A) Electrostatic stabilisation induced by the adsorption of charged species onto the surface of the nanoparticle and (B) steric stabilisation induced by a hydrophilic corona.

Nanoprecipitation of amphiphilic block co-polymers in an aqueous environment avoids the disadvantages seen with respect to electrostatically stabilised colloidal dispersions and their sensitivity to salt by accessing steric stabilisation (Figure 3.4, B). The hydrophilic segments of the polymer chains are able to extend into the solvent creating a corona around each nanoparticle.<sup>21</sup> Nanoparticles within this system are also subject to van der Waals forces which draw the particles together, therefore when two particles approach each other the solvated polymer chains within the corona of each nanoparticle are forced to overlap.<sup>21,24</sup> This overlap induces an excluded volume effect where the solvent molecules are forced out of the space now occupied by interpenetrating polymer chains increasing osmotic pressure and inducing a loss of entropy. Providing the hydrophilic polymer chains are well solvated, long enough and



sufficiently dense in the corona this effect is thermodynamically unfavourable resulting in repulsion and a colloiddally stable dispersion.<sup>21,24</sup>

### 3.1.2 Nanoparticle preparation *via* co-nanoprecipitation

As an adaptation of nanoprecipitation, co-nanoprecipitation (Figure 3.5), follows the same mechanism to form nanoparticles; however, two polymeric species of differing hydrophobicity can be dissolved in the organic, good solvent, phase resulting in particles that possess combined properties.<sup>25</sup> This technique, developed by Ford *et al*, was initially studied with the simultaneous co-nanoprecipitation of branched pHPMA along with PEG-*b*-pHPMA to achieve sterically stabilised nanoparticles.<sup>25</sup> These studies found that, as expected, the linear amphiphilic block co-polymer was incorporated into the branched architecture during the nanoprecipitation process forming monodispersed uniform particles without the need for filtration.<sup>25</sup> This adaptation of nanoprecipitation unlocks the major advantage of tuning the resultant particle properties by simply varying the components and their respective ratios within the good solvent phase. It also unlocked new scope for tackling salt stability issues as well as the creation of nanoparticles with mixed surface functionality.

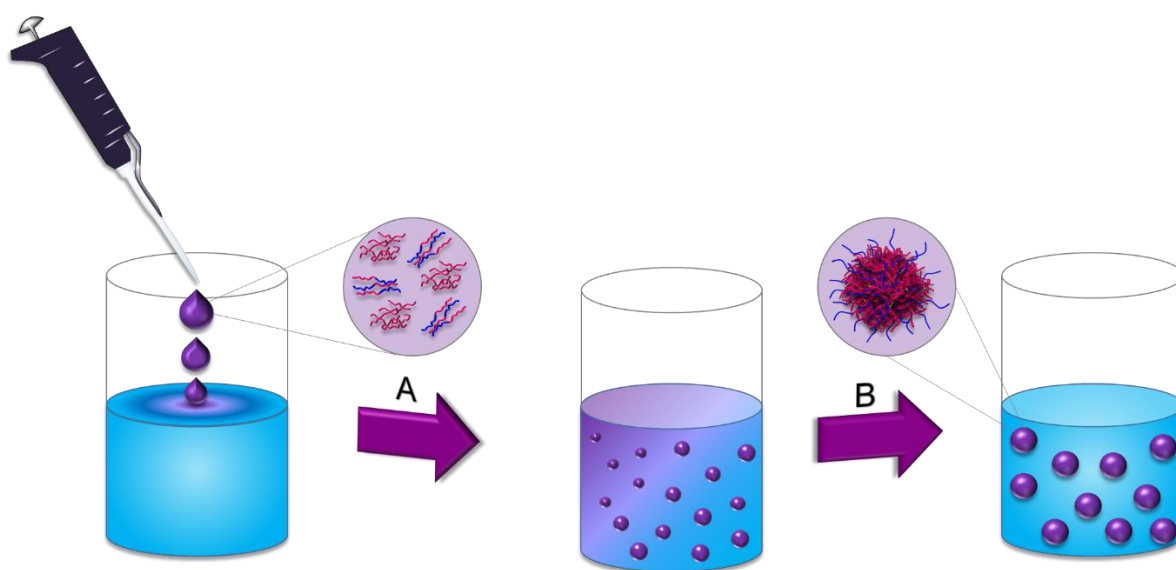


**Figure 3.5 – Representation of the co-nanoprecipitation of a branched hydrophobic polymer with an amphiphilic linear block co-polymer to form polymeric nanoparticles by;** (A) rapid addition of the miscible organic phase containing the polymeric species and (B) evaporation of the organic phase to yield an aqueous dispersion of nanoparticles.

Further studies have been completed within the Rannard group to further understand the co-nanoprecipitation process by employing a library of polymethacrylates and varying the experimental conditions of the technique.<sup>19</sup> In this vast body of research, nanoparticles were



achieved by the co-nanoprecipitation of branched hydrophobic polymers with linear amphiphilic block co-polymers, where entrapment of the hydrophilic block within the particle core and the effects of polymer composition and concentration were studied. Furthermore these particles were subjected to dilution and salt stability studies to further expand understanding in this area.<sup>19</sup> This research also successfully produced nanoparticle dispersions from the co-nanoprecipitation of linear hydrophobic polymers with linear amphiphilic block co-polymers which were previously unexplored. Finally this body of work further explored the successful encapsulation of a number of guest molecules to understand further the capabilities of this technique.<sup>19</sup>

### 3.1.3 Chapter aims

This chapter aims to explore the creation of a library of polyester nanoparticles using the materials synthesised by MSA catalysed ROP, defined in Chapter 2. Building on the work previously undertaken with methacrylate-based polymers, nanoprecipitation and co-nanoprecipitation techniques are intended to be studied in the context of polyesters. It is hypothesised that, as with vinyl polymers, these materials will yield a number of stable nanoparticle dispersions. These would then allow for further study of the stability of the nanoparticles produced by a series of salt studies to explore the suitability of these systems for use within a biological environment.

As detailed in Section 3.1.1 the nanoprecipitation mechanism of nanoparticles can be influenced by the conditions applied. Therefore it is thought that the study of good solvent choice would provide vital insight into the effects this has on the nanoparticle physicochemical properties. Direct comparisons hope to be drawn between acetone and tetrahydrofuran, *THF*, within this body of work. Expansion of (co)nanoprecipitations methods to the library of polymers synthesised using the four bespoke monomers detailed in Chapter 2 is hypothesised to help determine what role the structure of the polymer backbone plays in the physicochemical properties of the resultant nanoparticles. Utilising the advantageous ability to vary polymer components used within co-nanoprecipitation is hoped to highlight any favourable interactions that may be gained from the combinations of the amphiphilic block co-polymer and hydrophobic branched polymers explored.

Finally, initial exploration of the encapsulation abilities of these systems will aim to investigate the ability to incorporate guest molecules and the combining of nanoparticle growth mechanisms. It is hypothesised that the use of two hydrophobic guest molecules, which differ

greatly in molecular structure, will provide the best insight into the effects the presence of an additional molecule has on the co-nanoprecipitation process. Therefore Oil red O and docetaxel are to be utilised in these studies and the effects they have on the physicochemical properties of the resulting nanoparticles, at the time of synthesis and after storage, are to be assessed by dynamic light scattering, *DLS*, characterisation.

## **3.2 (Co)-Nanoprecipitation studies with poly( $\epsilon$ -caprolactone) based polymers**

### **3.2.1 (Co)-Nanoprecipitation studies using an acetone good solvent phase**

Preliminary investigations into the nanoprecipitation of polyesters were exclusively performed with a series of linear and branched PCL polymers (excluding PCL<sub>200</sub> and PCL<sub>200-co-BOD</sub><sub>0.7</sub> due low monomer conversion) and expanded to include A-B block PEG co-polymers at the time of co-nanoprecipitation. This allowed for the conditions of the nanoprecipitation, and subsequent co-nanoprecipitation, of all the polymer species to be determined. Nanoparticle dispersions were prepared by the method and conditions developed by Rannard and co-workers, where the selected polymer was dissolved in a chosen good solvent, either acetone or THF, at an initial concentration of 5 mg mL<sup>-1</sup>, and 1 mL of the resulting solution was rapidly added to deionised water targeting a final concentration 1 mg mL<sup>-1</sup> of polymer in water after good solvent evaporation.<sup>25</sup> The chosen good solvent for this study was initially defined as acetone which had previously been shown to produce well defined nanoparticle dispersions with both polyester and polymethacrylate-based materials.<sup>25,26</sup> Initial studies began with the analysis of the resulting unfiltered dispersions, formed from nanoprecipitation of single species, by DLS enabling the effects of both DP<sub>n</sub> and branched architecture on nanoparticle formation to be deduced (Table 3.1).

**Table 3.1 – DLS characterisation of PCL nanoparticles produced by nanoprecipitation from acetone;**

Sample	Z-Average Diameter (nm)		Number Average Diameter (nm)		PdI		Zeta Potential (mV)		Derived Count Rate (Attenuator)	
	Day 1	Day 7	Day 1	Day 7	Day 1	Day 7	Day 1	Day 7	Day 1	Day 7
PCL <sub>10</sub>					<i>Unstable</i>					
PCL <sub>20</sub>	85	85	55	55	0.110	0.120	-50	-55	255270 (5)	235595 (5)
PCL <sub>30</sub>	100	105	70	70	0.110	0.105	-55	-55	333035 (4)	328735 (5)
PCL <sub>40</sub>	100	100	70	65	0.110	0.115	-55	-45	331440 (4)	327555 (5)
PCL <sub>50</sub>	90	90	60	60	0.090	0.090	-60	-50	257215 (5)	247865 (5)
PCL <sub>60</sub>	95	95 <sup>a</sup>	65	70 <sup>a</sup>	0.090	0.085 <sup>a</sup>	-55	-50	318470 (5)	179085 (6) <sup>a</sup>
PCL <sub>80</sub>	75	85 <sup>a</sup>	50	45 <sup>a</sup>	0.095	0.200 <sup>a</sup>	-40	-60	136440 (6)	60305 (6) <sup>a</sup>
PCL <sub>100</sub>	75	80	50	45	0.115	0.190	-70	-55	114970 (6)	61855 (6)
PCL <sub>40-co-BOD</sub> <sub>0.7</sub>	75	80	50	50	0.105	0.115	-55	-55	129880 (6)	115345 (6)
PCL <sub>40-co-BOD</sub> <sub>0.6</sub>	85	85	60	55	0.090	0.105	-50	-60	218735 (5)	188010 (5)
PCL <sub>60-co-BOD</sub> <sub>0.7</sub>	75	70	50	45	0.110	0.130	-55	-55	90475 (6)	88745 (6)
PCL <sub>80-co-BOD</sub> <sub>0.7</sub>	70	70	45	45	0.130	0.115	-60	-50	82555 (6)	100590 (6)
PCL <sub>100-co-BOD</sub> <sub>0.7</sub>	70	75	50	45	0.095	0.120	-45	-50	103420 (6)	100885 (6)
PEG <sub>2K-b</sub> -PCL <sub>40</sub>	25 <sup>a</sup>	35 <sup>a</sup>	10 <sup>a</sup>	15 <sup>a</sup>	0.540 <sup>a</sup>	0.645 <sup>a</sup>	-30	-25	2585 (9) <sup>a</sup>	2585 (9) <sup>a</sup>
PEG <sub>5K-b</sub> -PCL <sub>40</sub>	25 <sup>a</sup>	35 <sup>a</sup>	15 <sup>a</sup>	15 <sup>a</sup>	0.285 <sup>a</sup>	0.510 <sup>a</sup>	-25	-25	1145 (9) <sup>a</sup>	1145 (9) <sup>a</sup>

<sup>a</sup> Multimodal distributions obtained for this measurement

DLS analysis established that particles were formed in all cases, apart from PCL<sub>10</sub>, with Z-average diameters,  $D_z$ , ranging from 75 nm to 100 nm for linear polymers and 70 nm to 85 nm for branched PCL (Table 3.1). The polydispersity index,  $PdI$ , of all the samples were below 0.2, this could be considered high, particularly when compared to polymethacrylates producing nanoparticle with  $PdI$  of 0.09 and above.<sup>25</sup> There was no evident correlation between the polymer architecture and  $PdI$  values which were comparable for samples where  $DP_n$  of the primary polymer chain was below 80 monomer units. On the other hand, there appeared to be a limit to chain length when acetone was used as a good solvent with PCL<sub>10</sub> being incapable of forming stable nanoparticles.

The decreased  $D_z$  of the particles formed from PCL<sub>x</sub>-co-BOD<sub>y</sub> correlated with studies carried out by Hatton *et al.* investigating the effects of high molecular weight branched material on the characteristics of the resulting nanoparticles.<sup>18</sup> This research indicated that the nanoprecipitation of a unimolecular species, containing a number of chains linked together, resulted in a well-defined nucleation-growth mechanism achieved by fast nucleation. As a consequence of many primary polymer chains linked together, larger nuclei which exceed the critical radius for nanoparticle formation, form faster leading to more monodisperse and smaller particles.<sup>18</sup> This is supported by the mechanistic principles of nanoprecipitation, that separate well-defined nucleation and growth phases results in more uniform dispersions.<sup>12-14</sup>

Precipitation of the amphiphilic block co-polymers alone also produced successful nanoparticle dispersions although the diameter of these particles potentially indicated a micelle-like structure. This would be expected due to PEG co-polymers typically being used for the creation of micelle structures.<sup>27</sup> The contrast between the PEGylated nanoparticles and hydrophobic PCL particles demonstrates the stability mechanisms involved in each system. It is clear that when PEG polymer segments are absent, electrostatic stability is the sole mechanism of stability as the zeta potentials are between -40 and -70 mV. Furthermore studies have shown that electrostatic stabilisation has characteristic zeta potentials of  $\pm 30$  mV and greater.<sup>20,21,24</sup>

The generation of negative zeta potentials at the slipping plane between water and nanoparticles, specifically hydrophobic in nature, is still not fully understood with a number of theories being submitted as to the cause. The two most utilised theories only consider the presence of hydroxide and hydronium ions within the aqueous phase therefore assuming that no other ions take part in the creation of a negatively charged interphase.<sup>28-30</sup> The first theory of this kind hypothesises that hydroxide ions within the aqueous phase absorb onto the

hydrophobic surface and thus creates the negative zeta potential characteristically seen with hydrophobic nanoparticles.<sup>29,30</sup> The alternative school of thought postulates that the interface between water and a hydrophobic surface is protonated generating hydronium ions. This causes water molecules to self-rearrange to accommodate these physio-adsorbed hydronium ions generating a negative zeta potential. More recently, a third hypothesis has been put forward which considers the presence of other ions within the aqueous phase for example sodium and chloride ions, but in particular carbon dioxide and subsequent bicarbonate ions present due to carbonation of water.<sup>28,31</sup> Investigations into this proposition firstly confirmed that bicarbonate ions were very good candidates for interacting with surfaces. Subsequently it was confirmed that bicarbonate ions have a large tendency to adsorb onto hydrophobic surfaces, particularly in the case of polymers.<sup>28</sup> The extension of this study to a range of pH values highlighted that bicarbonate ions have a lack of competition with other ions when adsorbing to the hydrophobic surface at neutral pH values between 6 and 9.<sup>28</sup> Additionally, as highlighted in Chapter 2 a number of carboxylic acid groups were formed during MSA catalysed ROP which would also contribute to the negative zeta potentials of nanoparticles formed from polymers synthesised in Chapter 2.

The presence of PEG chains saw a reduction in the zeta potential to  $\leq -30$  mV with the extension of the PEG chain length from 2000 to 5000 g mol<sup>-1</sup> resulting in a 5 mV decrease in the zeta potential as measured one day after formation. The reduction of the zeta potential of these particles is most likely due to the prevention of ion adsorption on the hydrophobic interface between the core and corona of the particle due to the steric hindrance of the hydrophilic PEG chain. Additionally the presence of these hydrophilic chains in the corona of the nanoparticles allows for the shielding of charge simultaneously as steric stability is imparted on the colloidal dispersion.<sup>21,24</sup> Furthermore the presence of the PEG corona on in the nanoparticle structure and the decreased zeta potential is thought to prevent the aggregation of the particles with salt addition seen with electrostatically charged nanoparticles.<sup>20,24</sup>

The benefit of both mechanisms of stability were explored by additional DLS analysis 7 days after initial synthesis with most of the systems synthesised producing results that are comparable between day 1 and day 7. Furthermore, the advantages of the branched architecture on the stability of the nanoparticle dispersion over time was also demonstrated with some linear PCL based nanoparticles failing to generate monomodal distributions.

Taking into consideration the results generated in Table 3.1 and studies performed by Hatton *et al.*, further exploration of nanoparticle formation was undertaken by co-nanoprecipitation of PCL<sub>40-co</sub>-BOD<sub>0.7</sub> with the amphiphilic A-B block co-polymers to achieve nanoparticles of reasonable size and stability.<sup>18</sup> Sterically stabilised particles were achieved by implementing the co-nanoprecipitation method developed by Ford *et al.* in which amphiphilic di-block co-polymers were included at various ratios within the organic phase containing PCL<sub>40-co</sub>-BOD<sub>0.7</sub> and then added to deionised water. The ratio of stabilising PEG<sub>x</sub>-*b*-PCL<sub>40</sub> to PCL<sub>40-co</sub>-BOD<sub>0.7</sub> was varied from 0 to 100 wt% for both PEG<sub>2K</sub>-*b*-PCL<sub>40</sub> and PEG<sub>5K</sub>-*b*-PCL<sub>40</sub> block co-polymers whilst maintaining a total polymer concentration of 5 mg mL<sup>-1</sup> in acetone and subsequently a final nanoparticle dispersion concentration of 1 mg mL<sup>-1</sup> in the aqueous phase once the co-nanoprecipitation process was complete. Stable nanoparticle dispersions were achieved in all cases with no significant differences observed in overall hydrodynamic radii or stability at corresponding ratios when using increased PEG chain lengths (Figure 3.6). The only meaningful difference between samples prepared with different amphiphilic PEG<sub>x</sub>-*b*-PCL<sub>40</sub> co-polymers that was observed was a small increase in zeta potential to less negative values when PEG<sub>5K</sub>-*b*-PCL<sub>40</sub> was utilised (Figure 3.6, C). Stability over 7 days was also observed throughout the series of nanoparticles with no significant trend witnessed over all ratios and between the two PEG<sub>x</sub>-*b*-PCL<sub>40</sub> polymers used.

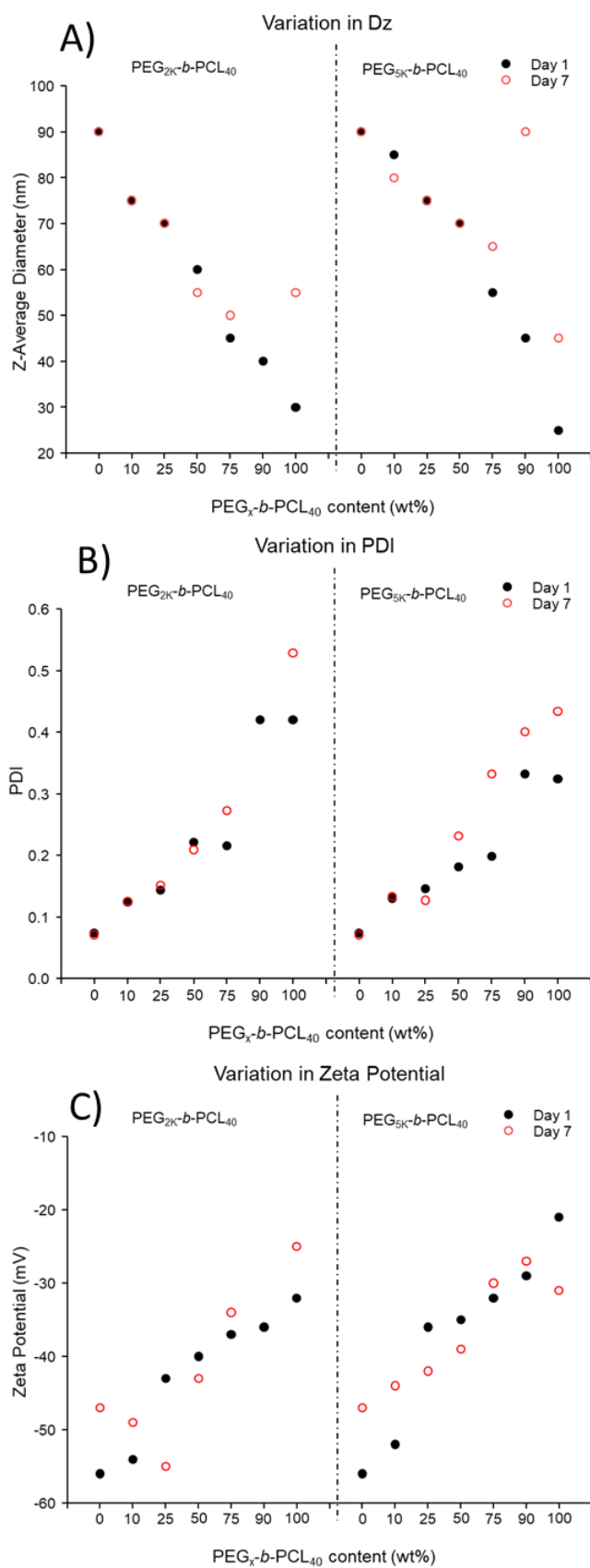


**Figure 3.6 – Graphical representation of changes in physicochemical characteristics of nanoparticles produced by co-nanoprecipitation with increasing PEG<sub>x</sub>-b-PCL<sub>40</sub> content (acetone) (A) Z-average diameter, (B) PDI and (C) zeta potential.**

The most significant trend was seen with the sequential increase in PEG<sub>x</sub>-*b*-PCL<sub>40</sub> content, irrespective of whether PEG<sub>2K</sub>-*b*-PCL<sub>40</sub> or PEG<sub>5K</sub>-*b*-PCL<sub>40</sub> was used to stabilise PCL<sub>40</sub>-*co*-BOD<sub>0.7</sub>. Firstly, considering the  $D_z$  of the particles, a decrease from 75 nm and 85 nm to 30 nm and 25 nm was observed for PEG<sub>2K</sub>-*b*-PCL<sub>40</sub> and PEG<sub>5K</sub>-*b*-PCL<sub>40</sub>, respectively, with increasing PEG<sub>x</sub>-*b*-PCL<sub>40</sub> content (Figure 3.6, A). This was to be expected due to the decreasing concentration of the hydrophobic branched PCL<sub>40</sub>-*co*-BOD<sub>0.7</sub> core-forming polymer within the nanoprecipitation mixture effectively increasing the concentration of amphiphilic stabilising block co-polymer and allowing a larger surface area (therefore, smaller particles) to be stabilised (Figure 3.7). Additionally  $D_z$  in all cases was equal to or below that of nanoprecipitated PCL<sub>40</sub>-*co*-BOD<sub>0.7</sub> further correlating with results observed by Hatton *et al.*<sup>18</sup>

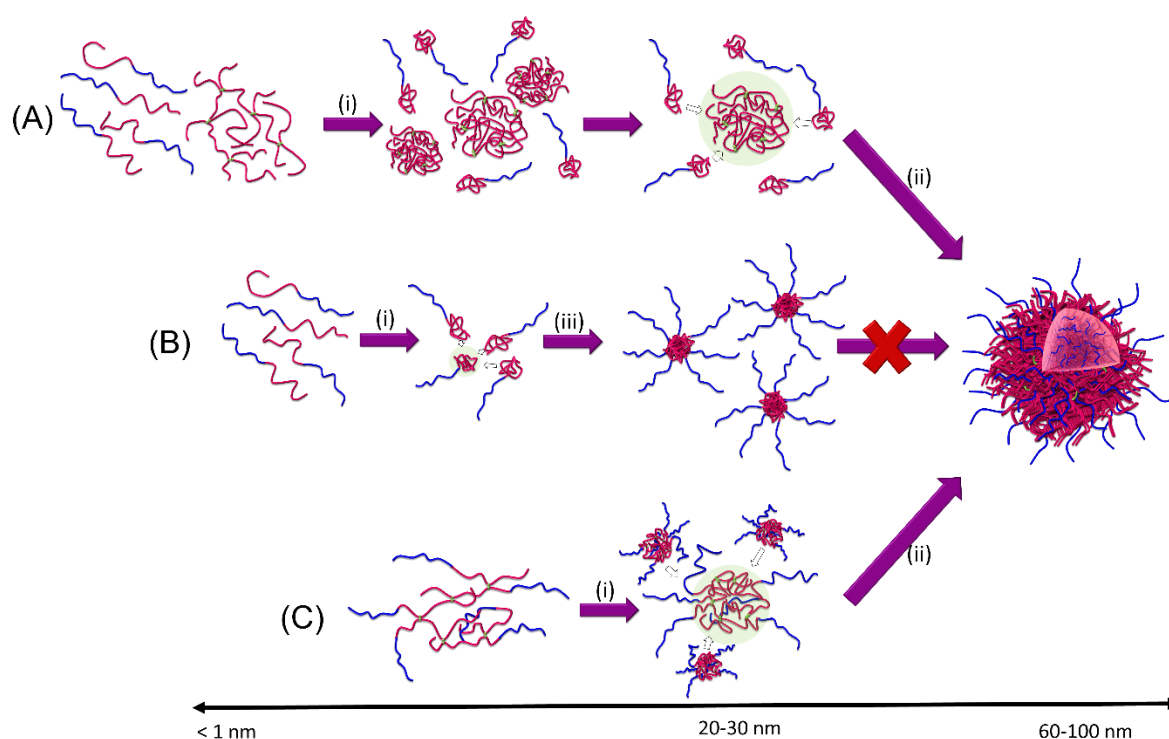


**Figure 3.7 – Schematic representation of the nucleation-growth mechanisms, during the (co)-nanoprecipitation process; dependant on varying polymer architecture; (A) co-nanoprecipitation of a hydrophobic branched polymer with an amphiphilic A-B block co-polymer resulting in sterically stabilised nanoparticles (with (i) nucleation and (ii) rapid growth), (B) nanoprecipitation of amphiphilic A-B block co-polymers resulting in the formation of micelle-like nanoparticles (with (i) nucleation and (iii) slow growth) and (C) nanoprecipitation of a amphiphilic branched A-B block copolyester resulting in similar behaviour described in (A) (with (i) nucleation and (ii) rapid growth) producing larger particles typically with within the range of > 60 nm.**



PdI increased with increasing PEG<sub>x</sub>-*b*-PCL<sub>40</sub> content, a phenomenon seen in previous work undertaken with pHPMA (Figure 3.6, B).<sup>25</sup> This may be attributed to the increasing concentration of amphiphilic block co-polymer diminishing the influence the branched architecture has on the fast nucleation step, and therefore limiting controlled nanoparticle formation. This was reflected by the lack of monomodal intensity-derived particle distributions when the percentage of PEG<sub>x</sub>-*b*-PCL<sub>40</sub> was  $\geq 75$  wt%. These distributions replicated those seen for 100 % PEG<sub>2K</sub>-*b*-PCL<sub>40</sub> and PEG<sub>5K</sub>-*b*-PCL<sub>40</sub> indicating successful incorporation of PEG<sub>x</sub>-*b*-PCL<sub>40</sub> in these systems. This could be a result of the size of these nanoparticles being on the limit of the DLS range.

Finally, studying the zeta potentials generated by each dispersion, increasing PEG<sub>x</sub>-*b*-PCL<sub>40</sub> content resulted in less negative zeta potentials confirming a shift towards more neutral particles and a predominant steric stabilisation as PEG<sub>x</sub>-*b*-PCL<sub>40</sub> content increased. This was also expected as dense PEG-derived coronas can be formed, shielding the surface charges and, leading to a lower measured zeta potential (Figure 3.8).<sup>28-30</sup> However, particles with  $\leq 50$  wt% PEG<sub>x</sub>-*b*-PCL<sub>40</sub> could still be characterised as electrostatically stabilised with zeta potentials below -35 mV suggesting that the PEG corona is not dense enough to shield the surface and a mixed stabilisation mechanism may be operating (Figure 3.8).<sup>20,21,24</sup>

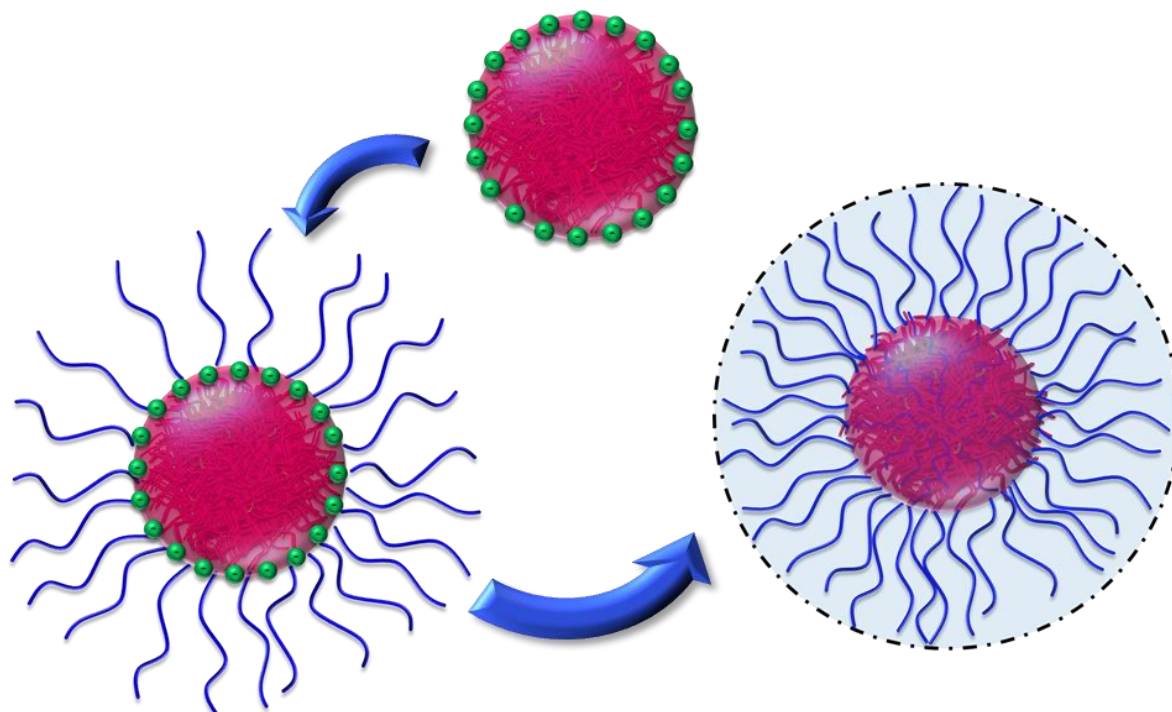


**Figure 3.8 – Increasing PEG<sub>x</sub>-*b*-PCL<sub>40</sub> content resulting in a shift from electrostatic stabilisation to steric stabilisation;** (top) electrostatic stabilisation, (left) combined steric and electrostatic stabilisation and (right) steric stabilisation.

### 3.2.1.1 Salt stability studies

The extent of steric stabilisation imparted on each nanoparticle dispersion, with increasing concentrations of PEG<sub>x</sub>-*b*-PCL<sub>40</sub>, and the variation in length of the PEG block, was evaluated through the addition of salt solution utilising the two methods outlined by Ford *et al.*<sup>25</sup> A study of salt stability, following the change in particle characteristics over seven days after a single 20 µL addition of 0.5 M NaCl<sub>(aq)</sub> to 1 mL of each nanoparticle dispersion was undertaken (Table 3.2, Figure 3.9). Firstly, considering the overall stability and amount of change to physicochemical properties in both the PEG<sub>2K</sub>-*b*-PCL<sub>40</sub> and PEG<sub>5K</sub>-*b*-PCL<sub>40</sub> stabilised systems, PEG<sub>5K</sub>-*b*-PCL<sub>40</sub> stabilised nanoparticles showed an increased resistance to salt addition. This was demonstrated by the smaller change in values for both  $D_z$  and PdI over the seven day period. Nonetheless there was a general increase in  $D_z$  values one day after addition suggesting that particles were beginning to aggregate.

The clearest trend was observed by the change in zeta potential of each system over time where it is also important to note the behaviour of 100 wt% PCL<sub>40</sub>-*co*-BOD<sub>0.7</sub> particles which showed an increase in the negativity of the particles (Table 3.2). It could be postulated that this is a result of bicarbonate and chloride ions being similar in their propensity to adsorb to a hydrophobic surface<sup>+++++</sup> which could increase the amount of charge available.<sup>28</sup> In systems where PEG<sub>2K</sub>-*b*-PCL<sub>40</sub> and PEG<sub>5K</sub>-*b*-PCL<sub>40</sub> were present, zeta potential reduced by approximately 50 % over the seven day period. This indicates a reduction in the finite barrier and repulsive electrostatic forces preventing aggregation, effectively increasing the influence of the attractive van der Waals forces and decreasing the distance between particles.<sup>20</sup> This reduction of electrostatic stabilisation most likely due to the shielding of charge by salt ions; also known as ‘salting-out’, leaves each system to rely solely on the steric stabilisation imparted on the nanoparticles by PEG<sub>2K</sub>-*b*-PCL<sub>40</sub> and PEG<sub>5K</sub>-*b*-PCL<sub>40</sub>. The small change in PdI and size over the series of nanoparticles stabilised by PEG<sub>5K</sub>-*b*-PCL<sub>40</sub> highlights the advantage of a longer PEG chain in the corona and its role in the stabilisation of the nanoparticles.

---

<sup>+++++</sup> This is determined by the examination of the polarizability and hydrophobicity of each ion by viscosity measurements and NMR analyses, as detailed by Yan *et al.* Bicarbonate and chloride ions are soft ions and therefore are more likely to interact with hydrophobic interfaces.<sup>28</sup>

**Table 3.2 – DLS characterisation of nanoparticles produced by (co)-nanoprecipitation with addition of 0.5 M NaCl<sub>(aq)</sub> (20 μL);**

Sample	Multiple 20 μL additions of 0.5 M NaCl <sub>(aq)</sub> Volume of salt added until aggregation (μL) <sup>b</sup>	Single 20 μL addition of 0.5 M NaCl <sub>(aq)</sub>											
		Z-Average Diameter (nm) <sup>c</sup>				PDI <sup>c</sup>				Zeta Potential (mV) <sup>c</sup>			
		No Salt	Instant	1 Day	7 Days	No Salt	Instant	1 Day	7 Days	No Salt	Instant	1 Day	7 Days
Ratio of PEG <sub>2K</sub> - <i>b</i> -PCL <sub>40</sub> : PCL <sub>40</sub> - <i>co</i> -BOD <sub>0.7</sub>													
0:100	140	90	85	95	90	0.074	0.084	0.124	0.123	-56	-45	-74	-92
10:90	20	75	75	75	80	0.124	0.118	0.120	0.111	-54	-27	-30	-27
25:75	20	70	70	70	70	0.143	0.112	0.151	0.121	-43	-21	-23	-25
50:50	20	60	55	60 <sup>a</sup>	60 <sup>a</sup>	0.221	0.173	0.245 <sup>a</sup>	0.199 <sup>a</sup>	-40	-17	-13	-12
75:25	40	45	55 <sup>a</sup>	55 <sup>a</sup>	50 <sup>a</sup>	0.215	0.292 <sup>a</sup>	0.338 <sup>a</sup>	0.231 <sup>a</sup>	-37	-15	-13	-14
90:10	140	40 <sup>a</sup>	45 <sup>a</sup>	50 <sup>a</sup>	55 <sup>a</sup>	0.420 <sup>a</sup>	0.361 <sup>a</sup>	0.463 <sup>a</sup>	0.593 <sup>a</sup>	-36	-10	-10	-21
100:0	>2000	30 <sup>a</sup>	47 <sup>a</sup>	65 <sup>a</sup>	60 <sup>a</sup>	0.420 <sup>a</sup>	0.537 <sup>a</sup>	0.658 <sup>a</sup>	0.677 <sup>a</sup>	-32	-7	-11	-10
Ratio of PEG <sub>5K</sub> - <i>b</i> -PCL <sub>40</sub> : PCL <sub>40</sub> - <i>co</i> -BOD <sub>0.7</sub>													
0:100	140	90	85	95	90	0.074	0.084	0.124	0.123	-56	-45	-74	-92
10:90	20	85	80	80	80	0.130	0.122	0.128	0.124	-52	-25	-19	-11
25:75	20	75	75	75	75	0.146	0.117	0.144	0.164	-36	-14	-12	-7
50:50	40	70	65	75	70 <sup>a</sup>	0.181	0.145	0.217	0.207 <sup>a</sup>	-35	-6	-5	-6
75:25	100	55	60 <sup>a</sup>	55 <sup>a</sup>	60 <sup>a</sup>	0.198	0.219 <sup>a</sup>	0.196 <sup>a</sup>	0.227 <sup>a</sup>	-32	-8	-6	-7
90:10	>2000	45 <sup>a</sup>	50 <sup>a</sup>	50 <sup>a</sup>	50 <sup>a</sup>	0.332 <sup>a</sup>	0.272 <sup>a</sup>	0.302 <sup>a</sup>	0.292 <sup>a</sup>	-29	-8	-5	-5
100:0	>2000	25 <sup>a</sup>	40 <sup>a</sup>	45 <sup>a</sup>	50 <sup>a</sup>	0.324 <sup>a</sup>	0.324 <sup>a</sup>	0.483 <sup>a</sup>	0.506 <sup>a</sup>	-21	-5	-8	-4

*a* Multimodal distributions obtained for this measurement, *b* volume of 0.5 M NaCl<sub>(aq)</sub> added until visible precipitation was observed, *c* DLS characterisation gained after a single 20 μL addition of 0.5 M NaCl<sub>(aq)</sub> to the aqueous dispersion.

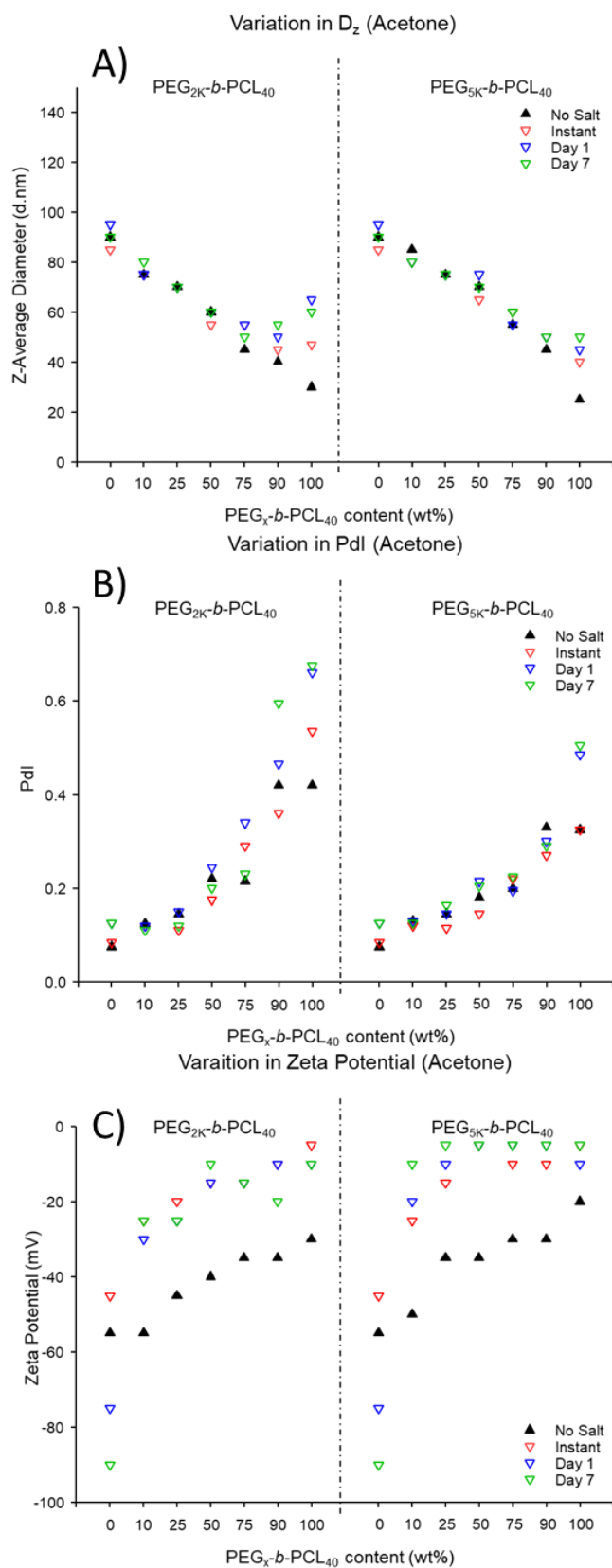


**Figure 3.9 – Graphical representation of changes in physicochemical characteristics with single 20  $\mu$ L addition of 0.5 M NaCl<sub>(aq)</sub> to 1 ML of each nanoparticle dispersion with increasing PEG<sub>x</sub>-b-PCL<sub>40</sub> content (acetone) (A) Z-average diameter, (B) Pdl and (C) zeta potential.**

Further exploration of the stability of the nanoparticles dispersions was conducted with the addition of 0.5 M NaCl<sub>(aq.)</sub> solution in aliquots (20  $\mu$ L) to 1 mL of each aqueous dispersion until visual precipitation occurred (Table 3.2). It was found that with increasing PEG<sub>x</sub>-*b*-PCL<sub>40</sub> content there was increased stability of the nanoparticles to salt addition. Interestingly when salt was added to the dispersion of 100 wt% PCL<sub>40</sub>-*co*-BOD<sub>0.7</sub> the nanoparticles displayed tolerance up to 140  $\mu$ L 0.5 M NaCl<sub>(aq.)</sub>. This resistance to salt combined with the large zeta potential value of -56 mV indicates the energy barrier between flocculation and aggregation, defined by DLVO theory, was greater within this system when compared to the systems containing PEG<sub>x</sub>-*b*-PCL<sub>40</sub>.<sup>20</sup> It is also important to note that there was a slight increase in stability with those particles that had PEG<sub>5K</sub>-*b*-PCL<sub>40</sub> present which was to be expected due to the longer hydrophilic block.

### **3.2.2 (Co)-Nanoprecipitation studies of PCL polymers using a THF good solvent phase**

The solvent used within the nanoprecipitation process can have an effect on the physicochemical properties of the nanoparticles formed. To explore this phenomenon the study detailed in Section 3.2.1 was repeated with THF acting as the good solvent, replacing acetone. The same series of polymers was utilised to allow for direct comparison of the data produced by both THF and acetone. Other parameters such as concentration of the polymer in the good solvent and final polymer concentration in water after solvent evaporation were fixed at 5 mg mL<sup>-1</sup> and 1 mg mL<sup>-1</sup>, respectively. As seen in Section 3.2.1, initial studies began with the synthesis of nanoparticles by nanoprecipitation of single species to assess stability and the physicochemical properties of the particles produced and the unfiltered samples were analysed by DLS (Table 3.3).

**Table 3.3 – DLS characterisation of PCL nanoparticles produce by nanoprecipitation from THF;**

Sample	Ratio (%)	Z-Average Diameter (nm)		Number Average Diameter (nm)		PDI		Zeta Potential (mV)		Derived Count Rate (Attenuator)	
		Day 1	Day 7	Day 1	Day 7	Day 1	Day 7	Day 1	Day 7	Day 1	Day 7
PCL <sub>10</sub>	100	540	530	365	370	0.410	0.360	-35	-40	36575 (6)	36410 (6)
PCL <sub>20</sub>	100	125	125	75	75	0.140	0.155	-55	-55	462355 (4)	472840 (4)
PCL <sub>30</sub>	100	140	140	95	90	0.135	0.155	-55	-60	438790 (4)	457700 (4)
PCL <sub>40</sub>	100	145	145	90	90	0.150	0.160	-55	-60	404735 (4)	420750 (4)
PCL <sub>50</sub>	100	115	115	70	70	0.135	0.135	-50	-60	417525 (4)	409140 (4)
PCL <sub>60</sub>	100	105	105	65	65	0.130	0.145	-55	-60	357560 (4)	382500 (4)
PCL <sub>80</sub>	100	100	95	55	50	0.150	0.155	-60	-65	326555 (5)	305080 (5)
PCL <sub>100</sub>	100	120	120	75	75	0.125	0.135	-60	-60	456435 (4)	480580 (4)
PCL <sub>40-co-BOD</sub> <sub>0.7</sub>	100	100	100	65	65	0.115	0.110	-50	-55	382840 (4)	344320 (4)
PCL <sub>40-co-BOD</sub> <sub>0.6</sub>	100	105	105	65	70	0.130	0.115	-55	-55	427705 (4)	447255 (4)
PCL <sub>60-co-BOD</sub> <sub>0.7</sub>	100	140	135	100	95	0.085	0.115	-50	-55	654825 (4)	650540 (4)
PCL <sub>80-co-BOD</sub> <sub>0.7</sub>	100	95	95	60	60	0.105	0.110	-55	-50	342630 (5)	329440 (4)
PCL <sub>100-co-BOD</sub> <sub>0.7</sub>	100	95	90	60	60	0.115	0.120	-50	-55	336960 (5)	331670 (5)

Upon initial observation the clearest difference seen when alternating the solvent used was the increase in both  $D_z$  and PDI of the nanoparticles nanoprecipitated from THF compared to acetone (Figure 3.10). This behaviour correlates with similar studies conducted with PEG-*b*-PCL and pHPMA, in which both types of polymers produced larger and less monodisperse samples with THF.<sup>25,26,32</sup> This phenomenon is largely the result of solvent/water interactions, solvent/polymer interactions, diffusion of the solvent and polymer and viscosity of the organic phase. A number of researchers have explored this area and the effects of solvent choice on the characteristics of the resultant nanoparticles; the consensus of these studies indicate that THF generally leads to larger particles than acetone.<sup>26,32</sup> Comparison between the nanoparticles produced from the organic solvents acetone and THF within this study indicates that viscosity of the organic phase should not vary significantly due to the concentration of polymer in solvent remaining constant.<sup>32,33</sup> Organic solvent/polymer interactions also play a role, however, in-depth analysis of the interactions with polymers is somewhat lacking.<sup>33</sup> The general consensus regarding this particular interaction is that higher solvent/polymer affinity results in reduced diffusion of the organic solvent into the water phase, and a shorter timescale for the creation of supersaturated polymer conditions due to the proportion of bound solvent.<sup>8</sup> As a result of this the nanoparticles generated using a solvent with higher solvent/polymer interactions will result in smaller nanoparticles which could suggest a stronger interaction between acetone and PCL than THF/PCL.<sup>8</sup>

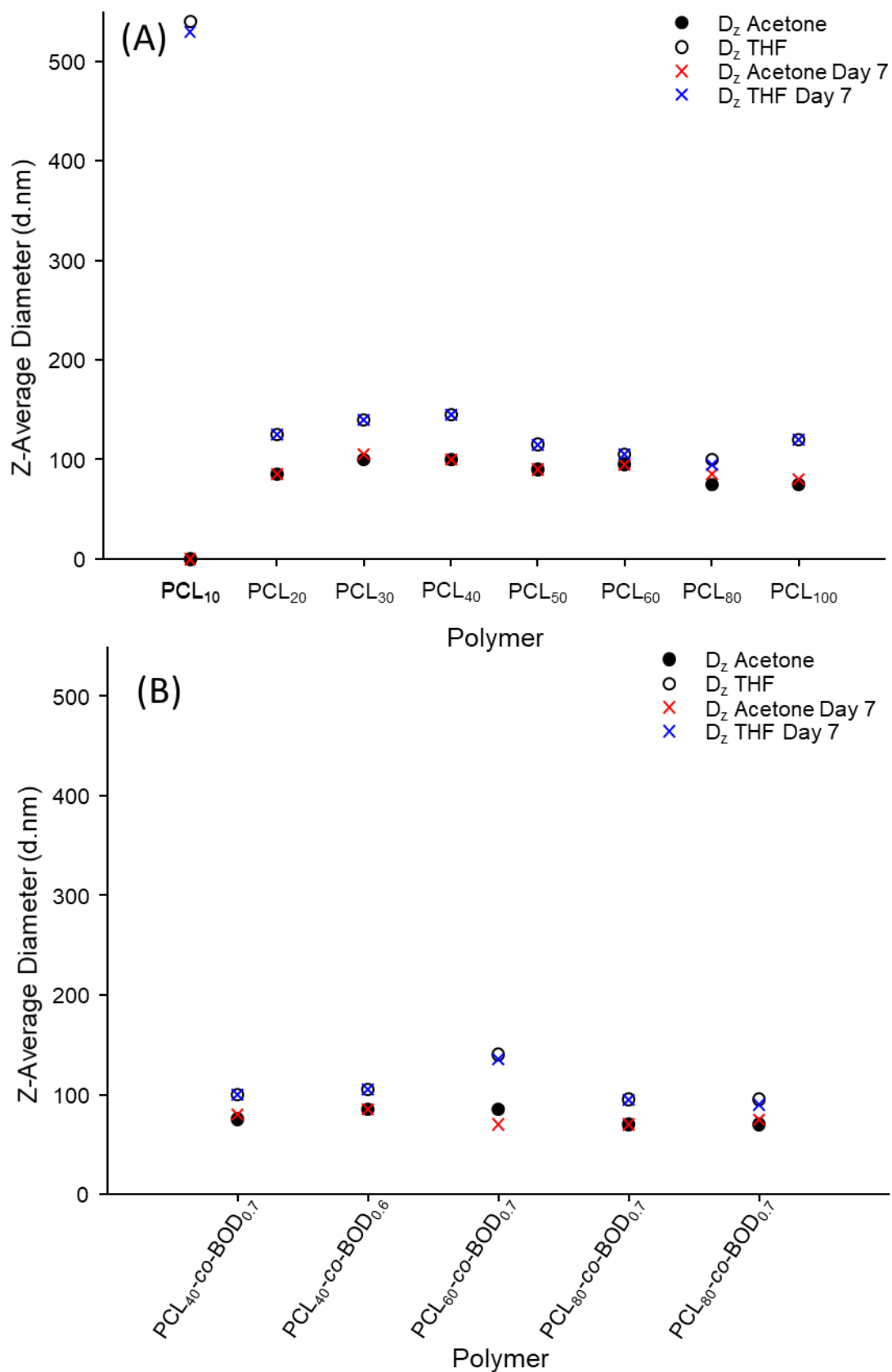


**Figure 3.10 – Graphical representation of changes in physicochemical characteristics with different solvents on day 1 and day 7 of nanoparticle synthesis; (A) linear PCL and (B) branched PCL.**



The role of solvent/water interactions has been most significantly cited within literature and an in-depth analysis of the solvent/water interactions has been performed by Galindo-Rodriguez *et al.* highlighting the definite dependence of nanoparticle size on the solvent nature.<sup>33</sup> Initial calculations were performed to determine the difference in solubility parameter,  $\Delta\delta_{sw}$ , of a given solvent,  $\delta_s$ , and water,  $\delta_w$ , using equation 3.2; where  $\delta_d$  denotes the dispersion force component,  $\delta_p$  is the polar component and  $\delta_h$  is the hydrogen bonding component, Subscripts s and w describe these partial parameters for solvent and water, respectively.<sup>33</sup>

$$\Delta\delta_{sw} = [(\delta_{d,s} - \delta_{d,w})^2 + (\delta_{p,s} - \delta_{p,w})^2 + (\delta_{h,s} - \delta_{h,w})^2]^{\frac{1}{2}} \quad \text{Equation 3.2}$$

These calculations determined that the smaller the value for  $\Delta\delta_{sw}$ , the higher the affinity of a given solvent for water resulting in smaller nanoparticles. Further definition of the affinity between water and a given solvent was undertaken by Galindo-Rodriguez *et al.* and Bilati *et al.* where the solvent/water interaction parameters,  $X_{sw}$ , were calculated for a number of solvents using equation 3.3; where  $V_s$  represents the molar volume of solvent,  $R$ , is the gas constant,  $T$ , temperature,  $\delta_s$  and  $\delta_w$ , total solubility parameters of solvent and water respectively.<sup>33,34</sup>

$$X_{sw} = \frac{V_s}{RT} (\delta_s - \delta_w)^2 \quad \text{Equation 3.3}$$

A lower value of  $X_{sw}$  signifies a higher affinity for water which promotes diffusion and polymer chain partitioning into the aqueous phase resulting in smaller nanoparticles.<sup>33,34</sup> The interaction parameters of acetone and THF are calculated to be 23.9 and 28.7 respectively<sup>\*\*\*\*\*</sup> by Lee *et al.* and therefore one would expect acetone to promote greater solvent diffusion upon addition to water and increased polymer chain partitioning correlating with the smaller particles produced in Section 3.2.1 when compared to THF.<sup>26,33</sup>

The co-nanoprecipitation study undertaken from acetone in Section 3.2.1 was replicated, keeping the parameters unchanged apart from using THF as the good solvent. Ratios of amphiphilic block co-polymer to PCL<sub>40</sub>-*co*-BOD<sub>0.7</sub> were increased from 0 wt% to 100 wt% for both PEG<sub>2K</sub>-*b*-PCL<sub>40</sub> and PEG<sub>5K</sub>-*b*-PCL<sub>40</sub>. Similar to the acetone model, successful, stable nanoparticle dispersions were achieved in all cases and similar trends could be derived from the plotting of DLS analysis with regards to  $D_z$ , PDI and zeta potential (Figure 3.11). On average

---

\*\*\*\*\* As a matter of context these values range from 0 for water-water, 11.4 for acetonitrile-water, 11 for ethanol-water, 18.7 for isopropyl alcohol-water and 32.5 for ethyl lactate-water. Therefore the difference between acetone and THF interaction with water could be classed as significant and high values.<sup>26,33,34</sup>

the  $D_z$  values for all the particles were higher than those produced using acetone as the good solvent (Figure 3.11, A). This indicates that the introduction of the hydrophilic PEG block does little to affect the solvent/polymer interactions or increase the affinity of THF for the polymer chains as this would have resulted in smaller particles. Interestingly, although PDI was higher when using THF and PEG<sub>x</sub>-*b*-PCL<sub>40</sub> was low; larger concentrations of PEG<sub>x</sub>-*b*-PCL<sub>40</sub> resulted in lower PDI than similar experiments using acetone and overall a smaller range in PDI throughout this series was observed.

Zeta potential, which is less reliant on the solvent interactions with water and polymer chains, showed a similar trend to particles generated using acetone, with less negative values observed with higher PEG<sub>x</sub>-*b*-PCL<sub>40</sub> content. This would be expected as zeta potential relies heavily on the composition of the nanoparticles. The decrease in negativity of the zeta potential values indicates a shift from electrostatic stabilisation, where ions, whether hydroxide or bicarbonate, are free to adsorb on the surface of the nanoparticles, imparting negative charge and contribution to the double layer hence stabilising the system.<sup>21,24,28-30</sup> Increased PEG<sub>x</sub>-*b*-PCL<sub>40</sub> content masks the surface of the nanoparticle preventing the adsorption of these ions and shields the charge whilst simultaneously imparting steric stability between nanoparticles preventing aggregation. Comparison with the results gained by co-nanoprecipitation from acetone, particles with increasing PEG<sub>5K</sub>-*b*-PCL<sub>40</sub> content showed a greater decrease in negative zeta potential than those stabilised PEG<sub>2K</sub>-*b*-PCL<sub>40</sub> which was expected due to the increased length of the hydrophilic block.

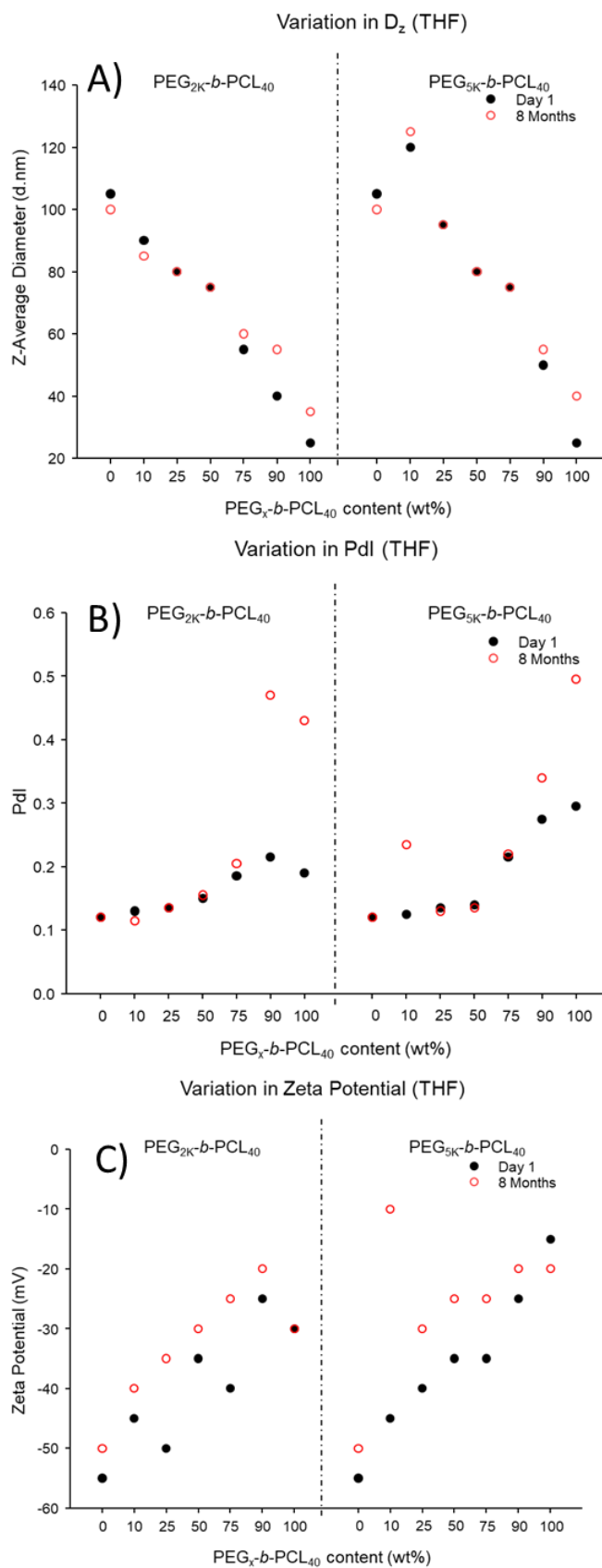


**Figure 3.11 – Graphical representation of changes in physicochemical characteristics of nanoparticles produced by co-nanoprecipitation with increasing  $PEG_x-b-PCL_{40}$  content (THF); (A) Z-average diameter, (B) Pdl and (C) zeta potential.**

Nonetheless although co-nanoprecipitation using acetone as the good solvent overall produced particles of smaller size and lower PdI, the results gained with THF are comparable especially with the inclusion of stability considerations. Additionally, reflecting on the trends determined from studies in both acetone and THF it is clear that a compromise must be made for favourable physicochemical characteristics to select a ratio of PEG<sub>x</sub>-*b*-PCL<sub>40</sub>: PCL<sub>40</sub>-*co*-BOD<sub>0.7</sub> for future studies. This compromise is best gained at the ratio of 50:50 wt% of the two polymer species, producing small particles of < 100 nm regardless of PEG length and PdI values of approximately 0.2. Moreover zeta potentials <-40 mV allows access to particles that have combined electrostatic and steric stability.

### 3.2.2.1 Salt stability studies

Salt studies were undertaken using the two separate methods detailed in Section 3.2.1.1 to allow for direct comparison to similar studies completed using acetone. The first method undertaken required the repeat analysis of each dispersion by DLS after a single 20  $\mu$ L addition of 0.5 M NaCl<sub>(aq)</sub> (Table 3.4, Figure 3.12). Upon comparison to nanoparticles precipitated from acetone the data expressed in Figure 3.12 indicated less variation in physicochemical properties when precipitated from THF. PdI and  $D_z$  values varied only slightly in the first 24 hours with the largest changes being measured on day 7 across the full series of nanoparticles which could indicate increased stability from these particles. The largest trend was observed when the change in zeta potential over time was considered (Figure 3.12, C), emulating analysis of particles formed from an acetone co-nanoprecipitation. Moreover particles containing 100 wt% PCL<sub>40</sub>-*co*-BOD<sub>0.7</sub> showed the same behaviour observed in the study detailed in Section 3.2.1.1 wherein zeta potential became more negative over time. As described in Section 3.2.1.1 this could be a result of bicarbonate and chloride ions having similar propensity to adsorb onto hydrophobic surfaces.<sup>28</sup>

**Table 3.4 – DLS characterisation of nanoparticles produced by nanoprecipitation (from THF) with the addition of 0.5 M NaCl<sub>(aq)</sub> (20 μL);**

Sample	Multiple 20 μL additions of 0.5 M NaCl <sub>(aq)</sub> Volume of salt added until aggregation (μL) <sup>b</sup>	Single 20 μL addition of 0.5 M NaCl <sub>(aq)</sub>											
		Z-Average Diameter (nm) <sup>c</sup>				PDI <sup>c</sup>			Zeta Potential (mV) <sup>c</sup>				
		No Salt	Instant	1 Day	7 Days	No Salt	Instant	1 Day	7 Days	No Salt	Instant	1 Day	7 Days
Ratio of PEG <sub>2K</sub> - <i>b</i> -PCL <sub>40</sub> : PCL <sub>40</sub> - <i>co</i> -BOD <sub>0.7</sub>													
0:100	120	105	100	100	100	0.120	0.115	0.115	0.140	-55	-65	-65	-60
10:90	20	90	85	85	85	0.130	0.095	0.120	0.105	-45	-30	-25	-25
25:75	20	80	80	80	75	0.135	0.115	0.135	0.120	-50	-20	-15	-20
50:50	40	75	70	70	70	0.150	0.105	0.130	0.120	-35	-10	-10	-10
75:25	60	55	55	55	55	0.185	0.150	0.165	0.160	-40	-15	-10	-10
90:10	> 2000	40	40	40	40	0.215	0.140	0.205	0.205	-25	-10	-10	-10
100:0	> 2000	25	30	30	35 <sup>a</sup>	0.190	0.100	0.205	0.305 <sup>a</sup>	-30	-10	-10	-10
Ratio of PEG <sub>5K</sub> - <i>b</i> -PCL <sub>40</sub> : PCL <sub>40</sub> - <i>co</i> -BOD <sub>0.7</sub>													
0:100	120	105	100	100	100	0.120	0.115	0.115	0.140	-55	-65	-65	-60
10:90	20	120	115	115	110	0.125	0.105	0.115	0.115	-45	-10	-10	-10
25:75	20	95	95	95	95	0.135	0.115	0.145	0.150	-40	-5	-5	-5
50:50	20	80	75	75	75	0.140	0.115	0.115	0.130	-35	-5	-5	-5
75:25	140	75	75	75	70	0.215	0.185	0.190	0.185	-35	-5	-5	-5
90:10	> 2000	50	50	55 <sup>a</sup>	60 <sup>a</sup>	0.275	0.210	0.255 <sup>a</sup>	0.250 <sup>a</sup>	-25	-5	-5	-5
100:0	> 2000	25 <sup>a</sup>	35 <sup>a</sup>	45 <sup>a</sup>	50 <sup>a</sup>	0.295 <sup>a</sup>	0.265 <sup>a</sup>	0.390 <sup>a</sup>	0.490 <sup>a</sup>	-15	-5	-5	-5

*a* Multimodal distributions obtained for this measurement, *b* volume of 0.5 M NaCl<sub>(aq)</sub> added until visible precipitation was observed, *c* DLS characterisation gained after a single 20 μL addition of 0.5 M NaCl<sub>(aq)</sub> to the aqueous dispersion.

The second salt stability study requiring multiple additions of 0.5 M NaCl<sub>(aq)</sub> (20  $\mu$ L) to 1 mL of each aqueous dispersion, showed little difference in the stability of the dispersions to results gained in Section 3.2.1.1 (Table 3.4). Nanoparticles synthesised from THF did require slightly more salt solution to induce aggregation although this was hard to determine visually and could not be classed as a significant difference between the two systems. Interestingly when PEG<sub>x</sub>-*b*-PCL<sub>40</sub> was absent, nanoparticles formed from 100 wt% PCL<sub>40-co</sub>-BOD<sub>0.7</sub> showed higher stability to salt requiring 120  $\mu$ L of 0.5 M NaCl<sub>(aq)</sub> to be added before aggregation occurred. It is clear the energy barrier between flocculation and aggregation was large therefore requiring a significant reduction before aggregation occurred.<sup>20</sup> This is indicated by the highly negative zeta potential of -55 mV which would require a larger number of positive Na<sup>+</sup> ions to shield the electronegative stability induced by the adsorption of negatively charged hydroxide or bicarbonate ions to the surface of the nanoparticles.<sup>28-30</sup> Furthermore the increasing concentration of PEG<sub>x</sub>-*b*-PCL<sub>40</sub> resulted in an increase in stability to salt addition with 90 wt% PEG<sub>x</sub>-*b*-PCL<sub>40</sub> content requiring > 2000  $\mu$ L of salt before any aggregation occurred. This reflects results observed in similar studies using acetone and indicates similar concentrations of salt can be tolerated by nanoparticles generated from either acetone or THF.

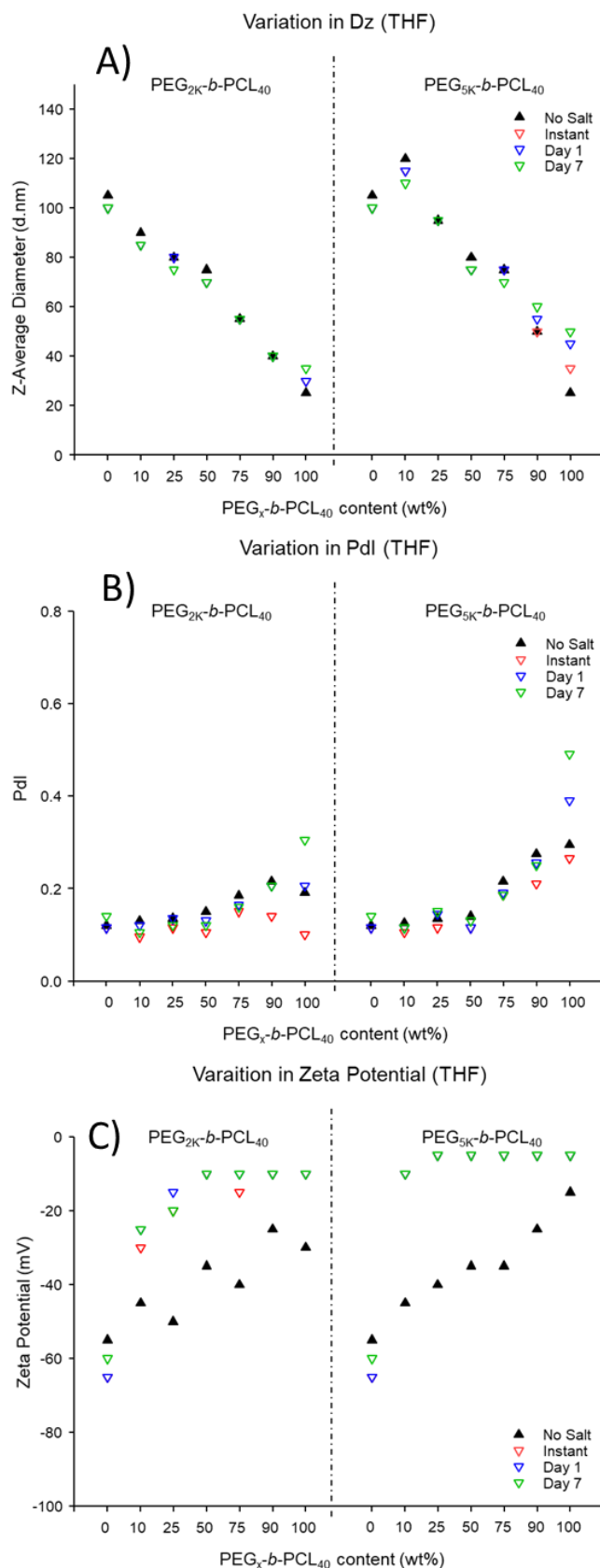


**Figure 3.12 – Graphical representation of changes in physicochemical characteristics with the addition of 20  $\mu$ L 0.5 M NaCl<sub>(aq)</sub> with increasing PEG<sub>x</sub>-b-PCL<sub>40</sub> content (THF) (A) Z-average diameter, (B) Pdl and (C) zeta potential.**

### 3.3 (Co)-nanoprecipitation utilising PSCM<sub>40-co-BOD</sub><sub>0.7</sub>

Investigations exploring the variation of the components used within the co-nanoprecipitation process were conducted with the selected ratio of 50:50 wt% amphiphilic di-block co-polymer to hydrophobic polymer, to be implemented for all future studies. It was thought that the versatility of this method would allow for the determination of the effects of polyester backbone chemistry on nanoparticle formation.<sup>25</sup> Following the studies carried out with PCL based polymers in both Sections 3.2.1 and 3.2.2, in combination with previous studies conducted by Hatton *et al.*, only branched co-polymers were studied.<sup>18</sup> Initial comparison between the five branched polymers (PCL<sub>40-co-BOD</sub><sub>0.7</sub>, PMOP<sub>40-co-BOD</sub><sub>0.7</sub>, PPOP<sub>40-co-BOD</sub><sub>0.7</sub>, PBOP<sub>40-co-BOD</sub><sub>0.7</sub> and PPHLOP<sub>40-co-BOD</sub><sub>0.7</sub>) synthesised in Sections 2.3.3.1 and 2.4.2.1 were undertaken with the nanoprecipitation of each polymer from THF; as this solvent resulted in less multimodal nanoparticle dispersions after seven days (Figure 3.13).

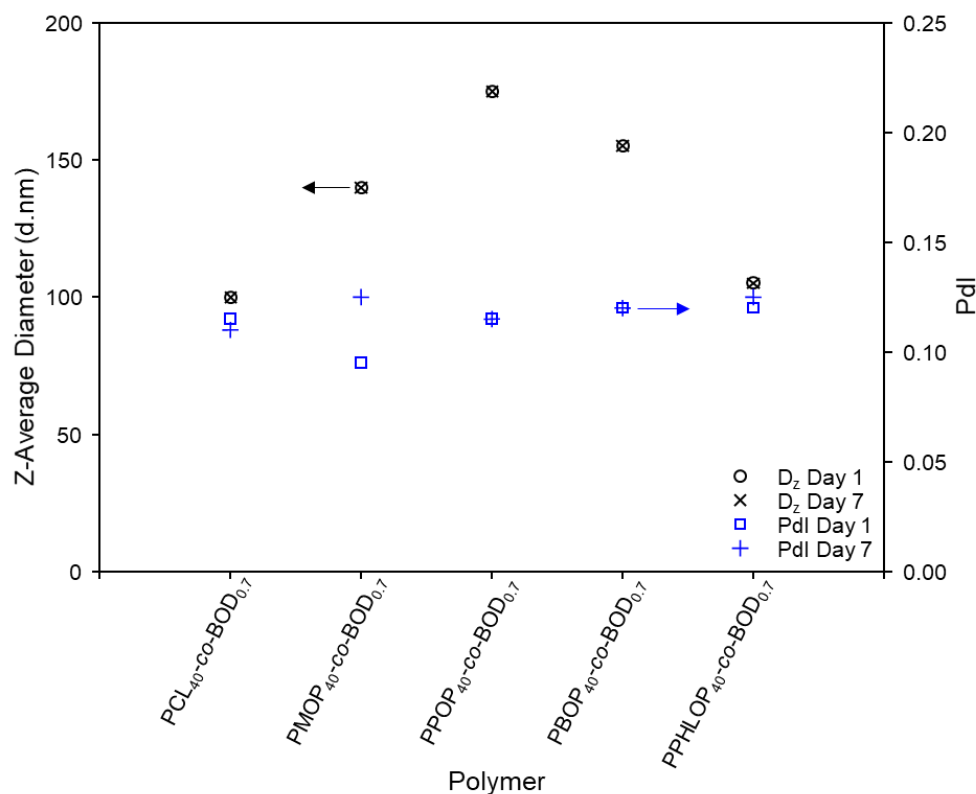


**Figure 3.13 – Graphical representation of changes in physicochemical characteristics with different PSCM<sub>40-co-BOD</sub><sub>0.7</sub> polymers** (○) Z-average diameter Day 1, (×) Z-average diameter Day 7, (□) Pdl Day 1 and (×) Pdl Day 7.

DLS analysis of the unfiltered samples revealed that the backbone of the hydrophobic branched polymer did effect the size of the nanoparticles although other physicochemical properties of the nanoparticles remained comparable to PCL<sub>40-co-BOD</sub><sub>0.7</sub>. As expected zeta potentials of all



five samples fell below -50 mV indicating complete electrostatic stability of the systems; this stability was sufficient enough to prevent aggregation with little change being observed over 7 days for all five systems.<sup>20,21,24</sup> PDI was also consistent between nanoparticles dispersions indicating that the solvent/polymer interactions were not playing a significant role in the control of the nanoparticle formation. However due to the backbone of each polymer being very similar to caprolactone, regardless of monomer used, this result would be expected.

$D_z$  values varied significantly depending on which monomer was used within the polymer backbone: PPOP<sub>40-co</sub>-BOD<sub>0.7</sub> generated the largest particles of 175 nm with the second largest at 155 nm produced by PBOP<sub>40-co</sub>-BOD<sub>0.7</sub>. This indicates that the bulky *iso*-propyl and *tert*-butyl groups present on the caprolactone ring of POP and BOP monomers and subsequently in the polymer backbone decrease the efficiency of the polymer chains packing close together upon collapse in the nucleation growth process. This prevention of the polymer chains' collapse into small nuclei and well organised adsorption of further groups within the growth process would most likely lead to the increase in nanoparticle hydrodynamic radius. This hypothesis would also be expected to play a role in PPHLOP<sub>40-co</sub>-BOD<sub>0.7</sub> nanoparticles however these particles had  $D_z$  values of 105 nm, only slightly larger than PCL<sub>40-co</sub>-BOD<sub>0.7</sub>. It can be speculated that this could be a result of  $\pi$  to  $\pi$  stacking induced by the phenyl side group.<sup>35</sup> These favourable intermolecular interactions would allow for chains to move closer to each other resulting in a more structured organisation of the chains and most likely reducing the size of the resulting nanoparticles. However it is important to keep in mind the probability of alignment is very small particularly in coiled polymer chains. Furthermore the modification of the polymer backbone with the addition of pendant alkyl groups may also alter the solvent/polymer interactions resulting in particles of varying sizes. This suggests that although the polymers are largely based on caprolactone-like monomers the small shift in alkyl side groups could have a significant effect on nanoparticle formation.

### **3.3.1 PEG-*b*-PCL<sub>40</sub> stabilised PSCM<sub>40-co</sub>-BOD<sub>0.7</sub> nanoparticles via co-nanoprecipitation**

After an initial study of branched polyester nanoprecipitation, a co-nanoprecipitation study was conducted utilising PCL derived A-B block co-polymers with each of the five branched polyester species detail in Section 3.3. Co-nanoprecipitation studies were performed with THF as the good solvent for the polymer and followed the same methodology detailed in Section 3.2.1 where 1 mL of polymer solution was added to 5 mL of water achieving a final

concentration of  $1 \text{ mg mL}^{-1}$  after solvent evaporation. DLS analysis was undertaken on unfiltered samples both on day 1 and day 7 to gain full understanding of both the physicochemical properties of the nanoparticle dispersions and their stability over time (Table 3.5).

The addition of  $\text{PEG}_x\text{-}b\text{-PCL}_{40}$  regardless of PEG block length resulted in a decrease in  $D_z$  for all the polymers compared to nanoprecipitation of 100 wt% branched species, for example co-nanoprecipitation of  $\text{PPOP}_{40}\text{-}co\text{-BOD}_{0.7}$  with  $\text{PEG}_{2K}\text{-}b\text{-PCL}_{40}$  and  $\text{PEG}_{5K}\text{-}b\text{-PCL}_{40}$  produced particles of 95 and 110 nm respectively (Table 3.5). This significant reduction in  $D_z$  from 175 nm without  $\text{PEG}_x\text{-}b\text{-PCL}_{40}$  was also observed with studies involving  $\text{PEG}_x\text{-}b\text{-PCL}_{40}$  and  $\text{PCL}_{40}\text{-}co\text{-BOD}_{0.7}$  although this was less significant when  $\text{PEG}_{5K}\text{-}b\text{-PCL}_{40}$  was used as the stabiliser (Table 3.5). This phenomenon is most likely caused by the additional steric stabilisation of the nanoparticles by the addition of a PEG corona, increasing the energy barrier needed to be overcome to result in aggregation.<sup>21,24</sup> Furthermore the combined steric and electrostatic stabilisation, inferred by the zeta potentials of all the nanoparticles being more negative or equal to -30 mV, causes the particles to reach stability at a smaller size than if reliant on electrostatic stabilisation alone.<sup>20,21,24</sup>

$D_z$  values for particles stabilised by  $\text{PEG}_{5K}\text{-}b\text{-PCL}_{40}$  were larger overall than particles stabilised by  $\text{PEG}_{2K}\text{-}b\text{-PCL}_{40}$  signifying the introduction of a larger PEG corona in the structure of the particles. Nonetheless these values, with the exception of  $\text{PPHLOP}_{40}\text{-}co\text{-BOD}_{0.7}$ , were smaller than those seen with 100 wt% branched hydrophobic polymer. This is again attributed to the gain of colloidal stability at a smaller size during the growth process due to the combination of both electrostatic and steric stabilisation.<sup>7,14,20,21</sup> Further consideration of  $D_z$  values of all ten co-nanoprecipitations highlighted the same trend observed in the absence of  $\text{PEG}_x\text{-}b\text{-PCL}_{40}$  with a peak in  $D_z$  being achieved with the presence of  $\text{PPOP}_{40}\text{-}co\text{-BOD}_{0.7}$  and  $\text{PPHLOP}_{40}\text{-}co\text{-BOD}_{0.7}$  producing particles similar in size to the  $\text{PCL}_{40}\text{-}co\text{-BOD}_{0.7}$  based dispersion regardless of PEG block length (Figure 3.14).

**Table 3.5 – DLS characterisation of nanoparticles produced by co-nanoprecipitation of PSCM<sub>40-co</sub>-BOD<sub>0.7</sub> with PEG<sub>x</sub>-*b*-PCL<sub>40</sub>**

Sample	Ratio	Z-Average Diameter (nm)		Number Average Diameter (nm)		PdI		Zeta Potential (mV)		Derived Count Rate (Attenuator)	
		Day 1	Day 7	Day 1	Day 7	Day 1	Day 7	Day 1	Day 7	Day 1	Day 7
PEG <sub>2K</sub> - <i>b</i> -PCL <sub>40</sub> : PCL <sub>40-co</sub> -BOD <sub>0.7</sub>	<b>50:50</b>	75	80	45	50	0.140	0.140	-40	-30	106045 (6)	89180 (6)
PEG <sub>2K</sub> - <i>b</i> -PCL <sub>40</sub> : PMOP <sub>40-co</sub> -BOD <sub>0.7</sub>	<b>50:50</b>	85	90	50	50	0.145	0.150	-35	-40	128700 (6)	122230 (6)
PEG <sub>2K</sub> - <i>b</i> -PCL <sub>40</sub> : PPOP <sub>40-co</sub> - BOD <sub>0.7</sub>	<b>50:50</b>	95	100	50	60	0.155	0.145	-40	-40	233800 (5)	148685 (6)
PEG <sub>2K</sub> - <i>b</i> -PCL <sub>40</sub> : PBOP <sub>40-co</sub> -BOD <sub>0.7</sub>	<b>50:50</b>	90	95	50	55	0.155	0.150	-40	-40	234285 (5)	223270 (5)
PEG <sub>2K</sub> - <i>b</i> -PCL <sub>40</sub> : PPHLOP <sub>40-co</sub> -BOD <sub>0.7</sub>	<b>50:50</b>	90	95	60	55	0.140	0.140	-40	-35	273960 (5)	234040 (5)
PEG <sub>5K</sub> - <i>b</i> -PCL <sub>40</sub> : PCL <sub>40-co</sub> -BOD <sub>0.7</sub>	<b>50:50</b>	100	100	60	60	0.150	0.155	-35	-30	120300 (6)	113380 (6)
PEG <sub>5K</sub> - <i>b</i> -PCL <sub>40</sub> : PMOP <sub>40-co</sub> -BOD <sub>0.7</sub>	<b>50:50</b>	100	105	55	60	0.155	0.150	-30	-35	119150 (6)	116530 (6)
PEG <sub>5K</sub> - <i>b</i> -PCL <sub>40</sub> : PPOP <sub>40-co</sub> -BOD <sub>0.7</sub>	<b>50:50</b>	110	115	60	75	0.135	0.140	-30	-30	247535 (5)	224620 (5)
PEG <sub>5K</sub> - <i>b</i> -PCL <sub>40</sub> : PBOP <sub>40-co</sub> -BOD <sub>0.7</sub>	<b>50:50</b>	110	110	60	60	0.175	0.165	-35	-30	202280 (5)	211695 (5)
PEG <sub>5K</sub> - <i>b</i> -PCL <sub>40</sub> : PPHLOP <sub>40-co</sub> -BOD <sub>0.7</sub>	<b>50:50</b>	100	100	65	60	0.120	0.140	-35	-25	355330 (5)	332050 (5)

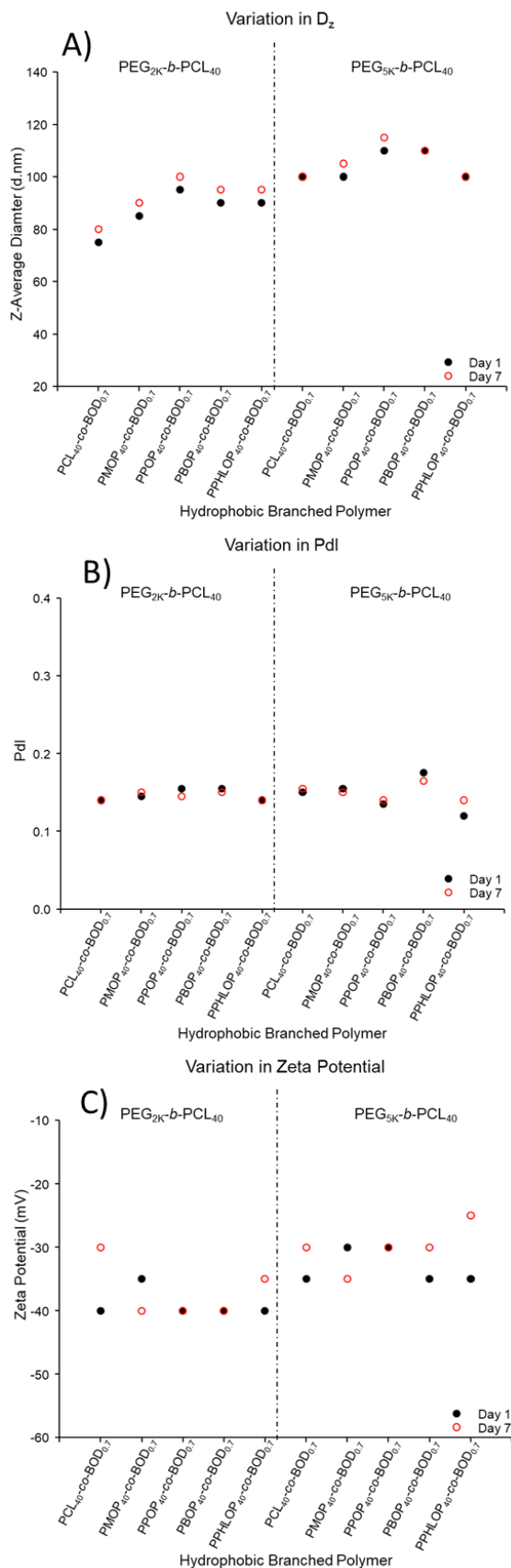


**Figure 3.14 – Graphical representation of physicochemical characteristics from the co-nanoprecipitation of 50:50 wt% PEG<sub>x</sub>-b-PCL<sub>40</sub>: PSCM<sub>40</sub>-co-BOD<sub>0.7</sub> (THF). (A) Z-average diameter, (B) Pdl and (C) zeta potential.**

Zeta potential, as mentioned previously, would indicate that electrostatic stabilisation would be taking part although it is hard to determine to what extent this may be (Figure 3.14, C).<sup>20,21,24</sup> It could be expected that complete resistance to salt addition would not be achieved by all ten dispersions particularly when compared to the results of the multiple addition of salt to PEG<sub>x</sub>-*b*-PCL<sub>40</sub>: PCL<sub>40</sub>-*co*-BOD<sub>0.7</sub> nanoparticles (Section 3.2.2.1). However a 50:50 wt% ratio of PEG<sub>x</sub>-*b*-PCL<sub>40</sub>: PCL<sub>40</sub>-*co*-BOD<sub>0.7</sub> in nanoparticles showed little variation over 7 days with the addition of only 20  $\mu$ L 0.5 M NaCl<sub>(aq.)</sub> solution which is promising when considering the nanoparticles described in this section, Section 3.3.1, and the potential application of drug vehicles.

Additionally limited variation in the physicochemical properties of all the nanoparticles stabilised by 50 wt% PEG<sub>2K</sub>-*b*-PCL<sub>40</sub> and PEG<sub>5K</sub>-*b*-PCL<sub>40</sub>, measured on day 7, indicated good stability over time. This further adds to the promising data that points to the successful use of these systems as vehicles for drug delivery.

### **3.3.2 PEG-*b*-PSCM<sub>40</sub> stabilised PSCM<sub>40</sub>-*co*-BOD<sub>0.7</sub> nanoparticles *via* (co)-nanoprecipitation**

A final exploration involving co-nanoprecipitation of the hydrophobic branched polyesters involved matching hydrophobic blocks of PEG<sub>5K</sub> block co-polymers with respect to polyester backbone chemistry. This enabled the study of the effects complementary hydrophobic polymer segments may have on the co-nanoprecipitation process. The first element of this examination was the nanoprecipitation of the linear PEG<sub>5K</sub> block co-polymers derived from each substituted caprolactone monomer, in the absence of the core-forming branched polyester, permitting the assessment of the influence of the monomer used in each co-polymer (Figure 3.15).

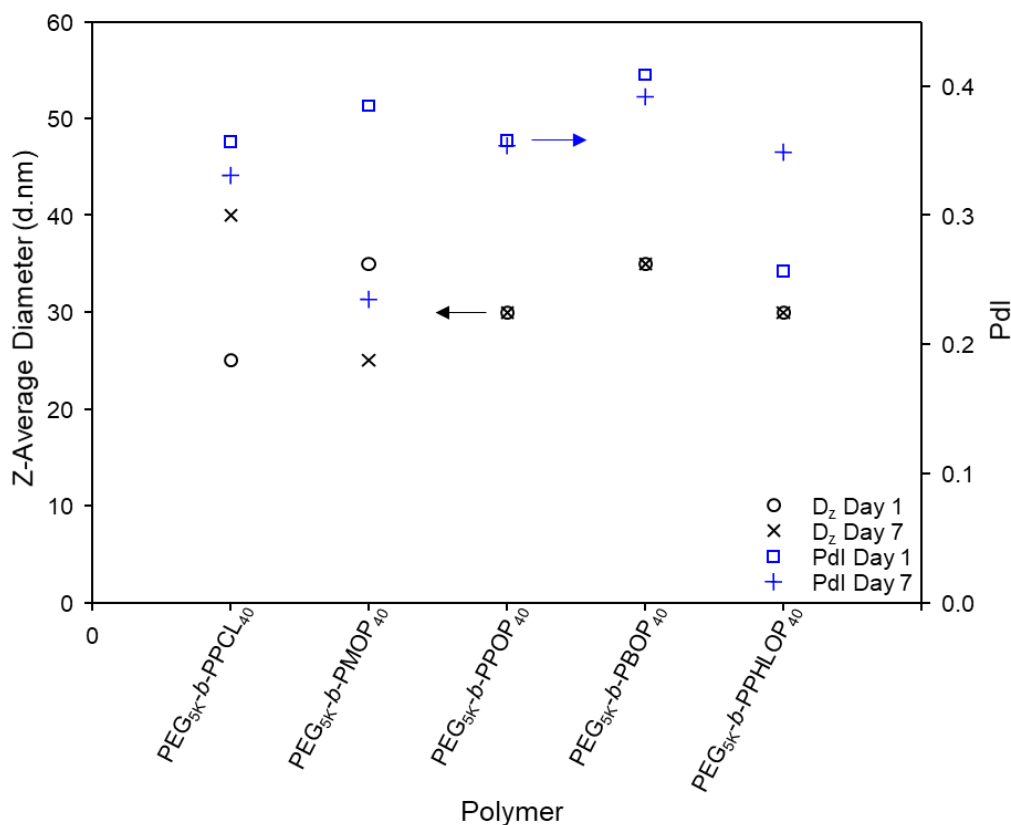


**Figure 3.15 – Graphical representation of changes in physicochemical characteristics of PEG<sub>5K</sub>-b-PSCM<sub>40</sub> nanoparticles prepared by nanoprecipitation.** (○) Z-average diameter Day 1, (×) Z-average diameter Day 7, (□) PDI Day 1 and (×) PDI Day 7.

Upon DLS characterisation it was clear that the polymers generated particles of micelle size and produced multimodal size distributions and large PDI values  $> 0.25$ . Therefore the results gained from this study could not be used to conclusively analyse trends in size and control between the five nanoparticle dispersions; however, it could be deduced that the addition of side chain functionality within the hydrophobic segments of the co-polymers led to larger particles than PEG<sub>5K</sub>-b-PCL<sub>40</sub>. Zeta potentials were significantly more positive than values seen for the co-nanoprecipitated or 100 wt% branched hydrophobic polymer particles described in Sections 3.3.1 and 3.3 respectively. The zeta potential values seen in this series, all  $\leq -30$  mV, indicate that the particles are most likely solely sterically stabilised by the PEG corona creating a barrier against aggregation.<sup>21,24</sup> This stability was indicated by the lack of variation in the physicochemical properties of each dispersion over 7 days reflected significantly in Figure 3.15.

The importance of matching the chemistry of the hydrophobic block of the stabilising amphiphilic A-B block co-polymer to the branched polyester was investigated by co-nanoprecipitations. The ratio of stabilising di-block co-polymer to hydrophobic branched

polymer was kept consistent at 50:50 wt% allowing direct comparison to the PEG<sub>5K</sub>-*b*-PCL<sub>40</sub> stabilised series. THF was also used as the good solvent within this study mitigating any effects imparted from organic solvent choice and allowing for direct comparison to previous work within this chapter.

DLS analysis of these systems when first co-nanoprecipitated revealed the production of larger particles than those produced by the PEG di-block co-polymers alone (Figure 3.16). This was to be expected as 50 wt% of the polymer mixture was now a bulky branched polymer of high molecular weight. There also seemed to be a shift in the stability mechanism of the particles to include electrostatic stabilisation. The increased concentration of hydrophobic material during the nucleation-growth process skews the stabilisation to favour combined steric and electrostatic stabilisation.<sup>28-30</sup> Interestingly the substitution of PEG<sub>5K</sub>-*b*-PCL<sub>40</sub> for the PEG co-polymer that is complementary to the hydrophobic branched core resulted in a reversal of the behaviour of the polymer with respect to size with PEG<sub>5K</sub>-*b*-PPOP<sub>40</sub>: PPOP<sub>40</sub>-*co*-BOD<sub>0.7</sub> (50:50 wt%) producing the smallest particles with a  $D_z$  value of 90 nm (Figure 3.16). This could indicate that use of complementary block co-polymers increases favourable polymer-polymer interactions and decreases the potential for phase separation during nanoparticles formation inducing favourable collapse of the polymer chains and thus producing smaller particles. This could also be an indication of the effects utilising a mixture of PEG<sub>5K</sub>-*b*-PCL<sub>40</sub> and hydrophobic branched polymer had on the solvent/polymer interactions, indicating that the mixture of hydrophobic polymers of differing structure reduced or scrambled solvent/polymer interactions resulting in larger particles.<sup>8</sup> If this were the case it would be expected that PPOP<sub>40</sub>-*co*-BOD<sub>0.7</sub> and PBOP<sub>40</sub>-*co*-BOD<sub>0.7</sub> would produce the largest particles when paired with PEG<sub>x</sub>-*b*-PCL<sub>40</sub> which is the trend observed in Section 3.3.1.

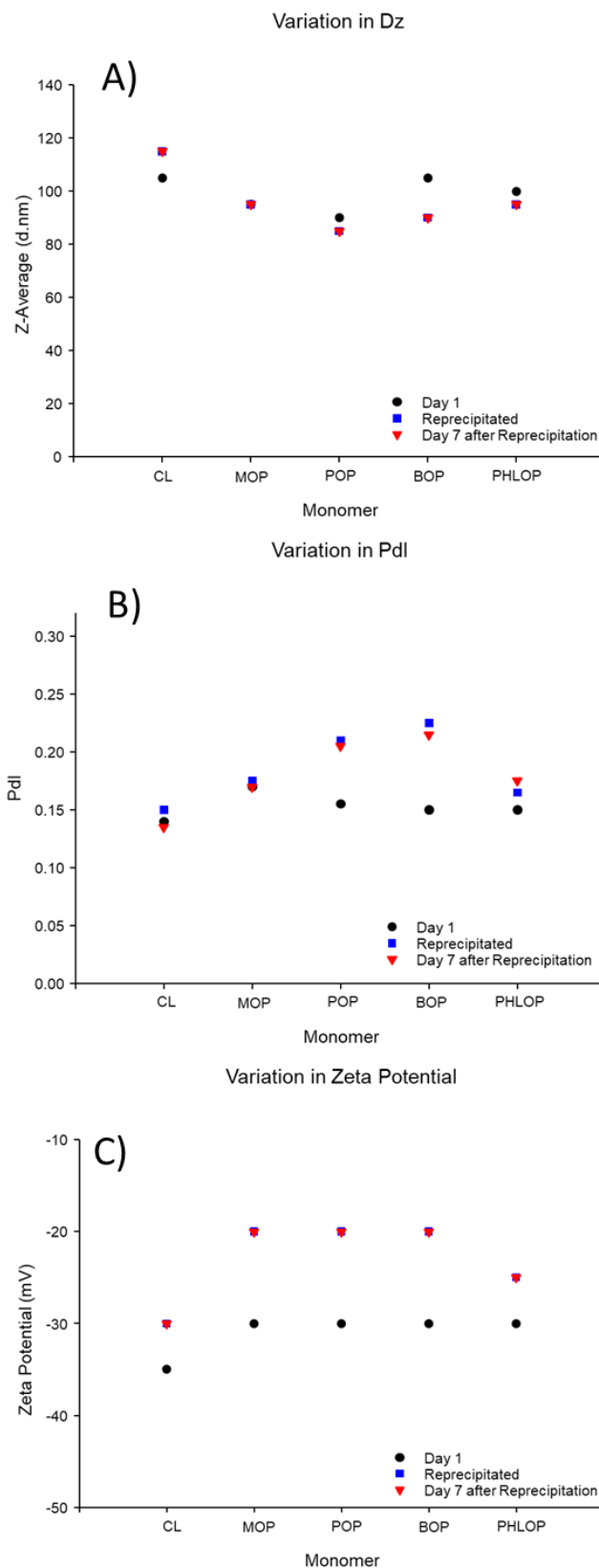


**Figure 3.16 – Graphical representation of changes in physicochemical characteristics of co-nanoprecipitation of complementary PEG<sub>5K</sub>-*b*-PSCM<sub>40</sub>: PSCM<sub>40</sub>-*co*-BOD<sub>0.7</sub> (50:50 wt%, THF) including results reprecipitated from stock solutions stored for 246 days. (A) Z-average diameter, (B) Pdl and (C) zeta potential.**



As an alternative investigation with this series of nanoparticles, the stock solutions of THF containing the polymers were kept at ambient temperature for a number of months to explore the possibility of reproducing the nanoparticles after storage. 246 days after first synthesis the THF solutions for the polymers mixtures were re-used in co-nanoprecipitation studies, generating samples with a final concentration in water of  $1 \text{ mg mL}^{-1}$  (Figure 3.16). Analysis indicated that nanoparticles produced from all five solutions were largely comparable to the initial results achieved with fresh solutions of polymer in THF particularly when  $D_z$  was considered. PDI and zeta potential did deviate from initial results more significantly with PDI increasing to include values  $> 0.2$  compared to values  $< 0.175$  for freshly produced nanoparticles. Zeta potential again increased becoming less negative after 246 days storage with an average reading of  $-20 \text{ mV}$  generated across the series of nanoparticles. Throughout these studies the same DLS apparatus and type of cuvette were used, where the measurement distance was fixed in order to rule out variation in the physicochemical properties of the nanoparticles resulting from measurement. A possible cause for the variation in parameters could be a result of greater solvation of the polymer over storage time or slight degradation of the polymers within solution due to storage at ambient temperature rather than in a colder environment.

Nonetheless the secondary results from the re-precipitation 246 days after the first use of the stock solutions correlated well with the analysis obtained seven days after the re-precipitation. This indicated that although it is unclear as to the cause of varying results between the first and second synthesis of the nanoparticle dispersions colloidal stability was still achieved. There was very limited change regarding  $D_z$ , PDI and zeta potential values over the 7 day period and this was also reflected by limited change in derived count rate of each solution signifying no aggregation or sedimentation. These results provide a fascinating insight into the nanoparticle formation and the stability imparted on these systems again combining steric and electrostatic stabilisation.

### **3.4 Model encapsulation *via* co-nanoprecipitation**

An exploration of the capabilities of the systems studied in Sections 3.2 and 3.3.1 to encapsulate hydrophobic guest molecules was undertaken for two different hydrophobic compounds namely Oil red O and an anticancer drug docetaxel (Figure 3.17). THF was used to dissolve the chosen polymers (50:50 wt% PEG<sub>x</sub>-*b*-PCL<sub>40</sub> to PCL/SCM<sub>40-co</sub>-BOD<sub>0.7</sub>) at a concentration of  $5 \text{ mg mL}^{-1}$  (5 mg polymer to 1 mL THF, varying the weight content of guest)

and the guest molecule (at a test loading of 2.43 wt%); 1 mL of this solutions mixture was added to water targeting a final concentration of 1 mg mL<sup>-1</sup> (1 mg polymer in 1 mL water, varying the weight content of guest to 2.43 wt%) after solvent evaporation.<sup>§§§§§§</sup>

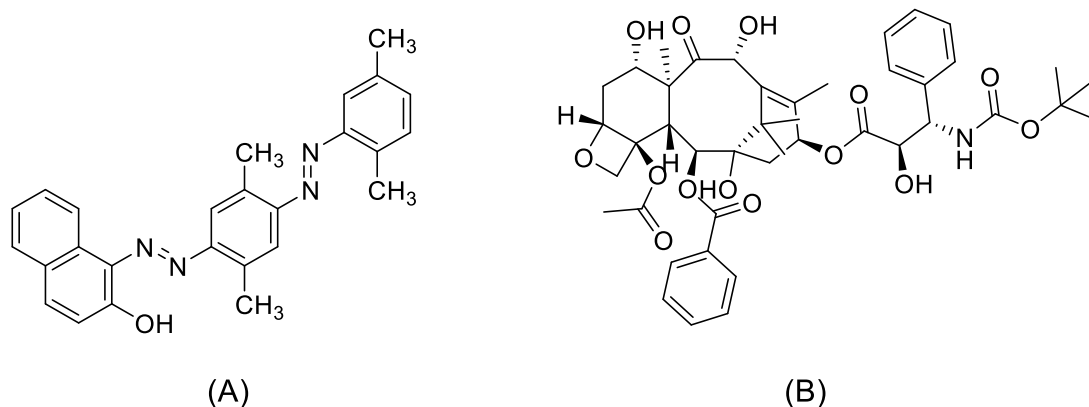


**Figure 3.17 -Molecular structures for guest molecules used in model encapsulation studies.** (A) Oil Red O and (B) docetaxel.

### 3.4.1 Encapsulation of Oil red O *via* co-nanoprecipitation

Oil red O is a molecule used to stain lipid and fat components in biological samples, and more recently in latent fingerprints, due to its highly hydrophobic nature which in turn make it the ideal model to test nanoparticle encapsulation capabilities.<sup>36</sup> Investigations were conducted with the encapsulation of Oil red O from a THF solution containing polymer and guest molecule. Here, PEG<sub>x</sub>-*b*-PCL<sub>40</sub> was used to stabilise nanoparticles formed from each of the hydrophobic branched polymers with 2.43 wt% Oil red O. The ratio of PEG<sub>x</sub>-*b*-PCL<sub>40</sub> to PCL/SCM<sub>40-co</sub>-BOD<sub>0.7</sub> was fixed at 50:50 wt% following the results gained in Section 3.2 aiming for a compromise between size, polydispersity and zeta potential of each dispersion. DLS analysis was performed on the unfiltered samples on the day of formation and 14 days after initial measurement to gauge whether these systems also possessed stability over time (Figure 3.18).

$D_z$  values of these systems revealed the same trend observed in the absence of Oil red O with the particles containing 50 wt% PPOP<sub>40-co</sub>-BOD<sub>0.7</sub> producing the largest particles when stabilised either by PEG<sub>2K</sub>-*b*-PCL<sub>40</sub> or PEG<sub>5K</sub>-*b*-PCL<sub>40</sub>. This indicated that the presence of this guest molecule had little effect on the nucleation-growth process or that its effect was

<sup>§§§§§§</sup> As these were concentrations based on the mass of only polymer in solvent (THF or water), the total solid concentration with 2.43 wt% guest is calculated to be 5.125 mg mL<sup>-1</sup> in THF and 1.025 mg mL<sup>-1</sup> in water. These equate to masses of 50 mg polymers and 1.25 mg guest molecule in 10 mL THF and 5 mg polymer and 0.125 mg guest molecule in 5 mL water.

negligible compared to the backbone of the hydrophobic branched polymer. Further consideration of the  $D_z$  values showed an overall increase in the size of the nanoparticles produced compared to the blank counterparts. The PDI and zeta potentials generated by each sample were also comparable to the corresponding blank systems. This, combined with the lack of aggregates within each dispersion, again reinforces the hypothesis that Oil red O encapsulation was successful.

Finally, repeat DLS measurements on the samples 14 days after first synthesis, and with storage at ambient temperature, highlighted their stability as little variation in all physicochemical properties was observed. This mirrors results observed for corresponding blank particles and is most likely due to the combined electrostatic and steric stability imparted on the particles by the PEG corona and hydrophobic particle core.<sup>21,24</sup> The results generated from this initial experiment were a promising step towards the ultimate goal of encapsulation of SN-38 within these systems. Although the drug loading capabilities with this molecule was low, the success at 2.43 wt% was encouraging in the fact that guest molecules had effectively no impact on the nucleation-growth process of co-nanoprecipitation.

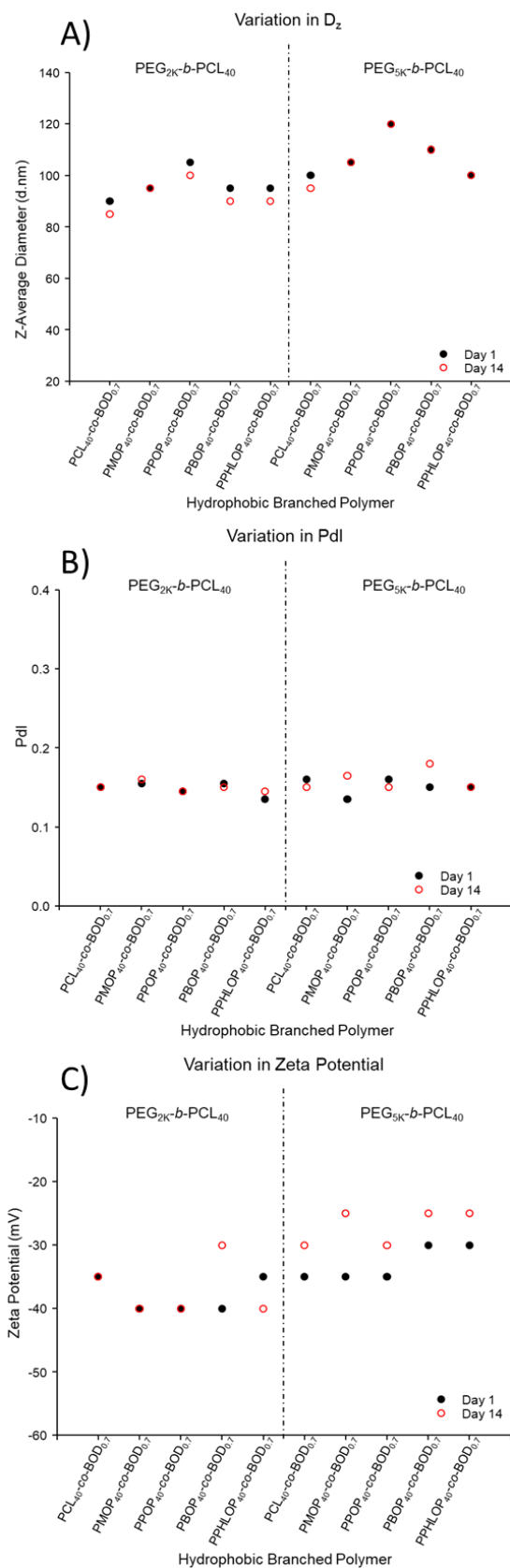


**Figure 3.18- Graphical representation of physicochemical characteristics from the co-nanoprecipitation of 50:50 wt% PEG<sub>x</sub>-b-PCL<sub>40</sub>: PSCM<sub>40</sub>-co-BOD<sub>0.7</sub> to encapsulate Oil red O (THF). (A) Z-average diameter, (B) Pdl and (C) zeta potential.**

### 3.4.2 Encapsulation of docetaxel *via* co-nanoprecipitation

Although Oil red O encapsulation was successful an additional model encapsulation study with docetaxel was conducted to study the diversity of chemical structures that may be incorporated using these novel polymers. Encapsulation of docetaxel was attempted at 2.43 wt% in PEG<sub>5K</sub>-*b*-PCL<sub>40</sub>: PCL/SCM<sub>40-co</sub>-BOD<sub>0.7</sub> (50:50 wt%) systems following the success in these conditions with Oil red O. Following the methodology used in all previous studies 1 mL of THF solution containing the polymers and drug (5 mg mL<sup>-1</sup>, 5 mg polymer to 1 mL THF, varying the weight content of guest to 2.43 wt%) was added to 5 mL of water targeting a final concentration of 1 mg mL<sup>-1</sup> (1 mg polymer in 1 mL water, varying the weight content of guest to 2.43wt%) after solvent evaporation. DLS analysis was performed on the unfiltered samples on the day of synthesis and 7 days later to study the stability of these systems and compare to the Oil red O containing nanodispersions (Figure 3.19).

Each of the nanoparticle dispersions successfully encapsulated docetaxel with no precipitation or sedimentation evident after THF evaporation. DLS analysis revealed that, similar to the Oil red O study,  $D_z$  values followed the same trend as the co-nanoprecipitation of the same systems without drug. The PEG<sub>5K</sub>-*b*-PCL<sub>40</sub>: PPOP<sub>40-co</sub>-BOD<sub>0.7</sub> (50:50 wt%) system therefore produced the largest particles of 100 nm. Nonetheless the diameters of all five systems were smaller than their blank counterparts although this does not indicate that encapsulation was unsuccessful especially when the appearance of each dispersion indicates no drug precipitate. The smaller  $D_z$  values for these systems indicate that docetaxel molecules are most likely acting as nuclei from which the nanoparticles can grow with well-defined, fast nucleation and growth steps.<sup>6,7</sup> PDI also followed a similar trend to the blank systems with the most polydisperse particles being produced when PMOP<sub>40-co</sub>-BOD<sub>0.7</sub> and PBOP<sub>40-co</sub>-BOD<sub>0.7</sub> were present in the hydrophobic branched core of the nanoparticles. Finally, zeta potential showed very little variability between all five systems and was indicative of a combination of both steric and electrostatic stabilisation at -30 mV.<sup>20,21,24</sup>

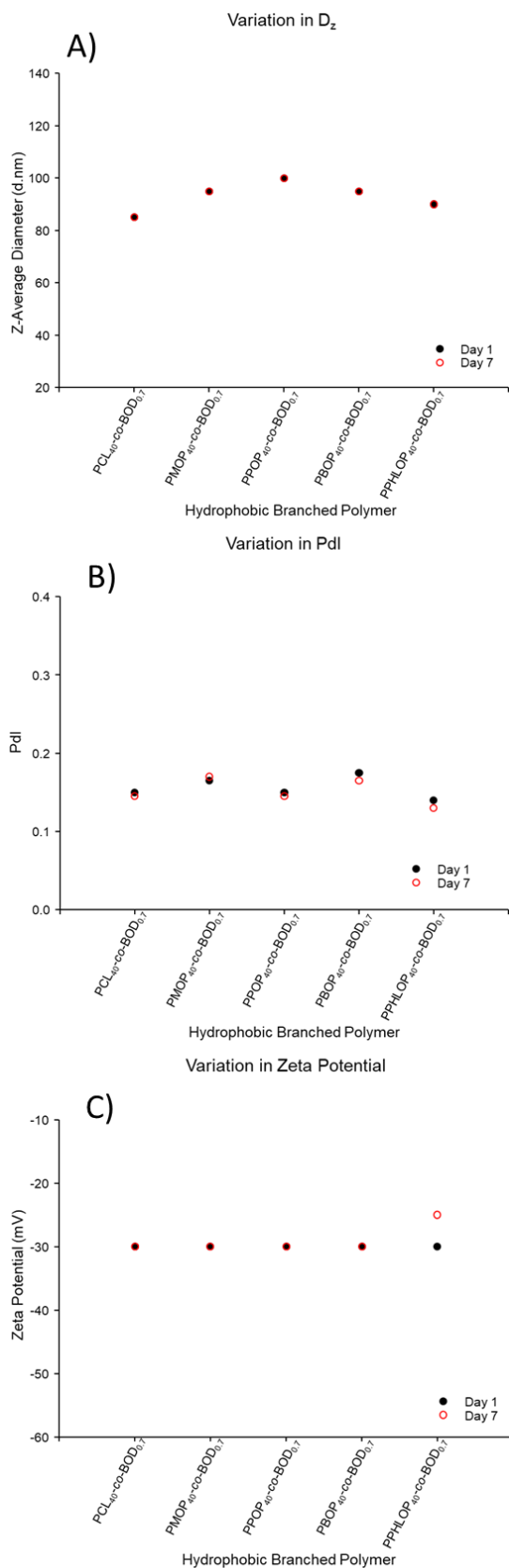


**Figure 3.19- Graphical representation of physicochemical characteristics from the co-nanoprecipitation of 50:50 wt% PEG<sub>5K</sub>-*b*-PCL<sub>40</sub>: PSCM<sub>40</sub>-*co*-BOD<sub>0.7</sub> to encapsulate docetaxel (THF). (A) Z-average diameter, (B) Pdl and (C) zeta potential.**

The stability of these systems was determined by repeated DLS characterisation seven days after first analysis was undertaken. Although the Oil red O systems were characterised on day 14, docetaxel containing nanoparticles showed very little variation in all characteristics after the seven day period (Figure 3.19). This was particularly reinforced by the similarities between derived count rate on day 1 and day 7 indicating that minimal to no sedimentation or aggregation had occurred upon storage at ambient temperature. The lack of aggregation of the particles was also indicated by the lack of variation in  $D_z$  over seven days. The confirmation of little change within all five systems give further evidence to the successful encapsulation of docetaxel.

The success of docetaxel encapsulation alongside that of Oil red O in the same systems generates promising evidence as to the capabilities of these systems to encapsulate hydrophobic guest/drug molecules. In addition, the stability of these systems over time would be beneficial for the use of these nanoparticle dispersions as drug delivery vehicles. The combination of the results gained in Section 3.4 also provides encouragement to expand encapsulation investigations to include SN-38 and SN-38 like drug molecules to ultimately fulfil one of the goals for this body of work.

### 3.5 Conclusions

In conclusion, initial exploration of co-nanoprecipitation, utilising PCL polymers indicated that branched architectures generated smaller nanoparticles than those of linear PCL. This trend regarding architecture followed previous findings from work completed by Hatton *et al.* and Flynn *et al.*, completed with polymethacrylates and indicated that the use of polyester based polymers did not cause a deviation from the trend they observed.<sup>18,19</sup>

Alternation of the organic solvent used to solvate the polymers to be nanoprecipitated, from acetone to THF, highlighted the role solvent played in the mechanism of formation of the nanoparticles. It is noted that solvent/water interactions play the greatest role in the increased size of nanoparticles synthesised from THF with regards to polyesters; with THF having a larger interaction parameter, 28.7, than acetone, 23.9, signifying a lower affinity for water and ultimately leading to larger particles. However the small increase in  $D_z$  and PDI in THF suggested that this effect was limited. Variety in size of nanoparticles produced with the variation of polymer backbone also indicated that solvent/polymer interactions played a role in the determination of particle size and must be considered during solvent selection.

Additionally the variation in polyester backbone appeared to have little effect on the successful nanoprecipitation of the branched polymers formed from substituted caprolactone monomers. Furthermore the mixed polyester backbone chemistry co-nanoprecipitation of these branched species with PEG<sub>x</sub>-*b*-PCL<sub>40</sub> had no discernible effect. This confirms that, if necessary, each linear amphiphilic A-B block polymer could be successfully co-nanoprecipitated with the complete branched polyester library.

Finally successful encapsulation of Oil red O and docetaxel at 2.43 wt% showed that the hydrophobic character of the polyester core aided the incorporation of guest molecules. Furthermore docetaxel containing nanoparticles possessed smaller  $D_z$  values than those without drug which may indicate drug molecules playing a role in nucleation.<sup>6,7</sup> The effective encapsulation of both Oil red O and docetaxel, which vary greatly in structure, would imply that co-nanoprecipitation is a viable route to SN-38 containing nanoparticles and offers a starting point for targeted drug content of 2.43 wt% with the view to optimise these systems.



**References**

- 1 A. Akbarzadeh, R. Rezaei-Sadabady, S. Davaran, S. W. Joo, N. Zarghami, Y. Hanifehpour, M. Samiei, M. Kouhi and K. Nejati-Koshki, *Nanoscale Res. Lett.*, 2013, **8**, 1–8.
- 2 E. Abbasi, S. F. Aval, A. Akbarzadeh, M. Milani, H. T. Nasrabadi, S. W. Joo, Y. Hanifehpour, K. Nejati-Koshki and R. Pashaei-Asl, *Nanoscale Res. Lett.*, 2014, **9**, 1–10.
- 3 W. Jin, W. Xu, H. Liang, Y. Li, S. Liu and B. Li, *Nanoemulsions for food: properties, production, characterization, and applications*, Elsevier Inc., 2016.
- 4 United States Patent, US 2010/0028444 A1, 2010, 1–44.
- 5 Y. Wang, P. Li, T. T. D. Tran, J. Zhang and L. Kong, *Nanomaterials*, 2016, **6**, 1–18.
- 6 S. M. D’Addio and R. K. Prud’homme, *Adv. Drug Deliv. Rev.*, 2011, **63**, 417–426.
- 7 C. J. Martínez Rivas, M. Tarhini, W. Badri, K. Miladi, H. Greige-Gerges, Q. A. Nazari, S. A. Galindo Rodríguez, R. Á. Román, H. Fessi and A. Elaissari, *Int. J. Pharm.*, 2017, **532**, 66–81.
- 8 S. Schubert, J. T. Delaney and U. S. Schubert, *Soft Matter*, 2011, **7**, 1581–1588.
- 9 United States Patent, US 5118528 A, 1992, 1–7.
- 10 N. T. K. Thanh, N. Maclean and S. Mahiddine, *Chem. Rev.*, 2014, **114**, 7610–7630.
- 11 C. B. Whitehead, S. Özkar and R. G. Finke, *Chem. Mater.*, 2019, **31**, 7116–7132.
- 12 F. Shiba and Y. Okawa, *J. Phys. Chem. B*, 2005, **109**, 21664–21668.
- 13 M. A. Watzky and R. G. Finke, *J. Am. Chem. Soc.*, 1997, **119**, 10382–10400.
- 14 E. Lepeltier, C. Bourgaux and P. Couvreur, *Adv. Drug Deliv. Rev.*, 2014, **71**, 86–97.
- 15 R. Botet, *J. Phys. Conf. Ser.*, 2012, **352**, 1–10.
- 16 P. Meakin, I. Majid, S. Havlin and H. Eugene Stanley, *J. Phys. A Gen. Phys.*, 1984, **17**, 975–981.
- 17 S. Jungblut, J. O. Joswig and A. Eychmüller, *Phys. Chem. Chem. Phys.*, 2019, **21**, 5723–5729.

- 18 F. L. Hatton, P. Chambon, A. C. Savage and S. P. Rannard, *Chem. Commun.*, 2016, **52**, 3915–3918.
- 19 S. Flynn, PhD Thesis, Univeristy of Liverpool, 2019.
- 20 D. Horinek, in *Encyclopedia of Applied Electrochemistry*, eds. G. Kreysa, K. Ota and R. F. Savinell, Springer, New York, NY, New York, 2014th edn., 2014, pp. 343–346.
- 21 T. I. Morozova, V. E. Lee, A. Z. Panagiotopoulos, R. K. Prud'Homme, R. D. Priestley and A. Nikoubashman, *Langmuir*, 2019, **35**, 709–717.
- 22 E. J. W. Verwey, *J. Phys. Colloid Chem.*, 1947, **51**, 631–636.
- 23 B. Derjaguin and L. Landau, *Prog. Surf. Sci.*, 1941, **50**, 633–662.
- 24 L. Wu, J. Zhang and W. Watanabe, *Adv. Drug Deliv. Rev.*, 2011, **63**, 456–469.
- 25 J. Ford, P. Chambon, J. North, F. L. Hatton, M. Giardiello, A. Owen and S. P. Rannard, *Macromolecules*, 2015, **48**, 1883–1893.
- 26 J. S. Lee, S. J. Hwang and D. S. Lee, *Macromol. Res.*, 2009, **17**, 72–78.
- 27 A. Varela-Moreira, Y. Shi, M. H. A. M. Fens, T. Lammers, W. E. Hennink and R. M. Schiffelers, *Mater. Chem. Front.*, 2017, **1**, 1485–1501.
- 28 X. Yan, M. Delgado, J. Aubry, O. Gribelin, A. Stocco, F. Boisson-Da Cruz, J. Bernard and F. Ganachaud, *J. Phys. Chem. Lett.*, 2018, **9**, 96–103.
- 29 J. K. Beattie, A. M. Djerdjev and G. G. Warr, *Faraday Discuss.*, 2008, **141**, 9–30.
- 30 K. Roger and B. Cabane, *Angew. Chemie - Int. Ed.*, 2012, **51**, 5625–5628.
- 31 B. W. Ninham and M. Boström, *Cell. Mol. Biol.*, 2005, **51**, 803–813.
- 32 P. Legrand, S. Lesieur, A. Bochot, R. Gref, W. Raatjes, G. Barratt and C. Vauthier, *Int. J. Pharm.*, 2007, **344**, 33–43.
- 33 S. Galindo-Rodriguez, E. Allémann, H. Fessi and E. Doelker, *Pharm. Res.*, 2004, **21**, 1428–1439.
- 34 U. Bilati, E. Allémann and E. Doelker, *Eur. J. Pharm. Sci.*, 2005, **24**, 67–75.
- 35 T. Nakano, *Polym. J.*, 2010, **42**, 103–123.
- 36 G. S. Bumbrah, G. S. Sodhi and J. Kaur, *Egypt. J. Forensic Sci.*, 2019, **9**, 3–9.

CHAPTER 3

37 P. Meakin and F. Family, *Phys. Rev. A*, 1987, **36**, 5498–5501.

# **CHAPTER 4**

## **SN-38 ENCAPSULATION AND PHARMACOLOGICAL STUDIES**

## 4.1 Introduction

There have been several systems that have succeeded in the encapsulation of SN-38 with the intent for intravenous delivery to tumour sites. A number of these systems involve polyester-based nanoparticles, such as PLGA, decorated with active targeting moieties specific to a selected form of cancer. For example, PEG-PCL based nanoparticles decorated with a cancer stem-cell-like antibody, CD133Ab, successfully encapsulated SN-38 by freeze-drying and dispersion and were shown to selectively target colorectal cancer cells, reducing tumour growth.<sup>1</sup> SN-38 was also encapsulated in PLGA microspheres, as an example of a non-active targeting system, synthesised by emulsion-solvent evaporation achieving 6.89 wt% drug content. *In vivo* analysis of these systems revealed that tumour growth was significantly inhibited; however these microspheres were directly injected into the tumour; therefore their ability to target the tumour site was not assessed.<sup>2</sup> Although these examples have shown that encapsulation of SN-38 is possible in a variety of systems encapsulation *via* co-nanoprecipitation seems to be lacking within literature reports with only a small number of examples; such as work encapsulating the drug within pHPMA based nanoparticles by Ford *et al.*<sup>3</sup>

Investigations completed in the previous chapters laid the foundation for the work to be carried out within this chapter with the ultimate goal of achieving the successful encapsulation of SN-38. The polymers produced in Chapter 2 showed both the versatility of MSA catalysed ROP, but more relevantly the use of novel substituted caprolactone monomers allowed the thermal adaptation of the resulting polymer species. Similarly, the alteration of architecture also allowed access to different thermal properties, although this effect was less pronounced. Furthermore, the application of the five mono-functional monomers, one bi-functional monomer and two initiators, targeting four different architectures, created a polymer library ideal for the exploration of nanoparticle formation and guest encapsulation. The differences in thermal properties and crystallinity, gained by the alteration of the polymer backbone, may allow the tuning of favourable interactions with SN-38 to increase the likelihood of encapsulation. Additionally, these interactions could also improve the encapsulation ability of the resulting nanoparticles, thereby increasing the drug loading achieved.

Following methods previously outlined by Rannard and co-workers, (co)-nanoprecipitation from acetone and THF allowed the exploration of the influence good solvent choice and amphiphilic stabiliser to branched polymer ratio have on nanoparticle formation in Chapter 3.

This defined the conditions for further studies investigating the impact of polymer architecture and monomer selection on the resultant physicochemical properties of the particles. The studies also allowed proof-of-concept encapsulation studies with Oil red O and docetaxel to confirm the potential for guest-host studies using drug molecules. Analysis of these systems after storage confirmed that the presence of a guest molecule had little effect on stability over time.

### 4.1.1 Chapter aims

This chapter aims to build on the work and insights gained in the previous chapters, mentioned above, and take steps towards the encapsulation and assessment of SN-38 within polyester nanoparticles. The encapsulation SN-38 and SN-38-derived drug molecules is expected to be possible but it is hypothesised that macromolecular architecture may influence the ability of each polymer to obtain significant drug loadings. Therefore this is expected to allow for the investigation of possible polymer-drug interactions. An initial target of 2.43 wt% drug loading is expected to allow for comparisons to Oil red O and docetaxel encapsulation and build a foundation to understand the impact of increased drug loading. Polymer-drug interactions and the consequences these have on drug encapsulation, and nanoparticle stability are also important to explore. Furthermore, it is postulated that the variability in thermal properties and crystallinity of the polymers may affect encapsulation and stability.

Pharmacological behaviour, specifically drug release, cytotoxicity, macrophage uptake and *in vivo* pKa studies, will help to gain a complete overview of the behaviour of these nanoparticles within a biological setting and offer a view of future medicinal value.

### 4.2 Encapsulation of SN-38-based drug molecules *via* co-nanoprecipitation

The encapsulation of SN-38 and SN-38 derivatives was conducted *via* co-nanoprecipitation using both PEG<sub>x</sub>-*b*-PCL<sub>40</sub> and PEG<sub>5K</sub>-*b*-PSCM<sub>40</sub> stabilising hydrophobic branched polymers which have already been shown to successfully form stable nanoparticle systems in the absence of drug (Chapter 3, Section 3.2 & 3.3). Studies were conducted following the same methodology implemented in Chapter 3 with the addition of 1 mL THF solution, containing polymer and drug (5 mg mL<sup>-1</sup> polymer concentration with varying amounts of drug) to 5 mL deionised water targeting a final concentration, after evaporation, of 1 mg mL<sup>-1</sup> (polymer concentration with varying amounts of drug).

### 4.2.1 Encapsulation of SN-38 pentanoate, *SN-38 P*, via co-nanoprecipitation

Considering that SN-38 has previously been shown to be notoriously problematic concerning encapsulation within literature reports,<sup>4</sup> studies began with the encapsulation of SN-38 pentanoate, *SN-38 P*, a ‘pro-drug’ like molecule based on SN-38, with a pentanoate group at carbon 10 (Figure 4.1, B). This was synthesised within the Rannard group by Dr A Dwyer via nucleophilic addition/elimination reaction between pentanoyl chloride and the phenolic group of the drug at room temperature for 12 hours under a nitrogen atmosphere; 4-dimethylaminopyridine, *DMAP*, was used as a catalyst (nucleophilic base) and *N,N*-diisopropylethylamine, *DIPEA*, as a scavenger and the product was purified by silica gel chromatography. As this molecule has a small alkyl chain variation compared to SN-38, this was more desirable as a model for SN-38 than irinotecan, which has been adapted specifically to mitigate the insolubility of SN-38 allowing for intravenous administration (Figure 4.1, A).

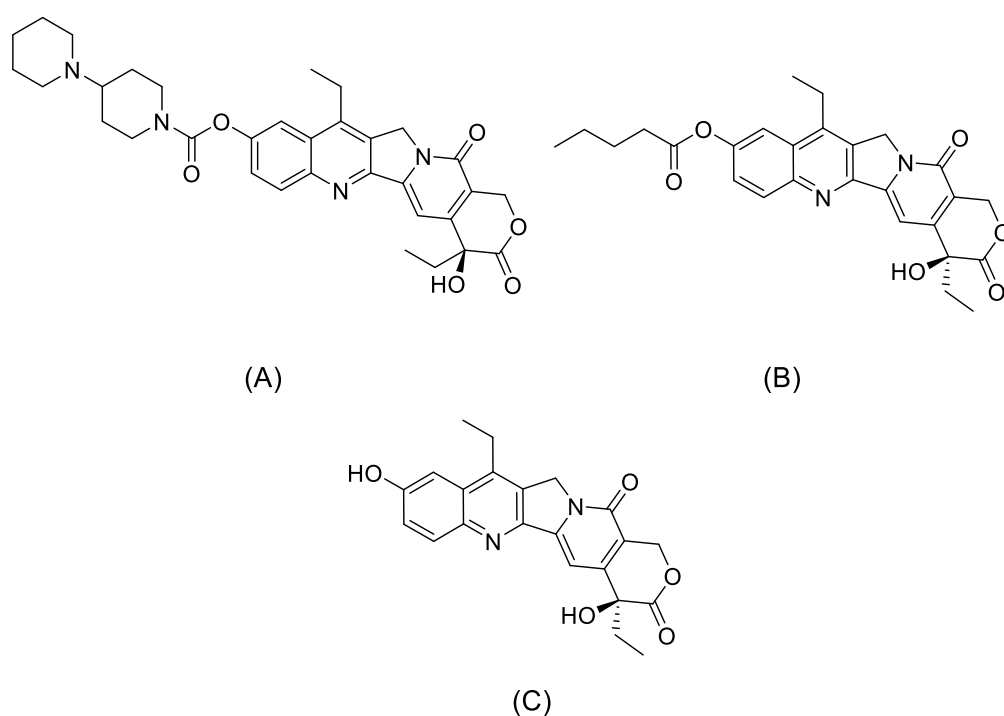


**Figure 4.1- Molecular structures for SN-38 and SN-38 derivatives.** (A) Irinotecan, (B) SN-38 Pentanoate, *SN-38 P*, and (C) SN-38.

Investigations began with a 2.43 wt% drug loading, as discussed above, maintaining the 50:50 wt% amphiphilic block co-polymer to hydrophobic branched polymer ratio. DLS analysis was conducted using unfiltered samples, allowing the physicochemical properties of each nanoparticle dispersion to be defined (Table 4.1).

**Table 4.1 – DLS characterisation of nanoparticles produced by co-nanoprecipitation with PEG<sub>x</sub>-*b*-PCL<sub>40</sub> or PEG<sub>5K</sub>-*b*-PSCM<sub>40</sub> (50:50 wt% ratio A-B block co-polymer to hydrophobic branched polyester) with SN-38 P at 2.43 wt% drug loading.**

Sample	Z-Average Diameter (nm)		Number Average Diameter (nm)		PdI		Zeta Potential (mV)		Derived Count Rate (Attenuator)	
	Day 1	Day 14	Day 1	Day 14	Day 1	Day 14	Day 1	Day 14	Day 1	Day 14
	PEG <sub>2K</sub> - <i>b</i> -PCL <sub>40</sub> : PCL <sub>40</sub> - <i>co</i> -BOD <sub>0.7</sub>	100	100	45	50	0.240	0.300	-25	-25	112125 (6)
PEG <sub>2K</sub> - <i>b</i> -PCL <sub>40</sub> : PMOP <sub>40</sub> - <i>co</i> -BOD <sub>0.7</sub>	105	105	45	50	0.290	0.290	-20	-20	117225 (6)	124740 (6)
PEG <sub>2K</sub> - <i>b</i> -PCL <sub>40</sub> : PPOP <sub>40</sub> - <i>co</i> -BOD <sub>0.7</sub>	115	115	65	65	0.165	0.160	-25	-25	324035 (5)	299575 (5)
PEG <sub>2K</sub> - <i>b</i> -PCL <sub>40</sub> : PBOP <sub>40</sub> - <i>co</i> -BOD <sub>0.7</sub>	105	100	55	50	0.315	0.265	-25	-20	139350 (6)	204695 (5)
PEG <sub>2K</sub> - <i>b</i> -PCL <sub>40</sub> : PPHLOP <sub>40</sub> - <i>co</i> -BOD <sub>0.7</sub>	95	90	50	50	0.185	0.190	-20	-20	303595 (5)	293575 (5)
PEG <sub>5K</sub> - <i>b</i> -PCL <sub>40</sub> : PCL <sub>40</sub> - <i>co</i> -BOD <sub>0.7</sub>	125	120	65	40	0.260	0.260	-20	-20	220770 (5)	224760 (5)
PEG <sub>5K</sub> - <i>b</i> -PCL <sub>40</sub> : PMOP <sub>40</sub> - <i>co</i> -BOD <sub>0.7</sub>	110	105	55	65	0.190	0.195	-25	-20	129950 (6)	196015 (5)
PEG <sub>5K</sub> - <i>b</i> -PCL <sub>40</sub> : PPOP <sub>40</sub> - <i>co</i> -BOD <sub>0.7</sub>	125	125	65	65	0.185	0.190	-25	-20	273780 (5)	266290 (5)
PEG <sub>5K</sub> - <i>b</i> -PCL <sub>40</sub> : PBOP <sub>40</sub> - <i>co</i> -BOD <sub>0.7</sub>	110	110	40	45	0.230	0.210	-25	-20	189380 (5)	124465 (6)
PEG <sub>5K</sub> - <i>b</i> -PCL <sub>40</sub> : PPHLOP <sub>40</sub> - <i>co</i> -BOD <sub>0.7</sub>	105	105	60	60	0.195	0.210	-20	-20	291720 (5)	305970 (5)
PEG <sub>5K</sub> - <i>b</i> -PMOP <sub>40</sub> : PMOP <sub>40</sub> - <i>co</i> -BOD <sub>0.7</sub>	105	100	60	60	0.210	0.170	-20	-20	120935 (6)	119985 (6)
PEG <sub>5K</sub> - <i>b</i> -PPOP <sub>40</sub> : PPOP <sub>40</sub> - <i>co</i> -BOD <sub>0.7</sub>	105	100	50	40	0.345	0.285	-20	-20	102740 (6)	97980 (6)
PEG <sub>5K</sub> - <i>b</i> -PBOP <sub>40</sub> : PBOP <sub>40</sub> - <i>co</i> -BOD <sub>0.7</sub>	110	100	40	50	0.265	0.240	-25	-20	102255 (6)	106700 (6)
PEG <sub>5K</sub> - <i>b</i> -PPHLOP <sub>40</sub> : PPHLOP <sub>40</sub> - <i>co</i> -BOD <sub>0.7</sub>	90	85	45	30	0.275	0.231	-23	-20	215170 (5)	191300 (5)



After solvent evaporation, it was immediately clear that nanoparticle formation was successful with no evident aggregation or precipitation. SN-38 P was assumed to be encapsulated within the nanoparticles due to the lack of precipitate around the glass and a lack of powder sedimentation. DLS characterisation confirmed the presence of nanoparticles in all cases with all dispersions appearing monomodal. When particles were stabilised by PEG<sub>2K</sub>-*b*-PCL<sub>40</sub>  $D_z$  values followed the same trend with varying hydrophobic branched polymer that was observed in Chapter 3 (Section 3.3) with PPOP<sub>40-*co*</sub>-BOD<sub>0.7</sub> based nanoparticles being the largest at 115 nm (Figure 4.2, A, Table 4.1). The PDI values for these five samples, however, did not follow a trend with the values varying significantly with the hydrophobic branched polymer used (Figure 4.2, B). The extension of the PEG block to PEG<sub>5K</sub>-*b*-PCL<sub>40</sub> resulted in larger particles, produced in all five cases, which was to be expected due to the larger PEG corona extending out into the aqueous phase increasing the hydrodynamic radius of the particles. PEG<sub>5K</sub>-*b*-PCL<sub>40</sub>: PPOP<sub>40-*co*</sub>-BOD<sub>0.7</sub> (50:50 wt%) produced the largest particles of 125 nm but this was equalled by PEG<sub>5K</sub>-*b*-PCL<sub>40</sub>: PCL<sub>40-*co*</sub>-BOD<sub>0.7</sub> deviating away from the trend observed with PEG<sub>2K</sub>-*b*-PCL<sub>40</sub> stabilised particles. Furthermore, there was a decrease in the PDI values for all the PEG<sub>5K</sub>-*b*-PCL<sub>40</sub> stabilised systems which was complemented by a decrease in variability between the hydrophobic branched polymers used.

When the hydrophobic block of the stabilising amphiphilic block co-polymer was matched to the hydrophobic branched polymer the trend in  $D_z$  observed in Chapter 3 (Section 3.3) was again replicated with an increase towards BOP based polymers ( $D_z = 110$  nm) followed by a decrease for PHLOP ( $D_z = 90$  nm) (Figure 4.3). PDI became more variable for this set of four systems and no real trend could be deduced. Considering the zeta potentials of all the systems, regardless of amphiphilic PEG co-polymer used, were between -20 and -25 mV this indicated the combined steric and electrostatic stabilisation which had been identified in Chapter 3.

DLS analysis 14 days after initial measurements showed more variability than had been detected in the equivalent systems in the absence of encapsulated guest molecules. This indicates the presence of sedimentation and suggests encapsulation of SN-38 P may not have been as successful as first thought. However, little variation in the derived count rates of all these systems suggests that the number of particles remains relatively constant signifying that sedimentation and aggregation are both minimal over 14 days storage under ambient conditions.

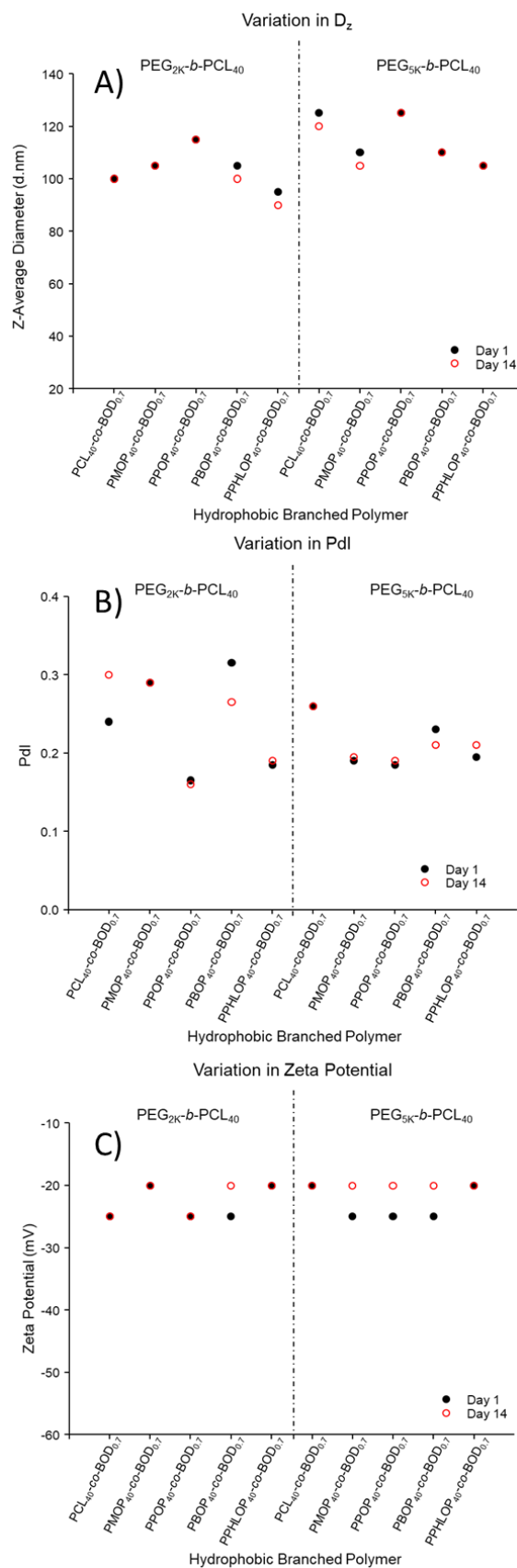


**Figure 4.2-** Graphical representation of physicochemical characteristics from the co-nanoprecipitation of 50:50 wt% PEG<sub>x</sub>-b-PCL<sub>40</sub>: PSCM<sub>40</sub>-co-BOD<sub>0.7</sub> to encapsulate SN-38 P (THF). (A) Z-average diameter, (B) PdI and (C) zeta potential.

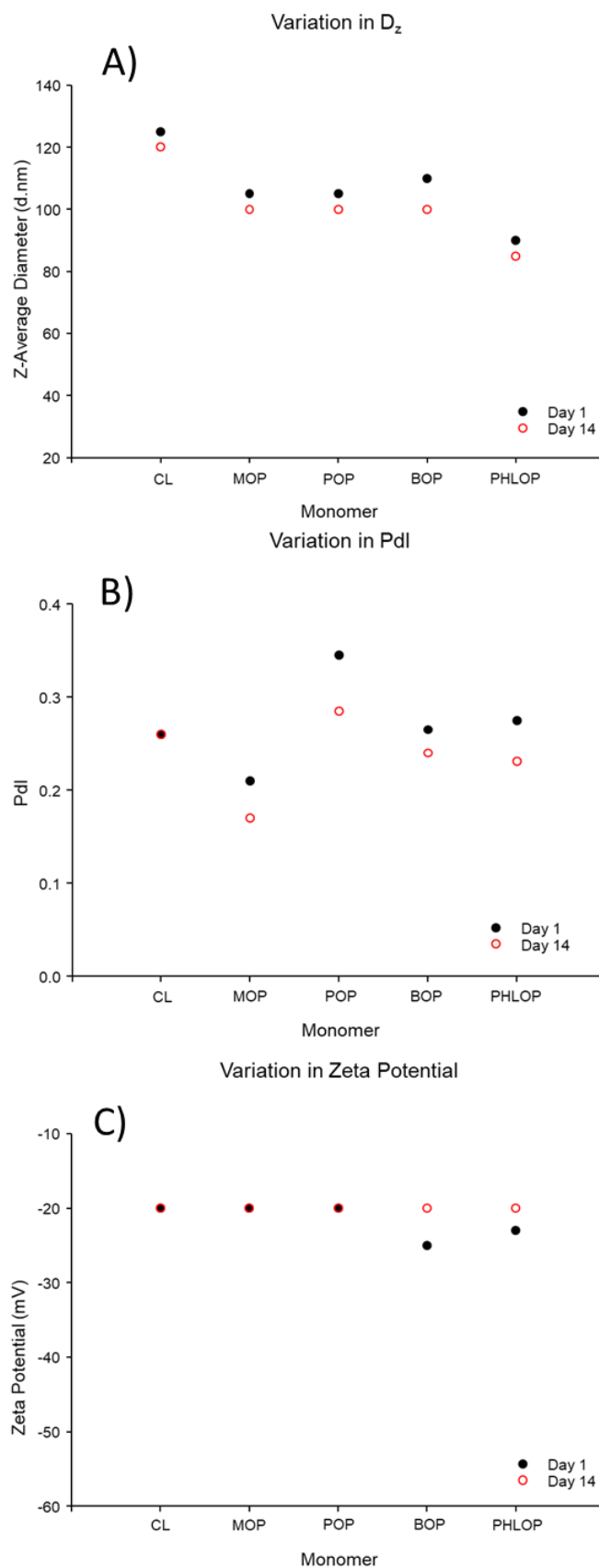


**Figure 4.3-** Graphical representation of physicochemical characteristics from the co-nanoprecipitation of 50:50 wt% PEG<sub>x</sub>-*b*-SCM<sub>40</sub>: PSCM<sub>40</sub>-*co*-BOD<sub>0.7</sub> to encapsulate SN-38 P (THF). (A) Z-average diameter, (B) Pdl and (C) zeta potential.

To gauge the potential of these systems to achieve higher drug loading, SN-38 P content was increased stepwise up to 5 wt%; however, this failed to produce dispersions in which all SN-38 P was contained within the nanoparticles as determined by aggregated material sticking to the sides of each glass vial after solvent evaporation. This material had the appearance of SN-38 P, which indicated that although encapsulation had failed, the formation of polymeric nanoparticles was not affected by the increased drug content. Nonetheless this result combined with evidence from Oil red O encapsulation indicates that there appears to be a limit to the drug loading capabilities of these systems synthesised by co-nanoprecipitation. However, further studies with a more extensive library of hydrophobic guest molecules could expand on whether this limit is universal or unique to specific guest molecules.

#### **4.2.2 Encapsulation of SN-38 *via* co-nanoprecipitation**

Promising encapsulation results generated with Oil red O, docetaxel and SN-38 P prompted investigations using SN-38 *via* co-nanoprecipitation. Several studies were undertaken replicating conditions detailed in Section 4.2.1 and targeting a drug loading of 2.43 wt%. Unfortunately, although encapsulation of this drug molecule has been achieved by co-nanoprecipitation with pHPMA based systems, each attempt utilising the polymers produced in Chapter 2 failed to successfully encapsulate SN-38.<sup>3</sup> At the time of organic solvent addition all nanoparticle dispersions showed no aggregation and/or solid precipitate present; however, after full solvent evaporation, particle dispersions had an iridescent “smoky” appearance thought to be the result of fine crystals of SN-38 (Additional Appendix, page 3). The lack of polymer precipitate would indicate that polyester nanoparticles were still obtained regardless of which polymer was used. Analysis of these samples by optical microscopy revealed the presence of spindle-like crystals which were assigned to SN-38 crystallising and precipitating into the aqueous phase (Figure 4.4).



**Figure 4.4-** Optical microscope images showing the presence of SN-38 crystals in the aqueous phase.

#### **4.2.2.1 Dilution studies of co-nanoprecipitation with guest molecules**

The phenomenon was further investigated with the implementation of dilution studies, a methodology first detailed by Ford *et al.* to explore the nanoprecipitation zone for pHPMA based polymers.<sup>5</sup> It was theorised that the implementation of this methodology would highlight the behaviour of the polyester mixtures (with and without drug) in aqueous solvent environments and therefore indicate any behavioural differences between polyester backbone chemistry and drug molecule presence. Here the polymers without drug, initially chosen as PEG<sub>5K</sub>-*b*-PCL<sub>40</sub>: PCL<sub>40</sub>-*co*-BOD<sub>0.7</sub> (50:50 wt%), were dissolved in THF at various concentrations from 1.5625 to 25 mg mL<sup>-1</sup>, maintaining a fixed final mass of polymer in 5 mL water of 12.5 mg after evaporation. The organic polymer solution was added to 5 mL of water at increasing volumes from 0.5 to 8 mL and DLS analysis was undertaken immediately after THF addition and after solvent evaporation. Plots of derived count rate, *DCR*, *PdI* and *D<sub>z</sub>* values both before and after solvent evaporation against volume of THF added, allowed for the behaviour of the polymers in various solvent mixtures to become clear (Figure 4.5).

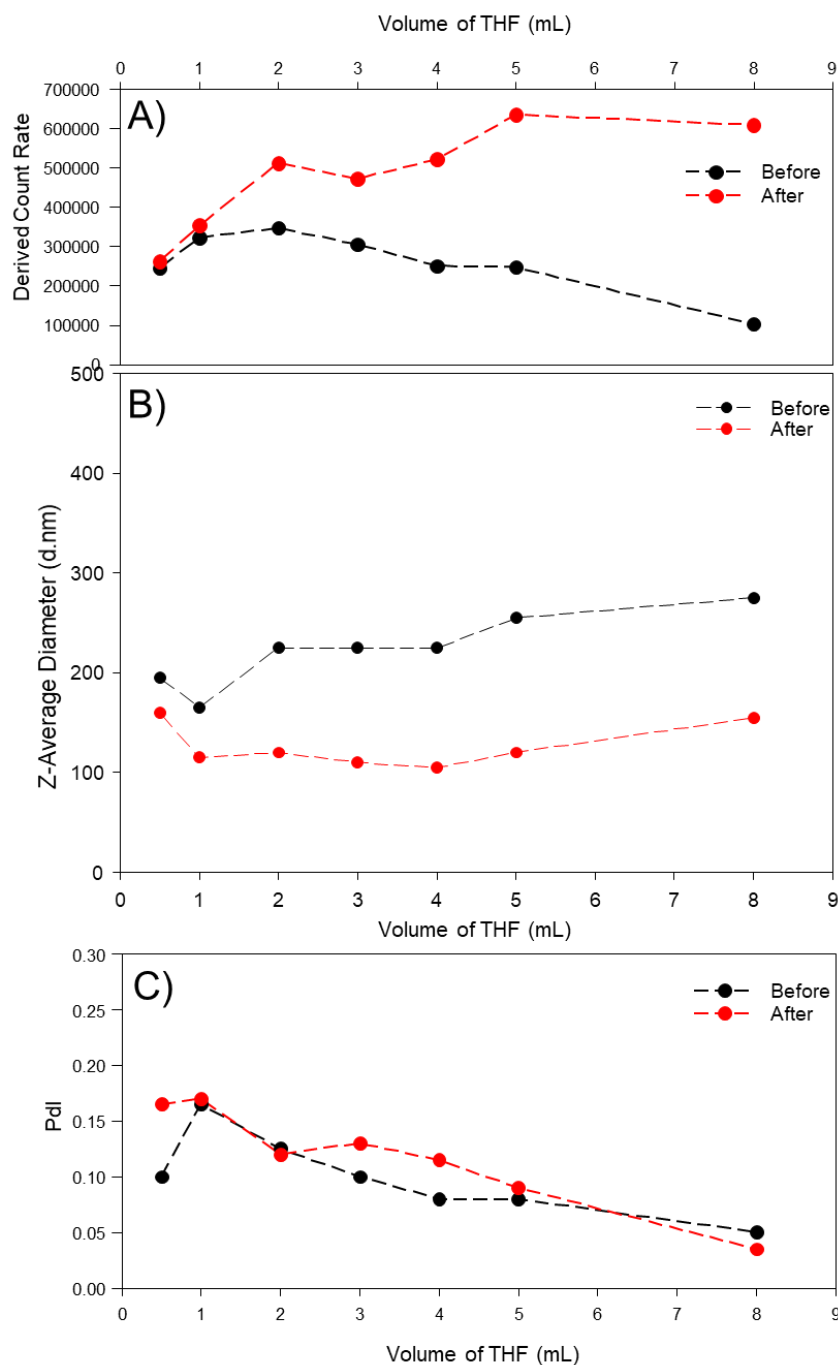


**Figure 4.5 – DLS studies of co-nanoprecipitation of PEG<sub>5K</sub>-*b*-PCL<sub>40</sub> with PCL<sub>40</sub>-*co*-BOD<sub>0.7</sub> varying the THF: 5 mL water ratios keeping a constant mass of polymer (12.5 mg) measured before (black) and after (red) solvent evaporation; (A) derived count rate, (B) Z-average diameter and (C) Pdl.**

The polyester-based systems studied here appear to be significantly more hydrophobic than the various pHPMA-derived materials studies by Ford *et al.*, forming nanoparticles upon instant organic solution addition up to and including a THF: water ratio of 8:5;<sup>5</sup> this suggests that such a solvent-rich aqueous mixture remains a poor solvent for PEG<sub>5K</sub>-*b*-PCL<sub>40</sub>: PCL<sub>40</sub>-*co*-BOD<sub>0.7</sub>

which is in stark contrast to the low concentrations of organic solvent that could be tolerated by pHPMA-derived nanoprecipitates.

The DCR generated for the PEG<sub>5K</sub>-*b*-PCL<sub>40</sub>: PCL<sub>40</sub>-*co*-BOD<sub>0.7</sub> co-nanoprecipitation at all volumes of THF additions indicated nanoprecipitate formation and this observation was mirrored in the  $D_z$  and PdI results of the nanoprecipitates with swollen nanoparticles present within the aqueous/solvent environment and smaller nanoparticles after solvent evaporation. In all instances of THF: water mixtures (from 0.5:5 to 8:5) nanoprecipitates were < 300 nm with PdI values between 0.050 and 0.165 which would indicate a fast nucleation step and rapid growth. The decrease in  $D_z$  values and increase in DCR is consistent with THF evaporation, causing the de-swelling of nanoparticles as trapped THF solvating polymer chains, exits the system. The lack of variability between PdI values before and after solvent evaporation would indicate that solvent evaporation does little to affect the monodispersity of the system which must be defined upon instant addition of the THF/polymer mixture to the aqueous phase. This further eludes to fast nucleation and a fast growth period with a rapid termination, as slow growth would most likely result in macro-precipitation with large  $D_z$  and PdI values.

The nanoprecipitation process was also studied in the presence of SN-38 dissolved in the THF solutions (12.5 mg polymer mass remained constant) to study the impact of a guest molecule. Here, PEG<sub>5K</sub>-*b*-PCL<sub>40</sub>: PCL<sub>40</sub>-*co*-BOD<sub>0.7</sub> and PEG<sub>5K</sub>-*b*-PCL<sub>40</sub>: PPOP<sub>40</sub>-*co*-BOD<sub>0.7</sub> (50:50 wt%) were both investigated to also analysed the impact of polyester chemistry on the nanoprecipitation outcomes; the drug content was fixed at a 2.43 wt% drug loading with respect to polymer. DLS analysis provided the DCR, PdI and  $D_z$  before and after evaporation which were all plotted against volume of THF added to 5 mL water (Figure 4.6).

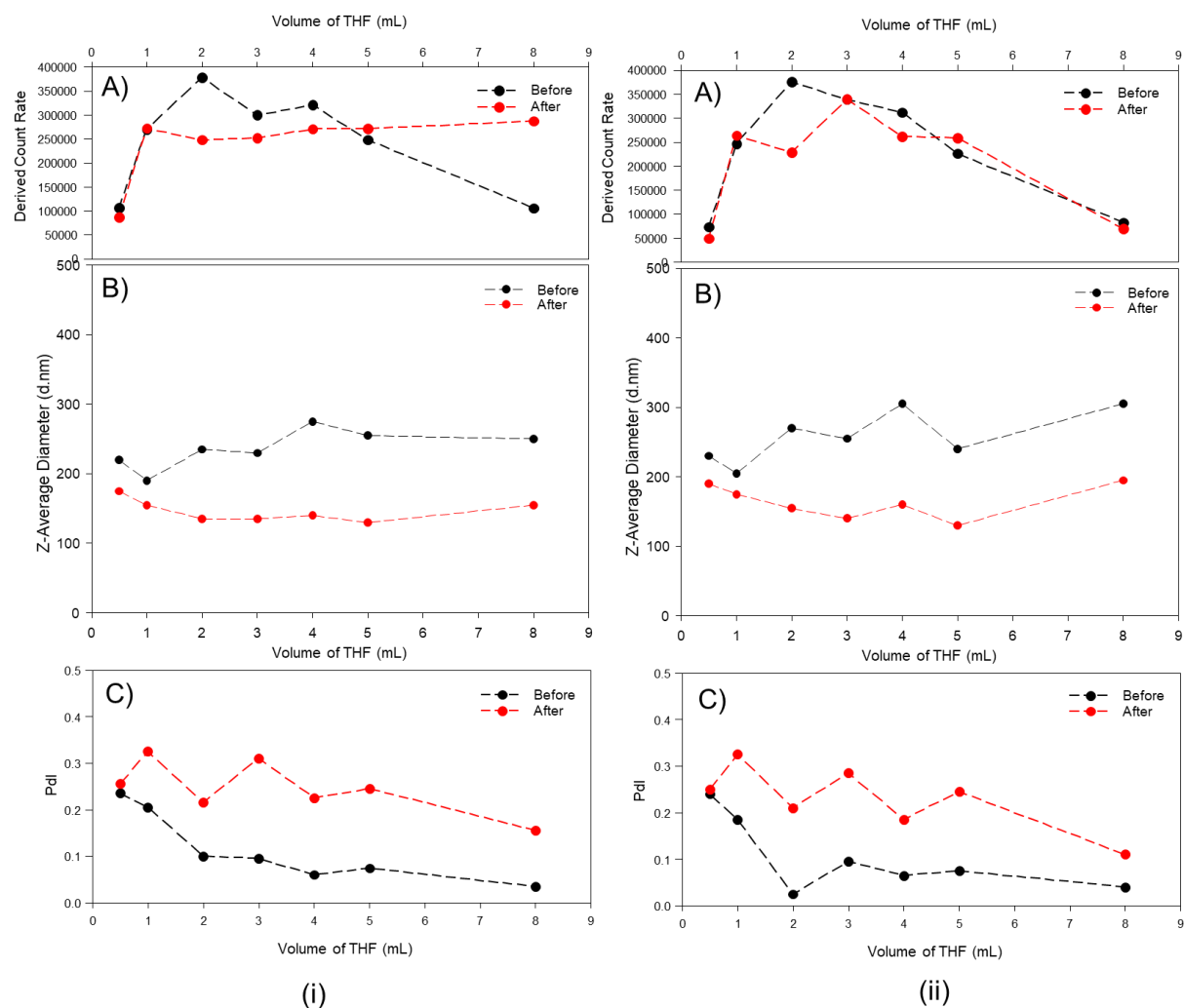


**Figure 4.6 – DLS studies of co-nanoprecipitation of PEG<sub>5K</sub>-*b*-PCL<sub>40</sub> and SN-38 with either PCL<sub>40</sub>-*co*-BOD<sub>0.7</sub> or PPOP<sub>40</sub>-*co*-BOD<sub>0.7</sub> varying the THF: 5 mL water ratios keeping a constant mass of polymer (12.5 mg) measured before (black) and after (red) solvent evaporation; (A) derived count rate, (B) Z-average diameter and (C) Pdl; for (i) PEG<sub>5K</sub>-*b*-PCL<sub>40</sub>: PCL<sub>40</sub>-*co*-BOD<sub>0.7</sub> and (ii) PEG<sub>5K</sub>-*b*-PCL<sub>40</sub>: PPOP<sub>40</sub>-*co*-BOD<sub>0.7</sub>.**



The chemistry of the hydrophobic branched polymer backbone appeared to have minimal effect on the behaviour of the nanoprecipitation with both systems producing highly similar results. The only significant difference between the two systems was a lack of increase in DCR for the PEG<sub>5K</sub>-*b*-PCL<sub>40</sub>: PPOP<sub>40</sub>-*co*-BOD<sub>0.7</sub> when 8 mL THF was added. This could indicate a change in the solvent/polymer interactions during the nanoprecipitation mechanism. Comparison to the blank PCL-based dispersions revealed that the presence of drug had little impact on the nanoprecipitation behaviour of each system. Nonetheless a greater increase in PDI after solvent evaporation was observed in the drug-containing systems. This was most likely due to drug crystals precipitating in the aqueous dispersions due to failed encapsulation. Combined with the decrease in  $D_z$  values after solvent evaporation, this reinforces the hypothesis (detailed in Section 4.2.2) that although encapsulation of SN-38 was unsuccessful polymeric nanoparticles were still formed. This would also indicate that the crystals observed in Figure 4.4 by optical microscopy were indeed indicative of the drug.

Finally, studies of the SN-38 nanoprecipitation in the absence of polymer were conducted. The final drug mass in 5 mL water was maintained at 0.3125 mg which reflected the concentrations and conditions used on the presence of polymer. The same treatment of the DLS data collected in the presence of organic solvent allowed the comparisons to be drawn with the previous two studies undertaken in this way (Figure 4.7). As the drug nanoparticles were unstable in an aqueous environment, DLS analysis was not undertaken after solvent evaporation as the data collected would have been inaccurate after sedimentation.

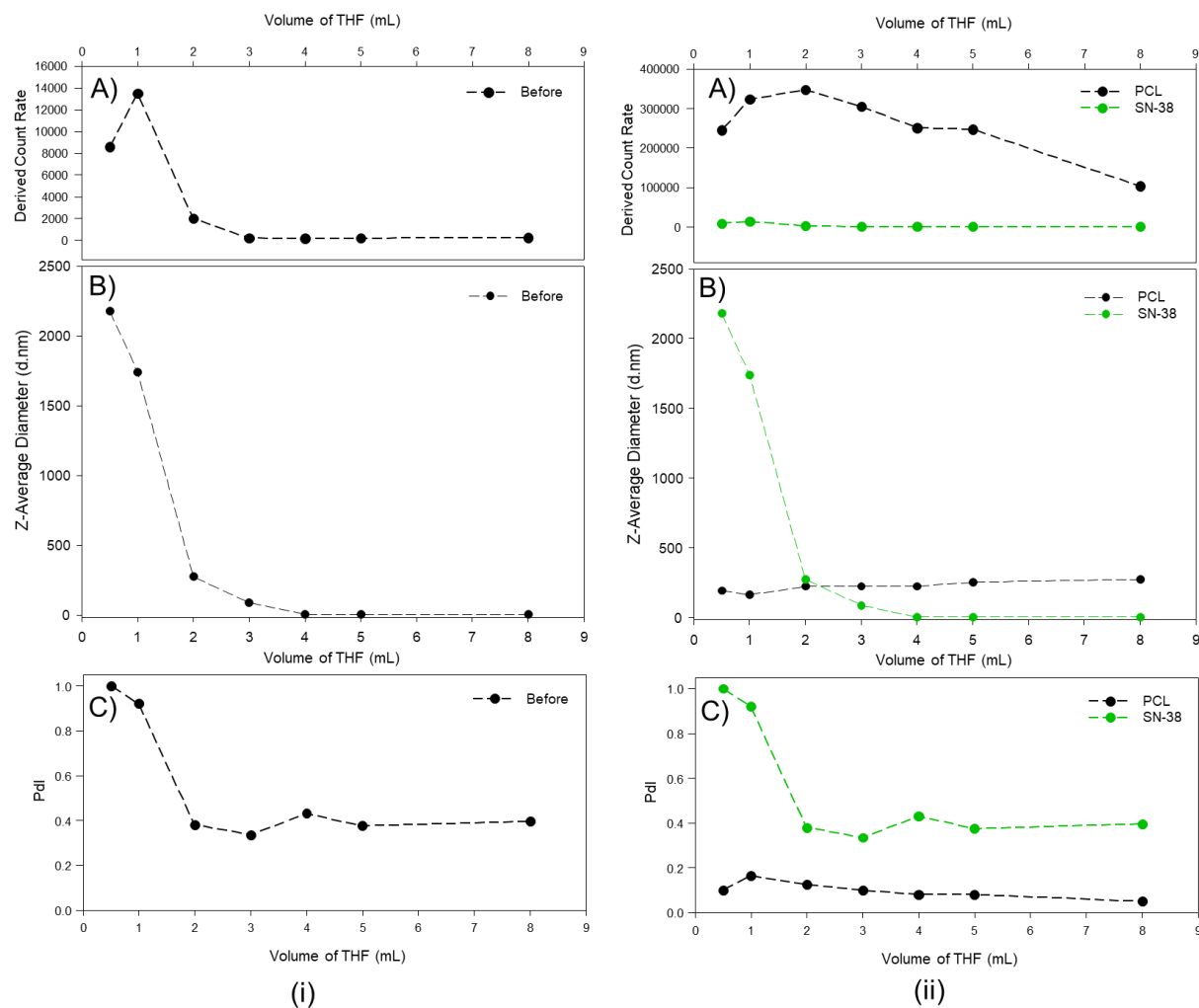


**Figure 4.7 – DLS studies of nanoprecipitation of SN-38 varying the THF: 5 mL water ratios keeping a constant drug mass in 5 mL water (0.3125 mg); (A) derived count rate, (B) Z-average diameter and (C) Pdl; for (i) SN-38 alone (solvent present) and (ii) SN-38 compared with PEG<sub>5K</sub>-*b*-PCL<sub>40</sub>: PCL<sub>40</sub>-*co*-BOD<sub>0.7</sub> with no drug (solvent present).**

Firstly, considering the DCR, when the THF volume increased above 1 mL addition, the DCR fell to 1980 kcps followed by values < 200 kcps indicative of a sample with very limited light scattering (Figure 4.7, i). This was mirrored in the  $D_z$  values which dropped dramatically when volumes of THF greater than 1 mL were added, and this would suggest that SN-38 is significantly soluble in THF/water mixtures containing low concentrations of THF. Comparison with the co-nanoprecipitation of PEG<sub>5K</sub>-*b*-PCL<sub>40</sub>: PCL<sub>40</sub>-*co*-BOD<sub>0.7</sub> (50:50 wt%) in the absence of SN-38 markedly highlights the different behaviour of the polymers and SN-38, especially at relatively low volumes of THF in water. When the volume of THF added to water is < 2 mL, the SN-38 seems to form large structures that may be crystallites or aggregates. This behaviour, when combined with increased solubility of SN-38 at higher ratios of THF: water, explains the failure of SN-38 encapsulation *via* co-nanoprecipitation described above.

It is hypothesised that utilising the co-nanoprecipitation method, detailed in Section 4.2.2, the addition of THF containing both the chosen polymer mixtures (e.g. 50:50 wt% PEG<sub>5K</sub>-*b*-PCL<sub>40</sub>: PCL<sub>40</sub>-*co*-BOD<sub>0.7</sub>) and SN-38 results in the instantaneous formation of polyester nanoparticles but SN-38 remains soluble within the THF/water mixture until solvent evaporation results in the precipitation of drug crystals. Given this remarkable behaviour, similar studies were conducted to evaluate the three species already shown to undergo successful encapsulation in this model but in the absence of polymer, namely Oil red O, docetaxel and SN-38 P (Figure 4.8). As may be expected, each of the guest molecules showed differences in the behaviour exhibited by SN-38 alone.

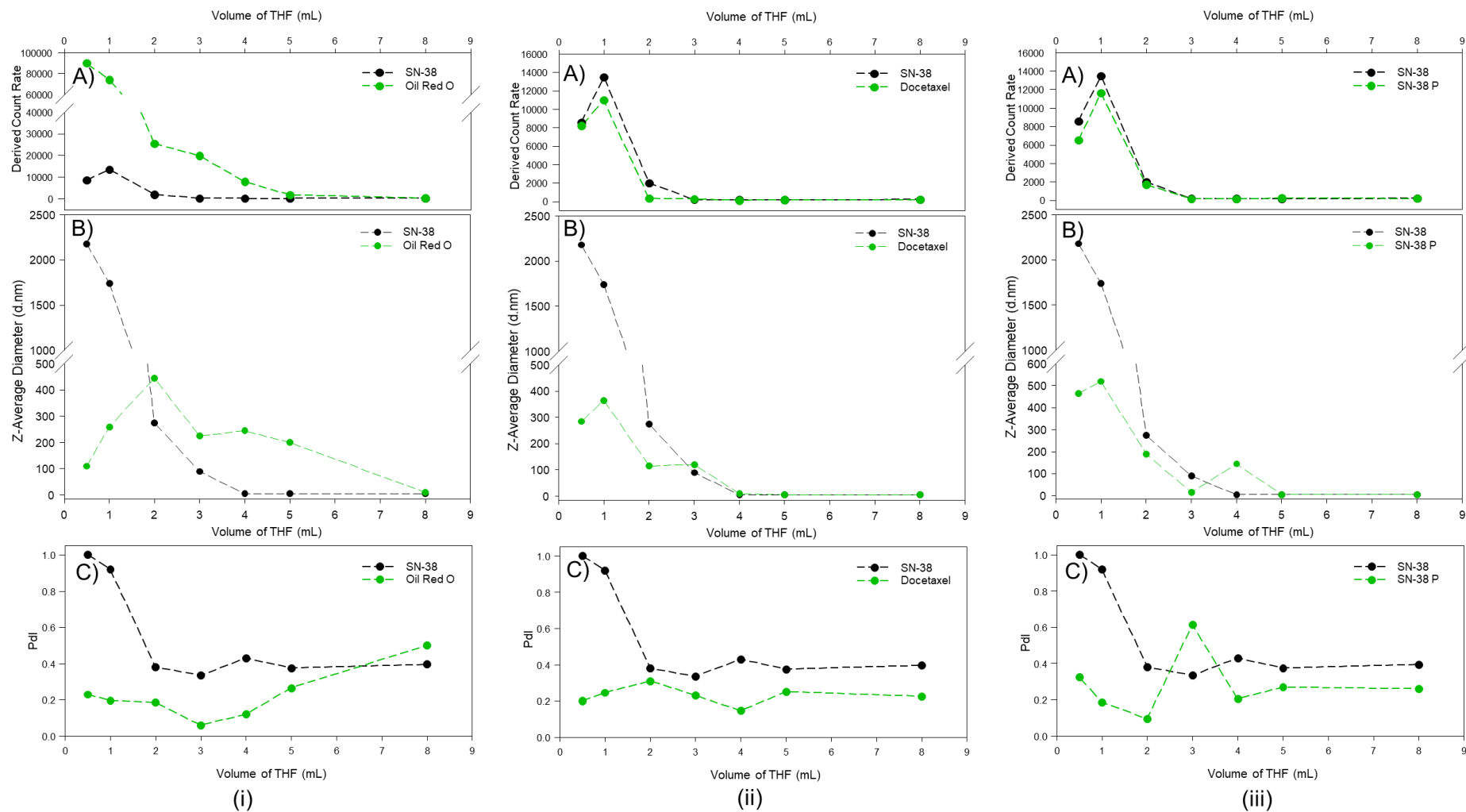


**Figure 4.8 – DLS studies of nanoprecipitation of guest molecules varying the THF: 5 mL water ratios keeping a constant drug mass in 5 mL water (0.3125 mg); compared to SN-38 (solvent present); (A) derived count rate, (B) Z-average diameter and (C) Pdl; for (i) Oil red O, (ii) Docetaxel and (iii) SN-38 P.**

Firstly, Oil red O showed an apparent decreased solubility in the THF: water mixtures compared to SN-38 with significant scattering and measurable nanoparticle diameters in mixtures containing up to 4-5 mL THF in water (Figure 4.8, i). This behaviour is more complementary to the nanoprecipitation behaviour of polyester-based nanoparticle systems, allowing encapsulation within polymer nanoparticles at relatively high THF concentrations.

Docetaxel and SN-38 P both showed less significant differences when compared to SN-38, particularly when observing the DCR generated by each system (Figure 4.8, ii & iii). Both drug molecules displayed similar DCR values to the corresponding SN-38 sample, indicating increased solubility in the THF: water mixture when the THF volume exceeded 2 mL. This was also reflected in the  $D_z$  values collected for both docetaxel and SN-38 P where  $D_z$  fell  $< 10$  nm when THF volumes were  $\geq 5$  mL. Nonetheless  $D_z$  values observed when the volume of THF was  $\leq 2$  mL for both docetaxel and SN-38 P were significantly smaller than those generated by SN-38 for the same volumes.

### **4.3 Evaluation of nanoparticle formation *via* a thin film hydration method using novel polyesters**

The failure to encapsulate SN-38 *via* co-nanoprecipitation, effectively ruled out this route for nanoparticle formation. It was hypothesised that processes that did not contain significant THF concentrations would allow both the polymers and drug guest molecule to be in a similarly unfavourable environment upon the addition of water; the hydrophobic nature of all the components would promote interactions whilst minimising the energy of the system and enable encapsulation. The most common technique involving the removal of organic solvent before water addition is thin film hydration; commonly used for the formation of liposomes. Typically, phospholipids are deposited onto a substrate or electrode and the resulting lipid bilayer films are reconstituted in water; rehydration times (a few minutes to several days) are known to define the physicochemical properties of the resulting liposomes. Further control of liposome properties can be achieved utilising ultrasonication.<sup>6</sup>

More recently polymeric nanoparticles have also been successfully synthesised by implementing this method with polyesters seeming popular within this research area. Zhang *et al.* produced ‘flower-like’ nanoparticles utilising PCL-PEG-PCL co-polymers to encapsulate doxorubicin *via* a thin film hydration method followed by ultrasonic dispersion. This method resulted in nanoparticles capable of encapsulating 8.72 wt% doxorubicin, with  $D_z$  values below 200 nm, which displayed enhanced tumour accumulation combined with long-term drug

release.<sup>7</sup> However the technique used required a large number of steps including dissolving polymer and drug in separate solvents.

Reports of a SN-38 specific study utilising thin film hydration methods to synthesise drug-loaded PEG-PCL nanoparticles have been published but little detail was provided to describe sonication conditions or the drug loading capabilities of the resulting particles. Nonetheless these particles were shown to eliminate colorectal cancer lung metastasis *in vivo*.<sup>8</sup> Following a review of the literature, it is also important to note that studies targeting polymeric nanoparticles *via* this route generally include a hydrophilic PEG block within the co-polymer to aid the hydration process.<sup>7-9</sup>

The bespoke polyesters with varying architectures and amphiphilicity synthesised within this study seemed to be ideal candidates for thin film hydration evaluation, whilst considering the concentrations and ratios of the polymers shown in Chapter 3 to form stable nanoparticles.

### 4.3.1 Thin film co-hydration using multiple polymeric species

Development of a thin film hydration method to synthesise well-defined particles utilised the same systems that had been investigated for co-nanoprecipitation, i.e. a hydrophobic branched polymer stabilised by an amphiphilic block co-polymer. As co-nanoprecipitation studies had revealed that 50:50 wt% ratio (amphiphilic block co-polymer to hydrophobic branched species) produced nanoparticle dispersions with the all-round best physicochemical properties, this ratio was used again. Exploration of thin film hydration methods utilised PEG<sub>5K</sub>-*b*-PCL<sub>40</sub> stabilised PCL<sub>40</sub>-*co*-BOD<sub>0.7</sub> and PPOP<sub>40</sub>-*co*-BOD<sub>0.7</sub> branched polymers in the presence and absence of SN-38 (2.43 wt%). Each thin film was created by the evaporation of a 5 mg mL<sup>-1</sup> THF/polymer solution (0.5 mL, with or without SN-38) to dryness using rotary evaporation under vacuum, followed by the addition of water (2.5 mL) to hydrate the resulting thin film to target a final polymer concentration of 1 mg mL<sup>-1</sup> in aqueous media.

Hydration was studied using either vortex mixing (approximately 5 minutes followed by sonication) or direct sonication of each sample after water addition; in all cases sonication was conducted for five minutes in an ultrasonic bath. Unfortunately, each sample displayed visible aggregation regardless of the method of hydration used, therefore further exploration was conducted implementing overnight stirring of each sample after water addition to provide a longer rehydration period. Sonication using a Covaris focussed ultrasound instrument was also implemented due to the direct and consistent sonication available using this more controllable

approach. Polymer and drug concentrations were kept consistent, targeting a final polymer concentration in water of  $1 \text{ mg mL}^{-1}$  and DLS characterisation was undertaken before and after sonication to determine the effects of sonication on the resulting dispersions. Samples were sonicated for 5 minutes when using the ultrasound bath; however, samples sonicated *via* the Covaris used a controlled and focused 70 W for 60 seconds.

Interestingly, particles containing only PCL based polymers failed to form stable dispersions both with and without SN-38, whereas 50:50 wt% PEG<sub>5K</sub>-*b*-PCL<sub>40</sub>: PPOP<sub>40-co</sub>-BOD<sub>0.7</sub> mixtures produced dispersions that could be readily characterised by DLS after sonication (Table 4.2). DLS characterisation before sonication indicated that dispersions containing PCL<sub>40-co</sub>-BOD<sub>0.7</sub> generally produced larger particles. Overall the DCR combined with the  $D_z$  values for each of the samples indicated the formation a small number of large particles. Once sonication was completed DLS characterisation of the dispersions produced by 50:50 wt% PEG<sub>5K</sub>-*b*-PCL<sub>40</sub>: PPOP<sub>40-co</sub>-BOD<sub>0.7</sub> showed a decrease in  $D_z$  to  $< 400 \text{ nm}$  and PdI to values below 0.6 whilst the DCR increased nearly two-fold in most cases, apart from the dispersion containing SN-38 which was treated with the Covaris (Table 4.2).

**Table 4.2- DLS characterisation of nanoparticles produced by thin film co-hydration, stabilised by PEG<sub>5K</sub>-*b*-PCL<sub>40</sub> without and with 2.43 wt% SN-38 investigating sonication techniques.**

SN-38 Loading (wt%)	Before Sonication <sup>a</sup>				Sonication method	After Sonication			
	Dz (nm)	Dn (nm)	PdI	Derived Count Rate (kcps)		Dz (nm)	Dn (nm)	PdI	Derived Count Rate (kcps)
PEG <sub>5K</sub> - <i>b</i> -PCL <sub>40</sub> : PCL <sub>40</sub> - <i>co</i> -BOD <sub>0.7</sub>									
0	1610	1255	0.355	276575 (4)	Ultrasound bath				Unstable
0	790	185	0.510	93880 (6)	Covaris				Unstable
2.43	910	265	0.650	106680 (6)	Ultrasound bath				Unstable
2.43	1060	235	0.665	82305 (6)	Covaris				Unstable
PEG <sub>5K</sub> - <i>b</i> -PCL <sub>40</sub> : PPOP <sub>40</sub> - <i>co</i> -BOD <sub>0.7</sub>									
0	505	145	0.515	61945 (6)	Ultrasound bath	340	95	0.460	107760 (5)
0	615	185	0.575	79705 (5)	Covaris	350	90	0.425	12035 (5)
2.43	790	260	0.705	69620 (6)	Ultrasound bath	335	105	0.525	126095 (5)
2.43	340	85	0.430	74710 (6)	Covaris	205	80	0.340	84115 (6)

<sup>a</sup> **DATA ACQUIRED NOT ACCURATE** - multimodal distributions obtained and data does not consistently meet DLS quality criteria for these measurements.

Analysis of the particle distributions (plotted against intensity) and correlograms for PEG<sub>5K</sub>-*b*-PCL<sub>40</sub>: PPOP<sub>40</sub>-*co*-BOD<sub>0.7</sub> particles indicated that before sonication all four samples were multimodal in appearance and could not be considered as successful dispersions (Figure 4.9). Correlograms also displayed similar results with only one sample, PEG<sub>5K</sub>-*b*-PCL<sub>40</sub>: PPOP<sub>40</sub>-*co*-BOD<sub>0.7</sub> containing SN-38 (treated with the Covaris), displaying an acceptable sigmoidal curve. Following sonication *via* an ultrasound bath, samples displayed only small changes in the particle distribution curves which was mirrored in the correlograms (Figure 4.9, B i & ii). The samples treated with the Covaris showed the particle distribution curves becoming less multimodal and more consistent over 3 measurements (Figure 4.9, B iii & iv). Regardless of the method of sonication, samples containing SN-38 were more unimodal which may signify an impact in the nanoparticle formation from the presence of drug in the solid state.



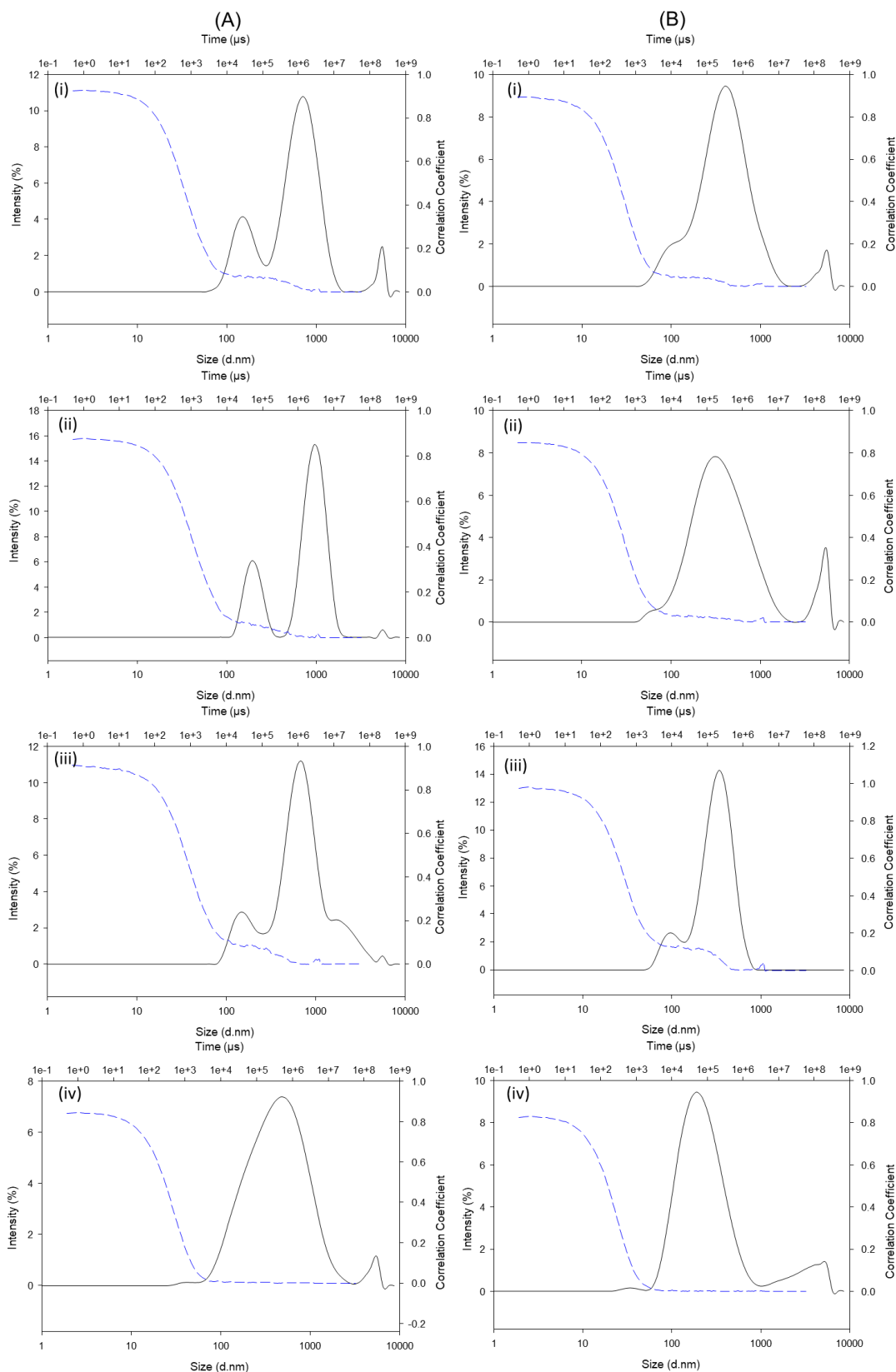


**Figure 4.9-** Size by intensity distributions (black) and correlograms (blue dashed) of nanoparticles generated from the co-hydration of PEG<sub>5K</sub>-*b*-PCL<sub>40</sub>: PPOP<sub>40</sub>-*co*-BOD<sub>0.7</sub> (50:50 wt%). (A) before sonication, (B) after sonication, (i & ii) ultra sound, (iii & iv) covaris and (i & iii) blank, (ii & iv) 2.43 wt% SN-38.

Although the particles formed in this study displayed physicochemical properties that were quite far from the desired dispersion characteristics, resembling those achievable by co-nanoprecipitation, successful SN-38 encapsulation was thought to have been achieved. Furthermore, the thin film hydration and sonication approach was shown to provide benefits that may allow optimisation. In summary, the steps used here were: 1) evaporation of 0.5 mL of a THF solution containing polymer (and drug) at a polymer concentration of 5 mg mL<sup>-1</sup> under vacuum to produce a 2.5 mg thin polymer film; 2) reconstitution by addition of 2.5 mL water to achieve a final polymer concentration of 1 mg mL<sup>-1</sup> by stirring vigorously overnight; 3) sonication using the Covaris focused ultrasound instrument for 60 seconds at 70 W at ≤ 14 °C (Figure 4.10). DLS characterisation was undertaken before and after sonication to fully assess the nanoparticle dispersions after each step.

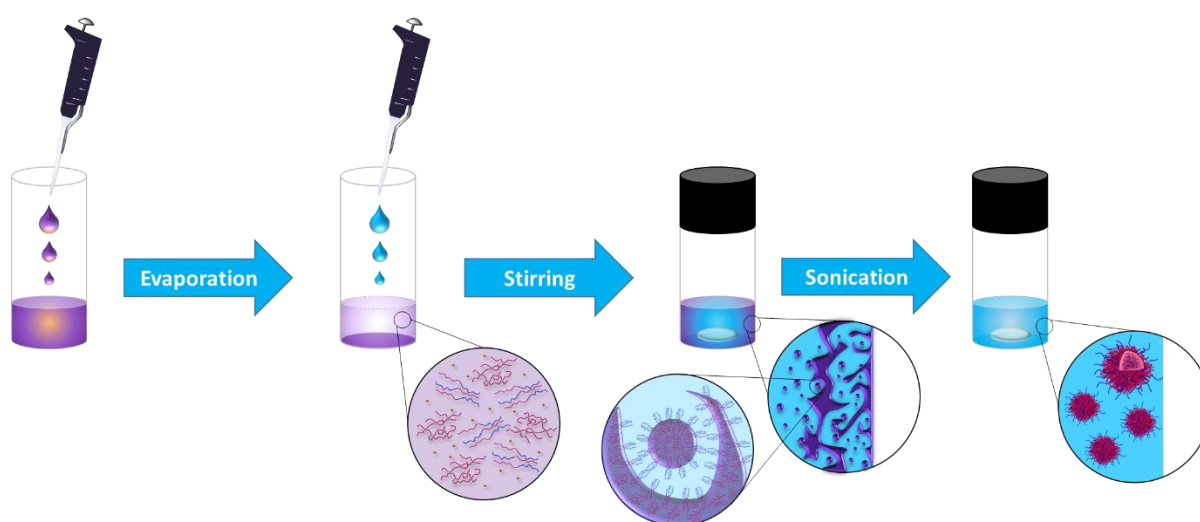


**Figure 4.10- Schematic representation of the thin film hydration method *via* co-hydration of a thin film formed from two polymeric species and SN-38.**

The whole series of hydrophobic branched species stabilised by PEG<sub>5K</sub>-*b*-PCL<sub>40</sub> at 50:50 wt% ratios (in the presence or absence of 2.43 wt% SN-38) was studied to evaluate the benefits of the different polymer chemistries. DLS characterisation before sonication revealed that nanoparticles containing PCL<sub>40</sub>-*co*-BOD<sub>0.7</sub> and PPHLOP<sub>40</sub>-*co*-BOD<sub>0.7</sub> produced the largest particles after hydration with both dispersions with and without SN-38 (4 samples in total) producing D<sub>z</sub> values > 800 nm three of which were > 1000 nm (Table 4.3).

**Table 4.3- DLS characterisation of nanoparticles produced by co-hydration stabilised by PEG<sub>5K</sub>-*b*-PCL<sub>40</sub> without drug and with 2.43 wt% SN-38.**

Hydrophobic branched Polymer	SN-38 Loading (wt%)	Before Sonication <sup>a</sup>				After Sonication				After 7 Days			
		Dz (nm)	Dn (nm)	PdI	Derived Count Rate (kcps)	Dz (nm)	Dn (nm)	PdI	Derived Count Rate (kcps)	Dz (nm)	Dn (nm)	PdI	Derived Count Rate (kcps)
PCL <sub>40-co</sub> -BOD <sub>0.7</sub>	0	820	345	0.580	250140 (5)	Unstable				Unstable			
PMOP <sub>40-co</sub> -BOD <sub>0.7</sub>	0	535	120	0.585	47920 (6)	220	75	0.470	62325 (6)	215	80	0.400	67940 (6)
PPOP <sub>40-co</sub> -BOD <sub>0.7</sub>	0	330	140	0.395	99800 (6)	200	80	0.345	89505 (6)	195	85	0.310	103730 (6)
PBOP <sub>40-co</sub> -BOD <sub>0.7</sub>	0	415	155	0.425	66725 (6)	230	75	0.310	76020 (6)	240	105	0.335	77175 (6)
PPHLOP <sub>40-co</sub> -BOD <sub>0.7</sub>	0	1375	345	0.560	271505 (4)	465	185	0.390	368935 (4)	495	210	0.425	377900 (4)
PCL <sub>40-co</sub> -BOD <sub>0.7</sub>	2.43	1080	590	0.580	174770 (5)	Unstable				Unstable			
PMOP <sub>40-co</sub> -BOD <sub>0.7</sub>	2.43	380	110	0.445	53735 (6)	250	45	0.455	66360 (6)	255	60	0.450	62610 (6)
PPOP <sub>40-co</sub> -BOD <sub>0.7</sub>	2.43	350	90	0.730	40495 (6)	265	35	0.390	28280 (7)	495	65	0.510	85415 (6)
PBOP <sub>40-co</sub> -BOD <sub>0.7</sub>	2.43	480	265	0.420	55650 (6)	275	50	0.370	74470 (6)	285	140	0.345	69775 (6)
PPHLOP <sub>40-co</sub> -BOD <sub>0.7</sub>	2.43	1625	965	0.685	161490 (4)	565	300	0.355	341585 (4)	590	360	0.360	318515 (4)

<sup>a</sup> **DATA ACQUIRED NOT ACCURATE** - multimodal distributions obtained and data does not consistently meet DLS quality criteria for these measurements.

Particles produced using PMOP<sub>40-co-BOD0.7</sub>, PPOP<sub>40-co-BOD0.7</sub> and PBOP<sub>40-co-BOD0.7</sub>, as the branched co-polymer component, successfully formed significantly smaller particles than other polymer combinations, following hydration. This could indicate that semi-crystallinity in the polymers impacts the nanoparticle formation *via* this method and it would be expected that both  $\epsilon$ -CL and PHLOP-based polymers would be semi-crystalline due to polymers synthesised from MOP, POP and BOP each possessing side chains that would prevent the uniform stacking of polymer chains; PHLOP differs here due to the  $\pi$ - $\pi$  stacking that could occur between chains and has the potential to interact with SN-38.<sup>10</sup>

The size by intensity distributions for each sample, regardless of drug presence, were multimodal over three measurements with at least two species clearly visible. After sonication it was clear that both blank and 2.43 wt% SN-38 containing dispersions of PEG<sub>5K-b</sub>-PCL<sub>40</sub>:PCL<sub>40-co-BOD0.7</sub> (50:50 wt%) were unsuccessful with visibly aggregation present; characterised as “smokiness”, emulating that seen during unsuccessful encapsulation *via* co-nanoprecipitation. The rest of the series were void of drug crystals and were successfully characterised by DLS.

DLS characterisation after sonication showed a progression towards a more unimodal distribution, particularly when drug was present, reflecting results gained in the initial studies for method development (Figure 4.11). Size by intensity distributions generated by all the dispersions without drug appeared to be less well-defined, however, this qualitative analysis generated by DLS could not be conclusive evidence of the role SN-38 during nanoparticle formation (Figure 4.11, A). All eight nanoparticle dispersions characterised by DLS after sonication revealed a decrease in  $D_z$  and PdI values producing particles of  $D_z$  values < 500 nm with SN-38 present and < 600 nm when SN-38 was absent (Table 4.3). PdI of each system was below 0.5; however all values were > 0.2 reflecting the relatively broad distributions (Figure 4.11).

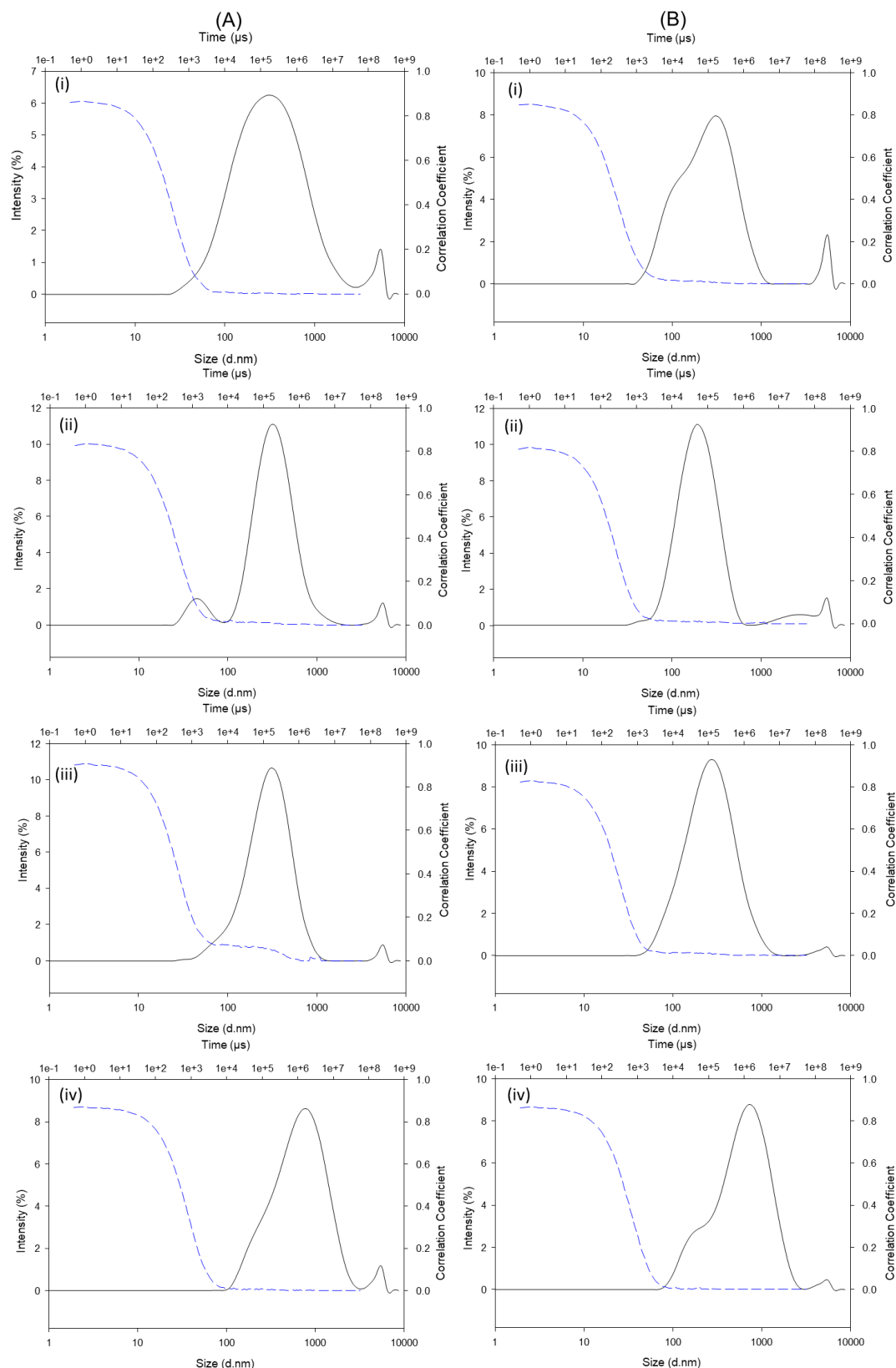


**Figure 4.11 – Size by intensity distributions (black) and correlograms (blue dashed) of nanoparticles generated from the co-hydration of thin films containing PEG<sub>5K</sub>-*b*-PCL<sub>40</sub> and a branched polyester after sonication (50:50 wt%); (A) blank, (B) 2.43 wt% SN-38; (i) PMOP<sub>40-co</sub>-BOD<sub>0.7</sub>, (ii) PPOP<sub>40-co</sub>-BOD<sub>0.7</sub>, (iii) PBOP<sub>40-co</sub>-BOD<sub>0.7</sub>, (iv) PPHLOP<sub>40-co</sub>-BOD<sub>0.7</sub>.**

Finally, DLS characterisation was undertaken after seven days storage under ambient conditions to assess stability and compare with nanoparticles synthesised *via* co-nanoprecipitation (Figure 4.12). The most significant changes in physicochemical properties were seen within pure polymer samples in the absence of drug, with  $D_z$  and PDI values increasing significantly, particularly for PMOP<sub>40-co</sub>-BOD<sub>0.7</sub> containing dispersions which increased from 265 nm (PDI = 0.390) to 495 nm (PDI = 0.510) (Table 4.3). Overall, samples containing SN-38 showed less variation over seven days.

Although monomodal particle distributions utilising this technique have yet to be achieved, the results gained from this study are promising and the method of nanoparticle formation developed here has created dispersions with encapsulated SN-38.

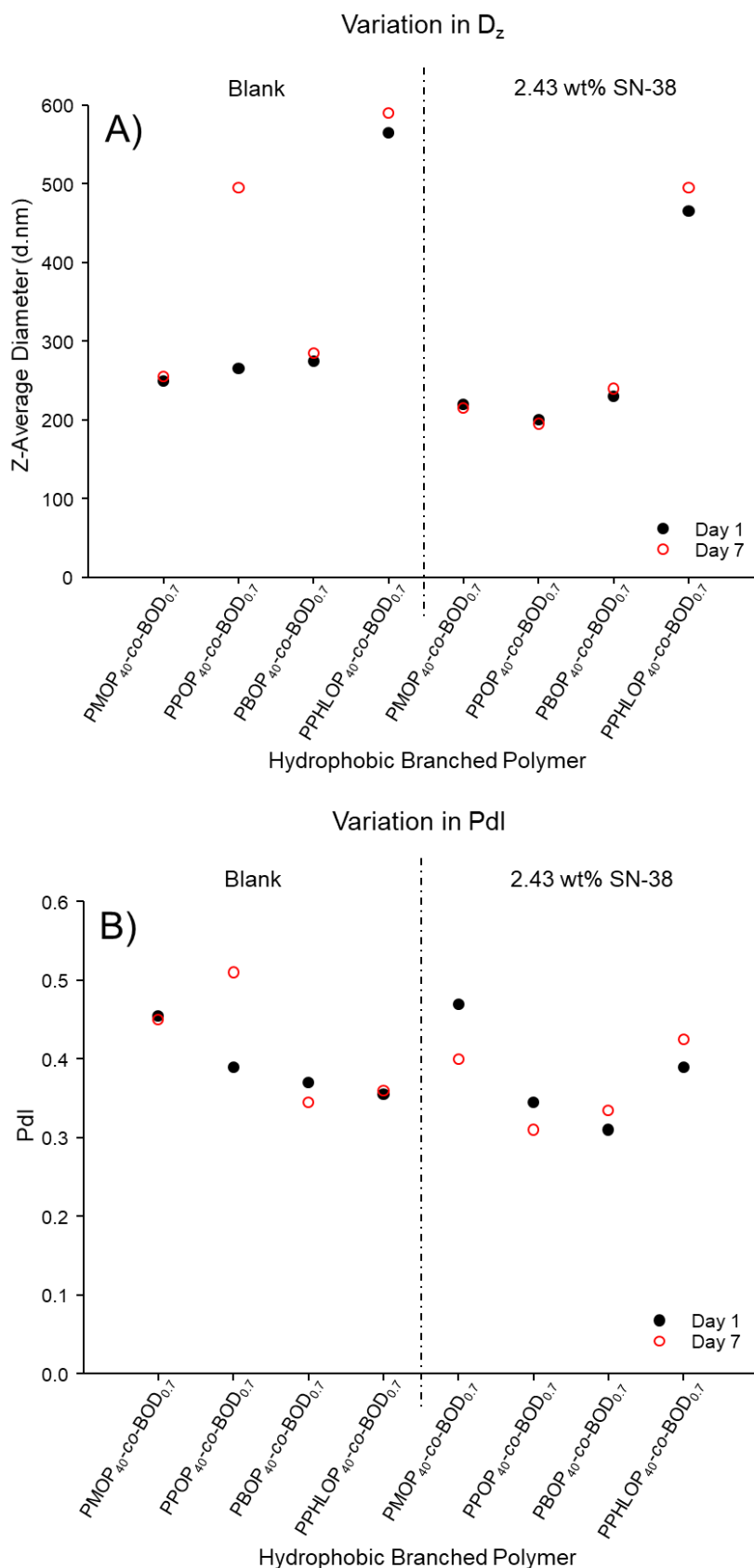


**Figure 4.12 - Graphical representation of variation in physicochemical characteristics of nanoparticles produced by co-hydration; stabilised by PEG<sub>5K</sub>-*b*-PCL<sub>40</sub> without drug and with 2.43 wt% SN-38 over 7 days. (A) Z-average diameter, (B) Pdl.**

### 4.3.2 Thin film hydration using single polymeric species

#### 4.3.2.1 Thin film hydration of branched amphiphilic PEG<sub>5K</sub>/polyester block co-polymers

The use of the branched amphiphilic polymers in a simple binary combination with SN-38 was evaluated using the thin film hydration method described above. It was hypothesised that the branched polyester-PEG co-polymers would be ideal for this investigation, encompassing all the components needed for successful co-nanoprecipitation into one polymeric species. The branched segments of the polymers allows for the formation of an amphiphilic film, deriving hydrophobicity from the branched polyester and hydrophilicity from the PEG<sub>5K</sub> block segments, that is expected to more readily rehydrate and offer steric stability to the resulting nanoparticles.<sup>11</sup> Following the methodology detailed in Section 4.3.1, initial investigations were undertaken both without drug and at 2.43 wt% SN-38 loading allowing comparisons to studies carried out in Section 4.3.1. DLS analysis was undertaken before and after sonication to reveal the changes that had occurred in each system (Table 4.4).

**Table 4.4- DLS characterisation of nanoparticles produced by thin film hydration of PEG<sub>5K</sub>-*b*-PCL/SCM<sub>40</sub>-co-BOD<sub>0.7</sub> without drug and with 2.43 wt% SN-38.**

Monomer	SN-38 Loading (wt%)	Before Sonication <sup>a</sup>				After Sonication			
		Dz (nm)	Dn (nm)	PdI	Derived Count Rate (kcps)	Dz (nm)	Dn (nm)	PdI	Derived Count Rate (kcps)
CL	0	150	40	0.465	23965 (7)	45	25	0.225	7360 (8)
MOP	0	9655	75	0.320	28340 (7)	55	30	0.155	13945 (7)
POP	0	695	100	0.935	52700 (6)	60	40	0.085	28400 (7)
BOP	0	9365	75	0.505	25565 (7)	55	40	0.090	31725 (7)
PHLOP	0	875	705	0.420	48605 (6)	90	40	0.195	72360 (6)
CL	2.43	235	75	0.520	64970 (6)	90	20	0.425	19070 (7)
MOP	2.43	1960	170	1	28855 (7)	70	25	0.235	21715 (7)
POP	2.43	445	165	0.790	58435 (6)	65	40	0.140	41660 (6)
BOP	2.43	605	80	0.860	57865 (6)	70	35	0.320	40155 (6)
PHLOP	2.43	1030	170	0.695	61970 (6)	75	40	0.230	68650 (6)

<sup>a</sup> **DATA ACQUIRED NOT ACCURATE** - multimodal distributions obtained and data does not consistently meet DLS quality criteria for these measurements.



Firstly, considering the five systems produced in the absence of drug (Table 4.4), initial rehydration of the thin films led to very broad multimodal distributions of the dispersed material. Sonication resulted in a dramatic decrease in  $D_z$  values to 45, 55, 60, 55 and 90 nm and PDI values reflected the more homogenous nature of the final nanoparticle dispersions (Table 4.4, Figure 4.13). The five nanoparticle dispersions produced in the absence of SN-38 showed  $D_z$  values below 100 nm and PDI values of  $< 0.3$  (Table 4.4) and unimodal intensity distributions after sonication (Figure 4.13). This was a remarkable result given the multimodal and broad distributions formed when using a 50:50 wt% mixture of a linear amphiphilic block co-polymer and a hydrophobic branched polyester described earlier.

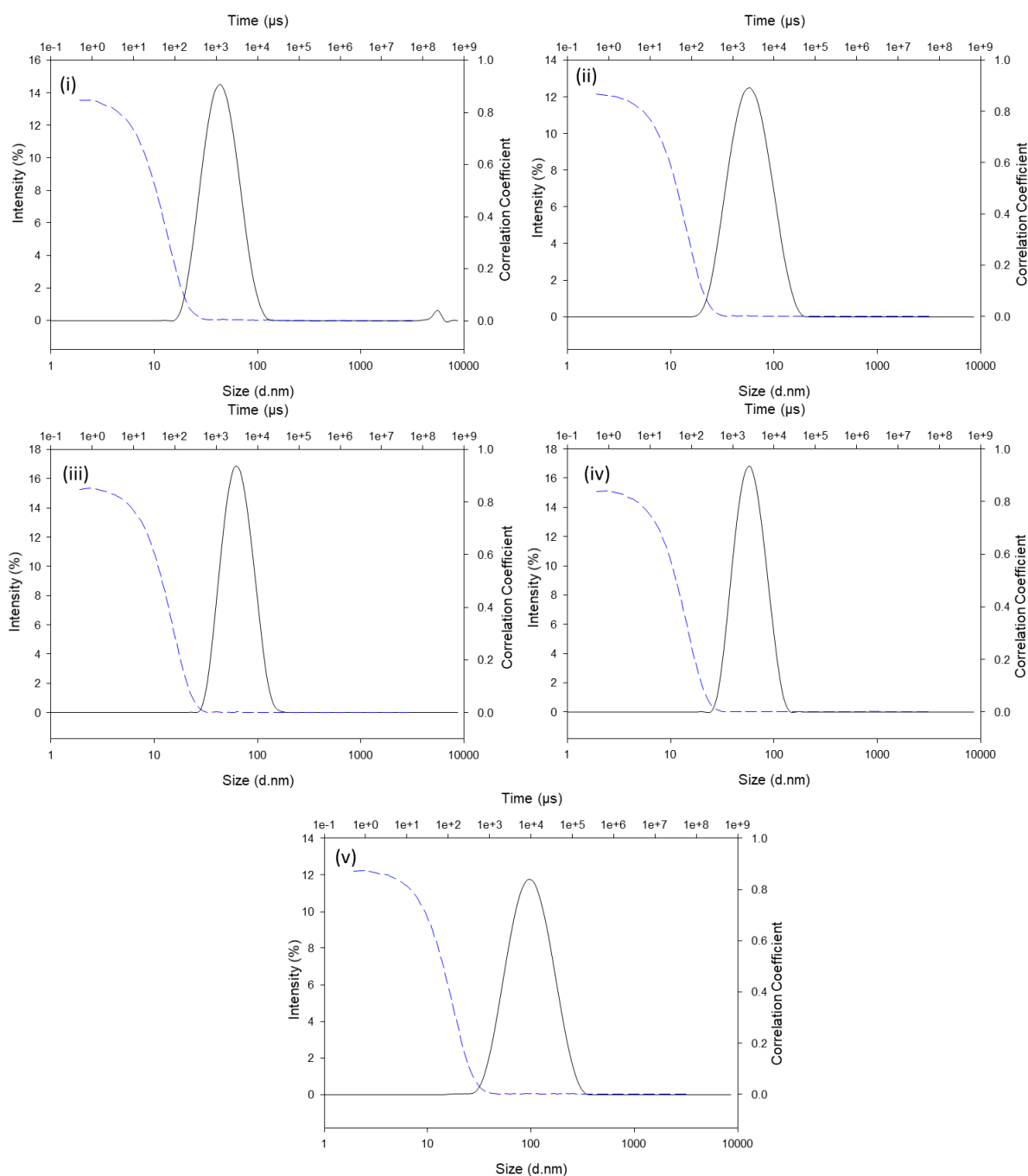


**Figure 4.13- Size by intensity distributions (black) and correlograms (blue dashed) of nanoparticles generated from thin films containing branched amphiphilic co-polymers after sonication (blank). (i) PEG<sub>5K</sub>-*b*-PCL<sub>40</sub>-*co*-BOD<sub>0.7</sub>, (ii) PEG<sub>5K</sub>-*b*-PMOP<sub>40</sub>-*co*-BOD<sub>0.7</sub>, (iii) PEG<sub>5K</sub>-*b*-PPOP<sub>40</sub>-*co*-BOD<sub>0.7</sub>, (iv) PEG<sub>5K</sub>-*b*-PBOP<sub>40</sub>-*co*-BOD<sub>0.7</sub> and (v) PEG<sub>5K</sub>-*b*-PPHLOP<sub>40</sub>-*co*-BOD<sub>0.7</sub>.**

The inclusion of 2.43 wt% SN-38 into the thin films, composed of amphiphilic block copolymers, yielded dispersions with unimodal distributions and  $D_z$  values < 100 nm; however, PDI values were considerably larger, than the counterparts formed without SN-38, ranging from 0.140 to 0.425. An increase in PDI values may not be unexpected as SN-38 particles may also

be present, nonetheless these values were lower than those obtained for the samples prepared in the absence of drug and with branched polyester present (Section 4.3.1). Interestingly, the ability of the branched amphiphilic co-polymers to generate narrow, monomodal particle distributions was not uniformly successful, suggesting an impact of the polymer chemistry in the formation process. For example, PEG<sub>5K</sub>-*b*-PCL<sub>40</sub>-*co*-BOD<sub>0.7</sub>, formed stable dispersions both in the presence and absences of SN-3; when SN-38 was present particle distributions were broad and multimodal (Figure 4.14, A). However, the use of PEG<sub>5K</sub>-*b*-PPOP<sub>40</sub>-*co*-BOD<sub>0.7</sub>, generated drug-loaded nanoparticles with monomodal distributions and low D<sub>z</sub> and PdI values (Table 4.4, Figure 4.14, B).

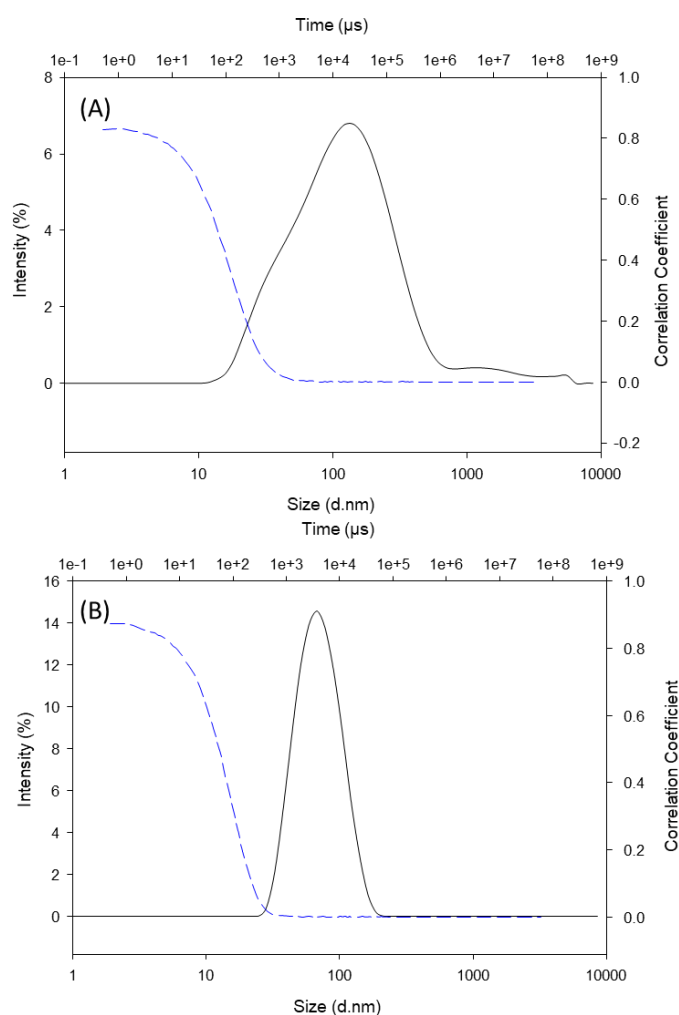


**Figure 4.14- Size by intensity distributions (black) and correlograms (blue dashed) of nanoparticles generated from thin films containing branched amphiphilic co-polymers after sonication in the presence of 2.43 wt% SN-38. (A) PEG<sub>5K</sub>-*b*-PCL<sub>40</sub>-*co*-BOD<sub>0.7</sub> (B) PEG<sub>5K</sub>-*b*-PPOP<sub>40</sub>-*co*-BOD<sub>0.7</sub>.**

The loading of SN-38 was increased incrementally to explore the capability of the approach to generate nanoparticles with high drug content. SN-38 was initially increased to 9.09 wt% and evaluated across each amphiphilic branched block co-polymer option (final polymer concentration in water = 0.5 mg mL<sup>-1</sup>); again, after sonication, successful drug-loaded nanoparticle dispersions were formed (Table 4.5).

**Table 4.5- DLS characterisation of nanoparticles produced by thin film hydration of PEG<sub>5K</sub>-*b*-PCL/SCM<sub>40</sub>-co-BOD<sub>0.7</sub> with 9.09 wt% SN-38.**

Monomer	SN-38 Loading (wt%)	Before Sonication <sup>a</sup>				After Sonication			
		Dz (nm)	Dn (nm)	PdI	Derived Count Rate (kcps)	Dz (nm)	Dn (nm)	PdI	Derived Count Rate (kcps)
CL	9.09	1005	300	0.805	111295 (6)	180	110	0.205	55970 (6)
MOP	9.09	525	80	0.620	67565 (6)	150	45	0.270	75245 (6)
POP	9.09	560	205	0.480	46695 (6)	105	45	0.255	48005 (6)
BOP	9.09	445	80	0.640	58200 (6)	105	35	0.280	50045 (6)
PHLOP	9.09	850	255	0.640	50000 (6)	100	35	0.405	52105 (6)

<sup>a</sup> **DATA ACQUIRED NOT ACCURATE** - multimodal distributions obtained and data does not consistently meet DLS quality criteria for these measurements.

SN-38 content was increased to values of 16.6, 33, 50, and 75 wt%, each maintaining a final polymer concentration of 1 mg mL<sup>-1</sup> in water. Overall, increasing SN-38 content with respect to polymer increased D<sub>z</sub> regardless of the polymer used within the system (Figure 4.15, A). These values ranged from 45 nm in the absence of drug (PEG<sub>5K</sub>-*b*-PCL<sub>40</sub>-co-BOD<sub>0.7</sub>) to 240 nm when the resulting nanoparticles contained 75 wt% SN-38 (PEG<sub>5K</sub>-*b*-PPHLOP<sub>40</sub>-co-BOD<sub>0.7</sub>). This was not completely to be expected as it may be possible to generate a greater number of nanoparticles as SN-38 dominates the hydrophobic “core” but it is also possible that a degree of crystallisation occurs at higher drug content. PdI values did not vary considerably with increasing SN-38 loading, with the exception of several samples with that lower drug loadings (Figure 4.15, B); there was a slight increase in PdI between 16.6 and 33 wt% drug loading which appeared to decrease as drug loading increased to 50 and 75 wt% (Figure 4.15, B).

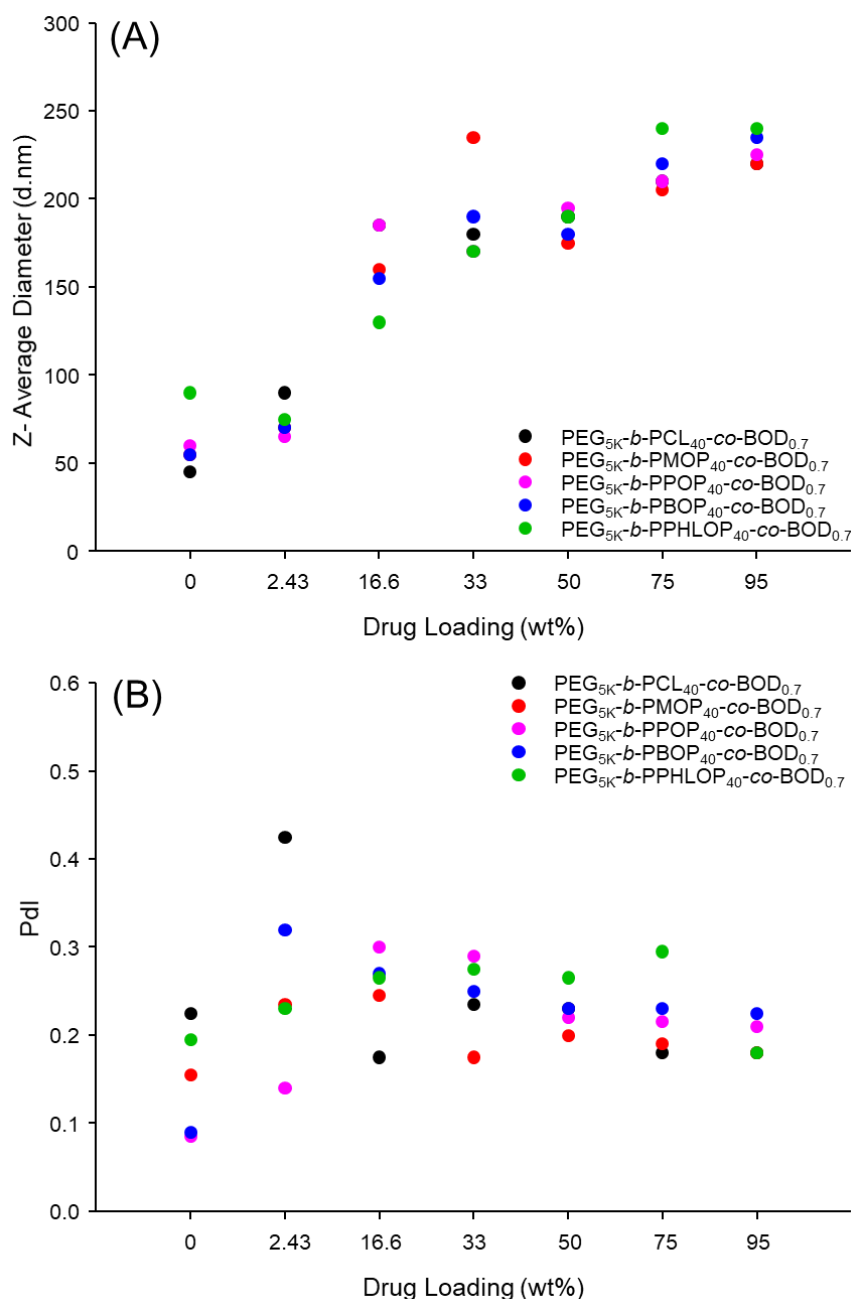


**Figure 4.15-** Graphical representation of physicochemical characteristics of nanoparticles generated *via* thin film hydration of PEG<sub>5K</sub>-b-PCL/SCM<sub>40</sub>-co-BOD<sub>0.7</sub> with increased SN-38 content. (A) Z-average diameter, (B) PdI.

The particle distributions observed before and after sonication reflected trends observed in earlier studies with a reduction in multimodality of each dispersion and subsequent, decrease in PdI. Monomodal particle distributions were observed for PEG<sub>5K</sub>-b-PMOP<sub>40</sub>-co-BOD<sub>0.7</sub> and PEG<sub>5K</sub>-b-PPOP<sub>40</sub>-co-BOD<sub>0.7</sub> after sonication regardless of drug content; however the other three polymers generated multimodal particle distributions after sonication at lower SN-38 loadings (Figure 4.16 & 4.17). At 50 wt% SN-38, small additional peaks, or artefacts, in all five samples were seen, possibly indicating the presence of un-encapsulated drug (Figure

4.17, A). SN-38 drug loadings were increased further to 95 wt% SN-38; due to the high drug content with respect to polymer the final polymer concentration was  $0.05 \text{ mg mL}^{-1}$  and SN-38 in water was  $1 \text{ mg mL}^{-1}$ . Surprisingly all five polymers produced stabilised nanoparticle dispersions with  $D_z$  values between 220-240 nm and PDI values  $<0.25$  in all cases (Figure 4.15, A & B). These values followed the trend of increasing  $D_z$  with increasing drug content; however, this increase was not as large as may have been expected. Interestingly after sonication all five dispersions produced monomodal distributions with only small artefacts present on single measurements for PEG<sub>5K</sub>-*b*-PBOP<sub>40-co</sub>-BOD<sub>0.7</sub> stabilised particles (Figure 4.17, C).

The overwhelming success of this technique for the hypothesised encapsulation of SN-38 highlights the significance differing solubility of the polymer and SN-38 in THF/water mixtures when attempting co-nanoprecipitation earlier (Section 4.2.2). The successful encapsulation of SN-38 *via* thin film hydration benefits from the solvent-free aqueous rehydration and the replacement of the hydrophobic branched polyester “core” component with SN-38 generates a film composed purely of amphiphilic branched block co-polymer and various ratios of drug. The ability to include such high drug content does suggest that detailed studies of the structure and stability are warranted before any pharmacological evaluation should be undertaken.

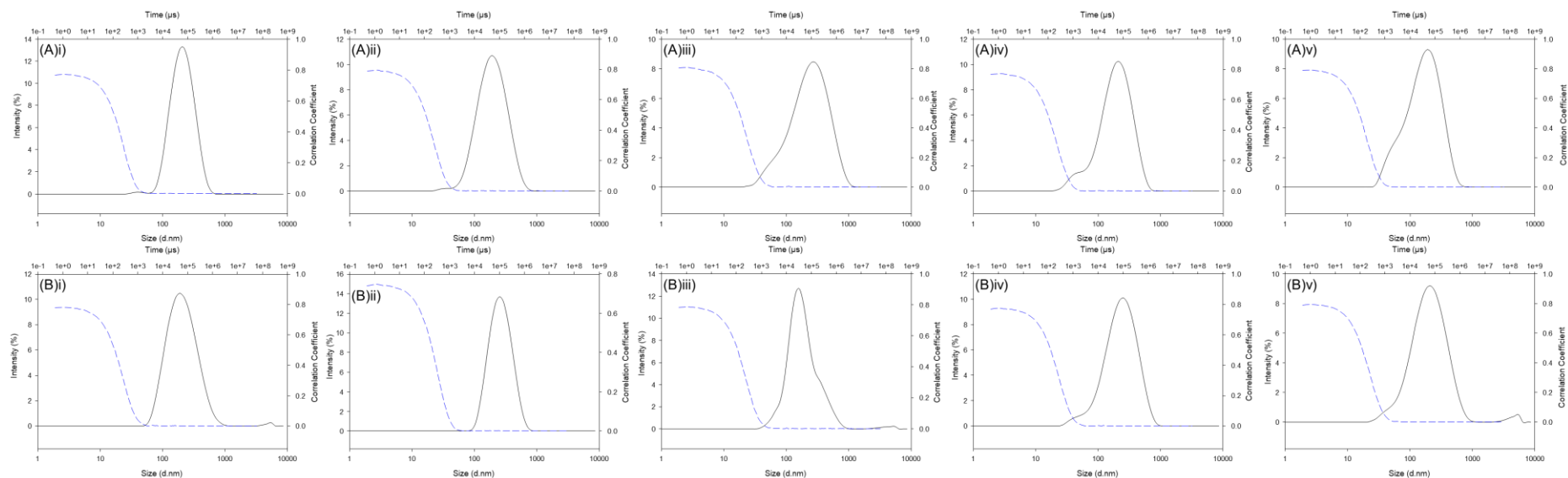


**Figure 4.16-** Size by intensity distribution (black) and correlograms (blue dashed) of nanoparticles generated from thin films containing branched amphiphilic co-polymers after sonication ((A) 16.6 wt% and (B) 33 wt% SN-38). (i) PEG<sub>5K</sub>-*b*-PCL<sub>40</sub>-*co*-BOD<sub>0.7</sub>, (ii) PEG<sub>5K</sub>-*b*-PMOP<sub>40</sub>-*co*-BOD<sub>0.7</sub>, (iii) PEG<sub>5K</sub>-*b*-PPOP<sub>40</sub>-*co*-BOD<sub>0.7</sub>, (iv) PEG<sub>5K</sub>-*b*-PBOP<sub>40</sub>-*co*-BOD<sub>0.7</sub> and (v) PEG<sub>5K</sub>-*b*-PPHLOP<sub>40</sub>-*co*-BOD<sub>0.7</sub>.

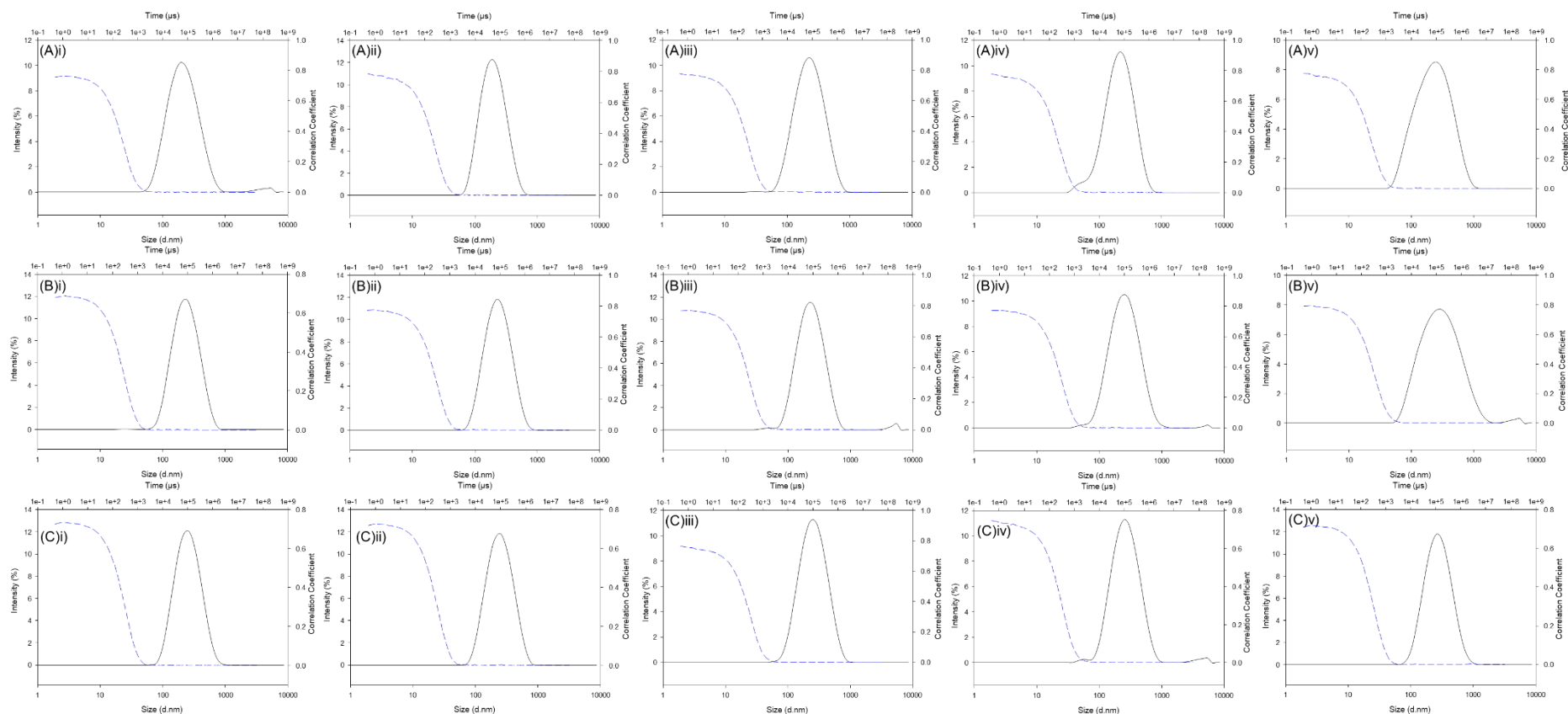


**Figure 4.17- Size by intensity distribution (black) and correlograms (blue dashed) of nanoparticles generated from thin films containing branched amphiphilic co-polymers after sonication ((A to C) 50, 75 & 95 wt% SN-38). (i) PEG<sub>5K</sub>-*b*-PCL<sub>40</sub>-*co*-BOD<sub>0.7</sub>, (ii) PEG<sub>5K</sub>-*b*-PMOP<sub>40</sub>-*co*-BOD<sub>0.7</sub>, (iii) PEG<sub>5K</sub>-*b*-PPOP<sub>40</sub>-*co*-BOD<sub>0.7</sub>, (iv) PEG<sub>5K</sub>-*b*-PBOP<sub>40</sub>-*co*-BOD<sub>0.7</sub> and (v) PEG<sub>5K</sub>-*b*-PPHLOP<sub>40</sub>-*co*-BOD<sub>0.7</sub>.**



### 4.3.2.2 Stability of nanoparticles created *via* thin film hydration of an amphiphilic branched polyester co-polymer and SN-38

Unlike aqueous nanoparticle dispersions generated *via* co-nanoprecipitation, thin film hydration offers a solid state sample format that has the potential to be stored for long periods of time before rehydration. Two avenues can therefore be explored to assess the stability of these samples: a) the stability of the dry thin film when stored and b) the stability of the aqueous dispersion after rehydration. It is hypothesised that the solid state storage with the thin film hydration approach will extend the storage time significantly when compared to those stored as an aqueous dispersion.

#### 4.3.2.2.1 Stability of dry thin films formed during the thin film hydration process

The polymers used in this study were PEG<sub>5K</sub>-*b*-PMOP<sub>40</sub>-*co*-BOD<sub>0.7</sub> and PEG<sub>5K</sub>-*b*-PPOP<sub>40</sub>-*co*-BOD<sub>0.7</sub> as both these polymers consistently produced monomodal nanoparticle dispersions over the whole range of drug loadings explored. SN-38 content used in this study was defined as 10, 30, 50 and 75 wt% to cover a large range that reflected the nanoparticles detailed in Section 4.3.2.1. Ten thin film samples were generated from each THF polymer/drug stock solution containing one of the selected polymers at each of the four drug loadings (Figure 4.18). The films were formed following the methodology developed in Section 4.3.1 resulting in a 1 mg mL<sup>-1</sup> polymer in water dispersion. Therefore, as the polymer mass remained constant (2.5 mg) in each thin film, the mass of SN-38 increased within the films and an increased light yellow colour was seen (Figure 4.18). Results were obtained over 10 time points by the rehydration, sonication and DLS characterisation of each film undertaken on the day of analysis occurring; a) every week for the first 5 time points followed by b) every 2 weeks for the last 5 time points.

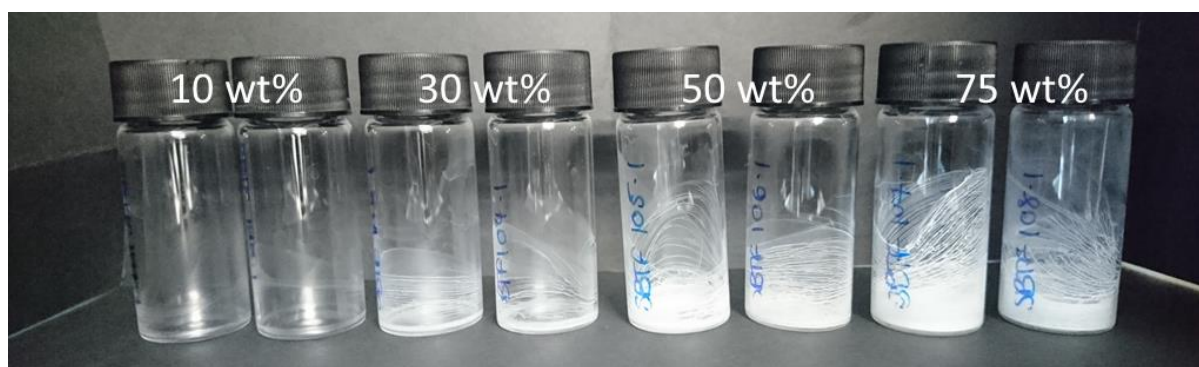


**Figure 4.18-** Picture of thin films with increasing drug loading; (right) PEG<sub>5K</sub>-*b*-PMOP<sub>40</sub>-*co*-BOD<sub>0.7</sub> and (left) PEG<sub>5K</sub>-*b*-PPOP<sub>40</sub>-*co*-BOD<sub>0.7</sub>.

Each sample was characterised by DLS before and after sonication; however the assessment of stability was substantially obtained from the variation of  $D_z$  and PDI over time after sonication of each thin film, rehydrated at the time of characterisation. On storage, the thin films appear to generate larger dispersions when rehydrated after weeks in the solid state at ambient temperature. The largest increase in  $D_z$  was seen with the highest SN-38 containing samples; when 10 wt% SN-38 was present there was a relatively small increase seen for both PEG<sub>5K</sub>-*b*-PMOP<sub>40-co</sub>-BOD<sub>0.7</sub> and PEG<sub>5K</sub>-*b*-PPOP<sub>40-co</sub>-BOD<sub>0.7</sub> over the full fourteen week dry film storage time frame. PEG<sub>5K</sub>-*b*-PMOP<sub>40-co</sub>-BOD<sub>0.7</sub> thin films did display more variability upon rehydration when  $\geq 30$  wt% SN-38 was present; however,  $D_z$  values seemed to plateau after 4 weeks of dry film storage (Figure 4.19, A). This may be the result of an energy minimisation, such as drug crystallisation or mass transportation, occurring within the thin film during storage which potentially discontinues after time periods above 4 weeks. PEG<sub>5K</sub>-*b*-PPOP<sub>40-co</sub>-BOD<sub>0.7</sub> also showed an increase in variability although this was markedly less than PEG<sub>5K</sub>-*b*-PMOP<sub>40-co</sub>-BOD<sub>0.7</sub> up until 75 wt% SN-38 by which point PEG<sub>5K</sub>-*b*-PPOP<sub>40-co</sub>-BOD<sub>0.7</sub> showed the most variability over the 14 week period (Figure 4.19, B). Nevertheless, the overall variation of  $D_z$  values for both polymeric species was relatively small which was encouraging, indicating that storage of these film at ambient temperature for use at a later date was possible.

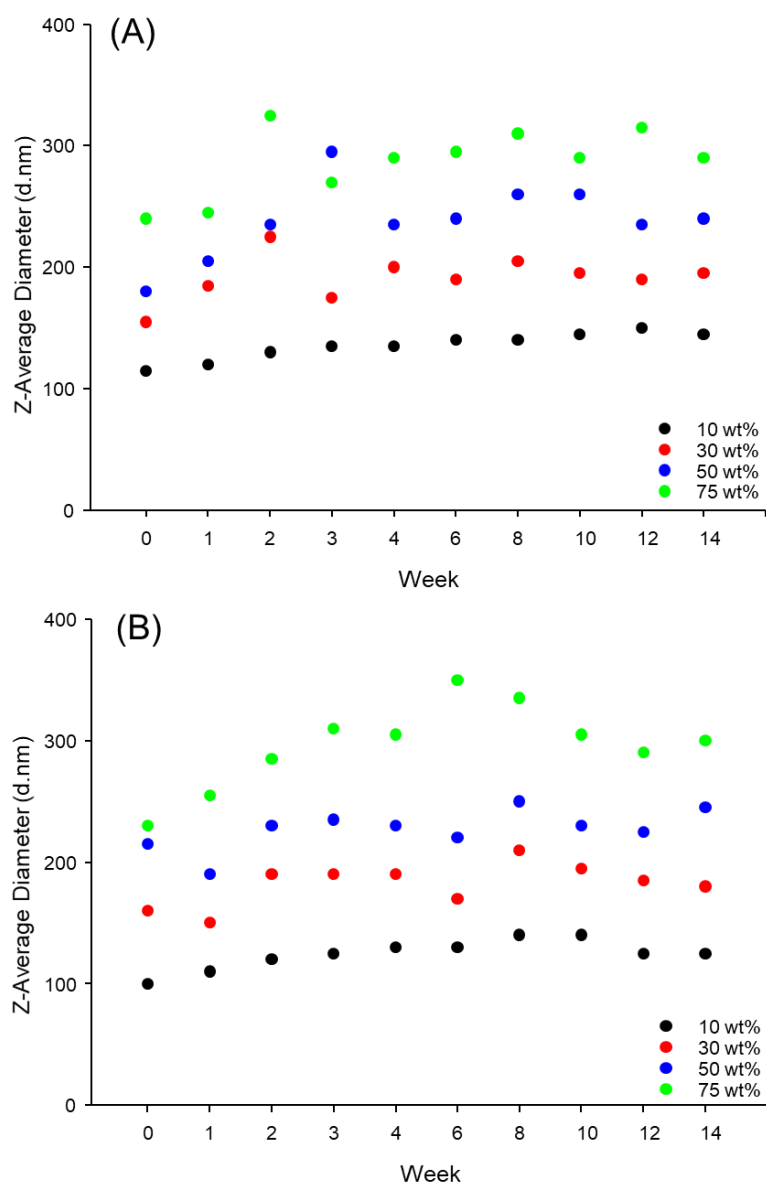


**Figure 4.19-** Graphical representation of variation in  $D_z$  with increased SN-38 content in the nanoparticles freshly produced *via* thin film hydration at each time point; stored in the solid state over a 14 week period and rehydrated upon the specified time of characterisation. (A) PEG<sub>5K</sub>-b-PMOP<sub>40-co</sub>-BOD<sub>0.7</sub>, (B) PEG<sub>5K</sub>-b-PPOP<sub>40-co</sub>-BOD<sub>0.7</sub>.

Similarly, the PdI values of each dispersion were monitored. PEG<sub>5K</sub>-b-PMOP<sub>40-co</sub>-BOD<sub>0.7</sub> samples showed relatively consistent PdI values within the re-dispersed samples when compared to PEG<sub>5K</sub>-b-PPOP<sub>40-co</sub>-BOD<sub>0.7</sub> derived samples across all SN-38 drug loadings; however, a similar trend to  $D_z$  was seen when SN-38 increased to 75 wt% (Figure 4.20, A & B). Both polymers systems showed the largest variation in PdI at this high drug content although no observed values were  $> 0.5$ . There was also no specific trend of increasing PdI with increasing SN-38 content which would indicate that the increased concentration of SN-38

does not negatively impact the mechanism for the formation of nanoparticles. Across the fourteen week study of dry film stability, the PDI values for 50 wt% drug loaded dispersions from both polymers, were consistently the lowest generated which appears to imply a beneficial drug loading; however, it is not clear why this is the case.

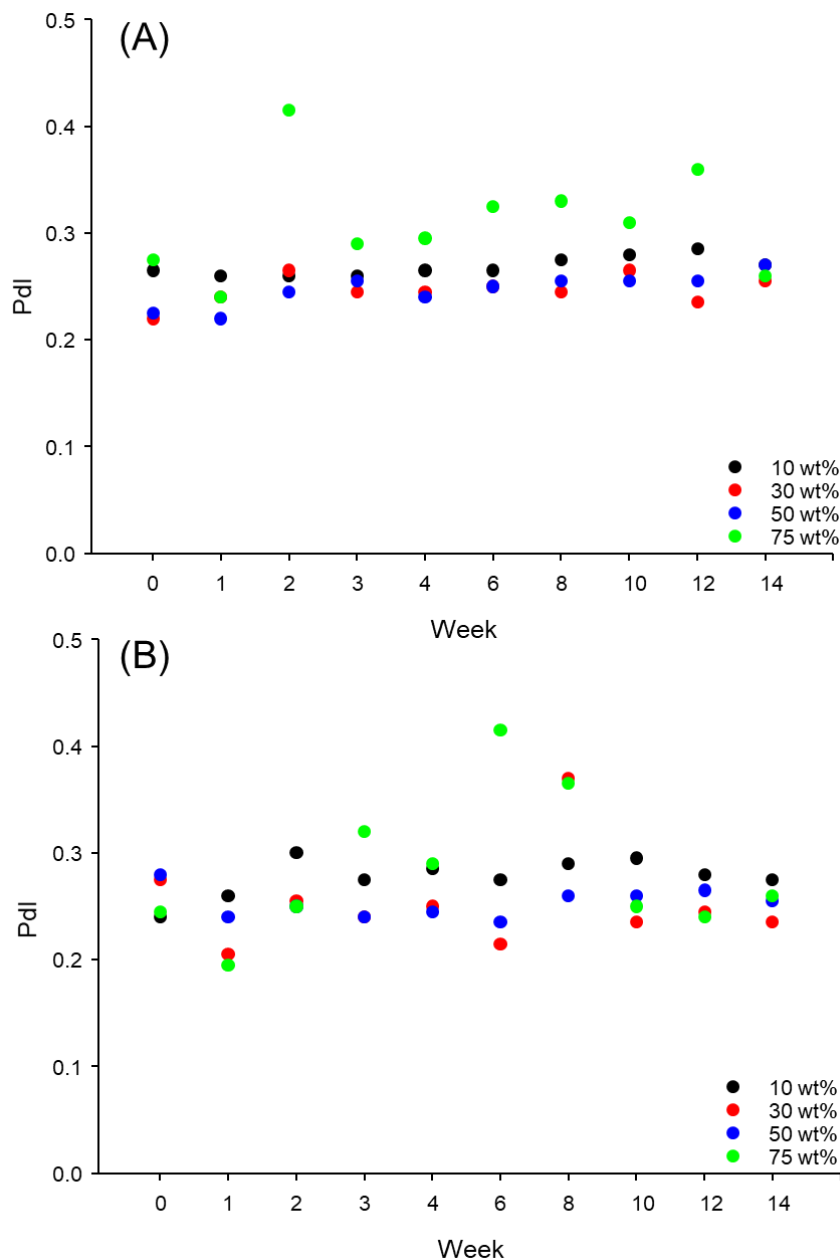


**Figure 4.20- Graphical representation of variation in PDI with increased SN-38 content in the nanoparticles freshly produced *via* thin film hydration at each time point; stored in the solid state over a 14 week period and rehydrated upon the specified time of characterisation (A) PEG<sub>5K</sub>-b-PMOP<sub>40</sub>-co-BOD<sub>0.7</sub>, (B) PEG<sub>5K</sub>-b-PPOP<sub>40</sub>-co-BOD<sub>0.7</sub>.**

Although some variability was seen in both  $D_z$  and PDI of the re-dispersed samples over the 14 weeks dry film stability study the storage of these thin films over this period did not impact the rehydration process and drug-loaded nanoparticles were consistently formed. Considering the targeted application for these nanoparticle dispersions, this would be an advantage over systems that must be stored in aqueous media, as liquid dispersions are notoriously difficult to store in ambient conditions.<sup>12</sup> Furthermore the data collected for samples containing > 50 wt% SN-38 was highly encouraging as it suggests that a high drug content does not have a detrimental effect on the stability of the dry thin films.

#### *4.3.2.2.2 Stability of aqueous dispersions formed from thin film hydration*

It was also important to analyse the stability of the aqueous dispersed systems, of increasing drug content, to understand the time frame for use after rehydration. As with all other studies, the methodology for the creation, hydration and sonication of each dispersion was kept constant; targeting a final polymer concentration of  $1 \text{ mg mL}^{-1}$  in water after rehydration (with the exception of 95 wt% SN-38 which required a  $0.05 \text{ mg mL}^{-1}$  polymer concentration). PEG<sub>5K</sub>-*b*-PCL<sub>40</sub>-*co*-BOD<sub>0.7</sub> was used throughout this study and SN-38 content was extended over a range of values, 2.43, 10, 16.6, 30, 33, 50, 75 and 95 wt%. Upon formation, by rehydration and sonication, DLS characterisation of the aqueous dispersion was undertaken on two consecutive days followed by measurements four and seven days after first analysis. This time frame was selected as it was assumed that in a clinical setting use 7 days after initial synthesis would be rare. Pictures of the dispersions taken before each measurement (Figure 4.21) allowed the presence of any sedimentation, forming on standing, to be recorded, as each sample was agitated before DLS analysis.

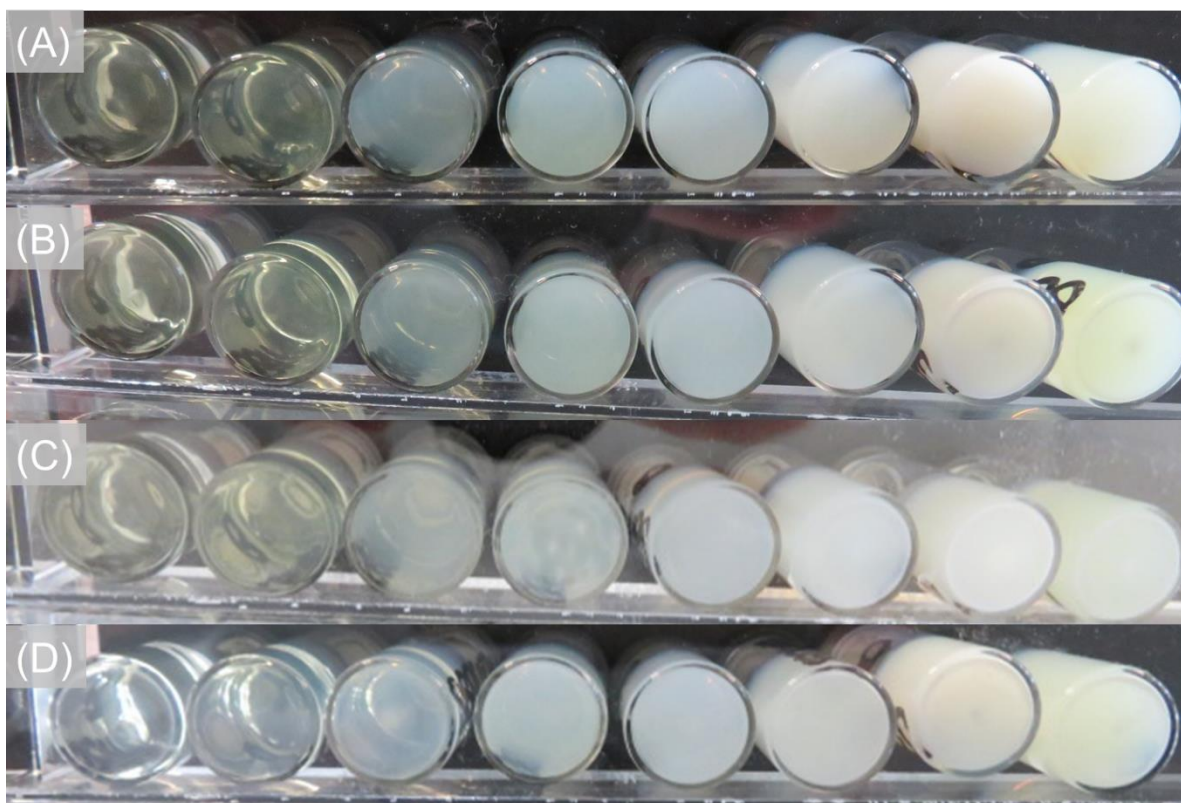


**Figure 4.21 - Photographs of PEG<sub>5K</sub>-*b*-PCL<sub>40</sub>-*co*-BOD<sub>0.7</sub> stabilised nanoparticles containing increasing amounts of SN-38 and stored for several days; (A) Day 0, (B) Day 2, (C) Day 4, (D) Day 7, (left to right) 2.43, 10, 16.6, 30, 33, 50, 75 and 95 wt%.**

Visual inspection of the samples indicated that sedimentation of a white/yellow powder, assumed to be drug, occurred two days after sonication for samples containing 75 and 95 wt% SN-38 (Figure 4.21, B). This was possibly due to the relatively low PEG<sub>5K</sub>-*b*-PCL<sub>40</sub>-*co*-BOD<sub>0.7</sub> content leading to aggregation and the larger initial particle sizes seen for these samples.<sup>13-15</sup> However, the turbidity of the two dispersions suggests that a large fraction of the nanoparticle distribution was well dispersed and sedimentation did not seem to increase significantly over seven days (Figure 4.21, B to D). Sedimentation was evident within samples after seven days of dispersion storage, except those containing 2.43 and 10 wt% SN-38 (Figure 4.21, D); DLS characterisation not only highlighted increasing  $D_z$  values but also the impact of drug content (Figure 4.22).

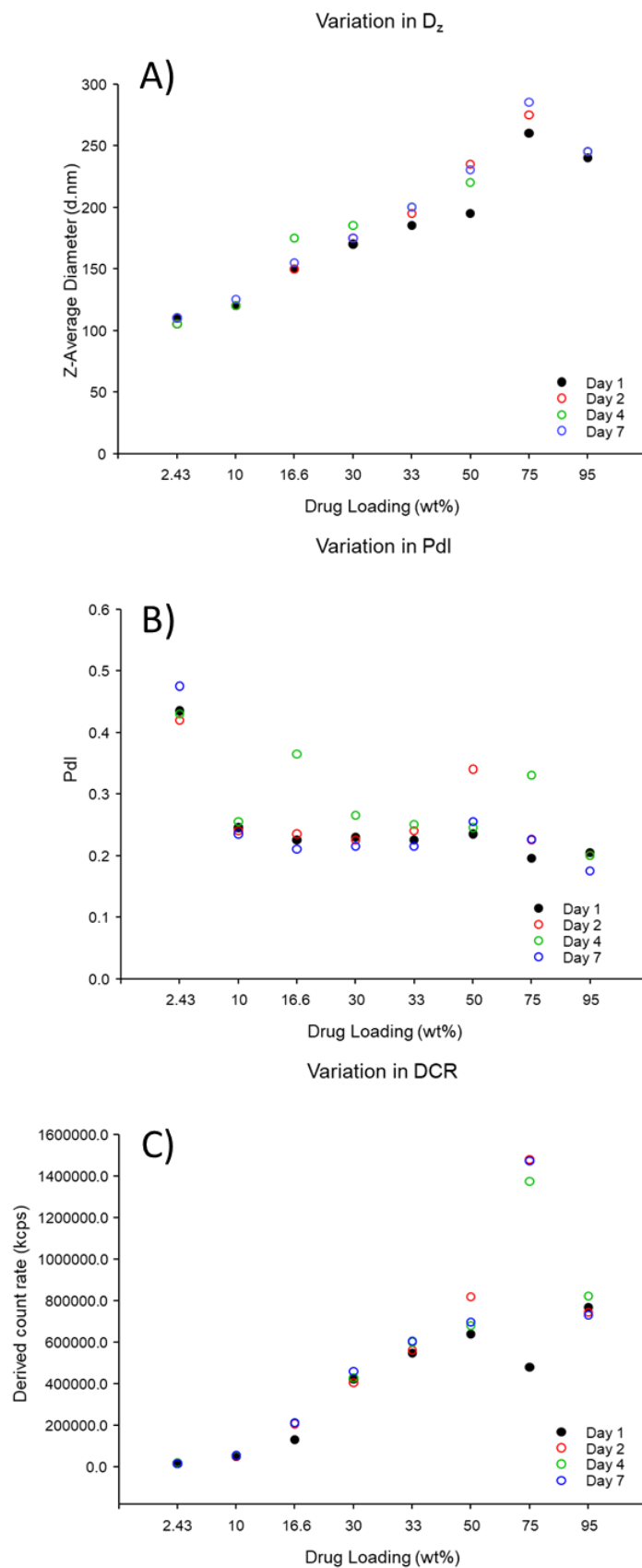


**Figure 4.22-** Graphical representation of the physicochemical characteristics of stored rehydrated dispersions containing PEG<sub>5K</sub>-*b*-PCL<sub>40</sub>-*co*-BOD<sub>0.7</sub> with varying SN-38 content. (A) Z-average diameter, (B) Pdl and (C) DCR.

Importantly, the  $D_z$  values measured immediately after rehydration and sonication replicated those seen in previous studies (Section 4.3.2.1), indicating the reproducibility of the thin film hydration method developed here (Figure 4.22, A). PdI values were also consistent with previous studies of thin film hydration using PEG<sub>5K</sub>-*b*-PCL<sub>40</sub>-*co*-BOD<sub>0.7</sub> showing the highest value for 2.43 wt% SN-38 at 0.435 and lower values at higher drug loadings (Figure 4.22, B). This implies that the drug has a favourable effect on the nanoparticle formation mechanism with PdI decreasing to <0.3 for all other samples (Figure 4.22, B). DCR increased with SN-38 content; however, a decrease in the attenuator was also observed which was to be expected as  $D_z$  values increases and samples became more turbid (Figure 4.22, C). When considering the variability in all three physicochemical properties, the nanoparticle dispersions containing 75 wt% SN-38 appear to be the least stable corresponding to the sedimentation also observed over the course of this study. Similarly, samples containing 50 wt% SN-38 showed greater variability of  $D_z$ , increasing from 195 nm to 235 nm after one day of storage.

As SN-38 content decreased below 50 wt%, there was an increase in the apparent stability of the suspensions, particularly at 2.43 and 10 wt%, showing little variation in all physicochemical properties and corresponding with visual observations. This suggests that the observed changes in  $D_z$ , PdI and DCR for these samples may be due to the re-dispersion of sedimented material before DLS characterisation. The increased variability and therefore decrease in stability of samples with increasing SN-38 content overtime is possibly a result in the reduction of polymer content relative to drug. This reduction in polymer may diminish the inferred steric and electrostatic stability gained from PEG<sub>5K</sub>-*b*-PCL<sub>40</sub>-*co*-BOD<sub>0.7</sub> therefore decreasing its ability to prevent sedimentation of drug crystals.

Although these results highlight some variability on storage over 7 days, it is important to consider the significant long-term storage benefits of the thin film hydration method and the ability to hydrate and sonicate at the time of administration. However, it is encouraging to note that a low variability was observed over the first four days of ambient storage of rehydrated/sonicated samples providing a considerable timeframe for storage and administration for these samples in a clinical setting.



### 4.3.2.3 Thin film hydration comparison using linear amphiphilic PEG<sub>5K</sub>/polyester block co-polymers

Linear PEG-polyester co-polymers were also investigated as candidate material within a series of thin film hydration studies containing increasing SN-38 concentrations to explore whether the branched architecture was essential for the behaviours and benefits described above. Drug loading was matched to the values investigated in Section 4.3.2.1, with the exception of 33 wt% (30 wt% used); additionally, 10 wt% SN-38 loaded samples were also included. All 5 linear PEG<sub>5K</sub> block co-polymers synthesised in Chapter 2, Sections 2.3.1.2 and 2.4.1.2 were studied using the methodology developed in Section 4.2.1 targeting a final polymer concentration in water (2.5 mL) of 1 mg mL<sup>-1</sup>; with exception for 95 wt% SN-38 loaded samples which required a polymer concentration of 0.05 mg mL<sup>-1</sup> and a drug concentration of 1 mg mL<sup>-1</sup> in water following rehydration.

Interestingly, rehydration of thin films composed of drug and linear amphiphilic block co-polymer also allowed nanoparticle formation. At SN-38 loading <16.6 wt%, considerable variation of outcomes was observed with the different polyester chemistries; this is in stark contrast to samples formed from the corresponding branched species. Significantly, PEG<sub>5K</sub>-*b*-PCL<sub>40</sub>, produced much larger particles than the other linear amphiphilic block co-polymers at <16.6 wt% drug loading (Figure 4.23, A). For example, at 2.43 wt% SN-38 content, the observed  $D_z$  values for linear block co-polymers of PEG<sub>5K</sub> and PMOP, PPOP, PBOP and PPHLOP all produced nanoparticles in the range of 65 to 75 nm but the presence of PEG<sub>5K</sub>-*b*-PCL<sub>40</sub> led to  $D_z = 300$  nm. Once drug loading surpassed 16.6 wt% all five polymeric species produced particles of similar  $D_z$  values (Figure 4.23, A) possibly suggesting that the drug behaviour is dominating the mechanism at these values. The branched polymer architecture appears, therefore, to dominate the mechanism at low SN-38 content.

When linear amphiphilic co-polymers are utilised, the observed  $D_z$  values appear to increase with increasing SN-38 loading, reflecting the trend observed when branched PEG/polyester co-polymers are used. Additionally, the measured  $D_z$  values were similar to those achieved with the branched species in all cases, regardless of SN-38 content; this may be an indication of the relatively low number of primary chains linked together within the branched co-polymers, therefore it could be rationalised that the impact of the branched architecture on

nanoparticle formations would not be as marked when comparing the systems detailed here and in Section 4.3.2.1.

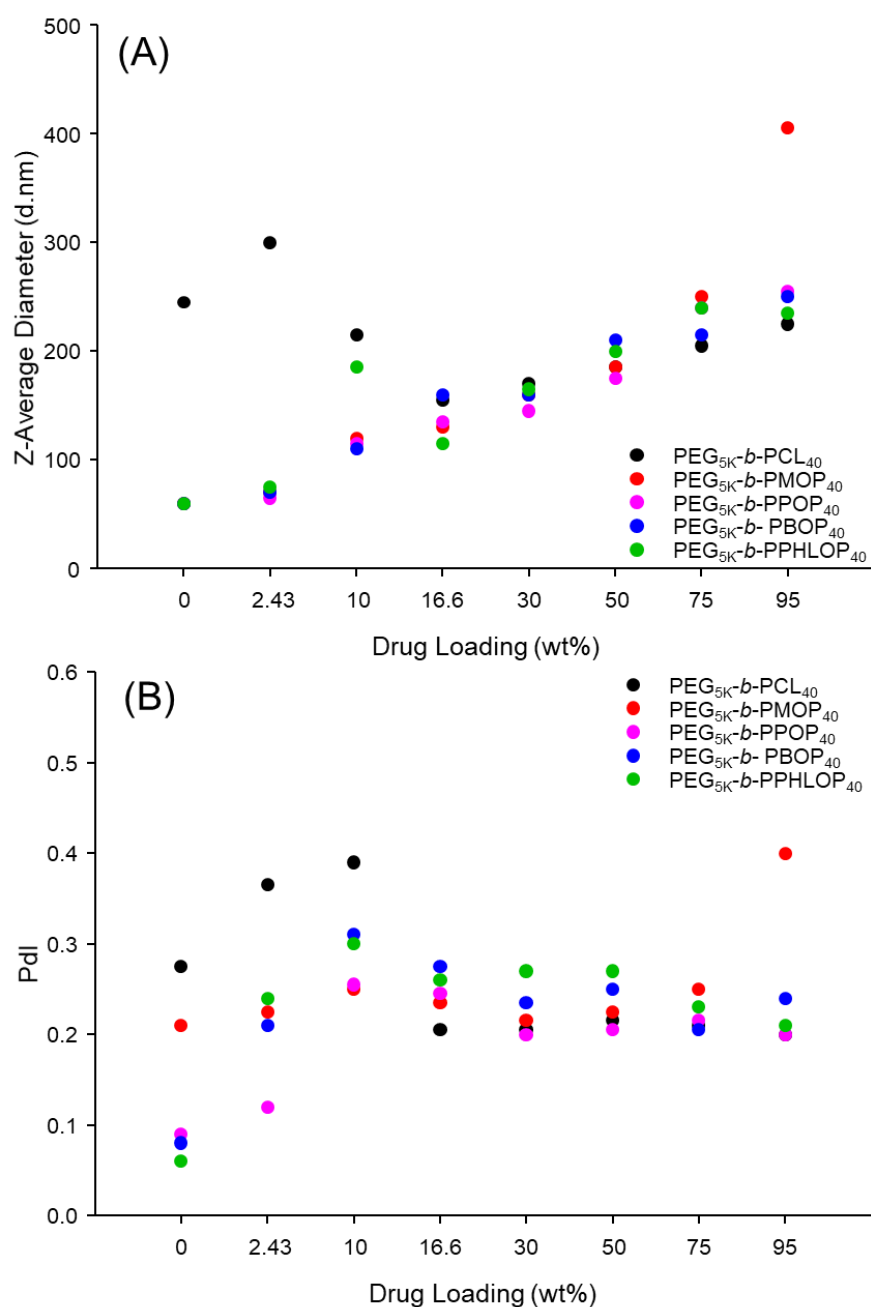


**Figure 4.23-** Graphical representation of physicochemical characteristics of nanoparticles generated *via* thin film hydration of PEG<sub>5K</sub>-b-PCL/SCM<sub>40</sub> with increased SN-38 content. (A) Z-average diameter, (B) Pdl.

The variation in the Pdl of dispersions formed using linear PEG<sub>5K</sub>/polyester amphiphilic block co-polymers and various SN-38 loadings did not appear to follow a clear trend although more consistency was seen > 16.6 wt% (Figure 4.23, B). This behaviour was not seen when branched

PEG<sub>5K</sub>/polyester block co-polymers were used. Nonetheless both branched and linear PEG co-polymer produced the largest variation between polymer species at 2.43 wt% SN-38; this again would be expected due to the higher amount of polymer in each system, therefore, determining the physicochemical characteristic of the nanoparticles.

The differences between nanoparticles synthesised using branched and linear PEG co-polymers were very small. This could be the result of two factors, firstly the number of primary polymer chains linked together in the branched PEG co-polymers is < 5 in all cases therefore the effects of the branched architecture may be difficult to determine. Secondly the method of synthesis for these nanoparticles differs considerably from co-nanoprecipitation and the aggregation-clustering mechanism is no longer operating. Therefore it is unclear whether the branched structure of the co-polymers offers the same benefits during the hydration of a polymeric thin film and if so to what extent. More in depth studies, adding small fractions of highly branched PEG<sub>5K</sub>/polyester block co-polymers to the polymers studied in Section 4.3.2.1 (adapted from those performed by Hatton *et al.* for nanoprecipitation) and applying the thin film hydration approach to these polymer mixtures would contribute to superior knowledge on this phenomenon.<sup>11</sup>

### **4.3.3 Mechanistic studies of the thin film hydration method using an amphiphilic branched co-polymers and SN-38**

The remarkable range of drug loading that was achieved within the thin film hydration method of nanoparticle formation provided a unique opportunity to probe the mechanism in some detail. The magnitude of this range was made clear when comparing the polymer to drug ratios achieved within the aqueous dispersions; these vary from 1:0.025 mg mL<sup>-1</sup> (2.43 wt% drug loading) to 1:19 mg mL<sup>-1</sup> (95 wt% drug loading). It is clear that the nanoparticles structure must change dramatically across such a wide range; drug encapsulation is more likely at high polymer ratios and drug particle stabilisation is more likely at low polymer ratios. It was, therefore, hypothesised that the continuum of drug loadings must lead to a transition in structure to a dispersion of solid drug nanoparticles, *SDN*, at higher drug loadings; polymeric nanoparticles are assumed to form below a critical drug loading value (Figure 4.24).

The methodology here appears to be relatively unique, as it is the only known system that allows both polymeric nanoparticles and *SDN* domains to be created by solely increasing the drug concentration. Investigation of the influence of drug loading on the structure of the

resulting nanoparticles was undertaken using a combination of techniques including; scanning electron microscopy, *SEM*, DSC and thermal analysis by structural characterisation, *TASC*.

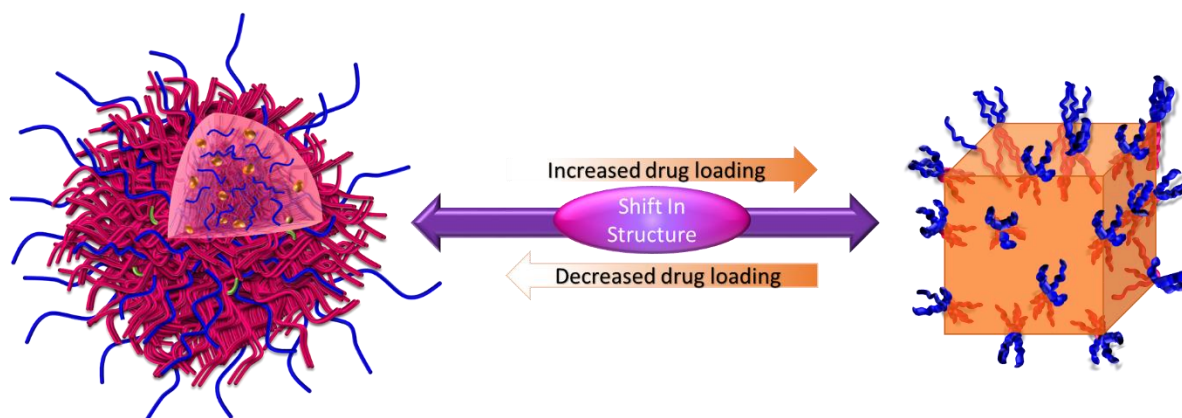


**Figure 4.24 - Representation of the transition between possible structures PEG-Polyester-BOD derived thin film dispersion result in, depending on drug loading wt%.**

#### **4.3.3.1 SEM studies of the thin film hydration method using amphiphilic branched polyester co-polymers**

SEM allowed a qualitative visualisation of the thin film methodology through the study of both the dry thin films and dried aqueous dispersions. Samples containing increasing SN-38 content were studied.

##### *4.3.3.1.1 SEM study of dry thin films formed before thin film hydration of PEG<sub>5K</sub>-PMOP<sub>40</sub>-BOD<sub>0.7</sub> and SN-38*

SEM imaging of dry thin films formed using PEG<sub>5K</sub>-PMOP<sub>40</sub>-BOD<sub>0.7</sub> at 5 mg mL<sup>-1</sup> in THF containing increasing SN-38 concentrations from 0 to 95 wt% (a thin film of 100 wt% SN-38 was also prepared to serve as a comparison). Each sample was prepared by pipetting a small volume of the THF mixture onto a silicon wafer atop an SEM stub and allowing solvent evaporation. Although this was not fully reflective of the vacuum solvent removal used to synthesise the thin films in Section 4.3.2, it was thought to be the best way to achieve thin films suitable for imaging by SEM. Once coated with chromium, images were obtained for a total of 8 samples (Figure 4.25 & 4.26).

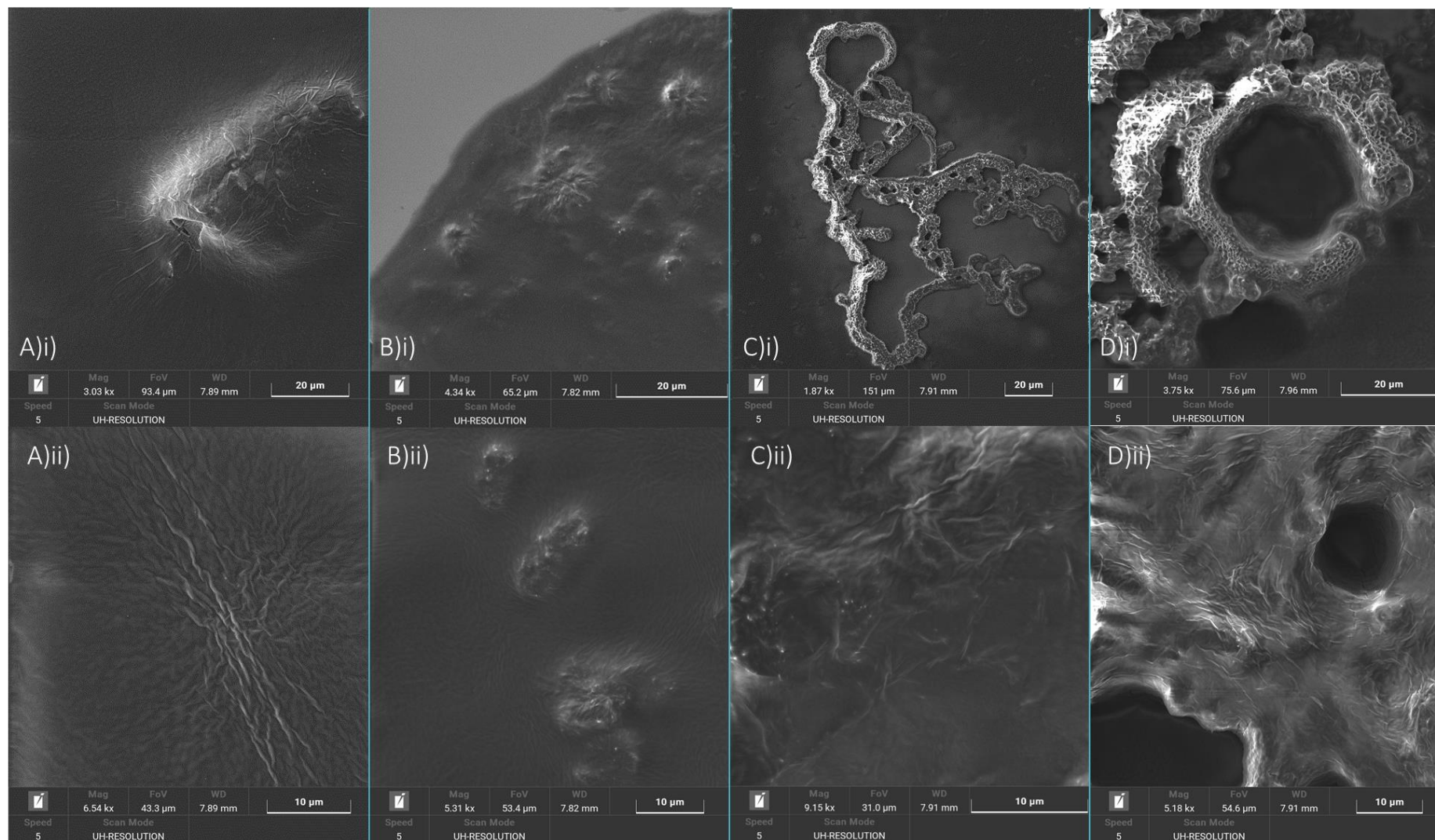


**Figure 4.25 – SEM images of PEG<sub>5K</sub>-b-PMOP<sub>40</sub>-co-BOD<sub>0.7</sub> thin films containing SN-38 at differing magnifications. (A) blank, (B) 10 wt%, (C) 20 wt% and (D) 30 wt%; lower magnification (top) and higher magnification (bottom).**



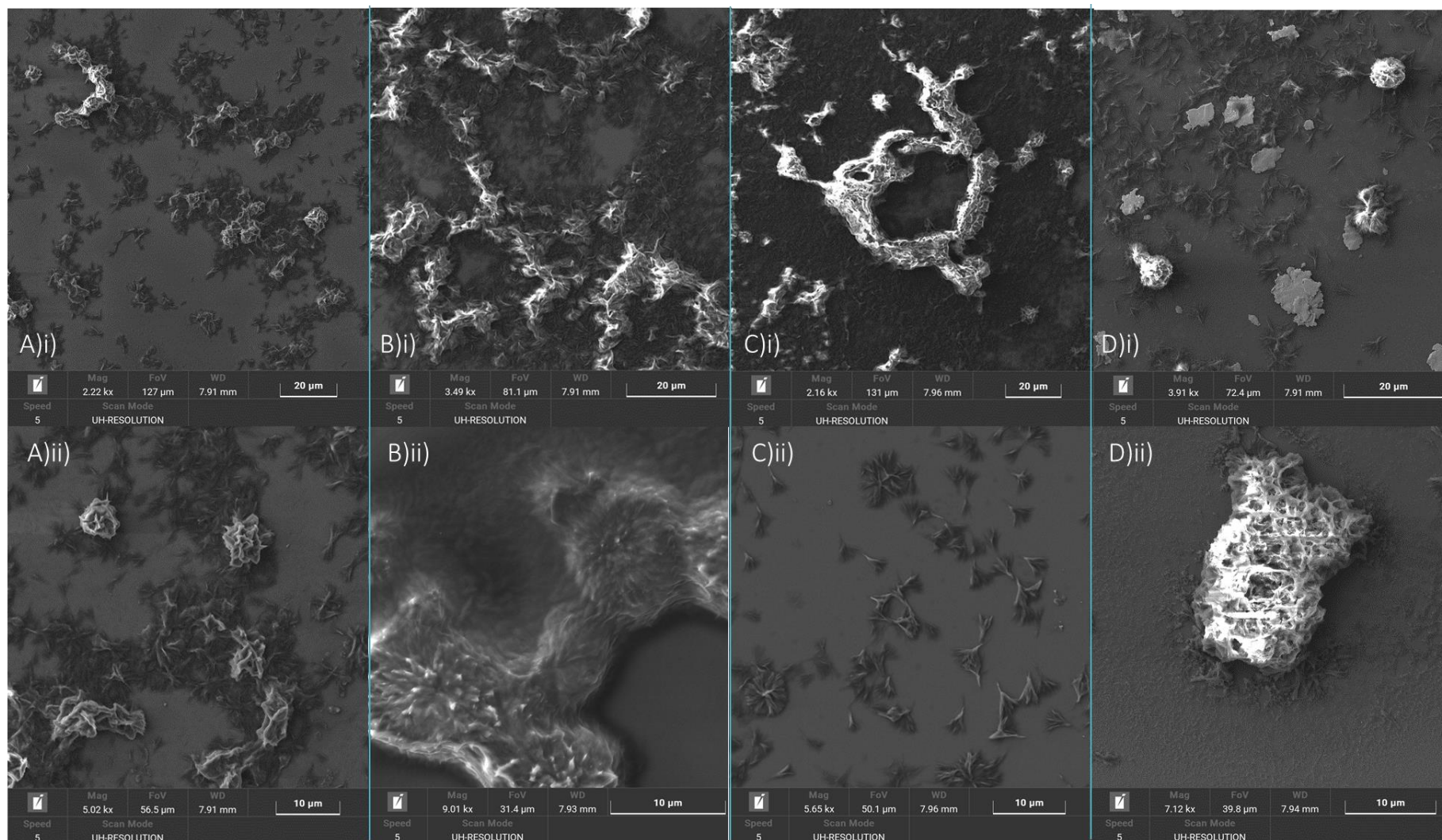


**Figure 4.26 – SEM images of PEG<sub>5K</sub>-*b*-PMOP<sub>40</sub>-*co*-BOD<sub>0.7</sub> thin films containing SN-38 at differing magnifications. (A) 50 wt%, (B) 75 wt%, (C) 95 wt% and (D) 100 wt%; lower magnification (top) and higher magnification (bottom).**

As the drug content increased the number and clarity of crystals increased, with clear crystalline structures being apparent in samples with  $\geq 50$  wt% SN-38 (Figures 4.25 & 4.26). These crystalline structures in each sample were characteristically needle-like in architecture indicating that these structures were the result of the same chemical species. The number of these crystalline architectures increased with increasing drug content therefore these were attributed to SN-38 not the polymer; when drug content was at 10 wt%; no definitive crystal structures could be distinguished (Figure 4.25 B).

Furthermore the role the polymer played during thin film formation appeared changed as drug loading increased and the relative amount of polymer decreased. Firstly, considering the thin film created without drug (Figure 4.25, A), the silicon wafer appeared to be coated in a complete polymer film. This was most evident when a drying artefact on the wafer was imaged (Figure 4.25, Aii) and a coating film seemed to be observed that conformed to the artefact. Further images of this sample showed that it had characteristic 'ripples' in the coating which was most likely the result of a drying effect. Similar images of the polymeric film were observed in samples containing 10, 20 and 30 wt% SN-38, shown by a similar 'rippling' effect in the film in each sample (Figure 4.25, B to D).

Once SN-38 content increased above 30 wt% the polymer coating was no longer evident and very different images were seen at 50, 75, 95 and 100 wt% drug loading (Figure 4.26). The lack of a discernible polymer film capable of impacting SN-38 crystals growth, or imaging, would suggest that the thin film is less homogeneous at drug loadings  $\geq 50$  wt%. When 100 wt% SN-38 was dried from the presence of planar, flake-like structures and needle-like crystals were observed (Figure 4.26, D) and these are not seen when polymer is present. This shows that the polymer still plays a role in the disruption of SN-38 crystallisation, even in very small amounts.

This reduction in the appearance of a coherent polymer film at higher drug loadings suggests that the nanoparticles that are being formed upon rehydration and sonication will no longer resemble a polymer particle with encapsulated drug but rather a transition towards a drug particles that is stabilised by polymer, resembling an SDN. This transition seems to occur between 20 and 50 wt% SN-38 content (Figure 4.27) however this is a preliminary qualitative

assessment and requires further investigation to confirm and refine the boundaries over which this structural change occurs.

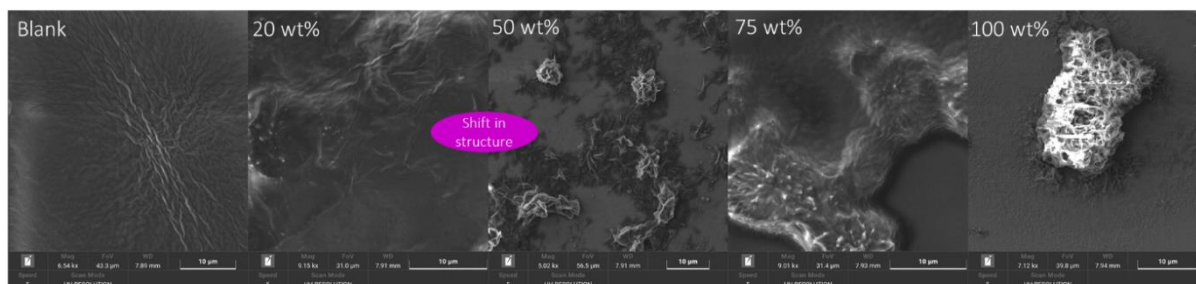


**Figure 4.27** – SEM images of PEG<sub>5K</sub>-*b*-PMOP<sub>40</sub>-*co*-BOD<sub>0.7</sub> thin films containing SN-38. (Pink oval) indicates where the shift in structure occurs.

#### 4.3.3.1.2 SEM study of filtered thin film dispersions formed via thin film hydration of PEG<sub>5K</sub>-PCL<sub>40</sub>-BOD<sub>0.7</sub> and SN-38

Studies of the morphological changes within the dispersed nanoparticles formed after hydration/sonication of the thin films were conducted by imaging a 0.2  $\mu\text{m}$  polytetrafluoroethylene, *PTFE*, filter, after filtration of a range of samples containing different drug loadings. This presented an opportunity to view the product particles rather than a model of the initial dry thin film. Before studies commenced, it was important to have a number of reference images, therefore an unused *PTFE* filter was imaged *via* SEM (Figure 4.28). Images of both the top (Figure 4.28, A) and bottom (Figure 4.28, B) revealed the considerable difference between the two sides of the filter. The top was more fibrous on the 20 to 30  $\mu\text{m}$  scales compared to the coarse, sub-micron, spindle-like fibres of the bottom with pores of around 3 to <1  $\mu\text{m}$  scale, indicating a gradient-like structure through the filter.



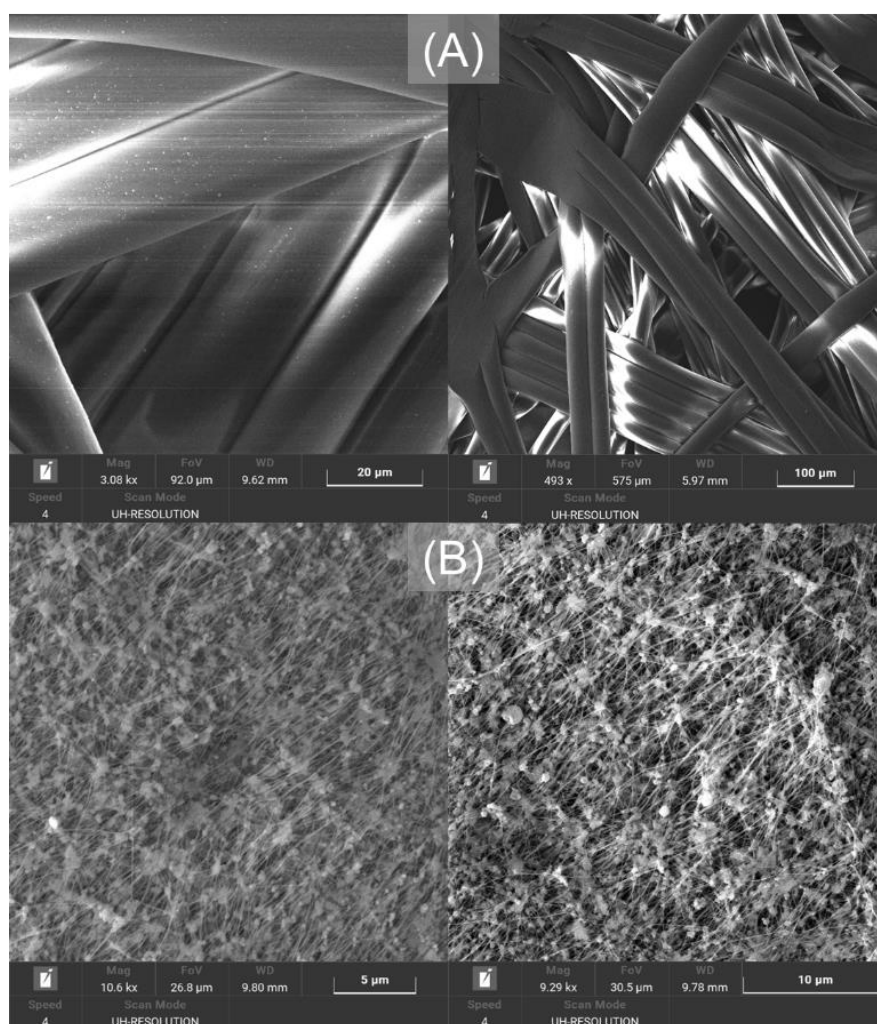


**Figure 4.28** – SEM images of a PTFE filter, unused. (A) top face of the filter and (B) bottom face.

PEG<sub>5K</sub>-*b*-PCL<sub>40</sub>-*co*-BOD<sub>0.7</sub> was selected as the amphiphilic branched block co-polymer for this study as it possessed the unsubstituted monomer repeat unit and the most crystalline polymeric structure; possibly advantageous for SEM imaging of nanoparticles. Drug loading ranged from 2.43, 10, 16.6, 30, 33, 50, 75 to 95 wt% to give a complete picture across the whole series of successful nanoparticle dispersions. Each dispersion was formed by the standard method, detailed in Section 4.3.1, and characterised by DLS before and after filtration (Table 4.6).

**Table 4.6 – DLS characterisation of nanoparticles produced by thin film hydration of PEG<sub>5K</sub>-*b*-PCL<sub>40</sub>-*co*-BOD<sub>0.7</sub> before and after filtration with increasing SN-38.**

SN-38 Loading (wt%)	Before Filtration				After Filtration			
	D <sub>z</sub> (nm)	D <sub>n</sub> (nm)	PdI	Derived Count Rate (kcps)	D <sub>z</sub> (nm)	D <sub>n</sub> (nm)	PdI	Derived Count Rate (kcps)
2.43	95	20	0.350	17815 (7)	80	20	0.245	14570 (7)
10	120	55	0.240	54475 (6)	110	65	0.210	45800 (6)
16.6	145	45	0.225	202980 (5)	125	60	0.185	78550 (6)
30	145	50	0.215	341010 (4)	130	80	0.160	218505 (5)
33	175	80	0.215	444475 (4)	160	80	0.230	352655 (4)
50	185	95	0.210	865905 (4)	170	100	0.180	622720 (4)
75	265	115	0.285	1251985 (3)	250	90	0.225	564025 (4)
95	235	95	0.220	725560 (4)	240	85	0.215	351960 (4)

It is important to note that comparative D<sub>z</sub> values to earlier studies using PEG<sub>5K</sub>-*b*-PCL<sub>40</sub>-*co*-BOD<sub>0.7</sub> in Section 4.3.2.1 were achieved, again indicating the reproducibility of this method. The incremental increase in D<sub>z</sub> with increasing SN-38 content, was also seen earlier. The comparison of data collected before and after filtration (Figure 4.29) showed a reduction in D<sub>z</sub>, PdI and DCR for each sample after filtration and confirmed the retention of larger particles on the filter even when D<sub>z</sub> of the nanoparticles was < 100 nm before filtration. As expected with the larger particles, produced with ≥ 75 wt% SN-38, a substantial drop in DCR (Figure 4.29, C) was observed with only a minimal decrease in D<sub>z</sub>, indicating the possibility of a large fraction of the dispersion being removed. Each filter was stored in a glass vial for several weeks to dry and then broken open to reveal the PTFE filter for imaging (both top and bottom faces, Figure 4.30 to 4.37).

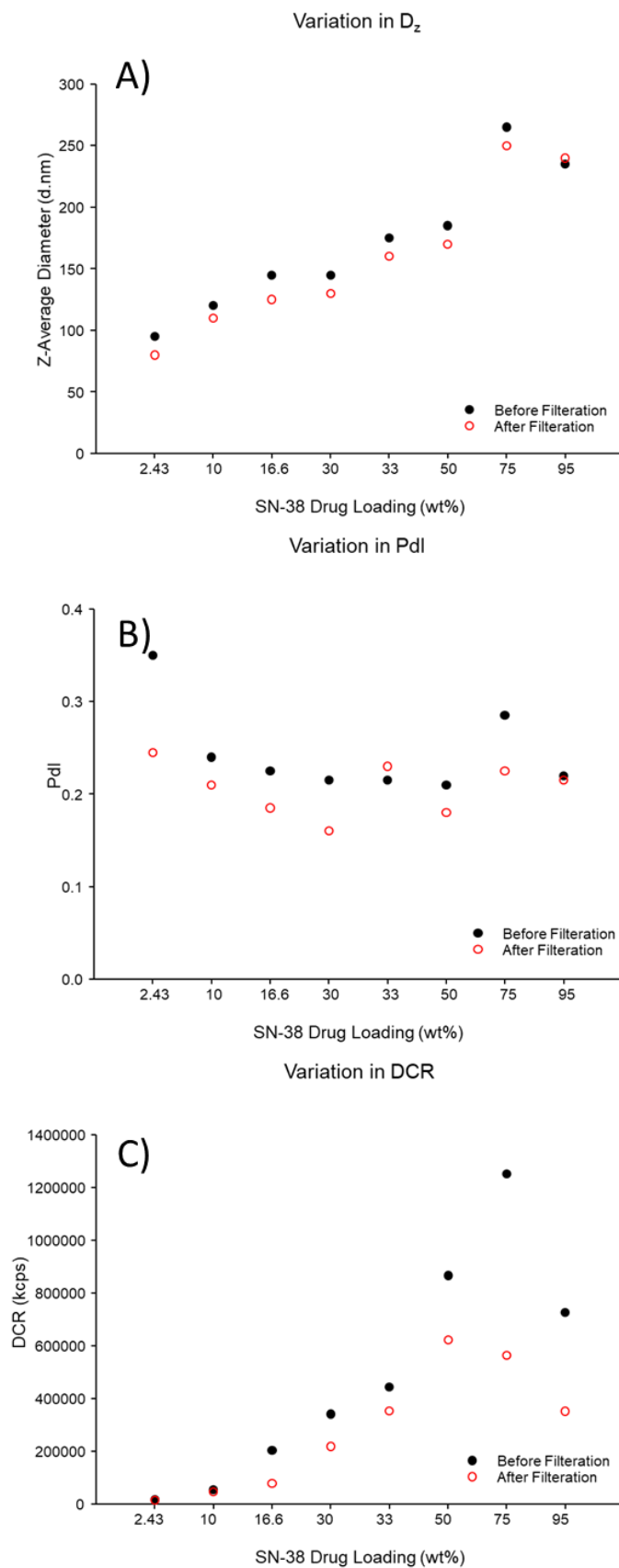


**Figure 4.29 – Graphical representation of changes in physicochemical characteristics before and after filtration of PEG<sub>5K</sub>-*b*-PCL<sub>40</sub>-*co*-BOD<sub>0.7</sub> dispersions containing increasing SN-38 content. (A) Z-average diameter, (B) Pdl and (C) DCR.**

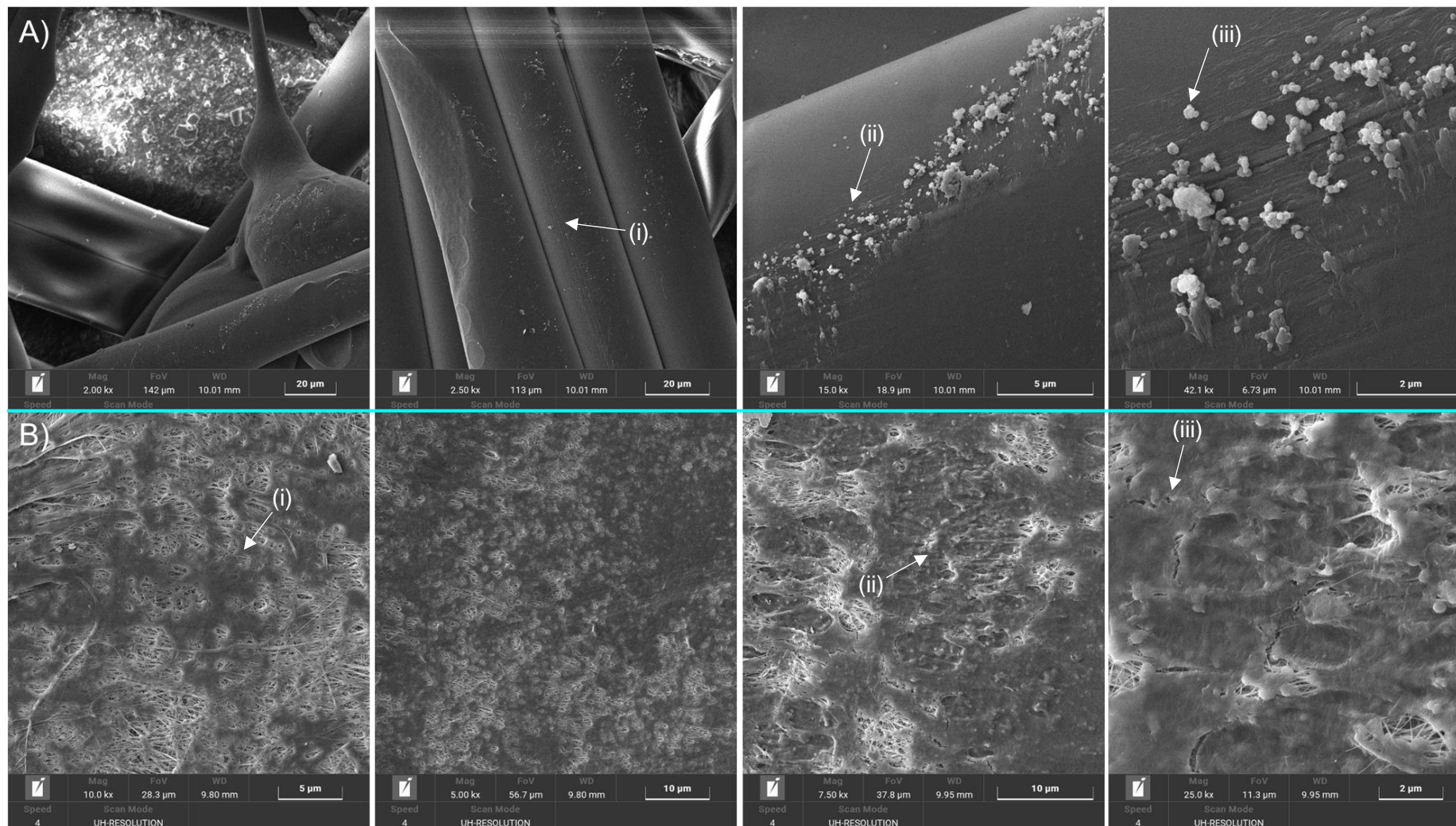


**Figure 4.30 – SEM images of a PTFE filter, used to filter PEG<sub>5K</sub>-*b*-PCL<sub>40</sub>-*co*-BOD<sub>0.7</sub> dispersion containing 2.43 wt% SN-38. (A) top face of the filter and (B) bottom face; (Ai to Aiii) indicating spherical nanoparticles and (Bi to Biii) indicating polymeric film.**



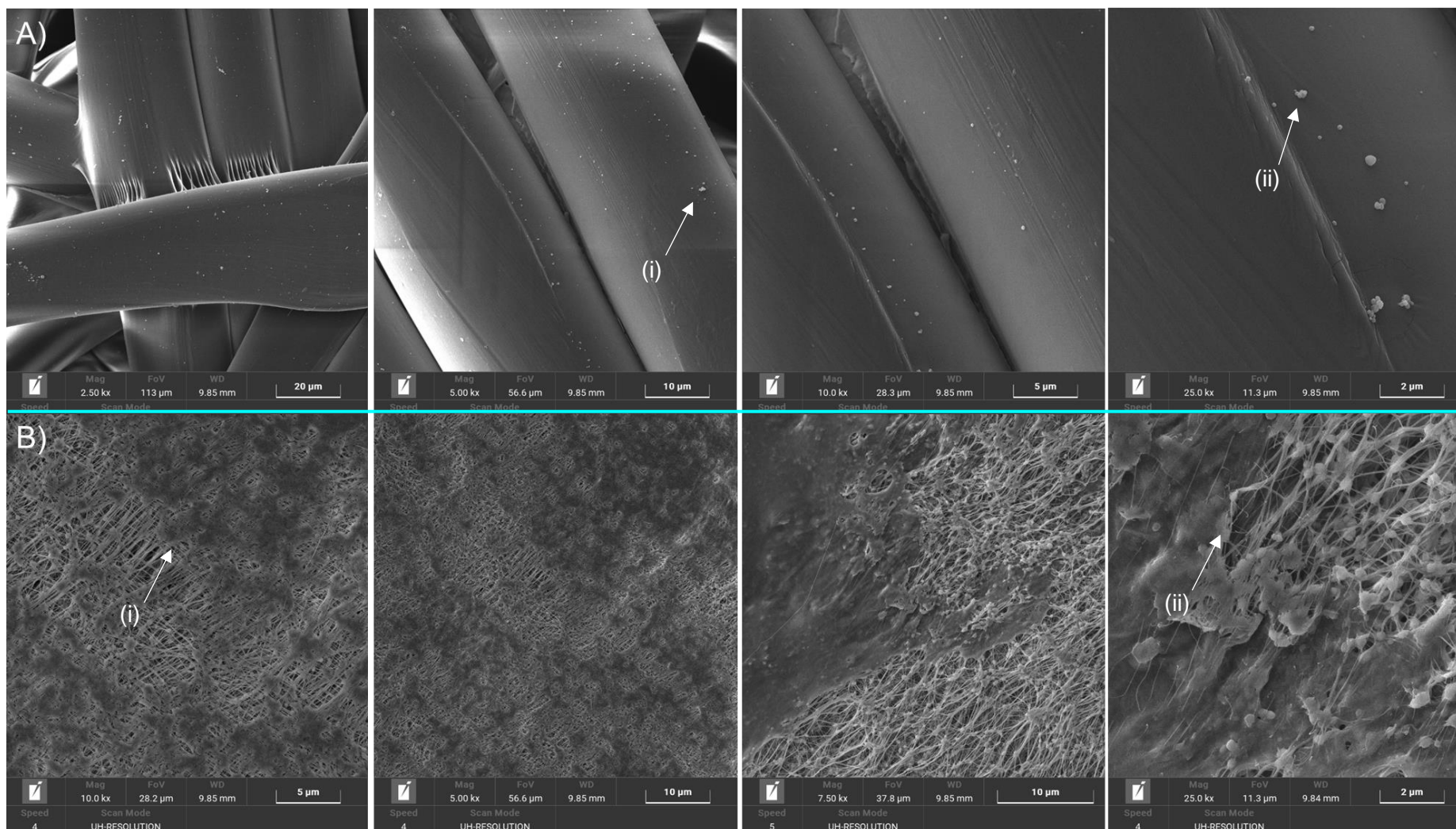


**Figure 4.31 – SEM images of a PTFE filter, used to filter PEG<sub>5K</sub>-*b*-PCL<sub>40</sub>-*co*-BOD<sub>0.7</sub> dispersion containing 10 wt% SN-38. (A) top face of the filter and (B) bottom face; (Ai & Aii) indicating spherical nanoparticles and (Bi & Bii) indicating polymeric film.**

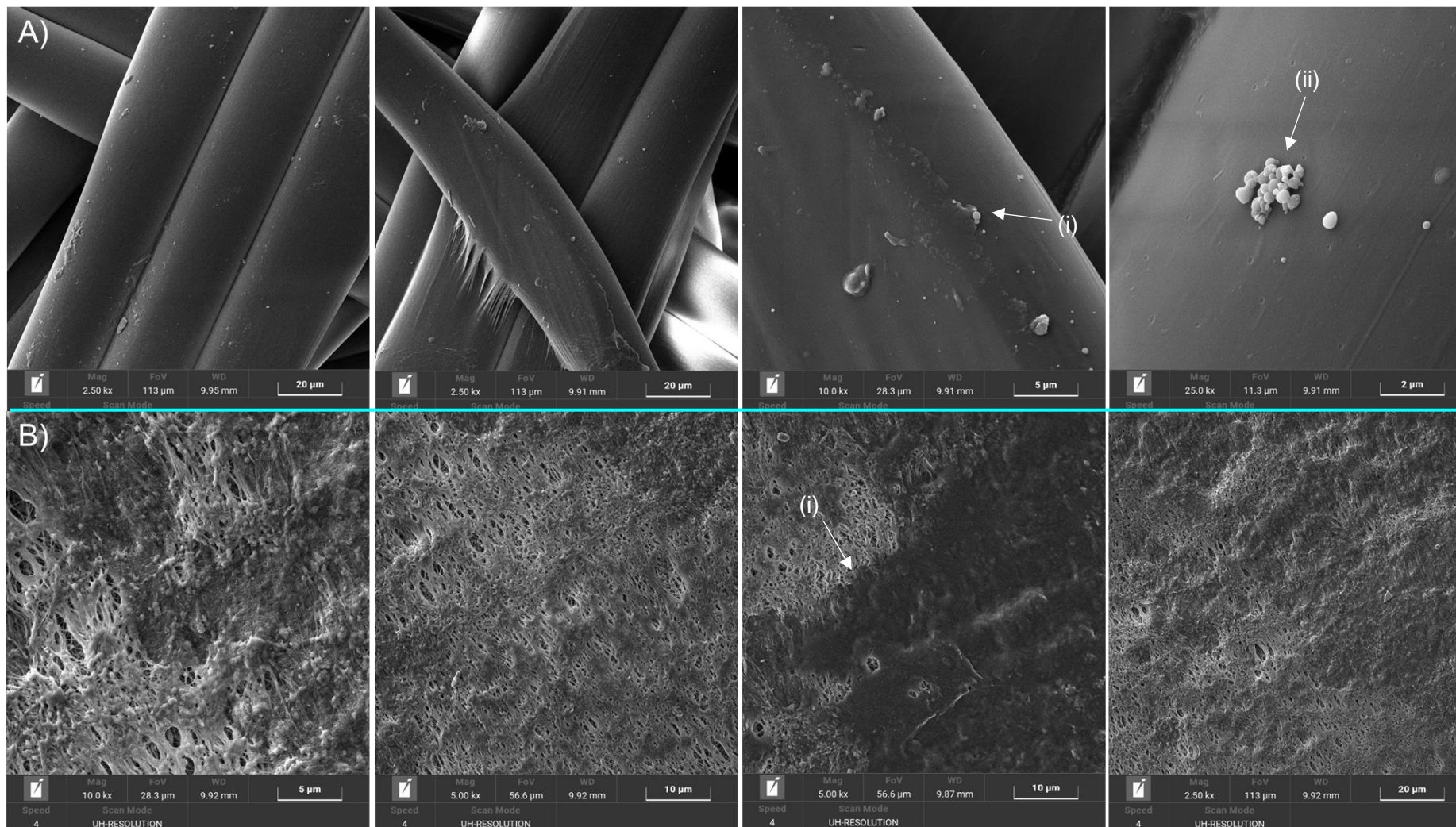


**Figure 4.32 – SEM images of a PTFE filter, used to filter PEG<sub>5K</sub>-*b*-PCL<sub>40</sub>-*co*-BOD<sub>0.7</sub> dispersion containing 16.6 wt% SN-38. (A) top face of the filter and (B) bottom face; (Ai & Aii) indicating spherical nanoparticles and (Bi) indicating polymeric film.**



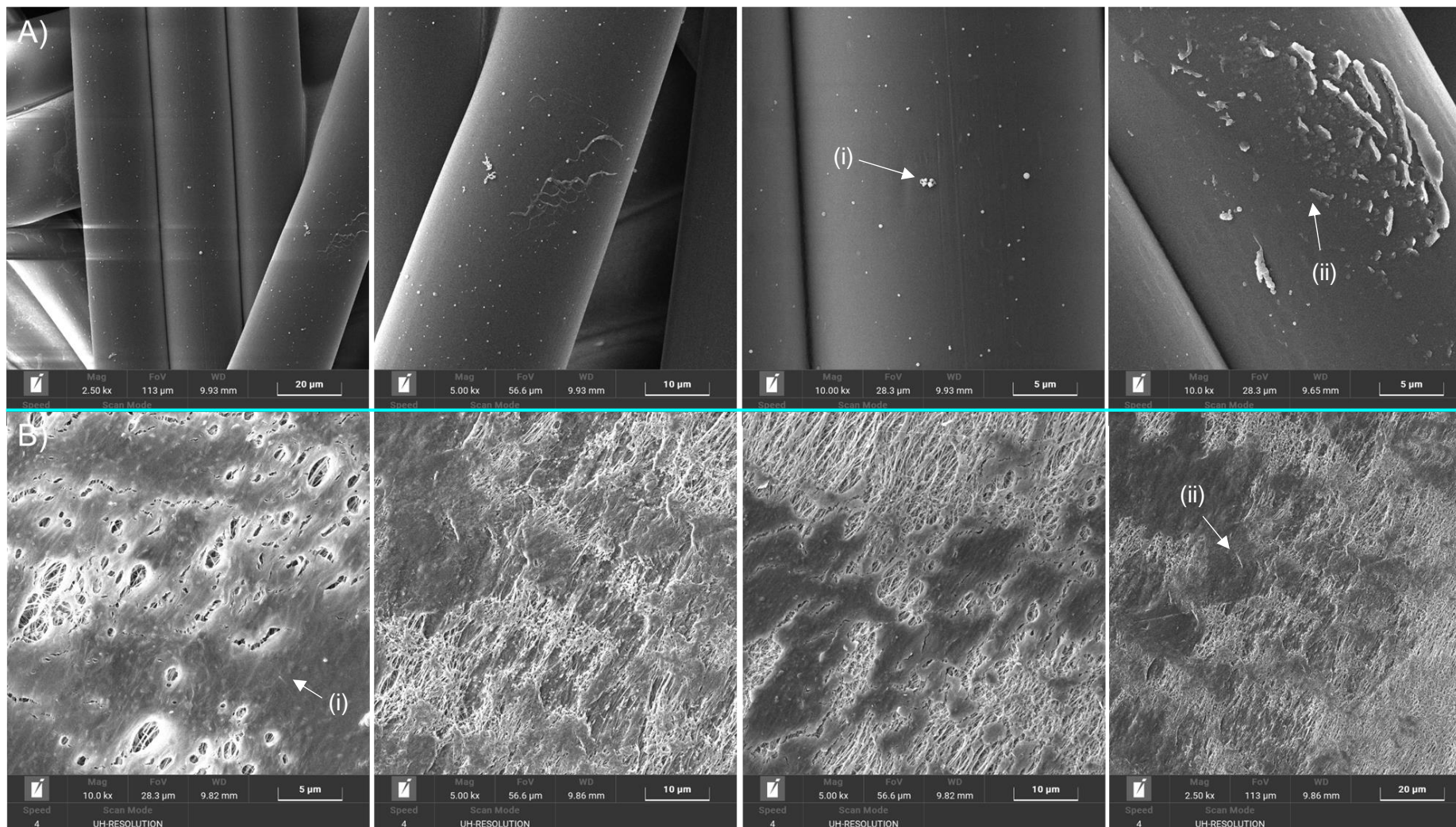


**Figure 4.33 – SEM images of a PTFE filter, used to filter PEG<sub>5K</sub>-*b*-PCL<sub>40</sub>-*co*-BOD<sub>0.7</sub> dispersion containing 30 wt% SN-38. (A) top face of the filter and (B) bottom face; (Ai) indicating spherical nanoparticles and (Aii) indicating drying effect and (Bi & Bii) indicating needle-like crystals within the polymeric film.**



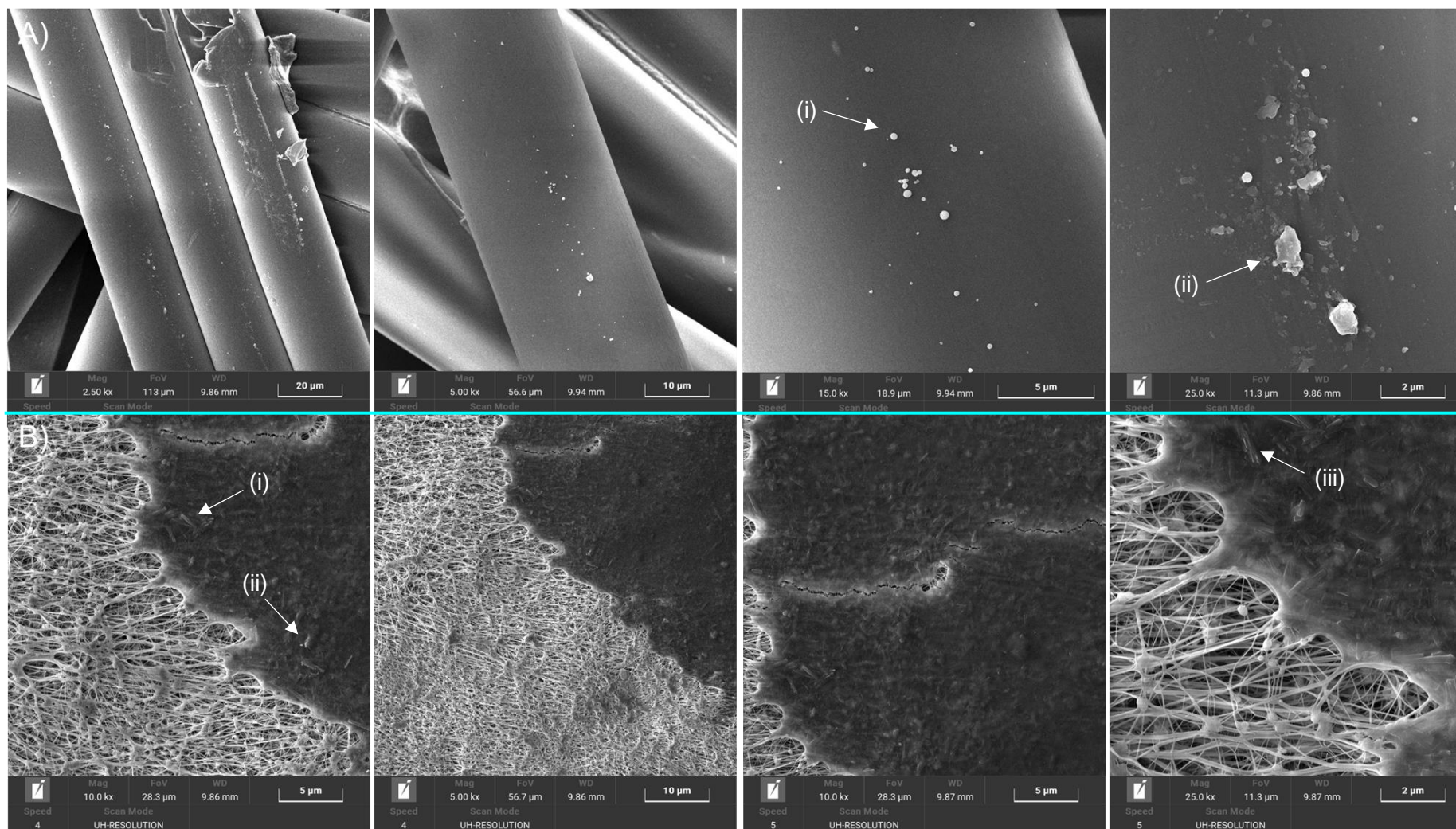


**Figure 4.34** – SEM images of a PTFE filter, used to filter PEG<sub>5K</sub>-*b*-PCL<sub>40</sub>-*co*-BOD<sub>0.7</sub> dispersion containing 33.3 wt% SN-38. (A) top face of the filter and (B) bottom face; (Ai) indicating spherical nanoparticles and (Aii) indicating planar artefacts and (Bi to Biii) indicating needle-like crystals within the polymeric film.



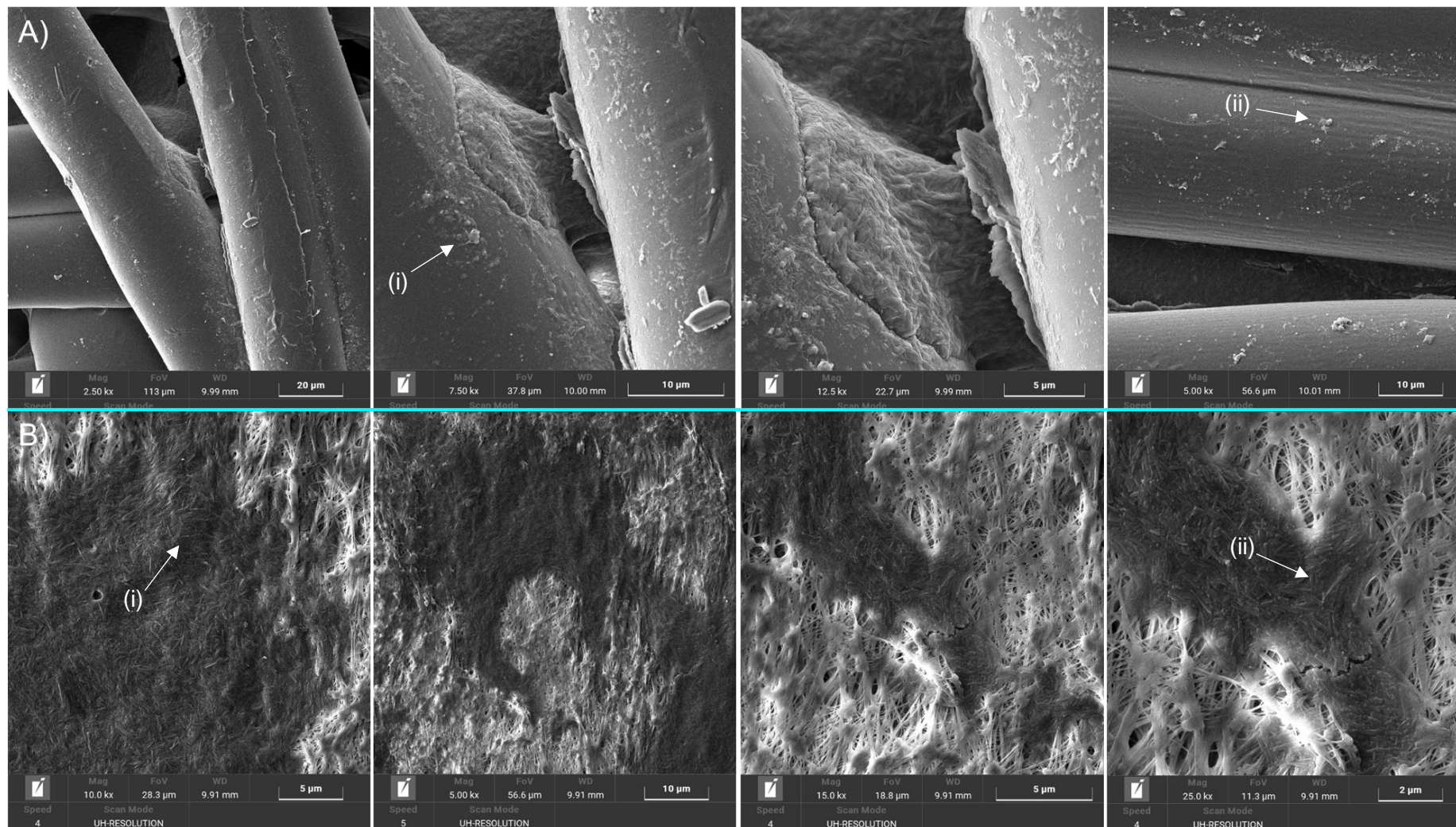


**Figure 4.35 – SEM images of a PTFE filter, used to filter PEG<sub>5K</sub>-*b*-PCL<sub>40</sub>-*co*-BOD<sub>0.7</sub> dispersion containing 50 wt% SN-38. (A) top face of the filter and (B) bottom face; (Ai & Aii) indicating planar artefacts/particles fused together and (Bi & Bii) indicating needle-like crystals within the polymeric film.**



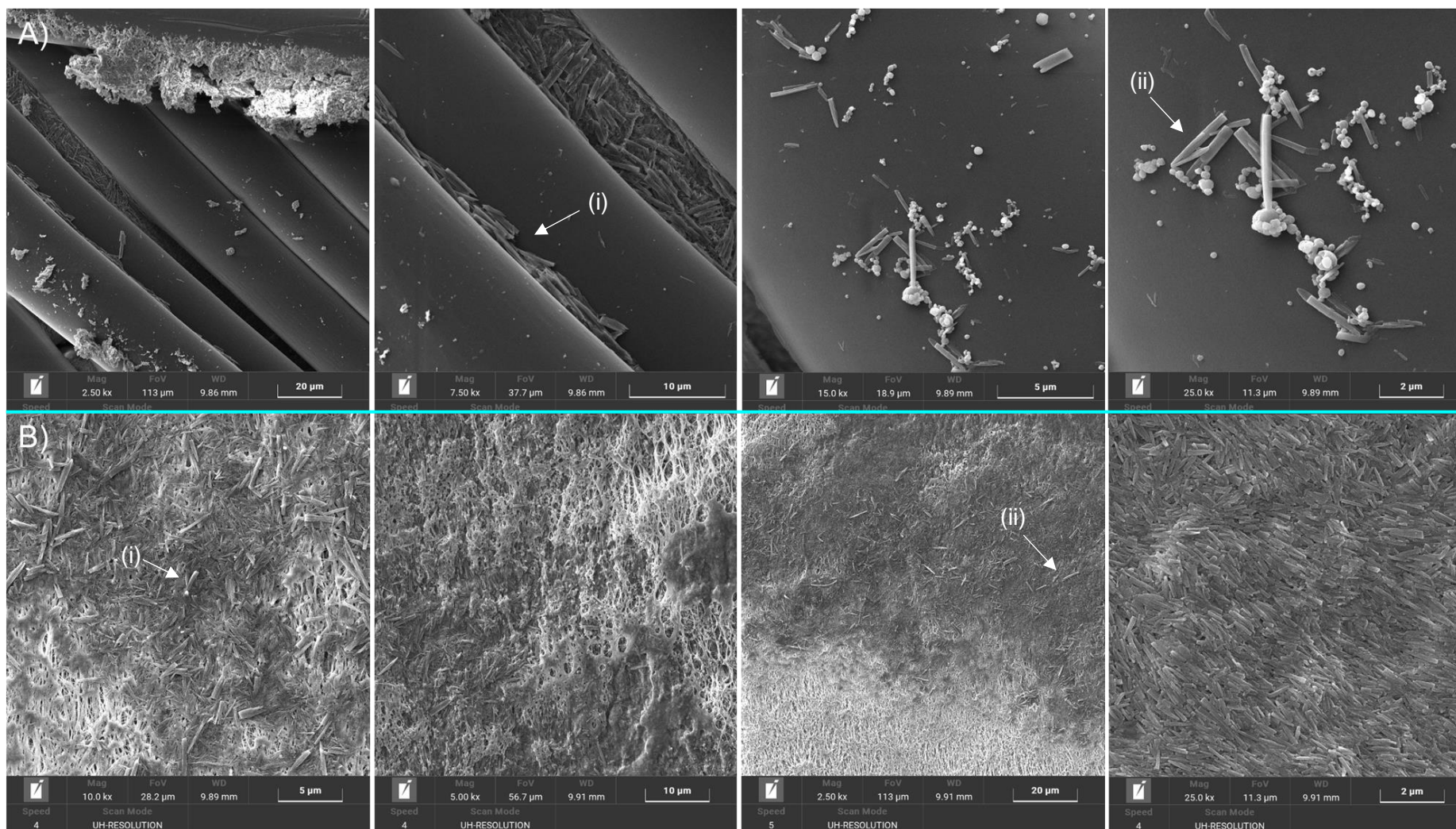


**Figure 4.36** – SEM images of a PTFE filter, used to filter PEG<sub>5K</sub>-*b*-PCL<sub>40</sub>-*co*-BOD<sub>0.7</sub> dispersion containing 75 wt% SN-38. (A) top face of the filter and (B) bottom face; (Ai & Aii) indicating needle-like crystals surrounded by spherical particles and (Bi & Bii) indicating needle-like crystals within the polymeric film.



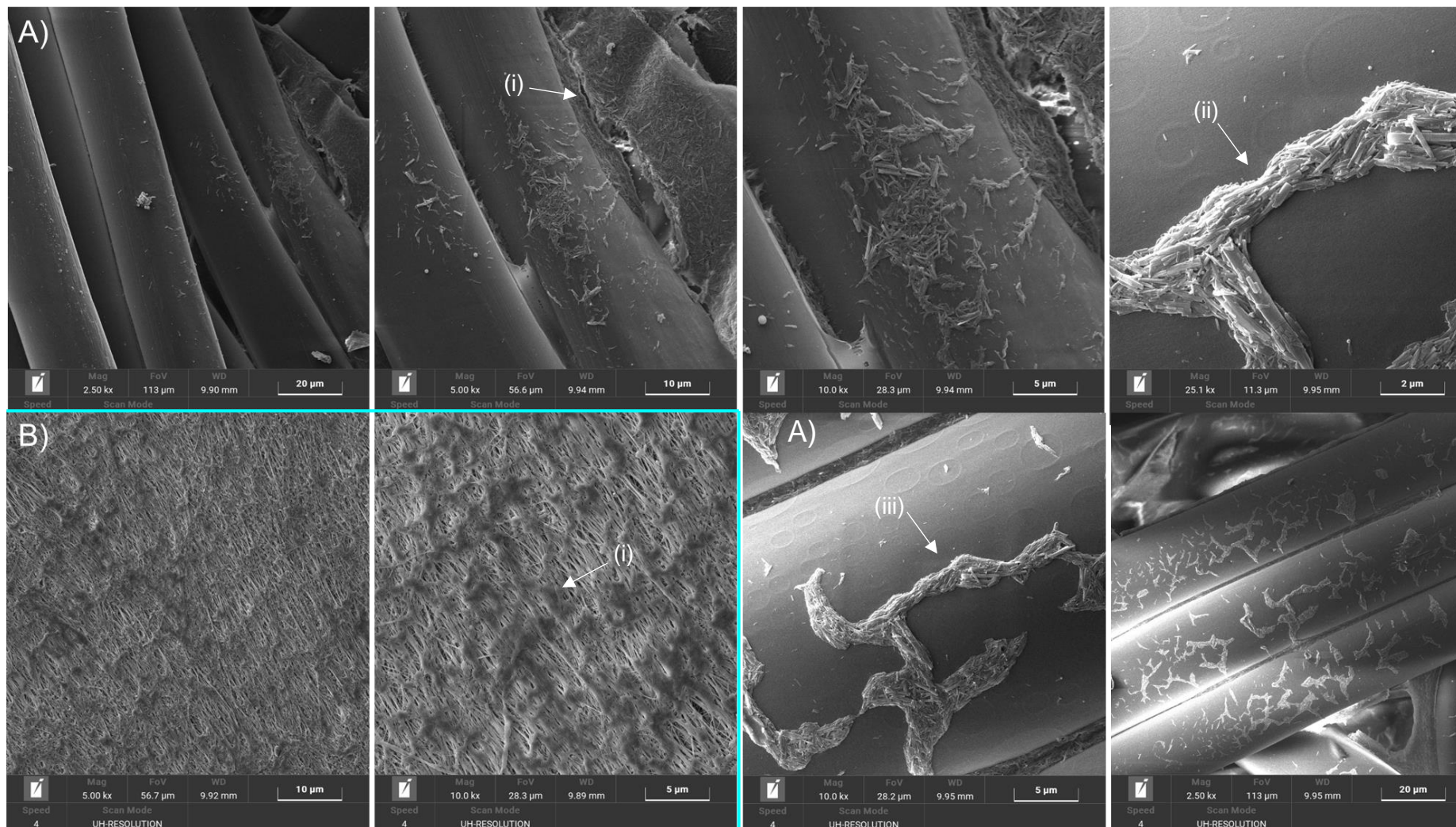


**Figure 4.37** – SEM images of a PTFE filter, used to filter  $\text{PEG}_{5K}\text{-}b\text{-PCL}_{40}\text{-}co\text{-BOD}_{0.7}$  dispersion containing 95 wt% SN-38. (A) top face of the filter and (B) bottom face; (Ai to Aiii) indicating trapped needle-like crystals and (Bi to Biii) indicating polymeric film void of crystals.

Inspection of the images of the top of the filter revealed that the nanoparticles of samples containing trends lower drug loadings of  $< 20$  wt% SN-38 were spherical in shape (Figure 4.30 to 4.32), mostly uniform in diameter with some larger particles appearing to be the result of coalescence in the process of drying the filter, and relatively low in number. The small number of particles is consistent with the majority of the sample passing through each filter and the low  $D_z$  and  $D_n$  of these samples. The bottom face of the filters used for dispersions containing  $< 20$  wt% SN-38 appeared to show the formation of a film covering the pores in the membrane; this is most likely a drying effect of the polymeric material trapped at the bottom face. The significance of these films cannot be overlooked; each film formed on the bottom face of the filter for samples with  $< 20$  wt% SN-38 showed no characteristically long and spindle-like drug crystals as described in Section 4.2.2.

Samples with increased SN-38 content ( $> 20$  wt%) displayed different behaviour, particularly when the bottom face of the filter was considered. The top face images for nanoparticles with SN-38 drug loadings of 30 and 33 wt% both contained spherical particles with small diameters; however, these appeared to be more polydisperse than those seen at lower SN-38 content (Figures 4.33 & 4.34). Additionally, a small number of planar objects were also present; which were previously only seen in dried solutions of SN-38. The formation of a film-like substance on the bottom face of the filters was seen at 30 and 33 wt% SN-38 drug loading; however, a small number of long, spindle-like drug crystals were also seen within this film. Images of the top face of filter wafers used from 50 to 95 wt% SN-38 content revealed drug crystals now trapped on the upper face the filter with larger film-like groups of crystals evident on all three samples (Figure 4.35 to 3.37). Non-spherical nanoparticles were also observed in all three samples (top face, Figure 4.35 to 4.37), which would indicate a more SDN-like structure. Additionally as the concentration of spindle-like crystals increased on the top face, the number of particles appeared to decrease, however, this was not quantified. The  $D_z$  of the particles present in dispersions containing  $\geq 75$  wt% SN-38 exceeding  $0.2 \mu\text{m}$  would lead one to expect increased trapping of particles when using these filters. The bottom faces of all three filter samples followed a similar trend in the number of crystals observed: increasing with increasing SN-38 content. Also, the crystals appeared to become more well-defined, which was to be expected due to the lack of polymer.

The SEM study of the PTFE filters allowed a narrowing of the range in which the transition from polymeric nanoparticle to SDN appears to occur. The lack of drug crystals on both the top and bottom face of the filter when drug content was  $\leq 16.6$  wt% combined with the presence

of drug crystals on the bottom face of the filter and more planar particles on the top face at 30 wt% SN-38 content would indicate the structure transition occurs between these two values.

#### **4.3.3.2 DSC of thin films formed before thin film hydration using PEG<sub>5K</sub>-*b*-PCL<sub>40</sub>-*co*-BOD<sub>0.7</sub> and SN-38**

The highlighting of a structural transition of the dispersed nanoparticles between 16.6 to 30 wt% SN-38 content via SEM allowed a focused and quantitative evaluation within this range of compositions using DSC analysis. Thin film homogeneity and SN-38 crystallinity was expected to give added insight; hypothesising that the structure of the initial films would play a meaningful role in defining the dispersions produced. Therefore the DSC study was conducted using PEG<sub>5K</sub>-*b*-PCL<sub>40</sub>-*co*-BOD<sub>0.7</sub> in thin films formed using methods described above. The dry thin films were formed inside vials before being sampled and analysed using DSC with a heat-cool-heat cycle between the temperatures of -90 °C and 250 °C.

To provide comparative data, both the polymer and the drug compound were analysed independently (Figure 4.38). PEG<sub>5K</sub>-*b*-PCL<sub>40</sub>-*co*-BOD<sub>0.7</sub> showed both a  $T_g$  and  $T_m$  at -55 °C and 51 °C respectively on the second heating cycle (Figure 4.38, A); this was consistent with the results obtained in Section 2.5. Peak enthalpy for the  $T_m$  of the polymer was 75.73 Jg<sup>-1</sup>. SN-38 produced a sharp  $T_m$  peak during the first heating cycle at 218 °C, consistent with literature values (Figure 4.38, B), and a peak enthalpy of 116.65 Jg<sup>-1</sup>.<sup>16</sup> This was the only peak observed in the heat-cool-heat cycle for SN-38 suggesting that decomposition may also occur under these conditions (i.e. no observable peak on the second heat cycle). Comparison of  $T_m$  peak enthalpy, of the polymer and drug, was expected to allow for an insight into the structural changes observed during SEM studies.

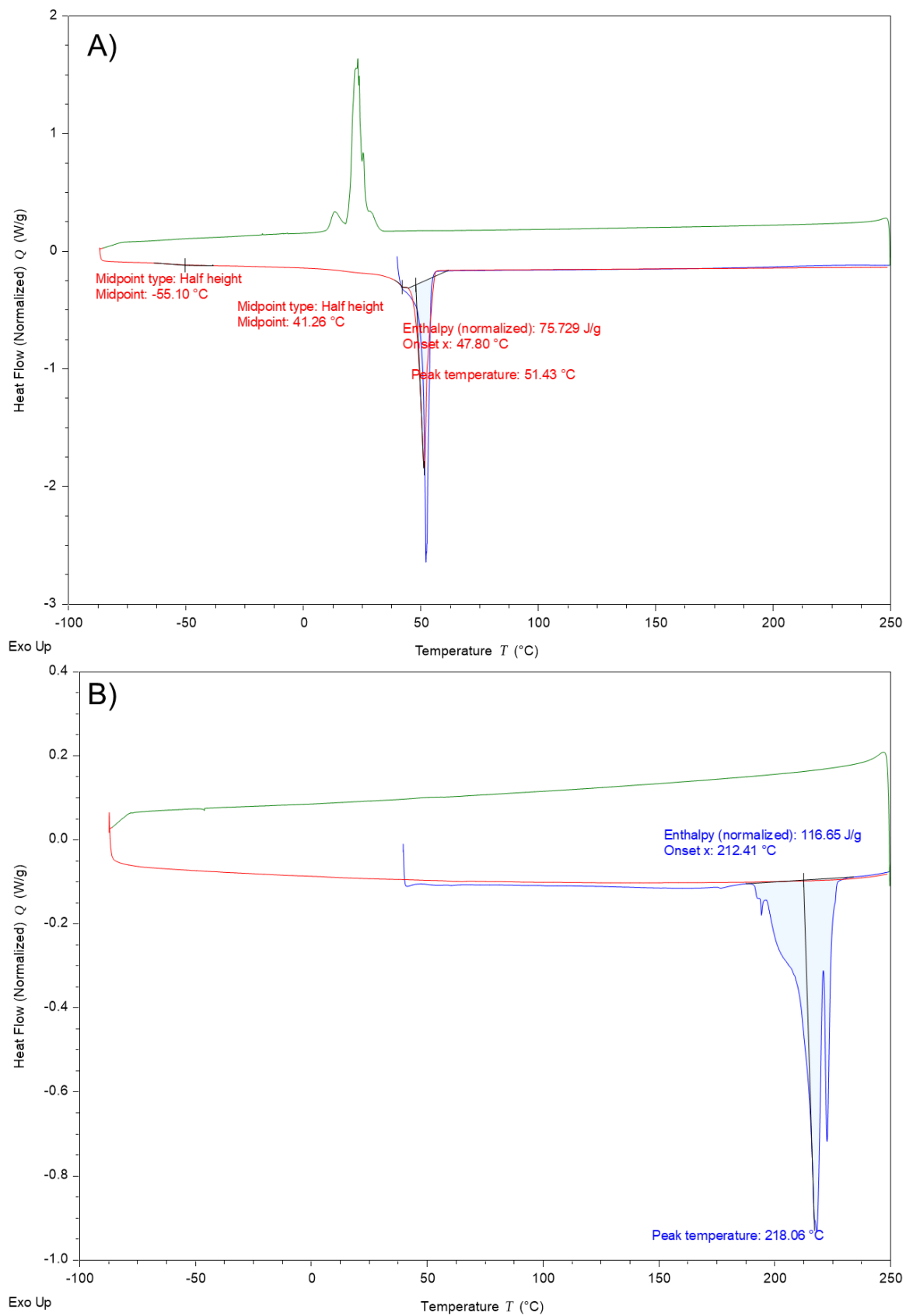


**Figure 4.38-** DSC analysis showing a heat-cool-heat cycle on; (A) PEG<sub>5K</sub>-*b*-PCL<sub>40</sub>-*co*-BOD<sub>0.7</sub>, (B) 100 wt% SN-38; (blue) first heat ramp, (green) cooling and (red) second heat ramp.

The combined polymer/drug containing dry thin films were studied across the compositions generated and  $T_m$  transitions for the polymer were well-defined and the respective peak enthalpies decreased linearly with increasing drug concentration, as would be expected (Figure 4.39). The slight increase from samples containing 0 to 2.5 wt% may be an anomaly however it could be postulated that the presence of SN-38 may encourage an increased crystallinity of the PEG chains within the polymer film therefore increasing the peak enthalpy when drug is present.

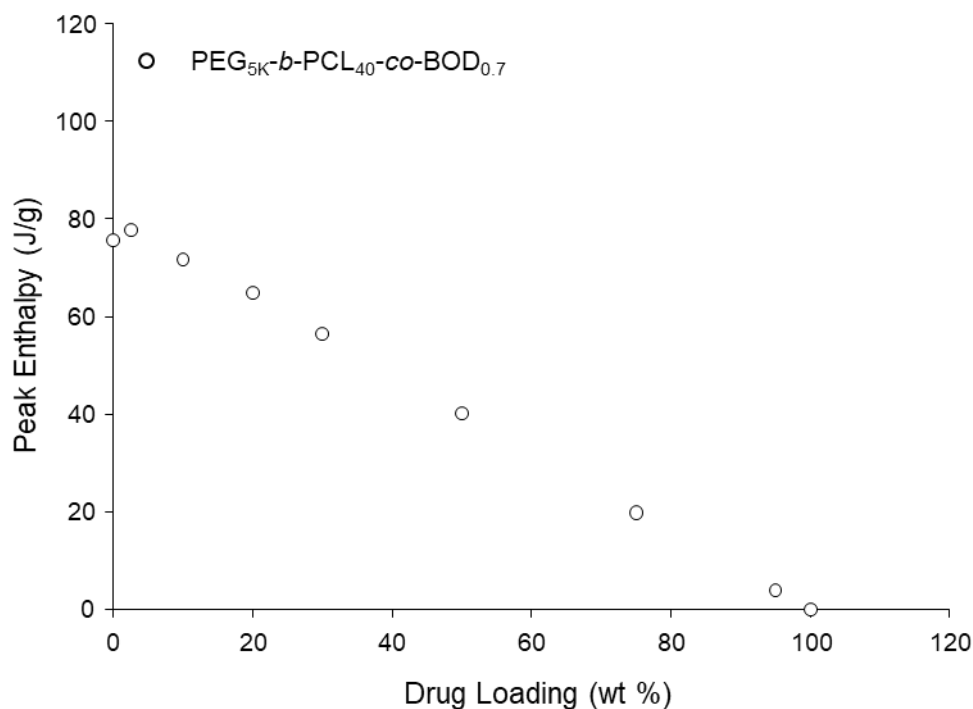


**Figure 4.39-** Graphical representation of changes in peak enthalpy of  $T_m$  peaks for  $\text{PEG}_{5\text{K}}\text{-}b\text{-PCL}_{40}\text{-}co\text{-BOD}_{0.7}$  with increasing SN-38 content.

As SN-38 only produced an endotherm during the first cycle of the heat-cool-heat analysis (Figure 4.38) in depth examination of the changes in SN-38 crystallinity, and therefore the role of the polymer in the thin film process, were solely focussed between 160 and 250 °C of the first heat cycle. When considering the full series of compositions generated an exotherm began to appear (approximately between 220 °C and 240 °C) at 30 wt% SN-38 drug loading and above. This was hypothesised to be the result of a secondary reaction (possibly oxidation or a reaction with the labile lactone ring) however this could also be an impurity given that this peak only appears within the samples containing 50 and 75 wt% SN-38 (Figure 4.40 & 4.41).

The nine samples studied were split into two groups with a single sample, 30 wt% SN-38, being present in both groups. The first group, consisting of dry thin films containing 0, 2.5, 10, 20 and 30 wt% SN-38, possessed very little, if any, real indication of SN-38 in a crystalline state

suggesting it was predominantly in an amorphous state (Figure 4.40). The thin film containing 30 wt% SN-38 however did show the beginnings of an endothermic peak formation at approximately 220 °C (Figure 4.40, pink) which would suggest the presence of crystalline domains of SN-38 forming within the thin film and the decline of homogeneity. This would also suggest the loss of amorphous molecular drug thought to be encapsulated within a polymer matrix and a possible transition to a new type of crystalline drug/polymer structure, resembling an SDN-like particle. Such DSC behaviour has been published by Prasad and Dangi who noted the disappearance of clear, sharp  $T_m$  peaks characteristic of crystalline SN-38 when encapsulated within chitosan and Eudragit® nanoparticles.<sup>17</sup> Further studies within the literature have eluded to the disappearance of  $T_m$  peaks for crystalline SN-38 when formulated as prodrug micelles or during ball milling.<sup>16,18,19</sup>

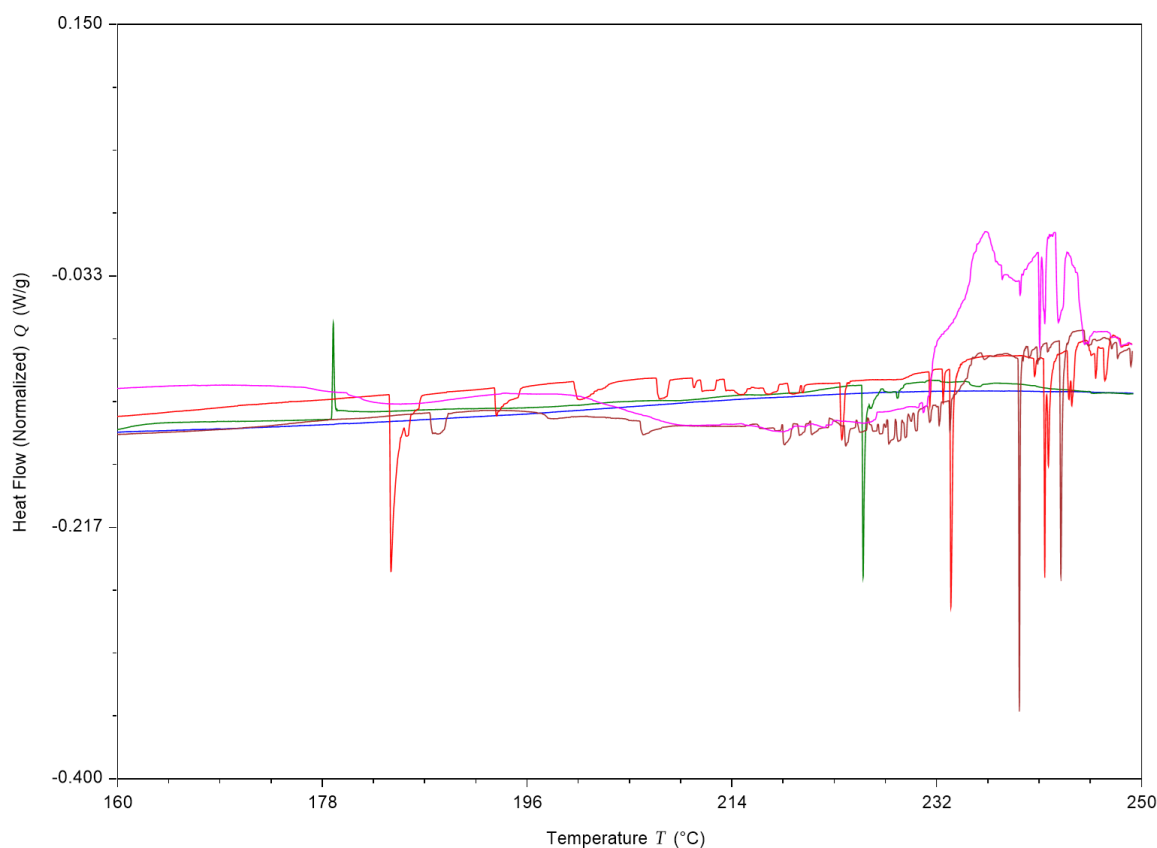


**Figure 4.40-** DSC analysis of the first heat ramp between 160 and 250 °C for SN-38 PEG<sub>5K</sub>-*b*-PCL<sub>40</sub>-*co*-BOD<sub>0.7</sub> thin films between 0 and 30 wt%; (blue) 0 wt%, (green) 2.5 wt%, (red) 10 wt%, (brown) 20 wt% and (pink) 30 wt%.

Investigation of the DSC thermograms for the second group of thin films, with SN-38 content ranging from 30, 50, 75, 95 and 100 wt%, displayed an increase of a  $T_m$  between 180 and 220 °C (Figure 4.41). Above 50 wt% the endotherm assigned to the melting of SN-38 became



sharper and more well-defined, suggesting an increase in SN-38 crystallinity within the thin film.

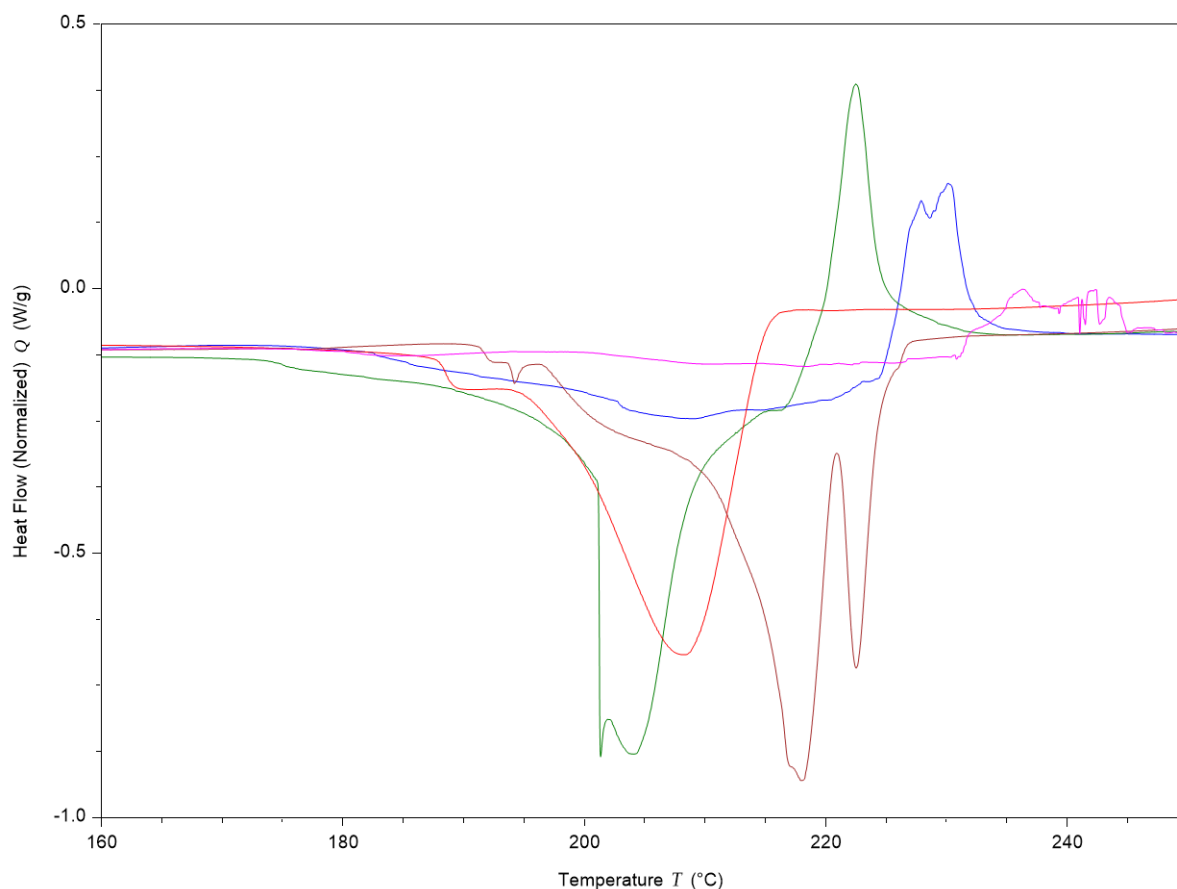


**Figure 4.41-** DSC analysis of the first heat ramp between 160 and 250 °C for SN-38 PEG<sub>5K</sub>-*b*-PCL<sub>40</sub>-*co*-BOD<sub>0.7</sub> thin films between 30 and 100 wt%; (pink) 30 wt%, (blue) 50 wt%, (green) 75 wt%, (red) 95 wt% and (brown) 100 wt%.

Further in-depth analysis was undertaken by the measurement of peak enthalpy of the SN-38 endotherm for each sample, however due to the minimal definition of this peak in samples containing low amounts of SN-38 the boundaries for this measurement were varied on a sample basis. All the endothermic peaks within the initial region >160 °C were included. As  $T_m$  of crystalline SN-38 were not highly detectable when SN-38 content was low, analysis suggested predominantly amorphous material was present. Plotting of peak enthalpy of both polymer (shown on its own in Figure 4.39) and drug vs. drug loading revealed a noticeable, and near-linear trend for SN-38 peak enthalpy at drug loadings >20 wt% (Figure 4.42); this supports the proposed transition from a polymer particle encapsulating drug to SDN-like particles within the dispersions as the homogeneity of the thin film decreased with increasing SN-38 content.

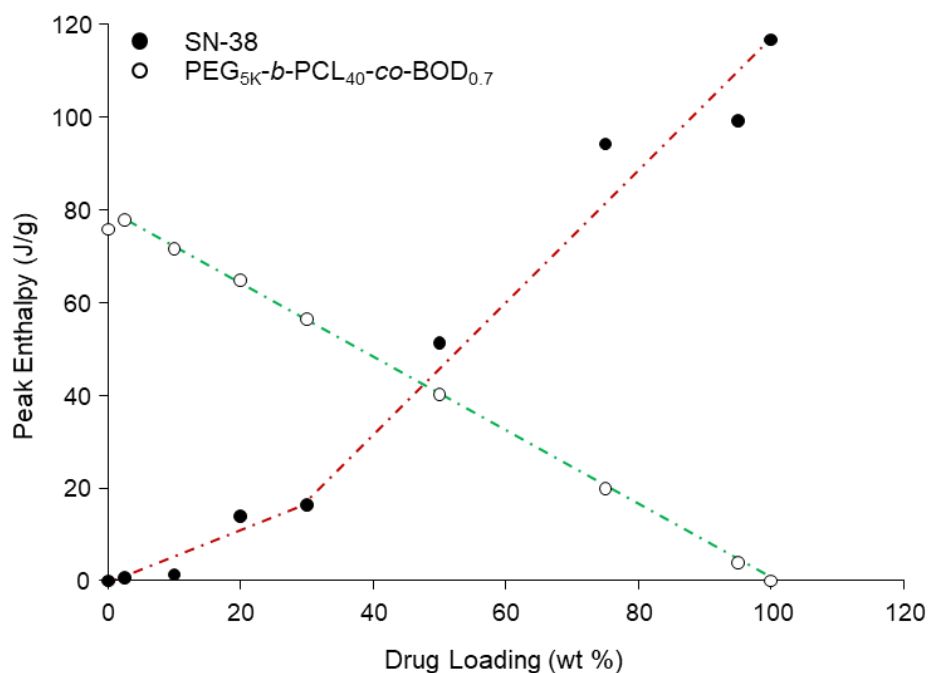


**Figure 4.42-** Graphical representation of changes in peak enthalpy of both  $T_m$  peaks for SN-38 and PEG<sub>5K</sub>-*b*-PCL<sub>40</sub>-*co*-BOD<sub>0.7</sub> with increasing SN-38 content; guidelines for gradient PEG<sub>5K</sub>-*b*-PCL<sub>40</sub>-*co*-BOD<sub>0.7</sub> (green) and the change in gradient for SN-38 (red).

#### 4.3.3.3 TASC of thin films formed before thin film hydration using PEG<sub>5K</sub>-*b*-PCL<sub>40</sub>-*co*-BOD<sub>0.7</sub> and SN-38

The thermal properties of the dry thin films were also evaluated using “thermal analysis by structural characterisation”, *TASC*, a technique expected to give a more in-depth picture of the thermal transitions at the time of melting. Developed by M. Reading, *TASC* allows changes in the sample to be analysed as heat and humidity increase by taking a number of pictures of the sample.<sup>20</sup> The *TASC* algorithm then quantifies the changes which are observed within a designated area, producing a change in gradient in the *TASC* output. Like DSC, the mid-point of these sigmoidal step changes can be used to define a  $T_g$  or  $T_m$  point within the sample being studied.<sup>20</sup> This technique requires no contact with the sample and is complementary to DSC, providing both qualitative and quantitative results.

Similar to other studies detailed in Section 4.3.3.2, PEG<sub>5K</sub>-*b*-PCL<sub>40</sub>-*co*-BOD<sub>0.7</sub> was selected for this study and thin films were created on 16 mm circular glass microscope cover slips by pipetting a small amount of the THF solution and allowing the solvent to evaporate. As with the SEM study of the dry thin films in Section 4.3.3.1.1, this method did not fully reflect the formation of thin films via vacuum solvent removal, however, it offered the best compromise to achieve thin films suitable for *TASC* analysis. Every film was heated from ambient

temperature to 250 °C following the determination of the  $T_m$  of SN-38 to be approximately 218 °C by DSC analysis (Section 4.3.3.2). Each sample examined was photographed at a rate of two pictures per second during the heating process allowing videos to be generated for each (see attached USB).

Again, comparative TASC analyses were conducted using 100 wt% PEG<sub>5K</sub>-*b*-PCL<sub>40</sub>-*co*-BOD<sub>0.7</sub> and 100 wt% SN-38. The thin film containing only PEG<sub>5K</sub>-*b*-PCL<sub>40</sub>-*co*-BOD<sub>0.7</sub> proved challenging to analyse due to transparency, resulting in considerable noise within the TASC analysis (Figure 4.43). Nonetheless, it was clear from the video generated that the polymer film began to melt between 47 and 65 °C. Following TASC analysis of the images, a change in gradient at 51.1 °C signified the  $T_m$  of the polymer (Figure 4.43) which was comparable to DSC analysis ( $T_m = 51.4$  °C, Section 4.3.3.2). As no other visual changes were observed in the thin film the changes in gradient between 800 and 1,050 seconds were considered as noise.

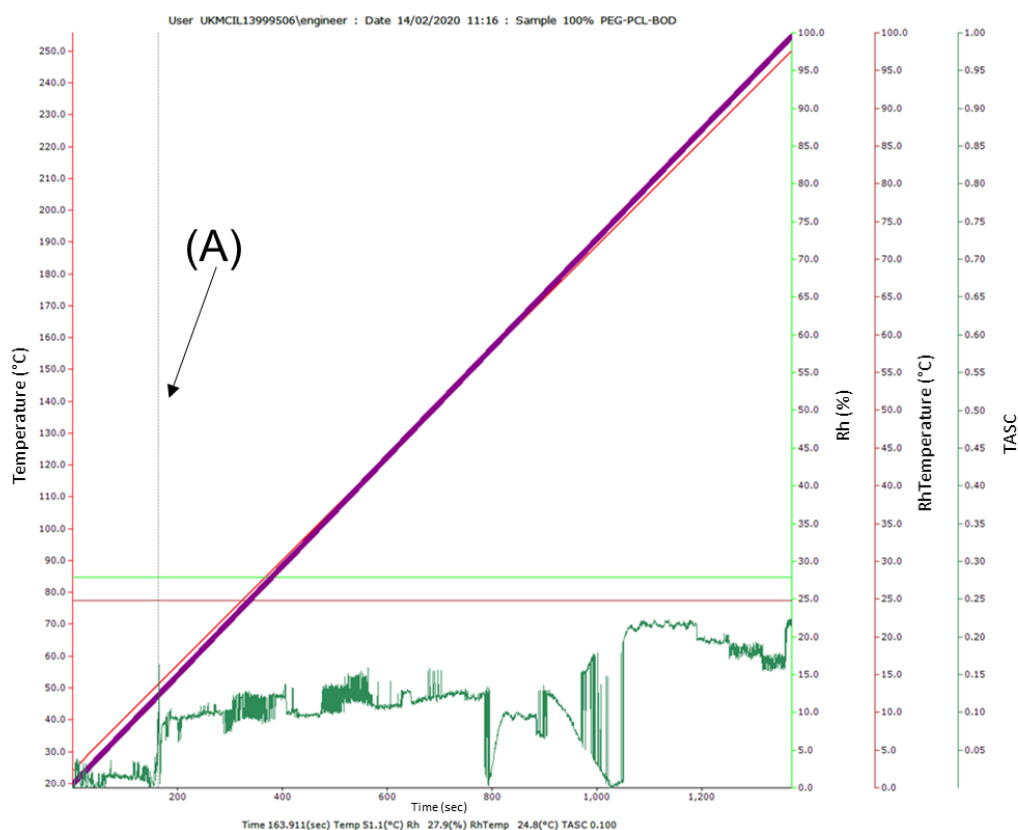


**Figure 4.43-** TASC analysis performed on a thin film of 100 wt% PEG<sub>5K</sub>-*b*-PCL<sub>40</sub>-*co*-BOD<sub>0.7</sub>; (A) Midpoint = 51.1 °C.

The opaque nature of the 100 wt% SN-38 film allowed for a considerable decrease in background noise in the TASC analysis, allowing a defined indication of changes within the sample during heating. Upon visual inspection the sample began to change colour at approximately 180 °C which may indicate some decomposition; two further visual

transformations occurred above this temperature which may indicate different SN-38 crystal habits and TASC analysis supported the presence of these transitions (midpoints values = 207.4 and 230.9 °C; Figure 4.44, A & B). Both of these values were inconsistent with the  $T_m$  of SN-38 observed by DSC ( $T_m = 218.1$  °C, Section 4.3.3.2) which may indicate a variation of crystal form. The sample appeared fully molten at 230.9 °C. Varied literature values for the melting point of SN-38, *via* DSC and melting point analysis, suggest that it is difficult to assign a consistent melting point, supporting the hypothesis that different crystal forms of the drug may exist.<sup>16,18,19,21</sup> However the discrepancies between the DSC and TASC observations could be linked to the increased accuracy of the DSC which is undertaken under inert atmosphere and requires different sample preparation which may influence the results obtained.

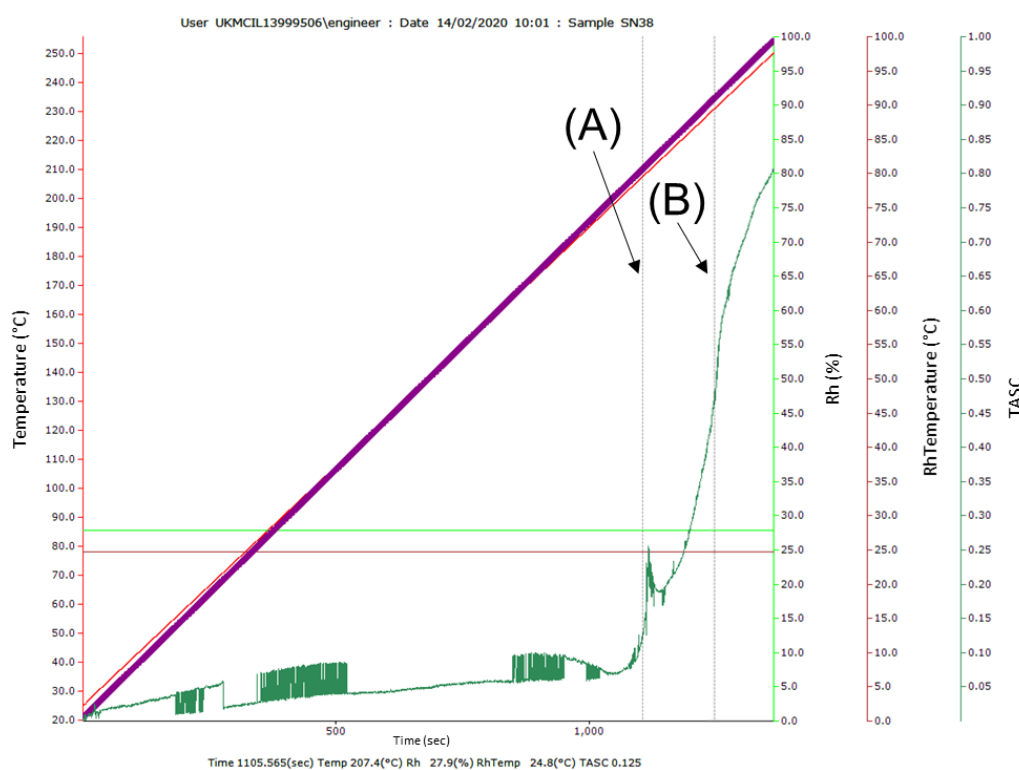


**Figure 4.44-** TASC analysis performed on a thin film of 100 wt% SN-38; (A) Midpoint = 207.4 °C and (B) Midpoint = 230.9 °C.

As the transition from drug-encapsulated polymeric nanoparticle to SDN appeared to occur between 10-30 wt% SN-38 by SEM and DSC investigations, thin films containing 10, 16.6 and 30 wt% SN-38 were analysed *via* TASC. Analysis of the PEG<sub>5K</sub>-*b*-PCL<sub>40</sub>-*co*-BOD<sub>0.7</sub> thin film containing 10 wt% SN-38 showed a clear loss of structure below 100 °C, associated with the melting of the polymer. A second structural change resembling the complete melting of all components of the film occurred above 200 °C; due to the movement of the slide during the measurement the background noise was relatively high, but a distinct melting point was

observed for the polymer at 52.1 °C which was comparable to both DSC and TASC analysis of the blank polymer film (Figure 4.45, A). A second gradient change was observed, spanning from 650-1,250 seconds, with a disappearance of thin film structures, at a midpoint value of 203.6 °C, which was assigned to SN-38 (Figure 4.45, B). It is also important to note that a change in colour from colourless/white to yellow was not observed in this sample. This broader, less defined peak for the apparent melting of SN-38, coupled with a lack of colour change, suggests that the crystallinity of the drug has been disrupted by the polymer and several forms of SN-38 may be present. The shift from crystalline to amorphous SN-38 has previously been noted in DSC studies within literature, indicated by a disappearance of a  $T_m$  peak at 200-230 °C when interacting with polymers or due to a processing technique such as grinding.<sup>16,18</sup>

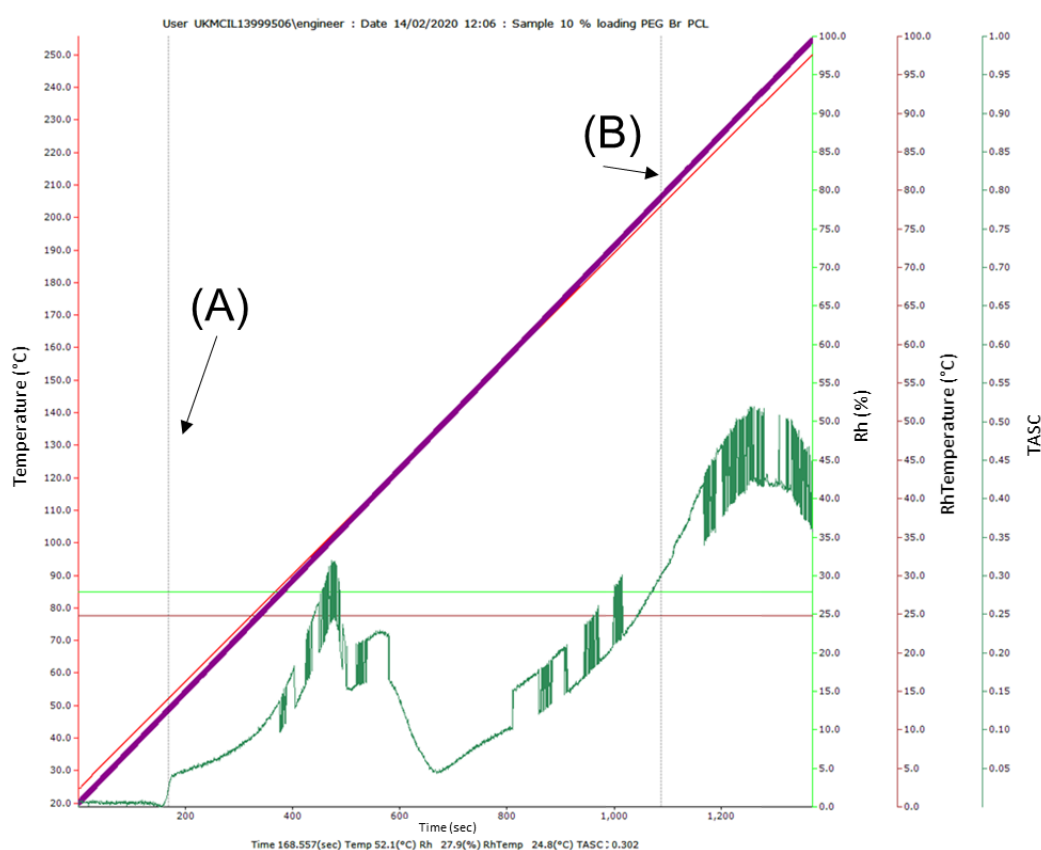


**Figure 4.45- TASC analysis performed on a thin film with PEG<sub>5K</sub>-*b*-PCL<sub>40</sub>-*co*-BOD<sub>0.7</sub> and 10 wt% SN-38; (A) Midpoint = 52.1 °C and (B) Midpoint = 203.6 °C.**

The visual assessment of the film containing 16.6 wt% SN-38 showed a total of 4 changes as temperature increased. This was confirmed by TASC analysis displaying four changes in gradient correlating to the visual transitions (Figure 4.46). The first midpoint value of 51.8 °C was confirmed as the polymer  $T_m$  correlating well with the values gained from previous TASC analysis and DSC of PEG<sub>5K</sub>-*b*-PCL<sub>40</sub>-*co*-BOD<sub>0.7</sub> (Figure 4.46, A). The second midpoint values

of 109.2 °C correlates within a change of film colour from a ‘cream’ to a dark grey, almost transparent film, which visually suggested the melting of another structure present although it is difficult to assign this (Figure 4.46, B). The sample proceeded to change to a yellow colour after this second transition, followed by a final melting. These last two changes were characterised in the TASC analysis as a broader peak with a less steep gradient and a sharper incline for the final transitions with midpoints values of 191.2 and 245.8 °C (Figure 4.46, C & D). Again this lack of definition for the melting point of SN-38 and multiple melting transitions within the sample suggests a disruption of the SN-38 crystallinity, potentially forming amorphous SN-38 or at least a number of crystal habits<sup>16,17,19</sup>

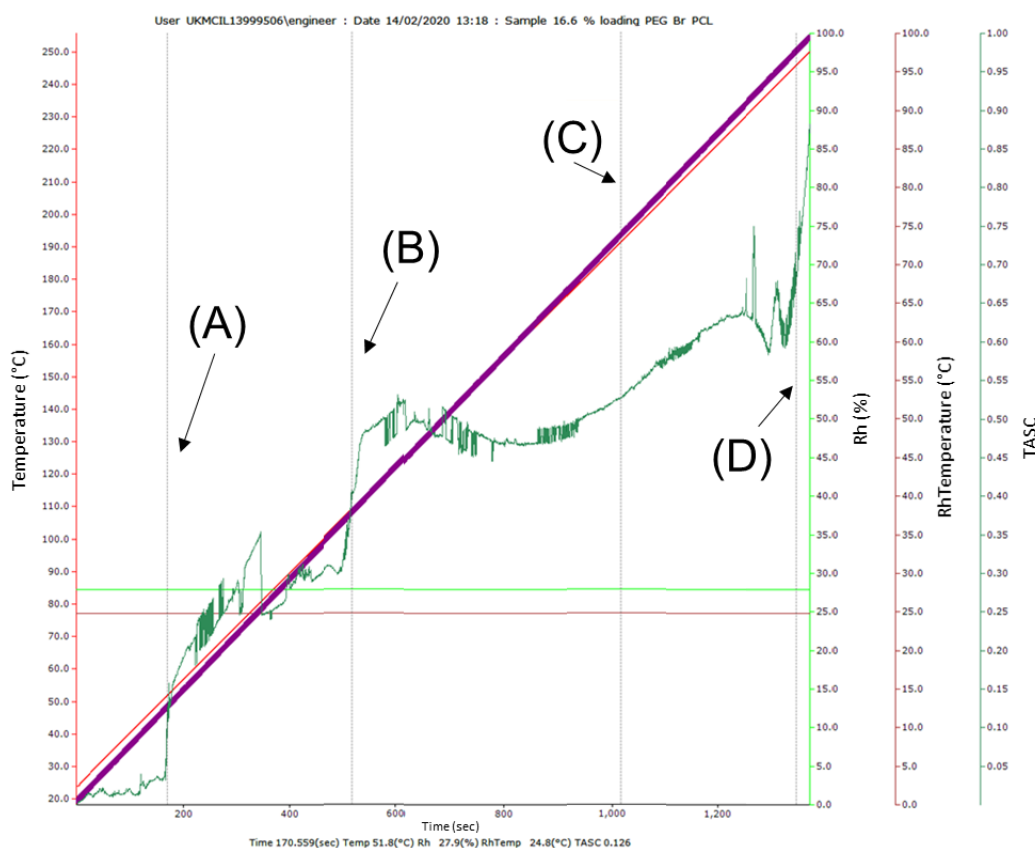


**Figure 4.46- TASC analysis performed on a thin film with PEG<sub>5K</sub>-*b*-PCL<sub>40</sub>-*co*-BOD<sub>0.7</sub> and 16.6 wt% SN-38; (A) Midpoint = 51.8 °C, (B) Midpoint = 109.2 °C, (C) Midpoint = 191.2 °C and (D) Midpoint = 245.8 °C.**

Finally, the dry thing film sample containing 30 wt% SN-38, showed areas of crystallinity when viewed under polarised light as indicated by the readily identified birefringent ‘Maltese cross’ structures within the overall image. Therefore, it was clear that the thin film was not homogeneous and either crystals of SN-38 or the crystallisation of PEG<sub>5K</sub> chains was present in the film. Visual inspection of the sample during the heating process confirmed that there were three changes within the sample, first a polymer melt followed by a change in colour from

white to grey/transparent. However, this was not consistent throughout the sample and resembled a melting point of the same unspecified species in the 16.6 wt% sample. The final change occurred over an extended period in which the sample underwent a colour change from white to yellow, followed by the complete melting of the sample. Due to the areas of crystalline drug, which only melted at high temperature, two separate TASC analyses were performed on the sample. The first area selected, referred to as *TASC 1*, was located close to the edge of the sample where the most significant change occurred at lower temperatures, particularly during the polymer melting point (Figure 4.47, i). The second area, referred to as *TASC 2*, focussed on the segment close to the Maltese crosses, as during the visual inspection it was evident less changes occurred in this area over the full heating cycle (Figure 4.47, ii).



**Figure 4.47** – Image defining the two areas used to complete TASC analysis; (i) TASC 1 and (ii) TASC 2.

TASC 1 analysis revealed three changes in gradient consistent with the visual observations made in the segment selected: 1) the polymer melting point at 52.2 °C, was consistent with the other values generated for PEG<sub>5K</sub>-*b*-PCL<sub>40</sub>-*co*-BOD<sub>0.7</sub> during this study (Figure 4.48, A); 2) a change that was assigned to the melting of an unknown species, possibly SN-38 in a different crystal form, occurred at 113.2 °C similar to the values generated with 16.6 wt% SN-38 (Figure 4.48, B); and 3) a long sloping gradient (Figure 4.48, C) with a midpoint value of 231.5 °C which was in the literature-reported melting point range of SN-38.<sup>16,21</sup>



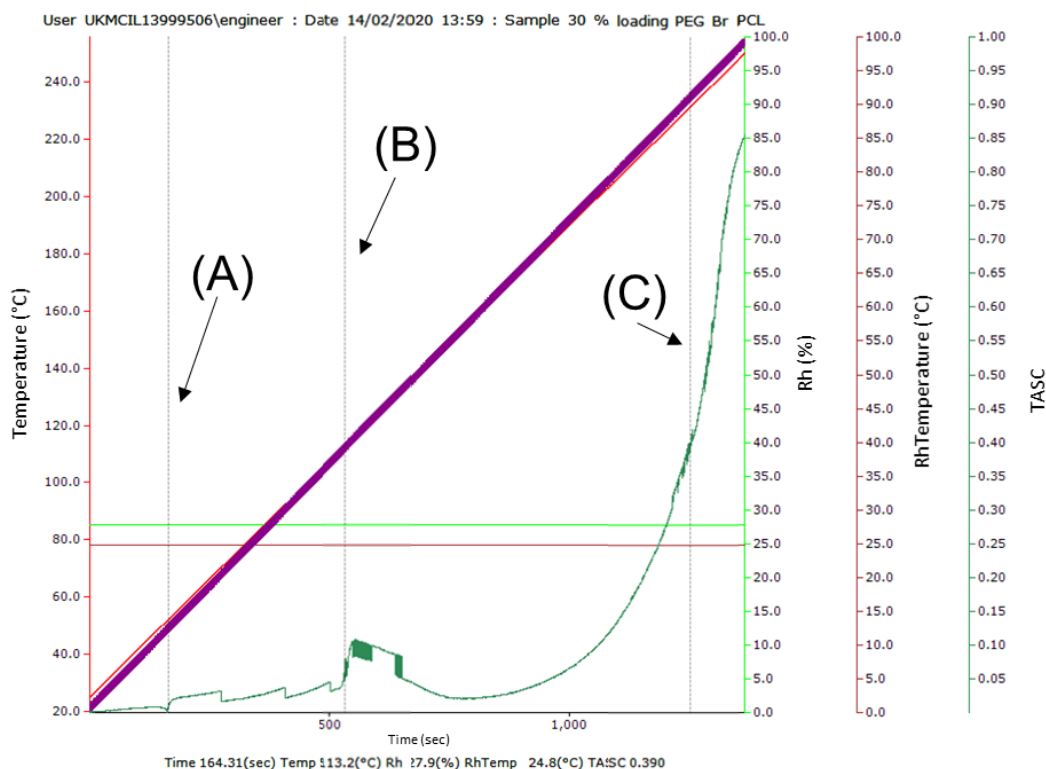


**Figure 4.48-** TASC 1 analysis performed on a thin film with PEG<sub>5K</sub>-*b*-PCL<sub>40</sub>-*co*-BOD<sub>0.7</sub> and 30 wt% SN-38; (A) Midpoint = 52.2 °C, (B) Midpoint = 113.2 °C and (C) Midpoint 231.5 °C

TASC 2 analysis revealed only one change in gradient at 238.0 °C, again within the literature range for the  $T_m$  of SN-38 (Figure 4.49, B).<sup>16</sup> The gradient, in this case, was much steeper than previously seen in thin films of lower SN-38 content, with less broadening at lower temperatures. The lack of changes throughout the rest of the TASC 2 analysis indicates that this segment of the 30 wt% sample probably contained only one crystalline form of SN-38. Therefore this supports the hypothesis that this thin film is not homogeneous. This would also lead the suggestion that the polymer content at 30 wt% SN-38 is insufficient to dominate the behaviour of the film during hydration/sonication and drug encapsulated polymeric nanoparticles are unlikely to form.



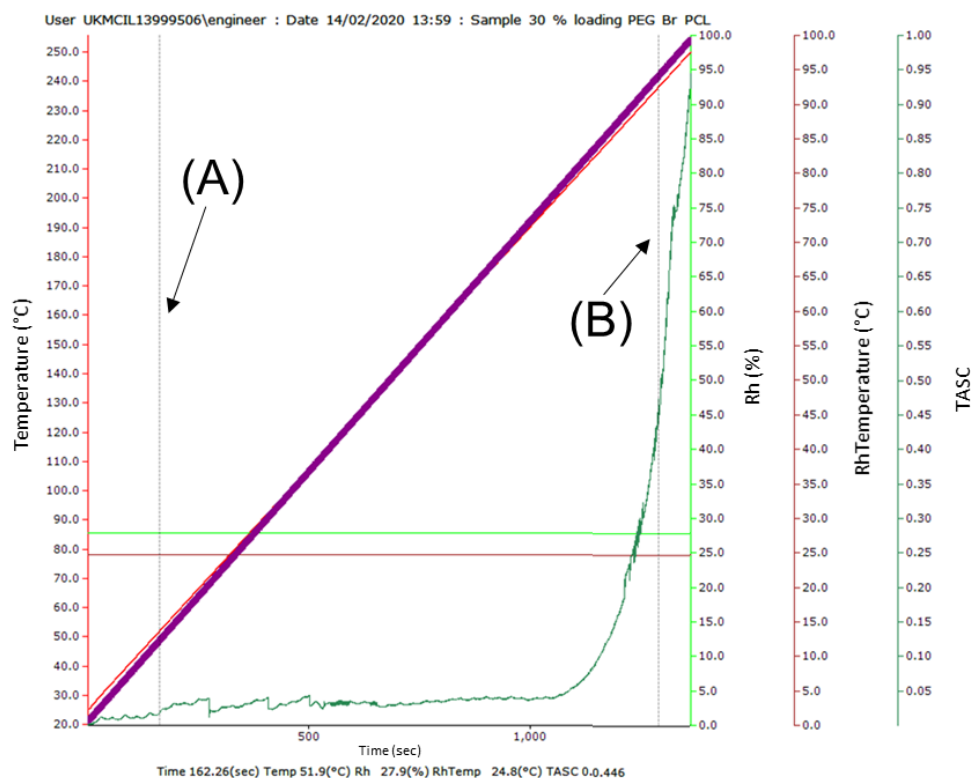


**Figure 4.49-** TASC 2 analysis performed on a thin film with PEG<sub>5K</sub>-*b*-PCL<sub>40</sub>-*co*-BOD<sub>0.7</sub> and 30 wt% SN-38; (A) Midpoint = 51.9 °C and (B) Midpoint = 238.0 °C.

#### 4.4 Pharmacological studies of SN-38 containing dispersions produced *via* thin film hydration of branched PEG<sub>5K</sub>/polyester co-polymers

Following the suggested successful encapsulation of SN-38 *via* thin film hydration, the resultant dispersions were subjected to pharmacological studies. *In vitro* studies were performed to assess the rate of SN-38 release, the cytotoxicity of the dispersions and finally the cellular uptake of each dispersion across the range of polymer and drug loading options. It was expected that *in vivo* studies would be possible after this *in vitro* evaluation. The work in this section was carried out by Mr Usman Arshad under the supervision of Professor Andrew Owen and Professor Chris Goldring in the Department of Molecular and Clinical Pharmacology at the University of Liverpool.

##### 4.4.1 Release rate studies

The library of nanoparticle dispersions selected for this study were based upon the branched PEG/polyester co-polymers that had achieved successful nanoparticle dispersions over a large range of drug loading values. All five branched PEG/polyester co-polymers were studied with SN-38 content of 10, 50 and 75 wt% as it was hypothesised that higher SN-38 content would

be more clinically valuable. Release rate studies were conducted using a well-plate rapid equilibrium dialysis, *RED*, assay in phosphate-buffered saline, *PBS*, at a dilution 20 times below that of SN-38 in PBS. Each time measurement required removal of the entire receptor well contents (Figure 4.50), whilst continuing until the concentration equilibrated across the membrane and in the nanoparticles. In this way, a maximum drug release of 50 % of the initial dose added to the donor well would be seen; the assay was typically conducted over 48 hours with full-well measurements taken every hour for the first 8 hours, then samples at 24 hours and finally at 48 hours.

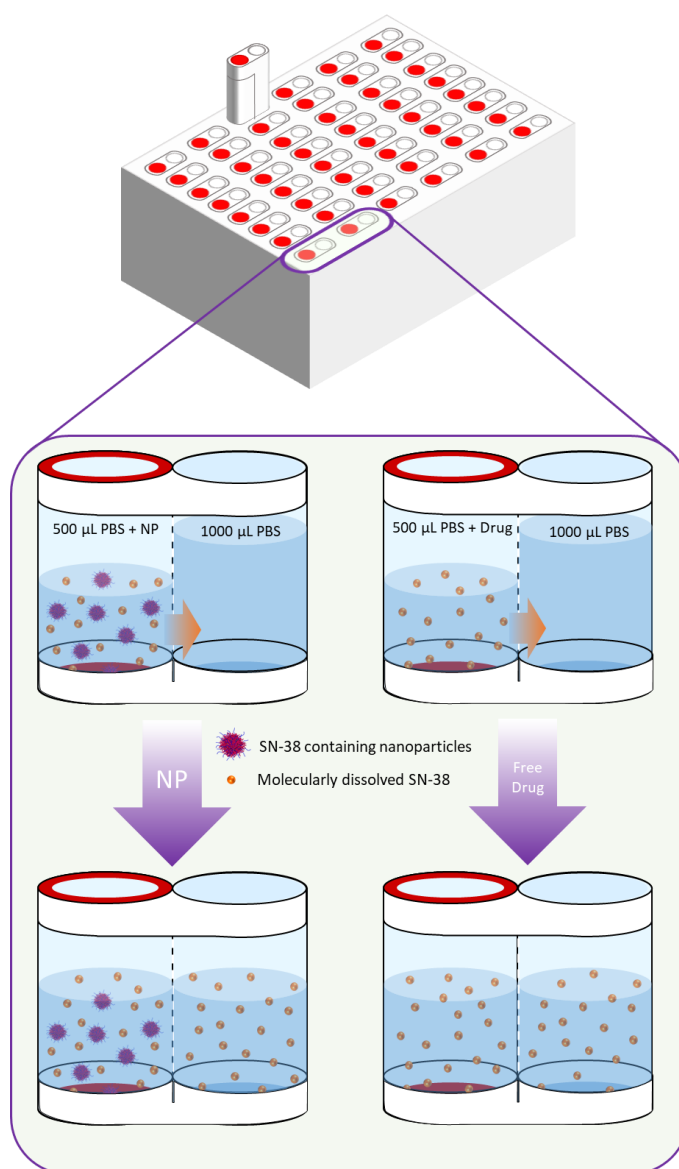


**Figure 4.50- Schematic representation of an RED assay; (A) nanoparticles containing drug and (B) free drug.**

Analysis of SN-38 release from each system with varying drug content and polymer chemistry was compared to free SN-38 to highlight any benefits of encapsulation and nanoparticle formation over the 48 hour study (Figure 4.51 , Appendix C). Every sample, regardless of drug content, appeared to replicate free drug release after 8 hours. Despite encapsulation within a polymeric nanoparticle or SDN-like structure all the nanoparticle systems appeared to have only slightly slower rates of release than that of free SN-38.

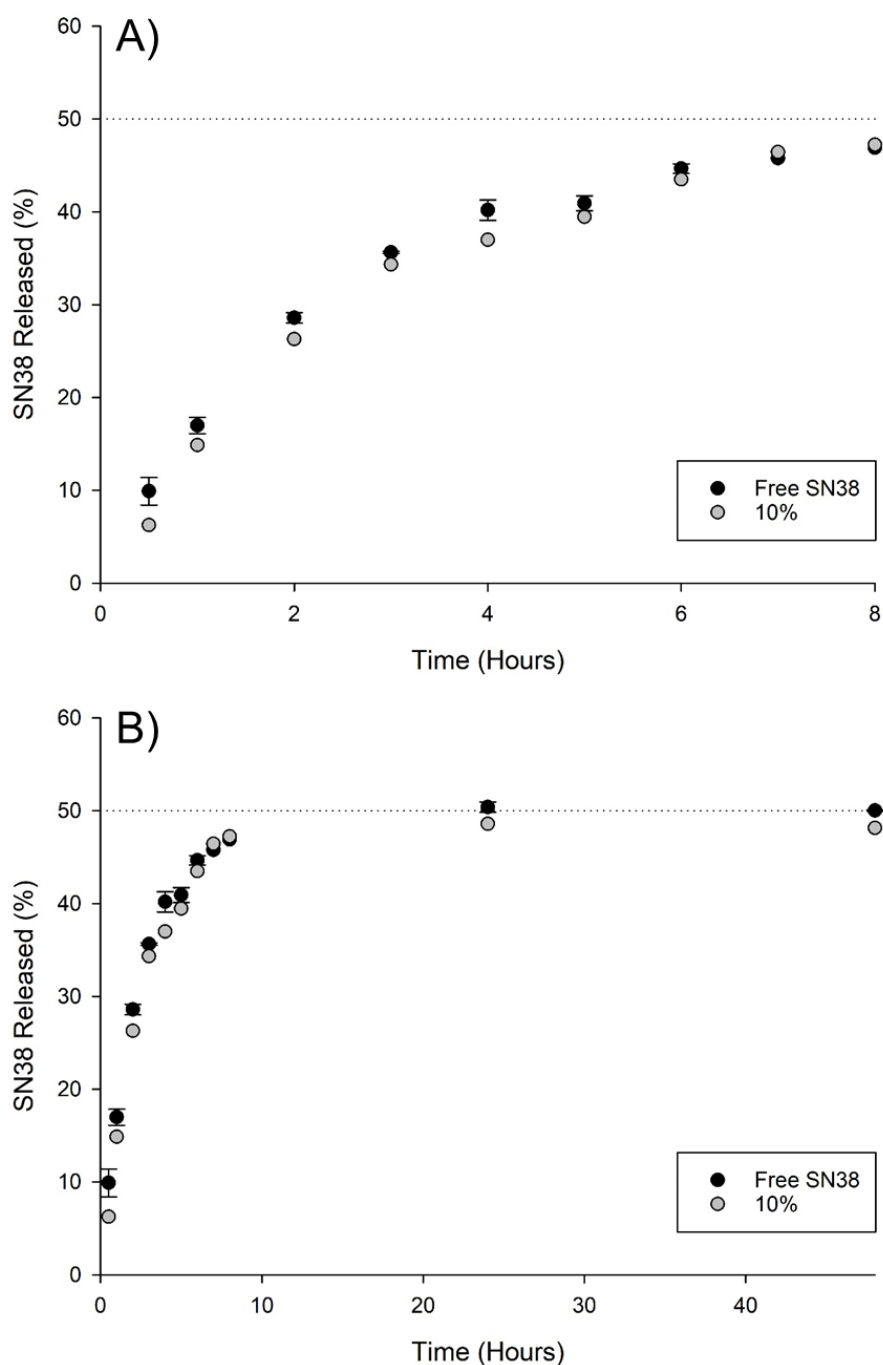


**Figure 4.51 – Example of a release rate curve produced *via* RED assay for a PEG<sub>5K</sub>-*b*-PCL<sub>40</sub>-*co*-BOD<sub>0.7</sub> nanoparticle dispersion containing 10 wt% SN-38; (A) the first 8 hours and (B) over 48 hours.**

To allow for a clear visual comparison, the data was replotted using bar charts, excluding 24 and 48 hour time points. Three charts were plotted, corresponding to various SN-38 drug loadings, each with free SN-38 as a comparison. Firstly 10 wt% SN-38 containing nanoparticle dispersions were considered which highlighted PEG<sub>5K</sub>-*b*-PCL<sub>40</sub>-*co*-BOD<sub>0.7</sub> and PEG<sub>5K</sub>-*b*-PMOP<sub>40</sub>-*co*-BOD<sub>0.7</sub> as the slowest releasing nanoparticle systems (Figure 4.52) at this drug loading. PEG<sub>5K</sub>-*b*-PMOP<sub>40</sub>-*co*-BOD<sub>0.7</sub> maintained a slower release than free SN-38 for 3 hours, whereas PEG<sub>5K</sub>-*b*-PCL<sub>40</sub>-*co*-BOD<sub>0.7</sub> showed a retarded rate until 6 hours had elapsed although the concentration of drug released at 2 hours was slightly higher than free drug.

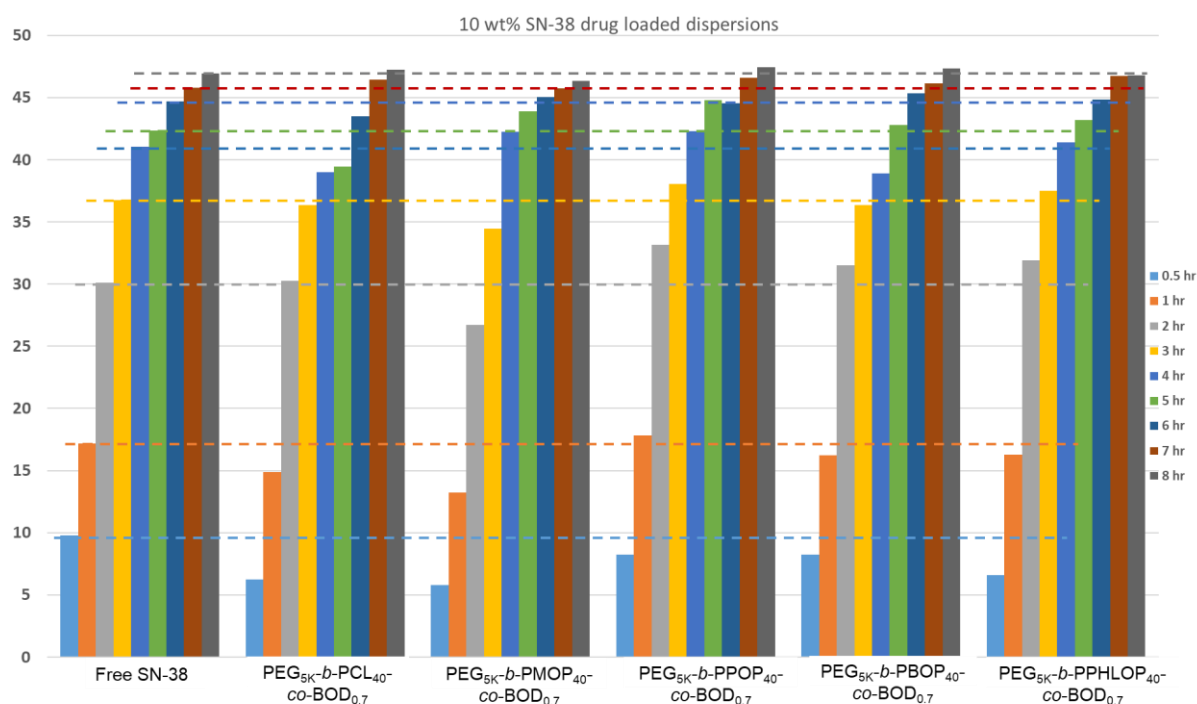


**Figure 4.52- RED assay equilibrium release rate (over 8 hours) for 10 wt% SN-38 containing samples generated from thin film hydration of branched PEG<sub>5K</sub>/polyester AB block co-polymers.**

Investigations of nanoparticle dispersions containing 50 wt% SN-38 portrayed the same trend with the only two samples displaying retardation in drug release, when compared to free SN-38, based on PEG<sub>5K</sub>-*b*-PCL<sub>40</sub>-*co*-BOD<sub>0.7</sub> and PEG<sub>5K</sub>-*b*-PMOP<sub>40</sub>-*co*-BOD<sub>0.7</sub> (Figure 4.53) PEG<sub>5K</sub>-*b*-PCL<sub>40</sub>-*co*-BOD<sub>0.7</sub> showed a longer delay in SN-38 release over 8 hours compared to both the 10 wt% containing sample and PEG<sub>5K</sub>-*b*-PMOP<sub>40</sub>-*co*-BOD<sub>0.7</sub>. PEG<sub>5K</sub>-*b*-PMOP<sub>40</sub>-*co*-BOD<sub>0.7</sub> again only maintained slower release than free SN-38 for 3 hours (Figure 4.53).

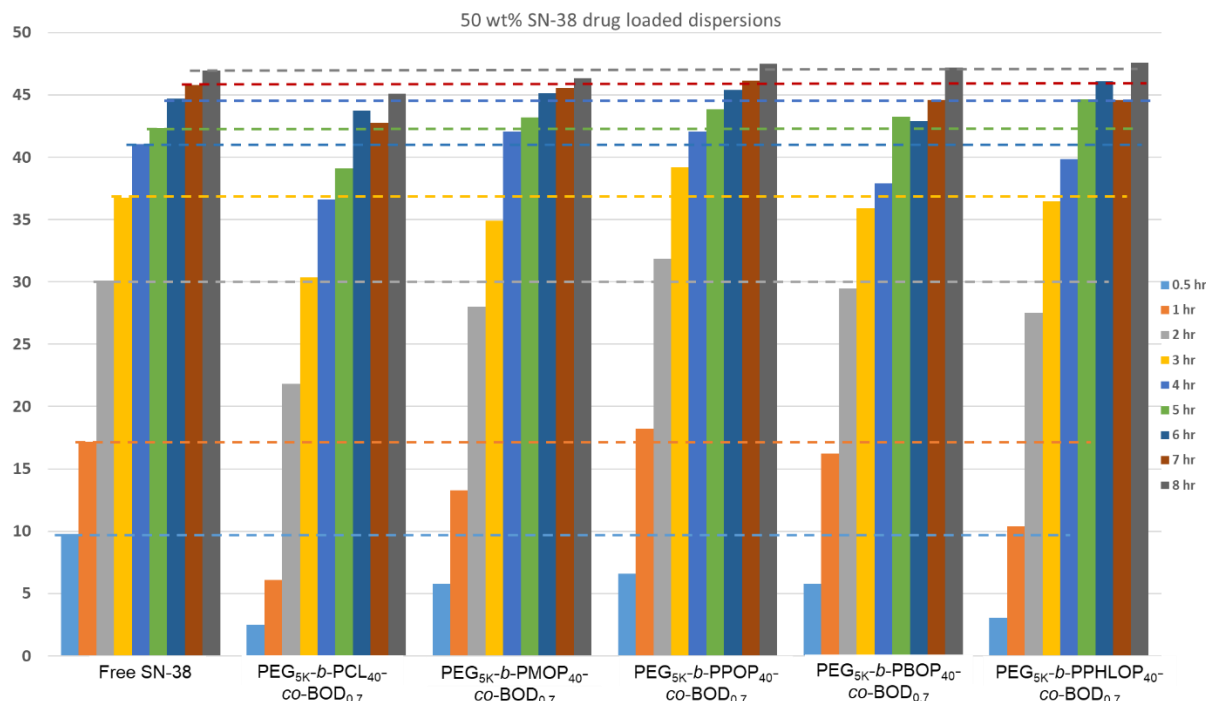


**Figure 4.53- RED assay equilibrium release rate (over 8 hours) for 50 wt% SN-38 containing samples generated from thin film hydration of branched PEG<sub>5K</sub>/polyester AB block co-polymers.**

The final group of nanoparticle dispersions (75 wt% SN-38) indicated that PEG<sub>5K</sub>-b-PCL<sub>40</sub>-co-BOD<sub>0.7</sub> released SN-38 significantly slower than the dispersions formed using the other four polymers (Figure 4.54); however, PEG<sub>5K</sub>-b-PBOP<sub>40</sub>-co-BOD<sub>0.7</sub> and PEG<sub>5K</sub>-b-PPHLOP<sub>40</sub>-co-BOD<sub>0.7</sub> derived dispersions now showed a slower release than free SN-38 over 5 hours (Figure 4.54). This was significantly longer than dispersions containing either 10 or 50 wt% SN-38 indicating possible benefits for clinical application. Given the DSC analysis of the polymers in Section 2.5, the altered thermal behaviour of these systems may play a part in affecting drug release rates.

SN-38 dispersion derived from PEG<sub>5K</sub>-b-PCL<sub>40</sub>-co-BOD<sub>0.7</sub> and PEG<sub>5K</sub>-b-PMOP<sub>40</sub>-co-BOD<sub>0.7</sub> were, therefore, selected for more in-depth pharmacological tests as it was hypothesised that these systems had the greatest potential for future *in vivo* experimentation. PEG<sub>5K</sub>-b-PCL<sub>40</sub>-co-BOD<sub>0.7</sub> systems at all three drug loadings and PEG<sub>5K</sub>-b-PMOP<sub>40</sub>-co-BOD<sub>0.7</sub> containing 10 and 50 wt% SN-38 were specifically selected.

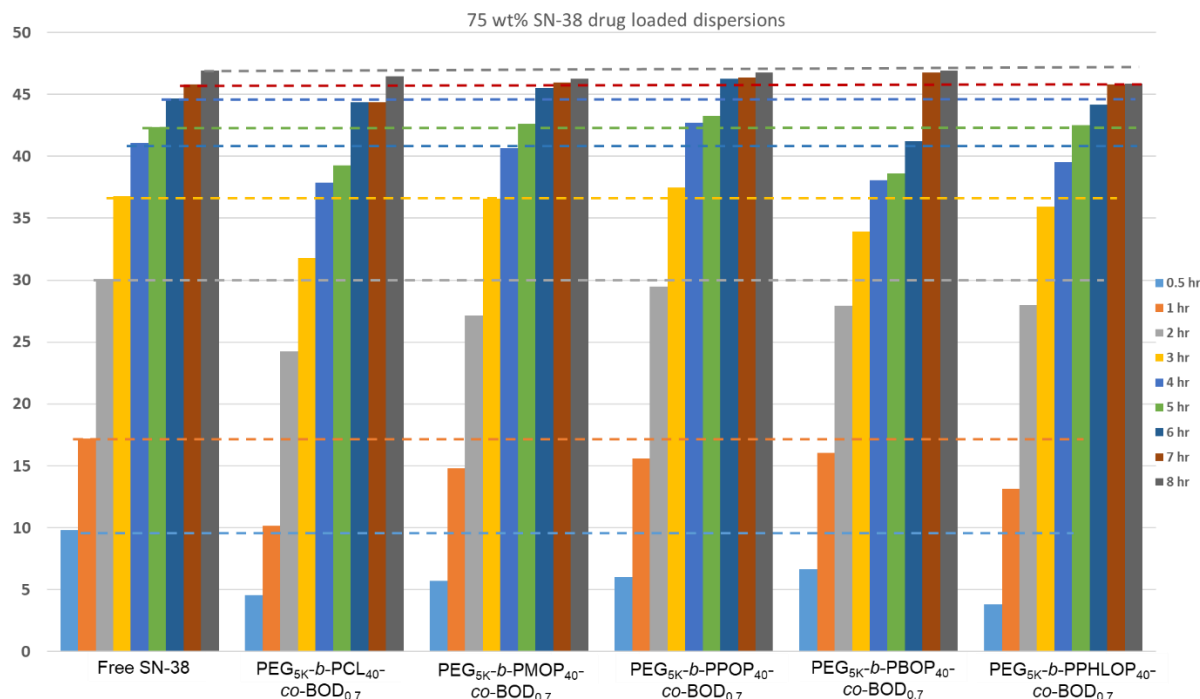


**Figure 4.54- RED assay equilibrium release rate (over 8 hours) for 75 wt% SN-38 containing samples generated from thin film hydration of branched PEG<sub>5K</sub>/polyester AB block co-polymers.**

#### 4.4.2 Cytotoxicity

Nanoparticle dispersions formed using PEG<sub>5K</sub>-b-PCL<sub>40</sub>-co-BOD<sub>0.7</sub> and PEG<sub>5K</sub>-b-PMOP<sub>40</sub>-co-BOD<sub>0.7</sub> containing 10, 50 and 75 wt% SN-38 were all evaluated using cytotoxicity assays. As PEG<sub>5K</sub>-b-PMOP<sub>40</sub>-co-BOD<sub>0.7</sub> showed slow release at SN-38 loadings of 10 or 50 wt%, this gave the opportunity to explore the impact of varying polymer structure relative to PCL. A number of cell lines were investigated, obtained from humans and mice; human colorectal cancer, *HCT 116*, murine colorectal cancer, *CT 26*, human colorectal adenocarcinoma, *LoVo*, and Dukes' type C colorectal adenocarcinoma, *DLD-1*, 2D cell lines were selected. Data collected after 72 hours, once each sample had achieved half maximal inhibitory concentration, *IC*<sub>50</sub>, was plotted with a comparison to SN-38 and irinotecan (Figure 4.55, A). Supplementary studies using 3D spheroids created with HCT 116 and CT 26 were also conducted and *IC*<sub>50</sub> values obtained after 144 hours (Figure 4.55, B).

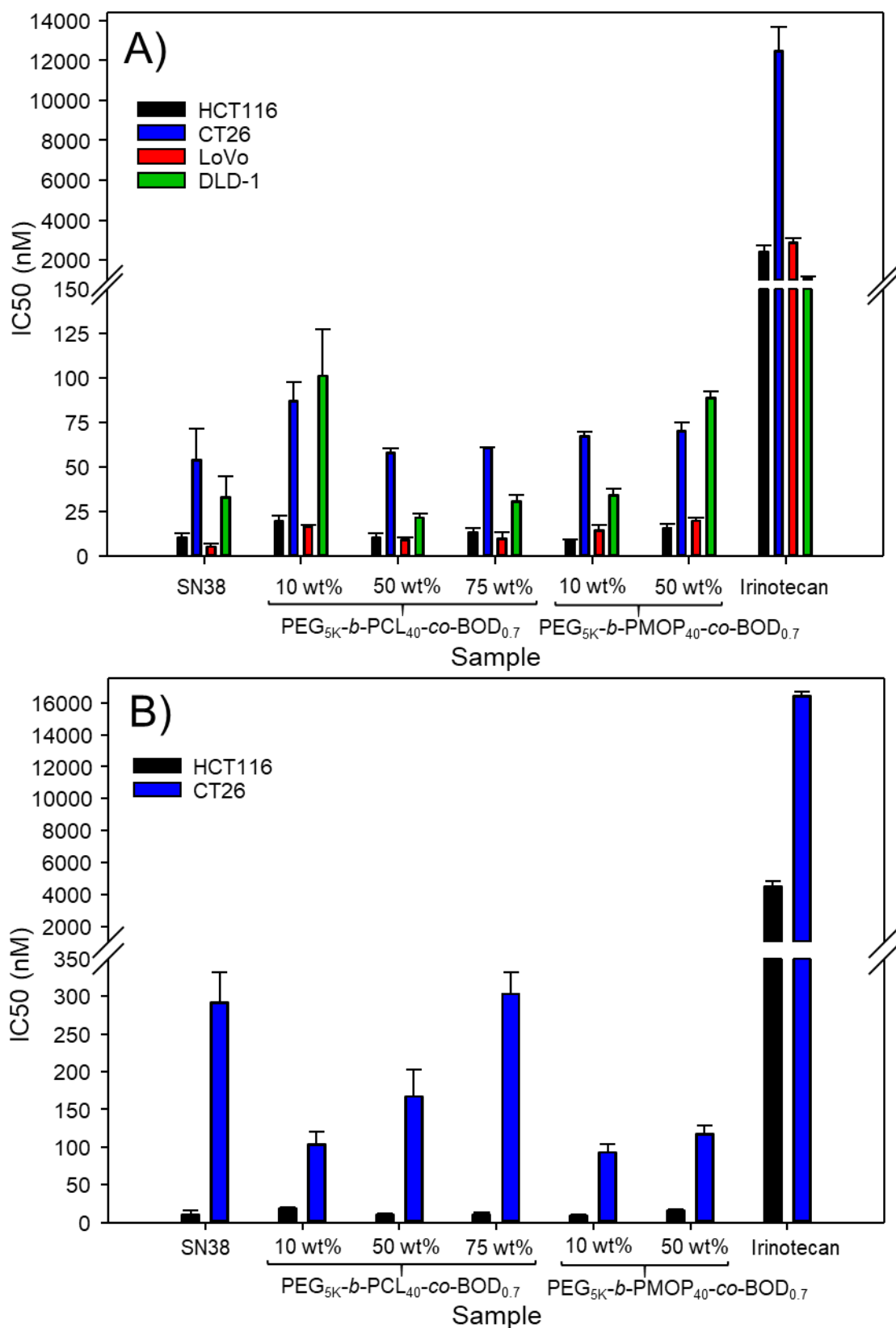


**Figure 4.55- Cytotoxicity studies of selected samples compared to SN-38 and irinotecan;**  
 (A) 2D cell lines plotted after 72 hours and (B) 3D spheroid cell lines plotted after 144 hours.

Overall samples showed very similar behaviour to SN-38, achieving  $IC_{50}$  values of similar magnitude, <150 nM regardless of the cell line used.  $IC_{50}$  values obtained from the human cell lines HCT 116 and LoVo offered the most comparable data to SN-38. No real trend was observed between the SN-38 drug loading within the nanoparticle dispersion and the  $IC_{50}$  values obtained. Furthermore the structural differences between nanoparticle and SDN, hypothesised to occur before 30 wt% SN-38 did not appear to affect toxicity. In studies utilising 3D spheroids all five nanoparticle dispersions had comparative toxicity to SN-38 when considering the HCT 116 cell line. CT 26 showed greater variability with both systems based on PEG<sub>5K</sub>-*b*-PMOP<sub>40-co</sub>-BOD<sub>0.7</sub> indicating lower toxicity than SN-38 alone. Nonetheless these studies supported 2D studies indicating that encapsulation of SN-38 did little to impact the efficacy of the drug.

#### 4.4.3 Macrophage uptake

In order for drug containing nanoparticles to have a therapeutic effect they must first avoid uptake and clearance from the circulatory system *via* macrophages, a type of white blood cell responsible for the removal of foreign artefacts from the body. Therefore a number of particle dispersions were assessed with regards to cellular accumulation in macrophages. The systems selected for this study were based on PEG<sub>5K</sub>-*b*-PCL<sub>40-co</sub>-BOD<sub>0.7</sub> and PEG<sub>5K</sub>-*b*-PMOP<sub>40-co</sub>-BOD<sub>0.7</sub> where PEG<sub>5K</sub>-*b*-PCL<sub>40-co</sub>-BOD<sub>0.7</sub> contained 10, 50 and 75 wt% SN-38 and PEG<sub>5K</sub>-*b*-PMOP<sub>40-co</sub>-BOD<sub>0.7</sub> contained 10 and 50 wt% SN-38. Free SN-38 was also studied as a control and comparison (Figure 4.56).



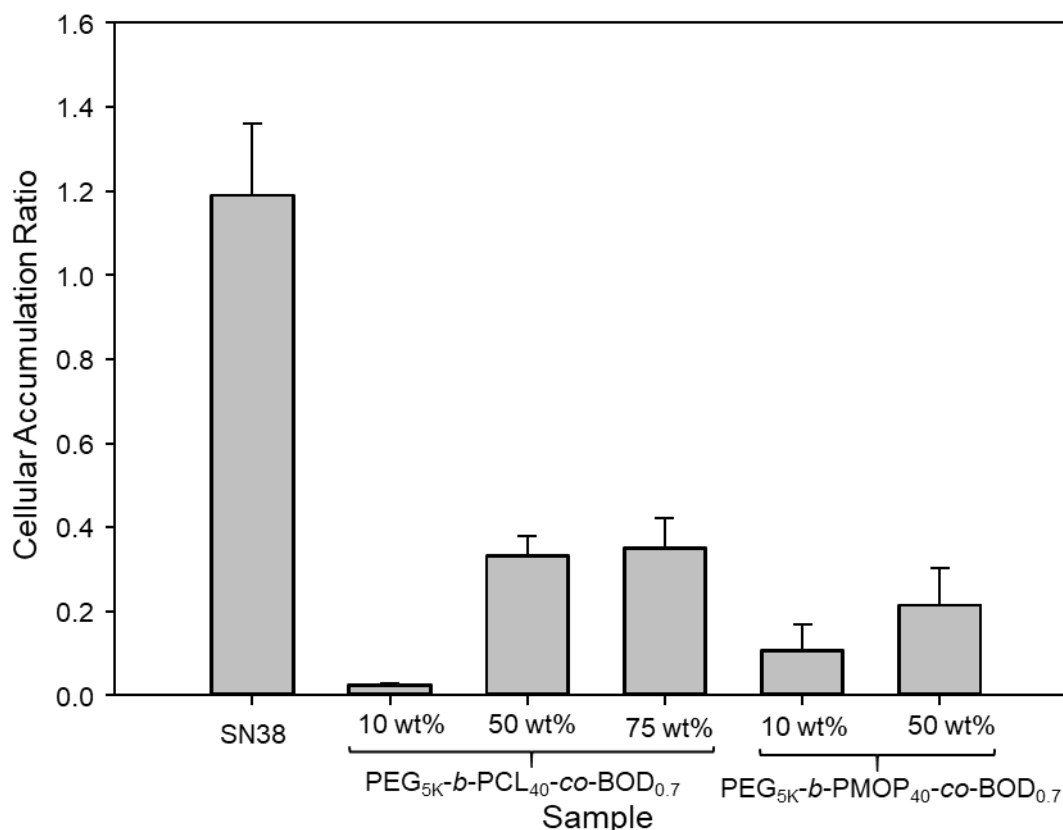


**Figure 4.56 – Graphical representation of cellular accumulation of nanoparticles in macrophages.**

Overall both systems containing 10 wt% SN-38 had the lowest cellular uptake whilst increasing SN-38 content to 50 and 75 wt% resulted in increased cellular uptake. Nonetheless the PEG<sub>5K</sub>-*b*-PCL<sub>40</sub>-*co*-BOD<sub>0.7</sub> system containing 10 wt% showed the least cellular uptake and would therefore be expected to display the longest circulation times *in vivo*. The trend of increasing cellular uptake with increased SN-38 suggests that these systems resemble the free drug which would complement the expected SDN structure when SN-38 is >30 wt%.

#### 4.4.4 *In vivo* Studies

The material selected for *in vivo* studies was PEG<sub>5K</sub>-*b*-PCL<sub>40</sub>-*co*-BOD<sub>0.7</sub> containing 10 wt% SN-38 due to the significantly lower cellular uptake suggesting that the circulation time of the nanoparticles within this dispersion would be the longest of the samples tested. Before *in vivo* studies could begin an increase in drug concentration was required from 0.11 mg mL<sup>-1</sup> in water to 0.44 mg mL<sup>-1</sup> to achieve the desired dosing regimen. Unfortunately, this study failed and due to COVID-19 subsequent studies to investigate this have been unable to be completed at this time.

## 4.5 Conclusion

In conclusion, the exploration of SN-38 encapsulation within nanoparticles generated from the library of polymers available, was hypothesised to build on the successful encapsulation studies conducted in Chapter 3. Further successful encapsulation of SN-38 P, at 2.43 wt%, *via* co-nanoprecipitation generated promising results hinting towards the potential to encapsulate SN-38 given the small variation in molecular structure. Unfortunately, SN-38 encapsulation *via* co-nanoprecipitation was unsuccessful regardless of polymer selection.

The implementation of a thin film hydration methodology, removing the presence of a THF/water mixture during nanoparticle formation, resulted in the first SN-38 containing nanoparticles within this body of work. Furthermore, method development showed that sonication of the nanoparticle dispersions was key to obtaining reproducible well-defined nanoparticles. The successful synthesis of nanoparticle dispersions, with SN-38 drug loadings between 2.43-95 wt%, highlighted the applicability of this method over a range of polymers and suggested a transition in nanostructure from polymeric nanoparticle to SDN, occurring between 16.6 and 30 wt%.

Promising signs for clinical application were also gained when samples were studied for storage which highlighted the remarkable length of time thin films could be retained between formation and successful reconstitution in water, without a detrimental effect on nanoparticle formation. Furthermore, exploration of the stability of the dispersions indicated at least one full working day in which administration could be achieved.

Finally, the formation of an aqueous dispersion of SN-38, with a large range of options regarding SN-38 drug loading a polymer backbone chemistry, does offer real potential for the future. Furthermore, although particles indicated slower drug release, little effect of encapsulation on the cytotoxicity of SN-38 and reduced macrophage uptake during pharmacological assessment, the efficacy of these formulations is yet to be shown.

**References**

- 1 S. T. Ning, S. Y. Lee, M. F. Wei, C. L. Peng, S. Y. F. Lin, M. H. Tsai, P. C. Lee, Y. H. Shih, C. Y. Lin, T. Y. Luo and M. J. Shieh, *ACS Appl. Mater. Interfaces*, 2016, **8**, 17793–17804.
- 2 Y. Hao, J. Liu, Q. Jia, J. Sui and G. Huang, *J. Drug Deliv. Sci. Technol.*, 2019, **53**, 101178.
- 3 J. Ford, PhD Thesis, University of Liverpool, 2015, URL: [https://livrepository.liverpool.ac.uk/2052220/1/FordJan\\_Sept2015\\_2052220.pdf.pdf](https://livrepository.liverpool.ac.uk/2052220/1/FordJan_Sept2015_2052220.pdf.pdf)
- 4 C. Wu, Y. Zhang, D. Yang, J. Zhang, J. Ma, D. Cheng, J. Chen and L. Deng, *Int. J. Nanomedicine*, 2019, **14**, 75–85.
- 5 J. Ford, P. Chambon, J. North, F. L. Hatton, M. Giardiello, A. Owen and S. P. Rannard, *Macromolecules*, 2015, **48**, 1883–1893.
- 6 Y. P. Patil and S. Jadhav, *Chem. Phys. Lipids*, 2014, **177**, 8–18.
- 7 L. Zhang, Z. Chen, H. Wang, S. Wu, K. Zhao, H. Sun, D. Kong, C. Wang, X. Leng and D. Zhu, *RSC Adv.*, 2016, **6**, 54727–54737.
- 8 P. Rychahou, Y. Bae, D. Reichel, Y. Y. Zaytseva, E. Y. Lee, D. Napier, H. L. Weiss, N. Roller, H. Frohman, A. T. Le and B. Mark Evers, *J. Control. Release*, 2018, **275**, 85–91.
- 9 X. Ai, L. Zhong, H. Niu and Z. He, *Asian J. Pharm. Sci.*, 2014, **9**, 244–250.
- 10 T. Nakano, *Polym. J.*, 2010, **42**, 103–123.
- 11 F. L. Hatton, P. Chambon, A. C. Savage and S. P. Rannard, *Chem. Commun.*, 2016, **52**, 3915–3918.
- 12 D. Lemoine, C. Francois, F. Kedzierewicz, V. Preat, M. Hoffman and P. Maincent, *Biomaterials*, 1996, **17**, 2191–2197.
- 13 T. I. Morozova, V. E. Lee, A. Z. Panagiotopoulos, R. K. Prud'Homme, R. D. Priestley and A. Nikoubashman, *Langmuir*, 2019, **35**, 709–717.
- 14 L. Wu, J. Zhang and W. Watanabe, *Adv. Drug Deliv. Rev.*, 2011, **63**, 456–469.
- 15 D. Horinek, in *Encyclopedia of Applied Electrochemistry*, eds. G. Kreysa, K. Ota and

- R. F. Savinell, Springer, New York, NY, New York, 2014th edn., 2014, pp. 343–346.
- 16 X. Sun, D. Zhu, Y. Cai, G. Shi, M. Gao and M. Zheng, *Int. J. Nanomedicine*, 2019, **14**, 2115–2126.
- 17 S. Prasad and J. S. Dangi, *Artif. Cells, Nanomedicine Biotechnol.*, 2016, **44**, 1824–1834.
- 18 Y. Liu, H. Y. Piao, Y. Gao, C. H. Xu, Y. Tian, L. H. Wang, J. W. Liu, B. Tang, M. J. Zou and G. Cheng, *Int. J. Nanomedicine*, 2015, **10**, 2295–2311.
- 19 F. Atyabi, A. Farkhondehfar, F. Esmaili and R. Dinarvand, *Acta Pharm.*, 2009, **59**, 133–144.
- 20 M. Reading, M. Morton, M. Antonijevic, D. Grandy, D. Hourston and a Lacey, 2014, 1083–1089.
- 21 R. B. Kolhatkar, P. Swaan and H. Ghandehari, *Pharm. Res.*, 2008, **25**, 1723–1729.

# **CHAPTER 5**

## **CONCLUSIONS AND FUTURE WORK**

## 5.1 Conclusions

The overall aim of this work was to understand the capabilities of polyester nanoparticles in the encapsulation of SN-38. Initial areas of investigation included: the synthesis of homo- and co-polyesters of varying architecture *via* MSA catalysed ROP, the implementation of substituted caprolactone monomers and the effects this caused on the thermal characteristics of the resultant polymers. Further essential studies, required to develop understanding before the encapsulation of SN-38 could be attempted, were nanoparticle synthesis *via* rapid co-nanoprecipitation and the consequences this method had on the ability to encapsulate guest molecules.

The hypotheses laid out in Chapter 1, as well as those that were developed over the course of study, have been examined successfully in the subsequent chapters to generate a comprehensive understanding of the different scientific aspects required to progress a new therapy option towards patient benefit. Blank nanoprecipitation and co-nanoprecipitation studies were initially used to develop knowledge in the context of the polymer library, based on  $\epsilon$ -CL and substituted caprolactone monomers. The MSA catalysed ROP technique provided a metal-free route to polymers of varying architecture, such as PEG block co-polymers and branched architecture, obtained using a ‘modified Strathclyde method’. The avoidance of tin-derived catalysts is of considerable importance as the removal of metal ions from the resulting polymers is essential for medical applications. By using a simple acid, the study extends the scope of the materials that have been demonstrated to be successfully polymerised using this approach.

Initial (co)nanoprecipitation studies, undertaken with PEG<sub>x</sub>-*b*-PCL<sub>40</sub> and linear and branched PCL, revealed that a decrease in size and PDI of the nanoparticles could be obtained by the application of a branched species when using acetone as the good solvent. This correlated well with previously reported results utilising polymethacrylates and shows that polyesters appear to behave in a similar way.<sup>1</sup> Co-nanoprecipitation of PCL<sub>40</sub>-*co*-BOD<sub>0.7</sub> with PEG<sub>x</sub>-*b*-PCL<sub>40</sub> revealed that with increased PEG<sub>x</sub>-*b*-PCL<sub>40</sub> content there was a reduction in zeta potential and an increase in salt stability which was key for future investigations within a biological setting. Due to the limited solubility of SN-38, discovered to be soluble in THF up to 4 mg mL<sup>-1</sup>, a study of the impact of varying the organic solvent within the nanoprecipitation process confirmed that larger and more disperse particles were formed, which was in line with previous nanoprecipitation reports but not readily predictable; for the PCL<sub>40</sub>-*co*-BOD<sub>0.7</sub>/PEG<sub>x</sub>-*b*-PCL<sub>40</sub>

systems, decreasing  $D_z$  and zeta potentials with increasing PEG<sub>x</sub>-*b*-PCL<sub>40</sub> content correlated with materials generated from acetone.

The various studies conducted here, suggested a 50:50 wt% amphiphilic block co-polymer to hydrophobic branched polymer ratio as the best compromise between  $D_z$ , PDI and zeta potentials of the resulting nanoparticles. Considering the polyester backbone variation, the original expectation of clear trends when progressing from MOP, POP, BOP to PHLOP structures was not fully observed; nanoparticle size did not seem to correlate with polymer chemistry but thermal characteristics varied in line with the behaviour of analogous polymers derived from chain-growth chemistry, such as polymethacrylates. DSC analysis indicated that addition of alkyl chain substituents decreased crystallinity and flexible side chains led to a decrease in  $T_g$  values (compared to  $\epsilon$ -CL based polymers) as may have been expected. Equally expected, more rigid side chains led to an increase in  $T_g$  above that of PCL. However, when substitution was present, nanoprecipitation led to nanoparticles that were larger than those containing PCL<sub>40</sub>-*co*-BOD<sub>0.7</sub>, regardless of the stabilising PEG co-polymer. For example, PPOP<sub>40</sub>-*co*-BOD<sub>0.7</sub> generated the largest particles which was most likely due to the increased steric hindrance in the polymer backbone; additionally studies that aimed to match the monomer chemistry of the hydrophobic branched polymer and the stabilising A-B block copolymer, showed no significant effect on the properties or stability of the resulting particles.

Across a range of guest molecules, namely Oil red O, docetaxel and SN-38 pro-drugs, Oil red O and docetaxel both formed highly stable nanoparticles with CL-derived polymers and SN-38 pro-drugs were successful using CL and substituted CL-derived A-B block co-polymers with no significant effect observed with the variation of amphiphilic block co-polymer. SN-38 was not able to be encapsulated *via* co-nanoprecipitation indicating a clear impact of the drug compound chemistry on the nanoprecipitation process. Comparisons between PCL and PPOP based systems and SN-38 revealed large solubility differences and these are important to consider when designing successful nanoprecipitation processes. Further confirmatory studies using Oil red O and docetaxel supported the conclusion that failure to encapsulate SN-38 *via* co-nanoprecipitation was a result of the differing solubility of the drug and the polymer.

In search of alternative nanoparticle formation processes, branched PEG co-polymers, and later linear PEG co-polymers, were identified as being able to successfully form SN-38-containing nanoparticles over a range of drug loadings from 2.43 to 95 wt%, using a thin film hydration method inspired by vesicle/liposome processing. MOP and POP based polymers consistently

producing the most monodisperse nanoparticle dispersions over the full range of drug loadings using this approach. A trend of increasing size with increasing SN-38 content was observed indicating that an increased amount of SN-38 was successfully stabilised by the amount of polymer that was present. The ability to achieve such high SN-38 content was highly surprising, but was rationalised as a transition from drug-containing polymeric nanoparticles (encapsulation mechanism) through to solid drug nanoparticle dispersions (stabilisation mechanism), also known as SDNs.

Various studies utilising SEM, DSC and TASC analysis were performed to attempt to define the transition from polymeric particles to SDNs. SEM of dry films and filtrates collected from nanoparticle dispersions, with increasing SN-38 content, suggested the transition occurred between 16.6 and 30 wt% SN-38, both DSC and TASC appeared to correlate with this conclusion. All three techniques universally indicated that the shift from polymeric nanoparticle to SDN also correlated with the appearance of SN-38 within the thin film.

Additionally, SN-38 containing thin films offer a solvent- and water-free storage option that may provide benefits over liquid dispersion. Dry thin films derived from PEG<sub>5K</sub>-*b*-PMOP<sub>40</sub>-*co*-BOD<sub>0.7</sub> and PEG<sub>5K</sub>-*b*-PPOP<sub>40</sub>-*co*-BOD<sub>0.7</sub> and containing 10, 30, 50 and 75 wt% SN-38 were shown to be reconstitutable after at least 14 weeks storage under ambient conditions, with little variation in  $D_z$  and PDI; however greater variability was observed at SN-38 contents over 30 wt%. In contrast, nanoparticle dispersions, based on PEG<sub>5K</sub>-*b*-PCL<sub>40</sub>-*co*-BOD<sub>0.7</sub>, with SN-38 content ranging from 2.43 and 95 wt% showed potential storage stability over several days. Collectively, this presents an opportunity for a clinical candidate to be stored for several months in a dry state, prepared by reconstitution within a hospital pharmacy and administered within a period of several days, under ambient conditions; for example, samples with  $\leq 33$  wt% SN-38 were shown to be stable for four days.

Finally, pharmacological assessments of branched PEG co-polymer systems containing 10, 50 and 75 wt% SN-38 indicated that the modification of the polymer backbone chemistries, had little effect on the release rate of SN-38 from the nanoparticles *in vitro*; PEG<sub>5K</sub>-*b*-PCL<sub>40</sub>-*co*-BOD<sub>0.7</sub> generated the slowest release rates across all three SN-38 concentrations. Cytotoxicity studies revealed that encapsulation within a polymeric nanostructure did not have a detrimental effect on the potency of SN-38, demonstrating similar IC<sub>50</sub> values to free SN-38. Cellular uptake however decreased when thought to be encapsulated within the polymer matrix for all



three drug concentrations when compared to free SN-38 suggesting that the nanoparticles would have extended circulation time within the body.

## 5.2 Future work

The completion of the work detailed within this thesis, whilst achieving SN-38 encapsulation, highlighted a number of areas that could be further explored. Each phase that led to the successful synthesis of SN-38 containing nanoparticles, from polymer synthesis to pharmacological assessment, provides opportunities for further study to expand the ideas explored within this body of work. For simplicity these shall be divided into the following sections;

### 5.2.1 Polymer synthesis

Evidence of transesterification reactions within PCL polymers, combined with the increase in molecular weight once full monomer conversion was reached, directs studies to investigate the optimum reaction time of the ‘modified Strathclyde method’ to produce a highly branched polymeric species. However, as the final polymer obtained from this method would most likely not possess primary chain lengths of the targeted  $DP_n$ , this conversely motivates exploration of the optimum conditions to achieve a branched species within the time it takes to reach full monomer conversion. This could be applied to both homo- and co-polymers, which within this body of work showed a lack of highly branched architecture, and may require additional investigation into alternative methods for the removal of water for the reaction mixture to further optimise the ‘modified Strathclyde method’.

Further studies utilising acid catalysed ROP utilising both MSA and TfOH, shown to be active for lactide, would also expand the boundaries of what can be achieved *via* this method.<sup>2</sup> The successful implementation of a ‘modified Strathclyde method’ utilising BOD and both BzA and PEG macroinitiators in the case of PCL would suggest that further studies involving a range branching units, monomers such as lactide and glycolide, and macroinitiators, such as PVP and dendrons, could greatly expand the library of polymers synthesised by this method. PVP block co-polymers would provide a favourable alternative to PEG due to PVP’s extremely low cytotoxicity, biocompatibility and non-ionic nature, however previous work conducted in this area would suggest that acid catalysed ROP with PVP initiators would require in depth study.<sup>3</sup> Application of dendron macroinitiators combined with the ‘modified Strathclyde

method' would provide a route to a new class of hyperbranched polydendron in which the hydrophobic segments would be biodegradable.

The synthesis of a number of statistical co-polymers based on  $\epsilon$ -CL, MOP, POP, BOP and PHLOP combined with DSC characterisation would give more insight into the effects the extending alkyl chain of the monomer had on the resulting polymer properties and crystallinity. Gradually increasing the substituted caprolactone monomer content within a co-polymerisation with  $\epsilon$ -CL would allow the point at which crystallinity was lost to be determined by the disappearance of a  $T_m$  peak. Extensive kinetic studies of the polymerisations of each substituted caprolactone monomer would provide invaluable insight into the effects, if any, of extending the alkyl side chain on the basicity of the monomer and therefore the rate of polymerisation. This would help to predict the sequence of monomers within statistical polymerisations.

The creation of four substituted caprolactone monomers and BOD *via* Baeyer-Villiger oxidation shows that simple monomer synthesis can be achieved utilising a selected cyclic ketone and therefore the library of polymers able to be created by MSA catalysed ROP is extensive and not limited to commercially available monomers. Further synthesis of monomers with increasing variety in side chain functionality based on  $\epsilon$ -CL, and possibly glycolide, could unlock an extensive range of new physicochemical properties in the resulting polymers. These polymers could subsequently be assessed in the formation of nanoparticles and the encapsulation of hydrophobic guest molecules. Furthermore, the implementation of an expensive library of monomers could also help to achieve more favourable pharmacological profiles for any drug-containing nanoparticles produced.

### **5.2.2 Nanoparticle formation and encapsulation *via* co-nanoprecipitation**

Extensive work concerning co-nanoprecipitation has been carried out within the Rannard group, however, the implementation of polyesters has been limited.<sup>4-6</sup> A wide-ranging study utilising: a) a number of different volatile solvents, b) a variety of polymer concentrations in the organic phase and c) the targeted final concentration in water, would provide a more complete assessment of the influence of solvent choice, concentration and polymer combination have on the resulting nanoparticle dispersions. Additional comparisons could then be drawn between polyester and polymethacrylate systems to evaluate whether any compromises are made by selecting a biodegradable polyester system.

Co-nanoprecipitation of the library of polymers within this thesis revealed that encapsulation of hydrophobic guest molecules was achievable only at low concentrations. Additional studies with a larger range of drug molecules and a variety of co-nanoprecipitation parameters could result in increased drug loadings of the molecules already studied and expand the potential of these systems.

Supplementary studies regarding the degradation of the polymer matrix when contained within a nanoparticle structure using lipase, and other enzymes found *in vivo*, would provide additional data to support or rule out the potential of these systems within a biological setting. This study is not limited to nanoparticles formed *via* co-nanoprecipitation but could also be extended to those formed by thin film hydration.

### **5.2.3 Nanoparticle formation and encapsulation *via* thin film hydration**

Further assessment of the thin films created within this body of work would provide greater understanding of what influences the particle structure and further refine the range in which the transition from polymeric nanoparticle to SDN occurs. This could be achieved by X-ray diffraction, cryo-SEM or TEM and energy-dispersive X-ray, *EDX*, analysis to give a more complete visual representation of the location and crystallinity of SN-38.

Given that the thin film hydration methodology provides an alternative route to nanoparticles, resulting in a favourable storage method shown to extend the shelf-life of these systems, the method could be applied to a variety of drug molecules. Furthermore the removal of organic solvent may also improve polymer-drug interactions with a variety of different drug molecules which may previously have been disregarded from study due to difficulty with encapsulation.

Assessment of nanoparticle degradation with varying drug content would provide a valuable insight into any effects of the structure of the nanoparticle on the degradation rate of the polymer. Coupled with release studies, degradation of the nanoparticles could highlight whether the degradation rate of the polymer matrix had any influence on the release of the drug.

### **5.2.4 Pharmacological assessment**

Assessment of SN-38 release using radio-labelled SN-38 would provide a valuable comparison to the RED analysis conducted within this body of work. Given that the release of SN-38 was only slightly slower when encapsulated within a polymeric nanostructure, radiometric analysis would provide greater resolution to distinguish any other effects the alteration of the polymer backbone had on SN-38 release.

Release rate studies of a larger library of nanoparticles, both synthesised within this body of work and further systems that could be synthesised in future - such as dispersions based on more highly branched PEG co-polymers, would allow for more trends to be evaluated. For example, obtaining release rate data for the complete range of SN-38 concentrations achieved when stabilised by PEG<sub>5K</sub>-*b*-PCL<sub>40</sub>-*co*-BOD<sub>0.7</sub> could highlight any trends associated with the shift from polymeric nanoparticle to SDN. This proposal could also apply to further pharmacological assessment such as cytotoxicity and macrophage uptake. Further assessment *in vivo*, possibly with direct injection intratumorally, would give a more complete view of the viability of these systems.

## References

- 1 F. L. Hatton, P. Chambon, A. C. Savage and S. P. Rannard, *Chem. Commun.*, 2016, **52**, 3915–3918.
- 2 S. Gazeau-Bureau, D. Delcroix, B. Martín-Vaca, D. Bourissou, C. Navarro and S. Magnet, *Macromolecules*, 2008, **41**, 3782–3784.
- 3 V. Carr, R. M., Oranu, A., & Khungar, *Curr. Opin. Chem. Biol.*, 2015, **28**, 181–193.
- 4 J. Ford, P. Chambon, J. North, F. L. Hatton, M. Giardiello, A. Owen and S. P. Rannard, *Macromolecules*, 2015, **48**, 1883–1893.
- 5 J. Ford, PhD Thesis, University of Liverpool, 2015, URL: [https://livrepository.liverpool.ac.uk/2052220/1/FordJan\\_Sept2015\\_2052220.pdf.pdf](https://livrepository.liverpool.ac.uk/2052220/1/FordJan_Sept2015_2052220.pdf.pdf)
- 6 S. Flynn, PhD Thesis, Univeristy of Liverpool, 2019.

# **CHAPTER 6**

## **EXPERIMENTAL PROCEDURES**

## 6.1 Materials

Toluene (anhydrous, >99.9 %), urea hydrogen peroxide (97 %), methanesulfonic acid ( $\geq 99$  %), benzyl alcohol (anhydrous, 99.8 %), 4-tert-butylcyclohexanone (99 %), 4-methylcyclohexanone (99 %), 4-phenylcyclohexanone ( $\geq 98$  %), 4-propylcyclohexanone ( $\geq 99$  %), *N,N*-triethylamine, *TEA* ( $\geq 99$ %), oil red O and deuterated chloroform,  $CDCl_3$ , were purchased from Sigma Aldrich and used as received.  $\epsilon$ -Caprolactone,  $\epsilon$ -*CL*, (97 %), was also purchased from Sigma Aldrich and purified by distillation over calcium hydride,  $CaH_2$ , or drying over 3 Å molecular sieves for at least 24 hours. Formic acid ( $\geq 98$  %) and aluminium oxide (activated, basic, Brockmann I) were purchased from Honeywell Fluka and used as received. Tetrahydrofuran, *THF*, *N,N'*-dimethylformamide, *DMF*, acetone, acetonitrile, methanol, *MeOH*, diethyl ether, hexane, ethyl acetate and chloroform,  $CHCl_3$ , all reagent grade were all purchased from Fischer Scientific. Docetaxel and SN-38 were purchased from Chemleader Biochemical. Pro-drug SN-38 pentanoate, *SN-38 P*, was synthesised and purified in the group by Dr Andrew Dwyer and used as provided (see Chapter 4).

## 6.2 Instrumentation and characterisation

### 6.2.1 Instrumentation

$^1H$  and  $^{13}C$ -nuclear magnetic resonance, *NMR*, was undertaken using a Bruker Avance III HD NMR spectrometer operating at 400 MHz for  $^1H$ -NMR and 100 MHz for  $^{13}C$ -NMR. The samples were acquired in  $CDCl_3$ ,  $D_2O$  or  $DMSO-d^6$ . Chemical shifts, quoted in parts per million, *ppm*, where in reference to the peak generated by trimethylsilane, *TMS*, at 0 ppm.

Elemental analysis was undertaken using a Thermo FlashEA 112 series CHNSO elemental analyser.

Chemical ionisation, *CI*, mass spectrometry was recorded using an Agilent GC/Q-TOP 7200 instrument using ammonium CI gas.

Triple detection size exclusion chromatography, *SEC*, used a Malvern Viscotek SEC Max equipped with a GPCmax VE2001 auto sampler, two Viscotek T6000 columns and a guard column. The detectors were a refractive index, RI detector (VE3580) and a 270 Dual Detector (light scattering and viscometer). The eluent system used was DMF containing 0.01 M LiBr at 60 °C with a flow rate of 1 mL min<sup>-1</sup>.

Single detection SEC was obtained using an Agilent 1260 Infinity II equipped with a PLgel 3 m Mixed-E 300 x 7.5 mm column and RI detector. The eluent system was DMF containing 0.01 M LiBr at 60 °C at a flow rate of 1 mL min<sup>-1</sup>. Calculations of  $M_n$  and  $M_w$  were determined using a conventional calibration method against poly(methyl methacrylate), *PMMA*, calibration standards ( $M_p = 850$  to 27,600 g mol<sup>-1</sup>).

Dynamic light scattering, *DLS*, was undertaken with a Malvern Zetasizer Nano ZS (4 mW He-Ne 633 nm laser) with a disposable folded cuvette, or a disposable cuvette (thin film nanoparticle dispersions at 25 °C).

Differential scanning calorimetry, *DSC*, utilised a DSC Discovery instrument using a T4P calibration of samples held within Tzero pans at temperatures between -90 and 500 °C under a nitrogen atmosphere at a pressure of 0.1 MPa.

Scanning electron microscopy, *SEM*, images were recorded using a Tescan S8000G focused ion beam/scanning electron microscope. After preparation of each sample on a SEM stub, detailed specifically in Chapter 4, each sample was sputter coating with chromium using a Quorum Technologies Q150T ES sputter coater for 15 seconds (120 mA).

Thermal analysis by structural characterisation, *TASC*, was undertaken at the Alderley Edge site of AstraZeneca using Linkcam scientific TASC apparatus.

## 6.2.2 Summary of characterisation

Substituted caprolactone monomers characterisation;

- <sup>1</sup>H-NMR, <sup>13</sup>C-NMR, CI mass spectrometry and CHNSO analysis.

Polymer characterisation;

- Monomer conversion and degree of polymerisation via chain end analysis were calculated using <sup>1</sup>H-NMR.
- Number-averaged and weight-averaged molecular weights,  $M_n$  and  $M_w$  respectively, polydispersity,  $D$ , dn/dc and Mark-Houwink value,  $\alpha$ , were determined by triple detection SEC.
- $M_n$  and  $M_w$  values for polymer samples obtained in Sections 2.3.2.1 and 2.3.2.2 were determined by single detection SEC.
- Thermal properties ( $T_g$  and  $T_m$ ) of the polymers were calculated using DSC.



Nanoparticle dispersions characterisation;

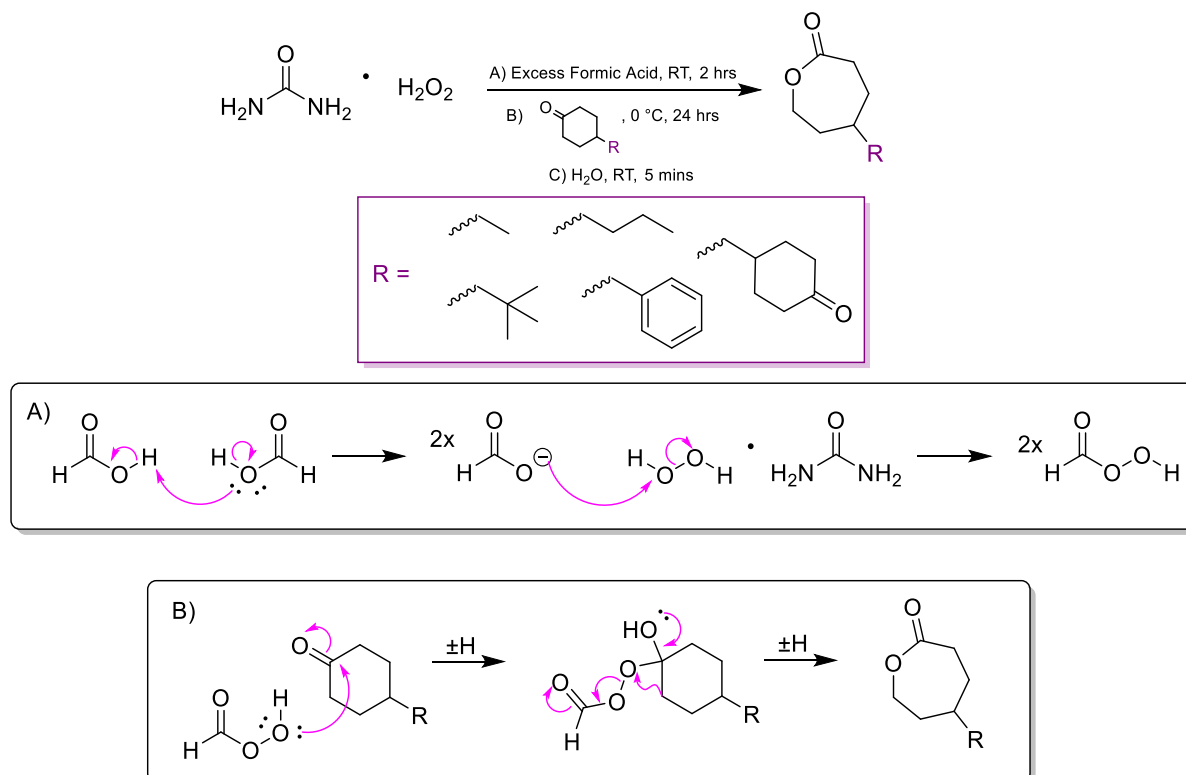
- Measurements of Z-average diameter, number-average diameter, zeta potential, derived count rate and PDI were determined by DLS at 25 °C at selected time points after nanoparticle formation.
- All samples, excluding those specified in Section 4.3.3.1.2 were unfiltered at the time of characterisation.
- Images of nanoparticle dispersions were obtained using SEM.

Thin film characterisation;

- Thermal properties ( $T_g$  and  $T_m$ ) of thin films were calculated using DSC.
- Further thermal analysis was undertaken using TASC microscopy.
- Images of thin films were obtained using SEM.

## 6.3 Methods for Chapter 2 – Polymer synthesis

### 6.3.1 Substituted caprolactone monomer and bis-lactone monomer synthesis



**Scheme 6.1 – Scheme representing the synthesis of substituted caprolactone monomers via Baeyer-Villiger oxidation**

### 6.3.1.1 General Baeyer-Villiger oxidation synthesis of substituted caprolactone monomers

Each monomer was synthesised on a 15 g scale by synthesising three 5 g batch reactions which were combined at the time of extraction/purification to reduce the risks associated with large amounts of peroxy-acid formation during the oxidation step.

Urea hydrogen peroxide, *UHP* (3 x 3 eq.) was added to excess formic acid (3 x 100 mL) and stirred at room temperature for 2 hours to allow for the formation of a peroxy-acid. The solution was then cooled to 0 °C before the selected cyclic ketone (3 x 5 g, 1 eq.) was added over 10 minutes. The mixture was then left stirring at 0 °C for 24 hours.

Water (3 x 100 mL) was then added followed by combination of the 3 batch reactions before extraction with chloroform (4 x 300 mL). The combined organic fractions were then washed with sodium bicarbonate (3 x 300 mL) and dried with sodium sulfate. The solution was filtered and the solvent removed before characterisation with <sup>1</sup>H NMR, <sup>13</sup>C NMR and mass spectrometry.

5-Methyloxepan-2-one, *MOP* (**1**) - The synthesis of 5-methyloxepan-2-one was carried out following the general Baeyer-Villiger oxidation method described above with UHP (3 x 12.58 g, 133.7 mmol, 3 eq.) and 4-methylcyclohexanone (3 x 5 g, 44.6 mmol, 1 eq.). The crude clear, colourless oil was purified by liquid chromatography on silica eluting with a polarity of ethyl acetate:hexane (25:75) (R<sub>f</sub>= 0.2) Yield: 9.64 g, clear, colourless oil (56.3 %). <sup>1</sup>H NMR (400 MHz, CDCl<sub>3</sub>) δ 4.42 – 4.12 (m, 2H), 2.73 – 2.54 (m, 2H), 1.99 – 1.83 (m, 2H), 1.84 – 1.71 (m, 1H), 1.57 – 1.44 (m, 1H), 1.34 (dtd, *J* = 13.9, 11.2, 2.8 Hz, 1H), 1.00 (d, *J* = 6.6 Hz, 3H). <sup>13</sup>C NMR (101 MHz, CDCl<sub>3</sub>) δ 176.06 (s), 68.09 (s), 37.25 (s), 35.26 (s), 33.21 (s), 30.78 (s), 22.12 (s), -25.14 – -25.34 (m). (Found: C, 65.41; H, 9.47; C<sub>8</sub>H<sub>12</sub>O<sub>2</sub> requires, C, 65.6; H, 9.44%).

5-Propyloxepan-2-one, *POP* (**2**) - UHP (3 x 10.06 g, 107 mmol, 3 eq.) and 4-propylcyclohexanone (3 x 5 g, 35.6mmol, 1 eq.). The crude clear, colourless oil was purified by liquid chromatography on silica eluting with a polarity of ethyl acetate:hexane (25:75) (R<sub>f</sub>= 0.25) Yield: 6.65 g, clear, colourless oil (39.8 %). <sup>1</sup>H NMR (400 MHz, CDCl<sub>3</sub>) δ 4.39 – 4.10 (m, 2H), 2.75 – 2.52 (m, 2H), 2.07 – 1.86 (m, 2H), 1.69 – 1.55 (m, 1H), 1.54 – 1.41 (m, 1H), 1.41 – 1.21 (m, 5H), 0.90 (t, *J* = 7.1 Hz, 3H). <sup>13</sup>C NMR (101 MHz, CDCl<sub>3</sub>) δ 176.14 (s), 68.19

(s), 39.91 (s), 38.65 (s), 35.34 (s), 33.19 (s), 28.88 (s), 19.85 (s), 14.14 (s). (Found: C, 69.58; H, 10.34; C<sub>9</sub>H<sub>16</sub>O<sub>2</sub> requires, C, 69.19; H, 10.32%).

5-(*tert*-Butyl)oxepan-2-one, *BOP* (**3**) - UHP (3 x 9.15 g, 97.2 mmol, 3 eq.) and 4-(*tert*-butyl)cyclohexanone (3 x 5 g, 32.4 mmol, 1 eq.). The crude white long crystals were purified by liquid chromatography on silica eluting with a polarity of ethyl acetate:hexane (25:75) (R<sub>f</sub>= 0.33) Yield: 10.49 g, white long crystals (63.3 %). <sup>1</sup>H NMR (400 MHz, CDCl<sub>3</sub>) δ 4.46 – 4.05 (m, 2H), 2.80 – 2.47 (m, 2H), 2.15 – 1.95 (m, 2H), 1.60 – 1.44 (m, 1H), 1.42 – 1.24 (m, 2H), 0.90 (s, 9H). <sup>13</sup>C NMR (101 MHz, CDCl<sub>3</sub>) δ 176.28 (s), 68.63 (s), 50.77 (s), 33.46 (s), 32.99 (s), 30.35 (s), 27.45 (s), 23.78(s). (Found: C, 70.42; H, 10.67; C<sub>10</sub>H<sub>18</sub>O<sub>2</sub> requires, C, 70.55; H, 10.66%).

5-Phenyloxepan-2-one, *PHLOP* (**4**) - UHP (3 x 8.1 g, 86.1 mmol, 3 eq.) and 4-phenylcyclohexanone (3 x 5 g, 28.7 mmol, 1 eq.). The crude white crystals were purified by liquid chromatography on silica eluting with a polarity of ethyl acetate:hexane (25:75) (R<sub>f</sub>= 0.15) Yield: 10.61 g, white/cream crystals (64.8 %). <sup>1</sup>H NMR (400 MHz, CDCl<sub>3</sub>) δ 7.40 – 7.08 (m, 5H), 4.43 – 4.23 (m, 2H), 2.92 – 2.66 (m, 3H), 2.24 – 1.60 (m, 3H), 1.93 – 1.73 (m, 1H). <sup>13</sup>C NMR (101 MHz, CDCl<sub>3</sub>) δ 175.72 (s), 144.98 (s), 128.79 (s), 126.88 (s), 126.63 (s), 68.26 (s), 47.24 (s), 36.75 (s), 33.72 (s), 30.34 (s). (Found: C, 75.58; H, 7.40; C<sub>12</sub>H<sub>14</sub>O<sub>2</sub> requires, C, 75.76; H, 7.42%).

### 6.3.1.2 Synthesis of 4,4'-bioxepanyl-7,7'-dione, BOD

Urea hydrogen peroxide, *UHP*, (15 g, 6 eq i.e. 3 eq per ketone) was added to excess formic acid (100 mL) and stirred for 2 hours at room temperature to allow for the formation of a peroxy-acid. The mixture was then placed in an ice bath before bicyclohexanone (5 g, 1 eq) was added over 10 minutes. This was then left stirring for 24 hours with periodic changing of the ice bath to control the exothermic reaction.

Water (100 mL) was then added and the organic fraction extracted with a chloroform wash (4 x 100 mL). A final wash of the organic layer was performed with sodium bicarbonate (3 x 100 mL). The organic fraction was dried over sodium sulfate for 24 hours. Finally the solution was filtered and the solvent removed liberating a white solid. Further purification was completed using liquid chromatography on silica, eluting from ethyl acetate: hexane (50:50), increasing to a polarity of ethyl acetate: hexane (100:0) (R<sub>f</sub> = 0.25), white solid. <sup>1</sup>H NMR (400 MHz, CDCl<sub>3</sub>) δ 4.22 (m, 4H), 2.82 – 2.51 (m, 4H), 1.98 – 1.80 (m, 4H), 1.73 – 1.57 (m, 4H),

1.56 – 1.39 (m, 2H).  $^{13}\text{C}$  NMR (101 MHz,  $\text{CDCl}_3$ )  $\delta$  175.38 (s), 68.07 (s), 45.94 (s), 33.33 (s), 32.27 (s), 32.04 (s), 26.00 (s), 25.79 (s). (Found: C, 63.39; H, 8.03;  $\text{C}_{12}\text{H}_{14}\text{O}_2$  requires, C, 63.70; H, 8.02%).

## 6.3.2 Acid Catalysed Ring Opening Polymerisation

### 6.3.2.1 Linear polymerisation of cyclic esters

In a typical synthesis, targeting a number average degree of polymerisation,  $DP_n = 40$ , a cyclic ester (**1-4**,  $\epsilon\text{-CL}$ , 2 g) was added to the reaction vessel, under an argon atmosphere, followed by anhydrous toluene (50 wt% for  $\epsilon\text{-CL}$  & **1/2**, 33 wt% for **3** and 25 wt% for **4**). The flask was transferred to an oil bath and stirred at 30 °C (48 °C for **4**). Benzyl alcohol (1 eq) acting as an initiator and methanesulfonic acid, *MSA*, (1 eq) were added consecutively. The flask was then sealed and left stirring at 30 °C (48 °C for **4**) for 1.5 hours for  $\epsilon\text{-CL}$  (3.5 hours for monomers **1-4**).

The resulting product was dissolved in chloroform and stirred with basic alumina before the catalyst was removed with a basic alumina column. A sample of the crude product was taken at this point for analysis by  $^1\text{H-NMR}$  in  $\text{CDCl}_3$ . The solution was reduced under vacuum and then precipitated/triturated in cold hexane (400 mL for precipitation, 2 x ~10 mL for trituration (**1-4**)) to liberate the pure polymer. The polymer was dried overnight under vacuum at 40-50 °C before analysis was completed with  $^1\text{H-NMR}$  in  $\text{CDCl}_3$  and triple detection SEC in DMF/LiBr at 60 °C.

### 6.3.2.2 Branched ring opening polymerisation of cyclic esters

The syntheses of branched polyesters (monomers **1-4**,  $\epsilon\text{-CL}$ ) were carried out following the procedure of linear ROP (as described in 6.3.2.1) with the addition of 4,4'-bioxepanyl-7,7'-dione, *BOD*, (for example, for a initiator: BOD ratio of 1:0.7, 41.63-104.07 g) to the reaction vessel before the addition of anhydrous toluene (w.r.t monomer: 50 wt% for  $\epsilon\text{-CL}$ , 33 wt% **1-3** and 25 wt% for **4**). These reactions also required an increased reaction temperature of 36 °C for  $\epsilon\text{-CL}$ , 38.5 °C for **1-3** and 61 °C for **4**. The ratio of initiator to BOD was varied from 1:0.8 to 1:0.6 (for  $\epsilon\text{-CL}$  exclusively) to determine the gelation point and follow the effects of a bis-lactone ester on molecular weight, detailed in Section 2.3.3.1.

### 6.3.2.3 Determining the presence of transesterification reactions in the ring opening polymerisation of PCL<sub>40</sub>

Synthesis of the linear polymer was carried out following the experimental procedures detailed in Section 6.3.2.1, targeting an average degree of polymerisation of 40 monomer units (4 g of  $\epsilon$ -CL) and undertaken in anhydrous toluene (50 wt%). Samples were taken under an argon atmosphere at different time points: before MSA addition,  $t_0$ , after 1.5 hours at full conversion,  $t_{1.5}$ , after 24 hours,  $t_{24}$ , and finally after 48 hours,  $t_{48}$ . MSA was removed from the aliquots ( $t_{1.5}$ ,  $t_{24}$  and  $t_{48}$ ) by a short basic alumina column in chloroform and then analysed by <sup>1</sup>H-NMR in CDCl<sub>3</sub> and single detection SEC in DMF/LiBr. Following completion of the experiment remaining polymer was purified by the procedure detailed in Section 6.3.2.1 and also analysed by <sup>1</sup>H-NMR in CDCl<sub>3</sub> and single detection SEC in DMF/LiBr.

### 6.3.2.4 Kinetic Studies of the ring opening polymerisation of $\epsilon$ -CL and $\epsilon$ -CL with BOD

Kinetic studies for both linear and branched polymerisations of CL were prepared in the same manner as detailed in Sections 6.3.2.1 and 6.3.2.2, targeting a DP<sub>n</sub> of 40 monomer units in each case and initiator to BOD ratio of 1:0.7 for the branched polymerisation. The scale of the reaction was undertaken with 3 g of  $\epsilon$ -CL and undertaken at 50 wt% dilution in anhydrous toluene, w.r.t monomer. A sample ( $t_0$ ) was taken before MSA addition, under Ar<sub>2</sub>, to give a representation of each polymerisation before it commenced. MSA was then added and samples (ca. 0.1 mL) were taken under Ar<sub>2</sub> over 1.5 hours. The purification and frequency of sampling was altered during this experiment due to purification problems, detailed in Section 2.3.2.1. In initial studies samples (ca. 0.1 mL) were taken every 5 minutes and purified by dissolution in chloroform followed by a small basic alumina column. Samples were analysed by <sup>1</sup>H-NMR in CDCl<sub>3</sub>.

For the investigation of purification method, two samples (0.1 mL) were taken at each time point; at 0, 27, 40, 60 and 90 minutes. Sample A for each time point was treated with basic alumina as detailed above whereas sample B was dissolved in toluene (1 mL) containing TEA (equimolar to the estimated MSA content in 0.1 mL polymer mixture).

Following the results of this investigations both linear and branched kinetic samples were treated with equimolar TEA. Preparation of each experiment was again undertaken following methodologies detailed in Sections 6.3.2.1 and 6.3.2.2, targeting a DP<sub>n</sub> of 40 monomer units in

each case and initiator to BOD ratio of 1:0.7 for the branched polymerisation. Initial time points (0.1 mL),  $t_0$ , were taken before MSA addition after the polymerisation mixtures were completely solvated at 30 and 36 °C for the linear and branched polymerisations respectively. Time points were then taken every 3 minutes for the first 30 minutes and then every 5 minutes until 1.5 hours had elapsed and each was added to 1 mL toluene containing TEA (equimolar to MSA). Each sample was filtered through cotton wool and analysed by  $^1\text{H-NMR}$  in  $\text{CDCl}_3$  and SEC analysis in DMF/LiBr at 60 °C (single detection for  $\text{PCL}_{40}$  and triple detection for  $\text{PCL}_{40-co-BOD_{0.7}}$ ) following evaporation of the toluene solution.

### 6.3.2.5 Poly(ethylene glycol) methyl ether initiated linear ring opening polymerisation of cyclic esters

Before the polymerisation, poly(ethylene glycol) methyl ether, *PEG-OH*, (2000 g mol<sup>-1</sup> or 5000 g mol<sup>-1</sup>) was dried overnight in a vacuum oven at 40-50 °C. In a typical reaction targeting a  $\text{DP}_n=40$  monomer units using a  $\text{PEG}_{5K}\text{-OH}$  initiator, the chosen cyclic ester (**1-4**,  $\epsilon\text{-CL}$ , 40 eq, 2 g) and initiator (1 eq) were weighed into a round bottom flask which was then equipped with a magnetic stirrer bar and sealed. The flask was sparged with  $\text{Ar}_2$  for ca. 10 minutes before the addition of toluene (50 wt% for  $\epsilon\text{-CL}$  & **1/2**, 33 wt% for **3** and 25 wt% for **4**). The flask was submerged in an oil bath pre-heated to 50 °C where MSA (1eq) was added following complete solubilisation of the initiator in the reaction mixture. The reaction mixture was left stirring for 2 hours for  $\epsilon\text{-CL}$  (3.75 hours for **1-4**).

The resulting polymer was dissolved in chloroform and stirred with basic alumina followed by catalyst removal via filtration through a basic alumina column. Here, an aliquot was taken for analysis by  $^1\text{H-NMR}$  in  $\text{CDCl}_3$ . The filter solution was then reduced to a minimal volume before precipitation/trituration in cold hexane (200 mL for precipitation, 2 x ~10 mL for trituration (**1-4**)). The resulting pure polymer was dried in a vacuum oven overnight at 40-50 °C followed by analysis by  $^1\text{H-NMR}$  ( $\text{CDCl}_3$ ) and SEC analysis in DMF/LiBr at 60 °C.

### 6.3.2.6 Poly(ethylene glycol) initiated branched ring opening polymerisation of cyclic esters

Again, the synthesis of  $\text{PEG}_{5K}\text{-OH}$  initiated branched polyesters with monomers **1-4** and  $\epsilon\text{-CL}$  were carried out following the procedure detailed in Section 6.3.2.5 targeting a  $\text{DP}_n$  of 40 monomer units with the addition of BOD (0.7 eq w.r.t 1 eq initiator) before the addition of toluene. The ratio of BOD to initiator was fixed at 0.7:1 following the results of the initial

studies detail in Section 2.3.3.1. Crude samples were taken for determination of monomer conversion by  $^1\text{H-NMR}$  in  $\text{CDCl}_3$  and pure polymers were analysed by both  $^1\text{H-NMR}$  in  $\text{CDCl}_3$  and SEC in DMF/LiBr at  $60\text{ }^\circ\text{C}$ .

Following this analysis the ratio of BOD to initiator was increased, exclusively with  $\epsilon\text{-CL}$ , to determine the gel point with the BOD to initiator ratio increments being 0.8:1, 0.9:1, 1:1, 1.2:1 and 1.5:1. Resultant polymers were analysed with both  $^1\text{H-NMR}$  and SEC in DMF/LiBr at  $60\text{ }^\circ\text{C}$ .

## 6.4 Methods for Chapter 3 – Particle formation

### 6.4.1 (Co)-Nanoprecipitation Studies

#### 6.4.1.1 Typical nanoprecipitation studies of polyesters

In a typical nanoprecipitation study, the selected polymer was dissolved in either acetone or THF at a concentration of  $5\text{ mgmL}^{-1}$ . Each solution was left mixing overnight to ensure full dissolution of the polymer. The organic solvent/polymer solution (1 mL) was then quickly added to de-ionised water (5 mL) contained within a 14 mL vial equipped with a magnetic stirrer bar. The mixture was left stirring vigorously at ambient temperature for approximately 24 hours to allow for full solvent evaporation. The resulting, unfiltered nanoparticle dispersion was then analysed by DLS and re-analysed after 7 or 14 days, unless otherwise specified.

#### 6.4.1.2 Typical co-nanoprecipitation studies of polyesters

In a typical co-nanoprecipitation study targeting a weight fraction of 75 wt% the selected branched polyester (e.g.  $\text{PCL}_{40}\text{-}co\text{-BOD}_{0.7}$ ) and 25 wt% of the chosen A-B block PEG co-polymer ( $\text{PEG}_x\text{-}b\text{-PCL}_{40}$ ), 40 mg in total was weighed out. This consisted of  $\text{PCL}_{40}\text{-}co\text{-BOD}_{0.7}$  (30 mg) and  $\text{PEG}_x\text{-}b\text{-PCL}_{40}$  (10 mg) which was then dissolved in the selected organic solvent, either THF or acetone (8 mL), to a concentration of  $5\text{ mgmL}^{-1}$  and mixed over ca. 24 hours to allow for complete dissolution. An aliquot (1 mL) of this solution was then rapidly added to de-ionised water (5 mL) stirring vigorously. The mixture was left at ambient temperature for 24 hours to allow for complete evaporation of organic solvent. This resulted in an aqueous dispersion at a final concentration of  $1\text{ mgmL}^{-1}$  which was subsequently analysed by DLS.

This method was implemented for a number of weight fractions for a large variation of branched polyester to AB block co-polymer combinations (specified in Chapter 3). These consisted of 100:0, 90:10, 75:25, 50:50 and 0:100 wt %.

## 6.4.2 Salt stability studies

### 6.4.2.1 Successive addition of NaCl to nanoparticle dispersions to determine salt stability

The chosen nanoparticle aqueous dispersion (1 mL), with a concentration of polymer in water of  $1 \text{ mgmL}^{-1}$  was added to a small 4 ml vial. Then, aliquots of 0.5 M NaCl (20  $\mu\text{L}$ ) were consecutively added, with agitation by vortex mixing and 30 second intervals between each addition (20 – 2000  $\mu\text{L}$ ). Additions were continued until visible aggregation could be seen or the 2000  $\mu\text{L}$  limit was reached and the volume noted. This was a qualitative method used to give a visual estimate of the solutions stability to be coupled with study of stability over time in the addition of salt detailed in section 6.5.2.2.

### 6.4.2.2 Time dependant salt stability study

Prior to the study, 1 mL of the chosen aqueous nanoparticle dispersion (concentration of  $1 \text{ mgmL}^{-1}$  polymer in water) was added to a 4 mL vial (after initial DLS characterisation). For the instant measurement, an aliquot of 0.5 M NaCl solution (20  $\mu\text{L}$ ) was added followed by agitation by vortex mixer followed by immediate DLS analysis. The sample was returned to the vial and re-analysed after 1 and 7 days of storage. The procedure was repeated for all co-nanoprecipitates involving PEG<sub>x</sub>-co-PCL<sub>40</sub> as the amphiphilic component.

### 6.4.3 Encapsulation of hydrophobic guest molecule via rapid co-nanoprecipitation

In a typical guest encapsulation study, *via* co-nanoprecipitation, using oil red O (2.43 wt%) targeting a weight fraction of 50 wt% the selected branched polyester (e.g. PCL<sub>40</sub>-co-BOD<sub>0.7</sub>) and 50 wt% of the chosen A-B block PEG co-polymer (PEG<sub>x</sub>-*b*-PCL<sub>40</sub>), oil red O was initially dissolved in THF ( $1 \text{ mgmL}^{-1}$ ) and left to dissolve overnight. The selected PEG co-polymer (10 mg) and branched polyester (10 mg) were dissolved in THF (3.48 mL) followed by the addition of the THF/oil red O mixture (0.52 mL). The resulting solutions ( $5 \text{ mgmL}^{-1}$  w.r.t polymer) were left to dissolve overnight, after which, an aliquot (1 mL) was rapidly added to de-ionised water (5 mL) under vigorous stirring. After organic solvent evaporation, the resulting aqueous dispersion ( $1 \text{ mgmL}^{-1}$ ) was characterised by DLS.



## 6.5 Methods for Chapter 4 – Encapsulation of active drug molecules

### 6.5.1 Encapsulation of SN-38 P via rapid co-nanoprecipitation

In a typical guest encapsulation study of SN-38 P (2.43 wt%), *via* co-nanoprecipitation, targeting a weight fraction of 50 wt% the selected branched polyester (e.g. PCL<sub>40-co</sub>-BOD<sub>0.7</sub>) and 50 wt% of the chosen A-B block PEG co-polymer (PEG<sub>5K-b</sub>-PCL<sub>40</sub> or PEG<sub>5K-b</sub>-BM<sub>40</sub>), SN-38 P was initially dissolved in THF (1 mgmL<sup>-1</sup>) and left to dissolve overnight. The selected PEG co-polymer (25 mg) and branched polyester (25 mg) were dissolved in THF (8.75 mL) followed by the addition of the THF/SN-38 P mixture (1.25 mL). The resulting solutions (5 mgmL<sup>-1</sup> w.r.t polymer) were left to dissolve overnight, after which, an aliquot (1 mL) was rapidly added to de-ionised water (5 mL) under vigorous stirring. After organic solvent evaporation, the resulting aqueous dispersion (1 mgmL<sup>-1</sup>) was characterised by DLS.

### 6.5.2 Encapsulation of SN-38 via rapid co-nanoprecipitation

First in order to select a suitable solvent which would enable the dissolution of both the polymer and SN-38 solubility tests were undertaken with SN-38 in a range of solvents (Table 6.1). It was found that only DMSO (1 mgmL<sup>-1</sup>), THF:acetonitrile (95:5 to 50:50, 1 mgmL<sup>-1</sup>) and THF (4 mgmL<sup>-1</sup>) were able to dissolve SN-38.

**Table 6.1 – Solubility studies conducted with SN-38 and various solvents.**

Solvent System	Dissolution?	Solvent System	Dissolution?
<b>THF: Acetonitrile</b> (50:50, 1 mgmL <sup>-1</sup> )	✓	<b>Acetone</b> (1 mg/mL)	✗
<b>THF: Acetonitrile</b> (75:25, 1 mgmL <sup>-1</sup> )	✓	<b>Dichloromethane</b> (1 mgmL <sup>-1</sup> )	✗
<b>THF: Acetonitrile</b> (90:10, 1 mgmL <sup>-1</sup> )	✓	<b>Methanol</b> (1 mgmL <sup>-1</sup> )	✗
<b>THF: Acetonitrile</b> (95:5, 1 mgmL <sup>-1</sup> )	✓	<b>Chloroform</b> (1 mgmL <sup>-1</sup> )	✗
<b>THF</b> (1 mgmL <sup>-1</sup> )	✓	<b>Ethanol</b> (1 mgmL <sup>-1</sup> )	✗
<b>THF</b> (2 mgmL <sup>-1</sup> )	✓	<b>Ethyl acetate</b> (1 mgmL <sup>-1</sup> )	✗
<b>THF</b> (3 mgmL <sup>-1</sup> )	✓	<b>Diethyl Ether</b> (1 mgmL <sup>-1</sup> )	✗
<b>THF</b> (4 mgmL <sup>-1</sup> )	✓	<b>Acetonitrile</b> (1 mgmL <sup>-1</sup> )	✗
<b>DMSO</b> (1 mgmL <sup>-1</sup> )	✓	<b>H<sub>2</sub>O</b> (1 mgmL <sup>-1</sup> )	✗

THF was selected for co-nanoprecipitation studies due to the low boiling point aiding solvent evaporation. In a typical co-nanoprecipitation study, targeting 2.43 wt% SN-38 loaded, 50:50 wt% linear PEG co-polymer and branched polyester (e.g. PEG<sub>5K</sub>-*b*-PCL<sub>40</sub>: PCL<sub>40</sub>-*co*-BOD<sub>0.7</sub>) nanoparticles, SN-38 was first dissolved in THF (1 mgmL<sup>-1</sup>) and left to mix for > 2 hours. 50 mg of polymer was weight out into a glass vial, consisting of PEG<sub>5K</sub>-*b*-PCL<sub>40</sub> (25 mg) and PCL<sub>40</sub>-*co*-BOD<sub>0.7</sub> (25 mg), and dissolved in THF (8.75 mL). THF/SN-38 mixture (1.25 mL) was then added to the same vial and the resulting solution (5 mgmL<sup>-1</sup> w.r.t polymer) was left to mix overnight. An aliquot (1 mL) of this solution was then rapidly added to de-ionised water (5 mL) under vigorous stirring and the organic solvent was left to evaporate over 24 hours targeting a final aqueous nanoparticle dispersion (1 mgmL<sup>-1</sup> w.r.t polymer) containing 2.43 wt% SN-38. This methodology was applied to various combinations of PEG<sub>x</sub>-*b*-PCL<sub>40</sub> stabilised branched polymers based on ε-CL, MOP, POP, BOP and PHLOP monomers. Unfortunately DLS characterisation was unable to be completed for any of these dispersion due to instability.

### 6.5.3 Variation of concentration: dilution studies

Studies were undertaken following methodology first published by Ford *et al.*<sup>1</sup>

#### 6.5.3.1 Varying the concentration of PEG<sub>5K</sub>-*b*-PCL<sub>40</sub> and branched polyesters in THF with and without hydrophobic guest present

In a typical dilution study based on a co-nanoprecipitation of 50 wt% PCL<sub>40</sub>-*co*-BOD<sub>0.7</sub>, 50 wt% PEG<sub>5K</sub>-*b*-PCL<sub>40</sub> and SN-38 content of 2.43 wt% final polymer content in de-ionised water (5 mL) was targeted to be 12.5 mg following solvent evaporation. Therefore a series of polymer/drug in THF solutions were made with concentrations (w.r.t polymer) between 1.5625 and 25 mgmL<sup>-1</sup>. SN-38 content was kept constant at 2.43 wt% regardless of polymer concentration in THF. All solutions were left to mix overnight to allow for full polymer and SN-38 dissolution. Then each THF mixture (concentrations specified in Table 6.2) was rapidly added to de-ionised water (0.5 mL to 8 mL, Table 6.2) with vigorous stirring. DLS characterisation was undertaken instantaneously after solvent addition and following full THF evaporation; both measurements were undertaken in a quartz cuvette.

This methodology was repeated for a 50 wt% PCL<sub>40</sub>-*co*-BOD<sub>0.7</sub>, to 50 wt% PEG<sub>5K</sub>-*b*-PCL<sub>40</sub> co-nanoprecipitation without SN-38 and also a 50 wt% PPOP<sub>40</sub>-*co*-BOD<sub>0.7</sub> to 50 wt% PEG<sub>5K</sub>-*b*-PCL<sub>40</sub> co-nanoprecipitation with 2.43 wt% SN-38.

**Table 6.2 – Concentration of polymers (50:50 wt%) combined PEG co-polymer and branched polyester, with and without SN-38, in THF targeting a final mass in water of 12.5 mg (w.r.t polymer) and 0.303 mg (w.r.t SN-38, 2.43 wt%).**

Entry	Volume of THF containing polymer (and drug) (mL)	Concentration of polymer in THF (mgmL <sup>-1</sup> )	Concentration of drug in THF (mgmL <sup>-1</sup> )	Volume of de-ionised water (mL)
Only polymer (50:50)				
1	0.5	25	-	5
2	1	12.5	-	5
3	2	6.25	-	5
4	3	4.167	-	5
5	4	3.125	-	5
6	5	2.5	-	5
7	8	1.5625	-	5
Polymer (50:50) and SN-38 (2.43 wt%)				
1	0.5	25	0.625	5
2	1	12.5	0.3125	5
3	2	6.25	0.15625	5
4	3	4.167	0.101475	5
5	4	3.125	0.078125	5
6	5	2.5	0.0625	5
7	8	1.5625	0.03906	5

### 6.5.3.2 Varying the concentration of a hydrophobic guest and trial of nanoparticle formation without polymer present

This study was completed using concentrations that reflect 2.43 wt% guest loading if the polymer was present at a constant mass in de-ionised water (5 mL) after THF evaporation (detailed in section 6.5.2.1). Therefore maintain a final guest mass in water (5 mL) of 0.303 mg after THF evaporation, with concentration of guest in THF varying from 0.03906 to 0.625 mgmL<sup>-1</sup> (Table 6.3). THF/guest mixtures were mixed overnight before additions of increasing volume (0.5 to 8 mL, Table 6.3) to de-ionised water (5 mL). DLS characterisation was only undertaken upon instant addition of each solution using a quartz cuvette.

**Table 6.3 – Concentration of guest molecules in THF targeting a final mass in water of 0.303 mg (2.43 wt%).**

Entry	Volume of THF containing polymer (and drug) (mL)	Concentration of polymer in THF (mgmL <sup>-1</sup> )	Concentration of drug in THF (mgmL <sup>-1</sup> )	Volume of de-ionised water (mL)
<b>Drug or guest only (2.43 wt%)</b>				
1	0.5	-	0.625	5
2	1	-	0.3125	5
3	2	-	0.15625	5
4	3	-	0.101475	5
5	4	-	0.078125	5
6	5	-	0.0625	5
7	8	-	0.03906	5

## 6.5.4 Thin film hydration

### 6.5.4.1 Typical thin film co-hydration of branched polyesters and PEG copolymers

In a typical thin film hydration study targeting a weight fraction of 50 wt% branched polyester (e.g. PCL<sub>40-co</sub>-BOD<sub>0.7</sub>) and 50 wt% PEG<sub>5K-b</sub>-PCL<sub>40</sub> and SN-38 content of 2.43 wt%, SN-38 (10 mg) was initially dissolved in THF (10 mL) at a concentration of 1 mgmL<sup>-1</sup> and left to mix for > 2 hours. PCL<sub>40-co</sub>-BOD<sub>0.7</sub> (10 mg) and PEG<sub>5K-b</sub>-PCL<sub>40</sub> (10 mg) were weighed out into a glass vial followed by THF (3.5 mL) and SN-38 solution in THF (0.5 mL). This was mixed overnight to allow for dissolution. An aliquot (0.5 mL) was then added to a new glass vial and the THF removed under vacuum. De-ionised water (2.5 mL) was added targeting an aqueous dispersion concentration of 1 mgmL<sup>-1</sup>. The method of mixing was then varied between 3 methods, vortex mixing for ca. 5 minutes, stirring vigorously overnight and sonication directly after water addition. Samples that were hydrated using vortex or by direct sonication were both sonicated using an ultrasound bath for 5 minutes. Samples which underwent vigorous stirring overnight were investigated with two methods of sonication, *via* ultrasound bath (5 minutes) or *via* a Covaris (60 seconds, 70 W at ≤ 14 °C). DLS characterisation was undertaken before and after sonication.

### 6.5.4.2 Typical thin film hydration of single species

In a typical thin film hydration study targeting a drug loading of 50 wt% SN-38 in a PEG<sub>5K</sub>-*b*-PMOP<sub>40-co</sub>-BOD<sub>0.7</sub> based dispersion, PEG<sub>5K</sub>-*b*-PMOP<sub>40-co</sub>-BOD<sub>0.7</sub> (25 mg) and SN-38 (25 mg) were added to a glass vial and dissolved in THF (5 mgmL<sup>-1</sup> w.r.t polymer). The solution was left to mix overnight to ensure dissolution. A small aliquot (0.5 mL) was transferred to another glass vial followed by removal of THF *via* rotary evaporation. The thin film was then hydrated by the addition of de-ionised water (2.5 mL) and vigorous stirring overnight. The resulting dispersion was then characterised by DLS before sonication was completed using a Covaris (60 seconds, 70 W at ≤ 14 °C). Following sonication nanoparticle dispersions were characterised by DLS again.

This methodology was repeated for both linear and branched PEG co-polymer with a number of SN-38 drug loading values, specified in Section 4.3.2.

### 6.5.5 Thin film hydration stability studies

#### 6.5.5.1 Stability of dry thin films

Thin films for this stability study were synthesised using the methodology detailed in Section 6.5.3.2 utilising either PEG<sub>5K</sub>-*b*-PMOP<sub>40-co</sub>-BOD<sub>0.7</sub> or PEG<sub>5K</sub>-*b*-PPOP<sub>40-co</sub>-BOD<sub>0.7</sub> and SN-38 drug loadings of 10, 30, 50 and 75 wt% maintaining a polymer in THF concentration of 5 mgmL<sup>-1</sup>. 10 thin films of each polymer and drug loading combination (80 in total) were created by the reduction of an aliquot of the polymer/drug/THF solution (0.5 mL) by rotary evaporation. Once the dry films were created the first time point, for each polymer and SN-38 content combination, was hydrated to a concentration of 1 mgmL<sup>-1</sup> by the addition of water (2.5 mL) with vigorous stirring overnight. Following DLS characterisation, each solution was transferred to a 4 mL vial and sonicated for 60 seconds at 70 W and ≤ 14 °C. Final DLS characterisation was then undertaken on the unfiltered aqueous dispersions.

The other 9 time points for each polymer drug combination were stored at ambient temperature and were hydrated and sonicated with the method detailed above once every week for the first 4 weeks followed by every 2 weeks for the final 10 weeks.

#### 6.5.4.2 Stability of nanoparticle dispersions

Thin film dispersions for the study of stability over time were synthesised using PEG<sub>5K</sub>-*b*-PCL<sub>40-co</sub>-BOD<sub>0.7</sub> with SN-38 contents of 2.43, 10, 16.6, 30, 33, 50, 75 and 95 wt% following

the methodology detailed in Section 6.5.3.2. DLS characterisation was not undertaken before sonication however the unfiltered samples were analysed directly after.

The samples were stored at ambient temperature and the bottom of the vials were photographed before further characterisation by DLS on days 2, 4 and 7 after synthesis. Each sample was agitated using a vortex mixer before DLS characterisation was carried out.

## 6.5.6 Mechanistic studies

### 6.5.6.1 SEM

The preparation of THF solutions containing polymer and SN-38 bound for SEM were prepared in the same manner as detailed in Section 6.5.3.2. For example, targeting SN-38 content of 50 wt%, the selected polymer (25 mg), either PEG<sub>5K</sub>-*b*-PMOP<sub>40-co</sub>-BOD<sub>0.7</sub> or PEG<sub>5K</sub>-*b*-PMOP<sub>40-co</sub>-BOD<sub>0.7</sub>, was weighed into a glass vial. SN-38 (25 mg) was then added before the mixture was dissolved in THF targeting a concentration w.r.t. polymer of 5 mgmL<sup>-1</sup>. The solution was left to mix overnight to ensure complete polymer and drug dissolution. This method was repeated for all targeted drug loadings (0 to 100 wt% SN-38) used in these SEM studies detailed in Section 4.3.3.1. Once dissolved the THF mixtures were treated in different ways specific to the investigation being undertaken detailed in Sections 6.5.5.1.1 and 6.5.5.1.2.

#### 6.5.6.1.1 SEM of the dry thin films

Thin films, suitable for SEM imaging, were created by the addition of a small aliquot ( $\leq 20 \mu\text{L}$ ) onto a silicon wafer atop a SEM stub. THF was then allowed to evaporate overnight resulting in a film of PEG<sub>5K</sub>-*b*-PMOP<sub>40-co</sub>-BOD<sub>0.7</sub> and SN-38. The resulting thin films was then analysed by SEM This was repeated for a number of different SN-38 concentrations between 0 and 100 wt%.

#### 6.5.6.1.2 SEM of filtered solutions

A aliquot of each THF solution (0.5 mL), with PEG<sub>5K</sub>-*b*-PCL<sub>40-co</sub>-BOD<sub>0.7</sub> (5 mgmL<sup>-1</sup> w.r.t. polymer) and SN-38 (0-100 wt%), was added to a glass vial. THF was removed using a rotary evaporation to create a thin film which was hydrated with de-ionised water (2.5 mL), targeting a concentration of 1 mgmL<sup>-1</sup> (w.r.t. polymer), and vigorously stirred overnight. Each solution was then transferred to a 4 mL glass vial and sonicated using a Covaris (60 seconds, 70 W at  $\leq 14 \text{ }^\circ\text{C}$ ). The resulting dispersions were characterised by DLS before being passed through a 0.2  $\mu\text{m}$  PTFE filter. Characterisation of the dispersions by DLS were repeated and the PTFE

filters left for at least 1 week. Once dry the filter wafers were removed and cut into 2 small squares which were stuck, one top face up and the other bottom face up, on a carbon tab atop a SEM stub.

### **6.5.6.2 Differential scanning calorimetry of dry thin films**

In a typical DSC experiment utilising a 75 wt% SN-38 containing thin film and PEG<sub>5K</sub>-*b*-PCL<sub>40</sub>-*co*-BOD<sub>0.7</sub> a solution of polymer and drug in THF (5 mgmL<sup>-1</sup> w.r.t polymer) was first prepared and left to mix overnight. An aliquot (2.5 mL) was then added to a glass vial and the organic solvent was removed under vacuum using a rotary evaporator. Once the dry film was formed the solid (8 to 10 mg) was scrapped out into a Tzero crucible and sealed to allow for DSC analysis to be undertaken.

This process was repeated for a range of SN-38 drug loading (0, 2.5, 10, 20, 30, 50, 75, 95 and 100 wt%).

### **6.5.6.3 Thermal analysis by structural analysis, TASC**

In a typical TASC measurement utilising a 30 wt% SN-38 loaded dry thin film created with PEG<sub>5K</sub>-*b*-PCL<sub>40</sub>-*co*-BOD<sub>0.7</sub>, a solution of polymer and drug was first dissolved in THF targeting a polymer concentration of 5 mgmL<sup>-1</sup>. After solubilisation of both solids at ambient temperature a small amount was pipetted onto the surface of a 16 mm circular round glass microscope cover slip to create the thin film. Once solvent evaporation was complete the film covered glass slide was placed on the heating mantel of the TASC microscope. Once the microscope was sufficiently focussed on a section of the sample that had clear structure the heating mantel was sealed and the microscope refocussed to give the best image for further TASC analysis on the data collected.

Once the apparatus had been set up and focused heating rate, temperature limits and picture rates were defined in the LINKCAM software. The heating rate was set at 10 °Cmin<sup>-1</sup> spanning a temperature range of ~ 25 °C to 250 °C to encompass the literature value of the melting point of SN-38. Pictures of the sample were taken at a rate of 2 per second for the duration of each experiment which allowed a video to be created for each sample measured as melting points were reached (attached DVD). Once the experiment run was completed, using the LINKCAM software, a video was made for each sample and TASC analysis ran on the data collected allowing for the creation of the structural analysis vs time vs temperature graphs seen in Section 4.3.3.3.

This process was repeated for a series of PEG<sub>5K</sub>-*b*-PCL<sub>40</sub>-*co*-BOD<sub>0.7</sub> thin films with increased drug loading from 0 to 100 wt% SN-38.

### 6.5.7 Pharmacological studies

Pharmacological studies were undertaken by Usman Ashard under the supervision of Prof. Andrew Owen and Prof. Chris Goldring

#### 6.5.7.1 Rapid equilibrium dialysis, RED, SN-38 release studies

In a typical rapid equilibrium assessing the release of SN-38 a dispersion of PEG<sub>5K</sub>-*b*-PCL<sub>40</sub>-*co*-BOD<sub>0.7</sub> with 50 wt% SN-38, the dispersion was first diluted with phosphate buffered saline, PBS, (250 ngmL<sup>-1</sup>, pH = 7.4). A control sample of SN-38 only, dissolve in DMSO (< 1% volume in PBS) was also prepared. An aliquot of each sample (0.5 mL) was then added to the donor compartment of a RED insert (8 kDa molecular weight cut off) and PBS (1 mL) added to the acceptor cell. This process was repeated for a total of 11 inserts per dispersion (one for each time point). Inserts were then stirred via orbital shaking (100 rpm, 37 °C) for 48 hours and the contents of each insert was removed at the specified time point (0.5, 1, 2, 3, 4, 5, 6, 7, 8, 24 and 48 hours). The collected aliquots were then analysed by LC-mass spectrometry to determine the percentage SN-38 released.

#### 6.5.7.2 Cytotoxicity studies

Cytotoxicity assessment of the dispersions were undertaken in both 2-dimensional and 3-dimensional assays. CT26, HTH116, DLDD-1 and LoVo cell lines (2000-5000 cells per well) were utilised for 2D assays, seeded for 24 hours (37 °C, 5 % CO<sub>2</sub>) on 96-well plates. HCT116 (1250 cells per well) and CT26 (1000 cells per well) were used for 3D spheroids; seeded for 5 days on low attachment plates. Nanoparticle dispersions, free SN-38 (0.1 % DMSO) and irinotecan (0.1 % DMSO) were used to replace the medium of the cells with increasing concentration (0.5 to 400 nM, 0.01 to 100 µM for irinotecan) and the cells were left for between 24 and 96 hours for 2D and 24 and 144 hours for 3D. Cell viability, calculated as a percentage of the control (0.1 % DSMO or corresponding blank nanoparticle dispersion), was measured using a CellTiter-Glo<sup>®</sup> Luminescent cell viability assay ( $\lambda = 570$  nm).

#### 6.5.7.3 Macrophage uptake

Before macrophage uptake assessment could begin, CD14+ monocytes were isolated by ficoll plaque separation of buffy coats and differentiated, using macrophage generation media DXF,



into M1 and M2 macrophages. These were then added to 6-well plates and treated with the selected nanoparticle dispersion (50  $\mu\text{M}$ ) for 24 hours. SN-38 concentration, both intra- and extra-cellular, was quantified with LC mass spectrometry.

## References

- 1 J. Ford, P. Chambon, J. North, F. L. Hatton, M. Giardiello, A. Owen and S. P. Rannard, *Macromolecules*, 2015, **48**, 1883–1893.

# APPENDIX

## A Chapter 2

### A.1 MSA catalysed ROP of $\epsilon$ -caprolactone

**Table A1 – Calculation of the average dn/dc value PCL polymers**

Target polymer	dn/dc
PCL <sub>40</sub>	0.0574
PCL <sub>50</sub>	0.0592
PCL <sub>60</sub>	0.0580
PCL <sub>80</sub>	0.0581
PCL <sub>100</sub>	0.0573
PCL <sub>40-co</sub> -BOD <sub>0.7</sub>	0.0621
PCL <sub>40-co</sub> -BOD <sub>0.6</sub>	0.0654
PCL <sub>60-co</sub> -BOD <sub>0.7</sub>	0.0622
PCL <sub>80-co</sub> -BOD <sub>0.7</sub>	0.0629
PCL <sub>100-co</sub> -BOD <sub>0.7</sub>	0.0618
Total	0.6044
Total number of values used	10
Average	0.06044

**Table A2 - Series of MSA catalysed ROP of  $\epsilon$ -CL with varied Degree of Polymerisation 10 to 200 monomer units with specific dn/dc values;**

Target polymer	Reaction time (hours)	<sup>1</sup> H-NMR				SEC <sup>c</sup>				
		Monomer conversion <sup>a</sup>	DP <sub>I</sub> by NMR (Initiator) <sup>d</sup>	M <sub>n</sub> by NMR (Initiator) <sup>e</sup> (gmol <sup>-1</sup> )	M <sub>n</sub> Theory <sup>b</sup> (gmol <sup>-1</sup> )	M <sub>n</sub> (g/mol)	M <sub>w</sub> (g/mol)	Đ	dn/dc	$\alpha$
PCL <sub>10</sub>	0.25	>99%	12	1,480	1,250				<i>f</i>	
PCL <sub>20</sub>	0.66	>99%	21	2,510	2,390				<i>f</i>	
PCL <sub>30</sub>	1	>99%	33	3,870	3,530	4,210	5,740	1.36	0.0584	0.79
PCL <sub>40</sub>	1.5	>99%	41	4,790	4,670	4,930	5,950	1.21	0.0574	0.82
PCL <sub>50</sub>	2	>99%	66	7,640	5,820	6,650	7,830	1.18	0.0592	0.84
PCL <sub>60</sub>	2.5	>99%	66	7,640	6,960	7,220	8,290	1.15	0.0580	0.98
PCL <sub>80</sub>	4	>99%	99	11,410	9,240	7,870	10,120	1.29	0.0581	0.69
PCL <sub>100</sub>	5	>99%	137	15,750	11,520	9,250	11,220	1.21	0.0573	0.71
PCL <sub>200</sub>	9	44 %	110	12,670	10,150	7,470	8,110	1.09	0.0579	0.92

*a* Determined by <sup>1</sup>H NMR (CDCl<sub>3</sub>, 400 MHz) of the crude samples, *b* Calculated using the equation:  $Mn_{theory} = (DP_{targeted} \times conv. \times Mr_{CL}) + Mr_{BzA}$ , *c* Determined by triple detection SEC with a mobile phase of DMF/LiBr 0.01 M (60 °C) at 1 mL min<sup>-1</sup>, *d* Calculated using the equation;  $DP_I = (\int 4.05/2 \div \int 5.1/2)$ , *e* Calculated using the equation:  $Mn_{NMR} = (DP_{I(Eq. 2.1)} \times Mr_{CL}) + Mr_{BzA}$ , *f* insufficient light scattering for calculation but RI chromatograms indicated monomodal distribution.

APPENDIX

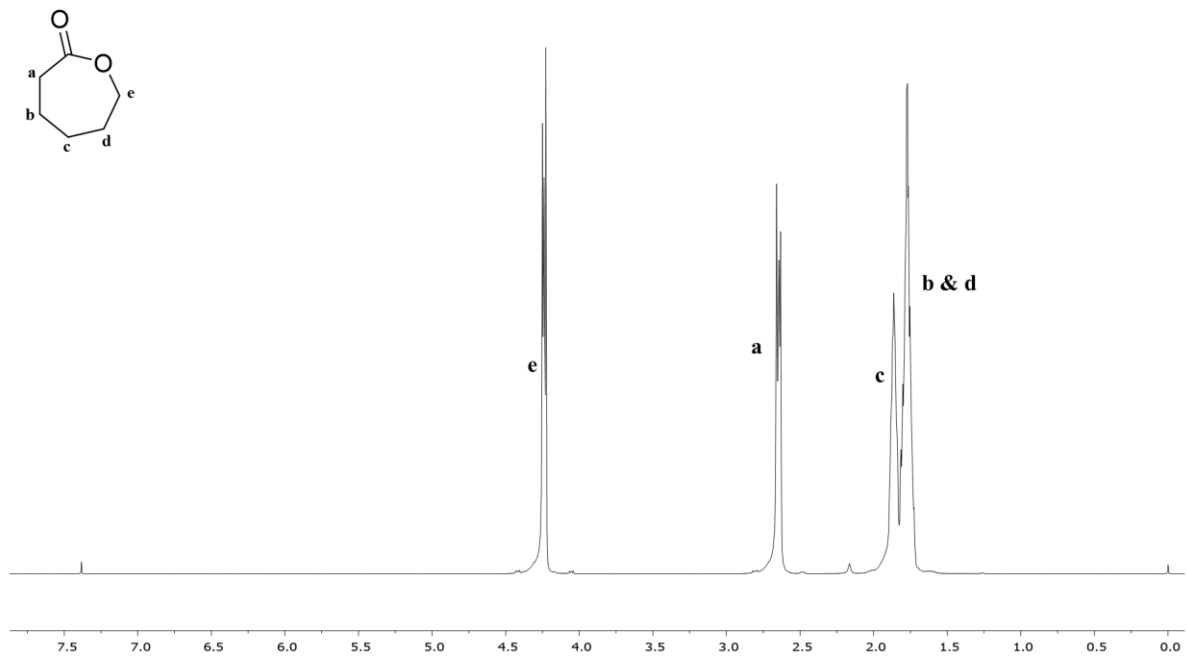


Figure A1 – <sup>1</sup>H-NMR (CDCl<sub>3</sub>, 400 MHz) of ε-caprolactone.

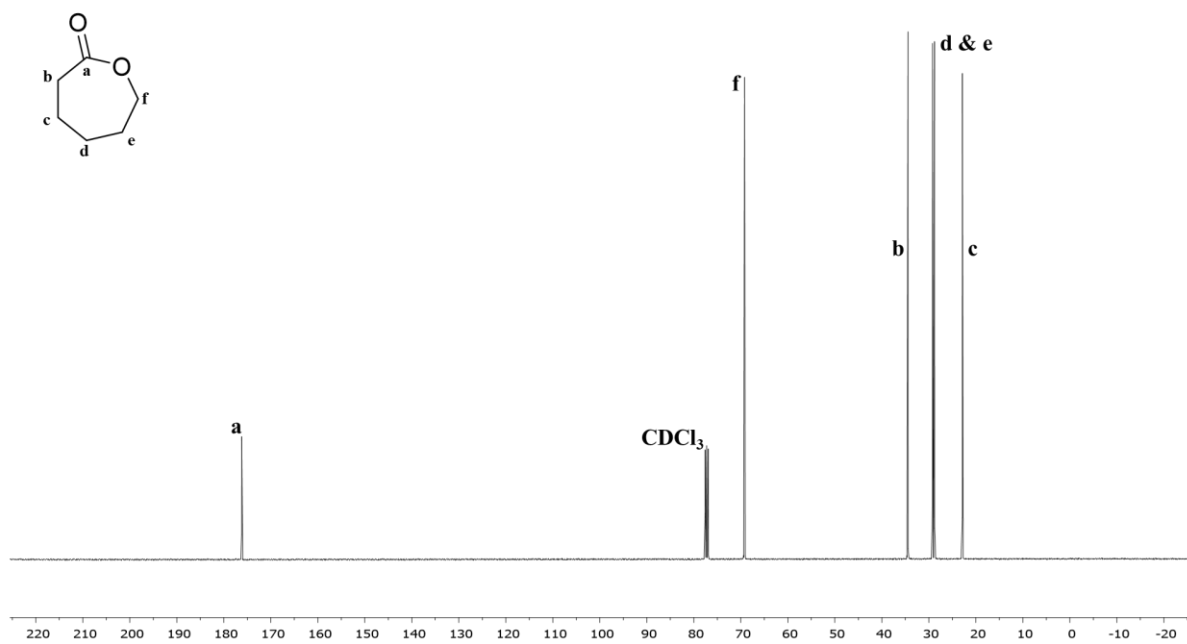
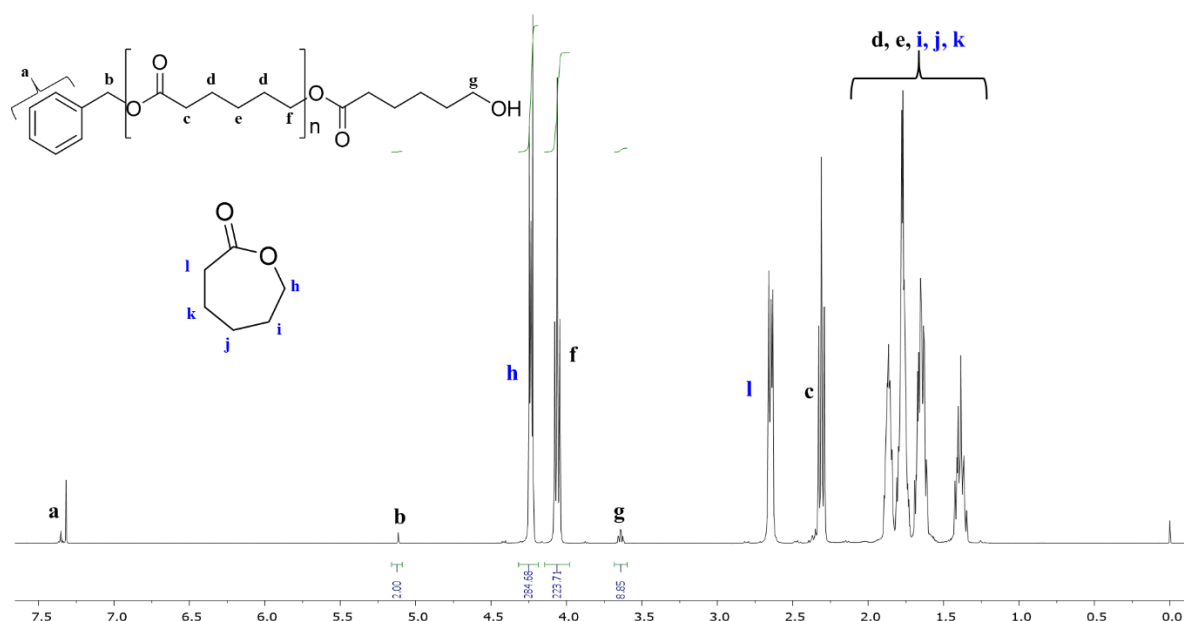


Figure A2 – <sup>13</sup>C-NMR (CDCl<sub>3</sub>, 400 MHz) of ε-caprolactone.



**Figure A3** –  $^1\text{H-NMR}$  ( $\text{CDCl}_3$ , 400 MHz) of crude  $\text{PCL}_{200}$ ; illustrating the polymer proton environments (4.05 ppm) and highlighting the peaks corresponding to the environments of the BZA initiator (5.1 ppm) and the chain end (3.6 ppm).

$$\text{monomer conversion (\%)} = \left( \frac{\int 4.05}{(\int 4.25 + \int 4.05)} \right) \times 100$$

**Equation for the calculation of monomer conversion for PCL polymers;** where  $\int 4.05$  = polymer proton environment f in Figure A3 and  $\int 4.25$  is the monomer proton environment h in Figure A3.

APPENDIX

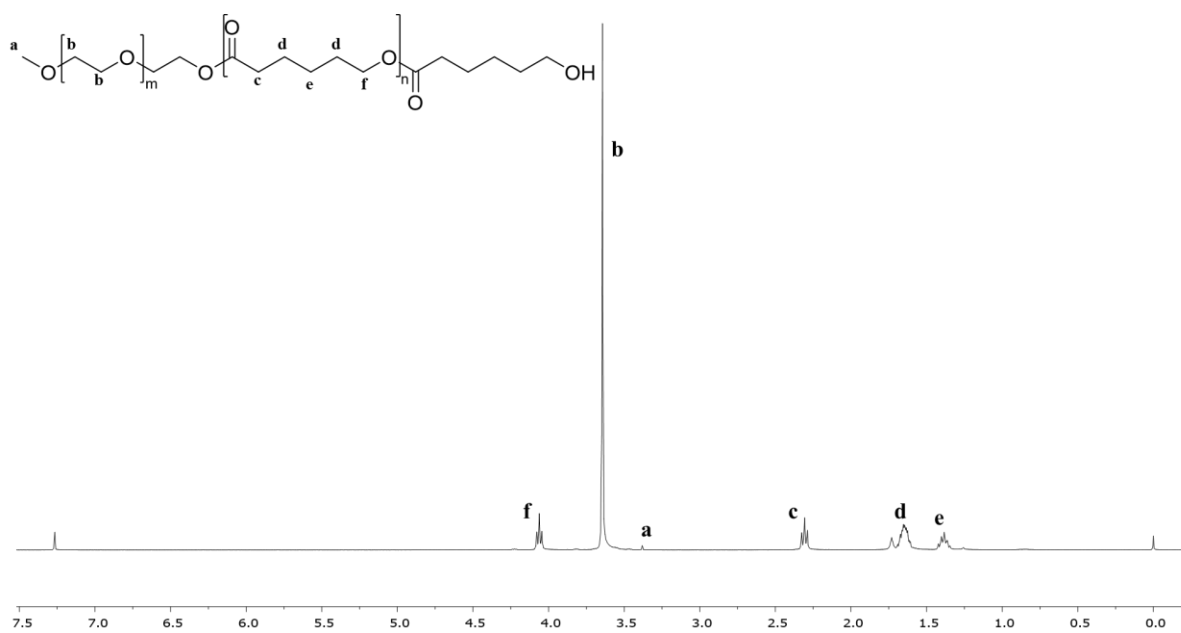


**Figure A4 – <sup>1</sup>H-NMR (CDCl<sub>3</sub>, 400 MHz) of purified PEG-*b*-PCL<sub>40</sub>;** illustrating the polymer proton environments (4.05 ppm) and highlighting the peaks corresponding to the environments of the PEG-OH initiator (3.7 ppm and 3.35 ppm).

**Table A3 –Kinetics of linear PCL<sub>40</sub> over 1.5 hours sampling every 3 minutes until t<sub>30</sub> then every 5 minutes normalised dn/dc = 0.06044;**

Time (min)	<sup>1</sup> H-NMR			Mn Theory <sup>b</sup> (g/mol)	SEC <sup>c</sup>			
	Monomer conversion <sup>a</sup>	DP <sub>I</sub> by NMR (Initiator)	M <sub>n</sub> by NMR (Initiator) (g/mol) <sup>d</sup>		M <sub>n</sub> (g/mol)	M <sub>w</sub> (g/mol)	DP <sub>GPC</sub>	Đ
3	17.8 %	8	1,020	920	1,630	1,630	13	1.001
6	22.9 %	10	1,250	1,150	1,970	2,010	16	1.022
9	37.8 %	15	1,820	1,830	2,130	2,210	18	1.037
12	54.6 %	21	2,510	2,600	2,510	2,700	21	1.074
15	68.8 %	27	3,190	3,250	2,890	3,160	24	1.092
18	86.1 %	33	3,870	4,040	3,390	3,690	29	1.088
21	95.3 %	37	4,330	4,460	3,700	4,050	31	1.095
24	96.5 %	39	4,560	4,510	3,910	4,370	33	1.118
27	99.8 %	39	4,560	4,660	3,940	4,430	34	1.124
30	99.9 %	39	4,560	4,670	4,010	4,570	34	1.139
35	99.9 %	39	4,560	4,670	4,130	4,780	35	1.158
40	99.6 %	39	4,560	4,670	4,180	5,000	36	1.197
45	99.6 %	39	4,560	4,670	4,220	5,080	36	1.202
50	99.3 %	39	4,560	4,670	4,270	5,240	36	1.227
55	99.9 %	40	4,670	4,670	4,390	5,420	38	1.236
60	99.8 %	39	4,560	4,670	4,400	5,430	38	1.235
65	99.6 %	39	4,560	4,670	4,500	5,600	38	1.244
70	99.9 %	39	4,560	4,670	4,610	5,720	39	1.241
75	99.9 %	40	4,670	4,670	4,580	5,960	39	1.303
80	99.9 %	40	4,670	4,670	4,500	5,720	38	1.270
85	99.7 %	40	4,670	4,670	4,640	6,070	40	1.309
90	99.9 %	40	4,670	4,670	4,620	6,580	40	1.423

*a* Determined by <sup>1</sup>H NMR (CDCl<sub>3</sub>, 400 MHz) of the crude samples, *b* Calculated using the equation:  $Mn_{theory} = (DP_{targeted} \times conv. \times M_{CL}) + M_{BZA}$ , *c* Determined by single detection SEC with a mobile phase of DMF/LiBr 0.01M at 1 mLmin<sup>-1</sup> w.r.t to poly(methyl methacrylate), *PMMA*, calibrants, *d* Calculated using the equation:  $Mn_{NMR} = (DP_{I(Eq. 2.14)} \times Mr_{CL}) + Mr_{BZA/PEG-OH}$ .



APPENDIX

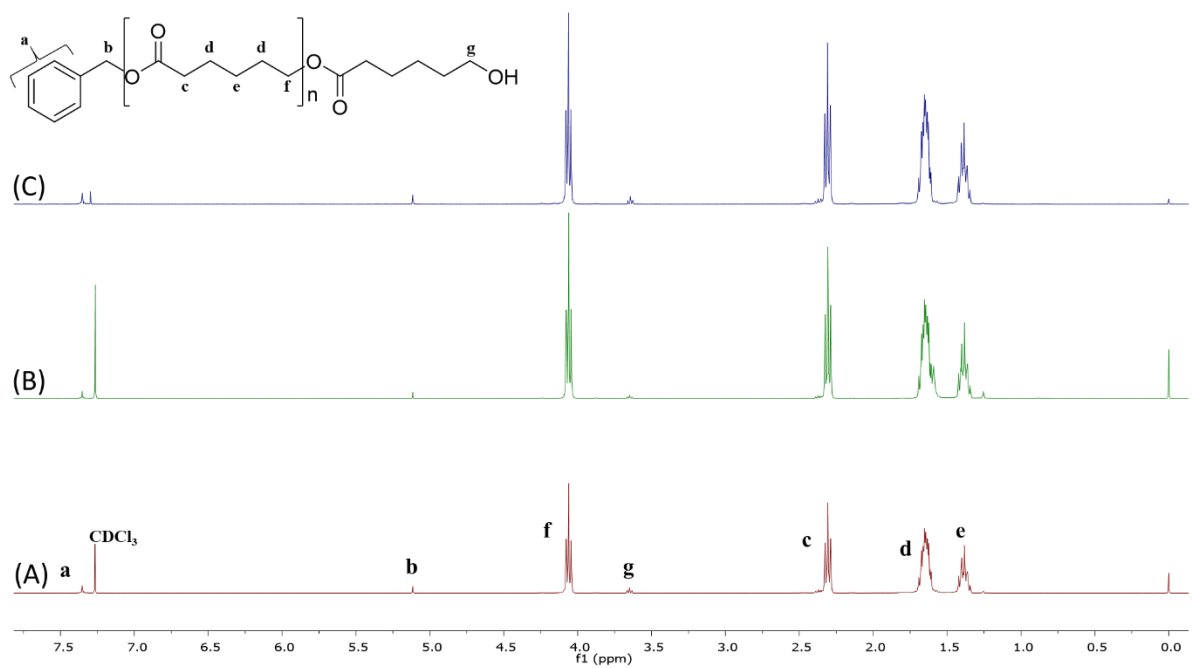


**Figure A5 – <sup>1</sup>H-NMR (CDCl<sub>3</sub>, 400 MHz) of PCL<sub>40</sub> at time points t<sub>1.5</sub>, t<sub>24</sub> and t<sub>48</sub> during transesterification experiment; (A) t<sub>1.5</sub>, (B) t<sub>24</sub> and (C) t<sub>48</sub>.**

**Table A4 - Series of BzA initiated MSA catalysed ROP of  $\epsilon$ -CL with BOD with varied Degree of Polymerisation 40 to 200 monomer units with specific dn/dc values;**

Target polymer	Reaction time (hours)	<sup>1</sup> H NMR		SEC <sup>b</sup>				
		Monomer conversion <sup>a</sup>	DP <sub>I</sub> by NMR (Initiator)	M <sub>n</sub> (gmol <sup>-1</sup> )	M <sub>w</sub> (gmol <sup>-1</sup> )	Đ	dn/dc	$\alpha$
PCL <sub>40-co</sub> -BOD <sub>0.8</sub>	1.5			<i>Gel</i>				
PCL <sub>40-co</sub> -BOD <sub>0.75</sub>	1.5	>99%	51		<i>Gel</i>			
PCL <sub>40-co</sub> -BOD <sub>0.7</sub>	1.5	>99%	51	11,780	248,230	21.1	0.0621	0.35
PCL <sub>40-co</sub> -BOD <sub>0.6</sub>	1.5	>99%	47	9,600	63,620	6.63	0.0654	0.35
PCL <sub>60-co</sub> -BOD <sub>0.7</sub>	2.5	>99%	74	11,690	72,460	6.20	0.0622	0.35
PCL <sub>80-co</sub> -BOD <sub>0.7</sub>	4	>99%	98	11,130	81,770	7.35	0.0629	0.35
PCL <sub>100-co</sub> -BOD <sub>0.7</sub>	5	>99%	116	12,910	61,070	4.73	0.0618	0.36
PCL <sub>200-co</sub> -BOD <sub>0.7</sub>	9	51 %	122	8,080	8,880	1.10	0.0598	0.59

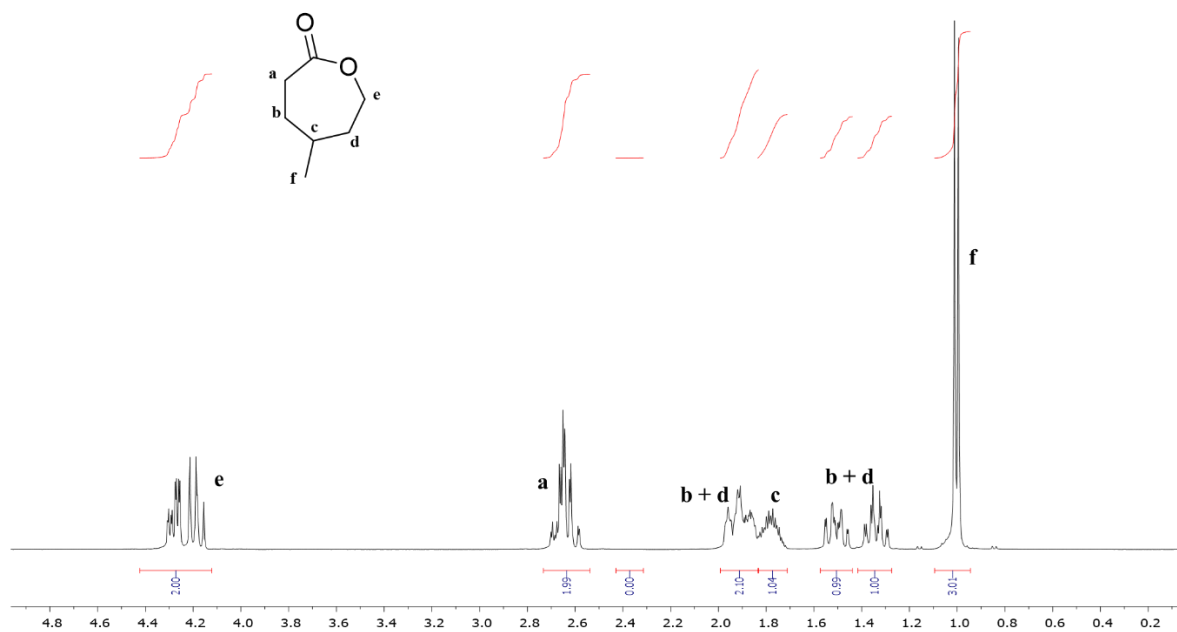
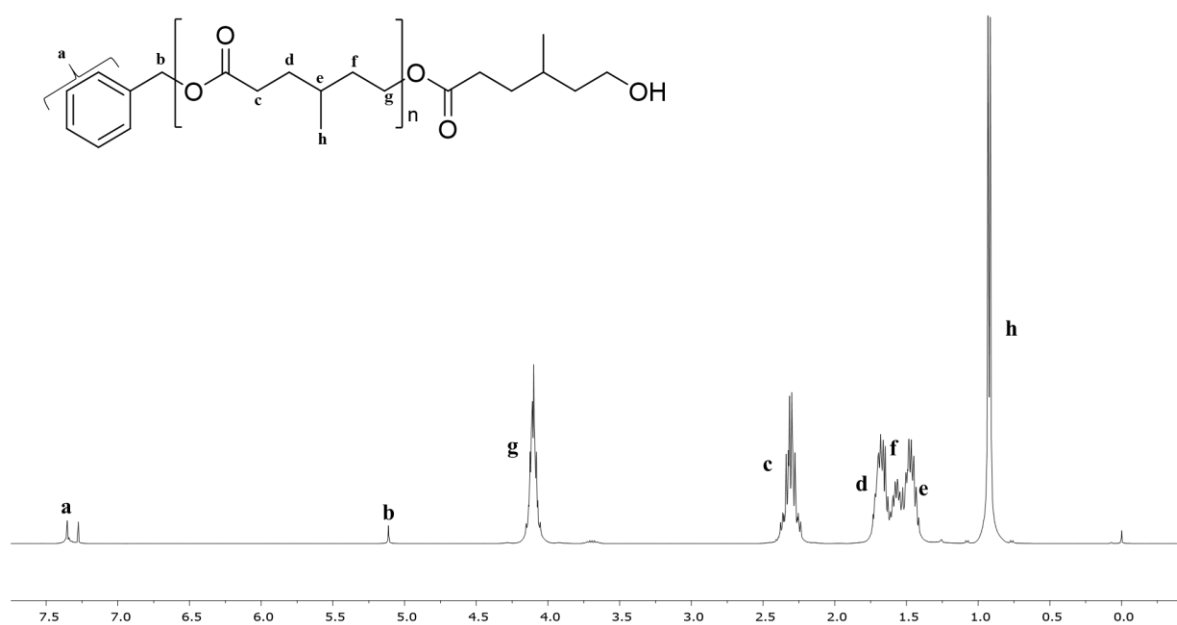
<sup>a</sup> Determined by <sup>1</sup>H NMR (CDCl<sub>3</sub>, 400 MHz) of the crude samples, <sup>b</sup> Determined by triple detection SEC with a mobile phase of DMF/LiBr 0.01M (60 °C) at 1 mLmin<sup>-1</sup>.

**Table A5 –Kinetics of branched PCL<sub>40-co</sub>-BOD<sub>0.7</sub> over 1.5 hours sampling every 3 minutes until t<sub>30</sub> then every 5 minutes normalised by dn/dc = 0.06044;**

Time (min)	<sup>1</sup> H-NMR		SEC <sup>b</sup>			
	Monomer conversion <sup>a</sup>	M <sub>n</sub> (g/mol)	M <sub>w</sub> (g/mol)	Đ	α	No. of linear chains (weight averaged)
3	10.3 %			- <sup>c</sup>		
6	23.1 %			- <sup>c</sup>		
9	37.4 %			- <sup>c</sup>		
12	49.7 %			- <sup>c</sup>		
15	64.6 %	2,600 <sup>c</sup>	2,910 <sup>c</sup>	1.12 <sup>c</sup>	0.079 <sup>c</sup>	0.62 <sup>c</sup>
18	83.5 %	1,860 <sup>c</sup>	2,570 <sup>c</sup>	1.38 <sup>c</sup>	0.60 <sup>c</sup>	0.55 <sup>c</sup>
21	89.5 %			- <sup>c</sup>		
24	96.3 %	3,620	8,300	2.29	0.32	1.77
27	98.2 %	6,210	9,210	1.48	0.38	1.97
30	99.8 %	4,380	9,050	2.07	0.42	1.93
35	>99 %	3,630	8,430	2.32	0.40	1.80
40	>99 %	4,570	10,450	2.29	0.39	2.23
45	-	5,240	11,890	2.27	0.40	2.54
50	-	3,610	11,240	3.11	0.37	2.40
55	-	5,090	12,730	2.50	0.39	2.72
60	-	5,740	13,830	2.41	0.40	2.96
65	-	5,660	15,150	2.68	0.38	3.24
70	-	3,050	13,670	4.48	0.45	2.92
75	-	5,970	17,260	2.89	0.36	3.69
80	-	3,910	17,190	4.40	0.37	3.67
85	-	5,310	18,880	3.56	0.37	4.03
90	-	6,880	21,450	3.09	0.38	4.60

<sup>a</sup> Determined by <sup>1</sup>H NMR (CDCl<sub>3</sub>, 400 MHz) of the crude samples, <sup>b</sup> Determined by triple detection SEC with a mobile phase of DMF/LiBr 0.01M at 1 mLmin<sup>-1</sup>, <sup>c</sup> insufficient light scattering for calculation but RI chromatograms indicated monomodal distribution.

## A.2 MSA catalysed ROP of substituted caprolactone monomers

Figure A6 – <sup>1</sup>H-NMR (CDCl<sub>3</sub>, 400 MHz) of purified MOP.Figure A7 – <sup>1</sup>H-NMR (CDCl<sub>3</sub>, 400 MHz) of purified PMOP<sub>40</sub>.

$$\text{monomer conversion (\%)} = \left( \frac{\int 4.10}{(\int 4.28 + \int 4.10)} \right) \times 100$$

**Equation for the calculation of monomer conversion for PMOP polymers;** where  $\int 4.10$  = polymer proton environment g in Figure A7 and  $\int 4.28$  = monomer proton environment e in Figure A6.

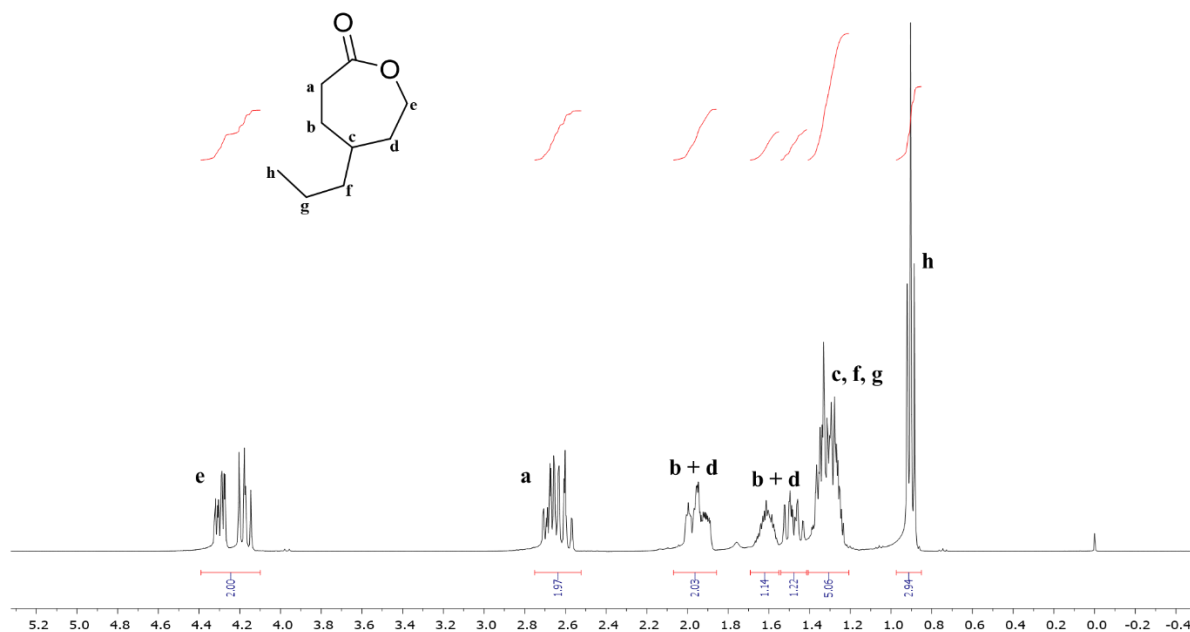


**Figure A8 –  $^1\text{H-NMR}$  ( $\text{CDCl}_3$ , 400 MHz) of purified POP.**

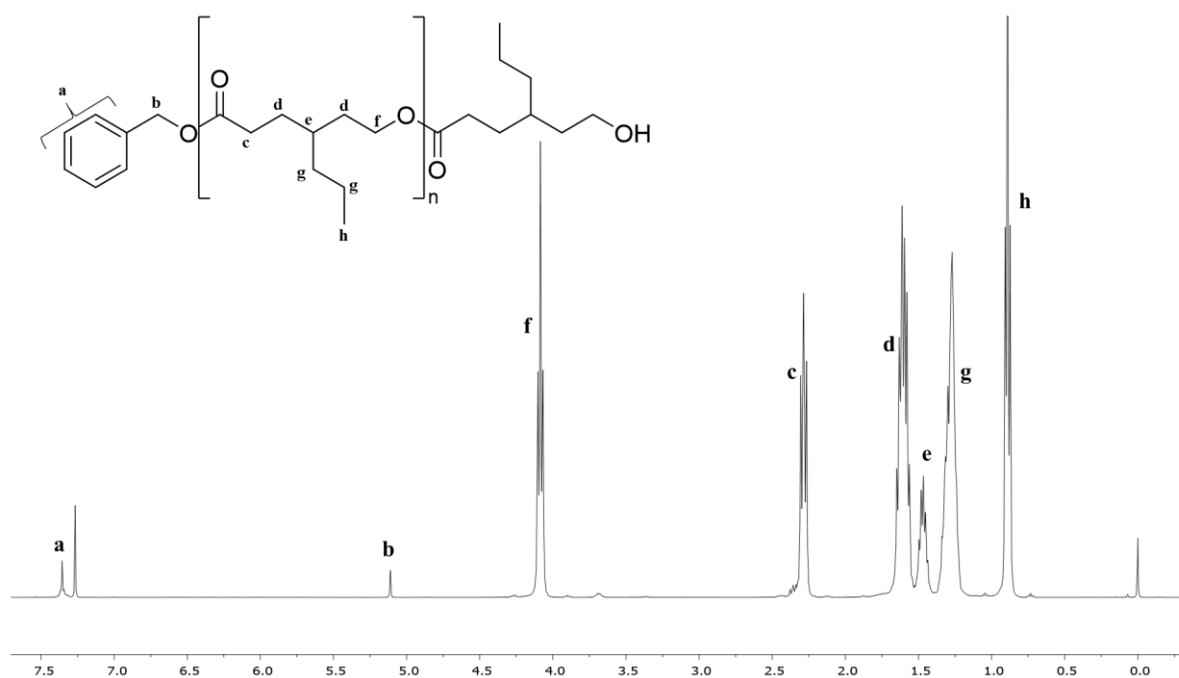


**Figure A9 –  $^1\text{H-NMR}$  ( $\text{CDCl}_3$ , 400 MHz) of purified PPOP<sub>40</sub>.**

$$\text{monomer conversion (\%)} = \left( \frac{\int 4.10}{(\int 4.28 + \int 4.10)} \right) \times 100$$

**Equation for the calculation of monomer conversion for PPOP polymers;** where  $\int 4.10$  = polymer proton environment f in Figure A9 and  $\int 4.28$  = monomer proton environment e in Figure A8.

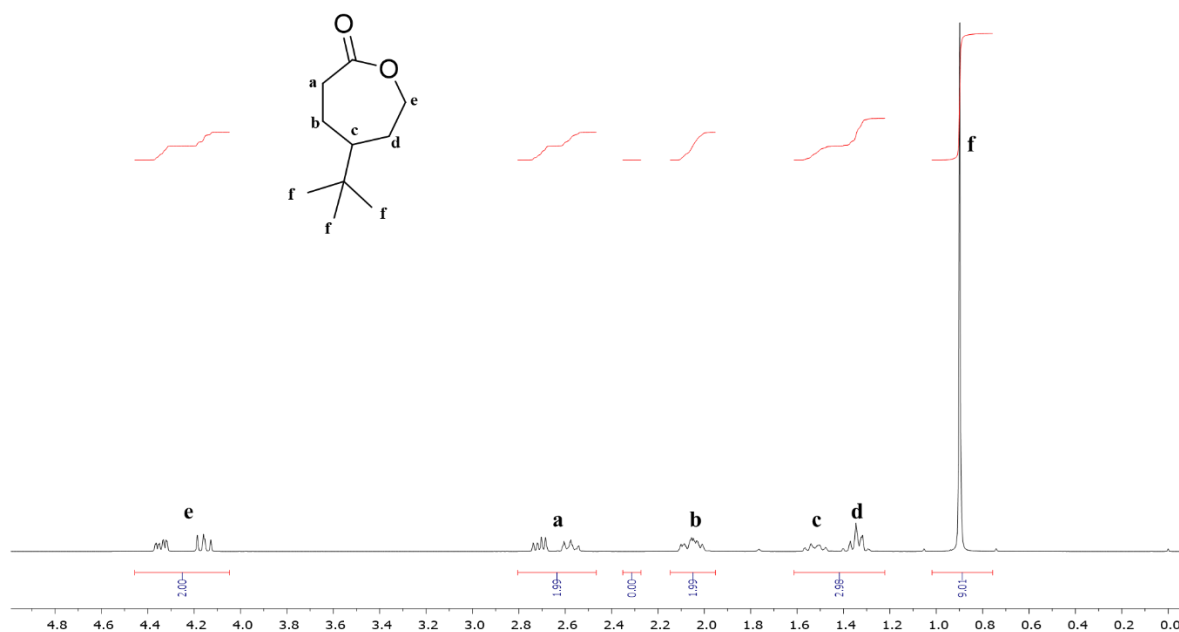


**Figure A10 –  $^1\text{H-NMR}$  ( $\text{CDCl}_3$ , 400 MHz) of purified BOP.**

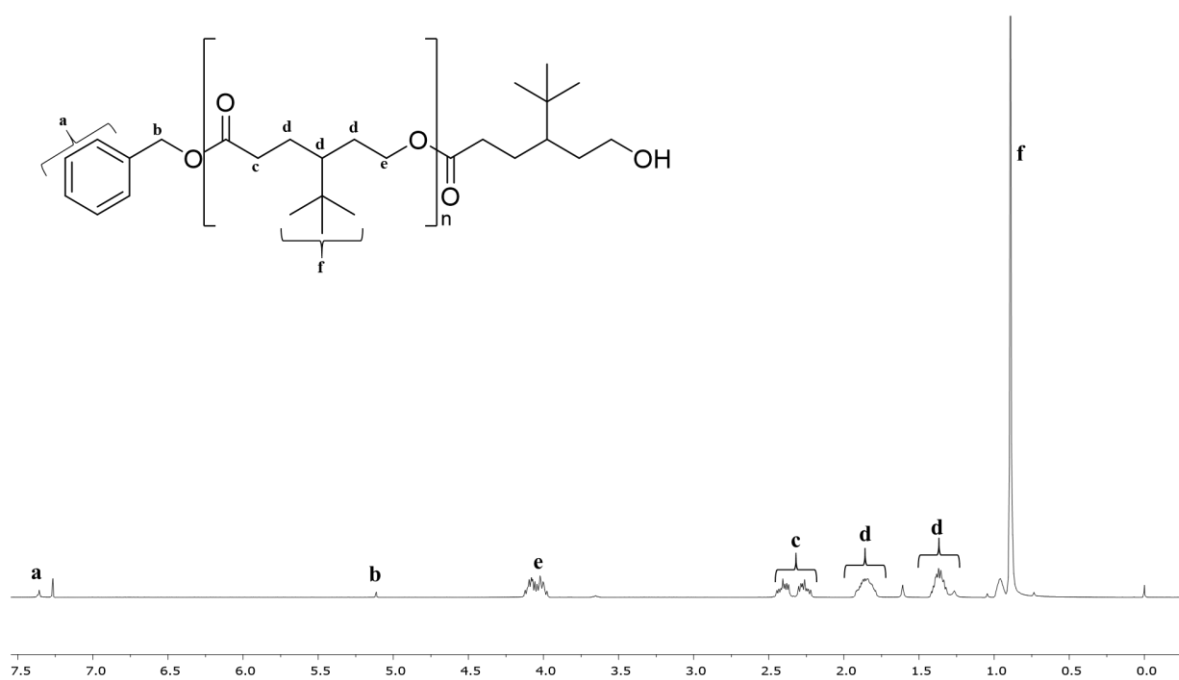


**Figure A11 –  $^1\text{H-NMR}$  ( $\text{CDCl}_3$ , 400 MHz) of purified PBOP<sub>40</sub>.**

$$\text{monomer conversion (\%)} = \left( \frac{\int 4.08}{(\int 4.25 + \int 4.08)} \right) \times 100$$

**Equation for the calculation of monomer conversion for PBOP polymers;** where  $\int 4.08$  = polymer proton environment e in Figure A11 and  $\int 4.25$  = monomer proton environment e in Figure A10.

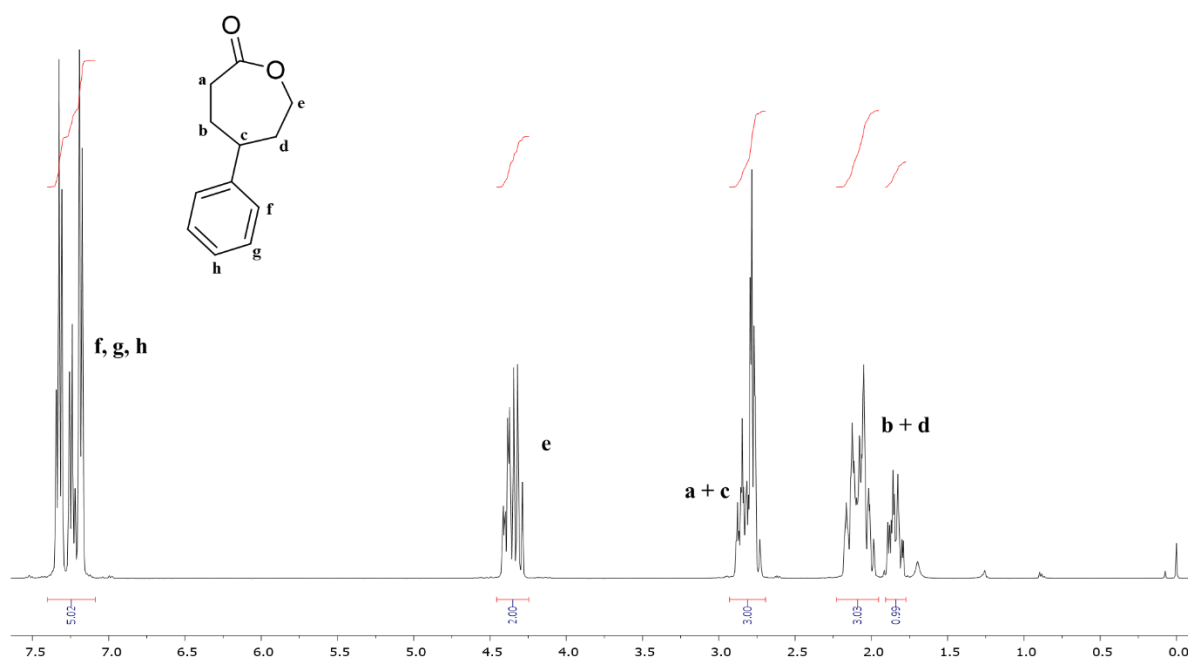


**Figure A12 –  $^1\text{H-NMR}$  ( $\text{CDCl}_3$ , 400 MHz) of purified PHLOP.**

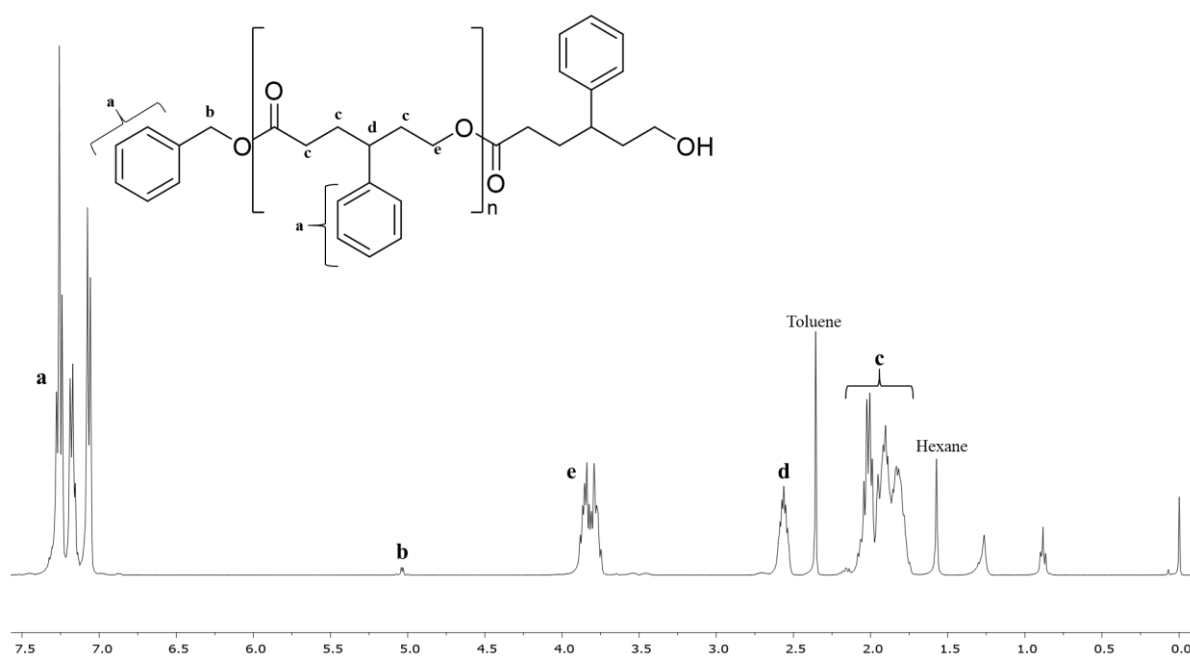


**Figure A13 –  $^1\text{H-NMR}$  ( $\text{CDCl}_3$ , 400 MHz) of purified PPHLOP<sub>40</sub>.**

$$\text{monomer conversion (\%)} = \left( \frac{(3 \times \int 2.56)}{(\int 2.70 + (3 \times \int 2.56))} \right) \times 100$$

**Equation for the calculation of monomer conversion for PPHLOP polymers;** where  $\int 2.56$  = polymer proton environment d in Figure A13 and  $\int 2.70$  = monomer proton environment c in Figure A12.

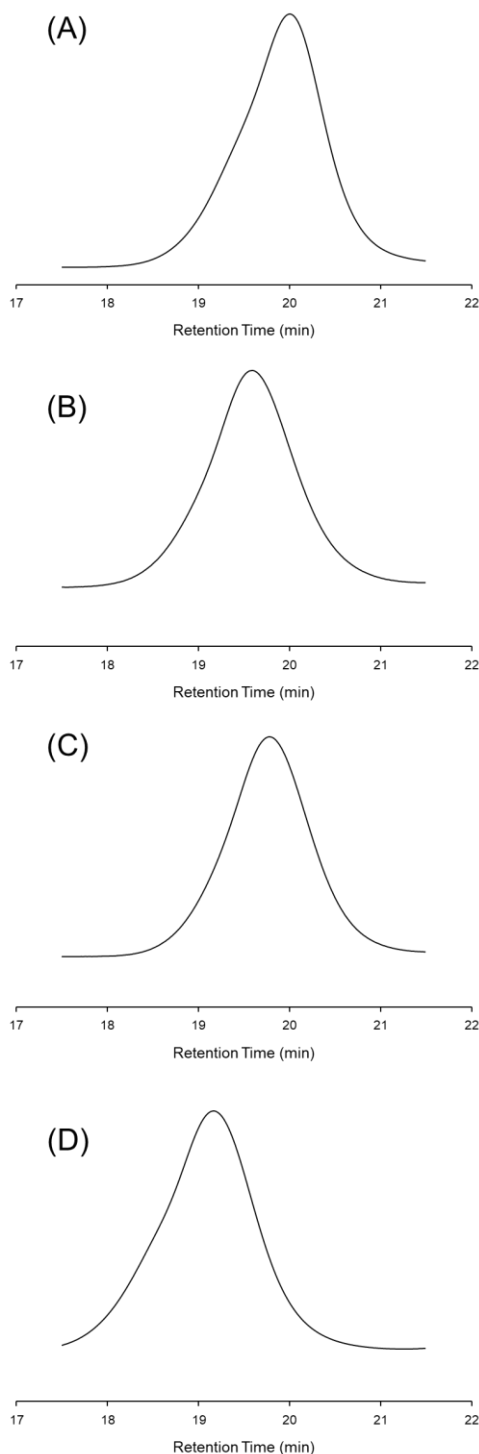


**Figure A14 – Refractive index, RI, detector output chromatograms of; (A) PMOP<sub>40</sub>, (B) PPOP<sub>40</sub>, (C) PBOP<sub>40</sub> and (D) PHLOP<sub>40</sub>.**



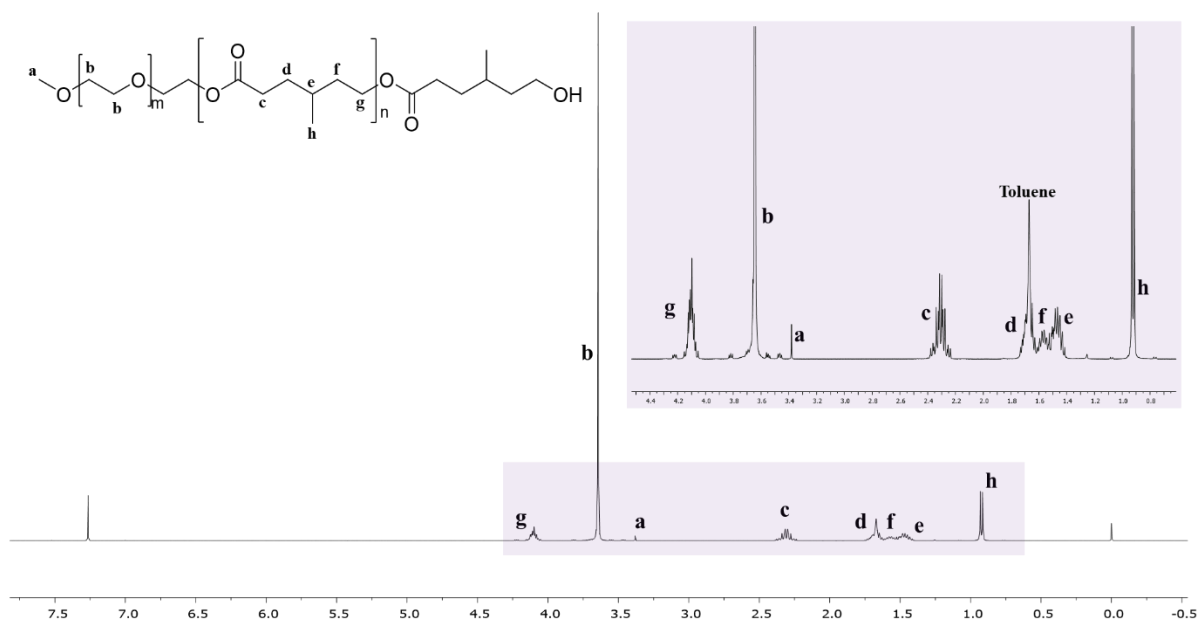


Figure A15 – <sup>1</sup>H-NMR (CDCl<sub>3</sub>, 400 MHz) of purified PEG<sub>5K</sub>-b-PMOP<sub>40</sub>;

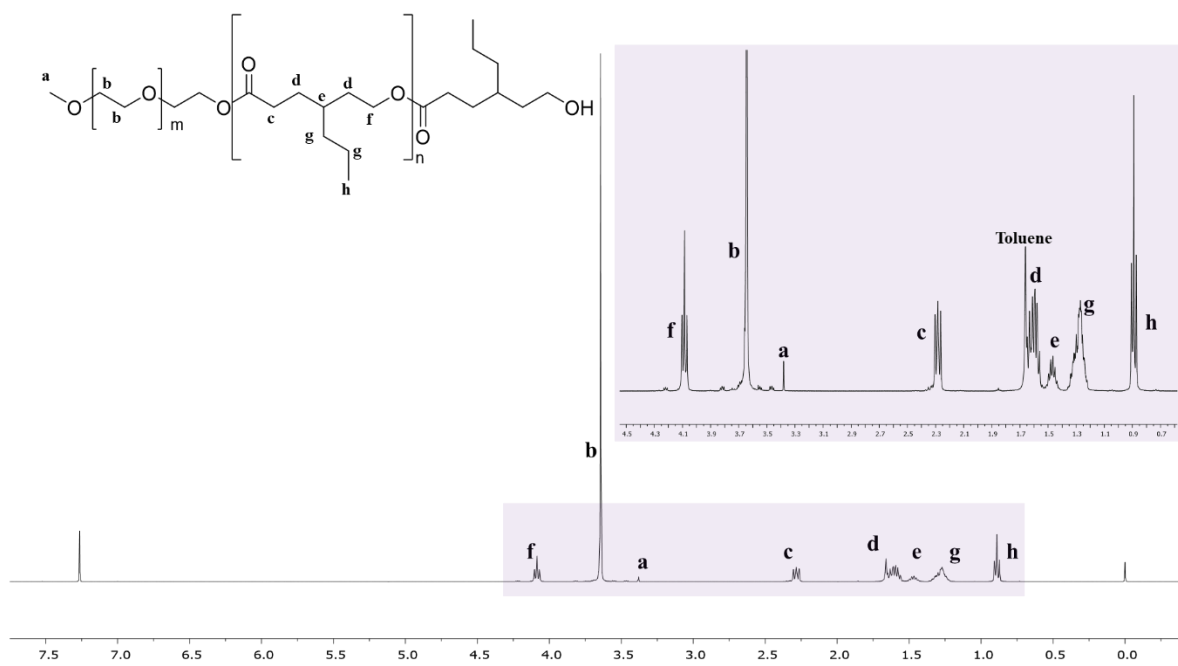


Figure A16 – <sup>1</sup>H-NMR (CDCl<sub>3</sub>, 400 MHz) of purified PEG<sub>5K</sub>-b-PPOP<sub>40</sub>;

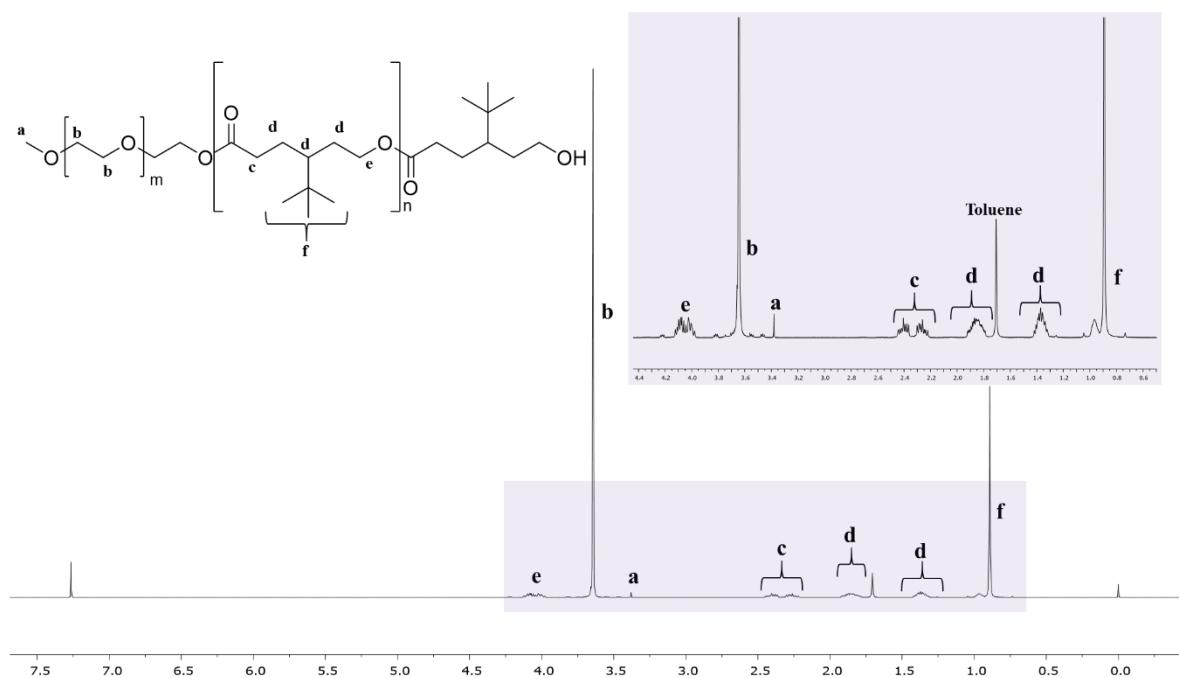


Figure A17 –  $^1\text{H-NMR}$  ( $\text{CDCl}_3$ , 400 MHz) of purified  $\text{PEG}_{5\text{K}}\text{-}b\text{-PBOP}_{40}$ ;

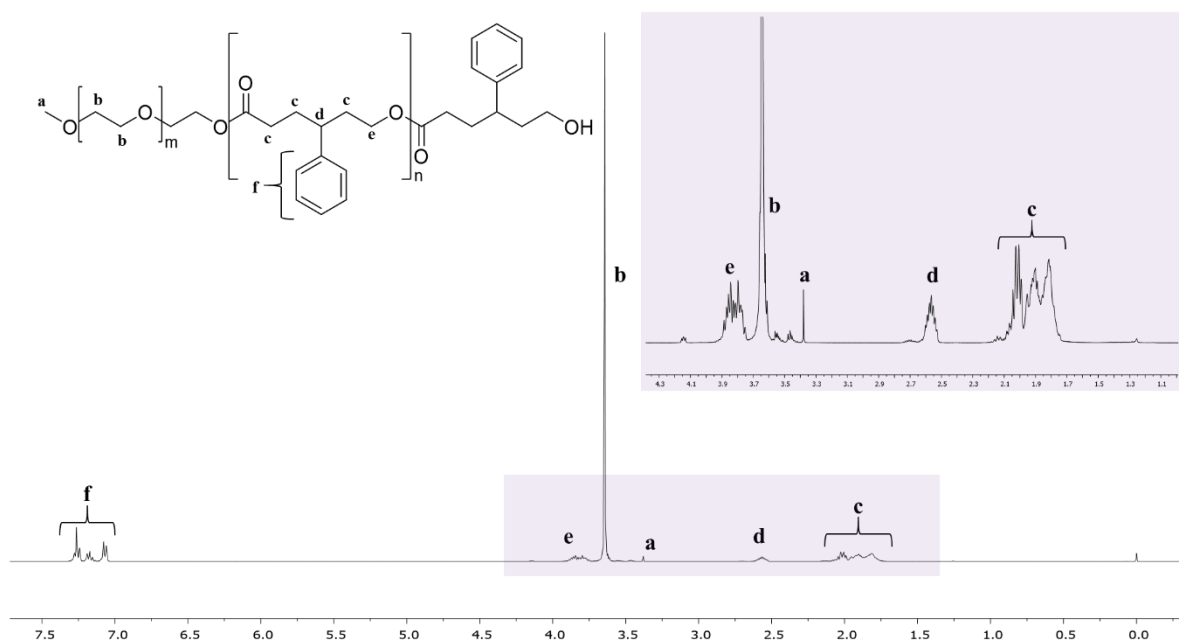
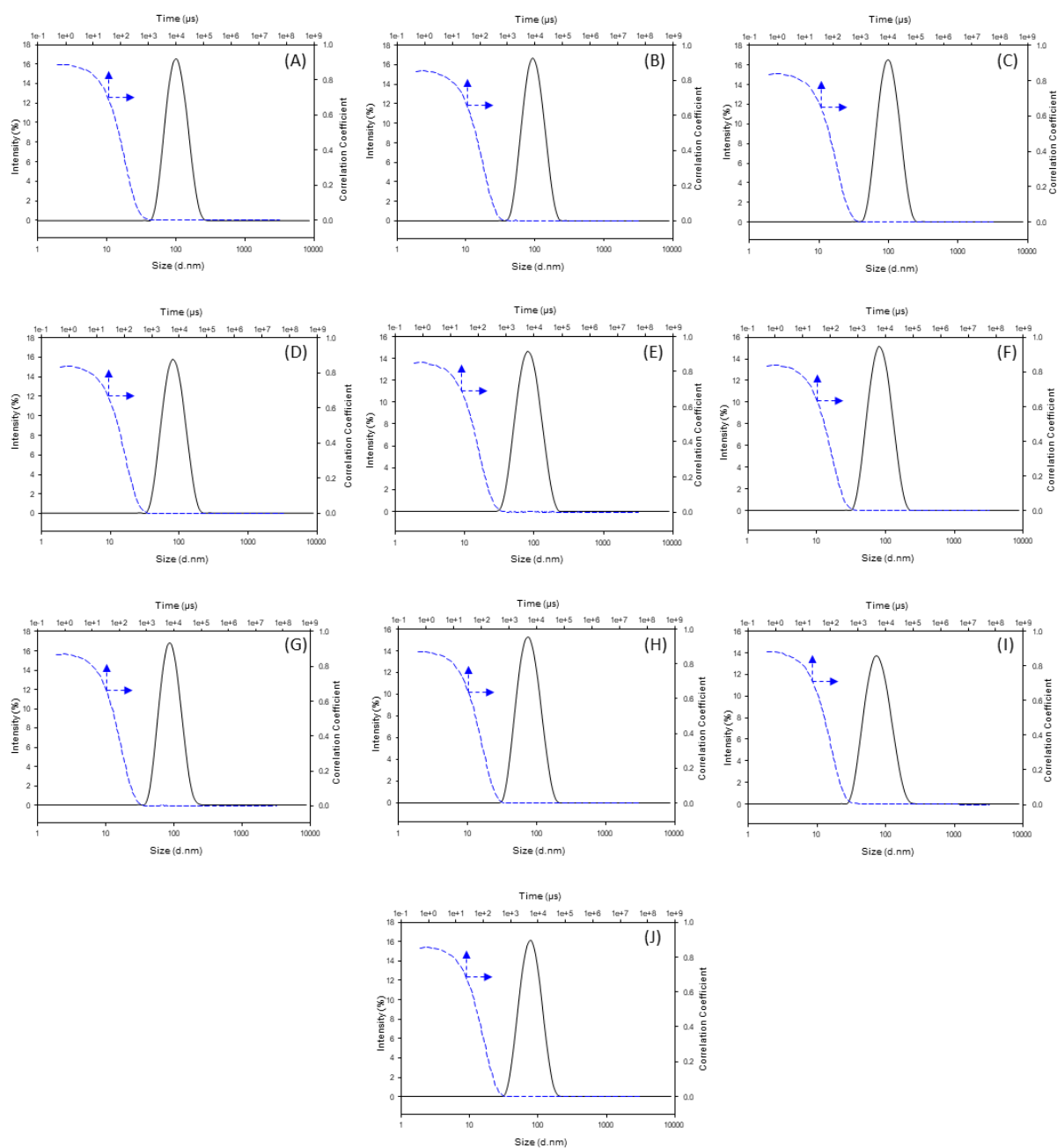


Figure A18 –  $^1\text{H-NMR}$  ( $\text{CDCl}_3$ , 400 MHz) of purified  $\text{PEG}_{5\text{K}}\text{-}b\text{-PPHLOP}_{40}$ ;

## B Chapter 3

Table B1 - DLS characterisation of PCL<sub>40</sub>-*co*-BOD<sub>0.7</sub> nanoparticles produced by co-nanoprecipitation with PEG<sub>x</sub>-*b*-PCL<sub>40</sub> from acetone;

Ratio (%)	Z-Average Diameter (nm)		Number Average Diameter (nm)		PdI		Zeta Potential (mV)		Derived Count Rate (Attenuator)	
	Day 1	Day 7	Day 1	Day 7	Day 1	Day 7	Day 1	Day 7	Day 1	Day 7
PEG <sub>2K</sub> - <i>b</i> -PCL <sub>40</sub> :										
PCL <sub>40</sub> - <i>co</i> -BOD <sub>0.7</sub>										
0:100	90	90	65	65	0.075	0.070	-55	-45	277760 (5)	299310 (5)
10:90	75	75	50	45	0.125	0.125	-55	-50	72410 (6)	89040 (6)
25:75	70	70	45	40	0.145	0.150	-45	-55	63380 (6)	21960 (7)
50:50	60	55	25	30	0.220	0.210	-40	-45	24295 (7)	13245 (7)
75:25	45	50	20	15	0.215	0.270	-35	-35	6160 (7)	8980 (7)
90:10	40	50	15	15	0.420	0.390	-35	-30	4910 (8)	7080 (8)
100:0	30	55	15	15	0.420	0.530	-30	-25	2125 (9)	3730 (8)
PEG <sub>5K</sub> - <i>b</i> -PCL <sub>40</sub> :										
PCL <sub>40</sub> - <i>co</i> -BOD <sub>0.7</sub>										
0:100	90	90	65	65	0.075	0.070	-55	-45	277760 (5)	299310 (5)
10:90	85	80	50	50	0.130	0.135	-50	-45	72120 (6)	88300 (6)
25:75	75	75	45	50	0.145	0.125	-35	-40	43570 (6)	49735 (6)
50:50	70	70	35	30	0.180	0.230	-35	-40	25770 (7)	18915 (7)
75:25	55	65	25	25	0.200	0.330	-30	-30	7890 (8)	8850 (8)
90:10	45	90	15	25	0.330	0.400	-30	-25	4255 (8)	19010 (7)
100:0	25	45	15	15	0.325	0.435	-20	-30	1050 (10)	1070 (9)



**Figure B1 – Example dynamic light scattering, DLS, average size distributions by intensity (black trace) and correlograms (blue dashed trace) of the nanoprecipitation of 100 % PCL of varying architecture from acetone (Day 1); A) PCL<sub>40</sub>, B) PCL<sub>50</sub>, C) PCL<sub>60</sub>, D) PCL<sub>80</sub>, E) PCL<sub>100</sub>, F) PCL<sub>40-co</sub>-BOD<sub>0.7</sub>, G) PCL<sub>40-co</sub>-BOD<sub>0.6</sub>, H) PCL<sub>60-co</sub>-BOD<sub>0.7</sub>, I) PCL<sub>80-co</sub>-BOD<sub>0.7</sub>, J) PCL<sub>100-co</sub>-BOD<sub>0.7</sub>.**

## APPENDIX

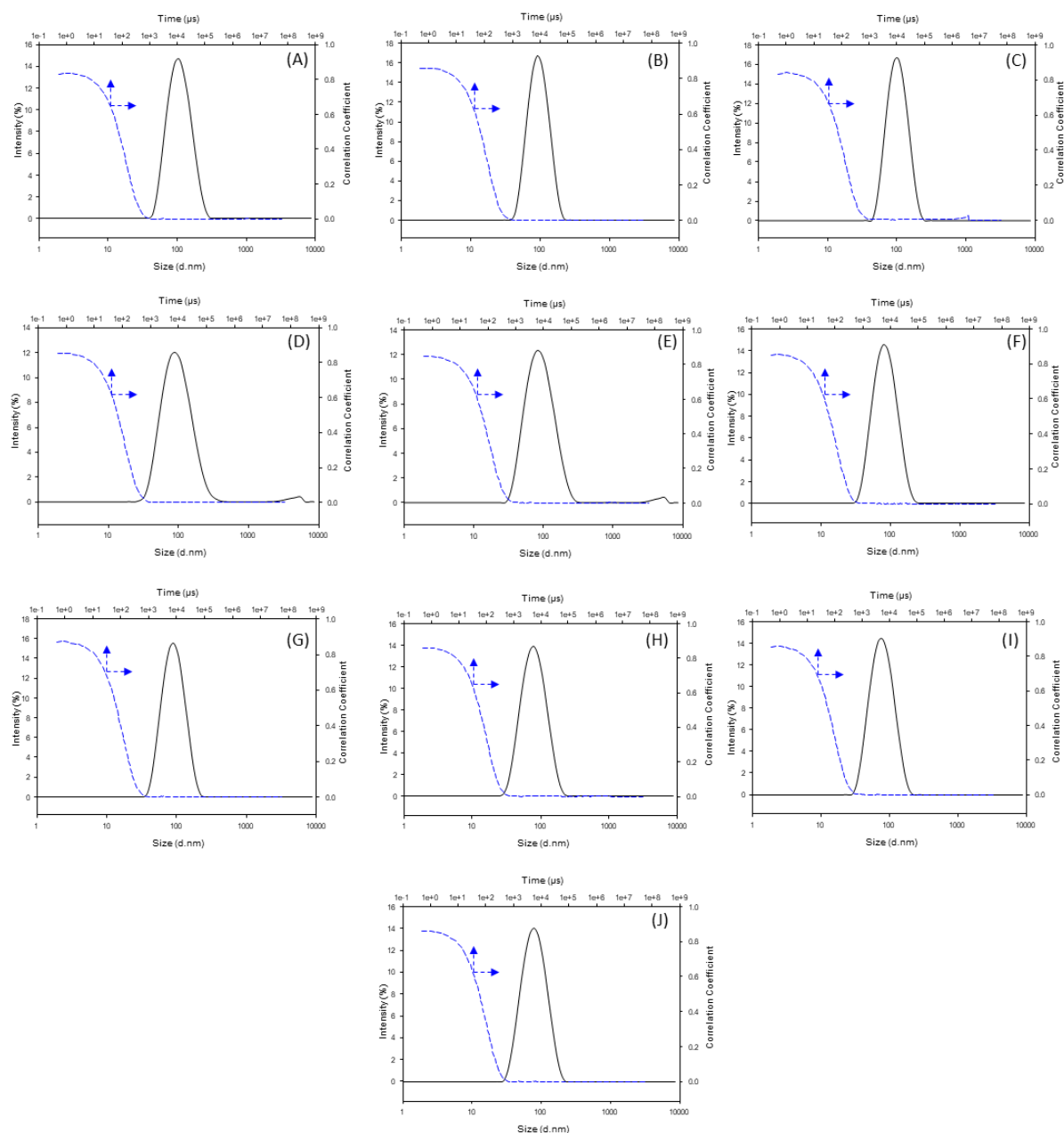


**Figure B2 – Example dynamic light scattering, DLS, average size distributions by intensity (black trace) and correlograms (blue dashed trace) of the nanoprecipitation of 100 % PCL of varying architecture from acetone (Day 1); A) PCL<sub>40</sub>, B) PCL<sub>50</sub>, C) PCL<sub>60</sub>, D) PCL<sub>80</sub>, E) PCL<sub>100</sub>, F) PCL<sub>40-co-BOD</sub><sub>0.7</sub>, G) PCL<sub>40-co-BOD</sub><sub>0.6</sub>, H) PCL<sub>60-co-BOD</sub><sub>0.7</sub>, I) PCL<sub>80-co-BOD</sub><sub>0.7</sub>, J) PCL<sub>100-co-BOD</sub><sub>0.7</sub>.**

## APPENDIX

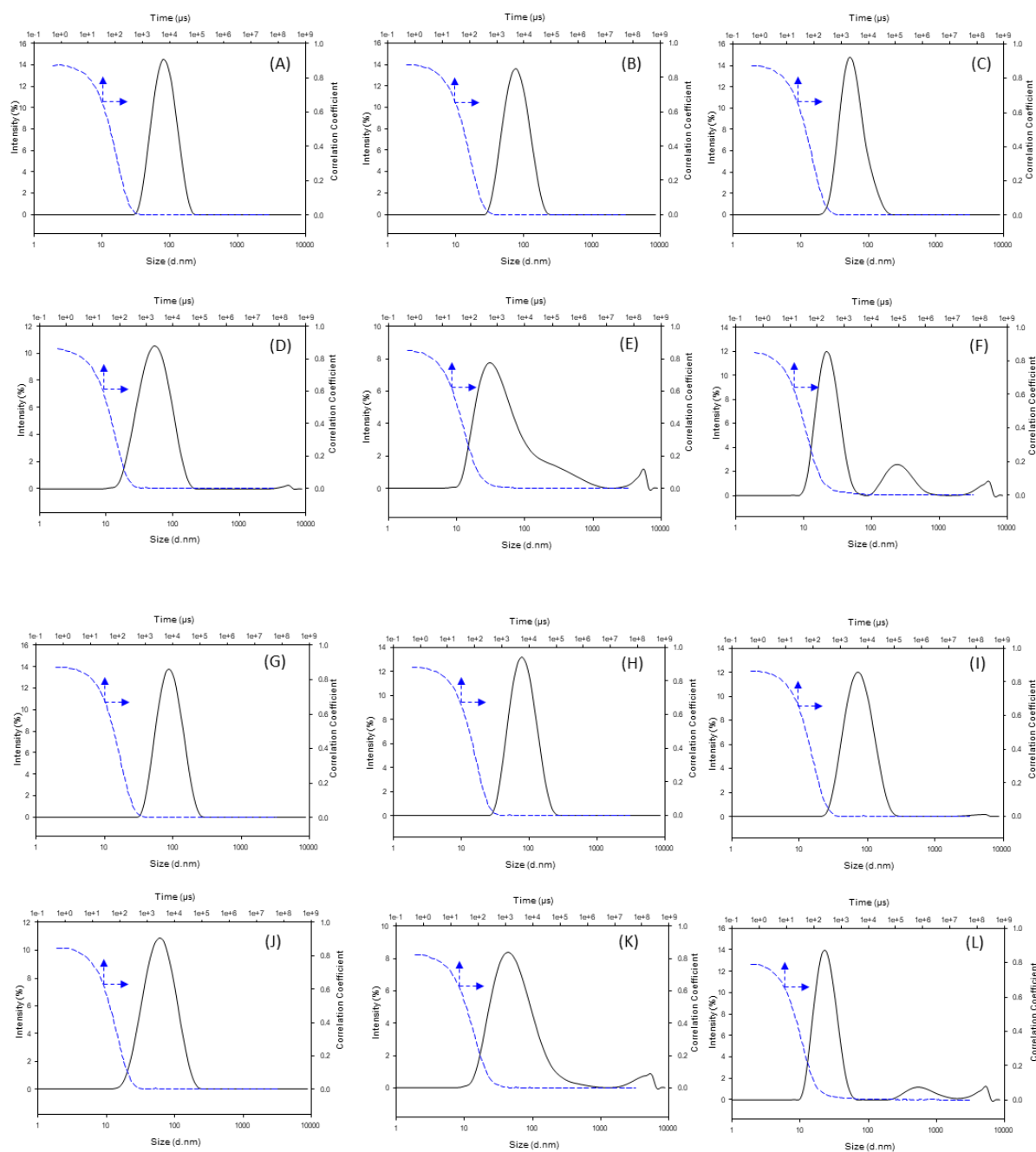


**Figure B3 – Dynamic light scattering average size distributions by intensity (black trace) and correlograms (blue dashed trace) of the co-nanoprecipitation of PEG-*b*-PCL<sub>40</sub>:PCL<sub>40</sub>-*co*-BOD<sub>0.7</sub> (acetone, Day 1). PEG<sub>2K</sub>-*b*-PCL<sub>40</sub> (A-F): A) 10:90, B) 25:75, C) 50:50, D) 75:25, E) 90:10, F) 100:0. PEG<sub>5K</sub>-*b*-PCL<sub>40</sub> (G-L): G) 10:90, H) 25:75, I) 50:50, J) 75:25, K) 90:10, L) 100:0.**

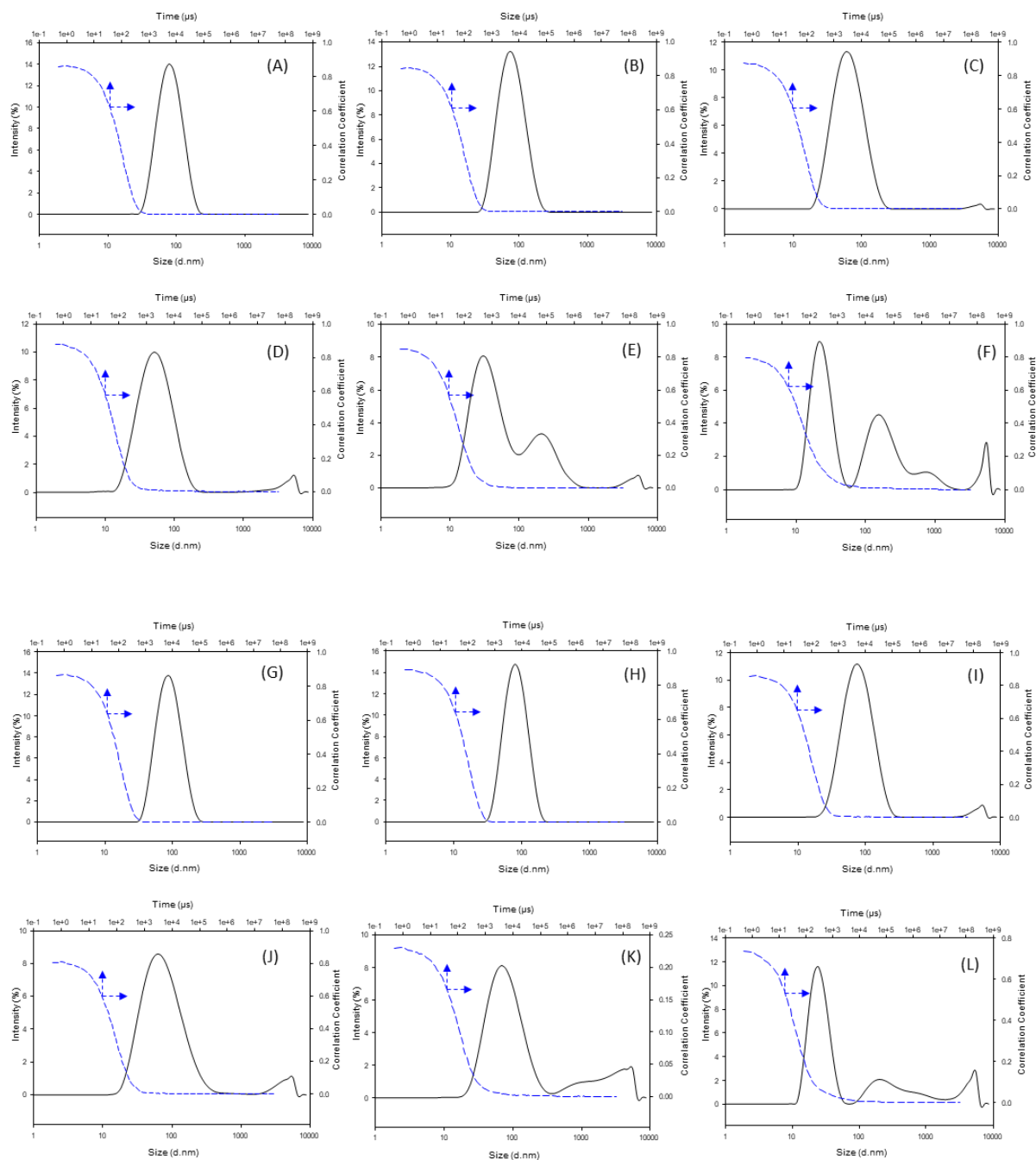


**Figure B4 – Dynamic light scattering average size distributions by intensity (black trace) and correlograms (blue dashed trace) of the co-nanoprecipitation of PEG-*b*-PCL<sub>40</sub>:PCL<sub>40</sub>-*co*-BOD<sub>0.7</sub> (acetone, Day 7).** PEG<sub>2K</sub>-*b*-PCL<sub>40</sub> (A-F): A) 10:90, B) 25:75, C) 50:50, D) 75:25, E) 90:10, F) 100:0. PEG<sub>5K</sub>-*b*-PCL<sub>40</sub> (G-L): G) 10:90, H) 25:75, I) 50:50, J) 75:25, K) 90:10, L) 100:0.

APPENDIX

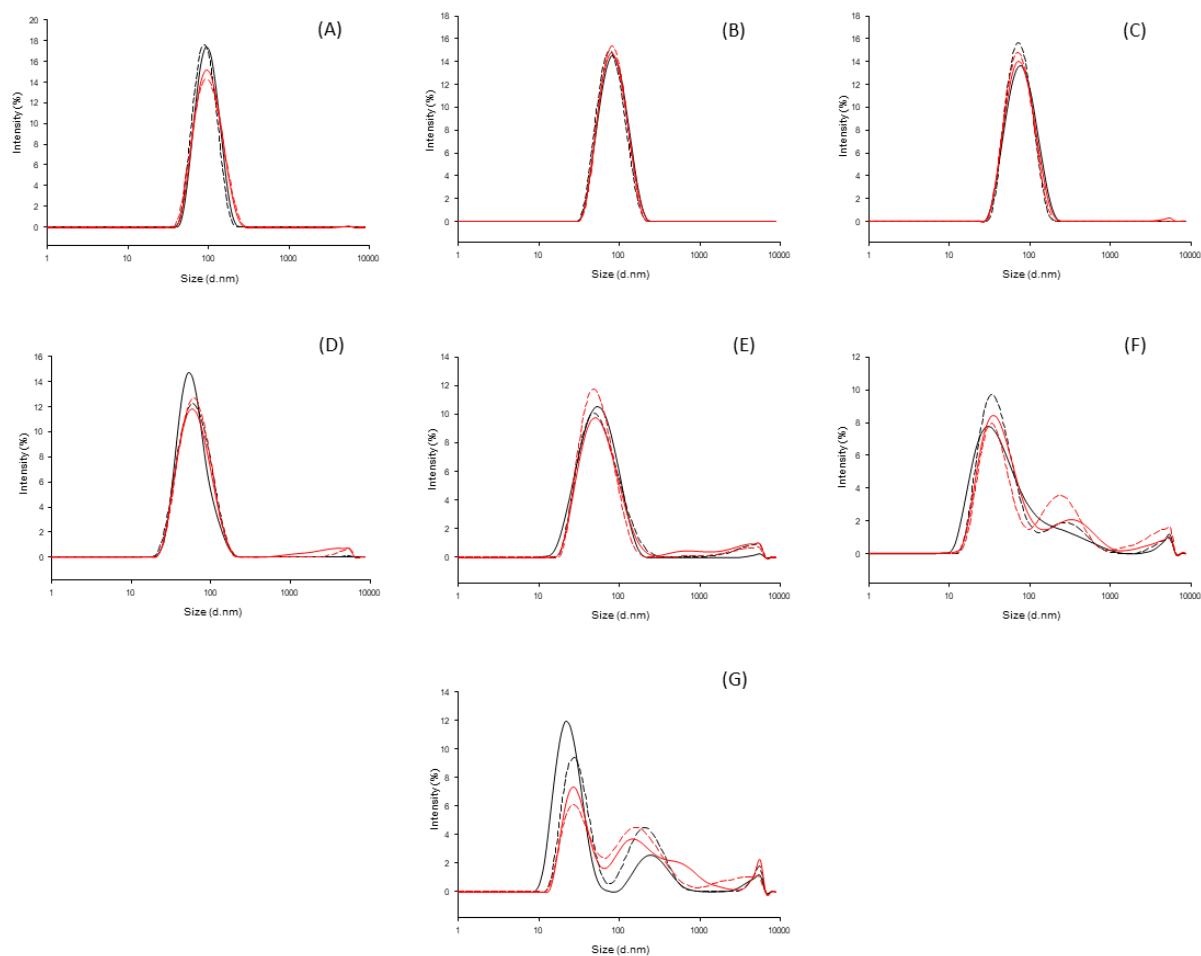


**Figure B5 – Dynamic light scattering average size distributions by intensity of dispersions following salt addition over time following NaCl addition (20  $\mu$ L of 0.5M NaCl) to 1 mL dispersions formed from the co-nanoprecipitation of PEG<sub>2K</sub>-*b*-PCL<sub>40</sub> and PCL<sub>40</sub>-*co*-BOD<sub>0.7</sub> (acetone):** No salt (black trace), Instant (black dashed trace), 24 hour (red trace) and 7 day (red dashed trace): A) 0:100, B) 10:90, C) 25:75, D) 50:50, E) 75:25, F) 90:10, G) 100:0.



APPENDIX

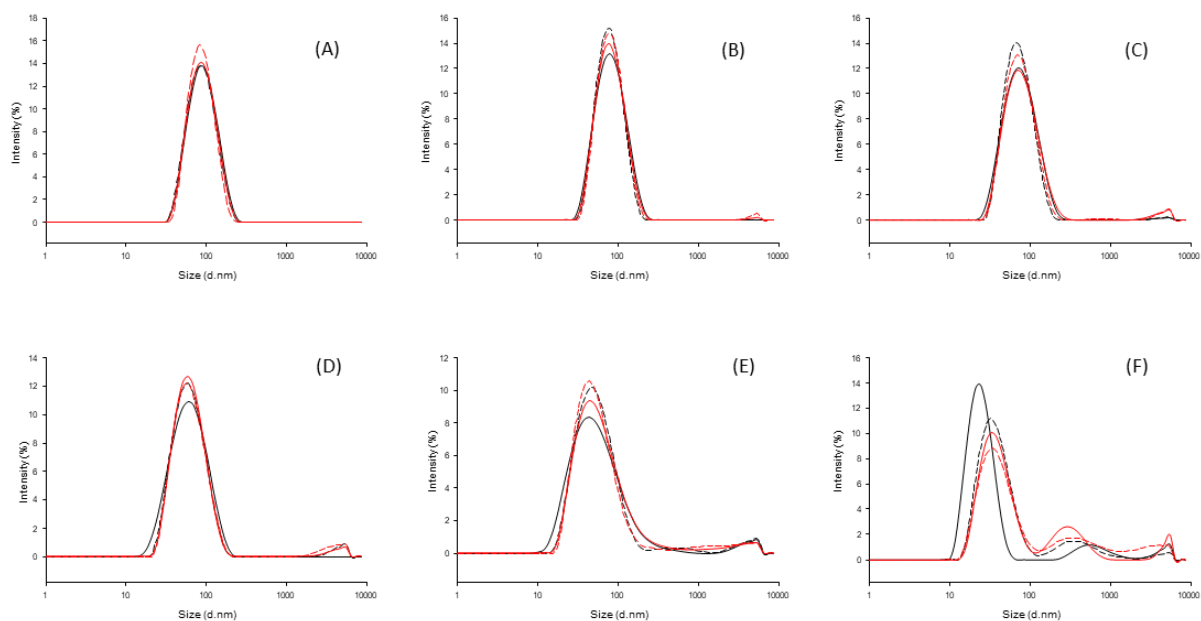


**Figure B6 – Dynamic light scattering average size distributions by intensity of dispersions following salt addition over time following NaCl addition (20  $\mu$ L of 0.5M NaCl) to 1 mL dispersions formed from the co-nanoprecipitation of PEG<sub>5K</sub>-*b*-PCL<sub>40</sub> and PCL<sub>40</sub>-*co*-BOD<sub>0.7</sub> (acetone):** No salt (black trace), Instant (black dashed trace), 24 hour (red trace) and 7 day (red dashed trace): A) 10:90, B) 25:75, C) 50:50, D) 75:25, E) 90:10, F) 100:0.

**Table B2 - DLS characterisation of PCL<sub>40</sub>-*co*-BOD<sub>0.7</sub> nanoparticles produced by co-nanoprecipitation with PEG<sub>x</sub>-*b*-PCL<sub>40</sub> from THF;**

Ratio (%)	Z-Average Diameter (nm)		Number Average Diameter (nm)		PdI		Zeta Potential (mV)		Derived Count Rate (Attenuator)		
	Day 1	8 Months	Day 1	8 Months	Day 1	8 Months	Day 1	8 Months	Day 1	8 Months	
PEG <sub>2K</sub> - <i>b</i> -PCL <sub>40</sub> : PCL <sub>40</sub> - <i>co</i> -BOD <sub>0.7</sub>											
0:100	105	100	70	65	0.120	0.120	-55	-50	365770 (4)	354715 (4)	
10:90	90	85	55	55	0.130	0.115	-45	-40	264530 (5)	260125 (5)	
25:75	80	80	40	45	0.135	0.135	-50	-35	133145 (6)	122515 (6)	
50:50	75	75	35	40	0.150	0.155	-35	-30	87830 (6)	83170 (6)	
75:25	55	60	15	25	0.185	0.205	-40	-25	30700 (7)	30480 (7)	
90:10	40	55	10	20	0.215	0.470	-25	-20	9590 (7)	12740 (7)	
100:0	25	35	15	15	0.190	0.430	-30	-30	4960 (8)	6300 (8)	
PEG <sub>5K</sub> - <i>b</i> -PCL <sub>40</sub> : PCL <sub>40</sub> - <i>co</i> -BOD <sub>0.7</sub>											
0:100	105	100	70	65	0.120	0.120	-55	-50	365770 (4)	354715 (4)	
10:90	120	130	80	65	0.125	0.235	-45	-10	380450 (4)	278480 (5)	
25:75	95	95	55	55	0.135	0.130	-40	-30	200675 (5)	226435 (5)	
50:50	80	80	45	45	0.140	0.135	-35	-25	63700 (6)	55275 (6)	
75:25	70	75	25	30	0.215	0.220	-35	-25	27795 (7)	27360 (7)	
90:10	50	55	20	15	0.275	0.340	-25	-20	7495 (8)	7805 (8)	
100:0	25	40	15	20	0.295	0.495	-15	-20	1805 (9)	2240 (9)	

**Table B3 - DLS characterisation of nanoparticles produced by nanoprecipitation of hydrophobic branched polyesters from THF;**

Sample	Z-Average Diameter (nm)		Number Average Diameter (nm)		PdI		Zeta Potential (mV)		Derived Count Rate (Attenuator)	
	Day 1	Day 7	Day 1	Day 7	Day 1	Day 7	Day 1	Day 7	Day 1	Day 7
PCL <sub>40-co</sub> -BOD <sub>0.7</sub>	100	100	65	65	0.115	0.110	-50	-55	382840 (4)	344320 (4)
PMOP <sub>40-co</sub> -BOD <sub>0.7</sub>	140	140	100	95	0.095	0.125	-60	-55	623425 (4)	598305 (4)
PPOP <sub>40-co</sub> -BOD <sub>0.7</sub>	175	175	125	125	0.115	0.115	-60	-60	42730 (4)	414365 (4)
PBOP <sub>40-co</sub> -BOD <sub>0.7</sub>	155	155	105	110	0.120	0.120	-65	-60	539900 (4)	523355 (4)
PPHLOP <sub>40-co</sub> -BOD <sub>0.7</sub>	105	105	75	75	0.120	0.125	-55	-50	504885 (3)	485895 (3)

**Table B4 - DLS characterisation of nanoparticles produced by nanoprecipitation of AB block co-polyesters from THF;**

Sample	Z-Average Diameter (nm)		Number Average Diameter (nm)		PdI		Zeta Potential (mV)		Derived Count Rate (Attenuator)	
	Day 1	Day 7	Day 1	Day 7	Day 1	Day 7	Day 1	Day 7	Day 1	Day 7
PEG <sub>5K-b</sub> -PCL <sub>40</sub>	25	40	15	15	0.355	0.331	-25	-20	1845 (9)	2240 (9)
PEG <sub>5K-b</sub> -PMOP <sub>40</sub>	35	25	15	15	0.385	0.235	-15	-15	2325 (9)	1800 (9)
PEG <sub>5K-b</sub> -PPOP <sub>40</sub>	30	30	15	15	0.360	0.355	-15	-10	2395 (9)	2510 (9)
PEG <sub>5K-b</sub> -PBOP <sub>40</sub>	35	35	15	20	0.410	0.390	-10	-15	1765 (9)	2300 (9)
PEG <sub>5K-b</sub> -PPHLOP <sub>40</sub>	30	30	15	15	0.255	0.350	-15	-15	5085 (8)	5840 (8)

**Table B5 - DLS characterisation of PCL/SCM<sub>40-co</sub>-BOD<sub>0.7</sub> nanoparticles produced by co-nanoprecipitation with PEG<sub>x</sub>-*b*-PCL/SCM<sub>40</sub> (50:50 wt%) from THF;**

Sample	Z-Average Diameter (nm)			Number Average Diameter (nm)			PdI			Zeta Potential (mV)			Derived Count Rate (Attenuator)		
	Day 1	Re-precip	Day 7	Day 1	Re-precip	Day 7	Day 1	Re-precip	Day 7	Day 1	Re-precip	Day 7	Day 1	Re-precip	Day 7
PEG <sub>5K</sub> - <i>b</i> -PCL <sub>40</sub> : PCL <sub>40-co</sub> -BOD <sub>0.7</sub>	105	115	115	65	70	75	0.140	0.150	0.135	-35	-30	-30	126615 (6)	276055 (5)	277115 (5)
PEG <sub>5K</sub> - <i>b</i> -PMOP <sub>40</sub> : PMOP <sub>40-co</sub> -BOD <sub>0.7</sub>	95	95	95	55	50	35	0.170	0.175	0.170	-30	-20	-20	115505 (6)	109385 (6)	8675 (6)
PEG <sub>5K</sub> - <i>b</i> -PPOP <sub>40</sub> : PPOP <sub>40-co</sub> -BOD <sub>0.7</sub>	90	85	85	50	35	40	0.155	0.210	0.205	-30	-20	-20	103360 (6)	76000 (6)	72360 (6)
PEG <sub>5K</sub> - <i>b</i> -PBOP <sub>40</sub> : PBOP <sub>40-co</sub> -BOD <sub>0.7</sub>	105	90	90	60	30	40	0.150	0.225	0.215	-30	-20	-20	217720 (5)	89895 (6)	70055 (6)
PEG <sub>5K</sub> - <i>b</i> -PPHLOP <sub>40</sub> : PPHLOP <sub>40-co</sub> -BOD <sub>0.7</sub>	100	95	95	55	45	40	0.150	0.165	0.175	-30	-25	-25	326360 (4)	313160 (5)	312955 (5)

**Table B6 - DLS characterisation of PCL<sub>40-co</sub>-BOD<sub>0.7</sub> nanoparticles produced by co-nanoprecipitation with PEG<sub>x</sub>-*b*-PCL<sub>40</sub> (50:50 wt%) from acetone with oil red O;**

Sample	Oil red O content (wt%)	Z-Average Diameter (nm)	Number Average Diameter (nm)	PdI	Zeta Potential (mV)	Derived Count Rate (Attenuator)
		Day 1	Day 1	Day 1	Day 1	Day 1
PEG <sub>2K</sub> - <i>b</i> -PCL <sub>40</sub> : PCL <sub>40-co</sub> -BOD <sub>0.7</sub>	2.43	80	25	0.210	-40	88726 (6)
PEG <sub>5K</sub> - <i>b</i> -PCL <sub>40</sub> : PCL <sub>40-co</sub> -BOD <sub>0.7</sub>	2.43	85	35	0.240	-30	64305 (6)
PEG <sub>2K</sub> - <i>b</i> -PCL <sub>40</sub> : PCL <sub>40-co</sub> -BOD <sub>0.7</sub>	4.76	80	40	0.210	-30	99535 (6)
PEG <sub>5K</sub> - <i>b</i> -PCL <sub>40</sub> : PCL <sub>40-co</sub> -BOD <sub>0.7</sub>	4.76	90	30	0.235	-35	75279 (6)

**Table B7 - DLS characterisation of PCL/SCM<sub>40-co</sub>-BOD<sub>0.7</sub> nanoparticles produced by co-nanoprecipitation with PEG<sub>2K</sub>-*b*-PCL<sub>40</sub> (50:50 wt%) from THF with oil red O (2.43 wt%);**

Sample	Z-Average Diameter (nm)		Number Average Diameter (nm)		PdI		Zeta Potential (mV)		Derived Count Rate (Attenuator)	
	Day 1	Day 14	Day 1	Day 14	Day 1	Day 14	Day 1	Day 14	Day 1	Day 14
PEG <sub>2K</sub> - <i>b</i> -PCL <sub>40</sub> : PCL <sub>40-co</sub> -BOD <sub>0.7</sub>	90	85	55	50	0.150	0.150	-35	-35	209940 (5)	222385 (5)
PEG <sub>2K</sub> - <i>b</i> -PCL <sub>40</sub> : PMOP <sub>40-co</sub> -BOD <sub>0.7</sub>	95	95	45	55	0.155	0.160	-40	-40	253405 (5)	263225 (5)
PEG <sub>2K</sub> - <i>b</i> -PCL <sub>40</sub> : PPOP <sub>40-co</sub> -BOD <sub>0.7</sub>	105	100	60	60	0.145	0.145	-40	-40	345115 (5)	318050 (4)
PEG <sub>2K</sub> - <i>b</i> -PCL <sub>40</sub> : PBOP <sub>40-co</sub> -BOD <sub>0.7</sub>	95	90	50	55	0.155	0.150	-40	-30	296235 (5)	299275 (5)
PEG <sub>2K</sub> - <i>b</i> -PCL <sub>40</sub> : PPHLOP <sub>40-co</sub> -BOD <sub>0.7</sub>	95	90	60	55	0.135	0.145	-35	-40	353115 (4)	367265 (4)

**Table B8 - DLS characterisation of PCL/SCM<sub>40-co</sub>-BOD<sub>0.7</sub> nanoparticles produced by co-nanoprecipitation with PEG<sub>5K</sub>-*b*-PCL<sub>40</sub> (50:50 wt%) from THF with oil red O (2.43 wt%);**

Sample	Z-Average Diameter (nm)		Number Average Diameter (nm)		PdI		Zeta Potential (mV)		Derived Count Rate (Attenuator)	
	Day 1	Day 14	Day 1	Day 14	Day 1	Day 14	Day 1	Day 14	Day 1	Day 14
PEG <sub>5K</sub> - <i>b</i> -PCL <sub>40</sub> : PCL <sub>40-co</sub> -BOD <sub>0.7</sub>	100	95	55	60	0.160	0.150	-35	-30	232530 (5)	228195 (5)
PEG <sub>5K</sub> - <i>b</i> -PCL <sub>40</sub> : PMOP <sub>40-co</sub> -BOD <sub>0.7</sub>	105	105	65	55	0.135	0.165	-35	-25	240675 (5)	228285 (5)
PEG <sub>5K</sub> - <i>b</i> -PCL <sub>40</sub> : PPOP <sub>40-co</sub> -BOD <sub>0.7</sub>	120	120	65	70	0.160	0.150	-35	-30	321140 (5)	309585 (5)
PEG <sub>5K</sub> - <i>b</i> -PCL <sub>40</sub> : PBOP <sub>40-co</sub> -BOD <sub>0.7</sub>	110	110	65	60	0.150	0.180	-30	-25	275075 (5)	274690 (5)
PEG <sub>5K</sub> - <i>b</i> -PCL <sub>40</sub> : PPHLOP <sub>40-co</sub> -BOD <sub>0.7</sub>	100	100	55	45	0.150	0.150	-30	-25	322390 (5)	320655 (5)

## APPENDIX

**Table B9 - DLS characterisation of PCL/SCM<sub>40-co</sub>-BOD<sub>0.7</sub> nanoparticles produced by co-nanoprecipitation with PEG<sub>x</sub>-*b*-PCL<sub>40</sub> (50:50 wt%) from THF with docetaxel (2.43 wt%);**

Sample	Z-Average Diameter (nm)		Number Average Diameter (nm)		PdI		Zeta Potential (mV)		Derived Count Rate (Attenuator)	
	Day 1	Day 7	Day 1	Day 7	Day 1	Day 7	Day 1	Day 7	Day 1	Day 7
PEG <sub>5K</sub> - <i>b</i> -PCL <sub>40</sub> : PCL <sub>40-co</sub> -BOD <sub>0.7</sub>	85	85	50	50	0.150	0.145	-30	-30	97190 (6)	96555 (6)
PEG <sub>5K</sub> - <i>b</i> -PCL <sub>40</sub> : PMOP <sub>40-co</sub> -BOD <sub>0.7</sub>	95	95	45	50	0.165	0.170	-30	-30	90640 (6)	90360 (6)
PEG <sub>5K</sub> - <i>b</i> -PCL <sub>40</sub> : PPOP <sub>40-co</sub> -BOD <sub>0.7</sub>	100	100	60	60	0.150	0.145	-30	-30	210315 (5)	132830 (6)
PEG <sub>5K</sub> - <i>b</i> -PCL <sub>40</sub> : BOP <sub>40-co</sub> -BOD <sub>0.7</sub>	95	95	50	45	0.175	0.165	-30	-30	108220 (6)	105190 (6)
PEG <sub>5K</sub> - <i>b</i> -PCL <sub>40</sub> : PPHLOP <sub>40-co</sub> -BOD <sub>0.7</sub>	90	90	55	55	0.140	0.130	-30	-25	233575 (5)	240620 (5)

**C Chapter 4****Table C1 - DLS characterisation of PCL<sub>40</sub>-*co*-BOD<sub>0.7</sub> nanoparticles produced by co-nanoprecipitation with PEG<sub>x</sub>-*b*-PCL<sub>40</sub> (50:50 wt%) varying the concentration of polymer within THF;**

THF Volume (mL)	Before Evaporation				After Evaporation			
	D <sub>z</sub> (nm)	D <sub>n</sub> (nm)	PdI	Derived Count Rate (kcps)	D <sub>z</sub> (nm)	D <sub>n</sub> (nm)	PdI	Derived Count Rate (kcps)
0.5	195	150	0.100	244090 (5)	160	100	0.165	261085
1	165	110	0.165	322300 (5)	115	70	0.170	352690
2	225	185	0.125	346280 (4)	120	80	0.120	511415
3	225	180	0.100	304380 (5)	110	65	0.130	471690
4	225	190	0.080	250400 (5)	105	70	0.115	521790
5	255	220	0.080	246595 (5)	120	85	0.090	634775
8	275	245	0.050	102670 (6)	155	130	0.035	608790

**Table C2 - DLS characterisation of PCL<sub>40</sub>-*co*-BOD<sub>0.7</sub> nanoparticles produced by co-nanoprecipitation with PEG<sub>x</sub>-*b*-PCL<sub>40</sub> (50:50 wt%) varying the concentration of polymer within THF with SN38 (2.43 wt%);**

THF Volume (mL)	Before Evaporation				After Evaporation			
	D <sub>z</sub> (nm)	D <sub>n</sub> (nm)	PdI	Derived Count Rate (kcps)	D <sub>z</sub> (nm)	D <sub>n</sub> (nm)	PdI	Derived Count Rate (kcps)
0.5	220	150	0.235	106010 (6)	175	90	0.255	86435 (6)
1	190	130	0.205	269765 (5)	155	85	0.325	271460 (5)
2	235	195	0.100	377920 (4)	135	85	0.215	247700 (5)
3	230	185	0.095	299145 (5)	135	75	0.310	252110 (4)
4	275	245	0.060	320840 (5)	140	95	0.225	270295 (5)
5	255	225	0.074	247720 (5)	130	90	0.245	270840 (5)
8	250	225	0.035	105365 (6)	155	120	0.155	287245 (4)



**Table C3 - DLS characterisation of PPOP<sub>40-co-BOD<sub>0.7</sub></sub>** nanoparticles produced by co-nanoprecipitation with PEG<sub>x-b-PCL<sub>40</sub></sub> (50:50 wt%) varying the concentration of polymer within THF with SN38 (2.43 wt%);

THF Volume (mL)	Before Evaporation				After Evaporation			
	D <sub>z</sub> (nm)	D <sub>n</sub> (nm)	PdI	Derived Count Rate (kcps)	D <sub>z</sub> (nm)	D <sub>n</sub> (nm)	PdI	Derived Count Rate (kcps)
0.5	230	135	0.240	72980 (6)	190	75	0.250	48350 (6)
1	205	140	0.185	246200 (5)	175	95	0.325	263330 (5)
2	270	245	0.025	374625 (4)	155	100	0.210	228280 (5)
3	255	215	0.095	338265 (5)	140	90	0.285	338840 (4)
4	305	265	0.065	311645 (5)	160	105	0.185	261360 (5)
5	240	210	0.075	225625 (5)	130	85	0.245	258240 (4)
8	305	275	0.040	82090 (6)	195	150	0.110	68740 (6)

**Table C4 - DLS characterisation of SN-38 (2.43 wt%) nanoprecipitated, varying the concentration within THF;**

THF Volume (mL)	Before Evaporation				After Evaporation			
	D <sub>z</sub> (nm)	D <sub>n</sub> (nm)	PdI	Derived Count Rate (kcps)	D <sub>z</sub> (nm)	D <sub>n</sub> (nm)	PdI	Derived Count Rate (kcps)
0.5	2180	320	1	8570 (7)			-	
1	1740	110	0.920	13470 (8)			-	
2	275	130	0.380	1980 (9)			-	
3	90	1	0.335	190 (11)			-	
4	5	1	0.430	150 (11)			-	
5	5	2	0.375	170 (11)			-	
8	5	2	0.395	215 (11)			-	

**Table C5 - DLS characterisation of oil red O (2.43 wt%) nanoprecipitated, varying the concentration within THF;**

THF Volume (mL)	Before Evaporation				After Evaporation			
	D <sub>z</sub> (nm)	D <sub>n</sub> (nm)	PdI	Derived Count Rate (kcps)	D <sub>z</sub> (nm)	D <sub>n</sub> (nm)	PdI	Derived Count Rate (kcps)
0.5	110	60	0.230	90040 (6)			-	
1	260	180	0.195	74175 (6)			-	
2	445	325	0.185	25450 (7)			-	
3	225	205	0.060	19800 (7)			-	
4	245	220	0.120	7935 (8)			-	
5	200	2	0.265	1770 (9)			-	
8	10	2	0.500	285 (11)			-	

**Table C6 - DLS characterisation of docetaxel (2.43 wt%) nanoprecipitated, varying the concentration within THF;**

THF Volume (mL)	Before Evaporation				After Evaporation			
	D <sub>z</sub> (nm)	D <sub>n</sub> (nm)	PdI	Derived Count Rate (kcps)	D <sub>z</sub> (nm)	D <sub>n</sub> (nm)	PdI	Derived Count Rate (kcps)
0.5	285	195	0.200	8210 (7)			-	
1	365	115	0.245	10990 (7)			-	
2	115	1	0.310	335 (11)			-	
3	120	1	0.230	245 (11)			-	
4	10	1	0.145	125 (11)			-	
5	5	2	0.250	165 (11)			-	
8	5	2	0.225	185 (11)			-	

**Table C7 - DLS characterisation of SN-38 P (2.43 wt%) nanoprecipitated, varying the concentration within THF;**

THF Volume (mL)	Before Evaporation				After Evaporation			
	D <sub>z</sub> (nm)	D <sub>n</sub> (nm)	PdI	Derived Count Rate (kcps)	D <sub>z</sub> (nm)	D <sub>n</sub> (nm)	PdI	Derived Count Rate (kcps)
0.5	465	340	0.325	6510 (7)			-	
1	520	455	0.185	11600 (8)			-	
2	190	175	0.095	1700 (9)			-	
3	15	1	0.615	145 (11)			-	
4	145	1	0.205	135 (11)			-	
5	5	2	0.270	230 (11)			-	
8	5	2	0.260	195 (11)			-	

**Table C8- DLS characterisation of nanoparticles produced by thin film hydration of PEG<sub>5K</sub>-*b*-PCL/SCM<sub>40</sub>-co-BOD<sub>0.7</sub> with 16.6 wt% SN-38.**

Polymer	SN-38 Loading (wt%)	Before Sonication				After Sonication			
		Dz (nm)	Dn (nm)	PdI	Derived Count Rate (kcps)	Dz (nm)	Dn (nm)	PdI	Derived Count Rate (kcps)
PEG <sub>5K</sub> - <i>b</i> -PCL <sub>40</sub> -co-BOD <sub>0.7</sub>	16.6	475	205	0.460	290325 (5)	185	100	0.175	331180 (5)
PEG <sub>5K</sub> - <i>b</i> -PMOP <sub>40</sub> -co-BOD <sub>0.7</sub>	16.6	900	120	0.550	251035 (5)	160	70	0.245	207530 (5)
PEG <sub>5K</sub> - <i>b</i> -PPOP <sub>40</sub> -co-BOD <sub>0.7</sub>	16.6	555	285	0.575	238275 (5)	185	40	0.300	353060 (4)
PEG <sub>5K</sub> - <i>b</i> -PBOP <sub>40</sub> -co-BOD <sub>0.7</sub>	16.6	865	350	0.665	167825 (5)	155	35	0.270	260065 (5)
PEG <sub>5K</sub> - <i>b</i> -PPHLOP <sub>40</sub> -co-BOD <sub>0.7</sub>	16.6	1280	375	0.695	170870 (5)	130	40	0.265	237490 (5)

**Table C9- DLS characterisation of nanoparticles produced by thin film hydration of PEG<sub>5K</sub>-*b*-PCL/SCM<sub>40</sub>-co-BOD<sub>0.7</sub> with 33 wt% SN-38.**

Polymer	SN-38 Loading (wt%)	Before Sonication				After Sonication			
		Dz (nm)	Dn (nm)	PdI	Derived Count Rate (kcps)	Dz (nm)	Dn (nm)	PdI	Derived Count Rate (kcps)
PEG <sub>5K</sub> - <i>b</i> -PCL <sub>40</sub> -co-BOD <sub>0.7</sub>	33	545	295	0.465	473705 (4)	180	95	0.235	521795 (4)
PEG <sub>5K</sub> - <i>b</i> -PMOP <sub>40</sub> -co-BOD <sub>0.7</sub>	33	1105	590	0.425	581815 (4)	235	180	0.175	665720 (4)
PEG <sub>5K</sub> - <i>b</i> -PPOP <sub>40</sub> -co-BOD <sub>0.7</sub>	33	985	340	0.590	372675 (4)	170	85	0.290	528390 (4)
PEG <sub>5K</sub> - <i>b</i> -PBOP <sub>40</sub> -co-BOD <sub>0.7</sub>	33	1305	520	0.470	434265 (4)	190	50	0.250	593615 (4)
PEG <sub>5K</sub> - <i>b</i> -PPHLOP <sub>40</sub> -co-BOD <sub>0.7</sub>	33	1160	505	0.505	247840 (5)	170	35	0.275	573890 (4)

**Table C10- DLS characterisation of nanoparticles produced by thin film hydration of PEG<sub>5K</sub>-*b*-PCL/SCM<sub>40</sub>-co-BOD<sub>0.7</sub> with 50 wt% SN-38.**

Polymer	SN-38 Loading (wt%)	Before Sonication				After Sonication			
		Dz (nm)	Dn (nm)	PdI	Derived Count Rate (kcps)	Dz (nm)	Dn (nm)	PdI	Derived Count Rate (kcps)
PEG <sub>5K</sub> - <i>b</i> -PCL <sub>40</sub> -co-BOD <sub>0.7</sub>	50	605	350	0.300	638270 (4)	190	95	0.230	827110 (4)
PEG <sub>5K</sub> - <i>b</i> -PMOP <sub>40</sub> -co-BOD <sub>0.7</sub>	50	770	475	0.425	690965 (4)	175	110	0.200	644090 (3)
PEG <sub>5K</sub> - <i>b</i> -PPOP <sub>40</sub> -co-BOD <sub>0.7</sub>	50	635	295	0.315	635990 (4)	195	90	0.220	686295 (3)
PEG <sub>5K</sub> - <i>b</i> -PBOP <sub>40</sub> -co-BOD <sub>0.7</sub>	50	-	-	-	-	180	50	0.230	678735 (3)
PEG <sub>5K</sub> - <i>b</i> -PPHLOP <sub>40</sub> -co-BOD <sub>0.7</sub>	50	710	230	0.440	524510 (4)	190	75	0.265	716495 (3)

**Table C11- DLS characterisation of nanoparticles produced by thin film hydration of PEG<sub>5K</sub>-*b*-PCL/SCM<sub>40</sub>-co-BOD<sub>0.7</sub> with 75 wt% SN-38.**

Polymer	SN-38 Loading (wt%)	Before Sonication				After Sonication			
		Dz (nm)	Dn (nm)	PdI	Derived Count Rate (kcps)	Dz (nm)	Dn (nm)	PdI	Derived Count Rate (kcps)
PEG <sub>5K</sub> - <i>b</i> -PCL <sub>40</sub> -co-BOD <sub>0.7</sub>	75	660	425	0.295	1230235 (3)	210	100	0.180	10445000 (4)
PEG <sub>5K</sub> - <i>b</i> -PMOP <sub>40</sub> -co-BOD <sub>0.7</sub>	75	895	280	0.335	600860 (4)	205	130	0.190	1572120 (3)
PEG <sub>5K</sub> - <i>b</i> -PPOP <sub>40</sub> -co-BOD <sub>0.7</sub>	75	965	360	0.445	833825 (3)	210	100	0.215	1629375 (3)
PEG <sub>5K</sub> - <i>b</i> -PBOP <sub>40</sub> -co-BOD <sub>0.7</sub>	75	835	325	0.465	1336680 (3)	220	105	0.230	1553435 (3)
PEG <sub>5K</sub> - <i>b</i> -PPHLOP <sub>40</sub> -co-BOD <sub>0.7</sub>	75	640	350	0.485	1178320 (3)	240	95	0.295	1317890 (3)

**Table C12- DLS characterisation of nanoparticles produced by thin film hydration of PEG<sub>5K</sub>-*b*-PCL/SCM<sub>40</sub>-co-BOD<sub>0.7</sub> with 95 wt% SN-38.**

Polymer	SN-38 Loading (wt%)	Before Sonication				After Sonication			
		Dz (nm)	Dn (nm)	PdI	Derived Count Rate (kcps)	Dz (nm)	Dn (nm)	PdI	Derived Count Rate (kcps)
PEG <sub>5K</sub> - <i>b</i> -PCL <sub>40</sub> -co-BOD <sub>0.7</sub>	95	705	410	0.410	370885 (4)	220	150	0.180	806915 (4)
PEG <sub>5K</sub> - <i>b</i> -PMOP <sub>40</sub> -co-BOD <sub>0.7</sub>	95	700	395	0.420	573080 (4)	220	135	0.180	743775 (4)
PEG <sub>5K</sub> - <i>b</i> -PPOP <sub>40</sub> -co-BOD <sub>0.7</sub>	95	710	380	0.385	509910 (4)	225	125	0.210	740720 (3)
PEG <sub>5K</sub> - <i>b</i> -PBOP <sub>40</sub> -co-BOD <sub>0.7</sub>	95	690	345	0.450	642095 (4)	235	115	0.225	740000 (3)
PEG <sub>5K</sub> - <i>b</i> -PPHLOP <sub>40</sub> -co-BOD <sub>0.7</sub>	95	565	170	0.500	551825 (4)	240	155	0.180	789680 (4)

**Table C13- DLS characterisation of nanoparticles produced by thin film hydration over 14 weeks (storage of dry thin film) of PEG<sub>5K</sub>-*b*-PMOP<sub>40-co-BOD</sub><sub>0.7</sub> or PEG<sub>5K</sub>-*b*-PPOP<sub>40-co-BOD</sub><sub>0.7</sub> with 10 wt% SN-38.**

SN-38 Loading (wt%)	Week	PEG <sub>5K</sub> - <i>b</i> -PMOP <sub>40-co-BOD</sub> <sub>0.7</sub>				PEG <sub>5K</sub> - <i>b</i> -PPOP <sub>40-co-BOD</sub> <sub>0.7</sub>			
		Dz (nm)	Dn (nm)	PdI	Derived Count Rate (kcps)	Dz (nm)	Dn (nm)	PdI	Derived Count Rate (kcps)
10	0	115	35	0.265	88630 (6)	100	40	0.240	81040 (6)
	1	120	25	0.260	76140 (6)	110	40	0.260	95215 (6)
	2	130	30	0.260	97285 (6)	120	40	0.300	89975 (6)
	3	135	30	0.260	92910 (6)	125	35	0.275	103775 (6)
	4	135	40	0.265	95595 (6)	130	35	0.285	108880 (6)
	6	140	30	0.265	103655 (6)	130	35	0.275	104200 (6)
	8	140	20	0.275	87535 (6)	140	40	0.290	105320 (6)
	10	145	25	0.280	91265 (6)	140	40	0.295	214710 (5)
	12	150	30	0.285	103845 (6)	125	35	0.280	102990 (6)
	14	145	35	0.270	100915 (4)	125	35	0.275	79010 (6)

**Table C14- DLS characterisation of nanoparticles produced by thin film hydration over 14 weeks (storage of dry thin film) of PEG<sub>5K</sub>-*b*-PMOP<sub>40-co</sub>-BOD<sub>0.7</sub> or PEG<sub>5K</sub>-*b*-PPOP<sub>40-co</sub>-BOD<sub>0.7</sub> with 30 wt% SN-38.**

SN-38 Loading (wt%)	Week	PEG <sub>5K</sub> - <i>b</i> -PMOP <sub>40-co</sub> -BOD <sub>0.7</sub>				PEG <sub>5K</sub> - <i>b</i> -PPOP <sub>40-co</sub> -BOD <sub>0.7</sub>			
		Dz (nm)	Dn (nm)	PdI	Derived Count Rate (kcps)	Dz (nm)	Dn (nm)	PdI	Derived Count Rate (kcps)
30	0	155	60	0.220	363970 (4)	160	50	0.275	570650 (4)
	1	185	55	0.240	571515 (4)	150	35	0.205	550095 (4)
	2	225	45	0.265	637310 (4)	190	60	0.255	709695 (4)
	3	175	65	0.245	547380 (4)	190	45	0.240	622045 (4)
	4	200	70	0.245	606750 (4)	190	75	0.250	698230 (4)
	6	190	65	0.250	559920 (4)	170	25	0.215	603530 (4)
	8	205	75	0.245	539150 (4)	210	60	0.370	523000 (4)
	10	195	80	0.265	592335 (4)	195	40	0.235	637265 (4)
	12	190	80	0.235	623690 (4)	185	50	0.245	621075 (4)
	14	195	75	0.255	628395 (4)	180	50	0.235	686075 (4)



**Table C15- DLS characterisation of nanoparticles produced by thin film hydration over 14 weeks (storage of dry thin film) of PEG<sub>5K</sub>-*b*-PMOP<sub>40-co</sub>-BOD<sub>0.7</sub> or PEG<sub>5K</sub>-*b*-PPOP<sub>40-co</sub>-BOD<sub>0.7</sub> with 50 wt% SN-38.**

SN-38 Loading (wt%)	Week	PEG <sub>5K</sub> - <i>b</i> -PMOP <sub>40-co</sub> -BOD <sub>0.7</sub>				PEG <sub>5K</sub> - <i>b</i> -PPOP <sub>40-co</sub> -BOD <sub>0.7</sub>			
		Dz (nm)	Dn (nm)	PdI	Derived Count Rate (kcps)	Dz (nm)	Dn (nm)	PdI	Derived Count Rate (kcps)
50	0	180	60	0.225	767665 (4)	215	75	0.280	632205 (3)
	1	205	70	0.220	780645 (4)	190	75	0.240	705255 (3)
	2	235	115	0.245	704125 (4)	230	85	0.250	68755 (4)
	3	295	100	0.255	661755 (4)	235	90	0.240	695045 (4)
	4	235	110	0.240	683935 (4)	230	95	0.245	749500 (4)
	6	240	120	0.250	840765 (4)	220	130	0.235	700340 (4)
	8	260	105	0.255	736865 (4)	250	75	0.260	736230 (4)
	10	260	50	0.255	788695 (4)	230	110	0.260	820770 (4)
	12	235	80	0.255	816295 (4)	225	105	0.265	693800 (4)
	14	240	45	0.270	844120 (4)	245	105	0.255	607920 (4)

**Table C16- DLS characterisation of nanoparticles produced by thin film hydration over 14 weeks (storage of dry thin film) of PEG<sub>5K</sub>-*b*-PMOP<sub>40-co</sub>-BOD<sub>0.7</sub> or PEG<sub>5K</sub>-*b*-PPOP<sub>40-co</sub>-BOD<sub>0.7</sub> with 75 wt% SN-38.**

SN-38 Loading (wt%)	Week	PEG <sub>5K</sub> - <i>b</i> -PMOP <sub>40-co</sub> -BOD <sub>0.7</sub>				PEG <sub>5K</sub> - <i>b</i> -PPOP <sub>40-co</sub> -BOD <sub>0.7</sub>			
		Dz (nm)	Dn (nm)	PdI	Derived Count Rate (kcps)	Dz (nm)	Dn (nm)	PdI	Derived Count Rate (kcps)
75	0	240	105	0.275	1516805 (3)	230	110	0.245	1696590 (3)
	1	245	130	0.240	1410785 (3)	255	165	0.195	450010 (4)
	2	325	125	0.415	1373315 (3)	285	140	0.250	1273535 (3)
	3	270	155	0.290	1172915 (3)	310	190	0.320	1349440 (3)
	4	290	90	0.295	1173995 (3)	305	120	0.290	1453770 (3)
	6	295	150	0.325	1108285 (3)	350	125	0.415	1630200 (3)
	8	310	150	0.330	1225360 (3)	335	150	0.365	1120890 (3)
	10	290	135	0.310	121965 (3)	305	120	0.250	1289650 (3)
	12	315	160	0.360	1133755 (3)	290	150	0.240	1299615 (3)
	14	290	110	0.260	1195695 (3)	300	140	0.260	1279395 (3)

**Table C17- DLS characterisation of nanoparticles produced by thin film hydration over 7 days (storage of dispersion) of PEG<sub>5K</sub>-*b*-PCL<sub>40</sub>-co-BOD<sub>0.7</sub> with increasing SN-38 content.**

SN-38 Loading (wt%)	Day 1				Day 2				Day 4				Day 7			
	Dz (nm)	Dn (nm)	PdI	Derived Count Rate (kcps)	Dz (nm)	Dn (nm)	PdI	Derived Count Rate (kcps)	Dz (nm)	Dn (nm)	PdI	Derived Count Rate (kcps)	Dz (nm)	Dn (nm)	PdI	Derived Count Rate (kcps)
2.43	110	25	0.435	16365 (7)	105	20	0.420	15305 (7)	105	25	0.430	17455 (7)	110	30	0.475	14490 (7)
10	120	70	0.245	49220 (6)	120	20	0.240	49805 (6)	120	25	0.255	50645 (6)	125	35	0.235	53910 (6)
16.6	150	55	0.225	131700 (6)	150	45	0.235	205625 (5)	175	65	0.365	212160 (5)	155	70	0.210	210440 (5)
30	170	85	0.230	420230 (4)	175	50	0.225	403705 (4)	185	80	0.265	427390 (4)	175	105	0.215	457375 (4)
33	185	90	0.225	547495 (4)	195	100	0.240	561165 (4)	200	105	0.250	599395 (4)	200	75	0.215	603305 (4)
50	195	100	0.235	637210 (3)	235	120	0.340	818365 (4)	220	65	0.245	677995 (3)	230	140	0.255	697115 (3)
75	260	105	0.195	479370 (4)	275	142	0.225	1477965 (3)	320	155	0.330	1373925 (3)	285	160	0.226	1471690 (3)
95	240	145	0.205	766700 (4)	245	130	0.200	745045 (4)	245	150	0.200	821900 (4)	245	150	0.175	729170 (4)

**Table C18- DLS characterisation of nanoparticles produced by thin film hydration of PEG<sub>5K</sub>-*b*-PCL/SCM<sub>40</sub> without drug and with 2.43 wt% SN-38.**

Polymer	SN-38 Loading (wt%)	Before Sonication				After Sonication			
		Dz (nm)	Dn (nm)	PdI	Derived Count Rate (kcps)	Dz (nm)	Dn (nm)	PdI	Derived Count Rate (kcps)
PEG <sub>5K</sub> - <i>b</i> -PCL <sub>40</sub>	0	840	285	0.735	55460 (6)	245	50	0.275	93975 (6)
PEG <sub>5K</sub> - <i>b</i> -PMOP <sub>40</sub>	0	420	45	0.71	43515 (6)	60	30	0.210	17015 (7)
PEG <sub>5K</sub> - <i>b</i> -PPOP <sub>40</sub>	0	8170	85	0.295	24485 (7)	60	40	0.090	28620 (7)
PEG <sub>5K</sub> - <i>b</i> -PBOP <sub>40</sub>	0	555	140	0.925	53095 (6)	60	40	0.080	25415 (7)
PEG <sub>5K</sub> - <i>b</i> -PPHLOP <sub>40</sub>	0	765	75	0.775	58685 (6)	60	45	0.060	53495 (6)
PEG <sub>5K</sub> - <i>b</i> -PCL <sub>40</sub>	2.43	945	185	0.805	104225 (6)	300	145	0.365	111010 (6)
PEG <sub>5K</sub> - <i>b</i> -PMOP <sub>40</sub>	2.43	345	60	0.835	51385 (6)	70	20	0.225	23375 (7)
PEG <sub>5K</sub> - <i>b</i> -PPOP <sub>40</sub>	2.43	485	165	0.735	58470 (6)	65	45	0.120	42095 (6)
PEG <sub>5K</sub> - <i>b</i> -PBOP <sub>40</sub>	2.43	9105	50	0.650	29515 (7)	70	40	0.210	31625 (7)
PEG <sub>5K</sub> - <i>b</i> -PPHLOP <sub>40</sub>	2.43	950	175	0.910	108235 (6)	75	40	0.240	72700 (6)

**Table C19- DLS characterisation of nanoparticles produced by thin film hydration of PEG<sub>5K</sub>-*b*-PCL/SCM<sub>40</sub> with 10 wt% SN-38.**

Polymer	SN-38 Loading (wt%)	Before Sonication				After Sonication			
		Dz (nm)	Dn (nm)	PdI	Derived Count Rate (kcps)	Dz (nm)	Dn (nm)	PdI	Derived Count Rate (kcps)
PEG <sub>5K</sub> - <i>b</i> -PCL <sub>40</sub>	10	480	150	0.485	96240 (6)	215	60	0.390	278555 (5)
PEG <sub>5K</sub> - <i>b</i> -PMOP <sub>40</sub>	10	265	55	0.300	102860 (6)	120	35	0.250	71535 (6)
PEG <sub>5K</sub> - <i>b</i> -PPOP <sub>40</sub>	10	405	160	0.600	82125 (6)	115	25	0.255	91625 (6)
PEG <sub>5K</sub> - <i>b</i> -PBOP <sub>40</sub>	10	370	105	0.505	92495 (6)	110	40	0.310	76590 (6)
PEG <sub>5K</sub> - <i>b</i> -PPHLOP <sub>40</sub>	10	560	150	0.910	158455 (6)	185	50	0.300	137205 (6)

**Table C20- DLS characterisation of nanoparticles produced by thin film hydration of PEG<sub>5K</sub>-*b*-PCL/SCM<sub>40</sub> with 16.6 wt% SN-38.**

Polymer	SN-38 Loading (wt%)	Before Sonication				After Sonication			
		Dz (nm)	Dn (nm)	PdI	Derived Count Rate (kcps)	Dz (nm)	Dn (nm)	PdI	Derived Count Rate (kcps)
PEG <sub>5K</sub> - <i>b</i> -PCL <sub>40</sub>	16.6	500	155	0.485	256055 (5)	155	85	0.205	343835 (4)
PEG <sub>5K</sub> - <i>b</i> -PMOP <sub>40</sub>	16.6	315	130	0.360	263100 (5)	130	35	0.235	229410 (5)
PEG <sub>5K</sub> - <i>b</i> -PPOP <sub>40</sub>	16.6	435	165	0.425	127605 (6)	135	30	0.245	224500 (5)
PEG <sub>5K</sub> - <i>b</i> -PBOP <sub>40</sub>	16.6	810	315	0.575	299695 (5)	160	50	0.275	345395 (5)
PEG <sub>5K</sub> - <i>b</i> -PPHLOP <sub>40</sub>	16.6	530	55	0.555	283945 (5)	115	30	0.260	232950 (5)

**Table C21- DLS characterisation of nanoparticles produced by thin film hydration of PEG<sub>5K</sub>-*b*-PCL/SCM<sub>40</sub> with 30 wt% SN-38.**

Polymer	SN-38 Loading (wt%)	Before Sonication				After Sonication			
		Dz (nm)	Dn (nm)	PdI	Derived Count Rate (kcps)	Dz (nm)	Dn (nm)	PdI	Derived Count Rate (kcps)
PEG <sub>5K</sub> - <i>b</i> -PCL <sub>40</sub>	30	530	235	0.530	622750 (4)	170	90	0.205	660765 (4)
PEG <sub>5K</sub> - <i>b</i> -PMOP <sub>40</sub>	30	385	65	0.335	459715 (4)	160	75	0.215	534475 (4)
PEG <sub>5K</sub> - <i>b</i> -PPOP <sub>40</sub>	30	530	105	0.465	431820 (4)	145	55	0.200	519425 (4)
PEG <sub>5K</sub> - <i>b</i> -PBOP <sub>40</sub>	30	530	105	0.430	432720 (4)	160	50	0.235	519805 (4)
PEG <sub>5K</sub> - <i>b</i> -PPHLOP <sub>40</sub>	30	735	165	0.560	567485 (4)	165	40	0.270	577555 (4)

**Table C22- DLS characterisation of nanoparticles produced by thin film hydration of PEG<sub>5K</sub>-*b*-PCL/SCM<sub>40</sub> with 50 wt% SN-38.**

Polymer	SN-38 Loading (wt%)	Before Sonication				After Sonication			
		Dz (nm)	Dn (nm)	PdI	Derived Count Rate (kcps)	Dz (nm)	Dn (nm)	PdI	Derived Count Rate (kcps)
PEG <sub>5K</sub> - <i>b</i> -PCL <sub>40</sub>	50	380	145	0.320	818150 (4)	185	110	0.215	670745 (3)
PEG <sub>5K</sub> - <i>b</i> -PMOP <sub>40</sub>	50	400	180	0.335	794120 (4)	185	80	0.225	691205 (3)
PEG <sub>5K</sub> - <i>b</i> -PPOP <sub>40</sub>	50	455	145	0.320	804440 (4)	175	50	0.205	722275 (3)
PEG <sub>5K</sub> - <i>b</i> -PBOP <sub>40</sub>	50	520	310	0.395	672820 (4)	210	80	0.250	759580 (3)
PEG <sub>5K</sub> - <i>b</i> -PPHLOP <sub>40</sub>	50	465	155	0.405	851245 (4)	200	50	0.270	743210 (3)

**Table C23- DLS characterisation of nanoparticles produced by thin film hydration of PEG<sub>5K</sub>-*b*-PCL/SCM<sub>40</sub> with 75 wt% SN-38.**

Polymer	SN-38 Loading (wt%)	Before Sonication				After Sonication			
		Dz (nm)	Dn (nm)	PdI	Derived Count Rate (kcps)	Dz (nm)	Dn (nm)	PdI	Derived Count Rate (kcps)
PEG <sub>5K</sub> - <i>b</i> -PCL <sub>40</sub>	75	425	250	0.295	727750 (4)	205	125	0.210	829735 (4)
PEG <sub>5K</sub> - <i>b</i> -PMOP <sub>40</sub>	75	705	285	0.445	1058640 (3)	250	135	0.250	152600 (3)
PEG <sub>5K</sub> - <i>b</i> -PPOP <sub>40</sub>	75	660	260	0.435	1270770 (3)	240	155	0.215	1541480 (3)
PEG <sub>5K</sub> - <i>b</i> -PBOP <sub>40</sub>	75	470	170	0.370	1185435 (3)	215	120	0.205	1423180 (3)
PEG <sub>5K</sub> - <i>b</i> -PPHLOP <sub>40</sub>	75	570	145	0.460	1315930 (3)	240	75	0.230	588885 (4)

**Table C24- DLS characterisation of nanoparticles produced by thin film hydration of PEG<sub>5K</sub>-*b*-PCL/SCM<sub>40</sub> with 95 wt% SN-38.**

Polymer	SN-38 Loading (wt%)	Before Sonication				After Sonication			
		Dz (nm)	Dn (nm)	PdI	Derived Count Rate (kcps)	Dz (nm)	Dn (nm)	PdI	Derived Count Rate (kcps)
PEG <sub>5K</sub> - <i>b</i> -PCL <sub>40</sub>	95	505	150	0.405	620010 (4)	225	130	0.200	794900 (4)
PEG <sub>5K</sub> - <i>b</i> -PMOP <sub>40</sub>	95	670	180	0.435	491705 (4)	405	130	0.400	766590 (4)
PEG <sub>5K</sub> - <i>b</i> -PPOP <sub>40</sub>	95	585	220	0.420	405560 (4)	255	175	0.200	734445 (4)
PEG <sub>5K</sub> - <i>b</i> -PBOP <sub>40</sub>	95	600	245	0.450	668160 (4)	250	120	0.240	771805 (4)
PEG <sub>5K</sub> - <i>b</i> -PPHLOP <sub>40</sub>	95	480	125	0.415	687495 (4)	235	140	0.210	741890 (4)

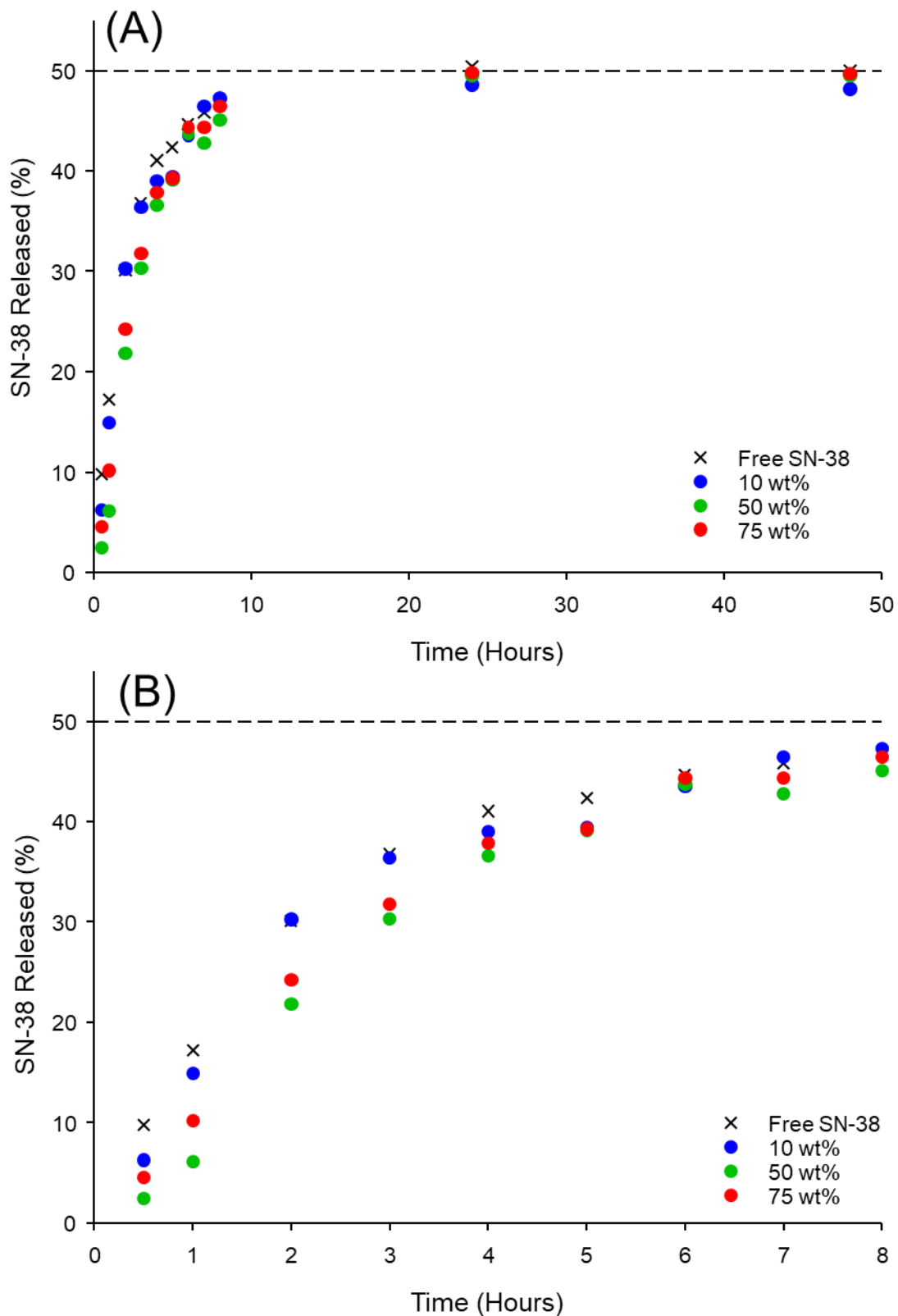


**Figure C1 –Release curves generated by RED assay for PEG<sub>5K</sub>-*b*-PCL<sub>40</sub>-*c*O-BOD<sub>0.7</sub> dispersions containing SN-38; (A) over 48 hours and (B) over 8 hours.**



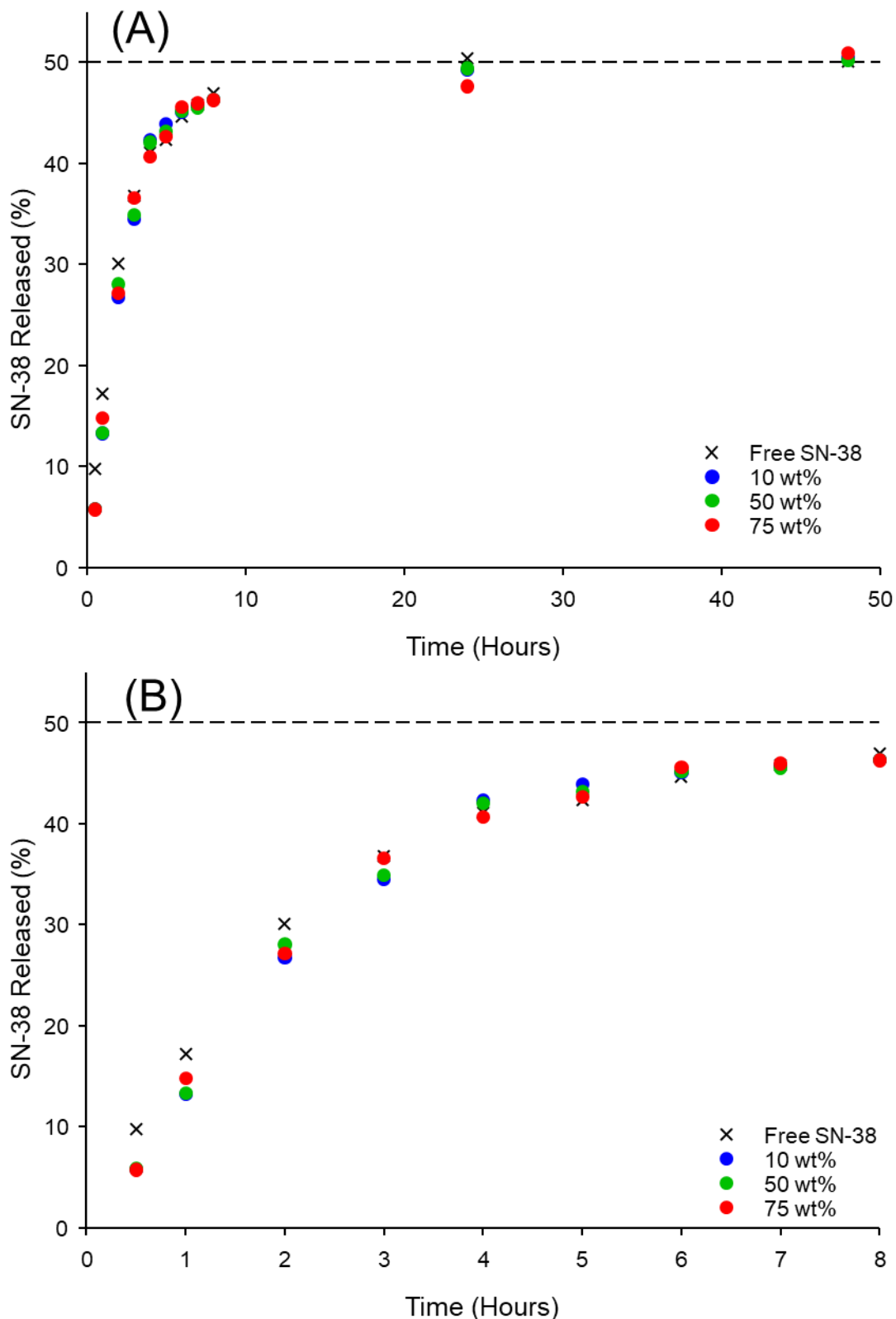


**Figure C2 – Release curves generated by RED assay for PEG<sub>5K</sub>-*b*-PMOP<sub>40-co</sub>-BOD<sub>0.7</sub> dispersions containing SN-38; (A) over 48 hours and (B) over 8 hours.**

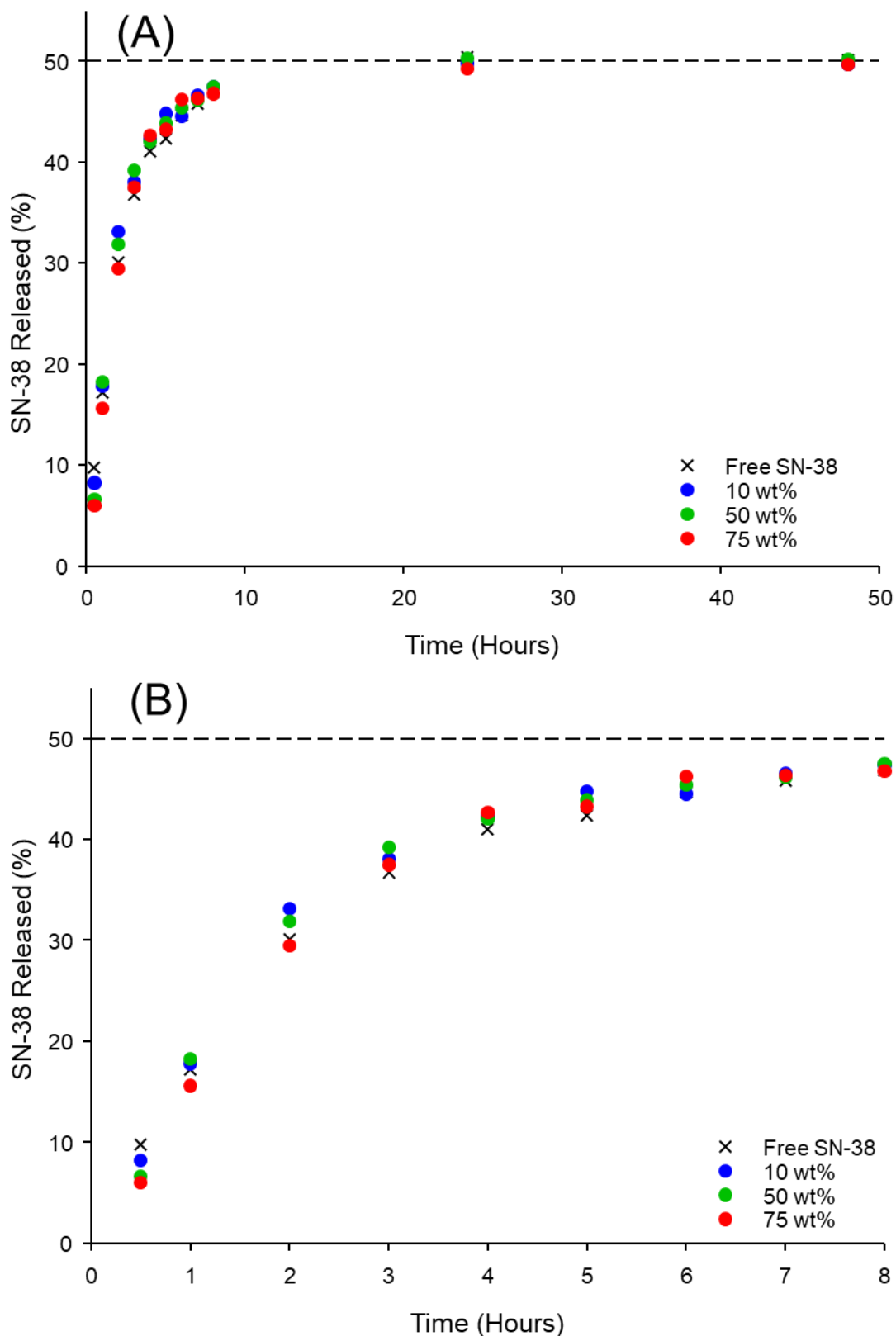


**Figure C3 – Release curves generated by RED assay for PEG<sub>5K</sub>-*b*-PPOP<sub>40-co</sub>-BOD<sub>0.7</sub> dispersions containing SN-38; (A) over 48 hours and (B) over 8 hours.**

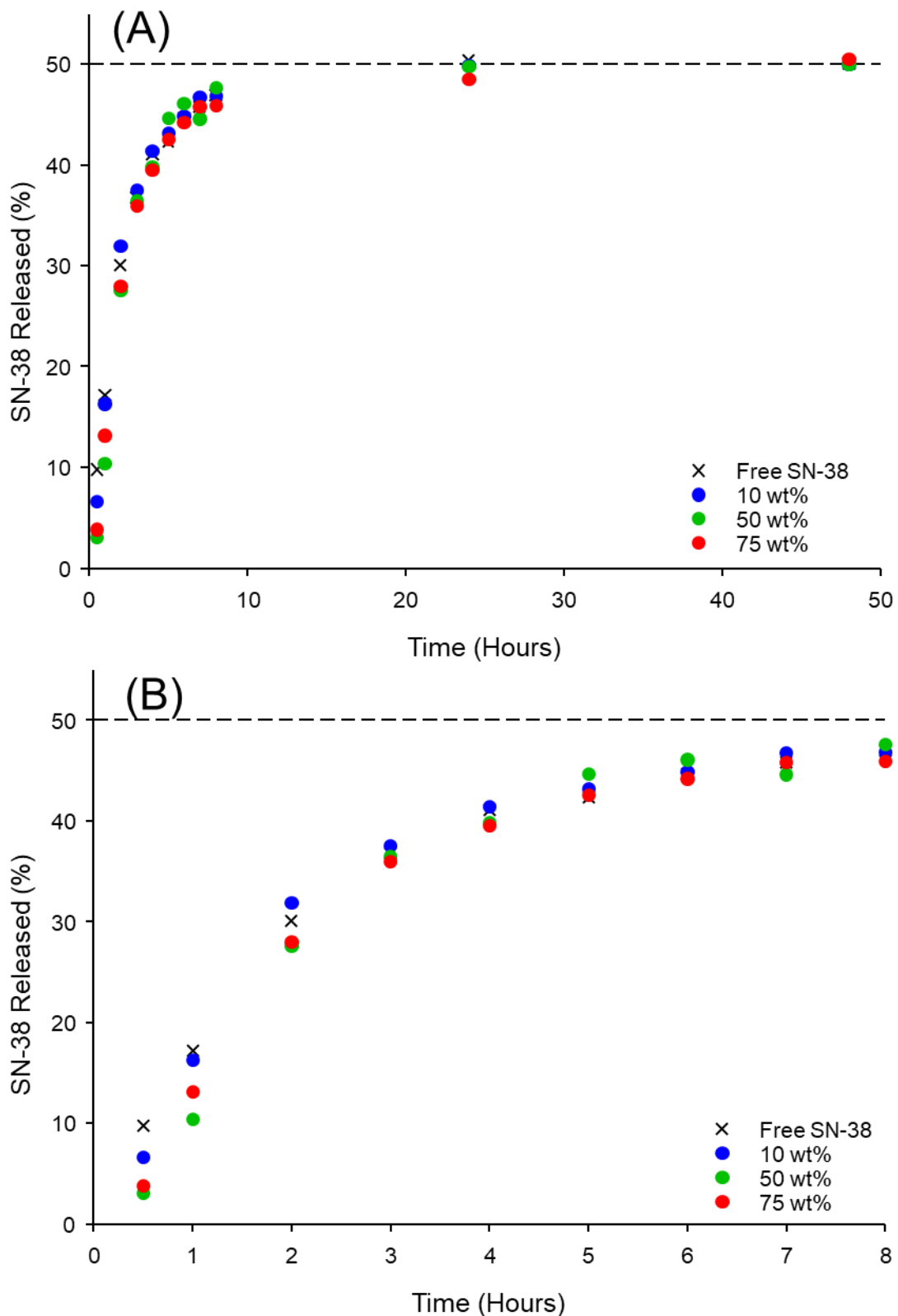


**Figure C4 – Release curves generated by RED assay for PEG<sub>5K</sub>-*b*-PBOP<sub>40</sub>-*co*-BOD<sub>0.7</sub> dispersions containing SN-38; (A) over 48 hours and (B) over 8 hours.**

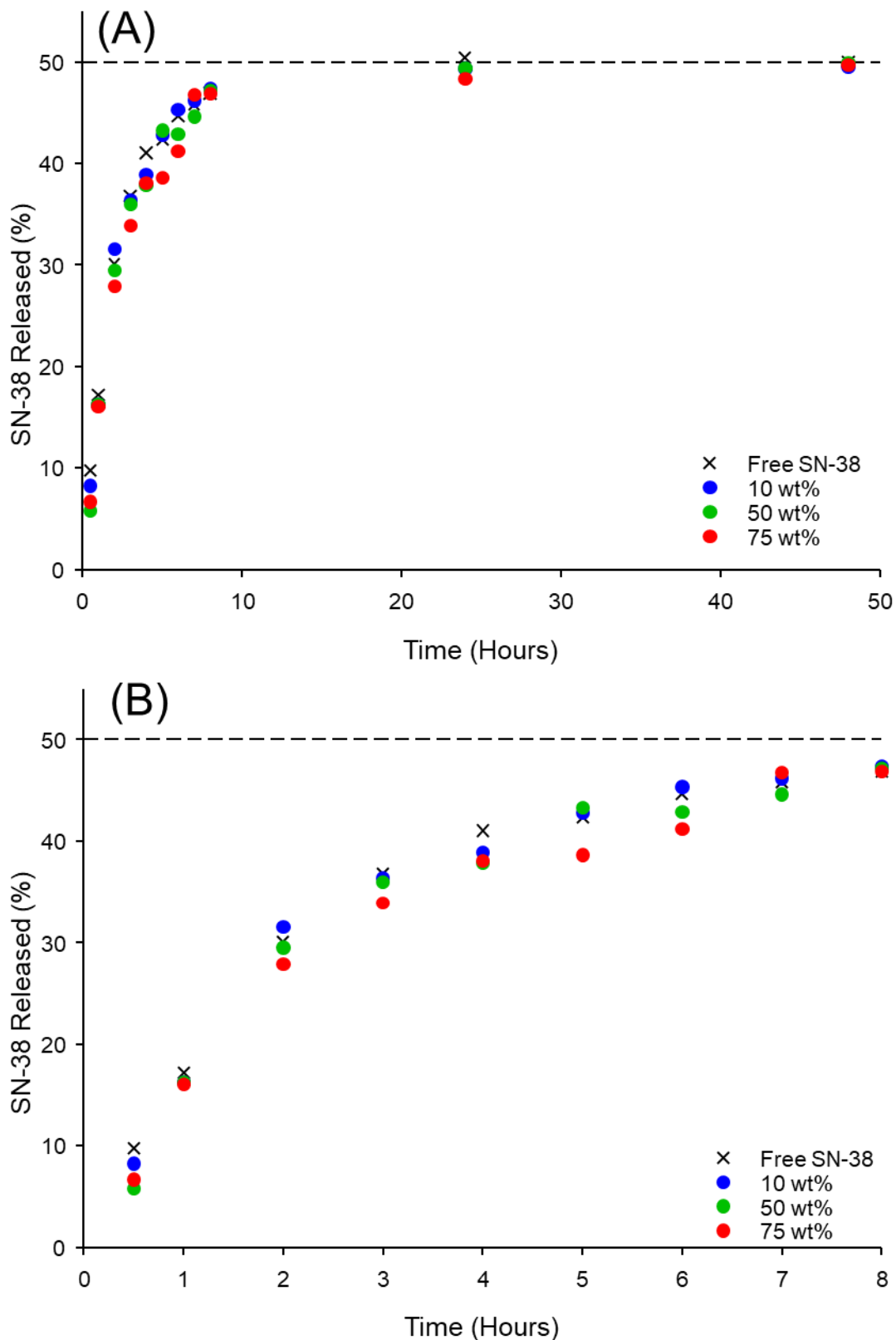


**Figure C5 – Release curves generated by RED assay for PEG<sub>5K</sub>-*b*-PPHLOP<sub>40-co</sub>-BOD<sub>0.7</sub> dispersions containing SN-38; (A) over 48 hours and (B) over 8 hours.**